Physics of the Solid State, Vol. 45, No. 11, 2003, pp. 2017–2024. Translated from Fizika Tverdogo Tela, Vol. 45, No. 11, 2003, pp. 1921–1927.

METALS AND SUPERCONDUCTORS

Longitudinal Response of the Spin System of a Metal to Modulated EPR Saturation at Arbitrary Modulation Frequency and Detuning of the Saturating Field

N. P. Fokina*, M. O. Élizbarashvili*, V. A. Atsarkin, and V. V. Demidov****

**Tbilisi State University, pr. Chavchavadze 3, Tbilisi, 380028 Georgia*

e-mail: n_fokina@caucasus.net

***Institute of Radio Engineering and Electronics, Russian Academy of Sciences, Moscow, 125009 Russia*

Received April 3, 2003

Abstract—The theory of the longitudinal (with respect to an external magnetic field) response of a combined spin system of localized paramagnetic centers (*s* subsystem) and free charge carriers (*e* subsystem) of a solid semiconductor to modulated saturation of EPR is developed. In contrast to relevant studies made earlier, the general case is considered of an arbitrary modulation frequency and arbitrary detuning of the saturating microwave field with respect to the central EPR frequency. A theoretical approach is used in which normal modes are considered in analyzing coupled oscillations of the spin magnetizations of the *s* and *e* subsystems. It is shown that, in the case of relaxation coupling between the subsystems, the longitudinal response recorded at the modulation frequency can be represented as the sum of the responses of the normal modes, each of which is described by a universal resonance lineshape that is different, in general, from the Lorentzian lineshape characteristic of EPR signals. In the extreme cases of weak and strong coupling, simple analytical formulas are derived. The results presented form a theoretical basis for applying the method of modulated longitudinal response for measuring very short longitudinal spin relaxation times in semiconductors with paramagnetic impurities. As an example, experimental data are presented for activated carbon containing stable free radicals.

1. INTRODUCTION

Measurements of the longitudinal (T_1) and transverse (T_2) electron spin relaxation times can provide valuable information on the amplitudes and correlation times of internal fluctuating fields in novel solid materials, such as high-temperature superconductors, fullerides, and manganites exhibiting colossal magnetoresistance. The relaxation time T_2 is usually determined from the EPR linewidth; however, inhomogeneous broadening frequently masks the effect of fluctuating fields. The longitudinal relaxation time in the materials mentioned above is short (10^{-7}–10^{-10} s) and cannot be measured using the conventional method based on pulsed or steady-state saturation of EPR. This difficulty was overcome using the improved technique for observing the longitudinal response first proposed in [1–3]. With this technique, the longitudinal relaxation time has recently been measured for a number of conducting materials [4–7]. In this method for measuring T_1 [1–7], the voltage induced across a pickup coil (oriented along the static magnetic field) is recorded; the signal is produced by the oscillating component of the longitudinal spin magnetization of a sample, which is the response of the spin system to modulation of the microwave (MW) radiation power saturating EPR. It is significant that a fairly low saturation level of EPR (with a saturation factor of the order of 10^{-3}–10^{-4}) is sufficient in this case, which makes it possible to measure very short relaxation times T_1.

In many of the novel solid materials mentioned above, as well as in other conductors with paramagnetic impurities, there are two types of paramagnetic particles ("spins"). Particles of one type (*s*) are localized paramagnetic centers, and particles of the other type (*e*) are itinerant charge carriers. Both these spin subsystems are coupled due to strong exchange interaction. Therefore, we should consider magnetic resonance for a strongly coupled system in which interaction between the two spin subsystems makes their precession complicated in character and significantly affects the resonance frequencies and damping (relaxation rates). In order to interpret an experimentally observed longitudinal response of such a system and extract information on the spin relaxation times, we need to invoke the theory of coupled oscillators.

This problem was partially solved in [8, 9], where the theory of coupled oscillators was used to calculate the EPR signal and the longitudinal response in a material with exchange-coupled *s* and *e* spin subsystems. However, the results obtained in those papers are valid

only in the case of low modulation frequencies or small (close to zero) detuning of the saturating MW field with respect to the spin resonance frequency.

For arbitrary modulation frequencies and detuning, the theory of longitudinal response has been developed only for one type of spins [1–3, 10]. In this paper, we extend the results obtained in [8, 9] for two interacting spin subsystems to the case of arbitrary values of the modulation frequency and detuning.

2. CALCULATION OF THE LONGITUDINAL RESPONSE OF RELAXATION-COUPLED SUBSYSTEMS OF LOCALIZED AND ITINERANT SPINS

We consider the spin system of a sample (normal conductor) containing a subsystem (*s*) of localized spins and a subsystem (*e*) of itinerant spins coupled via exchange interaction:

$$H_{ex} = -2J\sum_{i,i'} S_{si}S_{ei'}\delta(R_i - R_{i'}), \quad (1)$$

where S_{si} is a localized spin at a lattice site i and $S_{ei'}$ is an itinerant spin (we assume that $S_s = S_e = 1/2$). The sample is exposed to a static magnetic field $\mathbf{H}_0 \| z$ and an MW field $2\mathbf{H}_1\cos(\omega t) \| x$; *s* spins and *e* spins possess Zeeman energy, and *e* spins also have kinetic energy. Interaction (1) gives rise to a dynamic shift in the precession frequency of *s* and *e* spins via the molecular field and to spin relaxation, which is associated with the transfer of magnetization from the *s* subsystem to the *e* subsystem and *vice versa* [11, 12]. Experiments show that the dynamic shifts in the precession frequency, as a rule, are negligible [5, 6]. In what follows, we consider this case and assume, for simplicity, that the *g* factors of *s* and *e* spins are equal. Therefore, the resonance frequencies of *s* and *e* spins are also equal and the interaction between the magnetizations of the two spin subsystems is purely relaxational in character. As a result, the motion of the coupled transverse components of the *s*- and *e*-spin magnetizations is precession of two normal modes having normal (modal) decay rates (the linewidths of two EPR signals observed experimentally). For this reason, we write the equations of MW-field-modulated EPR saturation in terms of these transverse magnetization modes. We derive these equations in the same way as in [9] but take into account that, at a fairly high modulation frequency, each individual (*s*- and *e*-) spin subsystem is excited at three frequencies, one of which corresponds to main resonance and the other two are side frequencies.

We represent the Bloch–Hasegawa equations [11] for the transverse magnetization components of the *s* and *e* spins in the form of second-order differential equations. The longitudinal components will be described by first-order differential equations [12]. Thus, we have

$$\begin{aligned}
\ddot{M}_s^x + \omega_0^2 M_s^x + 2\omega_\delta'' \dot{M}_s^x + 2\omega_\alpha'' \dot{M}_e^x &= -\omega_0 \frac{g_s\mu_B}{\hbar} H^x M_s^x, \\
\ddot{M}_e^x + \omega_0^2 M_e^x + 2\omega_\gamma'' \dot{M}_e^x + 2\omega_\beta'' \dot{M}_s^x &= -\omega_0 \frac{g_e\mu_B}{\hbar} H^x M_e^x,
\end{aligned} \quad (2)$$

$$\begin{aligned}
\dot{M}_s^z + T_s^{-1} M_s^z - T_{es}^{-1} M_e^z &= \frac{M_s^0}{T_{sL}} - \frac{g_s\mu_B}{\hbar} H^x M_s^y, \\
\dot{M}_e^z + T_e^{-1} M_e^z - T_{se}^{-1} M_s^z &= \frac{M_e^0}{T_{eL}} - \frac{g_e\mu_B}{\hbar} H^x M_e^y.
\end{aligned} \quad (3)$$

Here, $\omega_\delta'' = T_{se}^{-1} + T_{sL}^{-1}$, $\omega_\gamma'' = T_{es}^{-1} + T_{eL}^{-1}$, $\omega_\alpha'' = -T_{es}^{-1}$, and $\omega_\beta'' = -T_{se}^{-1}$; T_{eL}^{-1} and T_{sL}^{-1} are the itinerant- and localized-spin relaxation rates to equilibrium with the lattice, respectively; and T_{se}^{-1} and T_{es}^{-1} are the Korringa and Overhauser relaxation rates, respectively, which can be written as

$$T_{se}^{-1} = \frac{4\pi}{\hbar}(\rho J)^2 k_B T, \quad T_{es}^{-1} = \frac{8\pi c}{3\hbar} S(S+1)\rho J^2,$$

where ρ is the density of states of conduction electrons at the Fermi level, J is the exchange integral, S and c are the spin and concentration of localized spins, T is the lattice temperature, and k_B is the Boltzmann constant. In the case when the *g* factors of the spins are equal, we have $T_{se}/T_{es} = \chi_s/\chi_e$ [11], where χ_s and χ_e are the static susceptibilities of localized and itinerant spins. If only the EPR line broadening mechanisms indicated above are operative, then, in the case of homogeneous EPR broadening, we have $T_s^{-1} = \omega_\delta''$ and $T_e^{-1} = \omega_\gamma''$. We introduced the designations ω_δ'' and ω_γ'', because later on we include inhomogeneous and dipole–dipole broadening, which affects ω_δ'' and ω_γ'' but leaves T_s^{-1} and T_e^{-1} unchanged.

Let us consider the case where an MW field of frequency $\omega \approx \omega_0$ (ω_0 is the resonance frequency, which is assumed to be the same for *s* and *e* spins) saturates EPR and is modulated with a frequency $\Omega \ll \omega_0$.

In actual practice, the MW radiation power is usually modulated. However, in the method in question, all harmonics of the periodic function $\sqrt{a + b\cos\Omega t}$, other than the harmonics with frequencies $\omega + \Omega$ and $\omega - \Omega$, are cut off in the experiment. Therefore, the time

dependence of the amplitude of the transverse MW field in Eq. (2) can be written as

$$-\frac{g\mu_B}{\hbar}H_x(t) = 2\sqrt{a+b\cos\Omega t}\cos\omega t \approx \frac{a_0}{2}\exp(-i\omega t) + \frac{a_1}{2}(\exp[-i(\omega+\Omega)t] + \exp[-i(\omega-\Omega)t]) + \text{c.c.}, \quad (4)$$

where a_0 and a_1 are the zeroth and first Fourier coefficients [13] of the function $\sqrt{a+b\cos\Omega t}$.

Thus, according to Eq. (4), the spin system is excited at three frequencies. Therefore, we consider the response of the system at these three frequencies:

$$M^x_{s,e} = \frac{1}{2}[u_{s,e\perp}(\omega) + iv_{s,e\perp}(\omega)]\exp(-i\omega t) + \frac{1}{4}[u_{s,e\perp}(\omega+\Omega) + iv_{s,e\perp}(\omega+\Omega)]\exp[-i(\omega+\Omega)t] + \frac{1}{4}[u_{s,e\perp}(\omega-\Omega) + iv_{s,e\perp}(\omega-\Omega)] \times \exp[-i(\omega-\Omega)t], \quad (5)$$

where $u_{s,e\perp}$ and $v_{s,e\perp}$ are slow transverse (Bloch) amplitudes satisfying the inequalities

$$|\dot u_{s,e\perp}(\omega, \omega\pm\Omega)| \ll |\omega u_{s,e\perp}(\omega, \omega\pm\Omega)|, \quad |\dot v_{s,e\perp}(\omega, \omega\pm\Omega)| \ll |\omega v_{s,e\perp}(\omega, \omega\pm\Omega)|. \quad (6)$$

Using Eqs. (6), we obtain the following equations for the individual Bloch precession amplitudes of *s* and *e* spins at the frequency ω:

$$\begin{aligned}
&\dot u_{s\perp}(\omega) + \Delta v_{s\perp}(\omega) + \omega''_\delta u_{s\perp}(\omega) + \omega''_\alpha u_{e\perp}(\omega) = 0,\\
&\dot v_{s\perp}(\omega) - \Delta u_{s\perp}(\omega) + \omega''_\delta v_{s\perp}(\omega) + \omega''_\alpha u_{e\perp}(\omega) = -\frac{g_s\mu_B}{\hbar}H_1 M^z_s,\\
&\dot u_{e\perp}(\omega) + \Delta v_{e\perp}(\omega) + \omega''_\gamma u_{e\perp}(\omega) + \omega''_\beta u_{s\perp}(\omega) = 0,\\
&\dot v_{e\perp}(\omega) - \Delta u_{e\perp}(\omega) + \omega''_\gamma v_{e\perp}(\omega) + \omega''_\beta u_{s\perp}(\omega) = -\frac{g_e\mu_B}{\hbar}H_1 M^z_e,
\end{aligned} \quad (7)$$

where $\Delta = \omega - \omega_0$. Equations for the transverse Bloch amplitudes at frequencies $\omega + \Omega$ and $\omega - \Omega$ can be obtained from Eqs. (7) by substituting $\Delta \pm \Omega$ for Δ.

In the absence of a driving force ($H_1 = 0$, $\Delta = 0$), the set of differential equations (7) reduces to two sets of equations. Each of these sets has the same secular equation,

$$(\omega'' - \omega''_\delta)(\omega'' - \omega''_\gamma) - \omega''_\alpha\omega''_\beta = 0. \quad (8)$$

Solutions $\omega''_{(t)}$ and $\omega''_{(-t)}$ to Eq. (8) are the normal-mode decay rates [14] (i.e., the EPR linewidths) of the coupled spin system under study. Here, *t* is the mode index, which stands for + or –; the index *t* always indicates the *s*-like mode and *t*, the *e*-like mode. Therefore, in the absence of dynamic *s*–*e* coupling ($\omega''_\alpha = \omega''_\beta = 0$), the normal-mode decay rates $\omega''_{(t)}$ and $\omega''_{(-t)}$ reduce to the partial decay rates ω''_δ and ω''_γ of the *s* and *e* spins, respectively. It should be noted that *t* stands for + or – depending on the actual type of the (+) and (–) modes.

As in [9], we pass over to the transverse Bloch amplitudes using the relations

$$\begin{aligned}
u_{s\perp}(\omega, \omega\pm\Omega) + iv_{s\perp}(\omega, \omega\pm\Omega) &= u_{(t)}(\omega, \omega\pm\Omega) + iv_{(t)}(\omega, \omega\pm\Omega) + k^{-1}_{(-t)}[u_{(-t)}(\omega, \omega\pm\Omega) + iv_{(-t)}(\omega, \omega\pm\Omega)],\\
u_{e\perp}(\omega, \omega\pm\Omega) + iv_{e\perp}(\omega, \omega\pm\Omega) &= k_{(t)}[u_{(t)}(\omega, \omega\pm\Omega) + iv_{(t)}(\omega, \omega\pm\Omega)] + u_{(-t)}(\omega, \omega\pm\Omega) + iv_{(-t)}(\omega, \omega\pm\Omega).
\end{aligned} \quad (9)$$

Here, $u_{(\pm t)}$ and $v_{(\pm t)}$ correspond to the modes with decay rates $\omega''_{(\pm t)}$ and the quantities $k_{(\pm t)}$ are defined as [9]

$$k_{(t)} = \frac{\omega''_{(t)} - \omega''_\delta}{\omega''_\alpha} = \frac{\omega''_\beta}{\omega''_{(t)} - \omega''_\gamma}, \quad k_{(-t)} = \frac{\omega''_{(-t)} - \omega''_\delta}{\omega''_\alpha} = \frac{\omega''_\beta}{\omega''_{(-t)} - \omega''_\gamma}. \quad (10)$$

Substituting Eqs. (9) into the first two equations in (7), we obtain decoupled equations which describe the evolution of the slow transverse *s*-like *t*-mode Bloch amplitudes:

$$\begin{aligned}
\dot u_{(t)}(\omega) &= -\Delta v_{(t)}(\omega) - \omega''_{(t)}u_{(t)}(\omega),\\
\dot v_{(t)}(\omega) &= \Delta u_{(t)}(\omega) - \omega''_{(t)}v_{(t)}(\omega) - \frac{a_0}{2}\tilde K_{s(t)}M^z_s,\\
\dot u_{(t)}(\omega\pm\Omega) &= -[\Delta\pm\Omega]v_{(t)}(\omega\pm\Omega) - \omega''_{(t)}u_{(t)}(\omega\pm\Omega),\\
\dot v_{(t)}(\omega\pm\Omega) &= [\Delta\pm\Omega]u_{(t)}(\omega\pm\Omega) - \omega''_{(t)}v_{(t)}(\omega\pm\Omega) - a_1\tilde K_{s(t)}M^z_s.
\end{aligned} \quad (11)$$

Equations for the slow Bloch amplitudes of the *e*-like (–*t*) mode can be obtained from Eqs. (11) by replacing $M^z_s \longrightarrow M^z_e$ and $\tilde K_{s(t)} \longrightarrow \tilde K_{e(-t)}$, where

$$\tilde K_{s(t)} = \frac{(\omega''_{(t)} - \omega''_\gamma)(1 + k_{(t)})}{\omega''_{(t)} - \omega''_{(-t)}}, \quad \tilde K_{e(-t)} = \frac{(\omega''_{(-t)} - \omega''_\delta)(1 + k^{-1}_{(-t)})}{\omega''_{(-t)} - \omega''_{(t)}}. \quad (12)$$

In the equation for the longitudinal magnetization component M_s^z, the term describing the interaction with the transverse microwave field can be written using Eqs. (4), (5), and (9); this equation takes the form

$$\begin{aligned}\dot{M}_s^z + \frac{M_s^z}{T_s} - \frac{M_e^z}{T_{es}} &= \frac{M_s^0}{\tau_s} + \left(\frac{a_0}{2} + a_1\cos\Omega t\right)[v_{(t)} + k_{(-t)}^{-1}v_{(t)}] \\ &+ \frac{a_0}{4}\cos\Omega t[v_{(t)}(\omega+\Omega) + v_{(t)}(\omega-\Omega) \\ &+ k_{(-t)}^{-1}[v_{(-t)}(\omega+\Omega) + v_{(-t)}(\omega-\Omega)]] \\ &- \frac{a_0}{4}\sin\Omega t[u_{(t)}(\omega+\Omega) - u_{(t)}(\omega-\Omega) \\ &+ k_{(-t)}^{-1}[u_{(-t)}(\omega+\Omega) - u_{(-t)}(\omega-\Omega)]].\end{aligned} \quad (13)$$

Now, we take into account other mechanisms of EPR line broadening for *s* spins. First, we include the dipole–dipole (dd) interaction between *s* spins. If all *s* spins have the same resonance frequency, the secular part of the dd interaction causes homogeneous EPR line broadening, which depends only on the secular dd interaction constants in the absence of exchange narrowing. In addition, the EPR line of *s* spins can be inhomogeneously broadened due to lattice defects, microscopic variations in the orientation of the crystallographic axes, hyperfine interaction with surrounding magnetic nuclei, etc. The effect of the scatter of the *s*-spin resonance frequencies on EPR in metals was consistently taken into account in this case in [15], where all *s* spins were characterized by different resonance frequencies and the *s*-spin magnetization spectral density, in addition to the *e*-spin magnetization, was included as a dynamic variable in the kinetic equations. To calculate the EPR signal, integration was performed over all resonance frequencies of *s* spins. However, in the case of inhomogeneous broadening, flip–flops of *s* spins having different resonance frequencies can occur due to the nonsecular part of their dd interaction. This effect can result in so-called fast spectral diffusion [16] within an inhomogeneously broadened EPR line. The spectral diffusion is called fast if it has a chance to involve the whole of the inhomogeneously broadened EPR line in a time less than any time of relaxation in the system under study. In this case, an inhomogeneously broadened EPR line transforms into a homogeneously broadened line, with its resonance frequency lying at the centroid of the line. The width of such a line includes (in the absence of narrowing mechanisms) contributions from the secular dd interaction and from the so-called local-field reservoir [16, 17].

We include the dd interaction between *s* spins in a metal in the cases where (i) this interaction results in homogeneous broadening of EPR lines or (ii) causes fast spectral diffusion in an inhomogeneously broadened EPR line. Let δ_s^0 be the contribution from one of these additional broadening mechanisms to the EPR linewidth of *s* spins in the absence of *e* spins in the sample. It was shown in [9, 11, 15] that, if the *s*–*e* coupling in a metal is sufficiently strong, then the contribution from an additional broadening mechanism to the EPR linewidth can become equal to a certain value δ^* different from the bare linewidth δ_s^0. The value δ^* was estimated in two extreme cases of the *s*–*e* coupling. If this coupling is weak ($T_{se}^{-1} \ll \delta_s^0$), then we have $\delta^* \approx \delta_s^0$. In the case of strong *s*–*e* coupling ($T_{se}^{-1} \gg \delta_s^0$), we have $\delta^* \approx (\delta_s^0)^2 T_{se}$. In [9, 11, 15], these relations were presented for the case of inhomogeneously broadened EPR lines. However, this exchange narrowing is fairly universal in character and, therefore, the relations indicated above can also be used in the case where δ_s^0 is the contribution from the secular part of the dd interaction to a uniformly broadened EPR line. In what follows, we include the additional broadening mechanisms indicated above by adding the quantity δ^* to the partial EPR linewidth of *s* spins [11] $T_{se}^{-1} + T_{sL}^{-1}$ in all expressions related to their motion in a transverse plane. The quantities characterizing this motion are labeled by the indices ($\pm t$), and the partial linewidth of *s* spins is taken to be

$$\omega_\delta'' = T_{se}^{-1} + T_{sL}^{-1} + \delta^*,$$

where, in the case of *s*–*e* coupling of arbitrary strength, the value of δ^* is intermediate between δ_s^0 and $(\delta_s^0)^2 T_{se}$.

We differentiate Eq. (13) twice and transform it by using Eq. (7) and replacing the slow amplitudes by their steady-state values in the third-order differential equation thus obtained. Then, we assume that a solution to this equation can be represented as the sum of a steady-state solution (without modulation) and a small addition $m_{sz}(t)$ due to modulation. In the case of weak EPR saturation (where the saturation factor is much less than unity), the time evolution of this small addition can be shown to be described by the equation[1]

[1] We note that, in [8, 9], the Bloch–Hasegawa equations were written only at frequency ω, which is valid if the harmonics with frequencies $\omega + \Omega$ and $\omega - \Omega$ overlap considerably with the fundamental resonance line, i.e., if the modulation frequency is much smaller than any decay rate in the system under study. Furthermore, in calculating the longitudinal response, second-order differential equations for $m_{sz}(t)$ and $m_{ez}(t)$ were used and transformed in much the same way as the third-order equation in this paper. As a result, the left-hand side of the second-order equations did not contain detuning and a number of effects associated with nonresonant EPR saturation were not included.

$$\ddot{m}_{sz} + (T_s^{-1} + 2\omega_\delta'')\ddot{m}_{sz}$$

$$+ [2T_s^{-1}\omega_\delta'' + \omega_\delta''^2 + 3T_{se}^{-1}T_{es}^{-1} + \Delta^2]\dot{m}_{sz}$$

$$+ [T_s^{-1}(\omega_\delta''^2 + \Delta^2) + T_{se}^{-1}T_{es}^{-1}(T_s^{-1} + \omega_\delta'' + \omega_\gamma'')]m_{sz}$$

$$- 3T_{es}^{-1}\ddot{m}_{ez} - T_{es}^{-1}[2T_e^{-1} + 3\omega_\delta'' + \omega_\gamma'']\dot{m}_{ez}$$

$$- T_{es}^{-1}[T_e^{-1}(\omega_\delta'' + \omega_\gamma'') + \omega_\delta''^2 + \Delta^2 + T_{se}^{-1}T_{es}^{-1}]m_{ez} \quad (14)$$

$$= -a_0a_1\tilde{K}_{s(t)}M_s^0\left\{\left[\omega_\delta'' - \frac{\omega_{(t)}''}{2}\frac{\Omega^2}{(\omega_{(t)}'')^2 + \Delta^2}\right.\right.$$

$$\left.\left. + k_{(-t)}^{-1}T_{se}^{-1}\right]\cos\Omega t + \Omega\left[\frac{3}{2} - \frac{\Delta^2}{(\omega_{(t)}'')^2 + \Delta^2}\right]\sin\Omega t\right\}$$

$$- a_0a_1k_{(-t)}^{-1}\tilde{K}_{e(-t)}M_e^0\left\{\left[\omega_\delta'' - \frac{\omega_{(-t)}''}{2}\frac{\Omega^2}{(\omega_{(-t)}'')^2 + \Delta^2}\right.\right.$$

$$\left.\left. + k_{(t)}^{-1}T_{se}^{-1}\right]\cos\Omega t - \Omega\left[\frac{3}{2} - \frac{\Delta^2}{(\omega_{(-t)}'')^2 + \Delta^2}\right]\sin\Omega t\right\}.$$

An analogous equation for e spins can be obtained from Eq. (14) by replacing $k_{(t)} \rightleftharpoons k_{(-t)}^{-1}$, $s \rightleftharpoons e$, $(t) \rightleftharpoons (-t)$, and $\delta \rightleftharpoons \gamma$.

Using the notation from [4–7], we represent the sum of m_{sz} and m_{ez}

$$m_{sz} + m_{ez} = (u_s + u_e)\cos\Omega t + (v_s + v_e)\sin\Omega t$$

in the form

$$m_{sz} + m_{ez} = \frac{1}{2}\{(u + iv)\exp(-i\Omega t) + (u - iv)\exp(i\Omega t)\}, \quad (15)$$

where $u = u_s + u_e$ and $v = v_s + v_e$ are the amplitudes of slow oscillation of the total longitudinal magnetization components that are in phase and $\pi/2$ out of phase with modulation, respectively. The voltage that is induced across a pickup coil oriented along the static magnetic field also consists of two components (one in phase and one in quadrature): $U = Au\Omega$ and $V = Av\Omega$, where A is the instrumental factor. Solving Eq. (14) and an analogous equation for $m_{ez}(t)$, we obtain the following expression for this voltage in complex form:

$$U + iV = -A\Omega\pi a_0a_1M_s^0K_{s(t)}$$
$$\times\frac{\Omega + i(\omega_{(-t)}'' - k_{(t)}\delta^*/(1 + k_{(t)}))}{\Omega + i\omega_{(-L)}''}$$
$$\times f(\Omega, \Delta, \omega_{(t)}'', \omega_{(L)}'')g_{(t)}(\omega - \omega_0) \quad (16)$$
$$- A\Omega\pi a_0a_1M_e^0K_{e(-t)}\frac{\Omega + i(\omega_{(t)}'' - \delta^*/(1 + k_{(-t)}^{-1}))}{\Omega + i\omega_{(L)}''}$$
$$\times f(\Omega, \Delta, \omega_{(-t)}'', \omega_{(-L)}'')g_{(-t)}(\omega - \omega_0),$$

where $K_{s(t)} = \tilde{K}_{s(t)}(1 + k_{(t)})$, $K_{e(-t)} = \tilde{K}_{e(-t)}(1 + k_{(-t)}^{-1})$, and the functions

$$g_{(\pm t)}(\omega - \omega_0) = \frac{\omega_{(\pm t)}''}{\pi}\frac{1}{(\omega - \omega_0)^2 + \omega_{(\pm t)}''^2}$$

describe the shape of EPR lines corresponding to different modes. The quantities $\omega_{(\pm L)}''$ and $k_{(\pm L)}$ are obtained from $\omega_{(\pm t)}''$ and $k_{(\pm t)}$, respectively, by replacing $\delta^* \longrightarrow 0$, and the functions $f(\Omega, \Delta, \omega_{(t)}'', \omega_{(L)}'')$, which were first defined in [2, 3] for the case of spins of one type, are given by

$$f(\Omega, \Delta, \omega_{(t)}'', \omega_{(L)}'')$$
$$= \frac{\omega_{(t)}''\left(1 - \frac{i\Omega}{2\omega_{(t)}''}\right)\left[\Omega + i\omega_{(t)}''\left(1 + \frac{\Delta^2}{(\omega_{(t)}'')^2}\right)\right]}{(\Omega + i\omega_{(L)}'')(\Omega + \Delta + i\omega_{(t)}'')(\Omega - \Delta + i\omega_{(t)}'')}. \quad (17)$$

At small values of detuning and (or) low MW-field modulation frequencies, the results of this paper coincide with those obtained in [9].

In the absence of s–e coupling, Eq. (16) reduces to the sum of individual complex signals of the longitudinal response of s and e spins, with each individual response coinciding with the expression derived in [2, 3] for the case of spins of one type (if the decay rates in Eqs. (16) and (17) are expressed in terms of the times T_1 and T_2). As seen from Eqs. (16) and (17), the ω dependence of the mode signals of the longitudinal response is different from the shape of the corresponding EPR lines (the frequency dependence of the individual response likewise differs from the shape of the individual EPR signal).

Distortion of the shape of a longitudinal response in the case where the modulation frequency is comparable to the relaxation rates and to detuning of the MW radiation frequency with respect to the center of the EPR line is exemplified in the figure. The experiment was conducted on samples of carbonized wood (activated carbon prepared using a special technology) containing stable surface free radicals for which the EPR linewidth

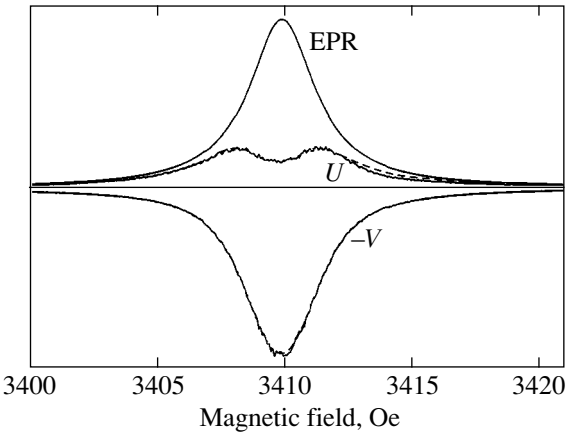

In-phase (*U*) and in-quadrature (*V*) components of the signal of the longitudinal response for one of the EPR lines of surface free radicals in carbonized wood recorded at room temperature in an oxygen-free atmosphere at a modulation frequency of 10^7 rad/s. The uppermost curve is the EPR (absorption) signal (in arbitrary units), and the dashed curves are calculations based on the formulas from [2, 3].

is very sensitive to the oxygen content in the environment [18]. The modulation frequency of the MW radiation power (wavelength 3.2 cm) was $\Omega = 10^7$ rad/s. The figure shows the in-phase and in-quadrature components of the longitudinal response (for convenience, the quantity $-V$ is plotted) and the EPR line (in arbitrary units), whose shape is described by a Lorentzian curve with a half-width of 1.6 Oe. (We note that the EPR spectrum in this material consists of two lines corresponding to paramagnetic centers that are located at physically different areas of the surface of the activated carbon; for the sake of simplicity, the second line is not shown in the figure.) It can be seen that the longitudinal response as a function of detuning differs in shape from the EPR (absorption) line. This difference is most evident for the signal *U*, which exhibits a dip at its center. The dashed curves are best fits to the signals *U* and *V* obtained using the formulas from [2, 3] with the parameters $T_1 = 2.2 \times 10^{-7}$ s and $T_2 = 7 \times 10^{-8}$ s. These theoretical curves are seen to agree well with the experimental data, which indicates that the conduction electrons in the activated carbon do not affect the signals of the longitudinal response.

Now, we consider several extreme cases of *s*–*e* coupling that are of interest for practical application of the modulation technique to metals with paramagnetic impurities.

We assume that, in a relaxation-coupled *s*–*e* spin system, the "coupling efficiency" is high in comparison with unity (the definition of this parameter for the case where oscillations are coupled with respect to their resonance frequencies is given in [14]). In our case of relaxation-coupled oscillators, the coupling efficiency was defined in [8, 9] as the ratio of the quantity characterizing the coupling of spins of two types to the difference of their partial decay rates:

$$\sigma = \frac{T_{se}^{-1} + T_{es}^{-1}}{\left|\delta^* + T_{sL}^{-1} - T_{eL}^{-1}\right|}. \tag{18}$$

If the coupling efficiency is high, i.e., $\sigma \gg 1$, or, in a different nomenclature, if there is an efficient relaxation "bottleneck" (RB) [11], then the decay rates of the normal modes of the transverse magnetization components can be approximated by the expressions

$$\omega''_{(t=+)} \approx T_{se}^{-1} + T_{es}^{-1} + \frac{\chi_e T_{sL}^{-1} + \chi_s T_{eL}^{-1}}{\chi_s + \chi_e} + \frac{\chi_e}{\chi_s + \chi_e}\delta^*,$$
$$\omega''_{(-t=-)} \approx \frac{\chi_s T_{sL}^{-1} + \chi_e T_{eL}^{-1}}{\chi_s + \chi_e} + \frac{\chi_s}{\chi_s + \chi_e}\delta_s^0. \tag{19}$$

The quantity δ^*, involved in the expression for the decay rate of the *s*-like normal mode, characterizes an additional broadening, as mentioned above. Under the condition $T_{se}^{-1} \gg \delta_s^0$, as shown in [9, Appendix], we have $\delta^* = (\delta_s^0)^2 T_{se}$, irrespective of whether the additional broadening is inhomogeneous in nature with fast spectral diffusion or is due to dipole–dipole interaction (this equation is associated with exchange narrowing, which takes place in the case of a high coupling efficiency [6, 15]). In the case of an efficient RB, the signal of the longitudinal response is due to narrow modes of transverse and longitudinal Bloch amplitudes enhanced by the *s*–*e* coupling. Under the conditions $T_{es}^{-1} + T_{eL}^{-1} < T_{se}^{-1} + T_{sL}^{-1} + \delta^*$ and $\delta^* \ll \min(T_{es}^{-1}, T_{se}^{-1})$ in the case of an efficient RB, the signal of the longitudinal response is proportional to the sum of the magnetizations of the *s* and *e* spins:

$$U + iV \approx -A\Omega a_0 a_1 \pi (M_s^0 + M_e^0)$$
$$\times f(\Omega, \Delta, \omega''_{(-t=-)}, \omega''_{(-L=-)}) g_{(-t=-)}(\omega - \omega_0). \tag{20}$$

In the case of low coupling efficiency ($\sigma \ll 1$) and under the assumption that $T_{es}^{-1} + T_{eL}^{-1} < T_{se}^{-1} + T_{sL}^{-1} + \delta_s^0$, the transverse normal mode decay rates are

$$\omega''_{(t=+)} \approx T_{se}^{-1} + T_{sL}^{-1} + \delta_s^0 + \frac{\sigma}{4}(T_{es}^{-1} + T_{se}^{-1}),$$
$$\omega''_{(-t=-)} \approx T_{es}^{-1} + T_{eL}^{-1} - \frac{\sigma}{4}(T_{es}^{-1} + T_{se}^{-1}). \tag{21}$$

The longitudinal normal mode decay rates $\omega''_{\pm L}$ are given by Eqs. (21) with $\delta_s^0 = 0$. In the case of low coupling efficiency, there is no exchange narrowing [6, 9, 15]. The complex signal of the longitudinal response in

the case of low coupling efficiency can be approximated by

$$U + iV \approx A\Omega a_0 a_1 M_s^0 \left(1 + \frac{\chi_s + \chi_e}{\chi_s}\frac{\sigma}{4}\right)^2 f(\Omega, \Delta, \omega''_{(t)}, \omega''_{(L)}) \times g_{(t)}(\omega - \omega_0) + A\Omega a_0 a_1 M_e^0 \left(1 - \frac{\chi_s + \chi_e}{\chi_e}\frac{\sigma}{4}\right)^2 \times f(\Omega, \Delta, \omega''_{(-t)}, \omega''_{(-L)}) g_{(-t)}(\omega - \omega_0). \quad (22)$$

In the case of $T_{eL}^{-1} \gg T_{es}^{-1}$, the *e* spins relax to equilibrium with the lattice so fast that their magnetization is always equal to its equilibrium value; i.e., an isothermal limit arises. In this case, temporal variations occur only in the *s* subsystem with the corresponding partial decay rates [12]. The signal of the longitudinal response is described by the first term in Eq. (22) with $\sigma = 0$.

When the signal of the longitudinal response can be described by one term (the isothermal limit or the efficient RB), the function $f(\Omega, \Delta, \omega''_{(t)}, \omega''_{(L)})$ has the form

$$f(\Omega, \Delta, T_{1eff}, T_{2eff}) = \frac{T_{2eff}^{-1}\left(1 - \frac{i\Omega T_{2eff}}{2}\right)[\Omega + iT_{2eff}^{-1}(1 + \Delta^2 (T_{2eff})^2)]}{(\Omega + iT_{1eff}^{-1})[(\Omega + iT_{2eff}^{-1})^2 - \Delta^2]}, \quad (23)$$

where, in the isothermal limit, the effective longitudinal and transverse relaxation rates are $T_{1eff}^{-1} = T_{se}^{-1} + T_{sL}^{-1}$ and $T_{2eff}^{-1} = T_{se}^{-1} + T_{sL}^{-1} + \delta_s^0$, respectively; in the case of the efficient RB, we have $T_{2eff}^{-1} = \omega''_-$ and $T_{1eff}^{-1} = \omega''_-|_{\delta^* = 0}$. Note that, in the case of large values of the detuning and the modulation frequency of the saturating MW field, the relaxation times T_{1eff} and T_{2eff} can be determined simultaneously and independently by analyzing the complicated shape of the signals *U* and *V*, as in the case exemplified in the figure, corresponding to the isothermal limit and weak *s*–*e* coupling. In the case of intermediate coupling, both terms in the longitudinal response in Eq. (16) are of importance and the relaxation characteristics of the coupled system of *s* and *e* spins can be determined using a fitting procedure, with $\omega''_{(\pm t)}$ and $\omega''_{(\pm L)}$ being adjustable parameters.

3. CONCLUSIONS

In this paper, we have derived an expression for the complex signal of the longitudinal response of the spin system in a metal containing both localized (*s*) and itinerant (*e*) spins; this expression is valid for arbitrary values of the detuning Δ and modulation frequency Ω of the saturating MW field. In two extreme cases for the coupling efficiency of *s* and *e* spins (the isothermal limit and efficient RB), the signal of the longitudinal response has been expressed in terms of the same function $f(\Omega, \Delta, T_{1eff}^{-1}, T_{2eff}^{-1})$ that was used earlier to describe the longitudinal response in systems with spins of one type [2, 3]; the effective relaxation rates T_{1eff}^{-1} and T_{2eff}^{-1} have been found to be different in these two extreme cases and have been expressed in terms of the microscopic parameters of the material. The experimentally measured EPR signals and longitudinal response of surface free radicals in activated carbon were adequately described by the theoretical expressions derived for the case of low coupling efficiency of paramagnetic centers with the conduction electrons. For arbitrary coupling efficiency, the signal of the longitudinal response was represented as the sum of two terms, each of which involves the same function *f*. In one term, the arguments of this function are Ω, Δ, $\omega''_{(t)}$, and $\omega''_{(L)}$, while in the other term, they are Ω, Δ, $\omega''_{(-t)}$, and $\omega''_{(-L)}$. The decay rates $\omega''_{(\pm t)}$ and $\omega''_{(\pm L)}$ of the transverse and longitudinal magnetization modes can be determined by fitting the expressions derived in this paper to the experimental data. The fact that the in-phase (*U*) and in-quadrature (*V*) components of the signal of the longitudinal response are described by the same set of parameters makes this problem easier. In addition, the parameters $\omega''_{\pm t}$ can be determined independently as the widths of the two mode lines obtained by decomposing an experimental EPR (absorption) signal into two Lorentzians [5, 6].

Thus, the theory developed in this paper can form the basis of an improved technique for measuring very short electron spin relaxation times in metals and (after the corresponding extension of the theory) in any solid material containing several types of exchange-coupled paramagnetic particles.

ACKNOWLEDGMENTS

This study was supported by the Tbilisi State University, the Swiss National Science Foundation (grant no. 7GEPJO62429), and the Russian Foundation for Basic Research (project no. 02-02-16219).

REFERENCES

1. J. Herve and J. Pescia, C. R. Acad. Sci. **251**, 665 (1960).
2. J. Herve, in *Proceedings of 1st International Conference on Paramagnetic Resonance*, Ed. by W. Low (Academic, New York, 1963), p. 689.
3. J. Pescia, Ann. Phys. (Paris) **10**, 389 (1965).
4. V. A. Atsarkin, G. A. Vasneva, and V. V. Demidov, Zh. Éksp. Teor. Fiz. **108** (3), 927 (1995) [JETP **81**, 509 (1995)]; Phys. Rev. B **52**, 1290 (1995).
5. V. A. Atsarkin, V. V. Demidov, and G. A. Vasneva, Phys. Rev. B **56** (15), 9448 (1997).

6. V. A. Atsarkin and V. V. Demidov, Zh. Éksp. Teor. Fiz. **113** (3), 1048 (1998) [JETP **86**, 572 (1998)].
7. V. A. Atsarkin, V. V. Demidov, G. A. Vasneva, and V. K. Conder, Phys. Rev. B **63**, 092405 (2001).
8. N. P. Fokina and K. O. Khutsishvili, Appl. Magn. Res. **17**, 503 (1999).
9. N. P. Fokina and K. O. Khutsishvili, Zh. Éksp. Teor. Fiz. **123** (1), 98 (2003) [JETP **96**, 83 (2003)].
10. G. Ablart and J. Pescia, Phys. Rev. B **22** (3), 1150 (1980).
11. S. E. Barnes, Adv. Phys. **30** (6), 801 (1981).
12. M. B. Walker, Phys. Rev. B **7** (7), 2920 (1973).
13. I. N. Bronshteĭn and K. A. Semendyaev, *Handbook on Mathematics* (Nauka, Moscow, 1981), p. 559.
14. V. V. Migulin, V. I. Medvedev, E. R. Mustel', and V. N. Parygin, *Foundations of the Oscillation Theory* (Nauka, Moscow, 1978), p. 245.
15. L. R. Tagirov and K. F. Trutnev, Zh. Éksp. Teor. Fiz. **86** (3), 1092 (1984) [Sov. Phys. JETP **59**, 638 (1984)].
16. L. L. Buishvili, M. D. Zviadadze, and G. R. Khutsishvili, Zh. Éksp. Teor. Fiz. **56** (1), 290 (1969) [Sov. Phys. JETP **29**, 159 (1969)].
17. V. A. Atsarkin, Zh. Éksp. Teor. Fiz. **56** (3), 769 (1970).
18. V. A. Atsarkin, V. V. Demidov, G. A. Vasneva, *et al.*, J. Magn. Reson. **149**, 85 (2001).

Translated by Yu. Epifanov

Physics of the Solid State, Vol. 45, No. 11, 2003, pp. 2025–2030. Translated from Fizika Tverdogo Tela, Vol. 45, No. 11, 2003, pp. 1928–1933.

METALS AND SUPERCONDUCTORS

Effect of Cation Composition on the Superconducting Properties and on the Microstructure of YBaCuO Thin Films

N. V. Vostokov, S. V. Gaponov, B. A. Gribkov, Yu. N. Drozdov, D. V. Masterov, V. L. Mironov, Yu. N. Nozdrin, and E. E. Pestov

Institute of Physics of Microstructures, Russian Academy of Sciences, Nizhni Novgorod, 603950 Russia

e-mail: masterov@ipm.sci-nnov.ru

Received April 9, 2003

Abstract—The surface morphology and superconducting properties of YBaCuO epitaxial films prepared through magnetron sputtering from targets of different cation composition were systematically studied. It was shown that small changes in the growth conditions and relatively small variations in the cation composition of the condensate noticeably affect the surface morphology of the films and their structural and superconducting properties, thus offering an efficient way of controlling the YBCO film parameters. It was found that the 90° off-axis configuration of the magnetron sputtering system permits realization of growth conditions in which the grown films do not contain CuO precipitates and exhibit good superconducting properties ($T_c \geq 88$ K, $j_c(77\text{ K}) \geq 4 \times 10^6$ A/cm^2). © *2003 MAIK "Nauka/Interperiodica".*

1. INTRODUCTION

It is common knowledge that the superconducting properties of $YBa_2Cu_3O_{7-\delta}$ (YBCO) films, such as the superconducting transition temperature, critical current, and microwave resistance, as well as the microstructure and surface morphology of the films, are determined by their cation composition. It has also been established that, irrespective of the method used to prepare YBCO films (laser ablation, magnetron sputtering, electron beam evaporation, metal-organic synthesis), the optimal superconducting characteristics are reached for nonstoichiometric compositions. Indeed, it was shown in [1–4] that films with the highest superconducting performance (zero-resistance temperature $T_{c0} > 90$ K, critical current density $j_c > 2$ MA/cm^2 at 77 K, surface microwave resistance $R_S < 1.0$ mΩ at 77 K and 10 GHz) are obtained in a condensate enriched strongly (up to 100% and more) by copper and yttrium in the course of film growth. However, particles of the secondary phase CuO, typically 0.5 μm in size and with a surface density of 10^8 cm^{-2}, create serious problems in the development of devices based on multilayered structures and Josephson junctions. Films in the stoichiometry region (1-2-3), while being more smooth and containing no YBCO secondary-phase particles, exhibit, as a rule, poorer superconducting properties ($T_{c0} < 88$ K, $j_c < 2$ MA/cm^2, $R_S > 2.0$ mΩ). To reach optimum superconducting and/or structural parameters of the films, one needs to vary their (integrated) cation composition over a broad range. The present communication reports on a study of the effect of cation composition on the superconducting properties and microstructure of YBCO thin films prepared through magnetron sputtering.

2. EXPERIMENTAL TECHNIQUE

The YBCO films were grown in a magnetron sputtering system in a 90° off-axis configuration [5]. Disk-shaped targets were used of the stoichiometric $Y_1Ba_2Cu_3O_7$ (1-2-3, KIB-1, Giredmet Company) and 1-2-2.5, 1-2-3.3, 1-2.25-3, and 1-2.6-3 compositions prepared at the IMP RAS. The target diameter was 40–60 mm, and the ablation zone diameter was 25 mm.

YBCO films 50–70 nm in thickness were grown on $NdGaO_3$ substrates under the following conditions: operating mixture pressure (1/1 Ar/O_2) 20 Pa, target voltage ~150 V, and discharge current 400 mA. The growth temperature T_d was varied from 690 to 760°C. The substrates were heated by a resistance heater using an In–Ga eutectic alloy. After the deposition, the working chamber was filled by oxygen to a pressure of 1 atm and the sample was cooled to room temperature for ~1 h.

The temperature of the superconducting transition was determined without contact using a near-field microwave microscope from the change in the third-harmonic response intensity within the temperature interval 4.2–92.0 K [6]. The sensitivity of this method was 10^{-14} W Hz^{-1}, and the spatial resolution was ~50 μm [7]. The critical (pinning) current was calculated using Bean's model from the measured remanent film magnetization [8] and reduced to the effective thickness of the 1-2-3 YBCO phase, which was derived from x-ray diffraction data.

The surface morphology and local electrical properties of the films were investigated using scanning probe microscopy (SPM) on a Solver setup (NT-MDT Company, Zelenograd). The film microstructure was studied

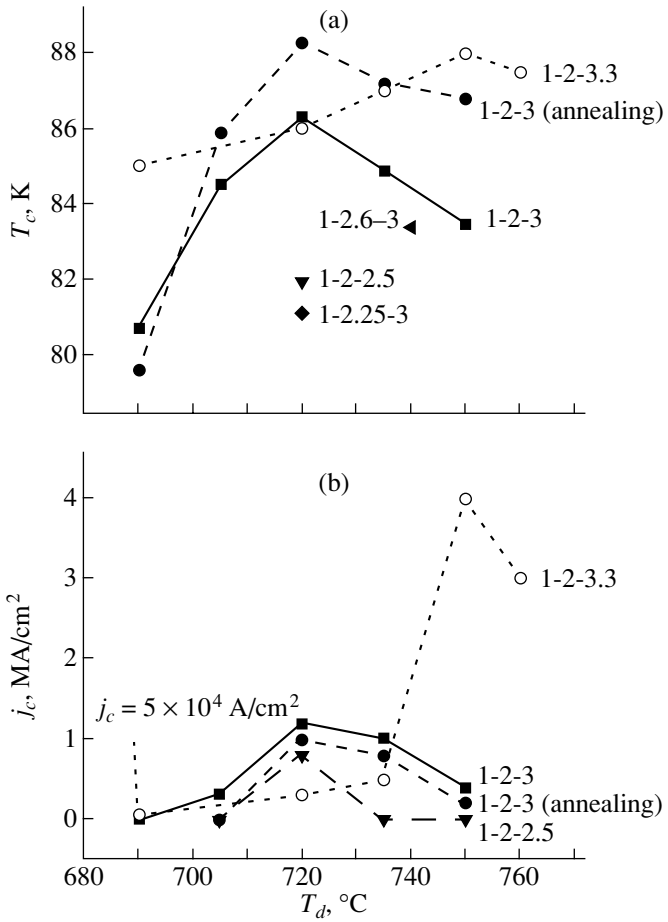

Fig. 1. Deposition temperature dependences of (a) the critical temperature and (b) the pinning current of YBCO films of different cation composition obtained in the 90° off-axis system.

using x-ray diffraction techniques on a DRON-4 diffractometer.

3. RESULTS AND DISCUSSION

Our planar-magnetron 90° off-axis deposition system makes it possible to exclude, to a considerable extent, the factors which are responsible for deviations of the condensate composition from the original composition of the target and are difficult to control (such as diffusion-induced changes in the target volume and the effect of secondary electrons on the growing film). Therefore, one can control the composition of the condensate on the growth surface by properly varying the cation composition of the targets employed and the growth conditions, primarily, the deposition temperature T_d. Figure 1 displays the critical temperature and pinning current (at 77 K) of YBCO epitaxial films plotted vs. deposition temperature for a range of cation compositions. We readily see that the superconducting properties of YBCO films of the stoichiometric composition (1-2-3) reach optimum values within a narrow (~10°C) interval of growth temperatures near 720°C.

3.1. Films of Stoichiometric (1-2-3) Composition

It was shown in [9] that the properties of YBCO films vary substantially in the course of low-temperature (T_{ann} < 200°C) vacuum annealing. Our studies revealed that post-growth vacuum annealing (T_{ann} ~ 200°C, duration 20–30 min) increases the superconducting transition temperature of 1-2-3 films by 1–3 K (Fig. 1a). This increase is accompanied by a decrease in the pinning current by 20–40% of the original value (Fig. 1b). These features in the variation of the film properties are apparently due to the formation of a peroxidized state in YBCO crystallites in the final stage of film growth (during cooling in an oxygen environment); in this state, the concentration of conduction holes in the Cu–O sheets deviates from the optimum value. In the course of subsequent annealing, the film looses part of the oxygen, thus optimizing the carrier concentration in the Cu–O sheets. A change in oxygen content in a film subjected to low-temperature annealing was detected by us from the increase in the lattice parameter c, whose magnitude is connected with the concentration p of conduction holes in the Cu–O sheet (reduced to one Cu atom) through the empirical relations [10, 11]

$$p = 0.187 - 0.21\delta,$$

$$c = 1.2771 - 0.01557(7 - \delta).$$

The oxygen concentration varies differently in crystallites of the YBCO phase and at grain boundaries in a film. As a result, the critical temperature of the YBCO matrix and the pinning current, which is governed primarily by intergrain (weak) links, respond differently to annealing (Fig. 1).

Atomic-force microscopy (AFM) studies showed that the films prepared in the 90° off-axis system through sputtering of a stoichiometric target at the optimum growth temperature have a uniform surface consisting of YBCO microblocks (an AFM image of the film surface is presented in Fig. 2).

The mean film roughness as determined from the AFM profile is less than 20 nm within a surface area of 10×10 μm. The roughness of the films prepared from a 1-2-3 target increases with increasing deposition temperature T_d. Figure 3 displays an AFM image of the surface of an YBCO film deposited at T_d = 750°C.

As seen from Figs. 1 and 3, the degradation of the superconducting properties of the film observed to occur with increasing T_d is accompanied by a roughening of the surface relief, which is associated, in part, with the formation of YBCO crystallite outgrowths. Note that the main structural characteristics of the film, namely, the half-width of the rocking curve (FWHM(005)YBCO) and the lattice parameter c, prac-

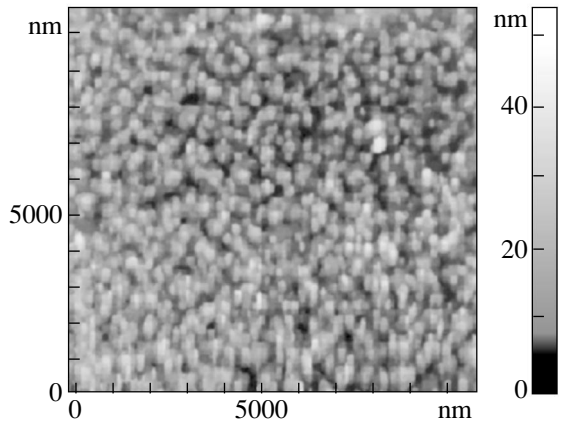

Fig. 2. AFM surface image of an 1-2-3 film grown in the 90° off-axis system at optimum growth temperature (720°C).

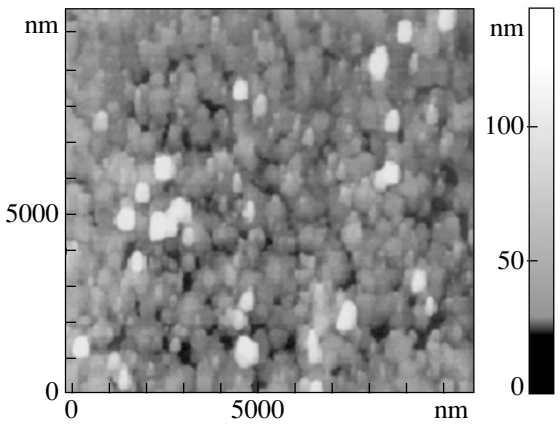

Fig. 3. AFM surface image of an 1-2-3 film grown in the 90° off-axis system at a growth temperature of 750°C.

tically do not change. An important feature of the films grown in the 90° off-axis system from targets of stoichiometric composition is that they do not have particles of secondary phases on their surface. The films are practically single phase and exhibit the following superconducting parameters: $T_{c0} > 86$ K and j_c up to 1.2×10^6 A/cm^2 at 77 K. Thus, the results obtained in our studies indicate that the cation composition of films prepared in a 90° off-axis configuration is identical to that of the original 1-2-3 target.

For comparison, Fig. 4 presents an AFM image of an YBCO film obtained in an inverted cylindrical magnetron sputtering (ICMS) system. As shown in [12–14], films prepared in an ICVS system are enriched in copper and yttrium due to diffusive mass transport occurring in the bulk of the target and selective reevaporation and desorption of YBCO components from the substrate and the surrounding parts of the system. The surface of these films exhibits CuO precipitates of hemispherical shape, with typical lateral dimensions of 0.5–1.0 μm and a height of up to 400–600 nm [13]. Films grown in an ICMS system had the same morphology within a broad deposition temperature range, from 600 to 750°C. Regions between precipitates have a typical block structure with a mean roughness of ~15 nm.

The local electrical properties of the films were studied using scanning tunneling microscopy (STM). We investigated the spatial distribution of the tunneling current between the probe and a sample and local current–voltage tunneling-junction characteristics at various points on the film surface. As follows from the STM measurements, the regions between CuO particles in a film have metallic conduction, as should be expected for the 1-2-3 YBCO phase above the critical temperature. The shape of the STM *I–V* curves obtained on the surface of CuO particles was typical of a metal–broad-band-gap semiconductor function.

A major factor determining the superconducting properties of films was shown in [4, 15, 16] to be cation disorder (CD) in the YBCO unit cell. This disorder consists, as a rule, in the formation of copper vacancies in the CuO chains and in the mutual substitution of Y and Ba atoms, which distorts the lattice. As a result of CD,

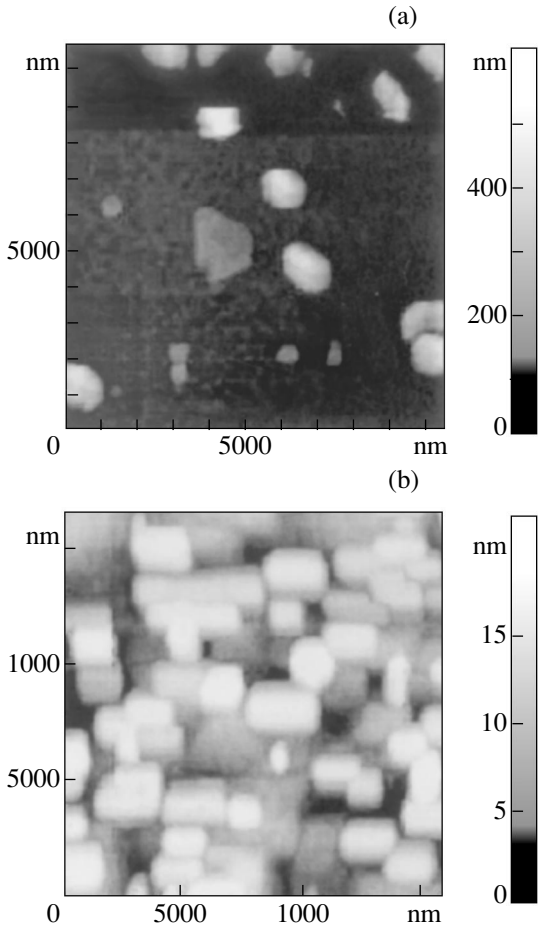

Fig. 4. AFM surface image of an YBCO film grown in inverted cylindrical magnetron sputtering system from a stoichiometric 1-2-3 target.

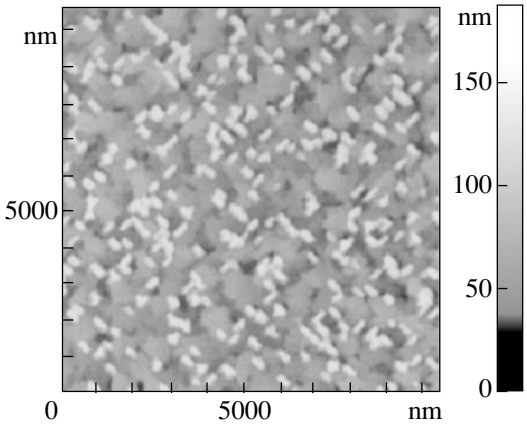

Fig. 5. AFM surface image of an 1-2-3.3 film grown in the 90° off-axis system at a growth temperature of 750°C.

the carrier concentration in YBCO films deviates from the optimal value, which degrades their superconducting properties. Obviously enough, the processes involved in CD depend, above all, on the cation composition of the condensate on the growth surface. In the ICMS deposition system, the crucial parameter is the Cu/Ba concentration ratio. In this system, at high deposition temperatures (above 720°C), Ba undergoes intense reevaporation, which brings about a change in the cation composition of the YBCO film and the formation of CuO secondary-phase particles. The regions near these particles exhibit modified properties (distorted relief and reduced tunneling conductivity) because of diffusive depletion in copper during film growth [13]. As a result of CD (the formation of copper vacancies), these regions possess degraded superconducting characteristics. In films obtained at high deposition temperatures (above 740°C), the relative volume of the nonuniformities actually representing CuO particles surrounded by such regions exceeds the current flow threshold, which degrades the superconducting properties dramatically. Furthermore, CuO particles contribute noticeably to resistive losses in the microwave range [17] and, hence, degrade the parameters of microwave devices. To study the effect of cation composition on the properties of YBCO films, a series of samples were deposited in the 90° off-axis system from nonstoichiometric targets of three types: 1-2-2.5 depleted in copper, 1-2.25-3 and 1-2.6-3 enriched in barium, and 1-2-3.3 enriched in copper.

3.2. Films with a Reduced Cu/Ba Cation Ratio

Our studies showed that YBCO films obtained from targets with compositions 1-2-2.5, 1-2.25-3, and 1-2.6-3, i.e., with a lower than stoichiometric Cu/Ba ratio, have poor superconducting properties (Fig. 1). Note that lowering the copper concentration (with respect to the 1-2-3 stoichiometry) degrades the superconducting properties more dramatically than increasing the concentration of Ba atoms. In particular, films prepared from 1-2-2.5 targets did not reveal any superconducting phases down to 4.2 K. Studies of the nonlinear properties of Ba-enriched films (target compositions 1-2.25-3 and 1-2.6-3) performed in the temperature range 4.2–92 K showed these films to have low critical temperatures (~82 K) and a strongly nonuniform (in T_c) phase composition. In our opinion, the poor superconducting properties of the films (or complete absence of superconductivity) are associated with CD in the YBCO unit cell. X-ray diffraction patterns of films with 1-2-2.5, 1-2.25-3, and 1-2.6-3 compositions prepared at $T_d \geq 720$°C showed them to have normal structural parameters; in particular, the lattice parameter was $c \leq 1.17$ nm. This apparently means that deposition in the 90° off-axis system does not involve reevaporation of Ba atoms from the growth surface, so that the Cu/Ba concentration ratio in a growing film remains nonoptimal (below the stoichiometric value). As a consequence, the excess of Ba gives rise to substitution of Ba for Y atoms and the integrated copper deficiency causes cation-vacancy formation in the Cu–O chains.

3.3. Films with an Enhanced Cu/Ba Cation Ratio

The surface morphology and electrical properties of films prepared from copper-enriched 1-2-3.3 targets were found to depend substantially on the deposition temperature. As is evident from Fig. 1, the deposition temperature optimal for this composition is 750°C. X-ray diffraction analysis showed these films to have a good microstructure. Films obtained at the optimum growth temperature have $T_{c0} = 88$–90 K. The films have a high critical current $j_c \geq 4 \times 10^6$ A/cm^2 at 77 K (reduced to the effective thickness of the *c*-oriented YBCO phase). Figure 5 displays an AFM image of the 1-2-3.3 YBCO film with the best superconducting characteristics.

The film features a well-developed surface relief. Two layers can be conventionally discriminated in the AFM image of the film. The bottom layer is made up of merged crystallites. The top layer consists of isolated microblocks with a real height, as derived from AFM profiles, of 50–70 nm. Our STM studies showed this film to feature highly uniform local electrical properties. Local STM *I–V* curves obtained in different film regions were indicative of metallic conduction. No dielectric inclusions were revealed on the film surface. It may be conjectured that, despite the targets used having been nonstoichiometric (Cu enriched), the growth microkinetics conditions (growth temperature, deposition rate, working-gas pressure) are, in this case, such that the formation of copper-containing particles is suppressed. X-ray diffraction analysis showed the presence of Y_2O_3 epitaxial inclusions (Bragg reflection angle $2\theta = 33.8°$), which are apparently distributed over the bulk of a film [18].

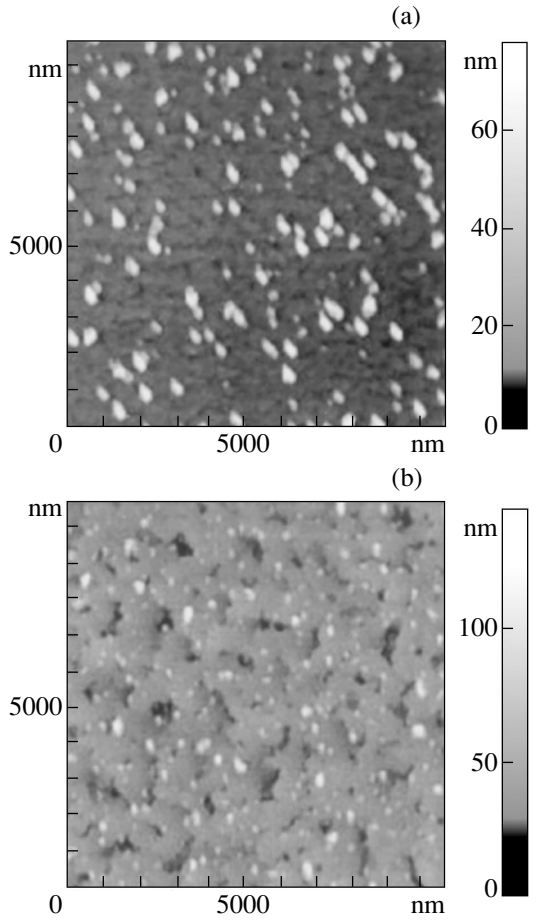

Fig. 6. AFM surface images of 1-2-3.3 films grown in the 90° off-axis system at growth temperatures of (a) 690 and (b) 720°C.

The surface morphology of 1-2-3.3 films grown at lower temperatures (Fig. 6) is similar to that of films prepared from stoichiometric targets in the ICMS system (Fig. 4). However, the films obtained in the 90° off-axis system are smoother. Figure 6a presents an AFM image of a film grown at T_d = 690°C. On the surface, particles about 60 nm high are clearly seen with characteristic lateral dimensions of 500 nm; these particles are apparently copper-containing precipitates. The surface roughness in the regions free of secondary-phase particles is within 5 nm. The film has a superconducting transition temperature T_{c0} = 85 K and a fairly low pinning current $j_c \geq 5 \times 10^4$ A/cm^2 (the sensitivity limit of magnetic measurements).

Thus, our studies show that the deposition of films from 1-2-3.3 targets at ~750°C and higher temperatures entails reevaporation of copper atoms from the growth surface. The enhanced copper concentration in the original condensate suppresses CD and, thus, favors the attainment of improved superconducting properties for the films. As a result, the films grown in the temperature interval T_d = 690–760°C from 1-2-3.3 targets (Fig. 1) have a critical temperature higher than 85 K.

4. CONCLUSIONS

Thus, we have carried out a systematic investigation of the growth, surface morphology, microstructure, and electrical properties of $YBa_2Cu_3O_{7-\delta}$ epitaxial films prepared through magnetron sputtering from targets differing in composition.

It has been established that the superconducting transition temperature of YBCO films obtained in the 90° off-axis system is extremely sensitive to the copper atomic concentration in the flow of sputtered material. When stoichiometric targets (1-2-3 composition) are employed, the optimal superconducting properties of films are reached within a narrow (~10°C) deposition temperature interval. A 10% excess of copper content above the stoichiometric value (1-2-3.3 composition) broadens the growth temperature (T_d) range within which the films exhibit fairly high superconducting properties (T_{c0} > 85 K). Films obtained from Cu-enriched targets feature a strongly developed surface morphology and higher superconducting transport characteristics compared to films grown from stoichiometric targets. If the percentage of copper is reduced (target composition 1-2-2.5), the films grown in the deposition temperature interval T_d = 705–750°C have practically no superconducting phases down to T = 4.2 K. Ba-enriched films (target compositions 1-2.25-3, 1-2.6-3) exhibit poor superconducting properties and, as revealed in studies of nonlinear characteristics, a strongly nonuniform (in T_c) phase composition. It has been established that the 90° off-axis magnetron sputtering configuration makes it possible to realize growth conditions in which the YBCO films obtained do not contain CuO particles and feature good superconducting properties, namely, T_{c0} up to 90 K and j_c in excess of 4 MA/cm^2 at 77 K.

Low-temperature vacuum annealing (T_{ann} ~ 200°C) of YBCO films prepared from stoichiometric targets in the 90° off-axis system increases the critical film temperature by 1–3 K while lowering the pinning current by 20–40%. Such annealing can be employed to attain the highest possible superconducting transition temperature for a given film, because it is reversible.

Thus, the surface morphology of films and their superconducting properties and structure are noticeably affected by small changes in the growth conditions and relatively small variations in the cation composition of the condensate, which provides the possibility of efficiently controlling the parameters of YBCO films. The growth conditions of YBCO films realized in practice permit one to optimize their surface morphology (so as to obtain, in particular, films which would not contain CuO particles on the surface); such optimization is a crucial requirement in the preparation of multilayered structures and the formation of topologically complex

configurations from photolithography. Conversely, in cases where fine treatment of the sample surfaces is not required, one can noticeably optimize the superconducting properties (critical temperature, pinning current) of films, which is of crucial importance in reaching the best possible operating parameters of YBCO-based devices.

ACKNOWLEDGMENTS

The authors are indebted to S.A. Churin and N.A. Korotkova for assistance in this study.

This study was supported by the Russian Foundation for Basic Research (project no. 02-02-16764) and the Ministry of Industry, Science, and Technologies of the Russian Federation, program "Research in Topical Areas of Science and Technology" (project on experimental and theoretical research aimed at creating a physical basis for the development of novel components and devices for superconducting electronics).

REFERENCES

1. B. Schaulte, M. Maul, P. Haussler, and H. Adrian, Appl. Phys. Lett. **62** (6), 633 (1993).
2. J. Hudner, O. Thomas, E. Mossang, *et al.*, J. Appl. Phys. **74** (7), 4631 (1993).
3. N. G. Chew, J. A. Edwards, R. G. Humphreys, *et al.*, IEEE Trans. Appl. Supercond. **5** (2), 1167 (1995).
4. W. Hattori, T. Yoshitake, and S. Tahara, IEEE Trans. Appl. Supercond. **11** (1), 3205 (2001).
5. A. K. Vorob'ev, N. V. Vostokov, S. V. Gaponov, *et al.*, Pis'ma Zh. Tekh. Fiz. **27** (5), 50 (2001) [Tech. Phys. Lett. **27**, 197 (2001)].
6. E. E. Pestov, Yu. N. Nozdrin, and V. V. Kurin, IEEE Trans. Appl. Supercond. **11** (1), 131 (2001).
7. E. E. Pestov, V. V. Kurin, Yu. N. Nozdrin, *et al.*, in *Extended Abstracts of 8th International Superconductive Electronics Conference (ISEC'01), Osaka, Japan, 2001*, p. 499.
8. Yu. N. Nozdrin, A. S. Mel'nikov, I. D. Tokman, *et al.*, IEEE Trans. Appl. Supercond. **9** (2), 1602 (1999).
9. Yu. N. Drozdov, S. A. Pavlov, and A. E. Parafin, Pis'ma Zh. Tekh. Fiz. **24** (1), 55 (1998) [Tech. Phys. Lett. **24**, 24 (1998)].
10. J. R. Tallon, C. Bernhard, H. Shaked, and R. L. Hitterman, Phys. Rev. B **51** (18), 12911 (1995).
11. M. Ohkudo, T. Kachi, T. Hioki, and J. Kawamoto, Appl. Phys. Lett. **55** (9), 899 (1989).
12. Yu. N. Drozdov, S. V. Gaponov, S. A. Gusev, *et al.*, Supercond. Sci. Technol. **9**, A166 (1996).
13. A. K. Vorobiev, Yu. N. Drozdov, S. A. Gusev, *et al.*, Supercond. Sci. Technol. **12**, 908 (1999).
14. M. N. Drozdov, S. V. Gaponov, S. A. Gusev, *et al.*, IEEE Trans. Appl. Supercond. **9** (2), 2371 (1999).
15. V. Matijasevic, P. Rosental, K. Shinohara, *et al.*, J. Mater. Res. **6** (4), 682 (1991).
16. J. L. MacManus-Driscoll, J. L. Alonso, P. C. Wang, *et al.*, Physica C (Amsterdam) **232**, 288 (1994).
17. J. Z. Liu, Y. J. Tian, L. Li, *et al.*, J. Appl. Phys. **77** (3), 1165 (1995).
18. T. I. Selinder, U. Helmersson, Z. Han, *et al.*, Physica C (Amsterdam) **202**, 69 (1992).

Translated by G. Skrebtsov

Physics of the Solid State, Vol. 45, No. 11, 2003, pp. 2031–2035. From Fizika Tverdogo Tela, Vol. 45, No. 11, 2003, pp. 1934–1937.

SEMICONDUCTORS AND DIELECTRICS

Capturing Properties of a Threefold Coordinated Silicon Atom in Silicon Nitride: Positive Correlation Energy Model*

V. A. Gritsenko[1], Yu. N. Novikov[1], A. V. Shaposhnikov[1], H. Wong[2], and G. M. Zhidomirov[3]

[1] *Institute of Semiconductor Physics, Siberian Branch, Russian Academy of Sciences, Novosibirsk, 630090 Russia*
e-mail: grits@isp.nsc.ru

[2] *Department of Electronic Engineering, Hong Kong, China*

[3] *Institute of Catalysis, Siberian Branch, Russian Academy of Sciences, Novosibirsk, 630090 Russia*

Received January 30, 2003

Abstract—The electronic structure and capturing properties of threefold coordinated silicon atoms (≡Si·) and the Si–Si bond in silicon nitride (Si_3N_4) were studied using the *ab initio* density functional theory. The results show that the previously proposed negative correlation energy (NCE) model is not applicable to Si_3N_4. The NCE model was proposed for interpreting the absence of the ESR signal for threefold coordinated silicon defects and suggested that an electron can transfer between two silicon defects. We proposed that the absence of this ESR signal is due to the creation of neutral diamagnetic Si–Si defects in Si_3N_4. This model offers the most fundamental theory for explaining the hole localization (memory) effect in silicon nitride. © *2003 MAIK "Nauka/Interperiodica".*

Carrier capturing in localized states or localization of electrons or holes is a fundamental process that governs the electronic properties of many amorphous solids, such as amorphous silicon, amorphous chalcogenides (*a*-Se, *a*-As_2S_3), and silicon nitride (Si_3N_4) films [1–4]. Amorphous Si_3N_4 is the most common material for observing this phenomenon, as it has a gigantic cross section (5×10^{-13} cm) for carrier capturing. An electron or a hole, after being injected into the Si_3N_4 film, can be captured by a deep trap with a lifetime in the localized state of more than ten years at room temperature [4]. This localization property is treated as a memory effect from the standpoint of application. Its practical application is the use of amorphous Si_3N_4 as a gate dielectric in SONOS (silicon–oxide–nitride–oxide–semiconductor) field effect transistors. Although this memory effect was discovered for more than thirty years ago and is widely used in modern silicon devices [2, 4–8], the exact nature and kind of defects responsible for the carrier localization in nitride films remain a subject of controversy. However, it has already been agreed that the localization of electrons and holes in the Si_3N_4 film is related to the intrinsic defects created by excess silicon atoms [2, 4, 8, 9].

The intrinsic defects in amorphous solids are believed to be due to dangling bonds. However, most of the defects could not be detected with the electron spin resonance (ESR) measurement in a number of amorphous semiconductors and wide-gap polar dielectrics, such as amorphous SiO_2 and Si_3N_4 films [1–4, 10]. The signal for an $N_3Si\cdot$ defect in silicon nitride, a threefold coordinated silicon atom with an unpaired electron, could be detected with ESR only after ultraviolet irradiation [11]. For a freshly synthesized nitride film, no related ESR signal can be detected. This observation was explained with the negative correlation energy (NCE) model [12, 13]. This model suggested that two diamagnetic defects, a positively charged N_3Si^+ and a negatively charged N_3Si^-:, can be formed from an $N_3Si\cdot$ (paramagnetic neutral defects in Si_3N_4) pair via the following reaction:

$$N_3Si\cdot + \cdot SiN_3 \longrightarrow N_3Si^+: + :^-SiN_3. \qquad (1)$$

In the NCE model, the repulsive energy (U_C) of the two electrons localized in the Si atom is overcompensated by the energy gain in lattice relaxation with an energy of U_L and the effective correlation energy $U = U_C + U_L$ becomes negative. According to the NCE model, reaction (1) is energetically favorable in the NCE model and the charged diamagnetic defects (N_3Si^+, N_3Si^-:) are electron and hole traps supposedly responsible for the memory effect in silicon nitride [2, 8, 14–17]. The most recent *ab initio* density functional theory (DFT) calculations [18] showed that the correlation energy for $N_3Si\cdot$ defects is equal to 0.1 eV and the distance between two $N_3Si\cdot$ defects was about 3.1 Å. Hence, the silicon dangling bonds can exchange electrons and the Coulomb interaction at this distance is strong. However, experiments in [4, 19, 20] showed that the electron trap density (N_t^e) and hole trap density

* This article was submitted by the authors in English.

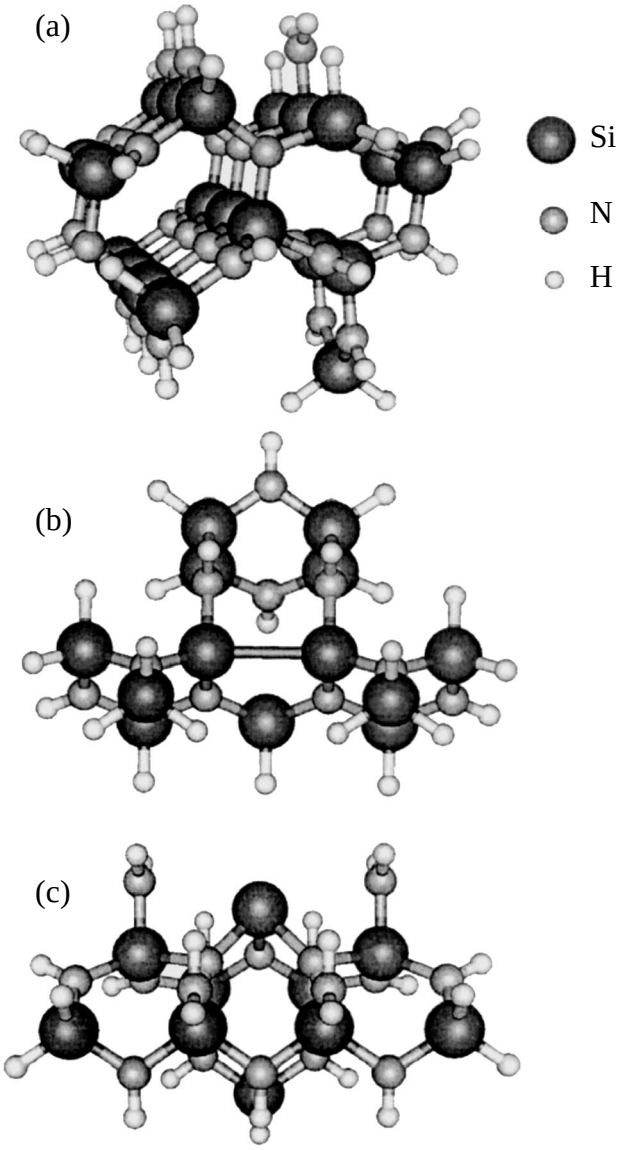

Fig. 1. Cluster models used in the simulation: (a) the 84-atom cluster for bulk nitride simulation, (b) the 56-atom cluster for the Si–Si bond simulation, and (c) the 55-atom cluster for the ≡Si· defect simulation.

(N_t^h) in Si_3N_4 are almost the same and are about 5×10^{18} cm^{-3}. The mean distance (a) between two traps in Si_3N_4 can be estimated from $a \approx (N_t)^{-1/3}$ and is about 60 Å, which is much larger than that used in the *ab initio* DFT calculation conducted by Pacchioni and Erbetta in [18]. At the distance estimated from the experimental trap density, the Coulomb interaction is too weak to make electron exchange between two $N_3Si\cdot$ defects occur. This data suggests that the defect distribution is highly localized within a tetrahedron or between adjacent tetrahedra of the network. In addition, if the distance between two defects is about 3.1 Å, other mechanisms of carrier localization are also possible. It has been suggested that electron and hole capturing could also occur at a neutral diamagnetic ≡Si–Si≡ defect [2, 4, 10, 20, 21]. The validity of these two models for Si_3N_4 is still under discussion. This paper aims to validate the NCE model and the Si–Si bond model in silicon nitride by using quantum-chemical DFT simulation. Quantum-chemical simulation has been successfully used for studying the electronic structures of the defects in silicon oxide and the electronic properties of other defects in Si_3N_4 films [18, 22–25].

The simulations were conducted on $N_3Si\cdot$ and N_3Si–SiN_3 defects created from the fragments of crystalline β-Si_3N_4. Figure 1 shows three clusters used in the simulation. The 84-atom cluster ($Si_{20}N_{28}H_{36}$) with a hydrogen-passivated surface (Fig. 1a) was used for simulating the bulk electronic structure of Si_3N_4 and for estimating the energy gain for carrier capturing. The 56-atom cluster $Si_{14}N_{12}H_{30}$ (shown in Fig. 1b) was used for simulating the capturing properties of the N_3Si–SiN_3 defect. The 55-atom $Si_{10}N_{18}H_{27}$ cluster (shown in Fig. 1c) was used for simulating the properties of the $N_3Si\cdot$ defect. Geometric relaxation of the Si atoms at different charged states was allowed during the simulation.

We performed *ab initio* DFT calculations using the ADF program [26], where the exchange-and-correlation (XC) functional consists of the generalized gradient approximation (GGA) part GGA–XC. The Kohn–Sham molecular orbits were constructed using Slater-type exponential basis functions, and the basis set includes the double-zeta basis with the polarization function for all atoms (i.e., the basis set III in ADF terminology). All electrons were included in the valence basis. In addition, the positions of all Si and N atoms were fully optimized at the nonlocal DFT level using the Becke form [27] of exchange and the Lee–Yang–Parr theory [28].

The energy gains for capturing an electron (ΔE^e) and a hole (ΔE^h) were calculated using the formulas

$$\Delta E^e = (E^-_{\text{bulk}} + E^0_{\text{defect}}) - (E^0_{\text{bulk}} + E^-_{\text{defect}}), \qquad (2)$$

$$\Delta E^h = (E^+_{\text{bulk}} + E^0_{\text{defect}}) - (E^0_{\text{bulk}} + E^+_{\text{defect}}), \qquad (3)$$

where E^0_{bulk}, E^-_{bulk}, and E^+_{bulk} are the total energies of the "bulk" clusters for Si_3N_4 in neutral, negative, and positive charge states, respectively, and E^0_{defect}, E^-_{defect}, and E^+_{defect} are the total energies for the defect clusters in neutral, negative, and positive charge states, respectively. If the value of the energy gain is positive, then capturing of an electron or a hole from the bulk of Si_3N_4 by the $N_3Si\cdot$ or N_3Si–SiN_3 defect will result in a release of energy.

The $N_3Si\cdot$ defect has been discussed intensively in the literature as a defect responsible for the carrier

localization in Si_3N_4 films [4, 8, 9, 18, 29–31]. In agreement with Pacchioni and Erbetta [18], our calculations show that the $N_3Si\cdot$ defect can be a trap for electrons. However, our results show that the $N_3Si\cdot$ defect cannot capture a hole, as this process is energetically unfavorable. This result was also obtained previously by Pacchioni and Erbetta [18]. However, the absence of the paramagnetic signal in a virgin Si_3N_4 film indicates that the $N_3Si\cdot$ defect should not be responsible for the memory effect [2, 10].

To ensure sufficient reliability of the cluster model for simulating the electronic structure of silicon nitride, we simulated the x-ray emission spectra of bulk Si_3N_4. The calculations were performed in the frozen orbital approximation. Dipole matrix elements were calculated between core (Si 1*s*, 2*p*, N 1*s*) orbits and valence orbits. These matrix elements include, in principle, all interatomic matrix elements between the Slater-type functions centered on different atoms. The calculated spectra were then broadened by convoluting the Lorentz curves with a width of 0.5 eV. We found that the Si 3*d* polarization functions must be included in the basis set in order to obtain an Si *L* x-ray emission spectrum that agrees with the experimental results. Our calculations also show that the contributions from Si *K* and N *K* emission spectra to the nonlocal transitions are negligible. Figure 2 shows our calculation results. Previous experimental results for Si *K*, Si *L*, and N *K* spectra [4] are also shown for comparison. In general, good agreement between the calculated and the experimental data is observed. The simulation results show that the main contributions to the valence band of silicon nitride are from N 2*p*, Si 3*s*, 3*p*, and 3*d* orbits.

To verify the NCE model, we calculated the total energies of the 55-atom cluster with the threefold coordinated silicon atom in three different charge states, $N_3Si\cdot$, N_3Si^+, and N_3Si^-:, using the DFT method. To estimate the long-range order lattice polarization during the charge trapping, we used the simplest approach based on the classical Born model [18]. According to this model, the long-range polarization will reduce the total cluster energy of the defect by 0.7 eV. Our simulation shows that the total energy of the two neutral clusters with the $N_3Si\cdot$ defect is 2.1 eV less than the total energies of the negatively charged N_3Si^- defect and the positively charged N_3Si^-: defects when the long-range polarization is taken into account. This indicates that the conversion of a pair of neutral threefold coordinated silicon atoms $N_3Si\cdot$ to a pair of charged diamagnetic states (N_3Si^+ and N_3Si^-:) according to reaction (1) is energetically unfavorable. Moreover, the energy gain U_L from the lattice distortion cannot overcompensate the large Coulomb repulsive energy U_C. Hence, the NCE model is not applicable to the carrier capturing of threefold coordinated silicon atoms in Si_3N_4. Instead, we proposed the formation of a neutral diamagnetic ≡Si–Si≡ bond from the ≡Si· defect pair with a positive correlation energy (PCE). The theory was proposed for silicon defects ($Si_3Si\cdot$) in amorphous silicon [32, 33] and the $O_3Si\cdot$ defect in SiO_2 films [34, 35].

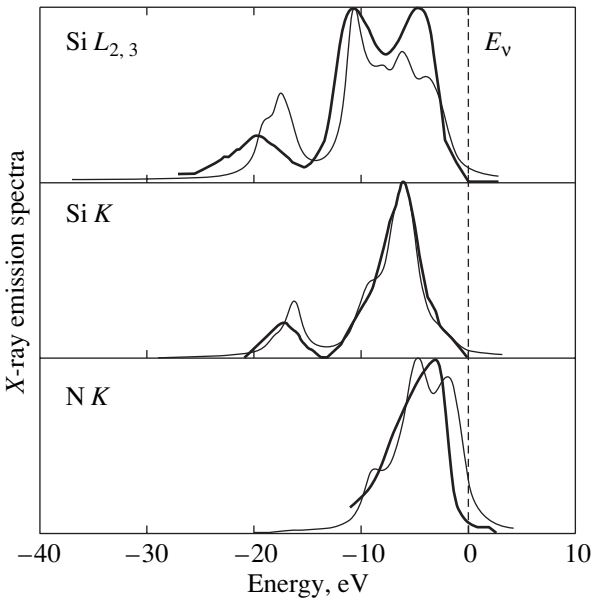

Fig. 2. X-ray emission spectra of silicon nitride calculated using the DFT theory (thin lines). Experimental results [4] are also shown for comparison (thick lines).

The Si–Si bond length in silicon is 2.35 Å, and the silicon–silicon distance in Si_3N_4 is about 3.1 Å [2]. In order to estimate the Si–Si bond length in the N_3Si–SiN_3 defect, we performed DFT calculations at MP2/6, QCISD/6, and B3LYP/6 levels [26]. The $(NH_2)_3Si$–$Si(NH_2)_3$ cluster was used for the simulation. To calculate the energy change of the cluster when the Si–Si bond length deviates from the optimized bond length, we first fixed the N–H bond length and the angle of SiNH in the cluster. According to the simulation, the optimal Si–Si bond length is 2.35 Å, which is the same as the Si–Si bond length in Si (see Fig. 3). To understand the charged state of a $(NH_2)_3Si$–$Si(NH_2)_3$ species, we calculated the Mulliken charge distribution on the two Si atoms of a $(NH_2)_3Si$–$Si(NH_2)_3$ cluster. The increase in the Si–Si bond length is accompanied by an increase in the total cluster energy and gives rise to a symmetric charge distribution in both of the Si atoms. Consequently, two paramagnetic $N_3Si\cdot$ species were created by breaking the Si–Si bond, i.e.,

$$N_3Si\text{–}SiN_3 \rightleftharpoons N_3Si\cdot + \cdot SiN_3. \quad (4)$$

The symmetric charge distribution obtained in this work shows that the creation of two charged N_3Si^+ and N_3Si^-: defects at a distance in the range of 2–3 Å is energetically unfavorable. Instead, the creation of a diamagnetic symmetric Si–Si bond is more favorable.

To determine the most favorable state of the Si atoms, we analyzed the total energies of different clus-

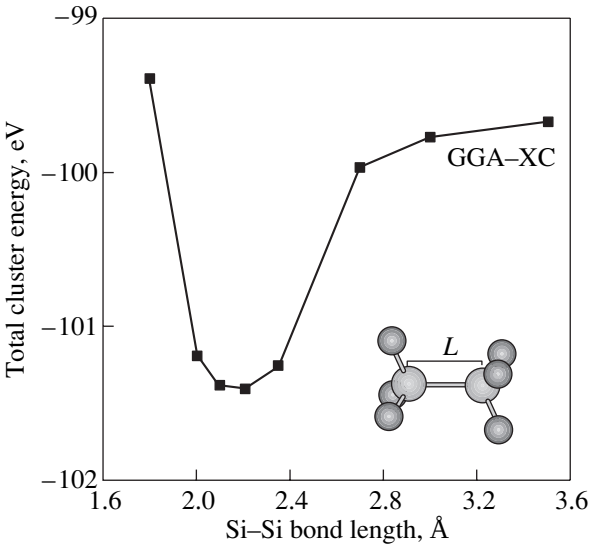

Fig. 3. Plot of the total energy of the $H_6N_3Si–SiN_3H_6$ cluster as a function of the Si–Si bond distance.

ters. The total energy of the $(NH_2)_3Si–Si(NH_2)_3$ cluster is 3.15 eV less than that of the two $(NH_2)_3Si\cdot$ defects, and the total energies of the N_3Si^+ and N_3Si^-: defects are 2.1 eV greater than that of the two $(NH_2)_3Si\cdot$ defects. Hence, the formation of neutral diamagnetic Si–Si bonds is the most favorable, the neutral paramagnetic state $N_3Si\cdot$ is less favorable, and the formation of diamagnetic charged N_3Si^+ and N_3Si^-: states is the least favorable.

We also performed a DFT calculation for a Si–Si bond with a captured hole or electron using the 56-atom $Si_{10}N_{18}H_{27}$ cluster. Our DFT simulation shows that the Si–Si bond in Si_3N_4 can capture a hole. This result is similar to the SiO_2 case. The calculated energy gain for the hole captured on the Si–Si bond is about 1 eV. The hole capturing on a Si–Si bond plays an important role in silicon devices with oxynitride acting as the gate dielectric [36]. Si–Si bonds were observed experimentally at the Si_3N_4–thermal oxide interface in [21]. Excess hole and electron capturings at the interface have also been found [37, 38].

The presence of Si–Si bonds naturally explains the absence of the ESR signal in the virgin Si_3N_4 film. The model also predicts that the Si–Si defect becomes paramagnetic after hole capturing. However, experiments have shown that carrier capturing in Si_3N_4 cannot be detected with ESR measurement [2, 10]. An explanation for the absence of the ESR signal in Si_3N_4 with captured carriers was proposed in [10, 38]. It was attributed to the spin coupling of the hole localized by the Si–Si bond as a result of resonance tunneling via nonoccupied traps [10, 38]. In fact, both electron and hole localization were found in silicon nitride. Since the Si–Si bond can capture an electron in amorphous silicon [32, 33], one may suggest that the Si–Si bond in Si_3N_4 can also capture an electron. However, the DFT results do not predict electron capturing by Si–Si bonds due to the negative energy gain. Thus, we have to find other possibilities for the electron capturing effect in silicon nitride. We have suggested that the electron localization in Si_3N_4 is due to the twofold coordinated nitrogen atom [39].

In conclusion, we believe that the creation of a pair of charged diamagnetic defects, $\equiv Si^+$ and $\equiv Si^-$:, from a neutral diamagnetic $\equiv Si\cdot$ defect pair with negative correlation energy (NCE) is invalid in silicon nitride for the following reasons.

(1) New *ab initio* DFT quantum-chemical simulation results suggest that hole capturing in the $N_3Si\cdot$ defect is energetically unfavorable.

(2) The energy gain U_L from the lattice distortion cannot overcompensate the large Coulomb repulsive energy U_C in the NCE model.

In this connection, we proposed the formation of a neutral diamagnetic $\equiv Si–Si\equiv$ bond from the $\equiv Si\cdot$ defects pair with the PCE. Simulation shows that the $\equiv Si–Si\equiv$ bond in Si_3N_4 can capture holes. This model explains the memory effect in silicon nitride.

ACKNOWLEDGMENTS

This work was supported by the Siberian Branch of the Russian Academy of Sciences (project no. 116) and by a project of the Russian Academy of Sciences.

This work was partially supported by research project no. 7001134 of City U.

REFERENCES

1. N. F. Mott and E. A. Davis, *Electronic Processes in Non-Crystalline Materials*, 2nd ed. (Clarendon, Oxford, 1979; Mir, Moscow, 1982).
2. W. L. Warren, J. Kanicki, J. Robertson, *et al.*, J. Appl. Phys. **74**, 4034 (1993).
3. V. A. Gritsenko, *Structure and Electronic Properties of Amorphous Dielectrics in Silicon MIS Structures* (Nauka, Novosibirsk, 1993).
4. V. A. Gritsenko, in *Silicon Nitride in Electronics*, Ed. by A. V. Rzhanov (Elsevier, New York, 1988).
5. H. Bachofer, H. Reisinger, E. Bertagnolli, and H. von Philipsborn, J. Appl. Phys. **89**, 2791 (2001).
6. J. Bu and M. H. White, Solid State Electron. **45**, 113 (2001).
7. B. Eitan, P. Pavan, I. Bloom, *et al.*, IEEE Electron Device Lett. **21**, 543 (2000).
8. Y. Yang and M. H. White, Solid State Electron. **44**, 949 (2000).
9. S. Fujita and A. Sasaki, J. Electrochem. Soc. **132**, 398 (1985).
10. V. A. Gritsenko and A. D. Milov, Pis'ma Zh. Éksp. Teor. Fiz. **64**, 489 (1996) [JETP Lett. **64**, 531 (1996)].

11. W. L. Warren and P. M. Lenahan, Phys. Rev. B **42**, 1773 (1990).
12. P. W. Anderson, Phys. Rev. Lett. **34**, 953 (1975).
13. R. A. Street and N. F. Mott, Phys. Rev. Lett. **35**, 1293 (1975).
14. J. Robertson, Appl. Phys. Lett. **44**, 415 (1984).
15. E. E. Meerson and S. P. Sinitsa, Microelectronics **16**, 37 (1987).
16. S. E. Gurri, P. M. Lenahan, D. T. Krick, *et al.*, Appl. Phys. Lett. **56**, 1359 (1990).
17. Y. Roizin and L. Tsibeskov, J. Non-Cryst. Solids **137–138**, 515 (1991).
18. G. Pacchioni and D. Erbetta, Phys. Rev. B **61**, 15005 (2000).
19. V. A. Gritsinko, E. E. Meerson, I. V. Travkov, and Yu. V. Goltviansky, Microelectronics **16**, 42 (1987).
20. Y. Kamigaki, S. Minami, and H. Kato, J. Appl. Phys. **68**, 2211 (1990).
21. V. A. Gritsenko, H. Wong, J. B. Xu, *et al.*, J. Appl. Phys. **86**, 3234 (1999).
22. G. Pacchioni, Phys. Rev. Lett. **79**, 753 (1997).
23. G. Pacchioni, G. Ierano, and A. M. Marquez, Phys. Rev. Lett. **81**, 377 (1998).
24. G. Pacchioni and D. Erbetta, Phys. Rev. B **60**, 12617 (1999).
25. C. Fonseca Guerra, J. G. Snijders, G. Te Velde, and E. J. Baerends, Theor. Chem. Acc. **99**, 391 (1998).
26. A. D. Becke, Phys. Rev. A **38**, 3098 (1988).
27. C. Lee, W. Yang, and R. G. Parr, Phys. Rev. B **37**, 785 (1988).
28. J. K. Rudra and W. B. Fowler, Phys. Rev. B **35**, 8223 (1987).
29. D. T. Krick, P. M. Lenahan, and J. Kanicki, Phys. Rev. B **38**, 8226 (1988).
30. J. Robertson, Philos. Mag. B **69**, 307 (1994).
31. T. Umeda, S. Yamasaki, J. Isoya, *et al.*, Phys. Rev. Lett. **77**, 4600 (1996).
32. T. Umeda, S. Yamasaki, J. Isoya, and K. Tanaka, Phys. Rev. B **62**, 15702 (2000).
33. W. B. Fowler, J. K. Rudra, M. E. Zvanut, and F. J. Feigle, Phys. Rev. B **41**, 8313 (1990).
34. W. L. Warren, E. H. Poindexter, M. Offenberg, and W. Muller-Warmuth, J. Electrochem. Soc. **139**, 872 (1992).
35. V. A. Gritsenko, J. B. Xu, R. M. Kwok, *et al.*, Phys. Rev. Lett. **35**, 1293 (1998).
36. E. Suzuki, Y. Hayashi, and T. Tsuchiya, Appl. Phys. Lett. **42**, 608 (1983).
37. Z. A. Weinberg, K. J. Stein, T. N. Nguen, and J. Y. Sun, Appl. Phys. Lett. **57**, 1248 (1990).
38. V. A. Gritsenko, Pis'ma Zh. Éksp. Teor. Fiz. **64**, 483 (1996) [JETP Lett. **64**, 525 (1996)].
39. Yu. N. Morokov, Yu. N. Novikov, V. A. Gritsenko, and H. Wong, Microelectron. Eng. **48**, 175 (1999).

Physics of the Solid State, Vol. 45, No. 11, 2003, pp. 2036–2038. Translated from Fizika Tverdogo Tela, Vol. 45, No. 11, 2003, pp. 1938–1940.

SEMICONDUCTORS AND DIELECTRICS

Observation of Bose Condensation in $(Pb_{0.4}Sn_{0.6})_{0.86}In_{0.14}Te$ Semiconductor Solid Solutions Using Mössbauer Spectroscopy

S. A. Nemov*, P. P. Seregin*, Yu. V. Kozhanova*, V. P. Volkov*, N. P. Seregin, S. M. Irkaev**, and D. V. Shamshur*****

**St. Petersburg State Polytechnical University, Politekhnicheskaya ul. 25, St. Petersburg, 195251 Russia*

***Institute of Analytical Instrumentation, Russian Academy of Sciences, St. Petersburg, 198103 Russia*

****Ioffe Physicotechnical Institute, Russian Academy of Sciences, Politekhnicheskaya ul. 26, St. Petersburg, 194021 Russia*

Received March 18, 2003

Abstract—^{73}As(^{73}Ge) Mössbauer emission spectroscopy is used to ascertain that the transition of the $(Pb_{0.4}Sn_{0.6})_{0.86}In_{0.14}Te$ solid solution to a superconducting state is accompanied by a change in electronic density at the cation sites, and spatial inhomogeneities in the Bose condensate of Cooper pairs are revealed. © *2003 MAIK "Nauka/Interperiodica".*

Semiconductors transfer to a superconducting state, as a rule, at temperatures as low as a few tenths of a degree Kelvin [1]. In this respect, $(Pb_{1-x}Sn_x)_{1-z}In_zTe$ semiconductor solid solutions are highly remarkable, as they exhibit the highest critical temperature observed thus far in semiconductors, 4.2 K [2].

Following the Bardeen–Cooper–Schrieffer (BCS) theory, superconductivity is due to the formation of a Bose condensate of Cooper pairs described by a common coherent wavefunction, with the electronic density distributions at lattice sites of the superconductor above and below the superconducting transition temperature T_c being different [3]. Studying superconducting materials with the use of the Mössbauer effect appears a promising area of investigating the properties of the Bose condensate; indeed, it becomes, in principle, possible to detect Bose condensation of Cooper pairs by measuring the temperature dependence of the center of gravity S in the Mössbauer spectra of superconductors [4]. This dependence contains three terms [5]: the first of them describes the dependence of the isomer shift I on volume V, the second allows for the effect of the second-order Doppler shift D, and the third describes the temperature dependence of the isomer shift I. The last term reflects the variation of electronic density at the sites of Mössbauer nuclei, and it is this effect that is expected to be observed as the matrix transfers to a superconducting state.

To make such a study, one has to choose an appropriate Mössbauer probe. In particular, attempts at detecting Bose condensation using Mössbauer spectroscopy on the ^{119}Sn isotope in the Nb_3Sn superconductor have not met with success [6]; the experimental $S(T)$ relation, in fact, could be fitted satisfactorily with the second-order Doppler shift, and no features in the behavior of $S(T)$ that could be assigned to a change in the electronic density on ^{119}Sn nuclei at lattice sites were observed. In addition, no anomalous variation in the magnitude of S in the Mössbauer spectra of ^{57}Fe impurity atoms in high-temperature superconductors has been found [7]. These observations are accounted for by the small magnitude of Δ/G (here, Δ is the largest attainable difference in isomer shifts of Mössbauer spectra between the normal and superconducting phases, G is the experimental width of the nuclear level), which does not exceed 6 for Mössbauer spectroscopy using the ^{57}Fe and ^{119}Sn isotopes.

To detect Bose condensation using Mössbauer spectroscopy, one obviously needs to employ a probe for which $\Delta/2G \gg 10$. In choosing objects for the study, the need to place Mössbauer probes at lattice sites should also be taken into account. These conditions were shown in [4] to be met for the ^{67}Zn Mössbauer probe in cuprate lattices in the ^{67}Cu(^{67}Zn) Mössbauer emission spectroscopy version. It was established, in particular, that the transition to a superconducting state changes the electronic density at the metal sites of cuprate lattices, and a relation was observed experimentally between the change in electronic density and the transition temperature of the crystal to a superconducting state. The expected change in the electronic density at the sites of ^{67}Zn nuclei in materials with $T_c < 10$ K turns out to be extremely small; therefore, reliable observation of a change in the electronic density upon the superconducting transition in $Pb_{1-x}Sn_xTe$:In-based semiconductors using ^{67}Zn spectroscopy is very unlikely [8].

The present paper reports on a study of Bose condensation in $(Pb_{1-x}Sn_x)_{1-z}In_zTe$-type semiconductors using Mössbauer emission spectroscopy on the ^{73}As(^{73}Ge) isotope. For ^{73}As, we have $\Delta/2G \sim 2000$ [9];

furthermore, the parent isotope ^{73}As can be doped during the preparation of $(Pb_{1-x}Sn_x)_{1-z}In_zTe$ solid solutions into the sites of both lead (tin) and tellurium [10].

The formation of the ^{73}Ge Mössbauer level after radioactive decay of the parent isotope ^{73}As is displayed schematically in [11]. In view of the fact that the ^{73}Ge daughter atom recoil energy due to the electron capture in ^{73}As and neutrino emission does not exceed the energy needed to displace atoms from their normal positions [12], one may reasonably expect the radioactive transformation not to displace germanium atoms from normal lattice sites and, hence, the parameters of ^{73}As(^{73}Ge) Mössbauer emission spectra to reflect the state of ^{73}Ge atoms localized on either the cation or the anion sublattice.

The ^{73}As radioactive isotope was obtained in the ^{74}Ge(p, $2n$) $\longrightarrow$ ^{73}As reaction, and the carrier-free ^{73}As isotope was isolated following a technique based on the large difference in volatilities between the target and parent atoms [13]. For this purpose, a proton-irradiated single-crystal germanium film containing ~98 at. % of the ^{74}Ge isotope was held for three months (to reduce the content of radioactive ^{74}As) and was then placed into an evacuated quartz ampoule. The ampoule end housing the target was heated for 5 h at 900 K in a tubular furnace. Upon opening the ampoule, ~80% of ^{73}As atoms turned out to be sorbed on its inner walls. The carrier-free ^{73}As deposit was removed with a nitric acid solution.

Mössbauer sources were prepared through diffusive doping of $(Pb_{1-x}Sn_x)_{1-z}In_zTe$ polycrystalline samples by radioactive ^{73}As in evacuated quartz ampoules at 773 K for 10 h, the concentration of arsenic impurity atoms being no greater than 10^{16} cm^{-3}. The starting $(Pb_{0.4}Sn_{0.6})_{0.86}In_{0.14}Te$ samples became superconducting at $T_c \approx 4.2$ K, whereas the starting $(Pb_{0.4}Sn_{0.6})_{0.97}In_{0.03}Te$ samples remained in the normal state down to 2 K. Diffusive annealing did not affect the value of T_c of $(Pb_{0.4}Sn_{0.6})_{0.86}In_{0.14}Te$ noticeably.

The ^{73}As(^{73}Ge) Mössbauer spectra were measured on an SM-2201 commercial spectrometer in the standard transmission geometry. The absorbers were either single-crystal ^{73}Ge (when obtaining spectra of the ^{73}Ge probe on the anion sublattice) or ^{73}GeTe (when obtaining spectra of the ^{73}Ge probe on the cation sublattice). All absorbers were enriched in ^{73}Ge to ~90 at. %.

We measured spectra with these absorbers and a Ge : ^{73}As source (a proton-irradiated ^{74}Ge single-crystal target held for two months and subsequently annealed at 500 K in a hydrogen environment for 5 h). The spectrum obtained with a ^{73}Ge absorber featured a single line with a half-width at half-maximum $G_{exp} = 30.8 \pm 0.5$ μm/s, which is substantially in excess of the natural ^{73}Ge line ($G_{nat} \sim 6.98$ μm/s) and is accounted for by incomplete annealing of radiation defects in the target used as the Mössbauer source. No resonance absorption was observed with the ^{73}GeTe absorber, which can be assigned to the large isomer shift (at least, larger than 10^3 μm/s) of the Mössbauer spectrum.

In full accordance with [10], the spectra of the sources $(Pb_{0.4}Sn_{0.6})_{0.86}In_{0.14}Te$:^{73}As and $(Pb_{0.4}Sn_{0.6})_{0.97}In_{0.3}Te$:^{73}As taken in the range 2–297 K are single lines; the widths of these spectra far exceed the natural width of the ^{73}Ge spectral line (for the spectra measured with the GeTe absorber, $G_{exp} \sim 50$ μm/s, and in the case of the Ge absorber, $G_{exp} \sim 100$ μm/s). At any rate, in the case of the ^{73}GeTe absorber, this broadening is partially due to the distorted cubic germanium atom environment in the GeTe lattice.

The spectra obtained with the ^{73}Ge absorber should be assigned to $^{73}Ge^0$ centers on the anion sublattice of the $(Pb_{1-x}Sn_x)_{1-z}In_zTe$ solid solution (the local environment of these centers contain lead atoms); the $^{73}Ge^0$ atoms form from the ^{73}As atoms on the anion sublattice of $(Pb_{1-x}Sn_x)_{1-z}In_zTe$. The spectrum measured with the ^{73}GeTe absorber is due to $^{73}Ge^{2+}$ centers on the cation sublattice of $(Pb_{1-x}Sn_x)_{1-z}In_zTe$ (the nearest environment of these centers have tellurium atoms), which obviously form from the ^{73}As atoms on the cation sublattice of $(Pb_{1-x}Sn_x)_{1-z}In_zTe$. Thus, one may conclude that arsenic impurity atoms in the $(Pb_{1-x}Sn_x)_{1-z}In_zTe$ lattice are localized on both the anion and cation sublattices.

As already mentioned, to detect Bose condensation of Cooper pairs in superconductors using Mössbauer spectroscopy, one has to measure the temperature dependence of the center of gravity S of a Mössbauer spectrum. At a constant pressure P, this relation can be written as

$$(\delta S/\delta T)_P = (\delta I/\delta \ln V)_T(\delta \ln V/\delta T)_P + (\delta D/\delta T)_P + (\delta I/\delta T)_V. \quad (1)$$

(The physical meaning of all three terms in Eq. (1) were given earlier.) Here,

$$I = \alpha\Delta|\Phi(0)|^2 \quad (2)$$

$\Delta|\Phi(0)|^2$ is the difference between the electronic densities on the nuclei under study in the two samples and α is a constant depending on the nuclear parameters of the isotope used.

As seen from the figure, the experimental temperature dependence of the center of gravity S of the spectrum corresponding to the ^{73}Ge probe on the cation sublattice of the $(Pb_{0.4}Sn_{0.6})_{0.97}In_{0.03}Te$ solid solution measured in the temperature range 2–297 K coincides with the theoretical relation derived for the temperature dependence of the second-order Doppler shift

$$(\delta D/\delta T)_P = -(3kE_0/2Mc^2)F(T/\Theta) \quad (3)$$

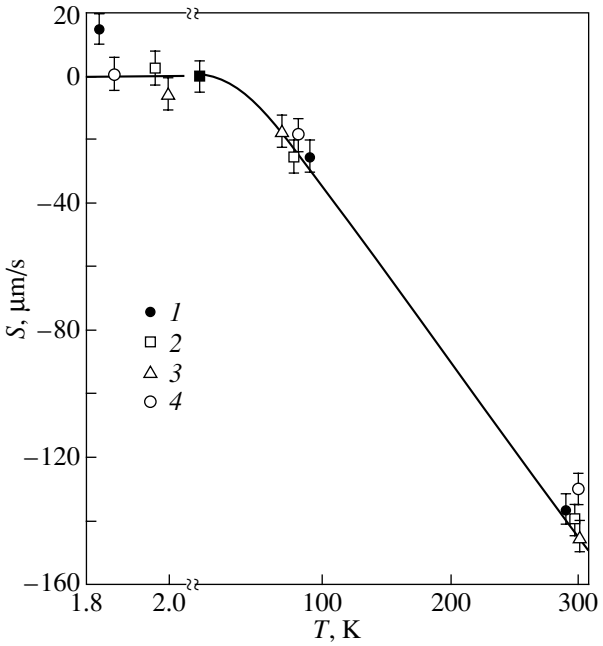

Temperature dependences of the position of the center of gravity S (relative to its position at 4.2 K) of Mössbauer spectra obtained for ^{73}Ge located on (*1*, *2*) cation sites and (*3*, *4*) anion sites of the solid solution sources (*1*, *3*) $(Pb_{0.4}Sn_{0.6})_{0.86}In_{0.14}Te$ and (*2*, *4*) $(Pb_{0.4}Sn_{0.6})_{0.97}In_{0.03}Te$. The solid line plots the theoretical temperature dependence of S for the case of the second-order Doppler shift at Θ = 130 K.

(k is the Boltzmann constant, E_0 is the isomer transition energy, M is the probe nucleus mass, c is the velocity of light in vacuum, Θ is the Debye temperature, $F(T/\Theta)$ is the Debye function), if one uses the Debye temperatures derived from heat capacity measurements [14].

In the case of the $(Pb_{0.4}Sn_{0.6})_{0.86}In_{0.14}Te$ superconducting solid solution, the $S(T)$ relation for the spectrum corresponding to the ^{73}Ge probe located on the cation sublattice of the solid solution at $T > T_c$ is also described by the second-order Doppler shift (3); for temperatures $T < T_c$, however, the quantity S depends on temperature more strongly than one would expect from Eq. (3), which suggests that in Eq. (1) one should take into account the temperature dependence of the isomer shift.

The situation is different in the case of the ^{73}Ge probe on the anion sublattice of the $(Pb_{1-x}Sn_x)_{1-z}In_zTe$ solid solutions. As is evident from the figure, the experimental temperature dependence of the center of gravity S of the spectrum in the 2- to 297-K temperature range practically coincides with the theoretical temperature dependence of the second-order Doppler shift for both the superconducting and the reference samples. This obviously indicates the presence of spatial inhomogeneities in the Bose condensate of Cooper pairs in the lattice of the $(Pb_{1-x}Sn_x)_{1-z}In_zTe$ solid solutions.

Thus, it has been established that the transition to a superconducting state brings about a change in the electronic density at the cation sites of the $(Pb_{0.4}Sn_{0.6})_{0.86}In_{0.14}Te$ solid solution and that the Bose condensate of Cooper pairs is spatially inhomogeneous.

ACKNOWLEDGMENTS

This study was supported by the Russian Foundation for Basic Research, project no. 02-02-17306.

REFERENCES

1. M. Cohen, G. Gladstone, M. A. Jensen, and J. R. Schrieffer, *Superconductivity*, Ed. by R. Parks (Marcel Dekker, New York, 1969; Mir, Moscow, 1972), Vols. 1 and 2.
2. R. V. Parfeniev, D. V. Shamshur, and M. F. Shakhov, J. Alloys Compd. **219**, 313 (1995).
3. J. R. Schrieffer, *Theory of Superconductivity* (Benjamin, New York, 1964; Nauka, Moscow, 1970).
4. N. P. Seregin and P. P. Seregin, Zh. Éksp. Teor. Fiz. **118**, 1421 (2000) [JETP **91**, 1230 (2000)].
5. D. L. Nagy, in *Mössbauer Spectroscopy of Frozen Solutions*, Ed. by A. Vertes and D. L. Nagy (Akademiai Kiado, Budapest, 1990; Mir, Moscow, 1998).
6. J. S. Shier and R. D. Taylor, Phys. Rev. **174**, 346 (1968).
7. Yun-Bo Wang, Guo-Hui Cao, Yang Li, *et al.*, Physica C (Amsterdam) **282–287**, 1087 (1997).
8. S. A. Nemov, N. P. Seregin, and S. M. Irkaev, Fiz. Tekh. Poluprovodn. (St. Petersburg) **36**, 1351 (2002) [Semiconductors **36**, 1267 (2002)].
9. A. Svane, J. Phys. C.: Solid State Phys. **21**, 5369 (1988).
10. S. A. Nemov, P. P. Seregin, S. M. Irkaev, and N. P. Seregin, Fiz. Tekh. Poluprovodn. (St. Petersburg) **37** (3), 279 (2003) [Semiconductors **37**, 263 (2003)].
11. *Radionuclide Decay Schemes. Energy and Intensity of Radiation* (Énergoatomizdat, Moscow, 1987), p. 147.
12. L. Pfeiffer, R. S. Raghavan, C. P. Lichtenwalner, and A. G. Cullis, Phys. Rev. B **12**, 4793 (1975); L. Pfeiffer, T. Kovacs, G. K. Celler, *et al.*, Phys. Rev. B **27**, 4018 (1983).
13. S. I. Bondarevskiĭ, V. V. Eremin, and N. P. Seregin, in *Fundamental Studies in Technical Universities: Proceedings of V All-Russian Conference on Problems in Science and Higher School, St. Petersburg, 2001*, p. 121.
14. Yu. I. Ravich, B. A. Efimova, and I. A. Smirnov, *Semiconducting Lead Chalcogenides* (Nauka, Moscow, 1968; Plenum, New York, 1970).

Translated by G. Skrebtsov

Physics of the Solid State, Vol. 45, No. 11, 2003, pp. 2039–2043. Translated from Fizika Tverdogo Tela, Vol. 45, No. 11, 2003, pp. 1941–1945.

SEMICONDUCTORS AND DIELECTRICS

Propagation of Nonequilibrium Acoustic Phonons in High-Purity Coarse-Grained ZnTe

V. S. Bagaev, T. I. Galkina, A. I. Sharkov, A. Yu. Klokov, V. P. Martovitskiĭ, V. V. Zaĭtsev, and Yu. V. Klevkov

Lebedev Physical Institute, Russian Academy of Sciences, Leninskiĭ pr. 53, Moscow, 119991 Russia

e-mail: shark@lebedev.ru

Received March 27, 2003

Abstract—Propagation of nonequilibrium acoustic phonons in coarse-grained ZnTe obtained through vacuum sublimation was studied using the heat pulse method under both optical and metallic-heater phonon generation. The phonon mean free paths in the samples studied were shown to be 14 μm and to be dominated by scattering from twin boundaries. © *2003 MAIK "Nauka/Interperiodica".*

1. INTRODUCTION

Studies of wide band-gap II–VI semiconductor compounds are stimulated by their numerous areas of possible application. All these compounds are semiconductors that exhibit direct transitions, which accounts for the high efficiency of the recombination radiation. In addition, they have fairly high electrooptical coefficients and comparatively low dielectric constants. These features stimulated original ideas, some of which have been implemented in new components and related devices. These are, first and foremost, light-emitting diodes and lasers operating in the near IR and visible regions, optical filters, solar cells, x-ray and gamma-radiation detectors, and high-sensitivity electrooptical sensors for coherent detection at frequencies above 30 THz [1]. Even such a property as a fairly low thermal conductivity, which is largely unfavorable for the above applications, may find use in developing thermal insulation layers (heat barriers) in some devices, as well as in the intercalation of some special-purpose ceramics.

Extensive application of the II–VI compounds is still impeded, however, by the serious technological difficulties inherent in preparing these substances with controllable electrophysical parameters. To eliminate these difficulties and develop a controlled technology for preparing single crystals, granular and polycrystalline materials, films, and related multilayer heterostructures, comprehensive studies of the complex processes involved in electron–phonon and interimpurity interactions and of the role played by extended defects in the formation of deep electronic states are presently being carried out (see, e.g., [2, 3]).

Information on acoustic-phonon mean free paths in the II–VI compounds, which is needed for low-temperature heat transport calculations, is practically lacking. This information can be derived, albeit very roughly, from thermal conductivity measurements. At the same time, the heat pulse technique permits one to obtain separate information on the propagation of longitudinal and transverse phonons. Indeed, separate arrival of phonons of different polarizations was detected in single-crystal ZnTe in [4].

Photoluminescence shows coarse-grained ZnTe prepared by vacuum sublimation to contain a considerably smaller number of impurities [2]; nevertheless, acoustic phonons should quite obviously undergo additional scattering from grain boundaries (as demonstrated in [5] for CVD-produced diamond films) and from twinning planes (as observed in CdTe in [6]). The present study was aimed at obtaining information on mean free paths of acoustic phonons in a coarse-grained material (ZnTe).

2. SAMPLE

Thick (1.5–2 mm) coarse-grained ZnTe condensates close in composition to the stoichiometric composition of the grains were deposited on the walls of a quartz tube at temperatures below 650°C in dynamic vacuum. The starting polycrystalline ZnTe was synthesized from preliminarily purified components at a temperature ~$0.5T_{melt}$, followed by triple purification from chemical impurities until it reached the stoichiometric composition (the so-called P_{min} point at 650°C). The total content of impurities was determined using spark mass spectrometry at an analytical center (laboratory of mass spectrometry and chromatography at GIREDMET). The total content of impurities in polycrystalline ZnTe (with exclusion of the gaseous impurities H, C, N, O, F, S, Cl) was found not to exceed 0.0006 wt %.

The ZnTe sample under study (ZT04) was a plate 10×5 mm in size and 1200 μm in thickness. Figure 1 presents a photograph of its surface made with a UNION-6551 optical microscope. To reveal the grain boundaries and emergence of twinning planes more

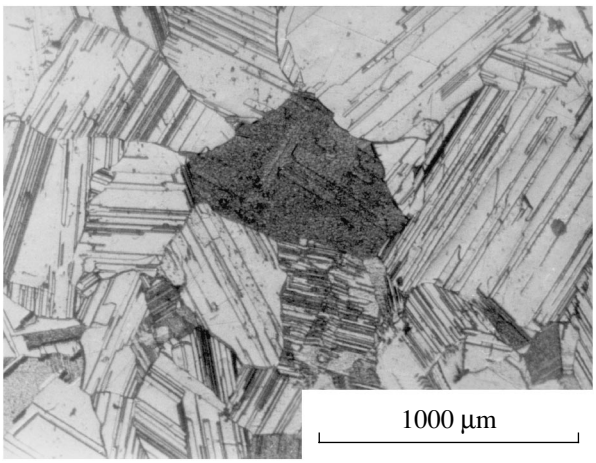

Fig. 1. Image of the ZnTe surface after etching with a 12.5 *N* NaOH solution. Polycrystalline structure of the material with a grain size of ~200 μm and emerging twin planes can be seen.

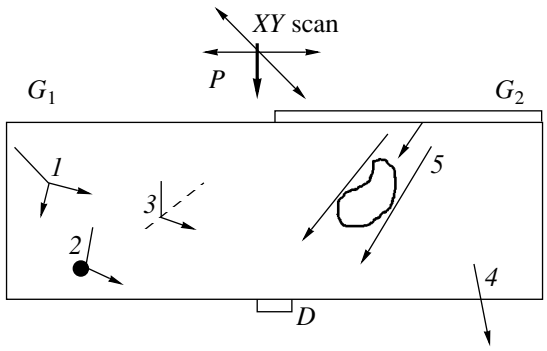

Fig. 2. Schematic of the experiment and the main processes occurring with nonequilibrium phonons. *P* stands for phonon generation by a pulsed laser beam that can sweep over the front surface of the sample; G_1 and G_2 refer to phonon generation by photoexcitation and gold film heating, respectively; and *D* denotes a thin-film superconducting bolometer: case *1* is spontaneous anharmonic phonon decay, *2* is phonon scattering from point defects, *3* is scattering from plane defects, *4* shows phonons exiting the sample into liquid helium, and *5* shows bolometer shadowing.

clearly, the sample was etched in a 12.5 *N* NaOH solution for 1 min. The sample is seen to consist of randomly oriented grains, a few tens to hundreds of micrometers in size, having a twin structure, with the distance between the twinning planes ranging typically from a few to tens of micrometers. In addition, on one side of the plate, separate clusters of pits up to two hundred micrometers in size were visible (Fig. 1).

X-ray characterization of the sample was carried out on a DRON-2.0 standard diffractometer by using a special technique [7] permitting determination of the orientation and structural perfection of an individual grain, as well as the presence of twins in it. The results obtained agree fully with the etch pattern displayed in Fig. 1. The reflection profiles corresponding to large Bragg angles {531} (Θ_B = 48.44°) and {620} (Θ_B = 53.13°) consist of narrow, well-separated $K_{\alpha 1}$, $K_{\alpha 2}$ peaks. This implies that microstrains are absent in the grains and that there are large regions of coherent x-ray scattering (>1000 Å). In most grains, one of the ⟨111⟩ directions lies in the plane of the plate; therefore, the grains in the plane of the plate are predominantly (100) oriented. In a few grains, the [111] direction emerges practically perpendicular to the sample surface. Such grains do not contain any twin layer traces in the etch pattern.

3. EXPERIMENTAL

The propagation of nonequilibrium acoustic phonons was studied using the heat pulse technique in transmission geometry, where phonons are generated on the sample side facing the detector. The schematic of the experiment and the main processes occurring with phonons are shown in Fig. 2. Nonequilibrium acoustic phonons are produced in the sample by pulsed excitation *P*; in this case, two methods of generating nonequilibrium phonons were employed, namely, photoexcitation of the sample surface G_1 by an LGI-21 pulsed nitrogen laser (λ = 337 nm, τ_P = 10 ns) and heating by these pulses of a 150-nm-thick gold film G_2 deposited on the sample surface. The spectra of emitted phonons differ in these two cases; in fact, in the former case, the generated phonons have a higher frequency (~3.1 THz) than in the latter case (<1.5 THz). After this, the phonons propagate along the sample while undergoing (*1*) spontaneous anharmonic decay and elastic scattering from (*2*) point defects (isotopes, impurity atoms) and (*3*) plane defects (grain boundaries, twinning planes). If a grain boundary is in contact with liquid helium, most of the phonons striking it leave the sample (as indicated by arrow *4*).

The arrival of nonequilibrium phonons was detected on a thin-film bridge-shaped superconducting bolometer *D* of granular aluminum [8], with a 50 × 70-μm detecting area. The sample was immersed in liquid helium at a temperature 1.8 K.

The measuring system included a RUZ-33 broadband preamplifier and a computer-controlled V9-5 gated voltage transducer. The time resolution of the recording system was about 5 ns. The laser beam could be swept over the front side of the plate to reveal features in the spatial distribution of nonequilibrium phonons in the sample.

The photoluminescence spectra were recorded at 5 K. Optical excitation was produced by a He–Cd laser with a photon energy of 2.808 eV (441.6 nm). The spectrum was analyzed using a double monochromator with a resolution of 0.1 meV. The PM tube output was measured in the photon-counting mode.

4. RESULTS AND DISCUSSION

Figure 3 presents a photoluminescence spectrum of the ZnTe sample. Note the high emission intensity in the edge region, which exhibits, besides the brightest A^0X line due to photoluminescence of the excitons localized at neutral acceptors, fairly intense radiation originating from the lower (LP) and upper (UP) polariton branches, as well as from the free-exciton excited state (n = 2 FE). Note that the existence of fairly strong intrinsic radiation in the exciton region, as well as its shape, attests to the high perfection of the crystallites and, furthermore, provides indirect evidence of a low acceptor concentration, whose average value does not exceed 10^{15} cm^{-3}. It should also be pointed out that the acceptor impurities are distributed nonuniformly in the sample, which is indicated by the asymmetric shape of the A^0X line having a long-wavelength tail. In addition to the main A^0X line, the spectrum also reveals the so-called two-hole transitions (the line notation is the same as that in [2]).

The long-wavelength part of the spectrum has weak lines (Y_1, Y_2) originating from extended defects. Note also that our samples do not reveal radiation due to oxygen, which is observed both in single crystals and in MBE-grown films [2, 9].

Thus, the undoped polycrystalline ZnTe samples studied here differ from the single crystals reported on in [10], on the one hand, in that the content of residual impurities in them is lower (by about two orders of magnitude) and the concentration of point nonstoichiometric defects is a few orders of magnitude lower, and, on the other, by the presence of a large number of plane defects (grain boundaries and twinning planes). This suggests that phonon scattering in polycrystalline samples should occur primarily from plane defects, such as twinning planes and grain boundaries, and, hence, have a different frequency behavior.

Figure 4 depicts a bolometer response over a time of ~50 ns recorded under photoexcitation of the ZnTe surface. The observed peak was assigned in [10] to the arrival of ZnTe photoluminescence, because direct propagation of light with a wavelength λ = 337 nm is ruled out. The amplitude of this peak and the decay time are substantially less than those observed in ZnTe single crystals [10], which should possibly be attributed to the photoluminescence centers being different (in [10] these centers are apparently oxygen atoms).

Figure 5 displays time-resolved bolometer responses to the arrival of nonequilibrium phonons produced in photoexcitation (filled circles) and by a heated gold film (open circles); the responses were measured under conditions where the phonons were generated directly opposite the detector. In these two cases, the responses are seen to be practically indistinguishable and to have a characteristic diffusive pattern, i.e., a long duration (~10 μs) and a smooth leading edge (~2 μs)

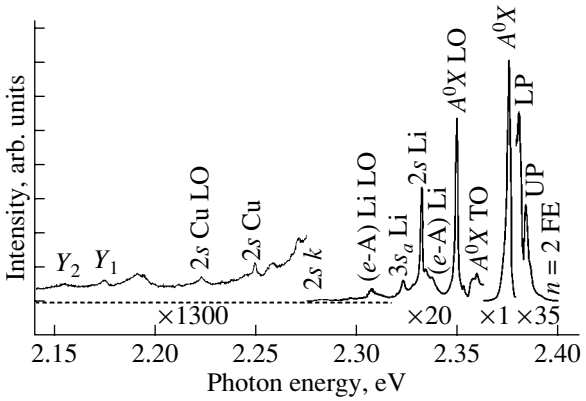

Fig. 3. Photoluminescence spectrum of polycrystalline ZnTe at 5 K; pump power 20 mW, excitation photon energy 2.808 eV, and spot size 0.5 mm.

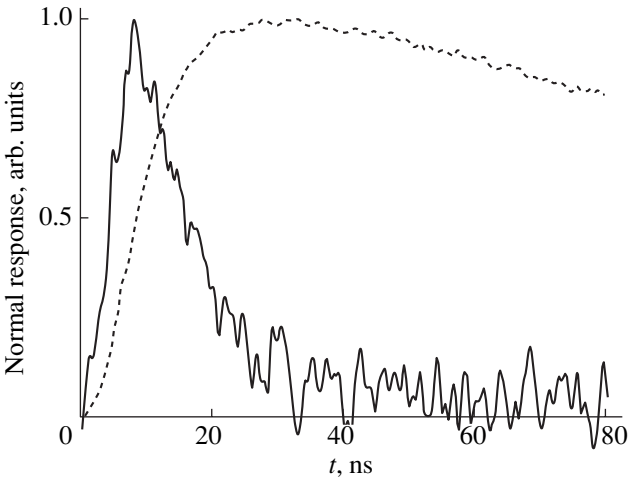

Fig. 4. Bolometer response to the arrival of photoluminescence radiation in the sample under study (solid line) and in a ZnTe single crystal [4, 10] (dashed line). The response amplitude is normalized to unity to make comparison of the time behavior possible.

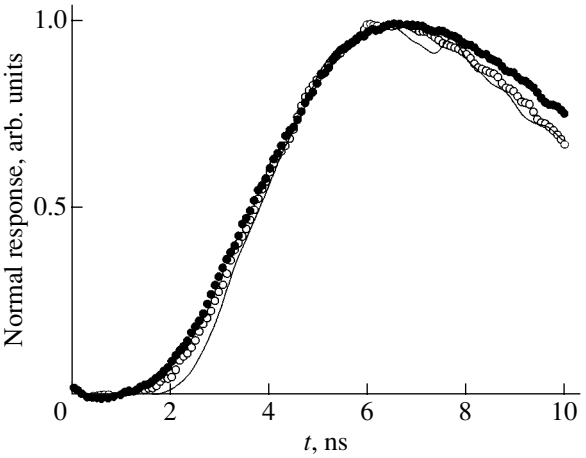

Fig. 5. Comparison of the experimental response obtained under photoexcitation (filled circles) and with a heated gold film (open circles) with Monte Carlo calculations performed for a phonon mean free path λ = 14 μm (solid line).

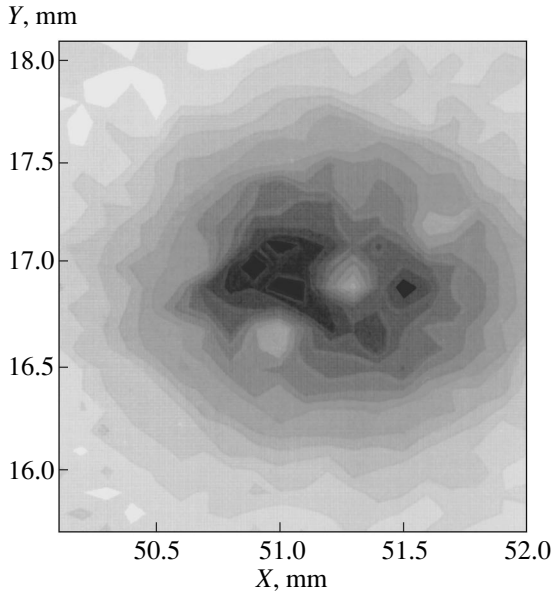

Fig. 6. Bolometer response intensity plotted vs. the position of the generation area (laser beam spot) on the front sample surface for detection time 6 μs. The bolometer was on the rear side of the sample at point (51.2, 17.0).

shifted noticeably with respect to the time of ballistic phonon arrival.

Similar responses were observed earlier on samples of coarse-grained CdTe [6]. These responses were analyzed by Monte Carlo modeling of nonequilibrium phonon propagation in the geometry of the experiment described in [11]. This analysis included a comparison of the effects produced on the response pattern by spontaneous decay and elastic scattering from point defects and from plane defects. It was shown that, in the cases where elastic scattering from point defects is dominant, the response observed even under very strong scattering has a sharp leading edge starting at the time of ballistic phonon transit. This is due to the fact that, because the mean free path for elastic scattering from point defects is strongly frequency dependent ($\tau \sim \nu^{-4}$), a certain part of the low-frequency phonons forming in the decay may have mean free paths comparable to the sample thickness; it is these phonons that account for the sharp leading edge. By contrast, the intensity of scattering from plane boundaries depends on phonon frequency only weakly [12], which places a constraint on the mean free paths of even low-frequency phonons. Therefore, in the case where elastic scattering from planar defects (grain boundaries, twinning planes) is dominant, the response has a characteristic diffusive pattern with a smoothly rising leading edge. Furthermore, the pattern of the response is, in this case, practically independent of the method by which the phonons were generated.

The experimental responses demonstrated in Fig. 5 permit the conclusion that scattering from plane defects is dominant here. Therefore, in the model used in the calculations (as in [6] for coarse-grained CdTe), the variable parameter was the frequency-independent phonon mean free path and the decay and scattering from point defects were neglected. The solid line in Fig. 5 shows the response calculated using the Monte Carlo method for the case where the phonon mean free path is 14 μm (the best fit value). Satisfactory agreement between the calculated and experimental response is seen. The fact that the mean free path is substantially shorter than the characteristic size of the grains making up the sample (Fig. 1) is accounted for by the additional phonon scattering from twin boundaries inside the grains, similar to the scattering observed in coarse-grained CdTe [6].

Figure 6 displays the pattern of the spatial distribution of the detector signal intensity (bolometer response) obtained by scanning the sample surface with a laser beam for a detection time of 6-μs. If the material were isotropic, the intensity would decrease smoothly as the beam moves away from the detector. In contradistinction to this, spatial nonuniformities in phonon arrivals, with dips in the signal intensity present in some directions can be seen in Fig. 6. This nonuniformity is apparently associated with the presence of either pores or defect clusters in grains, which scatter phonons significantly more strongly than does the surrounding material and thereby shadow the detector, as shown in Fig. 2 (case *5*).

5. CONCLUSIONS

To sum up, photoluminescence and propagation of acoustic phonons in high-purity stoichiometric coarse-grained ZnTe prepared through vacuum sublimation have been studied at liquid-helium temperatures. Phonon scattering was shown to occur primarily from twinning planes, and it is this scattering that determines the phonon mean free paths of ~14 μm.

ACKNOWLEDGMENTS

The authors are indebted to N.N. Sentyurina for chemical treatment of the samples and to V.S. Krivobok for assistance in the measurements.

This study was supported by the Russian Foundation for Basic Research (project nos. 02-02-17392, 01-02-16500) and by the RAS Commission for support to young scientists, 6th Competition (grant no. 24).

REFERENCES

1. Q. Wu and X.-C. Zhang, Appl. Phys. Lett. **71**, 1285 (1997); A. Leitenstorter, S. Hunshe, J. Shah, *et al.*, Appl. Phys. Lett. **74**, 1516 (1999).
2. V. S. Bagaev, V. V. Zaĭtsev, Yu. V. Klevkov, *et al.*, Fiz. Tekh. Poluprovodn. (St. Petersburg) **37** (3), 299 (2003) [Semiconductors **37**, 283 (2003)].

3. S. A. Medvedev, Yu. V. Klevkov, S. A. Kolosov, *et al.*, Fiz. Tekh. Poluprovodn. (St. Petersburg) **36** (8), 937 (2002) [Semiconductors **36**, 874 (2002)].
4. T. I. Galkina, A. Yu. Klokov, A. I. Sharkov, *et al.*, Physica B (Amsterdam) **316–317**, 243 (2002).
5. A. I. Sharkov, T. I. Galkina, A. Yu. Klokov, *et al.*, Diamond Relat. Mater. **9**, 1100 (2000).
6. A. Yu. Klokov, A. I. Sharkov, T. I. Galkina, and Yu. V. Klevkov, J. Russ. Laser Res. **21** (5), 478 (2000).
7. Yu. V. Klevkov, V. P. Martovitskiĭ, and S. A. Medvedev, Fiz. Tekh. Poluprovodn. (St. Petersburg) **37** (2), 129 (2003) [Semiconductors **37**, 119 (2003)].
8. A. S. Alekseev, A. Yu. Blinov, M. M. Bonch-Osmolovskiĭ, and T. I. Galkina, Kratk. Soobshch. Fiz. **11**, 12 (1984).
9. Y. Zhang, B. J. Skromme, and F. S. Turco-Sandroff, Phys. Rev. B **46** (7), 3872 (1992).
10. T. I. Galkina, A. Yu. Klokov, A. I. Sharkov, *et al.*, Fiz. Tekh. Poluprovodn. (St. Petersburg) **37** (5), 539 (2003) [Semiconductors **37**, 519 (2003)].
11. M. M. Bonch-Osmolovskiĭ, T. I. Galkina, A. Yu. Klokov, *et al.*, Fiz. Tverd. Tela (St. Petersburg) **38**, 1051 (1996) [Phys. Solid State **38**, 582 (1996)].
12. V. M. Mogilevskiĭ and A. F. Chudnovskiĭ, *Thermal Conductivity of Semiconductors* (Nauka, Moscow, 1972).

Translated by G. Skrebtsov

Physics of the Solid State, Vol. 45, No. 11, 2003, pp. 2044–2052. Translated from Fizika Tverdogo Tela, Vol. 45, No. 11, 2003, pp. 1946–1953.

SEMICONDUCTORS AND DIELECTRICS

Theory of Space-Charge Waves in Semiconductors with Negative Differential Conductivity

V. V. Bryksin*, P. Kleinert, and M. P. Petrov***

**Ioffe Physicotechnical Institute, Russian Academy of Sciences, Politekhnicheskaya ul. 26, St. Petersburg, 194021 Russia*
e-mail: vvb@mail.ioffe.ru; mpetr.shuv@pop.ioffe.rssi.ru
***Paul-Drude-Institut für Ferstkörperelektronik, Berlin, 10117 Germany*
e-mail: kl@pdi-berlin.de
Received April 1, 2003

Abstract—Phenomena that accompany optical excitation of eigenmodes of electron gas oscillation in semiconductors with an *N*-shaped current–voltage (*I–U*) characteristic in a strong electric field are investigated theoretically. The dependence of the current flowing through a sample on the oscillation frequency of the interference pattern of light illuminating the sample is analyzed. Nonsteady-state and nonuniform illumination produces an internal electric field, which interacts resonantly with the eigenmodes when the oscillation frequency of the interference pattern coincides with an eigenfrequency of electronic gas oscillation. As the maximum of the *I–U* curve is approached, the interaction becomes nonlinear in character. *© 2003 MAIK "Nauka/Interperiodica".*

1. INTRODUCTION

An electric current flowing through a semiconductor gives rise to free oscillations of the electron charge density (and, hence, of the internal electric field), which are called space-charge waves (SCWs). The theory of SCWs was developed fairly long ago [1]; however, experimental data on SCWs were very scarce [2] until optical methods for exciting and detecting SCWs came into use [3–7]. The most efficient method was developed only recently [8–10]. According to this method, an interference pattern of light (periodic grating) oscillating about a certain mean position is produced in a crystal. An interference pattern oscillating with a small amplitude can be represented as a combination of a fixed interference pattern (grating) and two gratings traveling in opposite directions. Illumination brings about the photogeneration of carriers, and, since an external electric field is applied to the crystal, a traveling grating produces a forced SCW. If the period and velocity of the forced SCW (which are dictated by the period and frequency of the interference pattern) coincide with the period and phase velocity of an SCW eigenmode, the SCW is excited resonantly.

An important advantage in optical methods is that an SCW can be excited that has a prescribed wave vector (by producing an interference pattern of the corresponding period) and the excitation regime can be changed (to linear or nonlinear) by varying the interference contrast *m*. The excited SCWs can be detected by both optical and electrical methods. For example, if a crystal exhibits a noticeable electrooptic effect, an SCW is accompanied by a refractive-index wave (traveling phase grating), which can cause diffraction of light [9]. The intensity of a diffracted beam is proportional to the SCW amplitude. In the case of the nonlinear excitation mode ($m \approx 1$), SCWs can be detected using a purely electric method [10], namely, by measuring the direct and the alternating current flowing through the sample.

To date, SCWs have been studied using relatively weak electric fields in which the current–voltage (*I–U*) characteristics are linear (ohmic) in character. On the other hand, materials that have *N*-shaped *I–U* characteristics in a strong electric field have been currently attracting considerable interest. In [11–14], it was shown theoretically that semiconductors with narrow electron energy bands have *N*-shaped *I–U* characteristics due to heating of the electron gas. The differential conductivity becomes negative in sufficiently strong fields, which gives rise to instability of the system with respect to inhomogeneous fluctuations in the electron density. As a result, a spatially inhomogeneous moving domain structure arises in the sample [15]. Phenomenologically, this is similar to the formation of Gunn domains in multivalley semiconductors [16]. The interest in materials with *N*-shaped *I–U* characteristics increased substantially after artificial GaAs/AlAs superlattices were synthesized, in which the differential conductivity becomes negative in relatively weak electric fields. In this respect, three-dimensional superlattices, which can be fabricated on the basis of zeolite matrices [17] or from artificial "quantum dots," hold even greater promise.

One might expect that, as the instability point is approached as the electric field is increased, the decay time of free electron density oscillations will increase

and, therefore, the quality factor of resonance effects caused by an external driving force will also increase. It should be noted that in semiconductors, in general, there are two branches in the spectrum of free oscillations of the electron density (and, therefore, of the internal electric field produced by the oscillating electron density). One of them is the low-frequency branch, for which $\Omega_1\tau < 1$, where τ is the recombination time in the case where free electrons are captured by traps [1, 18]. For the other, high-frequency, branch, we have $\Omega_2\tau > 1$; this branch is associated with electron gas oscillation without electron trapping. Here, Ω_1 and Ω_2 are the characteristic frequencies of free electron gas oscillations. We note that, in semiconductors with a high density of minority carriers, another type of instability can occur if the carrier drift velocity is sufficiently high [19]; this instability is not associated with the *N*-shaped *I–U* characteristic and is not considered here.

In this paper, we theoretically investigate free electron density oscillations with a long decay time occurring in semiconductor structures with *N*-shaped *I–U* characteristics in a strong electric field near the instability point. We also discuss possible experimental observations of such oscillations excited by an oscillating interference pattern. For this purpose, we calculate the dependence of the current flowing through a sample (in the vicinity of the point at which a domain structure forms) on the frequency of oscillation of the interference pattern. Schemes for the corresponding experiments are discussed briefly in the last section of this paper.

2. NONLINEAR EQUATIONS OF THE MODEL

We assume that, in an illuminated crystal, an oscillating interference pattern of light is formed and that its intensity W depends on the coordinate x and time t following the law

$$W(x, t) = W_0[1 + m\cos(K_g x + \Theta\cos\Omega t)], \quad (1)$$

where m is the interference contrast; Ω and Θ are the frequency and amplitude of the phase modulation, respectively; and K_g is the wave vector. Illumination of the crystal causes photoexcitation of electrons into the conduction band at a rate

$$g(x, t) = g_0[1 + m\cos(K_g x + \Theta\cos\Omega t)],$$

where the rate g_0 is proportional to the intensity W_0, with the proportionality coefficient depending on the photon energy, absorption coefficient of light, and quantum yield.

Photoionization produces a nonuniform concentration $n(x, t)$ of free electrons, which, in turn, generate a nonuniform electric field $E(x, t)$ in the crystal. These quantities obey a conventional set of nonlinear differential equations [20] (see also [21, 22]):

$$\frac{\partial n(x, t)}{\partial t} + \frac{n(x, t) - \tilde{n}_0}{\tau} = g_0[1 + h(x, t)] - \frac{\varepsilon}{4\pi e}\frac{\partial^2 E(x, t)}{\partial x \partial t}, \quad (2)$$

$$\frac{\varepsilon}{4\pi}\frac{\partial E(x, t)}{\partial t} + j(x, t) = I(t), \quad (3)$$

$$j(x, t) = en(x, t)v(E(x, t)) + eD(E(x, t))\frac{\partial n(x, t)}{\partial x}. \quad (4)$$

Here,

$$h(x, t) = m\cos(K_g x + \Theta\cos\Omega t), \quad (5)$$

$\tilde{n}_0$ is the equilibrium concentration of free electrons, ε is the dielectric constant of the crystal, $j(x, t)$ is the current density in the crystal, $I(t)$ is the total current density, v is the drift velocity, and D is the diffusion coefficient. Equations (2)–(4) are valid if there are many empty traps in the crystal and, hence, saturation effects are absent.

Note that the set of equations (2)–(4) differs essentially from the model investigated in [21, 22]. First, in this paper, we consider conducting crystals, for which the concentration of free electrons in the dark is nonzero, $\tilde{n}_0 \neq 0$. Second, the adiabatic approximation is not used and, therefore, $\partial n/\partial t \neq 0$ in Eq. (2). Third, we do not ignore the diffusion contribution to the current (proportional to $\propto \partial n/\partial x$) in Eq. (4).

However, the most essential difference from the study performed in [21, 22] is that, in this paper, we do not use the linear approximation with respect to the electric field in which Ohm's law is obeyed, the drift velocity is given by the relation $v = \mu E$, the diffusion coefficient D is independent of the field, and the Einstein relation $\mu = eD/kT$ between the mobility and diffusion coefficient takes place. In what follows, we assume that the drift velocity $v(E)$ becomes a decreasing function in a certain range and that the $D(E)$ dependence should be calculated independently from a microscopic model (see, e.g., [23, 24]). In particular, in the extreme case of a very strong field, we have $D(E) \propto E^{-2}$. For superlattices, for example, in the simplest relaxation time approximation, we have [12]

$$v(E) = \frac{\mu E}{1 + (E/E^{(0)})^2}. \quad (6)$$

The diffusion coefficient can be estimated from the Einstein relation

$$D(E) = \frac{kT\mu/e}{1 + (E/E^{(0)})^2}, \quad (7)$$

where $E^{(0)} = \hbar/(e\tau_s d_s)$ is a characteristic field, τ_s is the lifetime of the Stark ladder state, d_s is the superlattice period, μ is the mobility (in the range where Ohm's law is obeyed)

$$\mu = \frac{ed_s^2\tau_s\Delta}{2\hbar^2}\frac{I_1(\Delta/2kT)}{I_0(\Delta/2kT)},$$

$I_n(x)$ are modified Bessel functions, and Δ is the width of the allowed band. A more detailed analysis of the $D(E)$ dependence shows that, in Eq. (7), the crystal lattice temperature T has to be replaced by the effective temperature of the electron gas $T_{\text{eff}}(E)$ [24].

In order to determine the current in the external circuit $I(t)$, Eqs. (2)–(4) must be supplemented by a "boundary" condition. In our case, this condition is the Kirchhoff equation for the external circuit. If the external circuit contains an emf source with a voltage U across its terminals and a load of resistance R (including the internal resistance of the source), then Kirchhoff's law takes the form [22]

$$\int_0^L dxE(x, t) + RSI(t) = U,$$

where L and S are the length and cross-sectional area of the sample, respectively. Dividing this additional equation by L, we obtain

$$\frac{1}{L}\int_0^L dxE(x, t) + \rho I(t) = \Xi, \tag{8}$$

where $\Xi = U/L$ and $\rho = RS/L$.

Nonlinear equations (2)–(4) are very complicated. Therefore, in order to solve these equations analytically, we simplify them by assuming that the interference contrast is low, $m \ll 1$, and represent the sought quantities in the form

$$\begin{gathered}E(x, t) = E_0 + \delta E(x, t), \quad n(x, t) = n_0 + \delta n(x, t),\\ I(t) = I_0 + \delta I(t),\end{gathered} \tag{9}$$

where E_0, n_0, and I_0 are the field, carrier concentration, and the current in the external circuit, respectively, when the illumination of the crystal is constant and uniform; that is, these quantities are independent of the space coordinate and time and are a solution of Eqs. (2)–(4) at $m = 0$, i.e., when $h(x, t) = 0$:

$$n_0 = \tilde{n}_0 + g_0\tau, \quad I_0 = en_0v(E_0). \tag{10}$$

From condition (8), we obtain a third equation,

$$E_0 + \rho I_0 = \Xi. \tag{11}$$

Combining Eqs. (10) and (11) gives the following transcendental equation for the electric field E_0 within the sample under constant illumination and at the given voltage Ξ across the terminals of the emf source and the load (specific) resistance ρ:

$$E_0 + en_0v(E_0)\rho = \Xi. \tag{12}$$

The characteristic of the nonlinear element (the sample under study) described by Eq. (12) gives an implicit relation between the electric field within the sample and the voltage across the external emf source. If the $v(E_0)$ curve has a falling section, the following two different regimes are possible. For sufficiently small values of ρ, the $E_0(\Xi)$ function is single valued everywhere over the range $0 < \Xi < \infty$ (voltage-source regime). As ρ is increased, the $E_0(\Xi)$ function becomes ambiguous and Eq. (12) has three roots in a certain range of Ξ values (current-source regime); in this case, the *I–U* characteristic of the crystal exhibits hysteresis. In the falling section of the *I–U* curve, due to instability, measurements in the current-source regime are accompanied by the formation of moving domains and in the voltage-source regime, by the formation of a static inhomogeneous charge distribution [16]. In what follows, we restrict our consideration to the case of the voltage-source regime, where the $E_0(\Xi)$ function is single valued.

The quantities δE, δn, and δI in Eq. (9) vanish at $m = 0$. Therefore, they are small corrections in the case of a low interference contrast and we can keep only those nonlinear terms that are quadratic in δE and δn. Expanding the nonlinear quantities in the field in the vicinity of the working point E_0, we have

$$v(E_0 + \delta E) \cong v_0 + v_0'\delta E + \frac{1}{2}v_0''\delta E^2,$$

$$D(E_0 + \delta E) \cong D_0 + D_0'\delta E,$$

where $v_0 \equiv v(E_0)$, $v_0' \equiv dv_0/dE_0$, $v_0'' \equiv d^2v_0/dE_0^2$, etc. Introducing the dimensionless variables

$$z = K_g x, \quad T = \Omega t, \quad Y = \delta E\frac{v_0'}{v_0}, \quad \lambda = \frac{\delta n}{n_0},$$

$$f = \frac{\delta I}{en_0v_0}, \quad d = v_0K_g\tau,$$

$$\Lambda = \frac{D_0K_g}{v_0}, \quad \Lambda' = \frac{D_0'K_g}{v_0'},$$

we obtain the following equations for the dimensionless internal field $Y(z, T)$ and the nonuniform carrier concentration $\lambda(z, T)$:

$$\begin{gathered}\Omega\tau_M\frac{\partial Y}{\partial T} + Y + \lambda + \Lambda\frac{\partial\lambda}{\partial z} + \lambda Y\\ + \frac{v_0''v_0}{2v_0'^2}Y^2 + \Lambda' Y\frac{\partial\lambda}{\partial z} = f(T),\end{gathered} \tag{13}$$

$$\Omega\tau\frac{\partial\lambda}{\partial T}+\lambda=\frac{g_0\tau}{n_0}h(z,T)-\Omega\tau_M d\frac{\partial^2 Y}{\partial z\partial T}, \qquad (14)$$

where $\tau_M^{-1}=4\pi v_0' n_0/\varepsilon$.

3. DEPENDENCE OF CURRENT ON THE OSCILLATION FREQUENCY OF THE INTERFERENCE PATTERN

We seek a solution to Eqs. (13) and (14) in the form of a Fourier series in terms of the space coordinates and time:

$$Y(z,T)=\sum_{p,l=-\infty}^{\infty}Y_{p,l}\exp(ipz+ilT). \qquad (15)$$

In the Fourier representation, Eqs. (13) and (14) take the form

$$Y_{p,l}(1+i\Omega\tau_M l)+\lambda_{p,l}(1+i\Lambda p)$$
$$+\sum_{p',l'}Y_{p-p',l-l'}\left[\lambda_{p',l'}(1+i\Lambda' p')+Y_{p',l'}\frac{v_0'' v_0}{2v_0'^2}\right]=f_l\delta_{p,0}, \qquad (16)$$

$$\lambda_{p,l}(1+i\Omega\tau l)=\frac{g_0\tau}{n_0}h_{p,l}+\Omega\tau_M dpl Y_{p,l}, \qquad (17)$$

$$h_{p,l}=\frac{m}{2}J_l(\Theta)(\delta_{p,1}i^l+\delta_{p,-1}i^{-l}), \qquad (18)$$

where $J_l(\Theta)$ is a Bessel function.

Using Eq. (17), we eliminate $\lambda_{p,l}$ and obtain a closed equation for the Fourier components of the internal electric field $Y_{p,l}$:

$$f_l\delta_{p,0}=Y_{p,l}\left(1+i\Omega\tau_M l+\Omega\tau_M pl\frac{1+i\Delta p}{1+i\Omega\tau l}\right)$$
$$+\frac{g_0\tau}{n_0}h_{p,l}\frac{1+i\Lambda p}{1+i\Omega\tau l}+\sum_{p',l'}Y_{p-p',l-l'}\left[\frac{1+i\Lambda' p'}{1+i\Omega\tau l'}\right. \qquad (19)$$
$$\left.\times\left(\frac{g_0\tau}{n_0}h_{p',l'}+\Omega\tau_M dp'l'Y_{p',l'}\right)+Y_{p'l'}\frac{v_0'' v_0}{2v_0'^2}\right].$$

The additional equation (8) for the current f_l in the Fourier representation takes the form

$$Y_{0,l}=-\rho\sigma_d f_l, \qquad (20)$$

where $\sigma_d=en_0 v_0'$ is the differential conductivity of the material at the working point E_0.

Note that the Maxwell relaxation time τ_M, introduced above, becomes negative in the falling section of the *I–U* curve, which signifies that the ohmic component of the current "pulls" carriers into the region where their concentration is higher. In the region where the ohmic current component becomes greater than the diffusion component, instability arises and a domain structure can form.

The sought electric current f_l can be found from Eqs. (19) and (20) by setting $p=0$:

$$[1+\rho\sigma_d(1+i\Omega\tau_M l)]f_l-\frac{\rho^2\sigma_d^2 v_0'' v_0}{2v_0'^2}\sum_{l'}f_{l-l'}f_{l'}$$
$$=\sum_{l',p\neq 0}Y_{-p,l-l'}\left[\frac{1+i\Lambda' p}{1+i\Omega\tau l'}\left(\frac{g_0\tau}{n_0}h_{p,l'}+\Omega\tau_M dpl'Y_{p,l'}\right)\right. \qquad (21)$$
$$\left.+\frac{v_0'' v_0}{2v_0'^2}Y_{p,l'}\right].$$

Now, we find the Fourier components of the internal field $Y_{p,l}$ with $p\neq 0$ from Eq. (19). For $m\ll 1$, these components can be calculated analytically. Indeed, it is easy to verify that, for $m\ll 1$, we have $Y_{p,l}\propto m^{|p|}$ [22]. Therefore, for $p\geq 1$, the summation over p' in Eq. (19) can be performed from 1 to p. In this case, Eq. (19) reduces to a recurrent relation, from which $Y_{p,l}$ can be expressed in terms of $Y_{1,l}, Y_{2,l}, \ldots, Y_{p-1,l}$. The Fourier components with $p\leq -1$ can be found from the symmetry relations

$$Y_{-p,-l}=Y_{p,l}^*,\quad Y_{p,-l}(\Omega)=Y_{p,l}(-\Omega). \qquad (22)$$

In this approximation, to within terms linear in m, we obtain from Eq. (19)

$$Y_{p,l}=-\frac{g_0\tau}{n_0}h_{p,l}\left[\Omega\tau_M dpl+\frac{(1+i\Omega\tau_M l)(1+i\Omega\tau l)}{1+i\Lambda p}\right]^{-1}. \qquad (23)$$

In Eq. (23), only components $Y_{\pm 1,l}$ are nonzero [see Eq. (18)]. From Eq. (21), to within terms of order m^2, we obtain a closed expression for the current:

$$[1+\rho\sigma_d(1+i\Omega\tau_M l)]f_l=-\sum_{l',p=\pm 1}Y_{-p,l-l'}Y_{p,l'}$$
$$\times\left[\frac{(1+i\Lambda' p)(1+i\Omega\tau_M l')}{1+i\Lambda p}-\frac{v_0'' v_0}{2v_0'^2}\right]. \qquad (24)$$

Putting $l=0$ in Eq. (24) and using Eq. (23), we obtain, after simple algebra, the following final expres-

sion for the time-independent component of the dimensionless current in the external circuit f_0:

$$f_0 = -\frac{2}{(1+\rho\sigma_d)}\left(\frac{g_0\tau m}{2n_0}\right)^2\sum_l J_l^2(\Theta) \times \frac{1+\Lambda\Lambda'+\Omega\tau_M l(\Lambda-\Lambda')-(1+\Lambda^2)v_0''v_0/(2v_0'^2)}{\left|1+\Omega\tau_M dl-\Omega^2 l^2\tau\tau_M+i\Omega l[(1+\Lambda d)\tau_M+\tau]\right|^2}. \quad (25)$$

In the most interesting case of a small amplitude of phase modulation $\Theta \ll 1$, we obtain from Eq. (25) an expression for the change in the direct current caused by illumination of the sample:

$$\delta I_0(\Omega) = -\frac{en_0v_0}{(1+\rho\sigma_d)}\left(\frac{g_0\tau m}{2n_0}\right)^2\left\{(2-\Theta^2)A(0)+\frac{\Theta^2}{2\tau^2\tau_M^2} \times\left[\frac{A_-(\Omega)}{|\Omega-\Omega_1|^2|\Omega-\Omega_2|^2}+\frac{A_+(\Omega)}{|\Omega+\Omega_1|^2|\Omega+\Omega_2|^2}\right]\right\}, \quad (26)$$

where

$$A_\pm(\Omega) = 1+\Lambda\Lambda'-(1+\Lambda^2)\frac{v_0''v_0}{2v_0'^2}\pm\Omega\tau_M(\Lambda-\Lambda'), \quad (27)$$

$$\Omega_{1,2} = -\frac{1}{2\tau}\left[d+i\left(1+\frac{\tau}{\tau_M}+\Lambda d\right)\right] \pm\frac{1}{\tau}\sqrt{\frac{1}{4}\left[d+i\left(1+\frac{\tau}{\tau_M}+\Lambda d\right)\right]^2+\frac{\tau}{\tau_M}} = -\frac{1}{2}\left[K_g v_0+i\left(\frac{1}{\tau}+\frac{1}{\tau_M}+K_g^2D_0\right)\right] \pm\sqrt{\frac{1}{4}\left[K_g v_0+i\left(\frac{1}{\tau}+\frac{1}{\tau_M}+K_g^2D_0\right)\right]^2+\frac{1}{\tau\tau_M}}. \quad (28)$$

Now, we derive an expression for the first temporal Fourier component of the current. From Eqs. (24) and (23), after some mathematical manipulation, we obtain

$$\delta I_1(\Omega) = \frac{ien_0v_0\Theta}{1+\rho\sigma_d(1+i\Omega\tau_M)}\left(\frac{g_0\tau m}{2n_0}\right)^2\frac{1}{\tau\tau_M} \times\left[\frac{B_+(\Omega)}{(\Omega+\Omega_1)(\Omega+\Omega_2)}-\frac{B_-(\Omega)}{(\Omega-\Omega_1^*)(\Omega-\Omega_2^*)}\right], \quad (29)$$

where

$$B_\pm(\Omega) = A_\pm(\Omega)+i\Omega\tau_M(1+\Lambda\Lambda'). \quad (30)$$

From Eqs. (26) and (29), it can be seen that $\delta I_0(\Omega)$ and $\delta I_1(\Omega)$ have two resonance peaks, with resonance frequencies equal to $|\mathrm{Re}\,\Omega_{1,2}|$. These peaks become more pronounced as the quality factor of the system is increased, i.e., with decreasing the quantities $\mathrm{Im}\,\Omega_{1,2}$. In [22], only the branch associated with trap recharging was considered and, therefore, only one extremum was predicted and observed in the frequency dependence of both the static and varying components of the current. In this paper, we take into account both branches of the oscillation spectrum, with the consequence that two extrema (minima in the direct and maxima in the alternating component) are found to occur in each current component. The occurrence of these extrema in the frequency dependences of the direct and the alternating current is due to nonlinear interaction of SCWs and to scattering of SCWs by static charge grating associated with the static component in the interference pattern (1).

The minima of the direct current are due to the interaction of two SCWs, one of which is proportional to $m\Theta\exp(iK_gx+i\Omega t)$ and the other to $m\Theta\exp(-iK_gx-i\Omega t)$. The product of these expressions, describing the interaction between the SCWs, is equal to $m^2\Theta^2$ and does not depend on the space coordinates and time. This effect is similar to the rectification of light waves in nonlinear optics. The additional direct current due to this effect depends on the oscillation frequency of the interference pattern, because the excitation of SCWs is resonant in character. In [10], this effect was called the complete rectification of SCWs. The maxima in the frequency dependence of the alternating current are due to the scattering of waves $m\Theta\exp(iK_gx+i\Omega t)$ by the static charge grating, whose amplitude is proportional to $m\exp(-iK_gx)$. The product of these expressions, describing SCW scattering, is equal to $m^2\Theta\exp(i\Omega t)$ and, hence, depends on time but does not depend on the space coordinates. In [10], this effect was called the spatial rectification of SCWs. Note that the complete SCW rectification is independent of the technique used to excite SCWs, whereas the spatial rectification effect is closely related to the SCW-exciting technique (using an oscillating interference pattern).

4. OSCILLATION EIGENMODES

Here, we show that, physically, the frequency dependence of the current is resonant in character because the periodic internal electric field produced by nonuniform illumination of the crystal interacts with oscillation eigenmodes of the system. For this purpose, we show that the resonance frequencies $\Omega_{1,2}$ given by Eq. (28) coincide with the eigenfrequencies of electron gas oscillation. Let us trace the evolution of our system in the case where a nonuniform electron packet $\delta n^{(0)}(x)$ is formed at $t = 0$. This evolution is described by linearized equations (2)–(4):

$$\frac{\varepsilon}{4\pi e}\frac{\partial^2\delta E(x,t)}{\partial x\partial t}+\frac{\partial\delta n(x,t)}{\partial t}+\frac{\delta n(x,t)}{\tau} = 0, \quad (31)$$

$$\frac{\varepsilon}{4\pi e}\frac{\partial \delta E(x,t)}{\partial t} + v_0 \delta n(x,t) + n_0 v_0' \delta E(x,t) + D_0 \frac{\partial \delta n(x,t)}{\partial x} = 0. \quad (32)$$

Using the initial conditions $\delta n(x, 0) = \delta n^{(0)}(x)$ and $\delta E(x, 0) = 0$, we take the temporal Laplace transform and the spatial Fourier transform of both sides of Eqs. (31) and (32):

$$iqs\frac{\varepsilon}{4\pi e}\delta E(q,s) + \left(s + \frac{1}{\tau}\right)\delta n(q,s) = \delta n^{(0)}(q), \quad (33)$$

$$\left(s\frac{\varepsilon}{4\pi e} + n_0 v_0'\right)\delta E(q,s) + (v_0 + iqD_0)\delta n(q,s) = 0. \quad (34)$$

Here,

$$\delta n(q,s) = \int_{-\infty}^{\infty} dx \int_0^{\infty} dt\, \delta n(x,t) \exp(iqx - st). \quad (35)$$

The solution to Eqs. (33) and (34) has the form

$$\delta n(q,s) = \delta n^{(0)}(q)\frac{s + 1/\tau_M}{[s + i\Omega_1(q)][s + i\Omega_2(q)]}, \quad (36)$$

where $\Omega_{1,2}(q)$ are the oscillation eigenfrequencies of the system defined by Eq. (28) with K_g replaced by q.

Equation (28) gives the frequencies of two oscillation eigenmodes of the system consisting of the electron gas and electron traps in the crystal. It is convenient to investigate these modes in the extreme case of $(qv_0)^2 + (\tau^{-1} + \tau_M^{-1} + q^2D_0)^2 \gg |\tau\tau_M|^{-1}$, where the frequencies of these modes are sufficiently far apart from each other. In this case, we have

$$\Omega_1(q) = -qv_0 - i\left(\frac{1}{\tau} + \frac{1}{\tau_M} + q^2 D_0\right), \quad (37)$$

$$\Omega_2(q) = \frac{1}{\tau\tau_M}\frac{1}{qv_0 + i(\tau^{-1} + \tau_M^{-1} + q^2 D_0)}. \quad (38)$$

The first mode, described by Eq. (37), is associated with oscillations of the free electron gas, while the second mode [Eq. (38)] is associated with trap-recharging waves [1, 18].

It is important that these excitations are stable when the differential conductivity is positive, $\tau_M > 0$. In the falling section of the *I–U* curve, at $\tau_M < 0$, we have either $\mathrm{Im}\Omega_1 > 0$, $\mathrm{Im}\Omega_2 < 0$ (if $\tau^{-1} + \tau_M^{-1} + q^2D_0 < 0$) or, the reverse, $\mathrm{Im}\Omega_1 < 0$, $\mathrm{Im}\Omega_2 > 0$ (if $\tau^{-1} + \tau_M^{-1} + q^2D_0 > 0$). Therefore, in the falling section of the *I–U* curve, one of the oscillation eigenmodes is unstable. This conclusion becomes obvious if we take into account that $\Omega_1\Omega_2 = -(\tau\tau_M)^{-1}$. At the singular point $\tau^{-1} + \tau_M^{-1} + q^2D_0 = 0$, the decay times of both modes are infinite: $\mathrm{Im}\Omega_{1,2} = 0$, if $(qv_0)^2 > -4(\tau\tau_M)^{-1}$.

The branch Ω_1 is unstable with respect to long-wavelength fluctuations when $q^2D_0 + \tau^{-1} < -\tau_M^{-1}$. This instability is convective [25], i.e., the quantity $\delta n(x, t)$ in Eq. (35) at $x = 0$ decays with time, if $\tau^{-1} + v_0^2/(4D_0) > -\tau_M^{-1}$; therefore, in not very long samples, this instability may not bring about the formation of domains. The branch Ω_2 in the falling section of the *I–U* curve, on the contrary, is unstable to relatively short-wavelength fluctuations, when $\tau^{-1} + v_0^2/(4D_0) < -\tau_M^{-1}$, and its instability is absolute. The phase and group velocities of this oscillation mode are very small. Instability with respect to trap recharging was discussed in [26]. Note that, in the above treatment, we considered the simplest linear case of carrier recombination, in which the concentration of empty traps is high. In [1], more general results are presented for the dispersion relation of trap-recharging waves.

At a given sign of the wave vector **q**, the phase velocities of these two oscillation modes are oppositely directed, whereas the group velocities have the same direction, because the phase and group velocities of the mode Ω_2, described by Eq. (38), are oppositely directed.

5. DISCUSSION OF RESULTS

Relation (26) shows that the dependence of the dc component of the current flowing through the sample on the oscillation frequency of the interference pattern exhibits, in general, two minima at frequencies $\Omega = \Omega_{1,2}$, which are the oscillation eigenfrequencies of the semiconductor plasma in the case where carriers are recaptured by traps. One of these minima, at $\Omega = \Omega_2$, corresponding to the interaction with trap-recharging waves, was observed in [10] in dielectrics $Bi_{12}GeO_{20}$ and $Bi_{12}SiO_{20}$ in the region of the linear section of the *I–U* curve. In the case considered in this paper of a nonlinear *I–U* characteristic, this resonance occurs at the frequency

$$\Omega_{r2} = (K_g v_0 \tau\tau_M)^{-1} = \frac{4\pi n_0}{\varepsilon\tau K_g E_0}\frac{\sigma_d}{\sigma}, \quad (39)$$

where $\sigma = en_0v_0/E_0$ is the electrical conductivity of the sample. In superlattices for which the *I–U* curve has a falling section, the frequency Ω_{r2} in Eq. (39) decreases

with increasing applied electric field and vanishes at the inflection point of the *I–U* curve.

It should be noted, however, that in the vicinity of the point $\sigma_d = 0$ the expansion in powers of the small interference contrast m is invalid, because the m dependence is not analytic in this region. Near the maximum of the *I–U* characteristic, nonlinear effects become important, because the instability point with respect to spatially inhomogeneous electron density fluctuations is approached. In our model of carrier recombination, described by Eq. (2), in the falling section of the *I–U* curve at $\tau_M < 0$, one of the oscillation eigenmodes is unstable; namely, the first mode becomes unstable to long-wavelength oscillations at $\tau^{-1} + \tau_M^{-1} + q^2 D_0 < 0$ and the second mode becomes unstable to short-wavelength oscillations at $\tau^{-1} + \tau_M^{-1} + q^2 D_0 > 0$. The decay rates of these modes depend on the character of carrier recombination. In particular, even in the case of linear recombination, the right-hand side of Eq. (2) can contain a term proportional to the charge density, i.e., $\partial E(x, t)/\partial x$, which causes a significant renormalization of the decay rates of the modes Ω_1 and Ω_2. In principle, the results obtained above are valid not only in the stable section of the *I–U* curve (where $\sigma_d > 0$) but also in the falling section (at $\sigma_d < 0$) if the experimental conditions are such that a domain structure does not arise. Measurements near the maximum of the *I–U* curve ($\sigma_d = 0$) are of particular interest, because the dependence of the current on the interference contrast m is highly nonlinear in this range and one might expect a sharp decrease in the decay rate of free oscillations. However, the theory presented above is not valid in this range and the basic equations are essentially nonlinear even when the parameter $mg_0\tau/n_0$ is very small. We also note that the mechanism of the resonant dependence of the current flowing through a sample on the oscillation frequency of the interference pattern is similar in nature to the well-known enhancement of electromagnetic oscillations observed in multivalley semiconductors near the threshold for the formation of Gunn domains [16].

The results obtained above are valid for a wide range of values of the external electric field strength. In particular, in the case of a weak electric field, where Ohm's law is obeyed, $v_0 = \mu E_0$, $v_0' = v_0'' = D_0' = 0$, and diffusion can be ignored ($D_0 = 0$), Eqs. (26) and (29) in the adiabatic approximation ($\Omega\tau \longrightarrow 0$) reduce to the corresponding expressions for the direct and the alternating current from [22].

In the case where there is no external electric field and, hence, the current is diffuse in character, only an alternating current flows through the sample [20]. In this case, $v_0 = 0$ and, according to Eqs. (27) and (30), we have

$$A_\pm(\Omega) v_0 = B_\pm(\Omega) v_0 \longrightarrow \pm\Omega\tau_M K_g D_0.$$

Both eigenfrequencies $\Omega_{1,2}$ given by Eq. (28) are pure imaginary in this case:

$$\Omega_{1,2} = -\frac{i}{2}\left[\frac{1}{\tau} + \frac{1}{\tau_M} + K_g^2 D_0 \mp \sqrt{\left(\frac{1}{\tau} - \frac{1}{\tau_M}\right)^2 + 2\left(\frac{1}{\tau} + \frac{1}{\tau_M}\right)K_g^2 D_0 + K_g^4 D_0^2}\right].$$

Therefore, in the absence of an external electric field, we have from Eq. (26) that $\delta I_0 = 0$ and, according to Eq. (29), the alternating component of the current is

$$\delta I_1(\Omega) = \frac{2ien_0 K_g D_0 \Theta}{1 + \rho\sigma_d(1 + i\Omega\tau_M)}\left(\frac{g_0\tau m}{2n_0}\right)^2 \frac{\Omega}{\tau} \times \frac{1}{(\Omega + \Omega_1)(\Omega + \Omega_2)}. \quad (40)$$

This diffusion current induced by an oscillating interference pattern was investigated theoretically and experimentally in [27] in a dielectric ($n_0 = g_0\tau$, $\tau_M \gg \tau$) in the case of zero external load ($\rho = 0$) in the low-frequency limit $\Omega \ll |\Omega_2|$. In this extreme case, we have

$$\Omega_1 = -\frac{i}{\tau_M(1 + \tau K_g^2 D_0)}, \quad \Omega_2 = -i\left(\frac{1}{\tau} + K_g^2 D_0\right),$$

and Eq. (40) takes the form [27]

$$\delta I_1(\Omega) = \frac{en_0 K_g D_0 \Theta m^2}{2i} \frac{\Omega\tau_M}{1 + i\Omega\tau_M(1 + \tau K_g^2 D_0)}. \quad (41)$$

It is clear that, in the absence of an external field, the current is diffusive in character and, hence, its frequency dependence exhibits no resonance.

In closing, we make quantitative estimates and discuss possible experiments.

For well-studied sillenite-structure crystals ($Bi_{12}MeO_{20}$, where *Me* = Si, Ge, Ti), when illuminated with blue–green light of an intensity of the order of 100 mW/cm^2, the typical values of the parameters are $\mu \approx 0.2$–0.5 cm^2/V s, $\tau \approx 10^{-6}$ s, and $\tau_M \approx 3 \times 10^{-4}$ s. Under these conditions, in fields of the order of 10 kV/cm, the low-frequency branch of the spectrum lies around 100 Hz and the high-frequency branch lies around 10 MHz for the wave vector $K_g \approx 10^4$ cm^{-1}. In semi-insulating semiconductors GaAs : Cr and InP : Fe, the parameters depend strongly on the impurity content. For fairly high impurity concentrations (~10^{16} cm^{-3}), the low-frequency branch lies in the range 1–10 kHz in relatively high electric fields and the high-frequency branch is likely to lie in the range 10–100 MHz. In well-conducting semiconductors, the conditions for the experimental study of SCWs are less favorable, because the relaxation times τ_M and τ are very short in them ($\tau_M \sim 10^{-11}$–10^{-12} s, $\tau \sim 10^{-9}$–10^{-10} s). However, in materials exhibiting a negative differential conductiv-

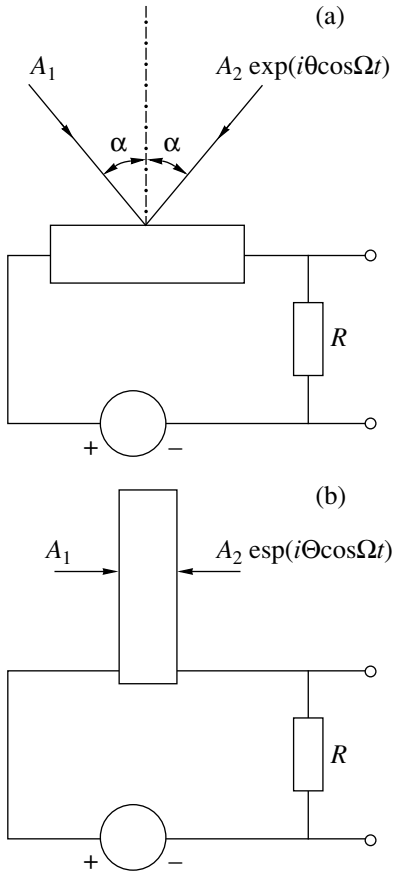

Fig. 1. Experimental setup (schematic) for optical excitation of space-charge waves by illuminating a crystal to produce an interference pattern oscillating about a mean position. Oscillations of the interference pattern are caused by phase modulation of one of the beams incident on the crystal; Ω and Θ are the frequency and amplitude of phase modulation. $A_1$and A_2 are the beams forming the interference pattern. R is the load resistance used to monitor both the direct and the alternating current in the crystal. (a) Transmission geometry (α is the angle of incidence of the beams) and (b) geometry with counter-propagating beams.

ity, with $\tau_M < 0$, the conditions for such experimental studies, on the contrary, may appear to be very favorable, because the oscillation decay rate can reach even zero in them.

We can propose two experimental schemes for observing the effects in question depending on sample size. If the spacing between electrodes is much larger than the period of the interference pattern (equal to $\lambda/2\sin\alpha$, where λ is the wavelength of light), then the transmission geometry is more convenient (Fig. 1a). In the case where the spacing between electrodes is small (as is the case, e.g., with superlattices to which an electric field is applied perpendicular to the layer plane), the geometry in which light beams propagate in opposite directions is preferable (Fig. 1b). In this geometry, the period of the interference pattern is $\lambda/2n$, where n is the refractive index of the layer under study. The wave vector of the grating in this case is very large, and the available trap concentration may be insufficient to study the low-frequency branch of the SCW spectrum. It should also be noted that, in the geometry with counter-propagating light beams, transparent electrodes have to be used.

ACKNOWLEDGMENTS

This study was supported by Deutsches Zentrum für Luft- und Raumfahrt and the Russian Foundation for Basic Research (project no. 02-02-17603).

REFERENCES

1. R. F. Kazarinov, R. A. Suris, and B. I. Fuks, Fiz. Tekh. Poluprovodn. (Leningrad) **7** (1), 149 (1973) [Sov. Phys. Semicond. **7**, 102 (1973)]; Fiz. Tekh. Poluprovodn. (Leningrad) **7** (3), 688 (1973) [Sov. Phys. Semicond. **7**, 480 (1973)].
2. N. G. Zhdanova, M. S. Kogan, R. A. Suris, and B. I. Fuks, Zh. Éksp. Teor. Fiz. **74** (2), 364 (1978) [Sov. Phys. JETP **47**, 189 (1978)].
3. J. P. Huignard and A. Marrakchi, Opt. Commun. **38** (8), 249 (1981).
4. S. I. Stepanov, V. V. Kulikov, and M. P. Petrov, Opt. Commun. **44** (1), 19 (1982).
5. G. Hamel, de Montchenault, B. Loiseaux, and J. P. Huignard, Electron. Lett. **22** (19), 1030 (1986).
6. B. I. Sturman, T. E. McClelland, D. J. Webb, *et al.*, J. Opt. Soc. Am. B **12** (9), 1621 (1995).
7. H. C. Pedersen, D. J. Webb, and Per M. Johansen, J. Opt. Soc. Am. B **15** (10), 2573 (1998).
8. M. P. Petrov, V. M. Petrov, V. V. Bryksin, *et al.*, Opt. Lett. **22** (14), 1083 (1997).
9. M. P. Petrov, V. V. Bryksin, V. M. Petrov, *et al.*, Phys. Rev. A **60** (3), 2413 (1999).
10. M. P. Petrov, V. V. Bryksin, H. Vogt, *et al.*, Phys. Rev. B **66** (8), 085107 (2002).
11. Yu. A. Bychkov and A. M. Dykhne, Zh. Éksp. Teor. Fiz. **48** (4), 1168 (1965) [Sov. Phys. JETP **21**, 779 (1965)].
12. L. Esaki and T. Tsu, IBM J. Res. Dev. **14** (1), 61 (1970).
13. V. V. Bryksin and Yu. A. Firsov, in *Proceedings of X International Conference on Physics of Semiconductors, Cambridge, USA, 1970*, p. 767.
14. V. V. Bryksin and Yu. A. Firsov, Zh. Éksp. Teor. Fiz. **61** (12), 2373 (1971) [Sov. Phys. JETP **34**, 1272 (1972)].
15. L. L. Bonilla, J. Phys.: Condens. Matter **14** (2), R341 (2002).
16. A. F. Volkov and Sh. M. Kogan, Usp. Fiz. Nauk **96** (4), 633 (1968) [Sov. Phys. Usp. **11**, 881 (1968)].
17. V. N. Bogomolov, A. I. Zadorozhniĭ, T. M. Pavlova, *et al.*, Pis'ma Zh. Éksp. Teor. Fiz. **31** (7), 406 (1980) [JETP Lett. **31**, 378 (1980)].

18. R. F. Kazarinov, R. A. Suris, and B. I. Fuks, Fiz. Tekh. Poluprovodn. (Leningrad) **6** (3), 572 (1972) [Sov. Phys. Semicond. **6**, 500 (1972)].
19. O. V. Konstantinov and V. I. Perel', Fiz. Tverd. Tela (Leningrad) **6** (11), 3364 (1964) [Sov. Phys. Solid State **6**, 2691 (1964)].
20. N. V. Kukhtarev, V. B. Markov, S. G. Odulov, *et al.*, Ferroelectrics **22** (4), 949 (1979).
21. V. V. Bryksin and M. P. Petrov, Fiz. Tverd. Tela (St. Petersburg) **40** (8), 1450 (1998) [Phys. Solid State **40**, 1317 (1998)].
22. V. V. Bryksin and M. P. Petrov, Fiz. Tverd. Tela (St. Petersburg) **44** (10), 1785 (2002) [Phys. Solid State **44**, 1869 (2002)].
23. B. Laikhtman and D. Miller, Phys. Rev. B **48** (8), 5395 (1993).
24. V. V. Bryksin and P. Kleinert, J. Phys.: Condens. Matter **15** (9), 1415 (2003).
25. L. D. Landau and E. M. Lifshitz, *Course of Theoretical Physics*, Vol. 6: *Fluid Mechanics*, 3rd ed. (Nauka, Moscow, 1986; Pergamon, New York, 1987).
26. B. K. Ridley, Proc. Phys. Soc. **86**, 637 (1965).
27. M. P. Petrov, I. A. Sokolov, S. I. Stepanov, and G. S. Trofimov, J. Appl. Phys. **68** (5), 2216 (1990).

Translated by Yu. Epifanov

Physics of the Solid State, Vol. 45, No. 11, 2003, pp. 2053–2059. Translated from Fizika Tverdogo Tela, Vol. 45, No. 11, 2003, pp. 1954–1960.

SEMICONDUCTORS AND DIELECTRICS

Numerical Simulation of the Temperature Dependence of the Ionization Energy of Hydrogen-Like Impurities in Semiconductors: Application to Transmutation-Doped Ge : Ga

N. A. Poklonskiĭ*, S. A. Vyrko*, A. G. Zabrodskiĭ, and S. V. Egorov****

**Belarussian State University, pr. F. Skarina 4, Minsk, 220050 Belarus*

***Ioffe Physicotechnical Institute, Russian Academy of Sciences, Politekhnicheskaya ul. 26, St. Petersburg, 194021 Russia*

e-mail: poklonski@bsu.by

Received April 1, 2003

Abstract—An electrostatic model describing the dependence of the thermal ionization energy of impurities on their concentration, compensation factor, and temperature is developed. The model takes into account the screening of impurity ions by holes (electrons) hopping from impurity to impurity, the change in the impurity-band width, and its displacement with respect to the edge of the valence band for acceptors (conduction band for donors). The displacement of the impurity band is due to the functional dependence of the hole (electron) affinity of the ionized acceptor (donor) on the screening of the Coulomb field of the ions. The spatial distribution of the impurity ions over the crystal was assumed to be Poisson-like, and the energy distribution was assumed to be normal (Gaussian). For the relatively low doping levels under investigation, the behavior of the density of states at the edges of the valence and conduction bands was assumed to be the same as for the undoped crystal. The results of the numerical study are in agreement with the decrease in the ionization energy that is experimentally observed for moderately compensated Ge : Ga as the temperature and the doping level are decreased. It is predicted that the temperature dependence of the thermal ionization energy has a small anomalous maximum at small compensation factors. © *2003 MAIK "Nauka/Interperiodica".*

1. INTRODUCTION

The thermal ionization energy is the energy required for the dissociation of the bound electron–donor (hole–acceptor) state at a given temperature due to thermal fluctuations.[1] The value of the thermal ionization energy determines the temperature dependence of the concentration of free charge carriers. In doped semiconductors, this concentration is determined by ionization–recombination equilibrium between the electrons (holes) and impurity atoms (see, for example, [1]). For hydrogen-like impurities, certain limiting dependences of the low-temperature thermal ionization energy (E_1) on the concentration and compensation factor of these impurities were analyzed in [2, 3]. While analyzing the ionization equilibrium in doped semiconductors, the energy E_1 is usually supposed to be dependent on temperature T by analogy with the temperature dependence of the activation energy for the reactions occurring in a molecular gas [4] or a plasma [5]. However, the particular $E_1(T)$ dependence for semiconductors has not been reliably determined either theoretically or experimentally. For example, the influence of the screening of ions on the degree of ionization of noncompensated hydrogen-like impurities was analyzed as a function of temperature for a special case in [6]. In [6–11], the dispersion of the impurity energy levels, i.e., the formation of an impurity band with a finite width in the energy gap of the semiconductor was not taken into account. At the same time, knowledge of the $E_1(T)$ dependence is of importance in analyzing the temperature dependences of the electrical conductivity [12], the thermopower [13], and the electron paramagnetic resonance spectra [14].

As an illustration, let us consider the following two examples. In [15], it was assumed that the nitrogen impurity in 6*H*-SiC : N is almost completely ionized at room temperature even at high doping levels; as a result, a highly underestimated (in comparison with the experimental data) critical concentration of about 2×10^{19} cm^{-3} was obtained for the metal–insulator transition. Taking into account the actually small degree of ionization of the nitrogen impurity leads to a quite different value of 2×10^{20} cm^{-3} [16]. According to estimates made in [17], it follows from the experimentally measured conductivity that the metal–insulator transition in type-IIa natural diamond single crystals (after ionic implantation of boron followed by annealing) occurs at a boron concentration of about 10^{21} cm^{-3}. At the same time, optical measurements (based on a sharp decrease in the radiant energy of the bound exciton) on growing boron-doped diamond films gave only 10^{20} cm^{-3} [18].

[1] The optical ionization energy is the minimum photon energy required for the transition of the electron (hole) from the bound state to the continuous-spectrum state at a fixed localizing potential (according to Franck and Condon).

This paper is devoted to a numerical study of the thermal ionization energy of hydrogen-like impurities in crystal semiconductors at relatively low doping levels, that is, far from the metal–insulator phase transition. The contribution from the excited states of the impurity to the statistics, as well as the broadening and shift of the impurity band[2] with respect to the edge of the allowed band closest to it, is taken into account. A comparison with the existing models [10, 21, 22] describing the temperature, concentration, and compensation dependences of the thermal ionization energy is made.

2. NECESSARY FORMULAS

Let us consider a *p*-type crystal semiconductor.[3] In this case, the equation of electrical neutrality is

$$p + KN = N_{-1}, \tag{1}$$

where p is the hole concentration in the valence (v) band, $N = N_0 + N_{-1}$ is the concentration of acceptors in charge states (0) and (–1), and K is the compensation factor of the acceptors due to their compensation by donors (KN is the concentration of positively charged donors).

At low temperatures, where the thermal ionization energy E_1 is determined, the de Broglie wavelength of the delocalized holes is large and they are not affected by the fluctuation potential; that is, the tail of the hole density of states in the v band can be neglected [26]. In this case, the concentration of the free holes is determined by the equation [21, 22]

$$p = \int_0^\infty g_v f_p dE = 2\left(\frac{2\pi m_p k_B T}{(2\pi\hbar)^2}\right)^{3/2} F_{1/2}\left(\frac{E_F}{k_B T}\right), \tag{2}$$

where $g_v = \frac{1}{2\pi^2}\left(\frac{2m_p}{\hbar^2}\right)^{3/2}\sqrt{E}$ is the density of states of holes with effective mass m_p and energy E in the v band of a crystal of unit volume, $f_p = \left[1 + \exp\left(\frac{E - E_F}{k_B T}\right)\right]^{-1}$ is the Fermi–Dirac distribution, $k_B T$ is the thermal energy, $E_F < 0$ is the Fermi level with respect to the top of the v band (the Fermi level lies in the band gap), and

$$F_j\left(\frac{E_F}{k_B T}\right) = \int_0^\infty \frac{t^j dt}{1 + \exp[t - (E_F/k_B T)]}\left(\int_0^\infty t^{j+1}\exp(-t)dt\right)^{-1}$$

is the Fermi–Dirac integral.

It should be noted that the calculation of the effective (density-of-states) mass m_p depends on the type of the particular semiconductor. In *p*-Ge, for example, the effective mass is determined by the effective masses of the light (m_l) and heavy (m_h) holes: $m_p = (m_h^{3/2} + m_l^{3/2})^{2/3} = 0.384 m_0$ [27–29]. The spin–orbit split-off energy subband is 290 meV below the top of the v band (at $T \approx 1.5$ K), which significantly exceeds the energy level of the Ga atoms ($I_a \approx 11.32$ meV). Thus, the contribution from this subband to the effective hole mass can be ignored. In the crystalline diamond, however, the contribution from the mass m_s in the spin–orbit split-off subband should be taken into account, because its splitting from the v band is only 6 meV in this case, which is much smaller than the energy level of the main acceptor impurity in diamond ($I_a \approx 370$ meV) [30]. For this reason, the effective hole density-of-states mass is now $m_p = (m_h^{3/2} + m_l^{3/2} + m_s^{3/2})^{2/3} = 1.249 m_0$, where $m_h = 1.08 m_0$, $m_l = 0.36 m_0$, and $m_s = 0.15 m_0$ [28, 29].

If the distribution of the energy levels of the ionized acceptors is Gaussian, then the concentration of the ionized acceptors in the energy gap of the crystal is [2, 3]

$$N_{-1} = N\int_{-\infty}^{+\infty} g_a f_{-1} d(E_a - \bar{E}_a) = N - N_0, \tag{3}$$

where

$$g_a = \frac{1}{W_a\sqrt{2\pi}}\exp\left(\frac{-(E_a - \bar{E}_a)^2}{2W_a^2}\right) \tag{4}$$

is the normal (Gaussian) probability density of the acceptor energy levels E_a with the average value $\bar{E}_a$;

$$f_{-1} = 1 - f_0 = \left[1 + \beta_a(l_t)\exp\left(\frac{E_a + E_F}{k_B T}\right)\right]^{-1} \tag{5}$$

is the probability that an acceptor with energy level E_a will be ionized; and $\beta_a(l_t) = \beta_a\sum_{l=1}^{l_t} l^2 \exp\left(\frac{(1 - l^2)E_a}{l^2 k_B T}\right)$ is the effective degeneracy factor of the hydrogen-like

[2] Here, the so-called classical impurity band is considered [19, 20] for which the shift of the energy level of an impurity atom with respect to the bottom of the conduction band or the top of the valence band of the crystal can be assumed equal to the electrostatic potential energy of the interaction between the impurity atom and the other charged impurities and delocalized carriers.

[3] The conductivity type is not of importance. We choose a *p*-type semiconductor in order to compare our results with the experimental data for moderately compensated *p*-Ge : Ga samples doped by thermal reactor neutrons [23–25].

acceptor [7–10, 21, 22] having l_t levels, namely, the ground state ($l = 1$) and $l_t - 1$ excited states.

In Eq. (5), it is taken into account that the degeneracy factor of the lth excited state of the acceptor in the (0) charge state is larger than that of the ground state by a factor of l^2 and is equal to $\beta_a l^2$. It is also assumed that the ionization energy of the acceptor in the lth excited state is $E_{-1} - E_0(l) = E_a/l^2$, where E_a is the ionization energy of the ground state ($l = 1$).

For p-Ge, the degeneracy factor of the ground state of hydrogen-like acceptors is $\beta_a = 4$, because only light and heavy holes are taken into account in the v band. For the p-type diamond, we have $\beta_a = 6$, since three hole subbands are of importance in considering at the thermal ionization of boron atoms.

If only the Coulomb interaction with the nearest neighbors (ionized impurities or holes) is taken into account, then the root-mean-square fluctuation of the acceptor potential energy in the (–1) charge state is [2, 3]

$$W_a \approx 1.64\frac{e^2}{4\pi\varepsilon}\left(\frac{8\pi}{3}N_{-1}\right)^{1/3}, \tag{6}$$

where $\varepsilon = \varepsilon_r\varepsilon_0$ is the dielectric permittivity of the crystal lattice and $2N_{-1} = p + KN + N_{-1}$ is the total concentration of point charges in the crystal.

The energy of the average acceptor level (in the middle of the acceptor band) decreases as the doping level increases, because the attracting Coulomb field of the ions is screened by the holes from the acceptor and v bands [2]:

$$\bar{E}_a = I_a - \frac{3e^2}{16\pi\varepsilon(\Lambda_s + d)}, \tag{7}$$

where $I_a = e^2/(8\pi\varepsilon a_H)$ is the energy level of an isolated acceptor above the top of the v band, a_H is the Bohr radius, Λ_s is the screening length of the electrostatic field, $d \approx 0.554[(1 + K)N]^{-1/3}$ is the average distance between the nearest neighbor impurity atoms, and e is the magnitude of the electronic charge.

The maximum number l_t of levels of the neutral acceptor can be estimated from the condition that the Bohr radius of the outer orbit of a hole $a_H(l_t) = e^2 l_t^2/(8\pi\varepsilon I_a)$ does not exceed half the average distance between the nearest neighbor impurity atoms [5]. From the equality $a_H(l_t) = d/2$, we obtain the following expression for the number of levels (ground and excited states):

$$l_t^2 = 0.554\frac{4\pi\varepsilon_r\varepsilon_0 I_a}{e^2[(1 + K)N]^{1/3}}, \tag{8}$$

where $(1 + K)N$ is the total concentration of the hydrogen-like acceptors and donors in the crystal and $l_t = 1, 2, 3, \ldots$ is the minimal integer.

It should be noted that, in p-Ge : Ga ($\varepsilon_r = 15.4$, $I_a = 11.32$ meV, $K = 0.35$), according to Eq. (8), the hole–acceptor bound state is absent at the concentration of Ga atoms $N > 2.23 \times 10^{17}$ cm^{-3}. The value of N estimated using Eq. (8) is close to the critical concentration of Ga atoms $N_M \approx 1.85 \times 10^{17}$ cm^{-3} [31], which corresponds to the metal–insulator phase transition (Mott transition) at the temperature $T \longrightarrow 0$ for $K = 0.35$.

If the screening of the Coulomb field of an ion by free holes (index p) and by holes hopping from acceptor to acceptor (index h) is taken into account, the screening length Λ_s is determined by the formulas [32]

$$\Lambda_s^{-2} = \Lambda_p^{-2} + \Lambda_h^{-2},$$

$$\Lambda_p^{-2} = \frac{e^2}{\varepsilon}\frac{\partial p}{\partial E_F} = \frac{e^2}{\varepsilon}\frac{2^{1/2}m_p^{3/2}}{\pi^2\hbar^3 k_B T}\int_0^\infty E^{1/2} f_p(1 - f_p)dE$$

$$= \frac{e^2 p}{\varepsilon k_B T}\frac{F_{-1/2}(E_F/k_B T)}{F_{1/2}(E_F/k_B T)}, \tag{9}$$

$$\Lambda_h^{-2} = \frac{-e^2}{\varepsilon}\frac{\partial N_{-1}}{\partial E_F} = \frac{e^2}{\varepsilon k_B T}N\int_{-\infty}^{+\infty} g_a f_0 f_{-1} d(E_a - \bar{E}_a).$$

For $p \ll K(1 - K)N$ at low temperatures, when $N_{-1} \approx KN$, Eq. (9) yields [2]

$$\Lambda_s^{-2} \approx \Lambda_h^{-2}$$

$$\approx \frac{e^2}{\varepsilon}\frac{N}{W_a\sqrt{2\pi}}\exp\left(\frac{-(E_F + \bar{E}_a + k_B T\ln\beta_a)^2}{2W_a^2}\right). \tag{10}$$

Substituting Eq. (6) into Eq. (10) at $T \longrightarrow 0$, we obtain $\Lambda_s \approx \Lambda_h \approx 0.82K^{1/6}N^{-1/3}\exp(\gamma_a^2/4)$, where the value of $\gamma_a = (E_F + \bar{E}_a)/W_a$ can be found from the equation $1 - \mathrm{erf}(\gamma_a/\sqrt{2}) = 2K$.

3. NUMERICAL STUDY OF THE THERMAL IONIZATION ENERGY

Let us compare the numerical results obtained by following this scheme and the experimentally observed thermal ionization energy E_1. The experimental value of the thermal ionization energy of hydrogen-like impurity atoms in a semiconductor can be found from the temperature dependence of the free-hole concentration $p(T)$ using the formula [10, 21, 22]

$$E_1 = -k_B\frac{d\ln(pT^{-3/2})}{d(1/T)}. \tag{11}$$

In what follows, we consider the $E_1(T)$ dependence for a moderately compensated p-Ge : Ga produced by neutron doping of the originally pure Ge [23–25]. We assume that the concentration of Ga atoms N is much smaller than the critical concentration N_M for the

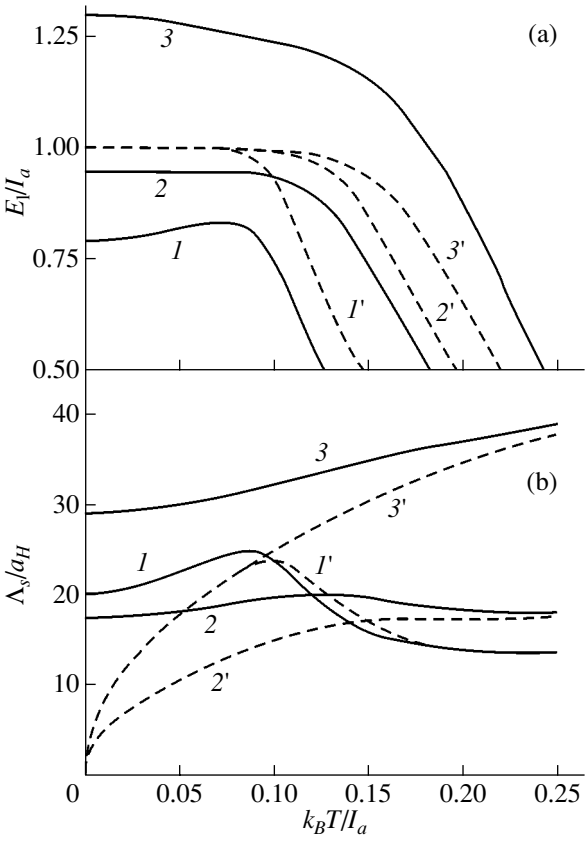

Fig. 1. Calculated temperature dependences of the thermal ionization energy E_1 of Ga atoms and of the screening length Λ_s of the Coulomb field of an impurity ion for different values of the compensation factor K of Ga atoms in *p*-Ge: (*1*, *1*') $K = 0.1$, (*2*, *2*') 0.5, and (*3*, *3*') 0.9. (a) Curves (*1*–*3*) show E_1 calculated for $I_a = 11.32$ meV and $N = 10^{15}$ cm^{-3} from Eq. (11) with the use of Eqs. (1)–(9); curves (*1*'–*3*') correspond to E_1 calculated for the case when $W_a \longrightarrow 0$ and $\bar{E}_a \longrightarrow I_a$ simultaneously. (b) Curves (*1*–*3*) show Λ_s calculated for $N = 10^{15}$ cm^{-3} from Eq. (9) with the use of Eqs. (1)–(8); curves (*1*'–*3*') are calculated from Eq. (9) for $W_a \longrightarrow 0$ and $\bar{E}_a \longrightarrow I_a$.

metal–insulator transition. Therefore, the divergence of the dielectric function at the critical point can be neglected and the dielectric function can be taken to be equal to its value for the pure material.

We calculate the temperature dependence of the thermal ionization energy of Ga atoms in Ge : Ga samples with $N = 10^{15}$ cm^{-3} and different compensation factors using the following parameters [27–29]: $I_a = 11.32$ meV, $m_p = 0.384m_0$, and $\varepsilon_r = 15.4$. The dependences calculated using Eq. (11) by employing Eqs. (1)–(9) are shown in Fig. 1a (curves *1*–*3*). For comparison, the temperature dependences of the ionization energy of hydrogen-like Ga acceptors in *p*-Ge are shown by dashed lines (curves *1*'–*3*'), which are calculated for the "ideal" semiconductor, that is, for an infinitely narrow acceptor band ($W_a \longrightarrow 0$) without considering its shift with respect to the top of the v band ($\bar{E}_a \longrightarrow I_a$). It is seen that if the broadening of the impurity band and its shift towards the v band are taken into account in accordance with the experimental data [33] for *n*-Ge : As, the thermal ionization energy E_1 of Ga atoms increases as the compensation factor increases.

According to our model, the thermal ionization energy E_1 slightly increases at $K = 0.1$ (Fig. 1a) in the low-temperature range, because the center of the impurity band $\bar{E}_a$ shifts from the v band deep into the band gap (due to an increase in the screening length, see Fig. 1b) and this shift exceeds the increase in the impurity band width W_a on heating.

Figure 1b shows the dependence of the screening length of the Coulomb field of an ion on the thermal energy k_BT; the screening length is measured in units of the Bohr radius $a_H = \varepsilon^2/8\pi\varepsilon I_a$, and the thermal energy is reduced to I_a. The dependence is calculated using Eq. (9) taking into account Eqs. (1)–(8). The nonmonotonic behavior of the screening length is noticeable at low temperatures, where the thermal ionization energy E_1 is virtually constant. If the finite width of the acceptor band is taken into account, then the screening length at $T \longrightarrow \infty$ does not vanish but tends to a finite value, because, in contrast to the case when $W_a \longrightarrow 0$ and $\bar{E}_a \longrightarrow I_a$ (dashed curves), the screening length is determined by the density of states in the impurity band at the Fermi level in this case. At high temperatures, where all acceptors are ionized, the screening length becomes equal to the Debye screening length, $\Lambda_s^{-2} \approx \Lambda_p^{-2} = e^2p/\varepsilon k_BT \approx (e^2/\varepsilon k_BT)(1 - K)N$, because the holes hopping from acceptor to acceptor do not contribute to the screening length in this case.

It should be noted that, at $p \ll K(1 - K)N$, the screening length given by Eq. (9) is equal to $\Lambda_s \approx \Lambda_h = [\varepsilon k_BT/e^2K(1 - K)N]^{1/2}$ for $W_a \longrightarrow 0$ [34, 35]; therefore, curves *1*' ($K = 0.05$) and *3*' ($K = 0.95$) coincide at low temperatures.

Figure 2 shows the dependence of the Fermi level E_F (curve *1*) on the compensation factor K for $T \longrightarrow 0$. This dependence is calculated from the equation of electrical neutrality $N_{-1} = KN$ by taking into account Eqs. (3)–(8). The circles show the numerically calculated dependence obtained in [19, 36]; dashed line *2* corresponds to the analytical expression for $-(E_F + I_a)/I_a$ derived in the framework of the model proposed in [20]. It should be noted that, for the case when $T \longrightarrow 0$, $W_a \longrightarrow 0$, and $\bar{E}_a \longrightarrow I_a$, the Fermi level tends to I_a for compensation factors $0 < K < 1$.

4. COMPARISON WITH THE EXPERIMENT

In Fig. 3, the symbols (squares, circles, triangles) show the temperature dependences calculated from Eq. (11) with the use of the experimental data from [12] for samples of the neutron transmutation–doped Ge : Ga with different doping levels.[4] The experimental values of $p(1/T)$ were approximated by a sixth-degree polynomial on a semilogarithmic scale, and then the reciprocal-temperature derivative was found analytically. It should be noted that, in the range of hopping conduction via acceptors, the dependence of $\ln p$ on $1/T$ was straightened according to the relationship $p = (eR_H)^{-1}(1 + \sigma_h/\sigma_v)^{-2}$ (see, for example, [7, 12, 37]), where $R_H = R_v$ is the Hall coefficient for holes in the v band and σ_v and σ_h are the conductivities corresponding to the band (v) and hopping (h) mechanisms of the hole transport, respectively. If $2 \times 10^{14} < N < 2 \times 10^{16}$ cm^{-3} and $K \approx 0.35$, then, according to the experimental data [12, 37], the conductivity due to holes in the v band σ_v becomes equal to the hopping conductivity σ_h via Ga atoms at the temperature T_h given by $T_h = 5.3 \times 10^{-4} N^{0.27}$, where $[T_h]$ = K and $[N]$ = cm^{-3}.

The curves in Fig. 3 show the temperature dependence of the thermal ionization energy calculated from Eq. (11) with the use of Eqs. (1)–(9). It is seen that the result obtained in our model is in good agreement with the experimentally observed dependence of the thermal ionization energy on the doping level and temperature.

Let us compare curves *1–3* in Fig. 3 with those calculated within a model that takes into account the "hopping" screening of the Coulomb field of the impurity ions at each act of thermal ionization of the corresponding neutral atom [38]. According to [38], the energy level of the "average" acceptor at high temperatures ($k_BT \gg W_a$) is given by

$$\bar{E}_a = I_a - \frac{e^3 N^{1/2}}{8\pi(\varepsilon_r\varepsilon_0)^{3/2}(k_BT)^{1/2}}(K+3)\sqrt{K(1-K)}. \quad (12)$$

Dashed line *1'* in Fig. 3 shows the $E_1(T)$ dependence calculated from Eq. (11) with the use of Eq. (12) for $N = 3.7 \times 10^{14}$ cm^{-3} and $K = 0.35$ in the infinitely narrow impurity band approximation, where g_a tends to the Dirac delta function $\delta(E_a - \bar{E}_a)$. For the concentrations corresponding to curves *2* and *3*, the values of $E_1(T)$ calculated from the model proposed in [38] are much smaller than $E_1/I_a = 0.5$.

Figure 4 shows the dependences of $-k_BT(dp/dE_F)$ on the position of the Fermi level $E_F < 0$ in the energy gap of p-Ge : Ga ($N = 6.3 \times 10^{15}$ cm^{-3}, $K = 0.35$) as the temperature increases from 10 to 100 K. These dependences are calculated using the method proposed in [39] with the use of Eqs. (1)–(9). It is seen that if the finite width of the acceptor band and the shift of this band towards the v band are taken into account, the agreement with the experimental data from [12] is, in general, better than in the case where $W_a \longrightarrow 0$ and $\bar{E}_a \longrightarrow I_a$.

[4] In [12], the experimental data were processed under the assumption that the Hall factor for holes in the v band is equal to 1 over the whole temperature range covered.

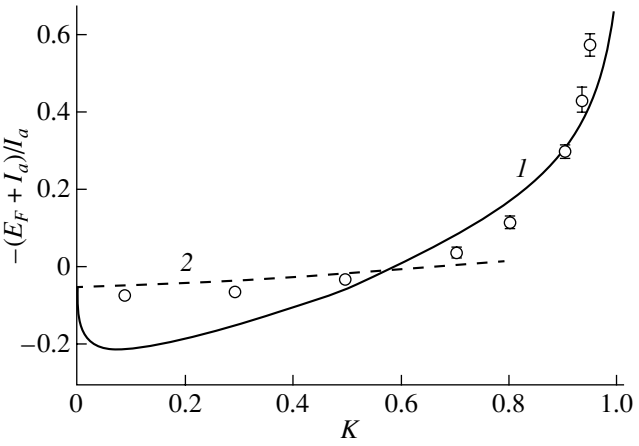

Fig. 2. (*1*) Dependence of the Fermi level E_F reduced to the ionization energy of a single Ga atom $I_a = 11.32$ meV in germanium on the compensation factor K for $N = 10^{15}$ cm^{-3} at temperature $T \longrightarrow 0$ (*1*). Circles show the results of the numerical study performed in [19, 36]; curve (*2*) corresponds to $-(E_F + I_a)/I_a$ calculated in the framework of the model proposed in [20].

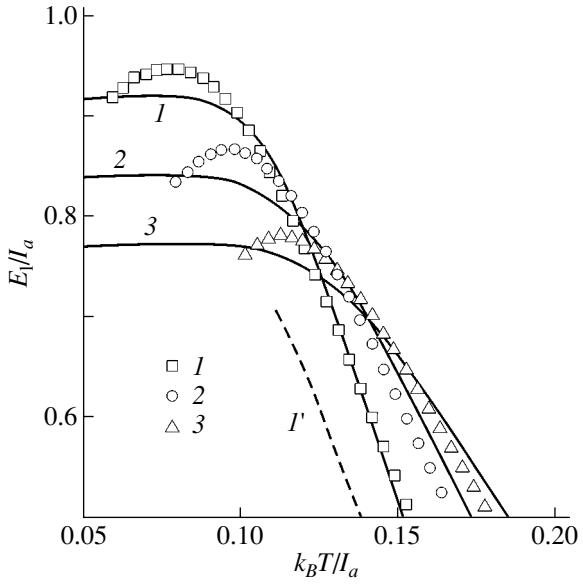

Fig. 3. Temperature dependence of the thermal ionization energy of Ga acceptors in p-Ge ($K = 0.35$). The points correspond to experimental data from [12]. Curves (*1–3*) show the $E_1(T)$ dependence calculated from Eq. (11) with the use of Eqs. (1)–(9); curve (*1'*) is calculated using the model proposed in [38]. (*1*, *1'*) $N = 3.7 \times 10^{14}$, (*2*) 2.3×10^{15}, and (*3*) 6.3×10^{15} cm^{-3}.

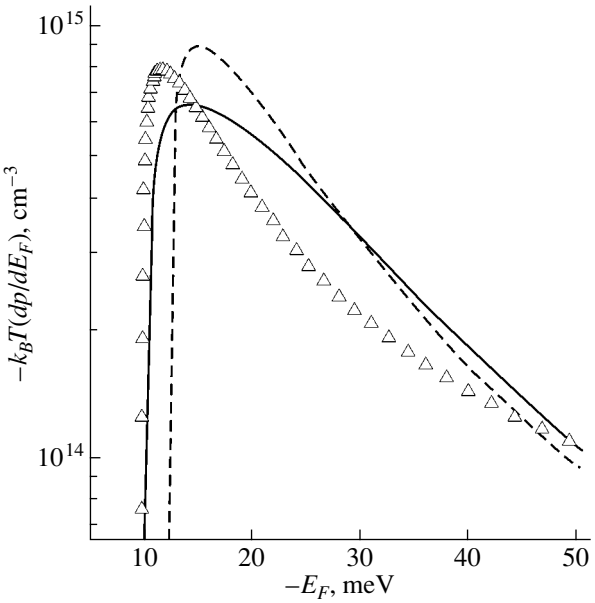

Fig. 4. Dependence of $-k_BT(dp/dE_F)$ on the position of the Fermi level in the band gap of *p*-Ge : Ga for $N = 6.3 \times 10^{15}$ cm^{-3} and $K = 0.35$. The experimental data (triangles) are taken from [12]; the solid line is calculated from Eqs. (1)–(9); the dashed line is calculated for $W_a \longrightarrow 0$ and $\bar{E}_a \longrightarrow I_a$.

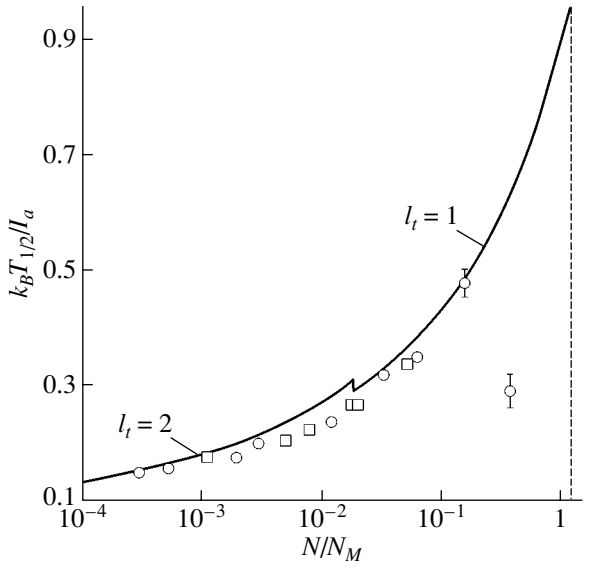

Fig. 5. Temperature $T_{1/2}$ at which half the neutral (for $T \longrightarrow 0$) Ga atoms are ionized on heating of *p*-Ge : Ga with a compensation factor $K \approx 0.35$ plotted as a function of the concentration of the Ga atoms N reduced to $N_M = 1.85 \times 10^{17}$ cm^{-3}. The solid line is calculated from Eqs. (1)–(9); the jump in this line is associated with the change in the number of excited states of the hydrogen-like Ga atom given by Eq. (8). The dashed line corresponds to $l_t < 1$ and $T_{1/2} \longrightarrow 0$. The points show values of $T_{1/2}$ calculated from experimental data from [12, 37].

The adequacy of our model can also be tested by analyzing the concentration dependence of the temperature $T_{1/2}$ at which exactly half the neutral (at $T \longrightarrow 0$) impurity atoms becomes ionized (Fig. 5). It can be derived from Eq. (1) that the relationship $p(T_{1/2}) = N_{-1}(T_{1/2}) - KN = (1 - K)N/2$ holds for $T_{1/2}$ (here, it is taken into account that KN acceptors are already ionized at $T \longrightarrow 0$). Thus, $p(T_{1/2})$ is the concentration of holes at the temperature $T_{1/2}$ where only half of the $(1 - K)N$ neutral acceptors are ionized: $N_{-1}(T_{1/2}) = (1 + K)N/2$. Knowing the concentration of acceptors N and their compensation factor K due to donors, one can estimate the value of $T_{1/2}$ from the experimental temperature dependence of the hole concentration by using the expression for $p(T_{1/2})$. Figure 5 shows the dependence of the temperature $T_{1/2}$ on the concentration of acceptors N (reduced to $N_M \approx 1.85 \times 10^{17}$ cm^{-3}) calculated by Eqs. (1)–(9) for *p*-Ge with the compensation factor $K \approx 0.35$. For comparison, the values of $T_{1/2}$ found using experimental data from [12, 37] and the procedure described above are also shown in Fig. 5. The downward deviation of the experimental point for the Ga concentration $N > 3 \times 10^{16}$ cm^{-3} from the calculated curve is due to the fact the metal–insulator transition is being approached and, seemingly, due to the effect of the tails of the density of states of the v band on the thermodynamics of the ionization processes. According to Eq. (8), the break of the solid curve in Fig. 5 is associated with the transition from the number of levels $l_t = 2$ to $l_t = 1$ (no excited states), which occurs as the concentration of the Ga atoms in Ge is increased. The dashed line corresponds to the case where there are no bound states in the system of a hole and a Ga atom (i.e., $l_t < 1$) and the temperature $T_{1/2} \longrightarrow 0$. It should be noted here that the calculated $T_{1/2}(N)$ dependence for the ideal crystal ($W_a \longrightarrow 0$; $\bar{E}_a \longrightarrow I_a$) actually coincides with the above calculation (solid curve in Fig. 5). Therefore, the finite width of the impurity band can be revealed only by using differential dependences (Figs. 1, 3, 4).

5. CONCLUSIONS

Thus, a theoretical description of the dependence of the thermal ionization energy of a hydrogen-like impurity on the temperature, concentration doping-impurity, and compensation factor of the impurity has been developed for crystal semiconductors in a region that is sufficiently far from the metal–insulator transition point. The model developed in this paper predicts the following feature in the temperature dependence of the thermal ionization energy for different values of the compensation factor: at intermediate and large values of the compensation factor, the thermal ionization energy drops with increasing temperature, whereas at small values of the compensation factor this energy can increase in a certain temperature range. The weak increase in the thermal ionization energy with tempera-

ture occurs because the center of the acceptor band shifts from the v band and this shift becomes larger than the acceptor band broadening as the temperature increases in the range $k_BT \ll I_a$.

The numerically calculated temperature dependence of the thermal ionization energy has been found to agree with the experimental data for moderately compensated Ge : Ga samples produced by neutron-transmutation doping.

ACKNOWLEDGMENTS

This work was supported by the Belarusian Foundation for Basic Research (project no. F01-199) and the Russian Foundation for Basic Research (project nos. 01-02-17813, 00-15-96750).

REFERENCES

1. E. V. Kuchis, *Galvanomagnetic Effects and Methods of Their Studies* (Radio i Svyaz', Moscow, 1990).
2. N. A. Poklonskiĭ, A. I. Syaglo, and G. Biskupski, Fiz. Tekh. Poluprovodn. (St. Petersburg) **33**, 415 (1999) [Semiconductors **33**, 402 (1999)].
3. N. A. Poklonskiĭ and A. I. Syaglo, Fiz. Tekh. Poluprovodn. (St. Petersburg) **33**, 402 (1999) [Semiconductors **33**, 391 (1999)].
4. W. Stiller, *Arrhenius Equation and Non-Equilibrium Kinetics* (Teubner, Leipzig, 1989; Mir, Moscow, 2000).
5. W. Ebeling, W. D. Kraeft, and D. Kremp, *Theory of Bound States and Ionization Equilibrium in Plasmas and Solids* (Akademie, Berlin, 1976; Mir, Moscow, 1979).
6. S. K. Chun, J. Appl. Phys. **80**, 4773 (1996).
7. J. S. Blakemore, *Semiconductor Statistics* (Pergamon, Oxford, 1962; Mir, Moscow, 1964).
8. B. I. Boltaks, M. K. Bakhadyrkhanov, S. M. Gorodetskiĭ, and G. S. Kulikov, *Compensated Silicon*, Ed. by B. I. Boltaks (Nauka, Leningrad, 1972).
9. A. G. Milnes, *Deep Impurities in Semiconductors* (Wiley, New York, 1973; Mir, Moscow, 1977).
10. V. O. Bariss and É. É. Klotyn'sh, *Determination of Local Level Parameters in Semiconductors* (Zinatne, Riga, 1978).
11. J. H. Nevin, H. T. Henderson, and K. L. Shen, Mater. Res. Bull. **17**, 1111 (1982).
12. A. G. Andreev, V. V. Voronkov, G. I. Voronkova, *et al.*, Fiz. Tekh. Poluprovodn. (St. Petersburg) **29**, 2218 (1995) [Semiconductors **29**, 1162 (1995)].
13. A. G. Andreev, A. G. Zabrodskiĭ, I. P. Zvyagin, and S. V. Egorov, Fiz. Tekh. Poluprovodn. (St. Petersburg) **31**, 1174 (1997) [Semiconductors **31**, 1008 (1997)].
14. A. I. Veĭnger, A. G. Zabrodskiĭ, and T. V. Tisnek, Fiz. Tekh. Poluprovodn. (St. Petersburg) **34**, 46 (2000) [Semiconductors **34**, 45 (2000)].
15. M. N. Alexander and D. F. Holcomb, Rev. Mod. Phys. **40**, 815 (1968).
16. M. V. Alekseenko, A. G. Zabrodskiĭ, and M. P. Timofeev, Fiz. Tekh. Poluprovodn. (Leningrad) **21**, 810 (1987) [Sov. Phys. Semicond. **21**, 494 (1987)].
17. T. Tshepe, J. F. Prins, and M. J. R. Hoch, Diamond Relat. Mater. **8**, 1508 (1999).
18. H. Sternschulte, T. Albrecht, K. Thonke, and R. Sauer, in *Proceedings of 23rd International Conference on the Physics of Semiconductors* (World Sci., Singapore, 1996), Vol. 1, p. 169.
19. B. I. Shklovskiĭ and A. L. Éfros, Fiz. Tekh. Poluprovodn. (Leningrad) **14**, 825 (1980) [Sov. Phys. Semicond. **14**, 487 (1980)].
20. Yu. Ya. Tkach and E. V. Chenskiĭ, Zh. Éksp. Teor. Fiz. **102**, 1683 (1992) [Sov. Phys. JETP **75**, 910 (1992)].
21. V. L. Bonch-Bruevich and S. G. Kalashnikov, *Physics of Semiconductors*, 2nd ed. (Nauka, Moscow, 1990).
22. K. Seeger, *Semiconductor Physics: an Introduction*, 7th ed. (Springer, Berlin, 1999).
23. A. G. Zabrodskiĭ and M. V. Alekseenko, Fiz. Tekh. Poluprovodn. (St. Petersburg) **28**, 168 (1994) [Semiconductors **28**, 101 (1994)].
24. *Neutron Transmutation Doping of Semiconductors*, Ed. by J. M. Meese (Plenum, New York, 1979; Mir, Moscow, 1982).
25. I. S. Shlimak, Fiz. Tverd. Tela (St. Petersburg) **41**, 794 (1999) [Phys. Solid State **41**, 716 (1999)].
26. J. M. Ziman, *Models of Disorder: the Theoretical Physics of Homogeneously Disordered Systems* (Cambridge Univ. Press, Cambridge, 1979; Mir, Moscow, 1982).
27. T. M. Lifshits, Prib. Tekh. Éksp., No. 1, 10 (1993).
28. *Semiconductors-Basic Data*, Ed. by O. Madelung (Springer, Berlin, 1996).
29. *Handbook Series on Semiconductor Parameters*, Ed. by M. Levinstein, S. Rumyantsev, and M. Shur (World Sci., Singapore, 1996 and 1999), Vols. 1 and 2.
30. V. S. Vavilov, Usp. Fiz. Nauk **167**, 17 (1997) [Phys. Usp. **40**, 15 (1997)].
31. A. G. Zabrodskii, A. G. Andreev, and S. V. Egorov, Phys. Status Solidi B **205**, 61 (1998).
32. N. A. Poklonskiĭ, Izv. Vyssh. Uchebn. Zaved., Fiz. **27**, 41 (1984).
33. I. S. Shlimak and V. V. Emtsev, Pis'ma Zh. Éksp. Teor. Fiz. **13**, 153 (1971) [JETP Lett. **13**, 107 (1971)].
34. N. A. Poklonski, V. F. Stelmakh, V. D. Tkachev, and S. V. Voitikov, Phys. Status Solidi B **88**, K165 (1978).
35. A. A. Uzakov and A. L. Éfros, Zh. Éksp. Teor. Fiz. **81**, 1940 (1981) [Sov. Phys. JETP **54**, 1028 (1981)].
36. N. V. Lien and B. I. Shklovskiĭ, Fiz. Tekh. Poluprovodn. (Leningrad) **13**, 1763 (1979) [Sov. Phys. Semicond. **13**, 1025 (1979)].
37. L. V. Govor, V. P. Dobrego, and N. A. Poklonskiĭ, Fiz. Tekh. Poluprovodn. (Leningrad) **18**, 2075 (1984) [Sov. Phys. Semicond. **18**, 1292 (1984)].
38. A. A. Uzakov and A. L. Éfros, Fiz. Tekh. Poluprovodn. (Leningrad) **21**, 922 (1987) [Sov. Phys. Semicond. **21**, 562 (1987)].
39. H.-J. Hoffmann, Appl. Phys. **19**, 307 (1979).

Translated by A. Poushnov

Physics of the Solid State, Vol. 45, No. 11, 2003, pp. 2060–2066. Translated from Fizika Tverdogo Tela, Vol. 45, No. 11, 2003, pp. 1961–1967.

SEMICONDUCTORS AND DIELECTRICS

Spectral Photoresistive Effect of the Field in CdS Crystals at Low Temperatures

A. S. Batyrev*, R. A. Bisengaliev*, N. V. Zhukova*, B. V. Novikov, and É. I. Chityrov****

** Kalmyk State University, Élista, 358000 Russia*

*** Research Institute of Physics, St. Petersburg State University, Ul'yanovskaya ul. 1, Petrodvorets, St. Petersburg, 198904 Russia*

e-mail: chityrov@mail.ru

Received March 18, 2003; in final form, April 14, 2003

Abstract—The influence of the surface electric field on the low-temperature (T = 77 K) photoconductivity spectra of CdS crystals in the region of exciton and interband transitions is experimentally studied by the field-effect method. The photoconductivity spectra of a semiconductor are numerically calculated in the framework of a model allowing for the dependence of the surface recombination rate of nonequilibrium charge carriers on the surface electric field. It is demonstrated that the surface electric field plays a decisive role in the formation of the fine spectral structure associated with the excitons. A correlation between the type of fine structure and the surface bending of the energy bands is revealed. It is shown that the surface electric field can be evaluated from the shape of the low-temperature photoconductivity spectrum of the semiconductor. *© 2003 MAIK "Nauka/Interperiodica".*

1. INTRODUCTION

Low-temperature band-edge photoconductivity spectra of CdS crystals and their evolution under the action of external factors have been studied in a large number of works.[1] Despite the great variety of photoconductivity spectra, Gross and Novikov [1] succeeded in separating characteristic types of spectra and, on this basis, classifying semiconductor crystals. Photoconductivity spectra are separated into two types, depending on whether maxima (first type) or minima (second type) of photocurrent correspond to exciton absorption lines. According to the spectroscopic classification proposed for semiconductor crystals with a natural surface, crystals can also be divided into two groups: the first group of crystals is characterized by first-type photoconductivity spectra measured in a dc electric field at T = 77 K, and the second group of crystals is characterized by second-type photoconductivity spectra measured under the same conditions.

Recent studies of low-temperature band-edge photoconductivity spectra of CdS crystals revealed a high sensitivity of these spectra and, especially, of their fine structure to external factors acting on the semiconductor. In particular, the band-edge photoconductivity spectra of CdS crystals at T = 77 K were investigated as a function of the transverse electric field in [2] and under exposure to IR light in [3]. In both works, it was found that the photoconductivity spectra undergo radical transformations up to a change in their type under external action. It was demonstrated that the inhomogeneous surface electric field together with small-sized and deep bulk centers substantially affect the structure of these spectra and, particularly, their fine structure. Furthermore, it was established that the partial contribution of bulk impurity states to band-edge photoconductivity of a semiconductor is completely suppressed upon exposure to IR light. A number of qualitative models were proposed to explain the phenomena observed.

According to [2], the influence of an inhomogeneous surface electric field on the photoconductivity spectra of CdS is associated with the dependence of the surface recombination rate of nonequilibrium charge carriers on the bending of energy bands near the surface of the semiconductor. Within this model, the type of photoconductivity spectrum is determined by the character of surface band bending. In particular, the first and second types of photoconductivity spectra correspond to the enriching (positive) and depleting (negative) band bendings, respectively. In the framework of the model proposed in [2], the structureless band-edge photoconductivity spectrum is attributed to flat (horizontal) bands near the surface of the semiconductor.

This study is a continuation of our earlier investigations into the influence of the surface electric field on the low-temperature photoconductivity spectra of CdS [2]. In the present work, we analyzed the effect of the surface electric field on the band-edge photoconductivity spectra of CdS crystals belonging not only to the first group (as is the case considered in [2]) but also to the second group. Moreover, the semiconductor sam-

[1] Regarding band-edge photoconductivity, we distinguish intrinsic band-edge photoconductivity due to exciton and interband transitions and band-edge photoconductivity governed by transitions involving small-sized (hydrogen-like) centers.

ples were exposed to IR light with the aim of excluding the bulk effects caused by impurity centers in the band-edge photoconductivity spectra. We also calculated numerically the intrinsic band-edge photoconductivity spectra of CdS crystals for different (in sign and strength) surface electric fields. The calculations were based on the solution of the continuity equation for nonequilibrium electrons under the boundary conditions determined by the surface recombination in an electric field near the surface of the semiconductor [4]. The calculated spectra agree well with the experimentally observed evolution of the photoconductivity spectra of CdS in the range of exciton and interband transitions in response to an external transverse electric field.

2. EXPERIMENTAL TECHNIQUE

The low-temperature (T = 77 K) photoconductivity spectra were measured with undoped CdS single crystals prepared in the form of plates 1–200 μm thick. The samples were placed in a capacitor cell. The cell made it possible to investigate the dependence of the photoconductivity spectrum on the potential of a field (control) capacitor plate with respect to the sample. Indium conducting ohmic contacts were evaporated onto the sample surface under vacuum with a residual pressure of ~10^{-3} Pa. Photoexcitation was performed as viewed from the control capacitor plate, which was a semitransparent tin dioxide (SnO_2) layer on a glass. The photoconductivity was excited by radiation separated using an MDR-2 wide-aperture monochromator from the continuous spectrum of a ribbon filament lamp with a power of 250 W. The samples were exposed to focused IR radiation separated by an IKS-1 glass optical filter from the radiation of a low-power (20 W) incandescent lamp (when required, the IR radiation intensity could be changed by varying the filament voltage). The pulling (measuring) voltage applied to the samples was provided by a dc power supply and did not exceed 100 V. The transverse electric field applied to the sample surface through a thin (≤10 μm) mica (muscovite) plate was produced by a dc stabilized voltage supply with the output voltage regulated in the range 0–2.5×10^3 V. The photoconductivity spectra were recorded with a V7-30 electrometric amplifier on the recording chart of a potentiometer upon continuous photoexcitation in the geometries $\mathbf{E} \perp \mathbf{C}$ or $\mathbf{E} \parallel \mathbf{C}$ and $\mathbf{k} \perp \mathbf{C}$ (where $\mathbf{E}$ is the electric vector of the light wave, $\mathbf{k}$ is the wave vector of the light wave, and $\mathbf{C}$ is the hexagonal axis of the crystal). In all the experiments, the spectral resolution was better than 8 Å.

3. RESULTS

Figure 1 shows the photoconductivity spectra of the CdS crystals belonging to the first group for different voltages U_n applied to the control electrode. The application of this voltage to the sample results in the depletion of the surface layer in majority charge carriers,

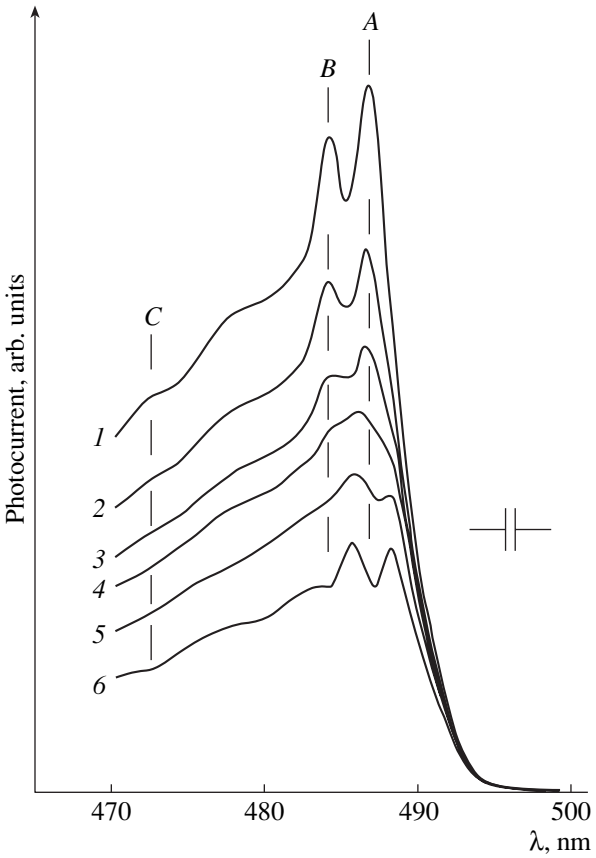

Fig. 1. Experimental photoconductivity spectra of a CdS crystal belonging to the first group for different voltages U_n applied to the control plate of the capacitor cell. $\mathbf{E} \perp \mathbf{C}$, $\mathbf{k} \perp \mathbf{C}$, T = 77 K. U_n = (*1*) 0, (*2*) –250, (*3*) –500, (*4*) –800, (*5*) –1200, and (*6*) –1900 V. Here and in Figs. 2 and 3, features *A*, *B*, and *C* are associated with the excitons generated from valence bands due to the crystalline and spin–orbit splittings.

namely, electrons. As can be seen from Fig. 1, the application of the depleting transverse electric field leads to a decrease in photosensitivity over the entire spectral range covered. An increase in the field strength is accompanied by a decrease in the photosensitivity. In this case, the spectrum of the first type (Fig. 1, curve *1*) gradually transforms into a spectrum of the second type (Fig. 1, curve *6*). The observed transformation of photoconductivity spectra of the first type with an increase in the depleting transverse electric field is reversible and occurs through an intermediate, virtually structureless photoconductivity spectrum (Fig. 1, curve *4*).

Characteristic changes in the low-temperature photoconductivity spectra upon application of an external transverse field are also observed for CdS crystals of the second group. For these crystals, as for crystals of the first group, the photosensitivity in the range of exciton and interband transitions increases at positive voltages U_n and decreases at negative voltages U_n Moreover, the photoconductivity spectra of these crystals can

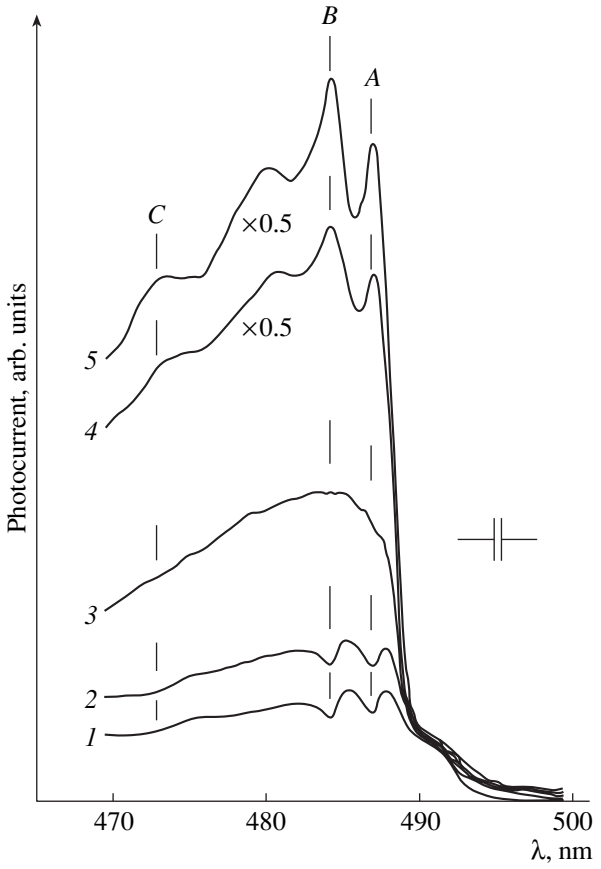

Fig. 2. Experimental photoconductivity spectra of a CdS crystal belonging to the second group for different voltages U_n applied to the control plate of the capacitor cell. $\mathbf{E} \perp \mathbf{C}$, $\mathbf{k} \perp \mathbf{C}$, $T = 77$ K. U_n = (*1*) 0, (*2*) 150, (*3*) 300, (*4*) 500, and (*5*) 600 V.

change qualitatively at positive voltages U_n. Actually, we observed for the first time that, for a number of CdS crystals of the second group, the photoconductivity spectrum of the second type reversibly transforms into a photoconductivity spectrum of the first type with an increase in the positive potential relative to the control plate of the capacitor cell (Fig. 2, curves *1–5*). Note that the photoconductivity spectrum at the intermediate stage of this transformation has a smooth (structureless) shape (Fig. 2, curves *3*).

Thus, the CdS crystals under investigation are characterized by the spectral photoresistive field effect, which resides in the quantitative and qualitative changes in the photoconductivity spectra in response to an external transverse electric field. In this case, the depleting transverse field ($U_n < 0$) always brings about a decrease in the photosensitivity and, at sufficiently high strengths, transformation of the photoconductivity spectrum of the first type to a photoconductivity spectrum of the second type. By contrast, the application of an enriching transverse field ($U_n > 0$) leads to an increase in the photosensitivity and can result in the transformation of the photoconductivity spectrum of the second type to a photoconductivity spectrum of the first type. In both cases, the transformation of the photoconductivity spectra with an increase in the transverse field strength involves two stages. At the first stage, the fine structure of the spectrum is smeared and almost completely disappears. Then, at the second stage, a fine structure of another type appears and becomes pronounced.

4. DISCUSSION

In semiconductors with direct allowed transitions, the intrinsic band-edge photoconduction proceeds in a thin surface layer (the layer thickness in CdS crystals is approximately equal to 10^{-5} cm) owing to the large optical absorption coefficient in the spectral region of exciton and interband transitions. As a result, the parameters (including the spectral characteristics) of the photoconduction depend on external and internal factors disturbing the state of the surface and (or) the surface region in a semiconductor. In particular, the latter factors involve an inhomogeneous electric field of a space charge generated in the surface layer due to the localization of charge carriers at levels of surface electron states. This factor is decisive in many optical and photoelectric processes [4, 5] occurring near the surface of a semiconductor. The inhomogeneous electric field can easily be controlled (over wide ranges) by varying the magnitude and sign of the space charge in the surface layer through an external transverse field (the field-effect method). In this respect, investigation into the influence of the external transverse field on the band-edge photoconductivity spectra of semiconductors makes it possible to establish uniquely how the surface electric field affects the photoconductivity spectra.

The mechanism of the influence of the surface field on the band-edge photoconductivity of a semiconductor is associated with the dependence of the surface recombination rate of nonequilibrium charge carriers on the bending of energy bands near the surface of the semiconductor. In monopolar semiconductors of the CdS type, the surface recombination rate is determined by the velocity of drift of minority charge carriers (holes) to the surface and increases with an increase in the drift velocity [4]. As a consequence, the lifetime of nonequilibrium majority charge carriers (electrons) near the surface of these semiconductors depends on the sign and the magnitude of surface band bending. Compared to the lifetime in the absence of band bending, the aforementioned lifetime increases with an increase in the enriching (positive) band bending in the vicinity of the surface and decreases with an increase in the depleting (negative) band bending. Consequently, the photoconductivity of a semiconductor upon excitation with strongly absorbed light should increase with an increase in the enriching band bending and decrease with an increase in the depleting band bending near the surface. Note that the most significant change in the

photoconductivity should be observed in the range of exciton resonances with the largest absorption coefficients in the edge spectral range. These inferences are supported by the experimental data (see Figs. 1, 2).

Therefore, the above mechanism of the influence of the surface electric field on the band-edge photoconductivity in monopolar semiconductors offers a qualitative explanation of the spectral photoresistive effect observed in the CdS crystals.

In order to describe quantitatively the influence of the surface electric field on the band-edge photoconductivity spectra of CdS crystals, we will use the results obtained by Nyberg and Colbow [4]. These authors solved the stationary one-dimensional continuity equation for nonequilibrium electrons under boundary conditions allowing for the surface recombination in the presence of an electric field at the surface of the semiconductor. The derived function of the electron distribution in the semiconductor along the X axis normal to the surface plane (the coordinate x increases from the surface deep into the sample) has the form

$$\Delta n(x) = \frac{\alpha I_0 \tau_n}{1-(\alpha L_a)^2} - \left[\exp(-\alpha x) - \frac{S_n - \mu_n E_s + \alpha D_n}{S_n - \mu_n E_s + D_n/L_a}\exp(-x/L_a)\right]. \quad (1)$$

Here, α is the absorption coefficient, I_0 is the excitation intensity (the number of photons absorbed by the semiconductor in a unit time per unit area), τ_n is the electron lifetime, L_a is the ambipolar-diffusion length, S_n is the surface recombination rate, μ_n is the electron mobility, E_s is the electric field strength at the surface of the semiconductor, and D_n is the electron diffusion coefficient.

Note that the parameters L_a and D_n entering into relationship (1) can be expressed through the basic photoelectric parameters of the semiconductor (such as the lifetimes and mobilities of charge carriers) according to the formulas [6]

$$L_a = \sqrt{\frac{2\mu_n\tau_n kT/e}{1+(\mu_n\tau_n)/(\mu_p\tau_p)}}, \quad D_n = \mu_n\frac{kT}{e}, \quad (2)$$

where k is the Boltzmann constant, e is the elementary charge, μ_p is the hole mobility, and τ_p is the hole lifetime (the second formula is known as the Einstein relation).

It should also be noted that expression (1) was derived for strongly absorbed light corresponding to the range of interband transitions under the implicit assumption that the quantum yield β is equal to unity. This assumption holds true in the spectral range of intrinsic band-edge photoconductivity in which $\beta \approx 1$ [7]. However, the validity of expression (1) over the entire range of the long-wavelength wing of exciton absorption line A ($n = 1$) is in doubt, because the quantum yield in this spectral range should decrease with a decrease in the photon energy.

The point is that the quantum yield in the spectral range of exciton states is determined by the interaction of excitons with phonons, defects [8, 9], and the surface electric field [5, 10]. In the case of the exciton–phonon interaction, the exciton dissociation is caused primarily by the interaction with optical phonons [8]. This interaction is predominantly responsible for the central part of the exciton absorption line, whereas the wings of the line are attributed to the interaction with acoustic phonons [11]. Therefore, in the long-wavelength range of exciton absorption line A ($n = 1$), the probability of exciton dissociation due to the interaction with phonons should decrease from the maximum of the line to its wing. The generation of free carriers through the interaction of excitons with defects is particularly efficient in the surface layer of the semiconductor, in which a higher concentration of defects leads to a severalfold increase in the probability of this interaction [12]. Consequently, in the spectral range of exciton state A ($n = 1$), the generation of free carriers through the exciton–defect interaction channel is efficient in the range of the absorption line at the maximum and is virtually suppressed in the range of the long-wavelength wing. The special role of the surface layer in the generation of free carriers through the exciton states is also dictated by the inhomogeneous surface electric field in which excitons can undergo electric-field and tunnel ionization. As in the preceding case, the efficiency of this channel of the contribution from excitons to the photoconductivity of the semiconductor changes in the range of the exciton absorption line and decreases when going from the range of the line maximum to the range of the line wing due to an increase in the depth of exciton generation owing to a decrease in the absorption coefficient.

From the above discussion, it follows that the quantum yield in the range of the long-wavelength wing of exciton absorption line A ($n = 1$) decreases with a decrease in the absorption coefficient. Note that processes responsible for the quantum yield in the range of the exciton resonance predominantly determine the shape of the exciton absorption line. Therefore, the function $\beta(\nu)$ describing the dependence of the quantum yield β on the frequency ν in this spectral range can be represented in the Lorentzian form

$$\beta(\nu) = \frac{\gamma^2}{(\nu-\nu_0)+\gamma^2}, \quad (3)$$

where ν_0 is the resonance frequency of the exciton and γ is a parameter of the order of the width of the exciton absorption line.

Relationships (1) and (3) allow us to calculate the intrinsic band-edge photoconductivity spectrum of the semiconductor. By integrating expression (1) from 0 to d (where d is the sample thickness) and multiplying the obtained result by β, we derive the expression for the

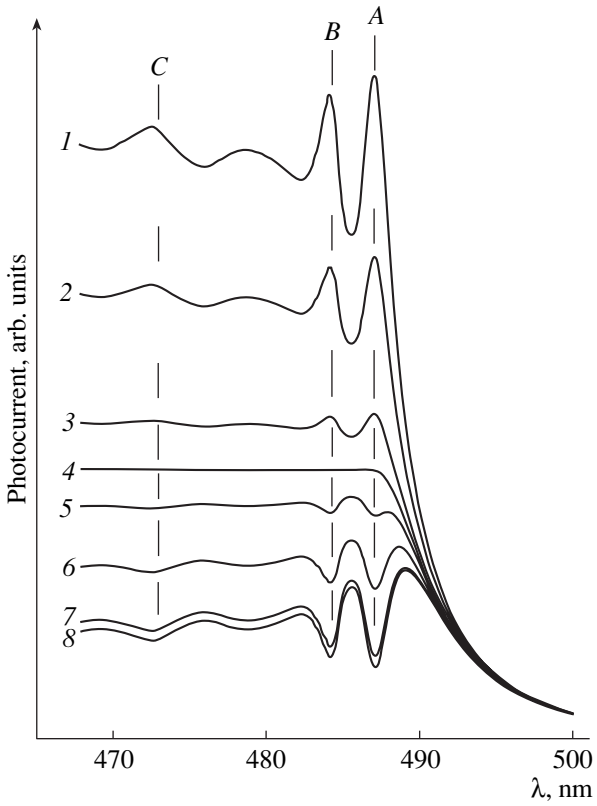

Fig. 3. Calculated photoconductivity spectra of a CdS crystal for different electric field strengths at the semiconductor surface. E_s = (*1*) 250, (*2*) 180, (*3*) 80, (*4*) 10, (*5*) –90, (*6*) –500, (*7*) -5×10^3, and (*8*) -5×10^4 V/cm.

number of nonequilibrium electrons per unit area of the illuminated sample surface:

$$\Delta N = \frac{\alpha\beta I_0 \tau_n}{1-(\alpha L_n)^2}\left[\frac{1}{\alpha}(1-\exp(-\alpha d)) - L_a \frac{S_n - \mu_n E_s + \alpha D_n}{S_n - \mu_n E_s + D_n/L_a}(1-\exp(-d/L_a))\right]. \quad (4)$$

Here, the quantum yield β depends on the frequency, is defined by expression (3) in the frequency range $\nu < \nu_0$, and is equal to unity at $\nu \geq \nu_0$ [7]. Since the photoconductivity is proportional to ΔN, relationship (4) provides a way of simulating the influence of the surface electric field on the band-edge photoconductivity spectra of the CdS crystal.

The photoconductivity spectra of the CdS crystal were numerically calculated from relationship (4) by varying the strength and sign of the electric field (parameter E_s) at the surface of the semiconductor. In these calculations, we used the absorption spectrum of CdS at $T = 77$ K taken from [8].[2] The parameters L_a and D_n were determined from formulas (2). The mobilities of charge carriers at $T = 77$ K, $\mu_n = 4 \times 10^3$ cm^2/(V s) and $\mu_p = 3$ cm^2/(V s), were taken from [13]. The lifetimes of charge carriers $\tau_n = 10^5$ s and $\tau_p = 10^{-8}$ s corresponded in order of magnitude to the averages of the data available in the literature [6, 14, 15]: $10^{-6} \leq \tau_n \leq 10^{-3}$ s and $10^{-10} \leq \tau_p \leq 10^{-6}$ s (when choosing τ_n, we also took into account that the electron lifetime decreases under exposure to IR light, which resulted in a decrease in the photoconductivity [3]). The energy parameter γ in expression (3) was taken equal to 2.2×10^{-2} eV. According to [16], the surface recombination rates in CdS fall in the range $S_n = 4 \times 10^4$–7×10^5 cm/s. We chose the surface recombination rate $S_n = 4 \times 10^4$ cm/s corresponding to the lower limit of this range. This choice was determined by the fact that our samples were optically perfect platelike CdS single crystals with a natural surface that were grown from a gas phase. The quality of the samples was checked against the exciton reflection spectra, which were very sensitive to the surface condition of the semiconductor [12]. This choice is justified by the high sensitivity of the photoconductivity spectra of the studied samples to the external transverse field. It is difficult to expect a similar sensitivity of the photoconductivity spectra to the transverse field for CdS crystals with a high density of surface states. Indeed, in this case, the observation of the effects brought about by the transverse field is complicated, because the charges induced by the field should be captured by the surface states [17].

Figure 3 shows the photoconductivity spectra of a CdS crystal (thickness $d = 150$ μm), which were calculated for different electric field strengths E_s at the semiconductor surface under the assumption of a constant excitation intensity I_0. The results of calculations confirm the inference that the surface electric field affects the photosensitivity and the shape of the photoconductivity spectrum of the semiconductor in the range of exciton and interband transitions.

According to the calculations, the enriching (positive) and slightly enriching or depleting (negative) fields satisfying the inequalities $E_s > S_n/\mu_n$ and $E_s < S_n/\mu_n$ ($S_n/\mu_n = 10$ V/cm) at the semiconductor surface correspond to photoconductivity spectra of the first and second types, respectively.[3] In the range of weak fields ($|E_s| < 10^2$ V/cm), the excitonic structure of the photoconductivity spectra is either weakly pronounced or absent altogether (Fig. 3, curves *3*–*5*). As the strength of the surface field increases, the excitonic structure becomes pronounced. Moreover, the photosensitivity in the spectral range under investigation changes signifi-

[2] Since the experimental absorption spectrum of CdS in [8] did not involve the necessary data on the absorption coefficient in the range of the long-wavelength wing of exciton line *A* ($n = 1$), the photoconductivity spectra of the CdS crystal in our case were calculated using the Lorentzian approximation of the line shape [12].

[3] Note that the range of positive fields in which the calculations in terms of the model proposed in [4] have a physical meaning is limited from above by the inequality $E_s < S_n/\mu_n + D_n/(\mu_n L_a)$. This limitation is caused by going beyond the scope of the used model in the range of strong positive fields.

cantly, i.e., increases for enriching surface fields and decreases for depleting surface fields. The characteristic values of $|E_s|$ at which the excitonic structure of the photoconductivity spectra is sufficiently pronounced are of the order of 10^2–10^3 V/cm for positive fields and 10^3–10^4 V/cm for negative fields (Fig. 3, curves *1*, *7*). These fields are substantially weaker than the critical field of exciton ionization $E_{\text{ion}} = 10^5$ V/cm [5].

It should be noted that the structureless (smooth) spectrum is reproduced by the calculations at a nonzero positive field $E_s = S_n/\mu_n = 10$ V/cm (Fig. 3, curve *4*). A weakly pronounced excitonic structure of the second type (this structure is indistinguishable on the scale of Fig. 3) corresponds to zero field. This result is important for the quantitative evaluation of the surface field from the strength of the external transverse field corresponding to the smooth photoconductivity spectrum. The smooth shape of the low-temperature photoconductivity spectrum of the semiconductor is usually explained by the absence of band bending near the surface of the semiconductor, i.e., by a zero value of E_s (see, for example, [18]). Now, it is clear that this holds accurate to within the term S_n/μ_n.

Therefore, the calculation of the low-temperature photoconductivity spectra of the CdS crystals in the framework of the model proposed by Nyberg and Colbow [4] reproduces the specific features of the spectral photoresistive effect observed in the semiconductor crystals. These are a change in the photosensitivity in the range of the exciton and interband light absorption and also a smoothing and reversal of the fine structure of the spectrum with an increase in the external transverse field.

A comparison of the results of calculations (Fig. 3) with the experimental data (Figs. 1, 2) shows that the model used is adequate to the real physical situation.

It is evident that, in semiconductor crystals of the first group, which, according to the results obtained in [10, 18, 19] and our calculations, are characterized by enriching band bending near the surface, the surface electric field E_s can change sign from positive to negative with an increase in the depleting transverse field. In turn, in crystals of the second group, which are characterized by photoconductivity spectra with a fine structure and, consequently, by depleting band bending near the surface (see [10, 18, 19] and Fig. 3), the surface electric field E_s can change sign from negative to positive with an increase in the enriching transverse field.

The results obtained led us to the unambiguous inference that the inhomogeneous electric field of the space-charge surface layer is the main factor responsible for the photosensitivity and structure of the low-temperature band-edge photoconductivity spectra of pure CdS crystals with a low surface recombination rate S_n. The space charge is generated upon the screening of the bulk of the semiconductor from the surface-charge field and brings about surface band bending. The surface electric field has a pronounced effect on the photoconductivity spectra of the CdS crystals, because it affects the surface recombination and, hence, the lifetime of nonequilibrium charge carriers near the surface of the semiconductor (see, for example, [20]). This also follows from relationship (1), in which the difference $S_n - \mu_n E_s$ has the physical meaning of the effective surface recombination rate [4]. Indeed, by designating $S_n^* \equiv S_n - \mu_n E_s$ in relationship (1) [4], we obtain an expression that coincides with the solution of the stationary continuity equation for a nonequilibrium concentration of charge carriers in the presence of surface recombination and the absence of a surface electric field (see, for example, [21]).

The effect of the surface electric field on the intrinsic band-edge photoconductivity spectra of a semiconductor can be phenomenologically taken into account by introducing the coordinate dependence of the electron lifetime in the surface layer with a thickness of the order of the depth of field penetration into the crystal. In this case, the depleting, zero, and weakly enriching surface fields ($E_s < S_n/\mu_n$) should correspond to the function $\tau_n(x)$ increasing to a constant bulk value, whereas the enriching surface field ($E_s > S_n/\mu_n$) should correspond to the function $\tau_n(x)$ decreasing to a constant bulk value (recall that the coordinate x is reckoned from the surface deep into the sample). The introduction of such a photoelectrically inhomogeneous surface layer enables us to simulate the effect of the surface electric field on the photoconductivity spectra of the semiconductor. In particular, this provides an explanation for the occurrence of two types of low-temperature photoconductivity spectra that directly (the first type) and inversely (the second type) correlate with the exciton optical absorption spectra [8].

It is obvious that the surface field $E_s = S_n/\mu_n$ should be related to the function $\tau_n(x) = \text{const}$. This corresponds to a photoelectric homogeneity near the surface and in the bulk of the semiconductor crystal and, as a consequence, a structureless (smooth) photoconductivity spectrum. In this situation, the positive surface electric field "compensates" for the photoelectric inhomogeneity that arises in the vicinity of the surface owing to the presence of surface recombination centers. These centers reduce the electron lifetime near the surface as compared to that in the semiconductor bulk and, hence, are responsible for the formation of the fine structure in photoconductivity spectra of the second type (even for an electrically neutral surface, i.e., at $E_s = 0$).

5. CONCLUSIONS

The above investigation allowed us to draw the inference that the intrinsic band-edge photoconductivity spectra of pure CdS crystals can be used as highly sensitive indicators of the surface electric field. A variation in the strength and sign of the surface electric field

makes it possible to change the photosensitivity of the semiconductor and also the structure and type of the photoconductivity spectra. This effect of the surface electric field on the photoconductivity spectra is associated with the dependence of the surface recombination rate and, consequently, the lifetime of nonequilibrium charge carriers on the bending of energy bands near the surface of the semiconductor.

The results obtained have demonstrated that the surface electric field is the decisive factor in the formation of the fine structure of the intrinsic band-edge photoconductivity spectra of pure CdS crystals. Moreover, these results give an insight into why a great variety of types of photoconductivity spectra can be observed for this compound and crystals of other II–VI semiconductors. It was shown that, in principle, the characteristics of the space-charge surface layer can be determined from the photoconductivity spectra of semiconductor crystals. However, the practical solution of this problem calls for further, primarily, theoretical investigation into the influence of the space-charge surface layer on the photoconductivity spectra of the semiconductor.

ACKNOWLEDGMENTS

We would like to thank É.D. Batyrev for his assistance in our studies and B.A. Kazennov for supplying the samples used in this work.

REFERENCES

1. E. F. Gross and B. V. Novikov, Fiz. Tverd. Tela (Leningrad) **1** (3), 357 (1959) [Sov. Phys. Solid State **1**, 321 (1959)].
2. A. S. Batyrev, R. A. Bisengaliev, O. É. Botov, *et al.*, Fiz. Tverd. Tela (St. Petersburg) **40** (5), 941 (1998) [Phys. Solid State **40**, 867 (1998)].
3. A. S. Batyrev, É. D. Batyrev, R. A. Bisengaliev, *et al.*, Fiz. Tverd. Tela (St. Petersburg) **41** (7), 1181 (1999) [Phys. Solid State **41**, 1075 (1999)].
4. D. W. Nyberg and K. Colbow, Can. J. Phys. **45**, 2833 (1967).
5. V. A. Kiselev, B. V. Novikov, and A. E. Cherednichenko, *Exciton Spectroscopy of Semiconductor Surface Regions* (Leningr. Gos. Univ., Leningrad, 1987).
6. *Physics and Chemistry of II–VI Compounds*, Ed. by M. Aven and J. S. Prener (North-Holland, Amsterdam, 1967; Mir, Moscow, 1970).
7. V. E. Lashkarev, E. A. Sal'kov, and V. A. Khvostov, in *Proceedings of IX International Conference on Semiconductor Physics, Moscow, 1968* (Nauka, Leningrad, 1969), p. 501.
8. J. Voigt and E. Ost, Phys. Status Solidi **33**, 381 (1969).
9. V. E. Lashkarev, E. A. Sal'kov, and V. A. Khvostov, in *Proceedings of 3rd International Conference on Photoconductivity, Stanford, USA, 1969*, p. 111.
10. K. Colbow, A. Jmaeff, and K. Yuen, Can. J. Phys. **48**, 57 (1970).
11. Y. Toyozawa, Tech. Rep. ISSP, No. SA-119, 3 (1964).
12. S. A. Permogorov, in *Physics of II–IV Compounds*, Ed. by A. N. Georgobiani and M. K. Sheĭnkman (Nauka, Moscow, 1986).
13. H. Fujita, K. Kobayashi, T. Kowai, and K. Shiga, J. Phys. Soc. Jpn. **20** (1), 109 (1965).
14. J. A. Bragagnolo and K. W. Böer, Phys. Status Solidi A **21**, 291 (1974).
15. N. B. Luk'yanchikova, *Fluctuation Phenomena in Semiconductors and Semiconductor Devices* (Radio i Svyaz', Moscow, 1990).
16. V. M. Leonov, A. G. Molchanov, Yu. M. Popov, and G. Kh. Talat, Fiz. Tekh. Poluprovodn. (Leningrad) **10** (8), 1434 (1976) [Sov. Phys. Semicond. **10**, 852 (1976)].
17. A. V. Rzhanov, *Electronic Processes on the Semiconductor Surface* (Nauka, Moscow, 1971).
18. E. Guche, in *Proceedings of IX International Conference on Semiconductor Physics, Moscow, 1968* (Nauka, Leningrad, 1969), p. 1223.
19. J. A. Bragagnolo, G. M. Storti, and K. W. Böer, Phys. Status Solidi A **24**, 147 (1974).
20. G. L. Bir, Fiz. Tverd. Tela (Leningrad) **1** (1), 67 (1959) [Sov. Phys. Solid State **1**, 62 (1959)].
21. R. A. Smith, *Semiconductors*, 2nd ed. (Cambridge Univ. Press, Cambridge, 1978; Mir, Moscow, 1982).

Translated by O. Borovik-Romanova

Physics of the Solid State, Vol. 45, No. 11, 2003, pp. 2067–2071. Translated from Fizika Tverdogo Tela, Vol. 45, No. 11, 2003, pp. 1968–1971.

SEMICONDUCTORS AND DIELECTRICS

Investigation into the Structural and Electrical Properties of Silver-Intercalated Zirconium Diselenide

A. N. Titov*, Z. A. Yagafarova, and N. N. Bikkulova****

** Ural State University, pr. Lenina 51, Yekaterinburg, 620083 Russia*

*** Sterlitamak State Pedagogical Institute, Sterlitamak, 453103 Russia*

e-mail: Alexander.Titov@usu.ru

Received April 23, 2003

Abstract—Silver-intercalated zirconium diselenides of the general formula Ag_xZrSe_2 are synthesized for the first time. The phase diagram of the Ag_xZrSe_2 compound is determined in the temperature range 423–523 K and at room temperature. An analysis has revealed the coexistence of two compounds, namely, $Ag_{0.125}ZrSe_2$ and $Ag_{0.25}ZrSe_2$, of which only the latter compound is stable at room temperature. The structural and electrical properties of Ag_xZrSe_2 diselenides are investigated. The results obtained indicate a polaron nature of charge-carrier localization. A comparison with isostructural intercalation compounds shows that free charge carriers play a dominant role in screening of the impurity potential. © *2003 MAIK "Nauka/Interperiodica".*

1. INTRODUCTION

Intercalation of transition metals and silver into titanium diselenide and titanium ditelluride leads to a lattice distortion (layers of the host lattice approach each other) and localization of charge carriers in the form of polarons of small radius [1]. It should be noted that the degree of localization of charge carriers for a heavier chalcogen atom proves to be considerably greater than that for other atoms. For example, no localization of charge carriers occurs upon intercalation of silver into titanium disulfide [2], whereas intercalation of iron into titanium disulfide leads to a very weak localization of charge carriers [3] (the polaron shift, which is defined as the energy of lattice deformation, becomes close to zero [4]). However, intercalation of these metals into titanium ditelluride brings about strong localization of charge carriers [1] even in the case where silver serves as an intercalant [5]. The difference in the degrees of localization of charge carriers in these lattices can be explained in terms of polarizability: the higher the polarizability of the lattice, the greater the degree of localization of charge carriers. In this case, proper allowance must be made for two main contributions to the lattice polarizability, namely, the polarizability of charge carriers, which is governed by the density of states at the Fermi level [2], and the polarizability of ion cores, which depends on the number of electron shells of the ions. A more complex situation arises with intercalation compounds of titanium dichalcogenides. This is associated with the fact that, in the sequence TiS_2–$TiSe_2$–$TiTe_2$, an increase in the density of states at the Fermi level due to an increase in the degree of overlap of the valence band and the conduction band [6] is accompanied by an increase in the polarizability of ion cores upon changing over to a heavier chalcogen atom. We believe that, in order to separate these contributions, it is necessary to investigate the structural and electrical properties of intercalation compounds of zirconium dichalcogenides and, in particular, zirconium diselenide $ZrSe_2$. This compound is isostructural to titanium dichalcogenides, exhibits semiconductor properties with a gap at the Fermi level (as is the case in TiS_2), and possesses an increased polarizability of ion cores (as compared to $TiSe_2$) due to the larger atomic weight of zirconium as compared to titanium. Therefore, by comparing the degrees of localization of charge carriers of $ZrSe_2$, TiS_2, and $TiSe_2$ upon their intercalation with the same metal, for example, silver, it is possible to determine the dominant contribution to the polarizability in the course of the formation of polarons. The purpose of the present work was to solve this problem.

2. SAMPLES AND EXPERIMENTAL TECHNIQUE

Samples used in our experiments were synthesized from the following elements: zirconium subjected to iodine cleaning (purity, 99.95), selenium of the OSCh 19-5 grade (purity, 99.999), and silver subjected to electrolytic cleaning (purity, 99.995). At the first stage of the synthesis, weighed portions of granular zirconium and selenium were placed in hermetically sealed and evacuated (to 10^{-5} Torr) silica glass ampules and were then sintered at temperatures in the range from 1100 to 1200 K for 7–10 days. Thereafter, the resultant compound $ZrSe_2$ and silver were mixed in the stoichiometric ratio. The mixture was placed in hermetically sealed and evacuated (to 10^{-5} Torr) Pyrex glass ampules and was then heated at temperatures in the range from 650 to 720 K for 100 h. The Ag_xZrSe_2 compounds thus

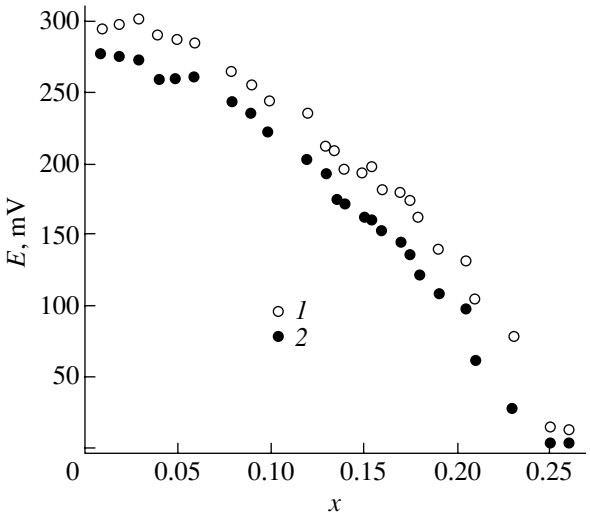

Fig. 1. Dependences of the partial free energy of formation of the Ag_xZrSe_2 compound on the silver content x at temperatures of (*1*) 573 and (*2*) 423 K.

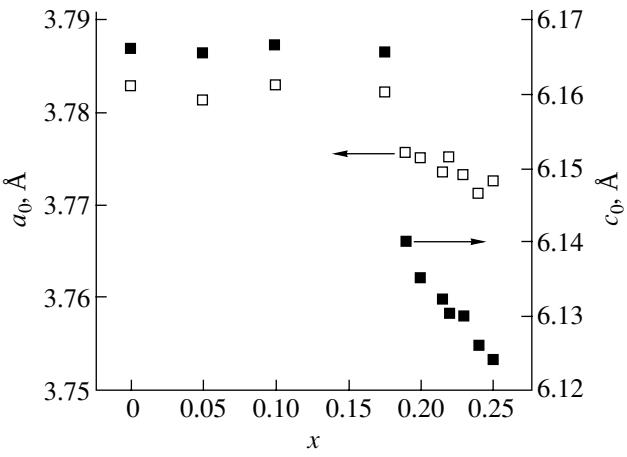

Fig. 2. Dependences of the lattice constants a_0 (open squares) and c_0 (closed squares) of the $ZrSe_2$ compound with a hexagonal structure on the intercalated silver content x at room temperature.

prepared, as a rule, were homogeneous to within the accuracy of the x-ray diffraction analysis (DRON-4-13 x-ray diffractometer, CuK_α radiation, room temperature). The electrical conductivity and the Seebeck coefficient were measured according to the standard four-point probe method with the use of polycrystalline cold-pressed samples. The nitrogen atmosphere used in the electrical measurements was preliminarily dried and purified from oxygen. The residual pressure of impurities was no higher than 10^{-15} Torr. Owing to the high mobility of silver ions in Ag_xZrSe_2 compounds, the technique of measuring the voltage difference (electromotive force) across the electrochemical cell was used to determine the concentration dependences of the thermodynamic functions and to construct isothermal sections of the phase diagram in the "silver content x–temperature T" coordinates. In these experiments, the silver content was varied using coulometric titration, i.e., by passing a current pulse of specified amplitude and width through the following electrochemical cell:

$$\text{Ag/AgI/Ag}_x\text{ZrSe}_2\text{/graphite.} \qquad (1)$$

For an electrochemical cell of this type, the operating temperature range is governed by the conditions under which the ionic conductivity of AgI (an electron filter suppressing electron conduction) is rather high and far exceeds the n-type conductivity. These conditions are satisfied in the temperature range 450–600 K, in which the ionic conductivity exceeds the n-type conductivity by a factor of 10^4. According to [7], the electromotive force E of electrochemical cell (1) is related to the chemical potential μ_{Ag} of a silver atom dissolved in Ag_xZrSe_2 through the expression

$$eE = -(\mu_0 - \mu_{Ag}), \qquad (2)$$

where e is the elementary charge and μ_0 is the chemical potential of a silver atom in a standard state (in bulk silver). Therefore, knowing the dependences of the emf E of electrochemical cell (1) on the temperature and silver content, we can determine the boundaries of the single-phase regions in the phase diagram.

3. RESULTS AND DISCUSSION

Figure 1 shows the dependences of the partial free energy of formation of the Ag_xZrSe_2 compound on the silver content x at two temperatures. As can be seen, these dependences are characteristic of materials in which the Fermi level is located between the bottom of the conduction band and the center of an impurity band of polaron nature [8]. This can also be judged from the formation of a two-phase region, which manifests itself in the form of a plateau in the dependence $E(x)$ and can be observed upon intercalation of even the first silver atoms. According to the Gibbs phase rule, the fact that the free energy of formation is independent of the concentration of one of the components under isothermal conditions at equal pressures can be explained only in terms of an inhomogeneous (non-single-phase) state of the sample. It should be noted that the Ag–$ZrSe_2$ system is characterized by two single-phase regions. Their boundaries are determined by the portions in the dependence $E(x)$ at T = 473 K in the concentration ranges $0.06 < x < 0.14$ and $0.175 < x < 0.23$.

Upon cooling of the sample to room temperature, the phase with a lower silver content most likely undergoes a decomposition of peritectic nature. This is indicated by the fact that the lattice parameters at room temperature do not depend on the content of intercalated silver in the range x = 0–0.175 (Fig. 2). In this region of compositions, the x-ray diffraction patterns of

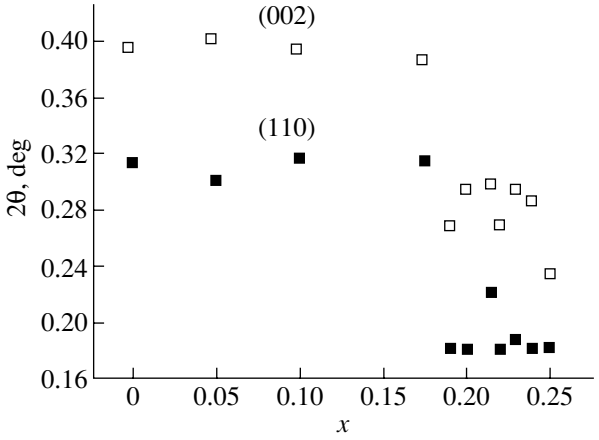

Fig. 3. Concentration dependences of the half-width of the diffraction lines (002) (open squares) and (110) (closed squares) on the silver content x in Ag_xZrSe_2 compounds (half-widths are expressed in terms of the diffraction angle 2θ).

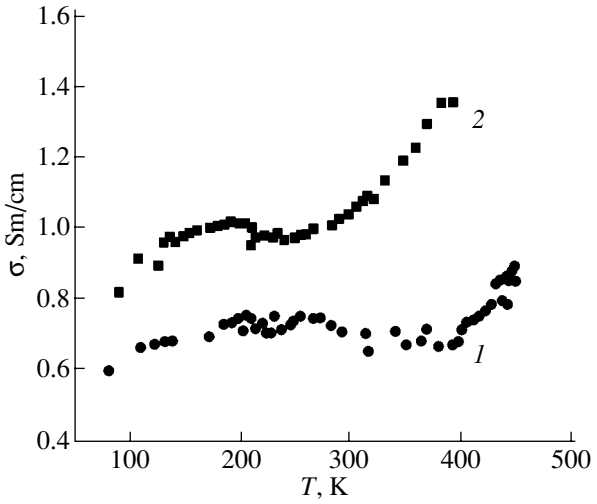

Fig. 4. Temperature dependences of the electrical conductivity for two single-phase Ag_xZrSe_2 compositions with silver contents x = (*1*) 0.20 and (*2*) 0.25 over the entire temperature range covered.

Ag_xZrSe_2 intercalation compounds are identical to the diffraction pattern obtained for the initial $ZrSe_2$ compound. The same situation was observed in the Ag–$TiSe_2$ system, for which the lattice parameters of the $TiSe_2$ and $Ag_{0.25}TiSe_2$ phases proved to be close to each other to such an extent that the diffraction lines of these phases could not be resolved [9]. These inference is in agreement with the concentration dependences of the half-width of the diffraction lines for the (110) and (002) reflections which correspond to the parameters a_0 and c_0 of the hexagonal lattice, respectively (Fig. 3). It can be seen from Fig. 3 that, in the system under investigation, there exist two composition regions for which the diffraction lines differ in width. Apparently, this circumstance is associated with the fact that the lattice parameters of the $ZrSe_2$ and $Ag_{0.175}ZrSe_2$ phases are also close to each other to such an extent that the diffraction lines of these phases cannot be resolved.

In the homogeneity region of the sole room-temperature stable phase, which can be designated as $Ag_{0.25}ZrSe_2$ or, what amounts to the same, $AgZr_4Se_8$, both lattice parameters, a_0 and c_0, decrease in the concentration range $x > 0.175$. This indicates that the volume of the unit cell of $ZrSe_2$ decreases upon incorporation of silver. The above behavior differs from that observed for intercalation compounds based on titanium dichalcogenides in which the contraction of the unit cell along the c axis is attended by an increase in the lattice parameter a_0, so that the total volume of the unit cell slightly increases with an increase in the intercalant content. It is generally believed that the observed decrease in the lattice parameter c_0 for intercalation compounds based on titanium dichalcogenides with charge-carrier localization of the polaron type is associated with a decrease in the distance between layers of the host lattice due to the formation of Ti–*Me*–Ti centers with covalent bonds (*Me* is an intercalated metal) [1, 4]. Most probably, the same is also true for Ag_xZrSe_2 intercalation compounds. The formation of these centers is usually explained by the hybridization of d_{z^2} orbitals of the host transition metal (Ti or Zr) and valence states of the intercalated metal (in our case, the 5*s* states of silver). The origin of the lattice contraction in the basal plane is not yet entirely understood. This behavior can also be explained by the formation of covalent bonds. However, the question regarding the sublattice and states associated with the formation of these bonds remains open.

The x-ray powder diffraction pattern of the $AgZr_4Se_8$ compound was indexed in a trigonal crystal system with space group $P\bar{3}m1$, which coincides with the space group of the initial $ZrSe_2$ compound. It is worth noting that no indication of silver ordering throughout the sample is revealed at room temperature. This is another argument in support of the polaron nature of the stability of the $AgZr_4Se_8$ phase, because the ordered state of intercalated silver becomes unstable at temperatures well below the point of polaron band collapse [10].

Figure 4 depicts the temperature dependences of the electrical conductivity for two Ag_xZrSe_2 compositions with silver contents x = 0.20 and 0.25. It can be seen from Fig. 4 that, although the concentration of electrons introduced with intercalated silver is relatively high ($\sim 10^{20}$ cm^{-3}), the temperature dependence of the electrical conductivity exhibits activation behavior. This suggests that, in contrast to the predictions made in the framework of the rigid-band model, the electrons introduced are not involved in the conduction band of $ZrSe_2$.

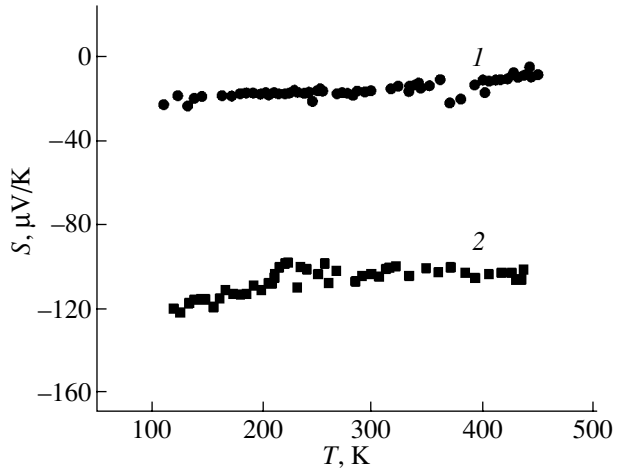

Fig. 5. Temperature dependences of the Seebeck coefficient for two single-phase Ag_xZrSe_2 compositions with silver contents x = (*1*) 0.25 and (*2*) 0.20 over the entire temperature range covered.

It seems likely that electron transfer upon intercalation occurs toward the band of hybrid Ag 5*s*–Zr 4*d* states localized in the vicinity of the Fermi level. The temperature dependence of the electrical conductivity at temperatures $T > 300$ K can be described by the expression $\sigma = \sigma_0 \exp(U/kT)$, where U is the activation energy. An increase in the magnitude of the electrical conductivity and, correspondingly, in the activation energy with an increase in the silver content x can be interpreted as resulting from the increase in the contribution made to the electrical conductivity by the localized electrons introduced with intercalated silver. This interpretation is in good agreement with the decrease in the Seebeck coefficient with increasing x. An analysis of the temperature dependence of the Seebeck coefficient revealed the presence of several types of charge carriers in Ag_xZrSe_2 (Fig. 5). It can be assumed that these carriers are silver impurity electrons and intrinsic electrons and holes of $ZrSe_2$. The Zr–Ag–Zr covalently bound centers serve as centers of localization of conduction electrons and strain centers of the lattice simultaneously. These objects can be treated as covalent polarons.

Thus, the experimental results lend support to the predicted polaron type of localization of charge carriers in the Ag–$ZrSe_2$ system. As was shown earlier in [8], the boundary of the single-phase state with a minimum intercalant content corresponds to the coincidence of the energies at the Fermi level and at the center of the polaron band (in our case, the band of hybrid Ag 5*s*–Zr 4*d* states). The concentration of electrons that need to be introduced into the material in order to ensure half filling of the polaron band depends on its position with respect to the Fermi level in the initial material, which, in turn, is determined by the effective ionization potential I_{eff} of the intercalated atom [4]. The effective ionization potential I_{eff} differs from the tabulated value by the screening constant γ; i.e., $I_{\text{eff}} = \gamma I_i$, where I_i is the ionization potential of a free atom or ion. For $TiSe_2$-based intercalation compounds, the screening constant is determined to be $\gamma = 1/33$ [4]. The ionization potential of the silver intercalated into $TiSe_2$ is estimated as $I_{\text{Ag}}^{\text{TiSe}_2} = \gamma 7.5763 \approx 0.23$ eV [11], which corresponds to the energy at the Fermi level located near the center of the polaron band. Therefore, intercalation of atoms whose ionization potential is less than $I_{\text{eff}} = 0.23$ eV should not lead to the formation of covalently bound centers. For $TiSe_2$-based intercalation compounds, the ionization potential of intercalated lithium $I_{\text{Li}}^{\text{TiSe}_2} = \gamma 5.3918 \approx 0.16$ eV is the closest in magnitude to the ionization potential of intercalated silver $I_{\text{Ag}}^{\text{TiSe}_2}$. It was proved that intercalation of lithium results in charge transfer from the intercalant to the lattice of $TiSe_2$; in this case, the introduced electrons remain completely free without any indication of electron localization [12]. This can be explained by the fact that the hybrid band formed upon incorporation of lithium is located very far above the Fermi level and, therefore, turns out to be empty. It is evident that, in the situation where silver atoms are intercalated into the $TiSe_2$ and $ZrSe_2$ compounds, the positions of the hybrid bands with respect to the Fermi level of the initial material should differ from each other because of the difference in the screening constants γ. Hence, if the dispersion of the polaron band is ignored, the width ratio of the two-phase regions for these materials should be equal to the ratio of their screening constants $\gamma(TiSe_2)/\gamma(ZrSe_2) = 1.31$. As a result, we obtain the quantity $\gamma(ZrSe_2) \approx 1/25$. Therefore, upon incorporation of lithium into $ZrSe_2$, the effective ionization potential of intercalated lithium $I_{\text{Li}}^{\text{ZrSe}_2}$ is approximately equal to 0.22 eV. This ionization potential is close to the critical value to such an extent that the formation of Ti–Li–Ti covalent centers (polarons) becomes quite possible.

According to experimental data available in the literature on the structural and electrical properties of $ZrSe_2$ diselenides containing lithium, the lattice parameters of intercalation compounds in the Li–$ZrSe_2$ system do not depend on the content of intercalated lithium up to $x = 0.4$. This composition corresponds to the crossover from semiconductor conductivity to metallic conductivity. An extended discussion of the nature of this crossover and the relevant experimental results is given in the review by Friend and Yoffe [13]. In our opinion, Berthier *et al.* [14] most clearly demonstrated that the two-phase region exists in the concentration range $0 < x < 0.4$. This suggests that intercalation of lithium into $ZrSe_2$ also leads to the formation of polarons. The shift observed in the concentration boundary of the phase instability upon replacement of silver by lithium is in good agreement with the fact that

the ionization potential of intercalated lithium is less than the ionization potential of intercalated silver. Moreover, the fact that the lattice parameters of the intercalation compounds do not depend on the intercalant content in the concentration range below the critical value confirms the validity of the proposed model.

4. CONCLUSIONS

Thus, the results obtained have demonstrated that the screening constant of the potential of the intercalated metal in $ZrSe_2$ is less than that in $TiSe_2$. The fundamental difference between these materials lies in the fact that, unlike the latter compound, the former compound is characterized by a gap at the Fermi level. Therefore, we can conclude that the presence of charge carriers capable of screening the potential of the intercalated ion and, thus, preventing the formation of covalent bonds between the intercalant and the host lattice is of crucial importance.

ACKNOWLEDGMENTS

This work was supported by the Russian Foundation for Basic Research, project nos. 01-03-32620 and 01-03-96502.

REFERENCES

1. A. Titov, S. Titova, M. Neumann, *et al.*, Mol. Cryst. Liq. Cryst. **311**, 161 (1998).
2. A. N. Titov and Kh. M. Bikkin, Fiz. Tverd. Tela (St. Petersburg) **34**, 3593 (1992) [Sov. Phys. Solid State **34**, 1924 (1992)].
3. M. Koyano, H. Negishi, Y. Ueda, *et al.*, Phys. Status Solidi B **138**, 357 (1986).
4. A. N. Titov, A. V. Dolgoshein, I. K. Bdikin, and S. G. Titova, Fiz. Tverd. Tela (St. Petersburg) **42**, 1567 (2000) [Phys. Solid State **42**, 1610 (2000)].
5. A. N. Titov, Izv. Ross. Akad. Nauk, Neorg. Mater. **33**, 534 (1997).
6. W. Bullet, J. Phys. C: Solid State Phys. **11**, 4501 (1978).
7. J. B. Wagner and C. Wagner, J. Chem. Phys. **26**, 1602 (1957).
8. A. N. Titov and A. V. Dolgoshein, Fiz. Tverd. Tela (St. Petersburg) **42**, 425 (2000) [Phys. Solid State **42**, 434 (2000)].
9. L. S. Krasavin, A. N. Titov, and V. M. Antropov, Fiz. Tverd. Tela (St. Petersburg) **40**, 2165 (1998) [Phys. Solid State **40**, 1962 (1998)].
10. A. N. Titov and S. G. Titova, Fiz. Tverd. Tela (St. Petersburg) **43**, 605 (2001) [Phys. Solid State **43**, 629 (2001)].
11. *Physical Quantities: A Handbook*, Ed. by I. S. Grigor'ev and E. Z. Meĭlikhov (Énergoatomizdat, Moscow, 1991).
12. P. C. Klipstein, C. M. Pereira, and R. H. Friend, Philos. Mag. B **56**, 531 (1987).
13. R. H. Friend and A. D. Yoffe, Adv. Phys. **36**, 1 (1987).
14. C. Berthier, Y. Chabre, P. Segransan, *et al.*, Solid State Ionics **5**, 379 (1981).

Translated by O. Borovik-Romanova

Physics of the Solid State, Vol. 45, No. 11, 2003, pp. 2072–2082. Translated from Fizika Tverdogo Tela, Vol. 45, No. 11, 2003, pp. 1972–1981.

SEMICONDUCTORS AND DIELECTRICS

Full Inclusion of Symmetry in Constructing Wannier Functions: Chemical Bonding in MgO and TiO_2 Crystals

R. A. Évarestov*, D. E. Usvyat*, and V. P. Smirnov**

**Chemistry Research Institute, St. Petersburg State University, ul. Pervogo Maya 100, Petrodvorets, St. Petersburg, 198504 Russia*

e-mail: evarest@hm.csa.ru

***St. Petersburg Institute of Precision Mechanics and Optics, St. Petersburg, 197101 Russia*

Received December 5, 2002; in final form, March 24, 2003

Abstract—Chemical bonding in MgO and TiO_2 crystals is analyzed using a minimal basis consisting of atomic-type Wannier functions (AWFs) centered at atomic sites in the crystal and constructed from Bloch states of the energy bands originating from the valence states of the atoms. A method proposed earlier for constructing Wannier functions is improved. Symmetrization of the initial Bloch function basis and symmetrical orthogonalization of the generalized Bloch functions greatly reduces computational effort. The prior symmetrization of the Bloch function basis is of fundamental importance in constructing AWFs, because the latter functions have to be centered at the atomic sites and possess the symmetry of the atomic functions in the crystal. The principle that should be followed in selecting the conduction bands originating from the valence states of the atoms of the crystal is formulated. The Bloch functions are calculated using the LCAO approximation within the Hartree–Fock method and density-functional theory. Using the calculated Bloch functions, a minimal valence AWF basis is constructed and calculations of the local characteristics of the electronic structure (atomic charge, bond order, atomic valence) are performed for the MgO and TiO_2 crystals. According to the analysis performed, the covalent component of the chemical bonding in the MgO crystal is negligibly small and TiO_2 is a mixed ionic and covalent crystal with pronounced covalent bonding. © *2003 MAIK "Nauka/Interperiodica".*

1. INTRODUCTION

The notion of chemical bonding [1–3] involves such quantities as the electron population and charge of an atom, bond population, bond order, etc. These quantities are local characteristics of the electronic structure of a crystal and cannot be calculated directly by using one-electron canonical orbitals of the crystal described by Bloch functions (BFs). Therefore, it is advantageous to use spatially localized Wannier functions (WFs) in this case [4]. The local properties of the electronic structure of a crystal are of importance not only in describing chemical bonding but also in modeling the charge transfer in a crystal, crystal defects, lattice dynamics, etc. and, therefore, can be estimated indirectly from experimental data.

The conventional scheme used to analyze the atomic populations is based on atomic-type functions. The typical atomic-function basis has been used, e.g., in [5], to calculate the electronic structure in the CO-LCAO approximation. The results of such an analysis depend on whether or not the diffuse AOs are included in the basis. The inclusion of these AOs allows one to refine variational calculations of energies based on BFs. However, when diffuse AOs are included, the results of population analysis depend essentially on the scheme (after Löwdin or Mulliken [5]) used and the interpretation of the calculated local characteristics of the electronic structure turns out to be difficult.

When the electronic structure is calculated in a plane-wave basis (or another nonatomic basis), the atomic-type function basis can generally be chosen within a certain arbitrariness and paradoxical results may be obtained. For example, in [6], the charges of the oxygen atoms in the ionic crystal MgO and covalently bonded crystal TiO_2 were calculated to be approximately the same (~–0.7). At the same time, calculations in the CO-LCAO approximation show that the crystal MgO is ionic and TiO_2 is partially ionic and partially covalent. However, the values of the local characteristics depend strongly on the scheme (after Löwdin or Mulliken) used for calculations [5].

The analysis of atomic populations in which an atomic-type Wannier function (AWF) basis is used does not suffer from these drawbacks [1]. The AWFs are constructed, by definition, from the BFs of occupied and empty energy bands originating from the valence states of the atoms (or ions) constituting the crystal. The AWFs are centered at atomic sites and possess the symmetry of the corresponding atomic functions in the crystal. The results obtained by this method are independent of the type of the basis (AO, plane-wave, or any other basis) used for electronic-structure calcula-

tions and of the number of AOs in the basis and the degree of their diffuseness. The AWFs used in analyzing the atomic populations allow one to relate the local properties of the electronic structure to the mutual arrangement of the one-electron energy bands.

Because the methods previously used to analyze the atomic populations in MgO and TiO_2 are inadequate, as indicated above, we describe chemical bonding in these crystals in terms of the AWFs.

In Section 2, we define the WFs and the AWFs and discuss their symmetry properties and a scheme for analyzing the atomic populations in terms of these functions. We also improve the method proposed in [7]. The improved method greatly reduces the magnitude of the calculations and can be applied to complex crystals with a fairly large number of atoms per unit cell. In Section 3, our calculations of the electronic structure of magnesium oxide MgO and titanium oxide TiO_2 (with the rutile structure) are described. The atomic-type WFs for the crystalline MgO and TiO_2 are constructed in Sections 4 and 5, respectively. In Section 6, we discuss the results of analyzing the chemical bonding in these crystals in terms of AWFs and the effect of electron correlation and of the size of a cyclic model on the local characteristics of the electronic structure.

2. ATOMIC-TYPE WANNIER FUNCTIONS AND CHEMICAL BONDING IN CRYSTALS

Wannier functions $W_m(\mathbf{r} - \mathbf{a_n})$ (where the index m labels the WFs related to a unit cell specified by the translation vector $\mathbf{a_n}$) are constructed from the Bloch functions $\varphi_{\tau\mathbf{k}}(\mathbf{r})$ of all states of the degenerate or nondegenerate energy band in question:

$$W_m(\mathbf{r}-\mathbf{a_n}) = L^{-1/2}\sum_{\mathbf{k}} e^{-i\mathbf{k}\mathbf{a_n}}\sum_{\tau} U_{\tau,m}(\mathbf{k})\varphi_{\tau\mathbf{k}}(\mathbf{r}) = L^{-1/2}\sum_{\mathbf{k}} e^{-i\mathbf{k}\mathbf{a_n}}\psi_{m\mathbf{k}}(\mathbf{r}), \quad (1)$$

$$\varphi_{\tau\mathbf{k}}(\mathbf{r}) = L^{-1/2}\sum_{m} U^{+}_{m,\tau}(\mathbf{k})\sum_{\mathbf{n}} e^{i\mathbf{k}\mathbf{a_n}}W_m(\mathbf{r}-\mathbf{a_n}) = \sum_{m} U^{+}_{m\tau}(\mathbf{k})\psi_{m\mathbf{k}}(\mathbf{r}). \quad (2)$$

Here, $\varphi_{\tau\mathbf{k}}(\mathbf{r})$ is the Bloch orbital corresponding to the state with a wave vector $\mathbf{k}$ and belonging to the energy band with the index τ and $U(\mathbf{k})$ is an arbitrary matrix. The functions $\psi_{m\mathbf{k}}(\mathbf{r})$ (the so-called generalized BFs) are the Fourier transforms of the WFs $W_m(\mathbf{r} - \mathbf{a_n})$. The WFs are orthonormalized if the matrices $U(\mathbf{k})$ are unitary. In the case of a nondegenerate energy band, matrices U reduce to phase factors $\exp(i\alpha_{\mathbf{k}})$. The particular choice of matrices $U(\mathbf{k})$ determines the degree of localization of the WFs.

It was shown in [8] that, in a one-dimensional model of a centrosymmetric crystal, the most localized WFs can be chosen real, possessing a certain inversion symmetry and decaying exponentially with distance. For a three-dimensional crystal, these properties of WFs have been proved only in the case of a nondegenerate energy band [9–11]. In general, the form of highly localized WFs in a three-dimensional crystal is nonunique and depends on the criterion for their localization. In the last decade, several efficient methods have been proposed for constructing the most localized WFs [7, 12–15]. Interest in the WFs has grown because of their application for studying a number of phenomena in solids.

(1) These functions are often used as a convenient basis in studying local effects produced by defects, excitons, etc. [16, 17].

(2) Certain physical quantities, such as the spontaneous polarization, dynamic Born charge, and piezoelectric constants, are expressed more simply in the basis of localized orbitals than in the Bloch function basis [18, 19].

(3) The WFs are of importance in designing rapid algorithms ("order N" methods) for calculating the electronic structure of a crystal [20, 21].

(4) The WF basis can be conveniently used to include the electron correlation effects in crystals [22].

(5) By using WFs, one can relate the electronic structure calculated in the Bloch function basis to the chemical bonding in the crystal [1–3].

There is a connection between the symmetry of the BFs of one-electron energy bands (degenerate or nondegenerate) and the symmetry of the corresponding WFs, which is due to the fact that both sets of functions are bases of a certain induced representation (IR) of the space group of the crystal [23–26].

To construct the AWFs for the MgO and TiO_2 crystals, we employ the variational method proposed in [7] and applied earlier for analyzing the chemical bonding in silicon and gallium arsenide in [1] and in silver halides in [2]. This method includes the following three steps: (i) symmetry analysis and selection of BFs (states of energy bands from which the WFs will be constructed); (ii) construction of the functions $V_m(\mathbf{r} - \mathbf{a_n})$ that are maximally localized (according to the criterion chosen for localization) but are not orthogonal to each other; and (iii) symmetric orthogonalization (after Löwdin [27]) of these functions to obtain WFs.

In this paper, we improve the method proposed in [7] as follows.

(1) As indicated above, the AWFs have to possess a certain symmetry (they have to transform according to a certain irreducible representation of the local site

symmetry group of the crystal). In constructing the functions $V_m(\mathbf{r} - \mathbf{a_n})$, we symmetrize the initial BF basis $\varphi_{\tau\mathbf{k}}(\mathbf{r})$ with respect to the irreducible representation of the local site symmetry group according to which the functions $V_m(\mathbf{r} - \mathbf{a_n})$ and $W_m(\mathbf{r} - \mathbf{a_n})$ transform. This procedure allows one to considerably reduce the number of variational parameters [independent elements of the matrices U in Eq. (1)], because, in this case, linearly independent symmetrized combinations of BFs (which are usually smaller in number than the BFs themselves) are used to construct the AWFs. Therefore, this symmetrization noticeably reduces the computational effort needed to perform the variational procedure. Furthermore, in constructing the AWFs, which have to be centered at the atomic sites and possess a certain symmetry, the BF basis symmetrization must be performed because, otherwise, the WFs obtained could be centered at points different from the atomic sites and might not possess the necessary symmetry since the reduction of a composite IR into simple IRs is ambiguous [25, 26].

Calculations can be optimized further by taking into account the time-reversal symmetry. In this case, for real AWFs, we have $U_{\tau,m}(\mathbf{k}) = U^*_{\tau,m}(-\mathbf{k})$.

(2) To perform symmetric orthogonalization, we pass over from the functions $V_m(\mathbf{r} - \mathbf{a_n})$ to their Fourier transforms $\tilde{\psi}_{m\mathbf{k}}(\mathbf{r})$ by using relations similar to Eq. (2). The functions $\tilde{\psi}_{m\mathbf{k}}(\mathbf{r})$ with different vectors $\mathbf{k}$ are orthogonal to each other, because these functions are of the Bloch type. Since the functions $V_m(\mathbf{r} - \mathbf{a_n})$ are not orthogonal to each other, the functions $\tilde{\psi}_{m\mathbf{k}}(\mathbf{r})$ with the same vector $\mathbf{k}$ can also be nonorthogonal [in contrast to the functions $\psi_{m\mathbf{k}}(\mathbf{r})$] and their normalization can be arbitrary. We perform the symmetric orthonormalization of these functions for each value of the wave vector $\mathbf{k}$ separately by using the Löwdin method. After this procedure, the functions $\tilde{\psi}_{m\mathbf{k}}(\mathbf{r})$ transform into $\psi_{m\mathbf{k}}(\mathbf{r})$. Taking the inverse Fourier transform (1), we obtain orthonormalized $W_m(\mathbf{r} - \mathbf{a_n})$.

In the unmodified version, the orthonormalization was performed for all $L \cdot N$ Wannier functions, where N is the number of energy sheets involved in the calculation and is equal to the number of WFs per primitive cell and L is the number of primitive cells in the cyclic model of the crystal. In the modified version, the orthogonalization is performed for each set of N functions separately. Since the orthogonalization after Löwdin involves diagonalization of matrices whose dimension is determined by the number of functions to be orthogonalized, the splitting of the space of nonorthogonal functions into orthogonal subspaces of a smaller dimension can significantly reduce the amount of calculations required.

(3) When choosing the BFs to construct the AWFs, particular attention should be given to vacant states (the conduction bands). The evolution of the orbitals involved in the formation of chemical bonding in a crystal (from atomic orbitals to crystal orbitals) can be described on the basis of the following qualitative considerations. Let us mentally increase the interatomic distances in a crystal to a large value without breaking the symmetry of the crystal lattice and then begin to decrease them to the equilibrium values. When the atoms are still far apart, the atomic levels corresponding to the minimal valence basis can be split by the crystal field only slightly and form narrow energy bands. In this case, the WFs are almost identical to the AOs. As the atoms approach each other further, the energy bands are affected noticeably and can even change their relative arrangement and the corresponding functions transform into the WFs of the crystal.

Therefore, in order to analyze the chemical bonding in a crystal, it is advantageous to choose, as localized functions, the AWFs corresponding to the minimal valence atomic basis [1]. The energy bands corresponding to such WFs are chosen so that the symmetry of the BFs of these bands allows one to construct AWFs. Further, since the positions of the bands originating from the atomic valence levels are unknown, we assume that these bands are such that their BFs allow one to construct the most localized AWFs. Such bands are usually the uppermost valence bands and certain empty bands, which are not necessarily the lowest in energy. We will specify an energy band by indicating the type of the AWF corresponding to this band and the atom at which this function is centered (e.g., *s* or *p* band of oxygen). The problem indicated above does not arise when WFs are constructed only from the BFs of occupied states (in semiconductors and insulators).

Symmetrization of the initial BF basis and symmetric orthogonalization of the generalized BFs significantly reduces the amount of calculations required, thus making it possible to apply this method to complex crystals with a large number of atoms per unit cell in which the states involved in the chemical bonding form complicated multisheeted energy bands.

Once a minimal valence AWF basis has been constructed, it can be used as an atomic-type basis to calculate the local characteristics of the electronic structure [1, 5]. Using the AWFs, analysis of the atomic populations can be performed either before their orthogonalization according to Löwdin or after it (analog of the analysis of the atomic populations in the AO basis after Mulliken and after Löwdin) [1]. Analysis of the atomic population [5] involves calculation of the density matrix in a basis of functions localized at atomic sites, in our case, in the AWF basis. Since the orthogonalized functions W and nonorthogonalized functions V are similar, we may expect the results of analyzing the atomic populations using these functions

to also be similar. Calculations performed for particular systems provide support for this conclusion and are discussed in Sections 4 and 5.

3. CALCULATION OF THE ELECTRONIC STRUCTURE OF MgO AND TiO_2 CRYSTALS

Crystalline magnesium oxide MgO and titanium oxide TiO_2 differ significantly in dielectric properties and the character of chemical bonding, which is due to the electron density distribution being much different in them. Crystal MgO (NaCl structure, fcc Bravais lattice, space group O_h^5) is ionic in character with a wide band gap (E_g = 7.8 eV). The large width of the upper oxygen valence band (approximately 8 eV) is indicative of significant oxygen–oxygen interaction [28]. Titanium oxide TiO_2 in the rutile structure (simple tetragonal Bravais lattice, space group D_{4h}^{14}, two formula units per primitive cell) is a semiconductor with a band gap of approximately 3 eV and with the metal–oxygen bond having a large degree of covalent character [29]. The upper oxygen valence band is also fairly wide (7.9 eV). The electronic structures of both compounds have been well studied experimentally and were calculated in several papers using an AO basis and a plane-wave basis [30, 31]. The calculations were carried out using the Hartree-Fock (HF) method [28, 32] and the density-functional theory (DFT) [30, 33], which includes electron correlations. The WFs of the valence bands of MgO were calculated quite recently in [3, 7]. The WFs for crystal TiO_2 are first constructed and discussed in this paper.

To construct AWFs by the method developed in [7], we calculated the BFs of the electronic states of MgO and TiO_2 nonempirically, with the help of the Crystal computer program [34] based on the Hartree–Fock method and density-functional theory in the CO-LCAO approximation. As a basis, we used atomic orbitals of the Gaussian type. For crystal MgO, we used the 8–6–1 basis (1*s*–2*sp*–3*sp*) for magnesium atoms and the 8–5–1 basis (1*s*–2*sp*–3*sp*) for oxygen atoms. For crystal TiO_2, the effect of core electrons was described by the Durand–Barthelat pseudopotential [35] and we used the (4–1)/1 (*d*/*sp*) basis for titanium atoms and the 3–1 (*sp*) basis for oxygen atoms. In [28], the exponents of the outer shell 3*sp* orbitals of Mg and O atoms in the MgO crystal (0.4 and 0.21, respectively) were found using the variational method in the HF approximation. In [32], using the same method for the TiO_2 crystal in the valence approximation, the exponents of the outer shell *sp* and *d* orbitals of titanium and *sp* orbitals of oxygen were found to be 0.484, 0.225, and 0.281, respectively. In both cases, by using the HF method and varying the orbital exponents, the parameters of the crystal structure were calculated and the results were found to be in good agreement with the experimental data: for MgO, the calculated lattice parameter is a = 4.201 Å (the experimental value a = 4.21 Å), and for TiO_2, the calculated parameters are a = 4.555 Å, c = 2.998 Å, and u = 0.306 Å (the experimental values a = 4.594 Å, c = 2.959 Å, u = 0.305 Å). We note that the calculated Gaussian outer shell orbitals are fairly diffuse and, for oxygen, are different in both crystals.

In our calculations, we used the basis AOs indicated above and the theoretical values of the structural parameters corresponding to them [28, 32]. Summation over the Brillouin zone (BZ) was performed using special points of the Monkhorst–Pack type [36]. For MgO, we used a $4 \times 4 \times 4$ set of special points; i.e., the infinite crystal is replaced, in fact, by a cyclic system of 64 primitive cells, for which the irreducible part of the BZ contains eight special points. For TiO_2, we used sets of $4 \times 4 \times 4$ and $2 \times 2 \times 3$ special points (18 and 6 points in the irreducible part of the BZ, respectively). For the $4 \times 4 \times 4$ sets of $\mathbf{k}$ points, the balance between calculated sums over the direct and reciprocal lattices [37] occurs if the sums over the direct lattice are calculated with an accuracy of 10^{-6} for all integrals of atomic functions except for the exchange integrals, for which the accuracy was 10^{-12} [34]. The calculations are carried out using both the HF method and the local-density approximation (LDA) [38].

The calculated band structures (for both the valence and conduction bands) of MgO and TiO_2 are shown in Figs. 1 and 2, respectively. In MgO (in accordance with the results of other calculations), the highest two valence bands are the oxygen *s*- and *p*-like bands, respectively, whereas the conduction bands are more complicated. The upper valence bands in TiO_2 are also oxygen *s*- and *p*-like bands; however, they consist of 4 and 12 branches, respectively, because the primitive cell of titanium oxide contains four oxygen atoms. The lowest conduction band in TiO_2 (consisting of 10 branches) is formed by the *d* states of two titanium atoms and is noticeably separated in energy from the upper conduction bands.

4. ATOMIC-TYPE WANNIER FUNCTIONS AND LOCAL CHARACTERISTICS OF THE ELECTRONIC STRUCTURE OF THE MgO CRYSTAL

Prior to constructing AWFs, one should analyze the symmetry of crystal orbitals of the valence and conduction bands on the basis of IRs of space groups [7]. Table 1 lists the irreducible representations of the wave-vector groups of symmetry points of the BZ induced by the atomic-function basis that was used for calculating the electronic structure of the MgO crystal. (The indices characterizing the irreducible representations of space groups are the same as those in [39].) This table also makes it possible to relate the symmetry of AWFs to the symmetry of the Bloch states if, instead of the atomic functions (the fourth column of the Table 1), the AWFs of the same symmetry are considered.

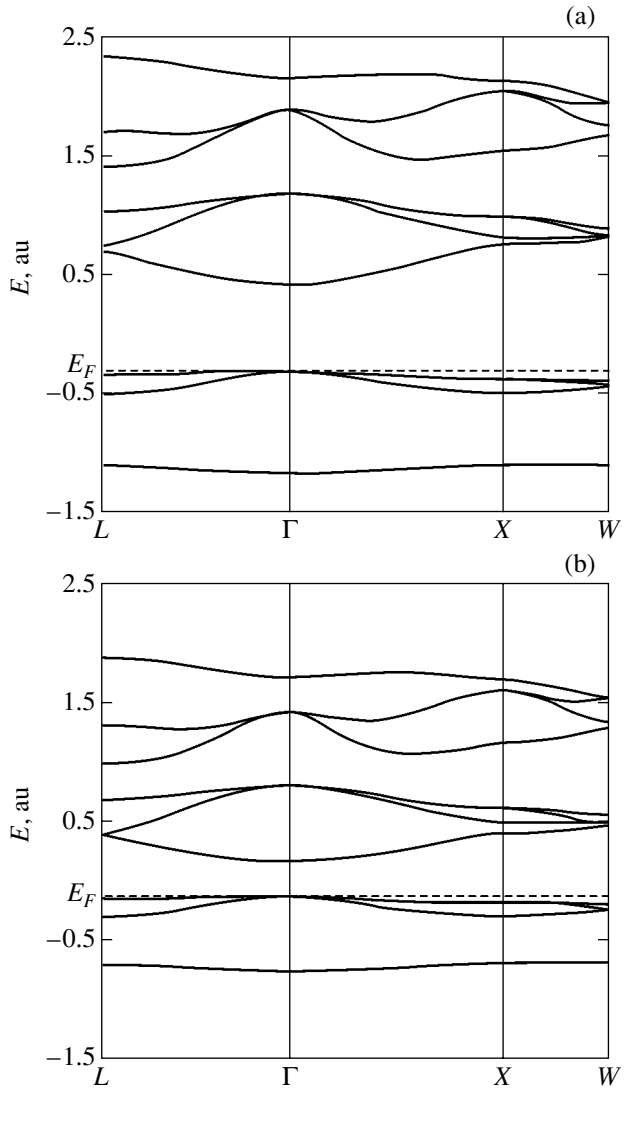

Fig. 1. Energy bands corresponding to occupied and empty states of crystal MgO as calculated using (a) the Hartree–Fock method and (b) density-functional theory. The Fermi energy is denoted by E_F and indicated by a dashed line.

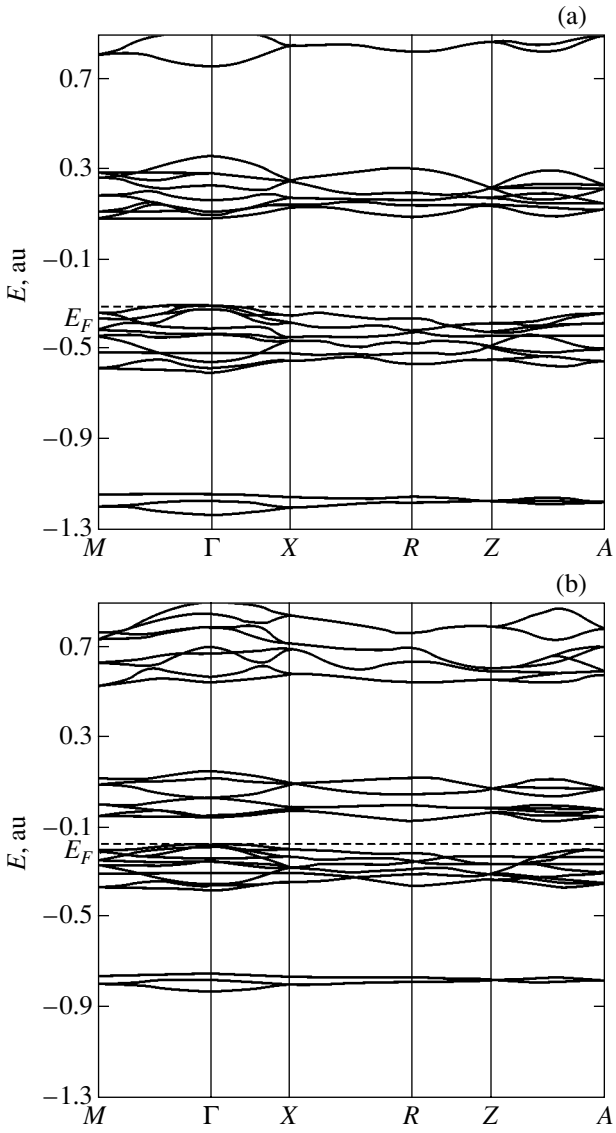

Fig. 2. Energy bands corresponding to the upper occupied and lower empty states of crystal TiO_2 as calculated using (a) the Hartree–Fock method and (b) density-functional theory.

In the MgO crystal (space group O_h^5, fcc lattice), both atoms occupy the Wyckoff positions with local symmetry $G_q = O_h$ (positions *a* and *b* for magnesium and oxygen atoms, respectively). The minimal basis involves the oxygen *s* and *p* functions and the magnesium *s* function. As mentioned above, in terms of symmetry (Table 1) and according to the maximal-localization principle for the corresponding WFs, the highest

Table 1. Induced representations of space group O_h^5

Atom	Wyckoff position	G_q	AO		Γ	*L*	*X*	*W*
Mg	*a* (000)	O_h	*s*	a_{1g}	1^+	1^+	1^+	1
			x, *y*, *z*	t_{1u}	4^-	2^-3^-	3^-5^-	25
O	$b\left(\frac{1}{2}\frac{1}{2}\frac{1}{2}\right)$	O_h	*s*	a_{1g}	1^+	2^-	1^+	2
			x, *y*, *z*	t_{1u}	4^-	1^+3^+	3^-5^-	15

Table 2. Characteristics of the magnesium *s* band

k point (projections onto reciprocal lattice basis vectors)	**k**-point symmetry		Numbers of symmetry-compatible empty states	Numbers of the levels corresponding to magnesium *s* band	Magnesium *s*-band energy, au
Γ (0 0 0)	O_h	1^+	1, 8	8	2.164
X (0 $\frac{1}{2}$ $\frac{1}{2}$)	D_{4h}	1^+	2, 5	2	0.821
L (0 0 $\frac{1}{2}$)	D_{3d}	1^+	2, 7	7	1.709
W ($\frac{1}{4}$ $\frac{1}{2}$ $\frac{3}{4}$)	D_{2d}	1	3, 6	6	1.767
Λ (0 0 $\frac{1}{4}$)	C_{3v}	1	1, 2, 7, 8	8	2.195
Δ (0 $\frac{1}{4}$ $\frac{1}{4}$)	C_{4v}	1	1, 2, 5, 8	8	2.251
(0 $\frac{1}{4}$ $\frac{3}{4}$)	C_{2v}	1	1, 3, 6, 8	8	2.154
(0 $\frac{1}{4}$ $\frac{1}{2}$)	C_s	1	1, 2, 3, 5, 7, 8	7	1.833

four-sheeted valence band is the oxygen *sp* band (with *s* and *p* subbands separated by an energy gap). To calculate the band structure, we chose a basis consisting of 18 AOs for which there are only eight energy levels in the conduction band at each **k** point. Therefore, in order to determine the magnesium *s* band, we must choose a level with symmetry compatible with the symmetry of the magnesium *s* function at each **k** point; these levels will allow us to construct the most localized WFs. The higher the symmetry of a point in the BZ, the smaller the number of energy levels with the appropriate symmetry that can be used to construct the magnesium *s*-like WF. For example, at the Γ or *X* point, only two of the eight levels have symmetry compatible with the symmetry of the magnesium *s* function. At a general position point in the BZ, symmetry does not impose any restrictions; therefore, any level can be used to construct any WF (we note that special points in our $4 \times 4 \times 4$ set are not general position points). The maximal WF localization principle allows us to conclude that the magnesium *s* band is fairly high in energy. Table 2 shows the position of the magnesium *s* band for each wave vector in the band structure calculated using the HF method in the basis of 18 AOs for the set of $4 \times 4 \times 4$ **k** points. Figure 3 shows the magnesium *s* AWF; this WF is constructed from the occupied states of the oxygen *sp* bands and the vacant states of the magnesium *s* band (Table 2).

Table 3 lists the values of the charge localized on an oxygen atom in the MgO crystal that are calculated, using different schemes, from the band structure determined using the HF and DFT methods. The bond orders and covalent contribution to the bonding calculated within the AWF method are close to zero, and the valence of both atoms is very accurately equal to 2. These results adequately characterize the ionic nature of the crystal MgO.

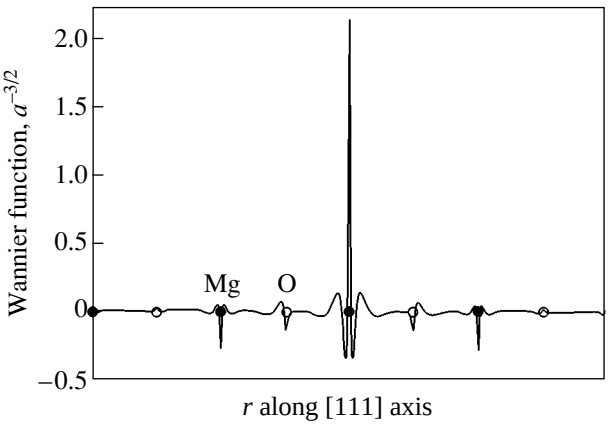

Fig. 3. Atomic-type *s*-like Wannier function centered at a magnesium atomic site (in units of $a^{-3/2}$, where *a* is the atomic length unit) along the [111] direction for a cyclic $4 \times 4 \times 4$ model of crystal MgO as constructed from Bloch functions calculated using the Hartree–Fock method.

Table 3. Atomic charges in crystal MgO

Scheme for analyzing atomic populations		Oxygen atomic charge, |*e*|
HF	Mulliken	–1.98
	Löwdin	–1.82
	Nonorthogonal AWFs	–2.00
	Orthogonal AWFs	–1.98
DFT (LDA)	Mulliken	–1.90
	Löwdin	–1.76
	Nonorthogonal AWFs	–1.99
	Orthogonal AWFs	–1.97
	Plane-wave basis [6]	–0.76

5. ATOMIC-TYPE WANNIER FUNCTIONS AND LOCAL CHARACTERISTICS OF THE ELECTRONIC STRUCTURE OF THE TiO_2 CRYSTAL

The titanium and oxygen atoms in the TiO_2 crystal occupy sites whose symmetry is described by the local groups $G_a = D_{2h}$ and $G_f = C_{2v}$ (Wyckoff positions *a*, *f*), respectively. The representations of the group D_{4h}^{14} induced by atomic-type functions centered at these sites are listed in Table 4. The indices characterizing the irreducible representations are the same as those used in [39].

The local symmetry of the positions of the metal and oxygen atoms in TiO_2 is lower than that in MgO. As a consequence, WFs of different types can have the same symmetry. In particular, the oxygen *s* and $(x + y)$ functions, included in the minimal basis, transform according to the irreducible representation a_1 of the group C_{2v} and the titanium *s*, $3z^2 - r^2$, and *xy* functions transform according to the representation a_g of the group D_{2h}.

The minimal valence basis for the TiO_2 crystal consists of the oxygen *s* and *p* functions and the titanium *s* and *d* functions. Symmetry analysis of the band states and of the degree of localization of WFs corresponding to different bands shows that the oxygen *sp* bands form the highest 16 bands of occupied states and the titanium *d* bands form the lowest 10 bands of empty states. The titanium *s* bands correspond to two bands of empty states lying at high energies (at different **k** points, the levels of these bands have indices from 39 to 44, as reckoned from the lowest empty band). These energies are ~3 au (the bottom of the conduction band corresponds to an energy of ~0.1 au). The titanium *d* and *s* AWFs (two *d* WFs and one *s* WF) of the same symmetry a_g are shown in Fig. 4 for the [001] and [110] directions.

To investigate the contribution from the titanium *s* band to the local characteristics, we analyzed the atomic populations both with the inclusion of the titanium *s* WFs (28 WFs per unit cell) and without them (26 WFs per unit cell). The data on the local characteristics of the electronic structure of TiO_2 are listed in Table 5.

6. DISCUSSION

It can be seen from Tables 3 and 5 that our results do not agree with the data from [6] not only in the values of the atomic charges but also in the relationship between the covalent contributions to the bonding in MgO and TiO_2. According to our results, the covalent character of bonding is much more pronounced in TiO_2 than in MgO, whereas according to the data from [6], both these crystals are partially ionic and partially covalent with a large amount of covalent character and with

Table 4. Induced representations of space group D_{4h}^{14}

Atom	Wyckoff position	G_q	AO		Γ, *M*	*Z*, *A*	*X*	*R*
Ti	*a*(000)	D_{2h}	s; $3z^2 - r^2$; xy	a_g	1^+4^+	1	2	1^+
			$x + y$	b_{3u}	5^-	4	2	1^-
			$x - y$	b_{2u}	5^-	3	2	1^-
			z	b_{1u}	2^-3^-	1	1	1^-
			$x^2 - y^2$	b_{1g}	2^+3^+	2	2	1^+
			$z(x + y)$	b_{2g}	5^+	3	1	1^+
			$z(x - y)$	b_{3g}	5^+	4	1	1^+
O	*f*(*pp*0)	C_{2v}	s; $x + y$	a_1	$1^+4^+5^-$	14	22	1^+1^-
			z	b_1	$2^-3^-5^+$	31	11	1^+1^-
			$x - y$	b_2	$2^+3^+5^-$	23	22	1^+1^-

Note: $D_{2h}(E, C_{2z}, U_{xy}, U_{x\bar{y}}, I, \sigma_z, \sigma_{xy}, \sigma_{x\bar{y}})$; $C_{2v}(E, U_{xy}, \sigma_z, \sigma_{x\bar{y}})$.

Table 5. Local characteristics of the electronic structure of crystal TiO_2

Bloch function computing method	Cyclic model	Scheme for analyzing atomic populations	Oxygen atomic charge, $\|e\|$	Orders of the shortest two Ti–O bonds	Covalence		Full valence	
					Ti	O	Ti	O
HF	$4 \times 4 \times 4$	Mulliken	–1.33	0.36, 0.30	2.15	1.24	3.94	2.08
		Löwdin	–0.86	0.56, 0.50	3.46	2.04	4.18	2.36
		Nonorthogonal AWFs	–1.38	0.35, 0.28	2.06	1.11	3.98	2.05
		Orthogonal AWFs	–1.30	0.38, 0.29	2.34	1.25	4.02	2.07
		26 nonorthogonal AWFs	–1.38	0.35, 0.28	2.06	1.11	3.98	2.05
		26 orthogonal AWFs	–1.35	0.37, 0.28	2.16	1.17	3.99	2.05
DFT	$4 \times 4 \times 4$	Mulliken	–0.89	0.52, 0.44	3.30	1.93	4.09	2.28
		Löwdin	–0.52	0.66, 0.58	4.29	2.52	4.53	2.62
		Nonorthogonal AWFs	–0.99	0.51, 0.40	3.15	1.70	4.11	2.16
		Orthogonal AWFs	–0.92	0.53, 0.41	3.39	1.81	4.19	2.19
		26 nonorthogonal AWFs	–0.99	0.51, 0.41	3.16	1.70	4.12	2.15
		26 orthogonal AWFs	–0.96	0.52, 0.41	3.23	1.74	4.13	2.17
	$2 \times 2 \times 3$	Mulliken	–0.90	0.52, 0.44	3.30	1.93	4.08	2.29
		Löwdin	–0.52	0.66, 0.58	4.29	2.52	4.53	2.62
		Nonorthogonal AWFs	–1.00	0.51, 0.40	3.15	1.69	4.11	2.15
		Orthogonal AWFs	–0.93	0.53, 0.41	3.34	1.79	4.17	2.18
Plane-wave basis [6]			–0.73	–	–	–	–	–

virtually equal charges localized on the oxygen atoms. Our results agree with the conventional view on the bonding in these crystals and with the results of other calculations.

The DFT method for calculating the electronic structure includes the effect of electron correlation. By comparing the results of analyzing the atomic populations based on the BFs calculated by the HF and DFT methods, we can estimate the effect of electron correlation on the chemical bonding. It can be seen from Table 3 that the electron correlation virtually does not affect the local properties of the electronic structure of the MgO ionic crystal. In the mixed ionic and covalent crystal TiO_2, on the contrary, the electron correlation increases the covalent contribution to the bonding (Table 5). This may be explained by the fact that the electron correlation manifests itself in a repulsion of electrons at small distances between them. This effect becomes significant for electrons forming a covalent bond. Therefore, the effect of electron correlation is more pronounced for more covalently bonded crystals.

The accuracy of calculating WFs depends on the number of BFs with different wave vectors included in the sum in Eq. (1). For the MgO isotropic cubic crystal, we used a set of $4 \times 4 \times 4 = 64$ **k** points. Calculations with a larger set of $8 \times 8 \times 8 = 512$ **k** points gave virtually the same results for both the total energy per unit cell (–274.6640 and –274.6642 au) and the energy at the valence band top (–0.3106 and –0.3105 au, respectively).

The crystal TiO_2 is anisotropic ($a \cong 1.5c$). Therefore, a set of **k** points might be obtained not only by a symmetrical split of reciprocal lattice vectors. With sets of $6 \times 6 \times 6 = 216$, $4 \times 4 \times 4 = 64$, and $2 \times 2 \times 3 = 12$ **k** points, the calculated total energy per unit cell is –69.7758, –69.7756, and –69.7744 au and the calculated one-electron energy at the valence band top is –0.3029, –0.3031, and –0.3030 au, respectively. Therefore, the set of 64 **k** points is appropriate for calculations. Even the set of 12 points gives virtually the same results for the WFs and, hence, for the local electronic properties (Table 5). We note that, in the latter case, the computational time is an order of magnitude shorter.

Now, we consider the dependence of the calculated local electronic structure on the scheme used to analyze the atomic populations. For the MgO crystal, the Mulliken and Lölwdin schemes for analyzing the atomic populations give virtually the same results (Table 3). The results are also not affected strongly when the AWF approach is used. The difference between the results obtained using these schemes is slightly larger for DFT than for HF calculations. When the atomic populations are analyzed in terms of an AO basis in the Löwdin scheme, the bonding becomes more covalent in character as one passes over from the HF to the DFT method. At the same time, the results obtained using orthogonal or nonorthogonal AWFs are similar for both the HF and

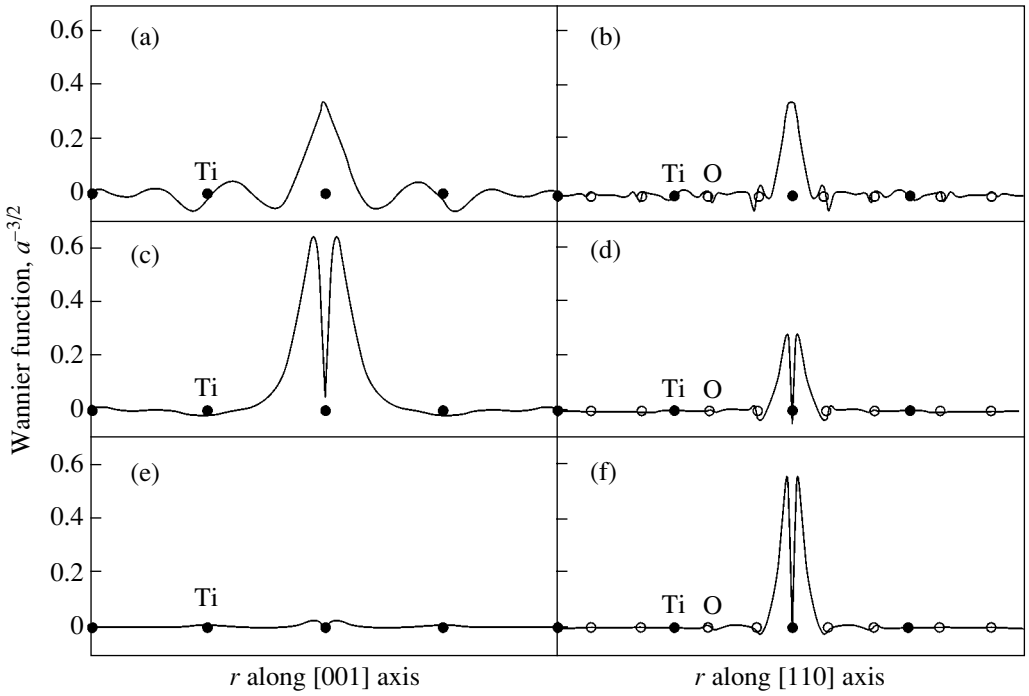

Fig. 4. Three AWFs centered at a titanium atomic site and having symmetry a_g for crystal TiO_2 (in units of $a^{-3/2}$, where a is the atomic length unit): (a, b) *s*-like function, (c, d) *d*-like function of the $3z^2 - r^2$ type, and (e, f) *d*-like function of the *xy* type along (a, c, e) the [001] axis and (b, d, f) the [110] axis. The Bloch functions are calculated within a cyclic $4 \times 4 \times 4$ model using the Hartree–Fock method.

DFT method and correspond to almost ionic bonding (with an oxygen charge equal to –2). Therefore, the occupied Bloch states are virtually orthogonal to the metal *s* AWF constructed from the entire set of valence bands and from the magnesium *s* band. Thus, the charge localized on the metal atom turns out to be small.

A different situation occurs in the case of TiO_2. The Mulliken and Löwdin schemes for analyzing the atomic populations give strongly different results. When based on orthogonal or nonorthogonal AWFs, the results of analysis become much less sensitive to the scheme used. Nevertheless, orthogonalization of AWFs affects the results more significantly than in the case of MgO, because the titanium *s* AWF is weakly localized and, therefore, overlaps noticeably with other AWFs. Such an overlap of the functions causes their deformation within the orthogonalization process, which can affect the values of the local characteristics calculated on the basis of these functions.

To determine the contribution from the titanium *s* states, we calculated the local characteristics with and without inclusion of these states. As seen from Table 5, the contribution from these states of the *s* band to the titanium atomic population is negligible, as in the case with the magnesium *s* band in MgO. The results obtained using nonorthogonal and orthogonal AWFs differ to a lesser extent if the *s* band is not included, because in this case the least localized titanium *s* function is not involved in the orthogonalization.

Thus, high-lying bands (in our case, metal *s* bands) virtually do not contribute to the electron population of the corresponding atoms. On the contrary, for low-lying bands (titanium *d* bands), strong mixing of the corresponding WFs with the oxygen states occurs, which increases the degree of covalent bonding. In the MgO crystal, there are no minimal-basis functions centered at the metal atoms and associated with an energy band lying near the oxygen bands. As a consequence, the degree of ionic bonding in this crystal is noticeably higher than that in titanium oxide, in which the minimal AWF basis contains such functions. For the same reason, the effect of electron correlation on the local characteristics is different in TiO_2 and MgO. Inclusion of the correlation (by using the DFT method) decreases the energy gap between the occupied and empty states in comparison with HF calculations. For the high-lying metal *s* bands in both crystals, this decrease in the energy gap is less perceptible than that for the titanium *d* bands; therefore, the covalent contribution from the latter bands to the bonding increases with the inclusion of electron correlation. We note that, in crystals with a significant degree of ionic bonding, the metal *s* bands lie at high energies; this fact is the reason for the ionic picture of the chemical bonding when the local characteristics are calculated using AWFs. However, if the

minimal basis includes metal AWFs corresponding to empty states, which are closer to occupied states than are the metal *s* states, then the degree of covalent bonding increases.

7. CONCLUSIONS

The main results of our study are as follows:

(1) The method proposed in [7] for constructing WFs has been improved:

(a) The initial BF basis has been symmetrized with respect to the irreducible representations of the local-symmetry groups of WF localization centers.

(b) Symmetric orthogonalization has been performed in the space of generalized BFs.

(c) A principle has been formulated that should be followed in selecting the conduction bands originating from the valence states of the atoms of the crystal.

The full inclusion of symmetry significantly reduces the magnitude of computations. Therefore, this method can be applied to complex crystals with a fairly large number of atoms per unit cell.

(2) The local characteristics of the electronic structures of the MgO and TiO_2 crystals, calculated using the HF and DFT methods, have been determined. In contrast to the earlier calculations, these results are self-consistent and agree with the empirical notion of the character of chemical bonding in these compounds.

(3) It has been found that the energy bands originating from the metal valence *s* states are empty and lie at fairly high energies.

(4) The local characteristics of the electronic structure were related to the mutual arrangement of the energy bands involved in the AWF construction.

(5) Using the TiO_2 crystal as an example, it was shown that the calculated atomic populations depend on the size of the cyclic model crystal only weakly.

(6) It was explained why the DFT method gives a larger degree of covalent bonding than the HF method only for rutile, even though the former method gives a smaller value of the band gap for both compounds (MgO, TiO_2).

We note that the method proposed in this paper for constructing AWFs can be applied in the cases where both an AO and a plane-wave basis are used to calculate the electronic structure of a crystal. Bloch states can be found both with inclusion of electron correlation (different versions of the DFT method) and without it (the HF method). Once the AWFs have been found, they can be used to calculate not only the local electronic structure of the crystal but also other physical properties that depend on them.

ACKNOWLEDGMENTS

This study was supported by the Russian Foundation for Basic Research, project nos. 02-03-32738 and 03-03-06124.

REFERENCES

1. V. P. Smirnov, R. A. Evarestov, and D. E. Usvyat, Int. J. Quantum Chem. **88**, 642 (2002).
2. R. A. Evarestov, V. P. Smirnov, and D. E. Usvyat, Int. J. Quantum Chem. (in press).
3. C. M. Zicovich-Wilson, A. Bert, C. Roetti, *et al.*, J. Chem. Phys. **116**, 1120 (2002).
4. G. Wannier, Phys. Rev. **52**, 191 (1937).
5. V. A. Veryazov, A. V. Leko, and R. A. Évarestov, Fiz. Tverd. Tela (St. Petersburg) **41**, 1407 (1999) [Phys. Solid State **41**, 1286 (1999)].
6. M. D. Segall, R. Shah, C. J. Pickard, *et al.*, Phys. Rev. B **54**, 16317 (1996).
7. V. P. Smirnov and D. E. Usvyat, Phys. Rev. B **64**, 245108 (2001).
8. W. Kohn, Phys. Rev. **115**, 809 (1959).
9. J. Des Cloizeaux, Phys. Rev. **135**, A698 (1964).
10. G. Nenciu, Commun. Math. Phys. **91**, 81 (1983).
11. E. K. Kudinov, Fiz. Tverd. Tela (St. Petersburg) **41**, 1582 (1999) [Phys. Solid State **41**, 1450 (1999)].
12. B. Sporkmann and H. Bross, Phys. Rev. B **49**, 10869 (1994).
13. N. Marzari and D. Vanderbilt, Phys. Rev. B **56**, 12847 (1997).
14. C. M. Zicovich-Wilson, R. Dovesi, and V. R. Saunders, J. Chem. Phys. **115**, 9708 (2001).
15. I. Mayer, G. Räther, and S. Suhai, Chem. Phys. Lett. **293**, 81 (1998).
16. P. Y. Yu and M. Cardona, *Fundamentals of Semiconductors* (Springer, Berlin, 1996).
17. J. P. Albert, C. Jouanin, D. Cassagne, and D. Bertho, Phys. Rev. B **61**, 4381 (2000).
18. Y. Noel, C. M. Zicovich-Wilson, B. Civalleri, *et al.*, Phys. Rev. B **65**, 014111 (2002).
19. P. Ghosez, J. Michenaud, and X. Gonze, Phys. Rev. B **58**, 6224 (1998).
20. S. Goedecker, Rev. Mod. Phys. **71**, 1085 (1999).
21. C.-K. Skylaris, A. A. Mostofi, P. D. Haynes, *et al.*, Phys. Rev. B **66**, 035119 (2002).
22. A. Shukla, M. Dolg, P. Fulde, and H. Stoll, Phys. Rev. B **60**, 5211 (1999).
23. J. Des Cloizeaux, Phys. Rev. **129**, 554 (1963).
24. O. V. Kovalev, *Representations of the Crystallographic Space Groups: Irreducible Representations, Induced Representations, and Corepresentations* (Nauka, Moscow, 1986; Gordon and Breach, Yverdon, Switzerland, 1993).
25. R. A. Evarestov and V. P. Smirnov, *Site Symmetry in Crystals: Theory and Applications* (Springer, New York, 1997), Springer Ser. Solid-State Sci., Vol. 108.
26. R. A. Évarestov and V. P. Smirnov, *Local Symmetry in Molecules and Crystals* (S.-Peterb. Gos. Univ., St. Petersburg, 1997).

27. P. Löwdin, Adv. Phys. **5**, 1 (1956).
28. M. Causa, R. Dovesi, S. Pisani, and C. Roetti, Phys. Rev. B **33**, 1308 (1986).
29. B. Silvi, N. Fourati, R. Nada, and C. R. A. Catlow, J. Phys. Chem. Solids **52**, 1005 (1991).
30. K. J. Chang and M. L. Cohen, Phys. Rev. B **30**, 4774 (1984).
31. K. M. Glassford and J. R. Chelikowsky, Phys. Rev. B **46**, 1284 (1992).
32. A. Fahmi, C. Minot, B. Silvi, and M. Causa, Phys. Rev. B **47**, 11717 (1993).
33. P. Reinhardt, B. A. Heβ, and M. Causa, Int. J. Quantum Chem. **58**, 297 (1996).
34. R. Dovesi, V. R. Saunders, C. Roetti, M. Causa, N. M. Harrison, R. Orlando, and E. Apra, *Crystal 95 User's Manual* (Torino Univ. Press, Torino, 1996).
35. P. Durand and J. C. Barthelat, Theor. Chim. Acta **38**, 283 (1975).
36. H. J. Monkhorst and J. D. Pack, Phys. Rev. B **13**, 5188 (1976).
37. R. A. Évarestov and I. I. Tupitsyn, Fiz. Tverd. Tela (St. Petersburg) **44**, 1582 (2002) [Phys. Solid State **44**, 1656 (2002)].
38. J. P. Perdew and A. Zunger, Phys. Rev. B **23**, 5048 (1981).
39. S. C. Miller and W. F. Love, *Tables of Irreducible Representations of Space Group and Co-Representations of Magnetic Space Groups* (Pruett, Boulder, Colo., 1967).

Translated by Yu. Epifanov

Physics of the Solid State, Vol. 45, No. 11, 2003, pp. 2083–2092. Translated from Fizika Tverdogo Tela, Vol. 45, No. 11, 2003, pp. 1982–1990.

SEMICONDUCTORS AND DIELECTRICS

Spin–Spin Interaction and the EPR Spectrum of $KDy(WO_4)_2$

I. M. Krygin[1], A. D. Prokhorov[1], V. P. Dyakonov[1,2], M. T. Borowiec[2], and H. Szymczak[2]

[1] *Donetsk Physicotechnical Institute, National Academy of Sciences of Ukraine, Donetsk, 83114 Ukraine*

[2] *Institute of Physics, Polish Academy of Sciences, Al. Lotnikyw 32/46, Warsaw, 02-668 Poland*

Received December 27, 2002; in final form, April 7, 2003

Abstract—The EPR spectrum of a $KDy(WO_4)_2$ monoclinic crystal is investigated. It is found that the EPR spectrum of magnetically concentrated materials at a low frequency (9.2 GHz) undergoes a substantial transformation in addition to the well-known broadening of the EPR lines. At low Dy^{3+} concentrations ($x < 10^{-2}$), the EPR spectrum of an isomorphic crystal, namely, $KY_{(1-x)}Dy_x(WO_4)_2$, is characterized by the parameters $g_x = 0$, $g_y = 1.54$, and $g_z = 14.6$. For a magnetically concentrated crystal $KDy(WO_4)_2$, the g values are as follows: $g_x = 0$, $g_y = 0.82$, and $g_z = 2.52$. It is demonstrated that the difference in the parameters is associated with the specific spin–spin interaction between Dy^{3+} ions, including the Dzyaloshinski interaction, which is not observed at high frequencies. © *2003 MAIK "Nauka/Interperiodica".*

1. INTRODUCTION

Considerable interest has been expressed by researchers in crystals of double tungstates of monoclinic symmetry for a number of reasons. First, these materials doped with rare-earth elements hold promise for producing laser action with unique properties [1–4]. Second, $KDy(WO_4)_2$ and $RbDy(WO_4)_2$ crystals at low temperatures undergo structural phase transitions of the Jahn–Teller type, during which lattice distortions occur without a change in symmetry [5–8]. At temperatures below 1 K, these crystals also undergo antiferromagnetic ordering [7–11].

Upon isomorphous substitution, the EPR spectra of magnetically diluted and magnetically concentrated compounds, as a rule, differ only in the absorption line width. The large line width for magnetically concentrated materials is explained by the considerable contribution of the spin–spin interaction to the EPR spectrum. This broadening leads to a smearing of the spectral structure. The smearing is determined by the ratio of the spin–spin interaction energy to the energy of the interaction responsible for the formation of the spectral structure. It should be noted that there are cases (see, for example, [12, 13]) where the EPR spectra of magnetically concentrated compounds exhibit a structure associated with the specific type of spin–spin interaction.

The spectroscopic splitting factor g entering into the Hamiltonian changes to a considerably lesser extent. This factor is a characteristic of the ground state of an impurity ion, which is determined by the symmetry and the electric crystal field of the matrix. In the homologous series of crystals, the crystal symmetry remains unchanged and only the unit cell parameters change quantitatively. Consequently, the g factor should also change only quantitatively, if at all. Numerous experiments have demonstrated that these changes in the g factor are within the limits of experimental error.

The $KDy(WO_4)_2$ paramagnetic crystal and the $KY(WO_4)_2$ diamagnetic crystal belong to the same homologous series. The unit cell parameters of these crystals differ by no more than 0.7%. Therefore, no substantial differences in the g factor can be expected for magnetically concentrated ($x = 1$) and magnetically diluted ($x < 10^{-2}$) $KY_{(1-x)}Dy_x(WO_4)_2$ crystals. However, the characteristics of the EPR spectra of the magnetically concentrated [7] and magnetically diluted [14] crystals differ qualitatively. At a frequency of ≈9.2 GHz, in crystals with a low dysprosium concentration, the g factor has ordinary values: $g_x = 0$, $g_y = 1.54$, and $g_z = 14.6$. In crystals with 100% Dy^{3+}, the g values are as follows: $g_x = 0$, $g_y = 0.82$, and $g_z = 2.52$ at temperatures above the phase transition point T_{spt} and $g_x = 0$, $g_y = 1.19$, and $g_z = 1.98$ at $T < T_{spt}$. Contradictory data on the g factor have been obtained from analyzing the magnetic susceptibility [10].

Earlier [15], we established that the strongest interaction is observed for Dy^{3+} ions located in the first (nn), fifth ($5n$), and ninth ($9n$) coordination shells. In this case, the spin–spin interaction is characterized by a considerable axial anisotropy, i.e., $|K_{zz}| \gg |K_{nm}|$ ($n, m = x, y, z$). The spin–spin interaction energy is comparable ($K_{zz(5n)} = -0.407$ cm^{-1}, $K_{zz(9n)} = -0.237$ cm^{-1}) and even exceeds ($K_{zz(nn)} = 1.49$ cm^{-1}) the energy of microwave photons ($h\nu = 0.308$ cm^{-1}) used in EPR experiments. For the other coordination shells, the spin–spin interaction is substantially weaker.

In the present work, we showed that the very specific, sufficiently strong spin–spin interaction between impurity ions is responsible for the qualitative transfor-

Table 1. Unit cell parameters (Å) and rhombohedral angles β (deg) in the structures of $KY(WO_4)_2$ and $KDy(WO_4)_2$ single crystals

Crystal	**a**	**b**	**c**	β	Reference
$KY(WO_4)_2$	8.11	10.35	7.54	93.3	[1]
$KDy(WO_4)_2$	8.05	10.32	7.52	94.4	[2]

Table 2. Coordinates *A*, *B*, and *C* (in terms of **a**, **b**, **c**) of rare-earth ions in the unit cells of $KY(WO_4)_2$ and $KDy(WO_4)_2$ crystals

Ion no.	*A*	*B*	*C*
1	0	0.2716	0.25
2	0.5	0.2284	0.25
3	0	0.7284	0.75
4	0.5	0.7716	0.75

mation of the EPR spectra with an increase in the concentration of Dy^{3+} ions.

2. CRYSTAL STRUCTURE

Potassium yttrium and potassium dysprosium double tungstates, $KY(WO_4)_2$ and $KDy(WO_4)_2$, are isomorphic crystals in the monoclinic system [16–18] with space-group symmetry $C_{2h}^6 = C2/c$. The unit cell contains four formula units. The unit cell parameters for both crystals are listed in Table 1. The coordinates of rare-earth ions in the unit cell are presented in Table 2. A fragment of the $KDy(WO_4)_2$ crystal is depicted in Fig. 1. To avoid overloading of the figure, only rare-earth ions located in two adjacent planes **ac** are shown by gray and open circles and bonding lines are drawn only for the *nn* pairs. The central ion from which the distances to the neighboring ions are reckoned is shown by the closed circle. The Dy^{3+} ions forming the 2*n* pairs (not shown in Fig. 1) occupy the lower **ac** plane and the **bc** plane involving the 3*n* pairs. The ions located within one unit cell bounded by the dashed straight lines are numbered in italic type in accordance with Table 2.

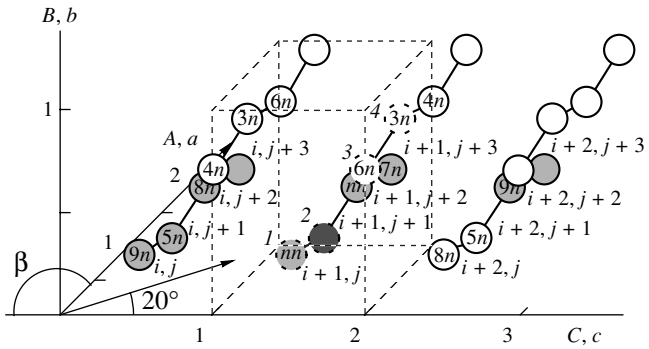

Fig. 1. A fragment of the $KDy(WO_4)_2$ crystal with sizes $L_1 = 4$ and $L_2 = 3$ and the axes of the laboratory coordinate system. β is the rhombohedral angle. Ions are numbered according to Hamiltonian (1). Numbering in italic type corresponds to Table 2. Dashed lines depict the unit cell and ions in it.

The nearest neighbor rare-earth ions (*nn*) are located in the **ab** plane and form slightly bent chains lying along the **a** axis. The bonding direction of the *nn* pair makes an angle of 6.3° with the **ac** plane. The Dy^{3+} ions forming the 5*n* and 9*n* pairs are located in the chains lying in the same plane **ac** at a distance *C* from the initial chain and, in turn, represent the *nn* pair. Therefore, the chains of the Dy^{3+} ions form planes perpendicular to the **b** axis. Note that the in-plane spin–spin interaction (with the dominant interaction along the chains) is appreciably stronger than the interplanar interaction.

3. THEORY

Let us consider a Dy^{3+} ion with the $4f^9$ electron configuration ($S = 5/2$, $L = 5$, $J = 15/2$, Landé factor $g_J = 4/3$). The ground state $^6H_{15/2}$ is split by the crystal field of monoclinic tungstate into eight Kramers doublets, of which the lowest doublet exhibits an EPR spectrum. The first and second excited doublets lie 10 and 135 cm^{-1} above the ground doublet, respectively [5, 6]. The even dysprosium isotopes (the natural abundance ^{evn}c is 56.1%) have a zero nuclear spin, whereas the odd isotopes ^{163}Dy (^{163}c = 24.97%) and ^{161}Dy (^{161}c = 18.88%) are characterized by the nuclear spin $I = 5/2$. For Dy^{3+} single ions in the studied matrix, the tensor *g* has the components $g_x = 0$, $g_y = 1.54$, and $g_z = 14.6$ and the components of the hyperfine interaction tensor for the odd isotopes are as follows: $^{163}A_z = 582.8 \times 10^{-4}$ cm^{-1}, $^{161}A_z = 416.5 \times 10^{-4}$ cm^{-1}, $^{163}A_y = 146 \times 10^{-4}$ cm^{-1}, and $^{161}A_y = 104 \times 10^{-4}$ cm^{-1} [14]. The directions of the principal axes of the tensors **g** and **A** are shown in Fig. 1. The **y** axis coincides with the **b** ($\mathbf{c}_2$) crystallographic axis, and the **z** axis lies in the **ac** plane and emerges from the acute angle between the **a** and **c** axes at an angle of 20° to the **c** axis.

Since the hyperfine interaction is considerably weaker than the spin–spin interaction, the former interaction is ignored in the further consideration, especially as the contribution of the even dysprosium isotopes (with a zero hyperfine interaction) amounts to more than half the total intensity of the spectrum of $KDy(WO_4)_2$. By disregarding also the interplanar interaction, the Hamiltonian for the plane formed by L_1

chains, each consisting of L_2 Dy^{3+} ions, at $\mathbf{B} \parallel \mathbf{z}$ can be written in the form

$$\hat{H} = g_z\mu_B B_z \sum_{i=1}^{L_1}\sum_{j=1}^{L_2}\hat{\mathbf{S}}_{z,i,j} + \sum_{i=1}^{L_1}\sum_{j=1}^{L_2-1}\hat{\mathbf{S}}_{i,j}\mathbf{K}_{(nn)}\hat{\mathbf{S}}_{i,j+1} + \sum_{i=1}^{L_1-1}\sum_{j=1}^{L_2}\hat{\mathbf{S}}_{i,j}\mathbf{K}_{(5n)}\hat{\mathbf{S}}_{i,j+1} + \sum_{i=1}^{L_1-1}\sum_{j=1}^{L_2-1}\hat{\mathbf{S}}_{i,j}\mathbf{K}_{(9n)}\hat{\mathbf{S}}_{i+1,j+1}. \quad (1)$$

Here, the first term describes the interaction of spins with an external constant magnetic field with induction B_z; the other terms characterize the spin–spin interaction of ions located in the first (nn), fifth ($5n$), and ninth ($9n$) coordination shells; the first and second subscripts on the spin operator $\hat{\mathbf{S}}$ indicate the number of the chain and the number of the ion in this chain (Fig. 1), respectively; μ_B is the Bohr magneton; $\mathbf{K}$ is the tensor of spin–spin interaction; and $S = 1/2$. The principal axes of the tensor of spectroscopic splitting g are used as the axes of the laboratory coordinate system. The axes of the laboratory coordinate system are shown in Fig. 1, in which the numbering of Dy^{3+} ions corresponds to the designations in Hamiltonian (1).

The contributions to the spin–spin interaction tensor $\mathbf{K}$ can be made by different mechanisms of spin–spin interaction, including the isotropic exchange (j) and magnetic dipole–dipole (MDD) interactions:

$$\mathbf{K} = \mathbf{K}^j + \mathbf{K}^{\mathrm{MDD}}. \quad (2)$$

To sufficient accuracy, we can calculate only the contribution of the magnetic dipole–dipole interaction [19]:

$$K_{nm}^{\mathrm{MDD}} = \mu_B r^{-3}(\delta_{nm} - 3l_n l_m)g_n g_m, \quad (3)$$

where r is the interionic distance, l_n and l_m are the direction cosines of the bonding direction with respect to the corresponding axis, and $\delta_{nm} = 1$ at $n = m$ and $\delta_{nm} = 0$ at $n \neq m$ ($n, m = x, y, z$).

The distance between Dy^{3+} ions is relatively large: two oxygen ions and one potassium ion are located even between the nearest neighbor Dy^{3+} ions. Therefore, it is highly improbable that the direct exchange interaction can occur between the Dy^{3+} ions. However, in any case, whether the isotropic exchange interaction is direct or indirect, this interaction can manifest itself in an anisotropic manner. Indeed, by ignoring the admixture of excited states, the tensor $\mathbf{K}^j$ (written in terms of effective spins) takes the anisotropic form [19]

$$K_{nm}^j = \left(\frac{g_{nm}}{g_j}\right)^2 (g_j - 1)^2 j. \quad (4)$$

From relationships (3) and (4), it follows that $\mathbf{K}^{\mathrm{MDD}}$ and $\mathbf{K}^j$ are symmetric tensors. With due regard for the rather low symmetry of the matrix, we should expect that the indirect exchange interaction is strongly anisotropic and can be either symmetric (s) or antisymmetric (as); in this case, the components of the tensors $\mathbf{K}^s$ and $\mathbf{K}^{as}$ satisfy the following conditions:

$$K_{mn}^s = K_{nm}^s, \quad K_{mn}^{as} = -K_{nm}^{as}, \quad K_{mm}^{as} = 0. \quad (5)$$

Consequently, relationship (2) can be rewritten in the form

$$\mathbf{K} = \mathbf{K}^s + \mathbf{K}^{as}. \quad (6)$$

Here, the contributions to the tensor $\mathbf{K}^s$ can be made by the magnetic dipole–dipole interaction and the direct (j), indirect isotropic (j_k), and symmetric anisotropic (j_s) exchange interactions:

$$\mathbf{K}^s = \mathbf{K}^{\mathrm{MDD}} + \mathbf{K}^j + \mathbf{K}^{jk} + \mathbf{K}^{js}. \quad (7)$$

However, according to Borisov and Klevtsova [16], pairs of Dy^{3+} ions in $KY_{0.99}Dy_{0.01}(WO_4)_2$ are characterized by the axial spin–spin interaction; i.e., all the components of the spin–spin interaction tensor $\mathbf{K}$ are negligible compared to the component K_{zz}. Hence, the solution of Hamiltonian (1) will be sought in the space of the wave functions

$$\phi_p = m_{p,1,1}, m_{p,1,2}m_{p,1,3}, \ldots, m_{p,1,L_2}, m_{p,2,l}, m_{p,2,2}m_{p,2,3}, \ldots, m_{p,2,L_2}, \ldots, m_{p,L_1,L_2}, \quad (8)$$

where $m_{p,i,j} = \pm 1/2$. The total number of states of the spin system is equal to 2^L, where $L = L_1L_2$.

Since Hamiltonian (1) in this case has only diagonal terms, the energy spectrum represents a set of levels linearly dependent on the magnetic field induction B_z and described by the pure wave functions (8); that is,

$$E_p = g_z\mu_B A_p B_z + D_p. \quad (9)$$

Here, p is the number of the energy level, $D_p = D_{p,0,0}K_{zz(nn)} + D_{p,1,0}K_{zz(5n)} + D_{p,1,1}K_{zz(9n)}$, and the nonzero coefficients $D_{p,k,l}$ and A_p are defined by the formulas

$$D_{p,k,l} = \left\langle \phi_p \middle| \sum_{i=1}^{L_1-k}\sum_{j=1}^{L_2-l}\hat{S}_{z,i,j}\hat{S}_{z,i+k,j+l} \middle| \phi_p \right\rangle = \sum_{i=1}^{L_1-k}\sum_{j=1}^{L_2-l} m_{p,i,j}m_{p,i+k,j+l},$$

$$A_p = \left\langle \phi_p \middle| \sum_{i=1}^{L_1}\sum_{j=1}^{L_2}\hat{S}_{z,i,j} \middle| \phi_p \right\rangle = \sum_{i=1}^{L_1}\sum_{j=1}^{L_2} m_{p,i,j}.$$

The probability W_{pq} of the transition from the pth level to the qth level is given by the relationship

$$W_{pq} \sim \left| \left\langle \phi_p \middle| \sum_{i=1}^{L_1}\sum_{j=1}^{L_2}\hat{S}_{y,i,j} \middle| \phi_q \right\rangle \right|^2. \quad (10)$$

The right-hand side of relationship (10) is equal to 0.25 when the projection of only one out of all the spins changes by 1 ($m_{p,i,j} = -m_{q,i,j}$). In all other cases, we have $W_{pq} = 0$. Consequently, the probabilities of all the allowed transitions are identical and the calculation of the EPR spectrum is reduced to simple geometric calculations involving the determination of all pairs of straight lines (9) with $W_{pq} \neq 0$ and calculation of the magnetic induction B_z necessary to satisfy the condition $|E_q - E_p| = h\nu$.

At high photon energies ($h\nu > |K_{zz(nn)}|$), the EPR spectrum of an ion pair ($L_1 = 1$, $L_2 = 2$) is represented by a doublet with lines at $B_0 \pm K_{zz(nn)}/2$, where $B_0 = h\nu/g_z\mu_B$. The EPR spectrum of an ion triad is given below. Similar calculations for longer chains include an exhaustion search for a very large number of straight lines and can be conveniently performed using a computer. As a result, we found that, at $L_1 = 1$ and arbitrary $L_2 > 2$, the EPR spectrum is an equidistant pentad with the lines located at

$$B_1 = B_0 - K_{zz(nn)}, \quad B_2 = B_0 - K_{zz(nn)}/2, \quad B_3 = B_0, \\ B_4 = B_0 + K_{zz(nn)}/2, \quad B_5 = B_0 + K_{zz(nn)} \tag{11}$$

and the intensity ratio

$$\left(1 - \frac{2}{L_2}\right) : \frac{4}{L_2} : \left(2 - \frac{4}{L_2}\right) : \frac{4}{L_2}\left(1 - \frac{4}{L_2}\right). \tag{12}$$

This implies that, as the chain length increases, the EPR spectrum transforms from the doublet B_2 and B_4 to the triplet B_1, B_3, and B_5. A similar result was obtained in our previous work [13] for a chain of ions bound through axial interaction.

Relationships (11) can be rewritten in the following form:

$$\Delta_{51} = 2K_{zz(nn)}, \quad \Delta_{42} = K_{zz(nn)}, \\ B_{51} = B_{42} = B_3 = B_0, \tag{13}$$

where $\Delta_{mk} = B_m - B_k$ and $B_{mk} = (B_m + B_k)/2$.

Similar calculations carried out for a square fragment of the plane at $L_1 = L_2 = 3$ and 4 showed that, for a sufficiently large fragment, each line of pentad (12) is split by the interaction with the Dy^{3+} ions located in the fifth coordination shell into the same pentad with $\Delta_{51(5n)} = 2K_{zz(5n)}$, $\Delta_{42(5n)} = K_{zz(5n)}$, and $B_{0(5n)} = B_0$. In turn, each of the 25 lines obtained is split by the spin–spin interaction with the Dy^{3+} ions located in the ninth coordination shell into a similar pentad with $\Delta_{51(9n)} = 2K_{zz(9n)}$ and $\Delta_{42(9n)} = K_{zz(9n)}$. For a real sample ($L_1, L_2 \longrightarrow \infty$), the EPR spectrum in the case of axial spin–spin interaction should consist of 27 lines broadened because of the interaction with more distant Dy^{3+} ions.

A decrease in the energy of microwave photons leads to a transformation of the EPR spectrum. It can be demonstrated that the transformation of the spectrum with a decrease in the frequency is formally reduced to reflection of the absorption lines located at negative inductions on the positive half-plane. At $h\nu < |K_{zz(nn)}/2|$, the EPR spectrum of a chain formed by the nearest neighbor ions is represented by pentad (12) with the lines located at

$$B_{51} = K_{zz(nn)}, \quad B_{42} = K_{zz(nn)/2}, \\ \Delta_{51} = \Delta_{42} = 2B_0, \quad B_3 = B_0. \tag{14}$$

Now, we consider how the symmetric and antisymmetric spin–spin interactions affect the EPR spectrum of the $KDy(WO_4)_2$ crystal. For this purpose, proper allowance must be made for the fact that a triad of interacting ions is the minimum configuration whose spectrum contains the lines observed not only in the spectrum of pairs but also in the spectrum of an infinite chain. On this basis, from analyzing the influence of the anisotropic exchange interaction on the locations of the first, third, and fifth lines, we can draw inferences regarding the transformation of the EPR spectrum due to off-diagonal components of the spin–spin interaction tensor **K**.

For the axial spin–spin interaction and **B** ∥ **z**, the energy spectrum of a triad formed by ions whose interaction is described by $K_{zz(nn)}$ ($L_1 = 1$, $L_2 = 3$) can be easily calculated in analytical form. From relationships (8)–(10), we derive the following energy spectrum and wave functions:

$$E_1 = -G - K_{zz}/2, \quad |\phi_1\rangle = |-1/2, +1/2, -1/2\rangle, \\ E_2 = G - K_{zz}/2, \quad |\phi_2\rangle = |+1/2, -1/2, +1/2\rangle, \\ E_3 = E_4 = -G \quad |\phi_3\rangle = |+1/2, -1/2, -1/2\rangle, \\ |\phi_4\rangle = |-1/2, -1/2, +1/2\rangle, \\ E_5 = E_6 = G \quad |\phi_5\rangle = |-1/2, +1/2, +1/2\rangle, \\ |\phi_6\rangle = |+1/2, +1/2, -1/2\rangle, \\ E_7 = -3G + K_{zz}/2 \quad |\phi_7\rangle = |-1/2, -1/2, -1/2\rangle, \\ E_8 = 3G + K_{zz}/2 \quad |\phi_8\rangle = |+1/2, +1/2, +1/2\rangle, \tag{15}$$

where $G = g_z\mu_B B_z/2$.

The E_7 level intersects the E_5 and E_6 levels at $B_{k1} = K_{zz}/4g_z\mu_B$; the E_2, E_3, and E_4 levels at $B_{k2} = K_{zz}/2g_z\mu_B$; and the E_1 level at $B_{k3} = K_{zz}/g_z\mu_B$. The allowed transitions with the same probability $W_{pq} \sim 0.25$ between the levels are as follows: $E_1 \rightleftharpoons E_5$, $E_1 \rightleftharpoons E_6$, $\underline{E_1 \longleftrightarrow E_7}$, $E_2 \rightleftharpoons E_3$, $E_2 \rightleftharpoons E_4$, $E_2 \rightleftharpoons E_8$, $\underline{E_3 \longleftrightarrow E_6}$, $E_3 \rightleftharpoons E_7$, $\underline{E_4 \longleftrightarrow E_5}$, $E_4 \rightleftharpoons E_7$, $E_5 \rightleftharpoons E_8$, and $E_6 \rightleftharpoons E_8$. The underlined transitions correspond to the spectrum of the infinite chain. The calculated energy spectrum is depicted by the solid lines in Fig. 2.

The tensor components K_{yz} and K_{yy} provide mixing of all the states. In this case, the energy spectrum and

the transition probabilities can be most conveniently calculated with a computer. The results of calculations are presented in Table 3 and Fig. 2. The component K_{yy} leads to the appearance of the energy gap at the point B_{k1} (Fig. 2, line *4*). The component K_{yz}^{as} removes the degeneracy of the E_3–E_6 levels at the point $B_z = 0$ and results in the appearance of the energy gap at the point B_{k2} (Fig. 2, line *2*). The component K_{yz}^{s} is responsible for the formation of the energy gap at the points B_{k2} and B_{k3} (Fig. 2, line *3*). These tensor components mix the wave functions and lead to a change in the transition probabilities at magnetic inductions B_z sufficiently close to the characteristic points. For other magnetic field inductions, the above components of the spin–spin interaction tensor **K** do not affect the energy spectrum.

Therefore, the antisymmetric spin–spin interaction has no noticeable effect on the B_1 and B_5 lines, shifts the B_3 line toward lower magnetic field inductions, and decreases its intensity, which becomes equal to zero at $B_z = 0$. By contrast, the component K_{yz}^{s} virtually does not affect the quartet E_3–E_6 and leads to a decrease in the separation between the B_1 and B_5 lines and in their intensities (the intensity of the B_5 line decreases to a greater extent).

Note that the aforementioned effects are most pronounced at frequencies comparable to splittings caused by the corresponding spin–spin interaction tensor components. For the sufficiently high energies of microwave photons used in experiments, the contribution from the off-diagonal components of the spin–spin interaction tensor **K** should be negligible in magnitude.

4. EXPERIMENTAL TECHNIQUE

Single crystals of $KDy(WO_4)_2$ were used as samples. The crystals were grown through spontaneous crystallization from a $K_2W_2O_7$ solution upon cooling from 950°C at a rate of 3°C/h. The linear dimensions of the grown crystals varied from 2 to 3 mm, and a number of crystals possessed a clearly pronounced faceting. The crystals were oriented using x-ray diffraction.

The EPR spectra measured at a frequency of 9244.5 MHz, **B** || **z**, and temperatures of 12 and 4.2 K (above and below the phase transition point T_{spt}, respectively) are shown by the solid lines in Fig. 3. Both spectra contain a line with a width of ≈130 mT at a magnetic field induction corresponding to $g_z = 2.53$ at $T = 12$ K and $g_z = 2.13$ at $T = 4.2$ K. At low inductions, there is an anomaly, which disappears with a decrease in the temperature.

The EPR spectrum measured at a frequency of 72 240 MHz, **B** || **z**, and $T = 4.2$ K is depicted by the solid line in Fig. 4. Unlike the low-frequency spectrum, the high-frequency EPR spectrum exhibits a pronounced triplet structure. The line intensities increase

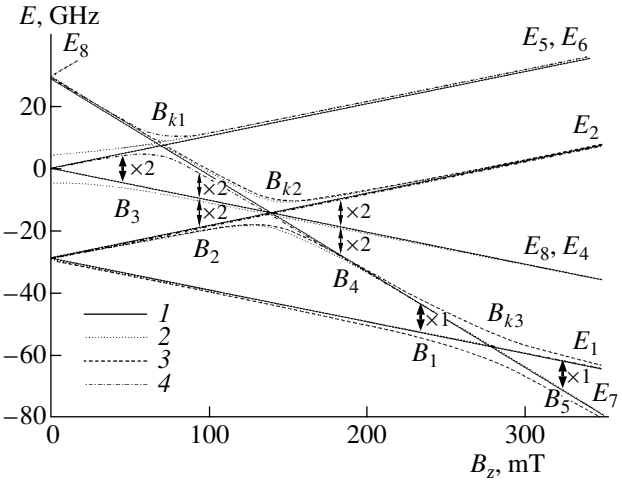

Fig. 2. Calculated energy spectra of a triad of interacting Dy^{3+} ions at **B** || **z** with due regard for (*1*) the axial spin–spin interaction ($K_{zz} = 1.9$ cm^{-1}) and (*2–4*) the low-symmetry components of the spin–spin interaction tensor: (*2*) antisymmetric ($K_{zz} = 1.9$ cm^{-1}, $K_{yz}^{as} = 0.3$ cm^{-1}), (*3*) symmetric ($K_{zz} = 1.9$ cm^{-1}, $K_{yz}^{s} = 0.3$ cm^{-1}), and (*4*) K_{yy} ($K_{zz} = 1.9$ cm^{-1}, $K_{yy} = 0.3$ cm^{-1}) components. In all calculations, it is assumed that $g_z = 14.6$. Components absent from the spin–spin interaction tensor **K** are equal to zero. Arrows indicate the allowed transitions for the axial spin–spin interaction at a frequency of 9244.5 MHz (0.3084 cm^{-1}). Heavy arrows correspond to the transitions in the EPR spectrum of an infinite chain. The transition multiplicity is given near arrows.

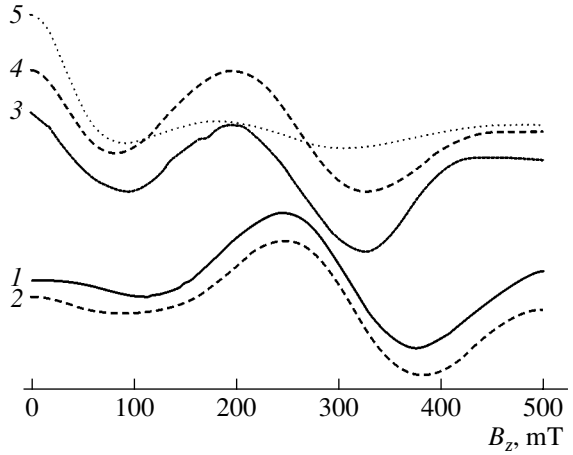

Fig. 3. (*1, 3*) Experimental and (*2, 4, 5*) calculated EPR spectra of $KDy(WO_4)_2$ at a frequency of 9244.5 MHz, **B** || **z**, and $T =$ (*1, 2, 5*) 4.2 and (*3, 4*) 12 K. The spectra are calculated according to (*2, 4*) the data presented in Table 4 and (*5*) the results obtained in [15]. All calculations are performed at $g_z = 14.6$ and $\Delta B = 70$ mT for a Gaussian line shape and with due regard for the freezing effect and the spin–spin interaction in the fifth and ninth coordination shells ($K_{zz(5n)} = -0.4074$ cm^{-1}, $K_{zz(9n)} = -0.2373$ cm^{-1}).

Table 3. Effect of the components K_{zz}, K_{yz}^{as}, K_{yz}^{s}, and K_{yy} of the spin–spin interaction tensor for Dy^{3+} ion triads in $KY_{1-x}Dy_x(WO_4)_2$ ($0 < x \le 1$) on the splitting of energy levels $\Delta E_{pq} = E_p - E_q$ (MHz) and the transition probabilities W_{pq} at characteristic points of the energy spectrum

K_{xz}^{as}	K_{yz}^{s}	K_{yy}	$B_z = 0$											
			ΔE_{43}	W_{43}	ΔE_{53}	W_{53}	ΔE_{63}	W_{63}	ΔE_{54}	W_{54}	ΔE_{64}	W_{64}	ΔE_{65}	W_{65}
0	0	0	0	0.25	0	0	0	0	0	0	0	0	0	0.25
0.3	0	0	0	0.41	8881	0	8881	0	8881	0	8881	0	0	0.11
0	0.3	0	0	0.14	0	0.027	0	0.052	0	0.042	0	0.17	4379	0
0	0	0.3	0	0.059	0	0.085	0	0.081	0	0.008	0	0.054	0	0.088
K_{xz}^{as}	K_{yz}^{s}	K_{yy}	$B_z = B_{k2}$											
			ΔE_{32}	W_{32}	ΔE_{42}	W_{42}	ΔE_{52}	W_{52}	ΔE_{43}	W_{43}	ΔE_{53}	W_{53}	ΔE_{54}	W_{54}
0	0	0	0	0	0	0.25	0	0.25	0	0.25	0	0.25	0	0
0.3	0	0	4123	0.012	4811	0	8912	0	678	0.99	4789	0.012	4101	0
0	0.3	0	4379	0	4608	0.001	8984	0.001	229	0	4605	0	4376	0.001
0	0	0.3	693	0	693	0	927	0.85	0	0	233	0	233	0.002
K_{yz}^{as}	K_{yz}^{s}	K_{yy}	$B_z = B_{k3}$											
			ΔE_{21}	W_{21}										
0	0	0	0	0.25										
0.3	0	0	236	0.24										
0	0.3	0	8934	0.009										
0	0	0.3	233	0.16										

Note: All calculations are performed at $g_z = 14.6$ and $K_{zz} = 1.9$ cm^{-1}, which results in $B_{k2} = 139.37$ mT and $B_{k3} = 278.74$ mT. The energy levels are numbered in increasing order. At $W_{pq} < 10^{-3}$, it is assumed that $W_{pq} = 0$.

with an increase in the magnetic field induction B_z, the width of each line is approximately equal to 120 mT, and $g_z \approx 14.6$.

5. DISCUSSION

Earlier [15], we studied the EPR spectra of Dy^{3+} ion pairs in $KY_{0.99}Dy_{0.01}(WO_4)_2$. According to the data obtained in [15], the dominant contribution to the spin–spin interaction tensor **K** is made by the isotropic exchange and magnetic dipole–dipole interactions [see formula (2)] and the spin–spin interaction for all types of pairs is axial in character. It is clear that the results obtained in [15] cannot be applied for calculating the spectrum of the crystal with the use of Hamiltonian (1) due to a great number of particles. For this reason, we will use a triad of interacting ions as a model. In this case, only the lines that correspond to the spectrum of the infinite chain, i.e., to the transitions between the E_3, E_4, E_5, and E_6 levels at $B_z < B_{k1}$ and the E_1 and E_7 levels at $B_z > B_{k2}$ (Fig. 2), are retained in the calculated spectrum. The calculations are performed taking into account that, for the crystal, (i) each line is split by the interaction with the Dy^{3+} ions located in the fifth and ninth coordination shells and (ii) each line is broadened because of the spin–spin interaction with more distant Dy^{3+} ions. The results of calculations at $\Delta B = 70$ mT (the width of each line is determined from the extrema of the derivative) with due regard for the data obtained in [15] ($g_z = 14.6$, $K_{zz(nn)} = 1.49$ cm^{-1}, $K_{zz(5n)} = -0.4074$ cm^{-1}, $K_{zz(9n)} = -0.2373$ cm^{-1}) are shown by curve *5* in Fig. 3. It can be seen from this figure that the results of calculations disagree with the experimental spectrum.

In [15], it was noted that, in the spectra of the 5*n* and 9*n* pairs, the hyperfine structure is identical to that of a single ion. On this basis, the conclusion was drawn that the nonaxial components of the spin–spin interaction tensor **K** for these pairs make an insignificant contribution. On the other hand, the spectrum of the *nn* pair is represented by a broad line without hyperfine structure. This circumstance, which was not explained in [15], may indicate that the spin–spin interaction tensor of the *nn* pair includes components that provide mixing of different states and are responsible for the disappearance of the hyperfine structure. The tensors $\mathbf{K}^{as}$ and $\mathbf{K}^{s}$ contain such components.

An impurity ion substituting for an ion in the matrix brings about distortion of the unit cell toward a unit cell characteristic of the impurity ion due to the difference in the ionic radii. A pair of closely spaced impurity ions

increases this distortion. For example, in rare-earth ethyl sulfates $Re(C_2H_5SO_4)_3 \cdot 9H_2O$, the unit cell parameter c is equal to the distance r_{nn} between the nearest neighbor rare-earth ions *Re*. According to [20], in $A_{(1-x)}B_x(C_2H_5H_2SO_4)_3 \cdot 9H_2O$ single crystals (A = La^{3+}, Y^{3+}, Tm^{3+}; B = Nd^{3+}, Ce^{3+}; isomorphous substitution), the parameter c of unit cells depends on the number k of neighboring ions B as follows:

$$c_k = c_B + (c_A - c_B)\exp(-0.592k), \qquad (16)$$

where c_k is the parameter c of the unit cells in which the B ion substitutes for the A ion and c_A and c_B are the parameters c for the pure $[A(C_2H_5H_2SO_4)_3 \cdot 9H_2O]$ and totally substituted $[B(C_2H_5H_2SO_4)_3 \cdot 9H_2O]$ matrices, respectively. To put it differently, as the length of a chain formed by impurity ions increases, the distance r_{nn} changes toward the distance characteristic of their own matrix.

The distance between rare-earth ions in $KDy(WO_4)_2$ is less than that in $KY(WO_4)_2$ (Table 2). Therefore, without going into detail on the quantitative analysis of the applicability of relationship (16) to rare-earth tungstates, we argue that the distance r_{nn} in Dy^{3+} ion pairs in $KY_{0.99}Dy_{0.01}(WO_4)_2$ can exceed the distance r_{nn} in $KDy(WO_4)_2$. Consequently, the spin–spin interaction of Dy^{3+} ions in $KDy(WO_4)_2$ can be stronger than that in the magnetically diluted matrix.

These circumstances were taken into account when choosing the tensor components K_{zz}, K_{yz}^{as}, K_{yz}^{s}, and K_{yy}. A comparison of calculated curves *2* and *4* with experimental spectra *1* and *3* (solid lines) in Fig. 3 demonstrates that the inclusion of the off-diagonal components of the spin–spin interaction tensor **K** leads to substantially better agreement with the experimental data. It should be noted that the component K_{zz} primarily affects the location of the B_1 and B_5 lines and the component K_{yz}^{s} determines the separation between them, whereas the components K_{yz}^{as} and K_{yy} compete with each other for the effect on the location and intensity of the B_3 line. In order to ensure uniqueness, the component K_{yy} was calculated provided that relationships (4) [i.e., $K_{zz}^{j}/K_{yy}^{j} = (g_z/g_x)^2$] and (7) are satisfied. Compared to the Lorentzian line shape, the Gaussian line shape is characterized by a flatter peak and steeper wings. The calculated spectra are described by Gaussian lines. This can be associated not with the random distribution of particles but primarily with the fact that the number of lines in the experimental spectrum is greater than the number of the lines used in calculations.

This surprisingly good agreement between the experimental and calculated data called for additional verification. Measurements carried out at a substantially higher frequency made it possible to draw the following inferences. (1) As follows from a theoretical analysis, the off-diagonal components of the spin–spin interaction tensor at a high photon energy do not significantly affect the absorption spectrum (curves *2* and *3* in Fig. 4 almost coincide with each other). (2) The positive sign of the component $K_{zz(nn)}$ is correctly predicted in [15], as can be judged from the "freezing" in the spectral range at low inductions. (3) The component $K_{zz(nn)}$ determined from the data at the low frequency corresponds to the spectrum observed at the high photon energy.

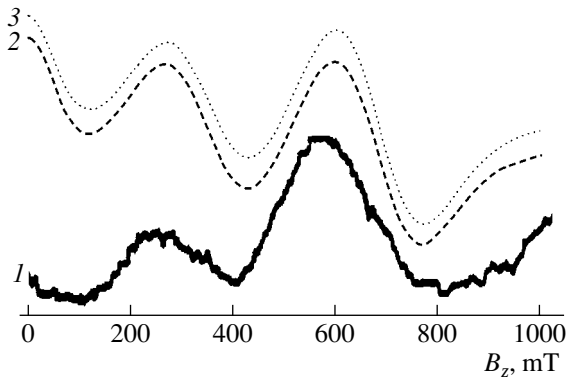

Fig. 4. (*1*) Experimental and (*2*, *3*) calculated EPR spectra of $KDy(WO_4)_2$ at a frequency of 72 240 MHz, **B** ∥ **z**, and T = 4.2 K. The spectra are calculated for (*2*) the axial spin–spin interaction ($K_{zz(nn)}$ = 2.24 cm^{-1}, all other tensor components K_{nn} are equal to zero) and (*3*) from the data presented in Table 4. All calculations are performed at g_z = 14.6 and ΔB = 120 mT for a Lorentzian line shape and with due regard for the freezing effect and the spin–spin interaction in the fifth and ninth coordination shells ($K_{zz(5n)}$ = –0.4074 cm^{-1}, $K_{zz(9n)}$ = –0.2373 cm^{-1}).

Note that the freezing effect at low frequencies ($h\nu \ll kT$) is substantially less pronounced than that at high frequencies ($h\nu \geq kT$). Therefore, the deviation of the relative intensities of the spectral lines from ratio (12) is determined by the low-symmetry components of the spin–spin interaction tensor **K** at the low frequency and the temperature at the high frequency. Thus, the results of the investigations performed with the magnetically concentrated materials at two considerably differing frequencies are not only consistent but also complement each other and demonstrate that the use of even a small chain fragment makes it possible to simulate the EPR spectrum of the real crystal with a high degree of accuracy.

The question arises as to why the off-diagonal components of the spin–spin interaction tensor **K** were not found in the spectrum of pairs in our previous work [15], in which we also used low-energy photons (9244.5 MHz).

Hamiltonian (1) for an ion pair at **B** ∥ **z** can be easily diagonalized at nonzero components K_{zz} and K_{yy} of the spin–spin interaction tensor. At L_1 = 1 and L_2 = 2, we

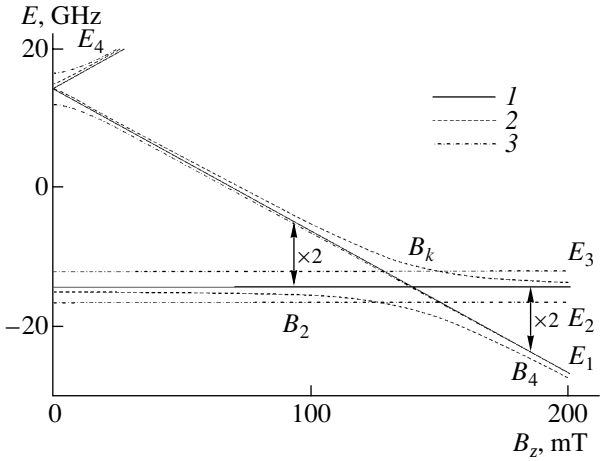

Fig. 5. Calculated energy spectra of a pair of interacting Dy^{3+} ions with due regard for (*1*) the axial spin–spin interaction (K_{zz} = 1.9 cm^{-1}, all other components of the tensor **K** are equal to zero) and (*2*, *3*) the low-symmetry components of the spin–spin interaction tensor **K**: (*2*) antisymmetric (K_{zz} = 1.9 cm^{-1}, K_{yz}^{as} = 0.3 cm^{-1}) and symmetric (K_{zz} = 1.9 cm^{-1}, K_{yz}^{s} = 0.3 cm^{-1}) and (*3*) K_{yy} (K_{zz} = 1.9 cm^{-1}, K_{yy} = 0.3 cm^{-1}) components. In all calculations, components absent from the spin–spin interaction tensor **K** are equal to zero and g_z = 14.6. Arrows indicate allowed transitions for the axial spin–spin interaction at a frequency of 9244.5 MHz. The transition multiplicity is given near arrows. Curves *3* are numbered according to relationships (17).

obtain the following energy spectrum and wave functions:

$$
\begin{aligned}
E_1 &= K_{zz}/4 - Q \\
|\phi_1\rangle &= A_+[(2G + Q)|-1/2, -1/2\rangle \\
&\quad - (K_{yy}/4) + 1/2, +1/2\,], \\
E_2 &= (-K_{zz} - K_{yy})/4 \\
|\phi_2\rangle &= \frac{1}{\sqrt{2}}[|+1/2, -1/2\rangle - |-1/2, +1/2\rangle], \\
E_3 &= (-K_{zz} + K_{yy})/4 \\
|\phi_3\rangle &= \frac{1}{\sqrt{2}}[|+1/2, -1/2\rangle + |-1/2, +1/2\rangle], \\
E_4 &= K_{zz}/4 + Q \\
|\phi_4\rangle &= A_-[(K_{yy}/4)|+1/2, +1/2\rangle \\
&\quad - (2G - Q)|-1/2, -1/2\rangle\,],
\end{aligned}
\tag{17}
$$

where

$$A_\pm = \frac{1}{\sqrt{2}}[(K_{yy}/4)^2 + 4G^2 \pm 2GQ]^{1/2},$$

$$Q = [4G^2 + (K_{yy}/4)^2]^{1/2}, \quad G = g_z\mu_B B_z/2.$$

The allowed transitions between the levels are as follows: $E_1 \rightleftharpoons E_3$ and $E_3 \rightleftharpoons E_4$. At a low photon energy, the lines in the absorption spectrum should be observed at the magnetic field inductions

$$
\begin{aligned}
B_2 &= (g_z\mu_B)^{-1}[(K_{zz}/2 - h\nu)(K_{zz}/2 - h\nu - K_{yy}/2)]^{1/2}, \\
B_4 &= (g_z\mu_B)^{-1} \\
&\quad \times [(K_{zz}/2 + h\nu)(K_{zz}/2 + h\nu - K_{yy}/2)]^{1/2}
\end{aligned}
\tag{18}
$$

with the transition probability (10) $W_{13} \sim [A_+(2G + Q - K_{yy}/4)]^2$. Consequently, an increase in the component K_{yy} is accompanied by a shift in the spectrum of pairs toward lower inductions of the external magnetic field, an increase in the separation between the lines, and a decrease in the spectral intensity.

Figure 5 shows the energy spectrum of the Dy^{3+} ion pair, which was calculated using a computer. It can be seen from this figure that the components K_{yz}^{as} and K_{yz}^{s} manifest themselves in the same way (dashed curves *2*) and lead to the appearance of an energy gap in the vicinity of the point B_k (a similar situation can be observed in the vicinity of the point B_{k2} in Fig. 2). Therefore, the effect of each component under consideration is reduced to a decrease in the separation between the B_2 and B_4 lines as compared to the separation calculated for the axial spin–spin interaction [see relationships (14)]:

$$\Delta_{42} = 2h\nu/g_z\mu_B = 90.4 \text{ mT}. \tag{19}$$

As a consequence, the contributions of the symmetric and antisymmetric spin–spin interactions to the EPR spectrum of the pair cannot be separated even at a low phonon energy.

Only one line, namely, B_4 at 154.5 mT, is observed in the absorption spectrum of the *nn* pairs of Dy^{3+} ions in $KY_{0.99}Dy_{0.01}(WO_4)_2$. The B_2 line overlaps with the spectrum of single ions and can be located in the range from 64.1 [see relationship (19)] to 69.2 mT (the upper boundary of the spectrum of single ions). The spectrum with B_2 = 64.1 mT and B_4 = 154.5 mT is uniquely described as follows: $K_{zz(nn)}$ = 1.49 cm^{-1} and $K_{yz(nn)}^{as}$ = $K_{yz(nn)}^{s}$ = 0. At the same time, the computer simulation of the EPR spectrum of pairs demonstrate that the spectrum with B_2 = 69.2 mT and B_4 = 154.5 mT can be described using an infinite number of variants, namely, from $K_{zz(nn)}$ = 1.525 cm^{-1}, $K_{yz(nn)}^{as}$ = 0.209 cm^{-1}, and $K_{yz(nn)}^{s}$ = 0 to $K_{zz(nn)}$ = 1.522 cm^{-1}, $K_{yz(nn)}^{as}$ = 0, and $K_{yz(nn)}^{s}$ = 0.144 cm^{-1}.

The results obtained are summarized in Table 4. By using these data and relationship (4), we found that

Table 4. Experimental and calculated contributions of different interaction mechanisms to the spin–spin interaction tensor for Dy^{3+} ions in the $KY_{0.99}Dy_{0.01}(WO_4)_2$ and $KDy(WO_4)_2$ matrices

		K_{zz}		K_{yz}^{as}		K_{yz}^{s}		K_{yy}	
Experiment	$KY_{0.99}Dy_{0.01}(WO_4)_2$	1.49–1.525		0–0.209		0–0.144		–	
	$KDy(WO_4)_2$	12 K	4.2 K	12 K	4.2 K	12 K	4.2 K	12 K	4.2 K
		1.9	2.24	0.304	0.311	0.3	0.3	0.0282	0.0320
Theory	Magnetic dipole–dipole interaction	0.7011	0.7011	0	0	0.0197	0.0197	0.0149	0.0149
	Isotropic symmetric (direct and indirect) exchange interaction	1.1989	1.5389	0	0	0	0	0.0133	0.0171
	Antisymmetric exchange interaction	0	0	0.304	0.311	0.2803	0.2803	0	0

Note: Only nonzero components (cm^{-1}) of the spin–spin interaction tensor **K** are given.

j_{nn} = (0.112–0.114) cm^{-1} for the nearest neighbor Dy^{3+} ion pair in $KY_{0.99}Dy_{0.01}(WO_4)_2$ and j_{nn} = 0.143 cm^{-1} at $T > T_{spt}$ and j_{nn} = 0.168 cm^{-1} at $T < T_{spt}$ for a similar pair in $KDy(WO_4)_2$. Therefore, we can make the following inferences. (1) The spin–spin interaction of the nearest neighbor Dy^{3+} ion pair in the magnetically diluted material is weaker than that in the magnetically concentrated material. For the measurements carried out at the same temperature, this unambiguously indicates a decrease in the interionic distance with an increase in the length of the chain formed by impurity ions; i.e., it qualitatively confirms the validity of expression (16). (2) The phase transition at 4.2 K < T_{spt} < 12 K is attended by an enhancement of the spin–spin interaction. It is unlikely that this circumstance can be associated with the thermal contraction of the crystal, because the temperature range is too narrow at a sufficiently low temperature. However, a unique conclusion cannot be drawn because low-temperature crystallographic data are not available.

6. CONCLUSIONS

Thus, the results obtained in this work can be summarized as follows.

(1) The use of a triad of interacting ions makes it possible to simulate the EPR spectra of magnetically concentrated materials with a high degree of accuracy.

(2) In order to reveal the low-symmetry components of the spin–spin interaction tensor, it is necessary to use microwave photons with a sufficiently low energy.

(3) The informative capability of the EPR spectrum of a triad formed by interacting ions is substantially higher than that of the pair of interacting ions.

(4) The Dzyaloshinski interaction between Dy^{3+} ions in $KY_{(1-x)}Dy_x(WO_4)_2$ ($0 < x \le 1$) was found experimentally.

(5) Upon substitution, an impurity ion distorts the unit cell toward the unit cell characteristic of this ion.

(6) The phase transition in $KDy(WO_4)_2$ is accompanied by an enhancement of the spin–spin interaction.

(7) The concentration dependence of the Dy^{3+} EPR spectrum of $KY_{(1-x)}Dy_x(WO_4)_2$ is associated with the specific spin–spin interaction in this material, and the spectrum of $KDy(WO_4)_2$ is adequately described by the spin Hamiltonian parameters characteristic of a single ion.

ACKNOWLEDGMENTS

We would like to thank A.G. Anders for his assistance in the experiments performed in the 4-mm range, G.Ya. Samsonova and L.F. Chernysh for growing high-quality single crystals, and V.I. Kamenev for his assistance in the orientation of single crystals.

This work was supported in part by the Committee of Scientific Research of Poland (KBN), project no. 2 PO3B 141 18.

REFERENCES

1. A. A. Kaminskiĭ, G. P. Verdun, V. Koeshner, *et al.*, Kvantovaya Élektron. (Moscow) **19**, 941 (1992).
2. M. C. Pujol, M. Rico, C. Zaldo, *et al.*, Appl. Phys. B **68**, 187 (1999).
3. A. A. Kaminskii, L. Li, A. V. Butahsin, *et al.*, Jpn. J. Appl. Phys. **36**, L107 (1997).
4. C. Zaldo, M. Rico, C. Cascales, *et al.*, J. Phys.: Condens. Matter **12**, 8531 (2000).
5. I. V. Skorobogatova and A. I. Zvyagin, Fiz. Nizk. Temp. **4** (6), 800 (1978) [Sov. J. Low Temp. Phys. **4**, 381 (1978)].
6. Yu. A. Popkov, V. I. Fomin, and L. N. Pelikh, Fiz. Nizk. Temp. **8** (11), 1210 (1982) [Sov. J. Low Temp. Phys. **8**, 614 (1982)].

7. M. T. Borowiec, V. Dyakonov, A. Nabialek, *et al.*, Physica B (Amsterdam) **240**, 21 (1997).
8. M. T. Borowiec, V. Dyakonov, V. Kamenev, *et al.*, Acta Phys. Pol. A **94**, 71 (1998).
9. V. Dyakonov, V. Markovich, V. Kovarskii, *et al.*, Phys. Solid State **40**, 691 (1998).
10. M. T. Borowiec, V. P. Dyakonov, E. Zubov, *et al.*, J. Phys. I **7**, 1639 (1997).
11. M. T. Borowiec, V. P. Dyakonov, A. Jedrzejczak, *et al.*, Phys. Lett. A **243**, 85 (1998).
12. R. J. Anderson and J. M. Baker, J. Phys. C: Solid State Phys. **4** (12), 1618 (1974).
13. I. M. Krygin and A. D. Prokhorov, Zh. Éksp. Teor. Fiz. **92** (2), 549 (1987) [Sov. Phys. JETP **65**, 311 (1987)].
14. M. T. Borowiec, V. P. Dyakonov, A. Prokhorov, and H. Szymczak, Phys. Rev. B **62**, 5834 (2000).
15. I. M. Krygin, A. D. Prokhorov, V. P. D'yakonov, *et al.*, Fiz. Tverd. Tela (St. Petersburg) **44** (8), 1513 (2002) [Phys. Solid State **44**, 1587 (2002)].
16. S. V. Borisov and R. F. Klevtsova, Kristallografiya **13** (3), 517 (1968) [Sov. Phys. Crystallogr. **13**, 420 (1968)].
17. P. V. Klevtsov and L. P. Kozeeva, Dokl. Akad. Nauk SSSR **185** (3), 571 (1969) [Sov. Phys. Dokl. **14**, 185 (1969)].
18. Yu. K. Vishchakas, I. V. Molchanov, A. V. Mikhaĭlov, *et al.*, Litov. Fiz. Sb. **28** (2), 224 (1988).
19. A. Abragam and B. Bleaney, *Electron Paramagnetic Resonance of Transition Ions* (Clarendon, Oxford, 1970; Mir, Moscow, 1972), Vol. 1.
20. I. M. Krygin and A. D. Prokhorov, Fiz. Tekh. Vys. Davlenii **25**, 70 (1987).

Translated by O. Borovik-Romanova

Physics of the Solid State, Vol. 45, No. 11, 2003, pp. 2093–2098. Translated from Fizika Tverdogo Tela, Vol. 45, No. 11, 2003, pp. 1991–1996.

SEMICONDUCTORS AND DIELECTRICS

Heat Transport over Nonmagnetic Lithium Chains in $LiCuVO_4$, a New One-Dimensional Superionic Conductor

L. S. Parfen'eva*, A. I. Shelykh*, I. A. Smirnov*, A. V. Prokof'ev, W. Assmus**, H. Misiorek***, J. Mucha***, A. Jezowski***, and I. G. Vasil'eva******

**Ioffe Physicotechnical Institute, Russian Academy of Sciences, Politekhnicheskaya ul. 26, St. Petersburg, 194021 Russia*
e-mail: igor.smirnov@pop.ioffe.rssi.ru

***Institute of Physics, Goethe University, Frankfurt am Main, 60054 Germany*

****Institute of Low-Temperature and Structural Research, Polish Academy of Sciences, Wroclaw 50-950, Poland*

*****Institute of Inorganic Chemistry, Siberian Division, Russian Academy of Sciences, pr. Akademika Lavrent'eva 3, Novosibirsk, 630090 Russia*

Received April 15, 2003

Abstract—The thermal conductivity of three single-crystal samples of the quasi-one-dimensional spin system of $LiCuVO_4$ with different concentrations of defects (primarily, vacancies on the lithium sublattice) was measured along the crystallographic *a* axis (along the nonmagnetic lithium chains) in the temperature interval 5–300 K. An increase in thermal conductivity from that of the crystal lattice was revealed for $T > 150$–200 K. This increase can be accounted for only by assuming $LiCuVO_4$ to be a superionic conductor. This assumption was confirmed by measuring its electrical conductivity in the temperature interval 300–500 K. Li^+ ions move over vacancies on the lithium sublattice (conducting channels) and act as charge carriers in $LiCuVO_4$. It is shown that $LiCuVO_4$ is a fairly good superionic conductor with application potential. © *2003 MAIK "Nauka/Interperiodica".*

1. INTRODUCTION

Studies of the thermal conductivity κ of low-dimensional and, particularly, quasi-one-dimensional (spin chains and spin ladders) and quasi-two-dimensional systems, in which heat transport by spinons has been detected, has spurred considerable recent experimental and theoretical interest at leading laboratories in Switzerland, Germany, Japan, France, and the USA (see [1–7] and references therein).

Papers [1–7] reported primarily on the measurement of κ of strontium cuprate single crystals of various composition. The present communication deals with the thermal conductivity of the quasi-one-dimensional single-crystal antiferromagnet $LiCuVO_4$.

$LiCuVO_4$ crystallizes in an orthorhombically distorted, inverted spinel structure. The V^{5+} nonmagnetic ions occupy tetrahedral voids, and the nonmagnetic Li^+ and magnetic Cu^{2+} ($S = 1/2$) ions are located in an ordered manner in octahedral voids of the anion sublattice [8] (Fig. 1a). The CuO_6 and LiO_6 octahedra form magnetic and nonmagnetic chains, which are aligned in $LiCuVO_4$ with the *b* and *a* crystallographic directions, respectively. Figure 1b presents the "rod" model of $LiCuVO_4$ [8, 9], which illustrates the arrangement of the magnetic and nonmagnetic chains.

There is copious information on the main physical parameters of $LiCuVO_4$, namely, its crystal structure [9, 10], magnetic susceptibility [11], heat capacity [12], and optical IR [13], ESR [11, 14], and NMR [15, 16] spectra, and techniques have been developed for growing fairly large single crystals [17] (see also references in the above-mentioned publications). The thermal conductivity of $LiCuVO_4$ has not been studied, although an analysis of its lattice, electronic, and magnon components would yield new valuable information on the physical nature of this compound.

The present communication reports on a study of the thermal conductivity (κ^a) and electrical conductivity (σ^a) of $LiCuVO_4$ for the case where the heat flow and electrical current propagate along the nonmagnetic lithium chains (along the crystallographic *a* axis). Investigation of the thermal conductivity of $LiCuVO_4$ with heat flow propagating along the magnetic copper chains will be dealt with in a separate paper.

2. SAMPLE PREPARATION AND EXPERIMENTAL TECHNIQUE

The $LiCuVO_4$ single crystals intended for use in measuring the thermal and electrical conductivity were grown using the technique developed in [17]. Because $LiCuVO_4$ is a thermally unstable compound, it cannot be melted. Therefore, $LiCuVO_4$ single crystals were grown from solutions below the decomposition temperature. The solvents used were $LiVO_3$ with a melting point of 620°C and a eutectic 53% $LiVO_3$ + 47% LiCl solution with a melting point of 520°C. From these

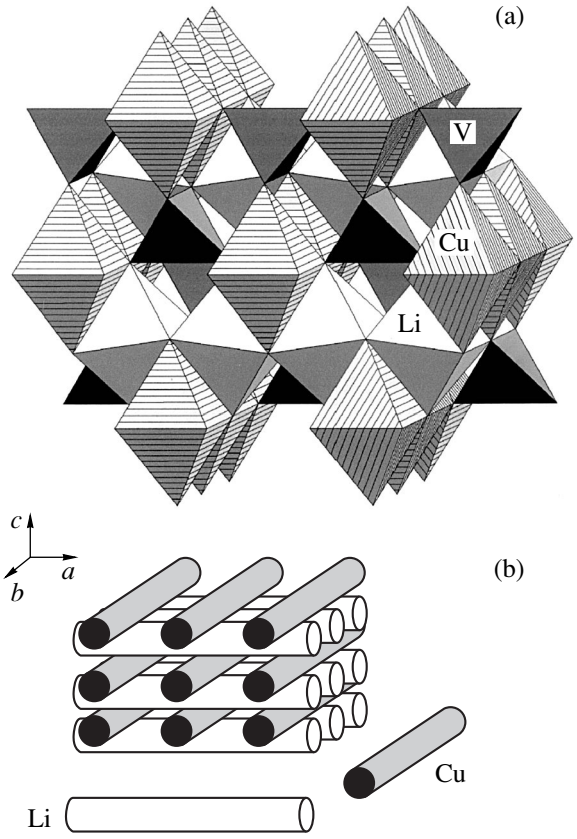

Fig. 1. (a) Structure of $LiCuVO_4$ [8]. One-dimensional (1D) chains of edge-sharing Li octahedra propagate along the *a* axis, and the 1D chains of Cu octahedra, likewise edge sharing, align with the *b* direction. The V octahedral, isolated from one another, connect the Cu and Li chains to form a 3D structure. (b) Rod model of $LiCuVO_4$ [8, 9]. Layers of Li and Cu rods alternate, and their directions are mutually perpendicular.

solutions, $LiCuVO_4$ crystallizes at 550 and 460°C, respectively [17].

$LiCuVO_4$ crystals were grown under slow cooling of the melts, in the interval 650–580°C from the solution in $LiVO_3$, and at 580–520°C from the solution in $LiVO_3$–LiCl. The $LiCuVO_4$ single crystals thus obtained will be called high- and low-temperature crystals, respectively, in what follows.

It was found that these two types of single crystals differ in both chemical composition and physical properties. This may be assigned to a different concentration of thermally induced defects forming in the course of their growth.

Our chemical analysis of a large number of the high- and low-temperature $LiCuVO_4$ single crystals prepared showed, despite a certain scatter in the results, that crystals of the first type have, on average, the composition $Li_{0.92}Cu_{1.03}VO_{4-x}$ and those of the second type have, on average, the composition $Li_{0.97}Cu_{1.00}VO_{4-x}$. Therefore, the high-temperature crystals deviate from stoichiometry more strongly than do the low-temperature crystals. Also, the former crystals have a deviation in the both lithium (a deficiency of about 8%) and copper content (an excess of about 3%). As follows from the above chemical formulas, the defects in both crystals are primarily vacancies on the lithium sublattice, and the high-temperature crystals also exhibit filling of the lithium sublattice by excess copper atoms.

It should be pointed out that we did not succeed in obtaining stoichiometric $LiCuVO_4$ either in the form of single crystals or in a powdered form even when the original oxide mixture had an exactly stoichiometric composition. Thus, lithium deficiency appears to be an intrinsic property of this compound.

To measure the thermal and electrical conductivity, we prepared three single-crystal samples of $LiCuVO_4$. Samples 1 and 2 were prepared from high-temperature single crystals, and sample 3, from low-temperature single crystals. According to x-ray diffraction analysis, in the interval $20 < T < 400$ K, none of the three samples underwent structural phase transitions similar to that observed in the strongly nonstoichiometric $Li_{1-x}CuVO_4$ [10].

Single-crystal samples 1, 2, and 3 had dimensions of $1 \times 2 \times 12$ mm, $0.8 \times 2 \times 7$ mm, and $0.7 \times 0.8 \times 6$ mm, respectively. The heat flow and electrical current were directed along the greatest dimension of a sample (the *a* axis of the crystal).

The thermal conductivity was measured in the 5- to 300-K temperature interval on a setup similar to that employed in [18]. The electrical conductivity was studied in the interval 300–500 K using the dc two-probe method.

3. EXPERIMENTAL RESULTS AND DISCUSSION

The measured $\kappa^a(T)$ dependences for samples 1, 2, and 3 are shown in Fig. 2. Note several features in the behavior of $\kappa^a(T)$ of these samples. We readily see that, in the $\kappa^a(T)$ dependence, there are two characteristic temperature ranges, 5–150(200) and 150(200)–300 K.

Consider first the behavior of thermal conductivity in the range 5–150(200) K.

(1) The thermal conductivity measured in this region is the crystal lattice conductivity κ^a_{ph}, because, as will be shown below, σ^a at 300 K in our samples is $\sim 10^{-6}$–10^{-7} Ω^{-1} cm^{-1} (to become still smaller at lower temperatures) and, thus, the electronic component of thermal conductivity is negligible. No other components of thermal conductivity are known to exist in this temperature region.

(2) The thermal conductivity κ^a_{ph} of all three samples at low temperatures [$T \le 10$ K, below the maximum in $\kappa^a_{ph}(T)$] increases with temperature (starting

from 5 K) following the law $\kappa_{ph}^{a} \sim T^2$, which indicates phonon scattering from dislocations [19].

(3) For temperatures above the maximum in thermal conductivity, the temperature dependence of $\kappa_{ph}^{a}(T)$ is different in the three samples studied. It is known that in this temperature region the $\kappa_{ph}(T)$ dependence can vary from κ_{ph} = const for heavily defected (amorphous) materials to $\kappa_{ph} \sim T^{-1}$ for defect-free crystalline materials [19]. For samples 1 and 2 (high-temperature single crystals), we obtained $\kappa_{ph}^{a} \sim T^{-n}$ with n equal to 0.25 and 0.37, respectively, which supports our conclusion from the preceding paragraph that in $LiCuVO_4$ single crystals prepared using the high-temperature technique there are a large number of defects which are, as already mentioned, primarily vacancies on the Li sublattice. As is evident from the thermal conductivity data, sample 1 contains a larger number of defects than sample 2. For sample 3 (a single crystal prepared using the low-temperature technology), $\kappa_{ph}^{a} \sim T^{-0.9}$, which is close to $\kappa_{ph}^{a} \sim T^{-1}$ for a defect-free crystal and implies a substantially lower defect concentration in this single crystal.

(4) The behavior of $\kappa_{ph}^{a}(T)$ of sample 1 reveals, at about 5 K, a noticeable deviation from the $\kappa_{ph}^{a} \sim T^2$ scaling obtained for the temperature range $T > 6$ K (see inset to Fig. 2). Close to this temperature, $LiCuVO_4$ also revealed a strong decrease in the magnetic susceptibility [11]. The anomaly observed in the behavior of κ_{ph}^{a} for $T < 5$ K is possibly due to a phase transition occurring at $T \sim 2.3$–2.4 K [11, 12], which transfers $LiCuVO_4$ from the one-dimensional antiferromagnet, by [12], according to a two-dimensional, or, according to [11], three-dimensional, antiferromagnet.

Interesting results on the behavior of $\kappa^a(T)$ were derived from an analysis of data on the second temperature range, 150(200)—300 K. It was found that, at $T \sim$ 150–200 K, all the samples studied here exhibit a deviation from the corresponding dependences $\kappa_{ph}^{a} \sim T^{-n}$ toward increasing thermal conductivity. The effect was the strongest for the more defected sample, sample 1 (Fig. 2). Now, what is the origin of the excess thermal conductivity$\Delta\kappa$ in these samples?

As already pointed out, at $\sigma_{300\,K}^{a} \sim 10^{-6}$–$10^{-7}\ \Omega^{-1}\,cm^{-1}$, one cannot expect a contribution from the electronic component of thermal conductivity. One could possibly assign the excess heat transport to the photon component of thermal conductivity, which scales as $\sim T^3/\alpha$ (where α is the optical absorption coefficient) [19]. As follows, however, from our preliminary data, at the wavelength $\lambda = 1.1$ μm, α is ~500 cm^{-1} (and it is very unlikely to become less for $\lambda > 1.1$ μm). For this value of α, the photon component of thermal conductivity should be very small. One could expect the appearance of an excess thermal conductivity due to the magnon component. In our case, however, this component is absent, because the measurements of $\kappa(T)$ are performed along the nonmagnetic lithium chains. There is, however, one more possibility for accounting for the

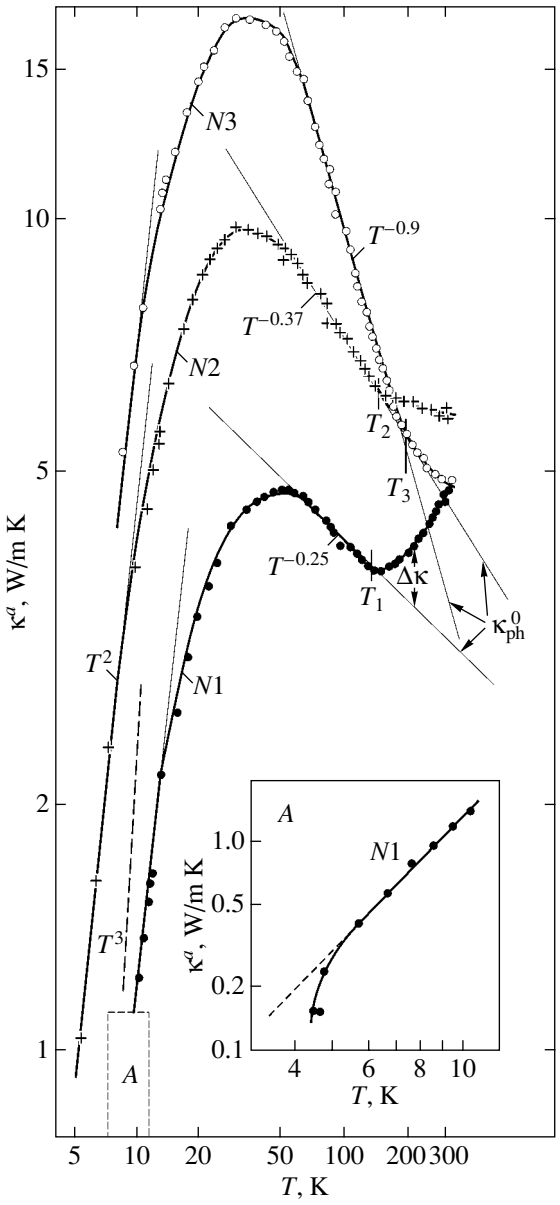

Fig. 2. Temperature dependence of κ^a along the a crystallographic direction plotted for the high-temperature (samples 1, 2) and low-temperature (sample 3) $LiCuVO_4$ single crystals. T_1, T_2, and T_3 are the temperatures at which the thermal conductivity of the samples starts to deviate from the relation $\kappa_{ph}^{a} \sim T^{-n}$. The quantity κ_{ph}^{0} is defined in the text. Dashed line corresponds to phonon scattering from crystal boundaries, $\kappa_{ph} \sim T^3$. Inset shows $\kappa^a(T)$ for sample 1 (region A of the main figure).

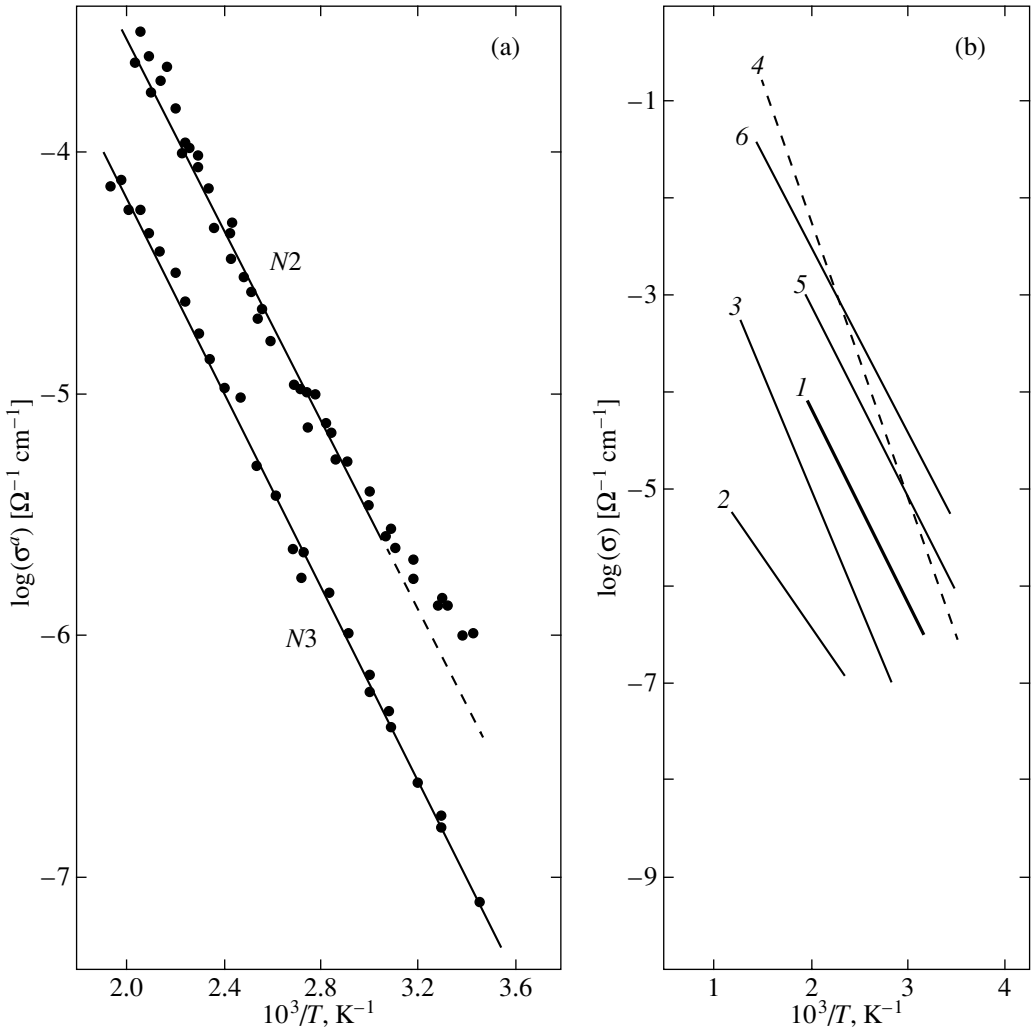

Fig. 3. (a) Temperature dependence of electrical conductivity σ^a of $LiCuVO_4$ samples 2 and 3. (b) Comparison of the magnitude and temperature dependence of σ^a of $LiCuVO_4$ sample 3 (line *1*) with literature data available for σof several lithium-based superionics [25] (lines *2*–*6*). (*2*) $Li_2TiIn(PO_4)_3$, (*3*) $Li_2ZrIn(PO_4)_3$, (*4*) Li_2FeCl_4, (*5*) $(La_{0.6}Li_{01})(Mg_{0.5}W_{0.5})O_3$, and (*6*) LiZrP.

excess thermal conductivity in the $LiCuVO_4$ samples studied by us.

There have been observations of excess thermal conductivity above the Debye temperature in the superionic conductors $Li_2B_4O_7$, LaF_3 [20], α-$LiIO_3$ [20, 21], α- and γ-AgSI [22], and α-AgI [23]; this is associated with an anomalous increase in the heat capacity of these materials in the superionic phase. Note that α-$LiIO_3$ and $Li_2B_4O_7$ are quasi-one-dimensional superionics with cation (Li^+) conduction. If the quasi-one-dimensional $LiCuVO_4$ is also a superionic conductor, this would account for the increase in the thermal conductivity it exhibits for $T > 150$–200 K.

We did not find any reports in the literature on measurements of the ionic conductivity in $LiCuVO_4$. A study [24] of the electrochemical properties of $LiCuVO_4$ pointed out, however, that this compound could have a fairly high ionic conductivity.

We measured σ^a in samples 2 and 3 in the temperature interval 300–500 K. The experimental results obtained are displayed in Fig. 3a. Figure 3b presents the data on $\sigma(T)$ for a number of lithium superionics taken from [25]. We readily see that $\sigma^a(T)$ for $LiCuVO_4$ (straight line *1*) lies in the middle of the band characterizing the family of lithium superionics.

The temperature dependence of the ionic electrical conductivity is described by the Arrhenius equation [25]

$$\sigma T = \sigma_0 \exp(-\Delta H/kT), \qquad (1)$$

where ΔH is the enthalpy of activation of the electrical conduction. The value of ΔH^a calculated for $LiCuVO_4$ samples 2 and 3 using Eq. (1) was found to be ~0.46 eV,

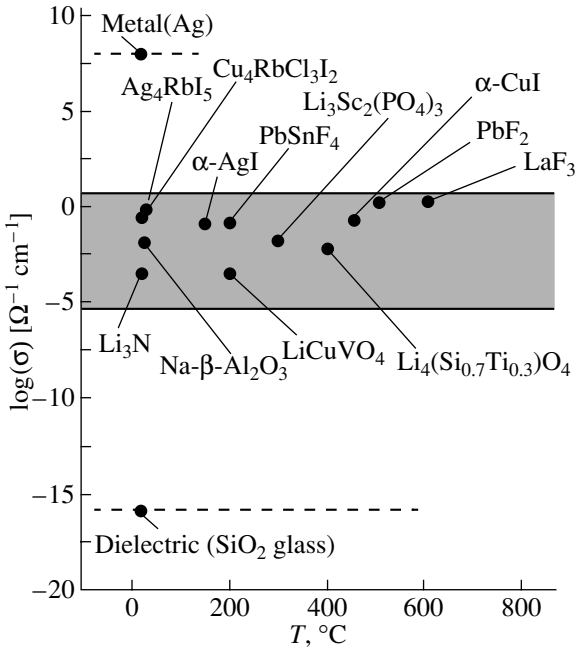

Fig. 4. Comparison of the values of $\log\sigma = f(10^3/T)$ for $LiCuVO_4$ (sample 3) and several superionics [25]. The materials corresponding to the shaded band belong, according to [25], to superionics with application potential.

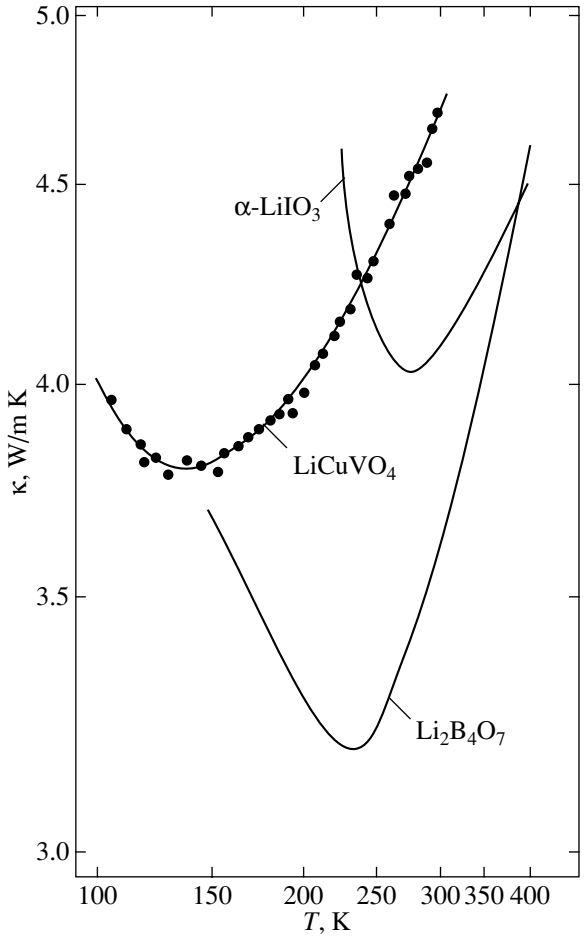

Fig. 5. Comparison of the behavior of $\kappa^a(T)$ of $LiCuVO_4$ (sample 1) and thermal conductivity of the quasi-one-dimensional superionics $Li_2B_4O_7$ and α-$LiIO_3$ [20].

which is in good agreement with the values of ΔH for the lithium-based superionics (see table).

Thus, our analysis of the data on $\sigma^a(T)$ for $LiCuVO_4$ suggests that this compound is a superionic conductor. The high concentration of vacancies on its lithium sublattice accounts for the high mobility of Li^+ ions at fairly low temperatures.

$LiCuVO_4$ can also be considered to be a superionic conductor with certain application potential (Fig. 4).[1]

Once $LiCuVO_4$ has been proven to be a good superionic conductor, the behavior of $\kappa^a(T)$ of $LiCuVO_4$ can be compared with that of the thermal conductivity of the related lithium-based, quasi-one-dimensional superionics α-$LiIO_3$ and $Li_2B_4O_7$ [20] (Fig. 5). All three superionics are seen to exhibit identical behavior. One may thus conclude that the excess thermal conductivity revealed to exist in $LiCuVO_4$ for temperatures $T >$ 150(200) K is connected with the nature of the superionic state of this material.

As already mentioned, the increased values of κ can be superionics is assigned to the heat capacity C_s of the superionic phase being higher than the classical Debye lattice heat capacity C_D^{ph} ($\Delta C = C_s - C_D^{ph}$, where ΔC relates to the excess heat capacity; see inset to Fig. 6). Unfortunately, we could not measure the heat capacity of $LiCuVO_4$ at high temperatures and the literature does not contain such information (the only data available relate to the heat capacity at low temperatures [12]). Therefore, our discussion of this problem can be based only on fairly scarce reports on the heat capacity of superionics [20].

Values of ΔH for some lithium-based superionics determined for $T > 300$ K [25]

Compound	ΔH, eV
$Li_2B_4O_7$	0.36
Li_3N	0.49 (‖ c axis)
γ-$Li_3Sc_2(PO_4)_3$	0.37
$Li_3Fe_2(PO_4)_3$	0.38 (‖ a axis)
	0.59 (‖ b axis)
$LiZr_2(PO_4)_3$	0.43
α-$LiIO_3$	0.30
$LiCuVO_4$	0.46

[1] We also measured $\sigma(T)$ of $LiCuVO_4$ with the current flowing along the b and c crystallographic directions. The data obtained will be published in a separate paper.

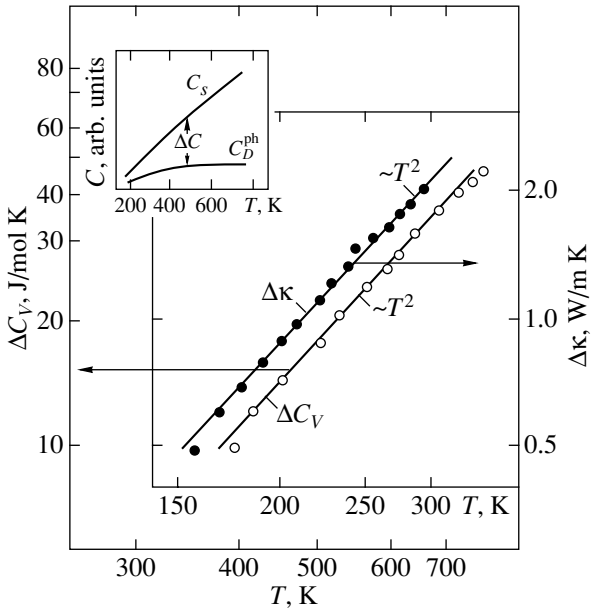

Fig. 6. Temperature behavior of Δκ for $LiCuVO_4$ sample 1 and of ΔC_V of the superionic LaF_3 [20]. Inset shows schematic of the temperature dependence of the heat capacity of superionic C_s and of the theoretical Debye lattice heat capacity C_D^{ph}.

The excess heat capacity of the superionic conductor LaF_3 scales with temperature as T^2 ($\Delta C_V \sim T^2$) [20], and $\Delta\kappa = (\kappa_{exp} - \kappa_{ph}^0)$ of the superionics $Li_2B_4O_7$ [20] and α-Ag_3SI [22] scales as $T^{2.5}$ and T^2, respectively.[2] We thus see that Δκ and ΔC_V obey the same (or similar) laws in the region of superionic conduction.

In the case of $LiCuVO_4$, we obtained that Δκ of sample 1 scales as T^2 for $T > 150$ K ($\Delta\kappa \sim T^2$, Fig. 6). This may be considered one more argument for the conclusion that the experimentally observed excess thermal conductivity in $LiCuVO_4$ is intimately connected with the nature of the superionic state of this material.

ACKNOWLEDGMENTS

This study was carried out within bilateral agreements between the Russian Academy of Sciences, Deutsche Forschungsgemeinschaft, and Polish Academy of Sciences and was supported by the Russian Foundation for Basic Research, project no. 02-02-17657.

[2] Here, κ_{exp} is the experimentally measured thermal conductivity and κ_{ph}^0 is the thermal conductivity extrapolated from the low-temperature region using the scaling $\kappa_{ph}^0 \sim T^{-n}$, where n is different for each of the samples studied (see separation of Δκ in Fig. 2).

REFERENCES

1. A. V. Sologubenko, K. Gianno, H. R. Ott, *et al.*, Physica B (Amsterdam) **284–288**, 1595 (2000).
2. A. V. Sologubenko, K. Gianno, H. R. Ott, *et al.*, Phys. Rev. Lett. **84** (12), 2714 (2000).
3. A. V. Sologubenko, E. Felder, K. Gianno, *et al.*, Phys. Rev. B **62** (10), R6108 (2000).
4. A. V. Sologubenko, K. Gianno, H. R. Ott, *et al.*, Phys. Rev. B **64**, 054412 (2001).
5. C. Hess, C. Baumann, U. Ammerahl, *et al.*, Phys. Rev. B **64**, 184305 (2001).
6. K. Kudo, S. Ishikawa, T. Noji, *et al.*, J. Phys. Soc. Jpn. **70** (2), 437 (2001).
7. C. Hess, U. Ammerahl, C. Baumann, *et al.*, Physica B (Amsterdam) **312–313**, 612 (2002).
8. M. A. Lafontaine, M. Leblanc, and G. Ferey, Acta Crystallogr. C **45**, 1205 (1989).
9. M. O. Keeffe and S. Andersson, Acta Crystallogr. A **33**, 914 (1977).
10. R. Kanno, Y. Kawamoto, Y. Takeda, *et al.*, J. Solid State Chem. **96**, 397 (1992).
11. A. N. Vasil'ev, L. A. Ponomarenko, H. Manaka, *et al.*, Phys. Rev. B **64**, 024 419 (2001).
12. M. Yamaguchi, T. Furuta, and M. Ishikawa, J. Phys. Soc. Jpn. **65** (9), 2998 (1996).
13. B. Gorshunov, P. Haas, M. Dressel, *et al.*, Eur. Phys. J. B **23**, 427 (2001).
14. H. A. Krug von Nidda, L. E. Svistov, M. V. Eremin, *et al.*, Phys. Rev. B **65**, 134445 (2002).
15. Ch. Kegler, N. Büttgen, H. A. Krug von Nidda, *et al.*, Eur. Phys. J. B **22**, 321 (2001).
16. T. Tanaka, H. Ishida, M. Matsumoto, and S. Wada, J. Phys. Soc. Jpn. **71** (1), 308 (2002).
17. A. V. Prokofiev, D. Wichert, and W. Assmus, J. Cryst. Growth **220**, 345 (2000).
18. A. Jezowski, J. Mucha, and G. Pompe, J. Phys. D: Appl. Phys. **7**, 1247 (1974).
19. V. S. Oskotskiĭ and I. A. Smirnov, *Defects in Crystals and Thermal Conductivity* (Nauka, Leningrad, 1972).
20. A. É. Aliev, V. F. Krivorotov, and P. K. Khabibullaev, Fiz. Tverd. Tela (St. Petersburg) **39** (9), 1548 (1997) [Phys. Solid State **39**, 1378 (1997)].
21. Ya. V. Burak, K. Ya. Borman, and I. S. Girnyk, Fiz. Tverd. Tela (Leningrad) **26** (12), 3692 (1984) [Sov. Phys. Solid State **26**, 2223 (1984)].
22. F. Saito, K. Toraki, and A. Kojima, J. Phys. Soc. Jpn. **62** (9), 3351 (1993).
23. M. C. Goetz and J. A. Cowen, Solid State Commun. **41** (4), 293 (1982).
24. R. Kanno and Y. Kawamoto, Solid State Ionics **40–41**, 576 (1990).
25. A. K. Ivanov-Shits and I. V. Murin, *Ionics of Solids* (S.-Peterb. Gos. Univ., St. Petersburg, 2000), Vol. 1.

Translated by G. Skrebtsov

Physics of the Solid State, Vol. 45, No. 11, 2003, pp. 2099–2103. Translated from Fizika Tverdogo Tela, Vol. 45, No. 11, 2003, pp. 1997–2001.

SEMICONDUCTORS AND DIELECTRICS

Effect of Magnetic Field on Tunneling Systems in Glasses

I. A. Chaban

Andreev Acoustical Institute, ul. Shvernika 4, Moscow, 117036 Russia

e-mail: chaban@akin.ru

Received April 29, 2003

Abstract—The effect of a magnetic field on two-level tunneling systems in dielectric glasses originates from the magnetic-field-induced rotation of nuclear spins and the ensuing rearrangement of ordered regions (clusters) in the glass structure. This process accounts for the observed variation of both the spontaneous-polarization echo amplitude and the dielectric constant in a magnetic field at low temperatures. The proposed theory is compared with experiment. © *2003 MAIK "Nauka/Interperiodica".*

1. INTRODUCTION

Until the early 1970s, it was expected that crystals and glasses would behave similarly at low temperatures, with the heat capacity and thermal conductivity, in accordance with the Debye model, scaling as T^3 as the absolute temperature tended to zero. It has been found, however, that below 1 K the heat capacity of glasses (we shall limit our consideration to dielectric glasses), unlike that of crystals, scales as T and the thermal conductivity scales as T^2. This is a typical behavior for the $BaO–Al_2O_3–SiO_2$ and a-$SiO_{2+x}C_yH_z$ glasses (whose experimentally measured characteristics will be treated below), as well as of the Ba_2O_3, $Na_2O–SiO_2–B_2O_3$, and many other compounds. Glassy glycerol was shown to behave in a similar manner [1]. Besides certain features revealed in the thermal properties, it was found that dielectric glasses respond unusually to the propagation of sonic, shear, and electromagnetic waves. In particular, they exhibit a saturation effect; namely, if a glass has been exposed to a high-intensity ultrasonic signal, then the next signal, sonic or electromagnetic, close in frequency but of a lower intensity propagates with a considerably lower damping than it would in the absence of the signal. It can be added that the glass will retain memory of the primary irradiation for 10^{-6} s at 1 K. An extensive review on the properties of glasses at low temperatures has been written by Hunklinger and Arnold [2]. For later reviews, the reader can be referred to [3, 4].

2. PROPOSED MODELS

Several models have been proposed to account for these unusual properties of glasses. The model put forward by Anderson, Halperin, Varma, and Phillips (AHVP) has proved the most successful [5, 6]. This model assumes that in a glass there are atoms or groups of atoms which may reside in two potential wells separated by a potential barrier from each other. The potential-well depths and barrier heights are assumed to be variable within broad ranges and to be distributed in such a way that an ensemble of these two-level systems (TLSs) is characterized by a constant probability density of energy level splitting E. The two levels are connected by tunneling transitions.

This model is capable of accounting for many properties of glasses at low temperatures. However, in certain cases, it was found to disagree with experiment. The disagreements relate to the dependence of the heat capacity on the duration of measurement, to the difference between the E distributions derived from thermal studies and sound absorption measurements, to the temperature behavior of the velocity and damping of sound, to the temperature dependences of the real and imaginary parts of the dielectric constant, etc. These discrepancies have recently been attracting particular attention. It is presently assumed that glasses contain tunneling TLSs, but their nature remains unclear.

It is the nature of these systems that was the subject of our earlier study [7]. In that study, tunneling TLSs were considered as ordered regions (clusters) in a glass structure that have a nonequidistant set of energy levels; consideration can be limited to the two lowest ones in certain cases. This approach eliminated a number of difficulties inherent in the AHVP model and provided a correct estimate of the magnitude of E.

3. EFFECT OF A MAGNETIC FIELD ON TUNNELING SYSTEMS

This problem has again attracted attention of the present author after the publication of the paper by Luding, Enss, Strehlow, and Hunklinger [8], which describes a study of spontaneous-polarization echo in the dielectric multicomponent glass $BaO–Al_2O_3–SiO_2$ observed in static magnetic fields. The echo amplitude was found [8] to grow quickly with increasing magnetic field B. In certain cases, the echo amplitude increases approximately threefold with B increasing from 0 to

1063-7834/03/4511-2099$24.00

230 mT. This observation suggests, as pointed out in [8], that the coupling of the tunneling systems with a magnetic field is remarkably strong and cannot be accounted for within current theories. It was also found [8] that the relaxation times are practically independent of magnetic field. The same glass as that investigated in [8] was reported in [9, 10] to exhibit a variation in the real and imaginary parts of the dielectric constant, ε' and ε'', under application of a static magnetic field. The observed relative change in ε', $\delta\varepsilon'(B)/\varepsilon'(0)$, was of the order of 10^{-4}. Similar variations in the dielectric constant in a magnetic field were observed to occur in the a-$SiO_{2+x}C_yH_z$ glass [11]. We show here that the interpretation of TLSs proposed in [7] is capable of accounting for the strong coupling between tunneling TLSs and a magnetic field.

Let us dwell in more detail on the ideas underlying paper [7]. Molten glasses are typical high-viscosity liquids. Such liquids exhibit characteristic features in the propagation of sonic, shear, and electromagnetic waves, more specifically, half-integral-power-law dependences of the damping coefficient and velocity dispersion on frequency, proportionality of the characteristic time to viscosity, a shift in the damping maximum from the center of the dispersion curve, very broad dispersion spectral ranges, etc. To explain these features, a nonlocal diffusion theory was proposed in [12], which treated a high-viscosity liquid as a two-phase system consisting of a disordered liquid and regions (clusters) ordered to a certain extent. It was assumed that the concentration of voids (places not occupied by molecules in the state of complete order) in ordered regions has an equilibrium value characteristic of the given external conditions. A variation in the external conditions (for instance, a change in the pressure) changes this equilibrium value and cause rearrangement of the ordered regions. Since this process requires an additional free volume (voids) or elimination of its excess, new equilibrium concentrations of voids set in through their diffusion through the boundaries of the ordered regions. Because this process takes a certain time, the change in the volume lags behind the change in the pressure. This lag entails anomalous damping and dispersion in the propagation velocity of sonic waves. This reasoning applies equally to shear and electromagnetic waves. This theory provided an explanation for numerous experimental data concerning wave propagation in high-viscosity liquids (glycerol, 1,3-butanediol, tetracetene, hexanetriol, 2-methyl pentanediol-2,4, pentachlorobiphenyl, molten B_2O_3, Na_2O–SiO_2–B_2O_3 glasses, etc.). Moreover, it was shown in [13] that the features characteristic of the glass formation point (such as jumps in the heat capacity and in the thermal expansion coefficient) can be accounted for by assuming that the ordered regions begin to contact one another at this point, so that the relative volume occupied by them will virtually no longer grow with decreasing temperature. This suggests that glass consists of nearly touching ordered regions separated by layers of a disordered phase. The smallest possible change in the free volume of an ordered region is associated with the appearance or elimination of one void. Accordingly, an ordered region should have a discrete nonequidistant set of energy levels. At low temperatures, only the lowest two levels can play a significant role and the ordered regions can be considered to be TLSs.

Turning back now to the effect of a magnetic field on TLSs observed in [8–11], it appears appropriate to recall here the results reported in [14]. That communication deals with the unusual behavior of the longitudinal relaxation time T_1 of NMR observed to occur in high-viscosity liquids with a variation in temperature. It was found that in such liquids, in particular, in glycerol, T_1 varies as a square root of viscosity [15]. Such a dependence cannot be interpreted in terms of the theory of Blombergen, Purcell, and Pound [16] and Kubo and Tomita [17], according to which the motion of molecules in a liquid is no more than Brownian motion and a rotation of individual molecules. This theory predicts that T_1 should be proportional to viscosity. It was found possible to explain the half-integral-power-law dependence of T_1 on viscosity in terms of the same mechanism as the features in wave propagation in high-viscosity liquids [14]. Indeed, this was accomplished by assuming a high-viscosity liquid to be a two-component medium consisting of ordered regions embedded in a disordered liquid. It was also assumed that a magnetic field aligns nuclear spins in ordered regions and that it is this effect that brings about their rearrangement. The initial state of an ordered region is recovered through diffusion of voids through its boundary; this process accounts for the half-integral-power-law dependence of T_1 on viscosity.

The increase in the amplitude of the spontaneous-polarization echo observed in [8] can also be explained, as will be shown later, in terms of rearrangement of the ordered regions caused by a magnetic-field-induced rotation of nuclear spins.

Molecules of dielectric glasses do not have constant magnetic moments associated with their electron shells. These molecules, however, have atoms possessing nuclear spins. In glycerol and in the a-$SiO_{2+x}C_yH_z$ glass studied in [11], the hydrogen atom has a spin, and in the BaO–Al_2O_3–SiO_2 glass, the spin of an aluminum nucleus is nonzero. The rearrangement of ordered regions occurs, at both high and low temperatures, through the removal or acquisition of voids. However, at low temperatures, in contrast to the high-temperature range, this process involves tunneling of atoms through barriers.

4. CALCULATION AND COMPARISON WITH EXPERIMENTAL DATA

Magnetic-field-induced rearrangement of ordered regions may change the dipole moment of an ordered region p, the tunneling probability (proportional to Δ_0), and the energy difference E between the lowest two levels. All these quantities enter into the expression for the amplitude A of the polarization two-pulse echo signal [8]:

$$A = A_0 \sin^3\theta_1, \tag{1}$$

where

$$A_0 \propto N\tanh(E/2kT)(p\Delta_0/E),$$

$$\theta_1 = (2\pi\Delta_0\tau_1/Eh)(\mathbf{p}\mathbf{F}_0),$$

τ_1 is the duration of the first electromagnetic pulse propagated (the second pulse is twice as long), N is the number of ordered regions (TLSs), k is the Boltzmann constant, h is the Planck constant, and $\mathbf{F}_0$ is the amplitude of the ac electric field.

Now, let us discuss the following three questions: which of the quantities p, Δ_0, or E entering into Eq. (1) contributes most to the variation of the echo signal amplitude when a magnetic field is switched on; how can we relate the observed relative variation of the real part of the dielectric constant induced by a magnetic field, $\delta\varepsilon'(B)/\varepsilon'(0)$, to the results obtained in [8] for the echo signal amplitude; and at what temperatures and magnetic fields does the echo signal amplitude become magnetic-field independent? The conclusions we come to will be compared with experimental data.

We may recall that the relaxation times were found in [8] to depend only weakly on magnetic field. This means that the potential barriers and, hence, the quantity Δ_0 vary only slightly when a magnetic field is switched on. In this case, the splitting energy E should also change only slightly. Therefore, the variation of the echo signal amplitude should be associated primarily with that of the dipole moment of the ordered region p.

According to [9, 10], in the $BaO–Al_2O_3–SiO_2$ glass, we have $[\varepsilon'(B) - \varepsilon'(0)]/\varepsilon(0) \cong 10^{-4}$ at temperatures of the order of a few tens of millikelvins, B values of about 0.1 T, and frequencies of about 1 kHz. The molecules of this glass are polar and possess a fairly high dielectric susceptibility χ compared to unity. Therefore, the above relation can be recast as

$$\delta\chi(B)/(1+\chi(0)) \cong \delta\chi(B)/\chi(0)$$
$$= \Delta P(B)/P(0) \cong 10^{-4},$$

where P is the polarization. Electric and magnetic fields act directly on each molecule, with the order and energy of an ordered region changing discretely. This discreteness can be disregarded in the estimates made below, although it does introduce some corrections. The polarization and dipole moment p_0 of a molecule for $p_0F_0/kT \ll 1$ are related through

$$P(0) = np_{0z} = np_0(p_0F_0/3kT),$$

where F_0 is the electric field strength, n is the number of molecules per unit volume, and p_{0z} is the component of p_0 along the electric field. Accordingly,

$$\Delta P(B) = 2n\Delta p_0(B)(p_0F_0/3kT)(\mu B/3kT),$$

where μ is the nuclear magnetic moment, $\Delta p_0(B)$ is the magnetic-field-induced change of the dipole moment of a molecule, and the last factor arises in averaging over all molecules in a unit volume. The above expressions can be combined to yield

$$\delta\varepsilon'(B)/\varepsilon'(0) \cong \Delta P(B)/P(0)$$
$$= (\Delta p_0(B)/p_0(0))(2\mu B/3kT) = 10^{-4}.$$

The nuclear magnetic moments μ are of the order of 10^{-26} J/T. For $B \cong 0.1$ T and $T \cong 0.1$ K, we have $2\mu B/3kT \cong 10^{-3}$. Substituting this figure into the last relation, we obtain

$$\Delta p_0(B)/p_0(0) \cong \Delta p(B)/p(0) \cong 10^{-1}.$$

Because of the simplifications made, $\Delta p(B) = n_0\Delta p_0(B)$, and $p(0) = n_0p_0(0)$, where n_0 is the number of molecules in an ordered region. The quantity $\Delta p(B)/p(0)$ should first grow linearly with increasing B for sufficiently low magnetic fields and after that saturate.

The proportionality of $\delta\varepsilon'(B)/\varepsilon'(0)$ to the B/T ratio is borne out by experiment. As seen from the graphs presented in [9, 10], $\delta\varepsilon'(B)/\varepsilon'(0)$ increases with decreasing temperature and increasing magnetic field for not very high $\mu B/kT$.

The above estimates can now be used to calculate the quantity θ_1 entering into Eq. (1) and its change $\Delta\theta_1(B)$ caused when a magnetic field is switched on. Supposing that $\Delta_0 \cong 10^{-26}$ J, $E \cong 0.1$ K $= 10^{-24}$ J, $\tau_1 = 10^{-7}$ s, $F_0 \cong 10^2$ V/m, and $p \cong 10^{-26}$ A s m (assuming an ordered region to contain $n_0 = 10^3$ molecules), we find $\theta_1 \cong 1$ and $\Delta\theta_1(B) \cong 0.1$. Thus, for $F_0 = 10^2$ V/m, θ_1 is comparable to unity and $\Delta\theta_1(B)$ is an order of magnitude smaller. These quantities vary with temperature and electric field strength. In addition, the quantity $\Delta\theta_1(B)$ also varies with magnetic field B. A more accurate analysis of the experimental data presented in [8] yields $\theta_1 = 1/3$ and $\Delta\theta_1(B) = 1/30$ for $F_0 = 10^2$ V/m. As F_0 increases by a factor of 4.5, θ_1 approaches $\pi/2$ and $A(0)$ takes on its maximum value, which is in full agreement with [8].

The amplitude ratio of the echo signals in a magnetic field and without it can be presented in the form

$$A(B)/A(0)$$
$$= [1 + \Delta p(B)/p(0)]\sin^3(\theta_1 + \Delta\theta_1)/\sin^3\theta_1. \tag{2}$$

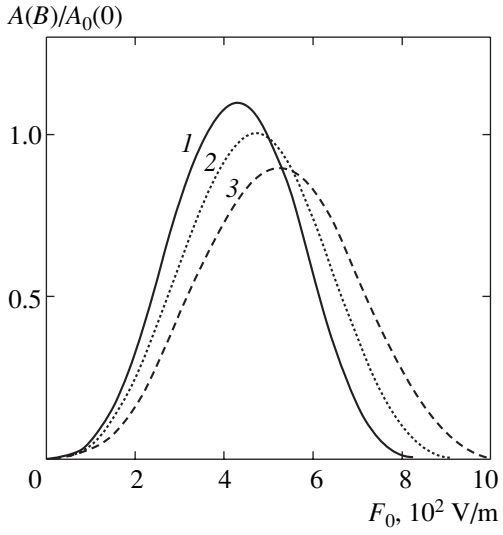

Fig. 1. Echo signal amplitude plotted vs. electric field amplitude F_0 for $\Delta p(B)/p(0)$ equal to (*1*) 0.1, (*2*) 0, and (*3*) –0.1, as predicted from theory.

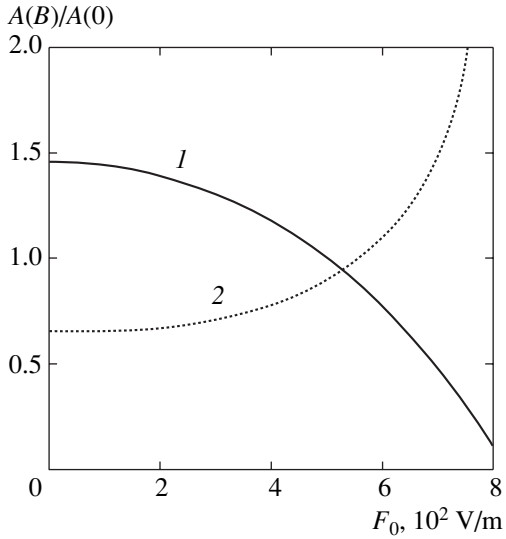

Fig. 2. Ratio of echo signal amplitudes with a magnetic field and in its absence, $A(B)/A(0)$, plotted vs. F_0 for $\Delta p(B)/p(0)$ equal to (*1*) 0.1 and (*2*) –0.1.

The smallness of $\Delta\theta_1(B)$ compared to unity permits us to recast this expression as

$$A(B)/A(0) = [1 + \Delta p(B)/p(0)][1 + \Delta\theta_1(B)\cot\theta_1]^3. \quad (3)$$

Because θ_1 varies with electric field amplitude and temperature, the second term in the second set of brackets in Eq. (3) can be both positive and negative, depending on the sign of $\cot\theta_1$; in other words, the echo signal amplitude can both increase and decrease with the application of a magnetic field. For large values of $\cot\theta_1$, the echo signal amplitude can grow by a few times, as observed experimentally [8]. As θ_1 increases, a second extremum (minimum) can appear in the graph relating the amplitude of the echo signal to that of the electric field, as observed in [8]. Thus, it follows that a large variation in the echo signal amplitude and a small variation in the dielectric constant are not in contradiction. Figure 1 plots the echo signal amplitude vs. the electric field amplitude F_0 [in units of the maximum echo signal amplitude with no magnetic field applied $A_0(0)$] for $\Delta p(B)/p(0) = 0.1$, 0 (with no magnetic field applied), and –0.1, as well as for $\theta_1 = 1/3$ and $\Delta\theta_1(B) = 1/30$ for $F_0 = 10^2$ V/m (curves *1–3*). Figure 2 shows the dependence of $A(B)/A(0)$ on electric field amplitude F_0 plotted for $\Delta p(B)/p(0) = 0.1$ and –0.1 (curves *1*, *2*).

Let us estimate the values of the temperatures and B values at which the magnetic field would no longer affect the echo signal amplitude and the dielectric constant. For $B = 0.1$ T, we have $\mu B \cong 10^{-27}$ J. Because in an ordered region there are about $n_0 = 10^3$ molecules, $n_0\mu B \cong 10^{-24}$ J. This quantity should be larger than the splitting energy E, which is also of the order of 10^{-24} J; otherwise, a magnetic field will not be able to rearrange an ordered region. This places a constraint on B; namely, magnetic field B should be higher than approximately 0.1 T. This is in accord with the experimental data from [8]. On the other hand, the energy $n_0\mu B$ must exceed kT. This imposes a constraint on temperature in that it should be less than 0.1 K. Indeed, as revealed in [11], the dielectric constant no longer varies in a magnetic field at temperatures above 0.1 K.

Magnetic fields less than about 0.1 T should also no longer affect the echo signal amplitude. As a result, a transition region appears in the B dependence of $A(B)/A(0)$ in which this ratio decreases with increasing B ($\Delta p(B)/p(0) < 0$), exactly what was observed in [8]. The course of this dependence is shown graphically in Fig. 3.

5. DISCUSSION OF RESULTS

The explanation of the effect of a magnetic field on TLSs in terms of nuclear spin rotation was unjustifiably rejected in [8] because of the large difference between the longitudinal relaxation time T_1 in NMR measured in glasses at low temperatures [18] and the longitudinal relaxation time T_1^0 observed in spontaneous polarization echoes. As will be shown below, however, this difference does not give any valid grounds for ruling out the explanation in terms of nuclear spin rotation.

Indeed, T_1 in NMR is connected intimately with the thermal motion (both Brownian and due to a rearrangement of ordered regions) of the dipole–dipole interacting nuclear spins, which generates ac magnetic fields that return the magnetization to equilibrium after the

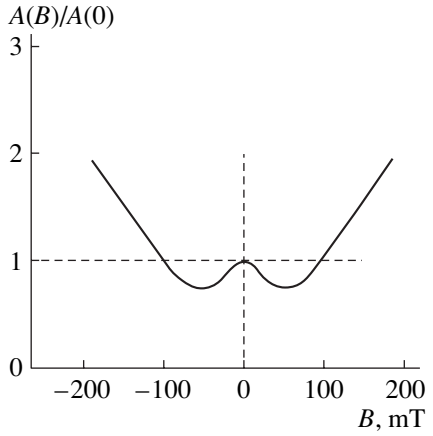

Fig. 3. Echo signal amplitude ratio with and without a magnetic field, $A(B)/A(0)$, plotted vs. magnetic field.

magnetic field is switched off. The expression for T_1 contains the time required for thermal motion to rearrange the whole ordered region [14]. The time T_1^0 in the polarization echo is also connected with a rearrangement of ordered regions, whose equilibrium state varies under the action of an ac electric field at a frequency of the order of 1 GHz. At such high frequencies, only narrow boundary layers in ordered regions will have enough time to rearrange. In this time, only a small number of tunneling transitions of atoms will occur through barriers to new equilibrium positions. Reverse transitions take place only through resonant one-photon emission. It is these processes that govern the time T_1^0, which is shown experimentally to be substantially shorter than T_1.

To explain the effect of a magnetic field on polarization echo amplitude, it was suggested in [8] that magnetic fields create mesoscopic current loops in glasses. In the last paper that came to the attention of the present author [19], nuclear quadrupoles were invoked to explain this effect.

6. CONCLUSIONS

The main results of the above analysis are as follows. The effect of a magnetic field on the dielectric constant and on the amplitude of the spontaneous-polarization echo observed in dielectric glasses at low temperatures has been connected with nuclear spin orientation in a magnetic field and the associated rearrangement of ordered regions. This effect of a magnetic field is a strong argument for the earlier assumption that the tunneling two-level systems are actually ordered regions (clusters) in the glass structure which have a discrete nonequidistant set of energy levels and are readily capable of rearranging under variation of external conditions (pressure, electric and magnetic field, etc.). These clusters are natural nanostructures with a high application potential.

ACKNOWLEDGMENTS

This study was supported by the Russian Foundation for Basic Research, project no. 03-02-17499.

REFERENCES

1. C. Talon, Q. W. Zou, M. A. Ramos, *et al.*, Phys. Rev. B **65**, 012203 (2002).
2. S. Hunklinger and W. Arnold, *Physical Acoustics*, Ed. by R. N. Thurston and W. P. Mason (Academic, New York, 1976), Vol. 12.
3. *Amorphous Solids*, Ed. by W. A. Phillips (Springer, Berlin, 1984), Topics in Current Physics, Vol. 24.
4. S. Hunklinger and A. K. Raychaudhuri, *Progress in Low Temperature Physics*, Ed. by D. F. Brewer (North-Holland, Amsterdam, 1986), Vol. 9.
5. P. W. Anderson, P. I. Halperin, and C. M. Varma, Philos. Mag. **25** (1), 1 (1972).
6. W. A. Phillips, J. Low Temp. Phys. **7** (3/4), 351 (1972).
7. I. A. Chaban, Fiz. Tverd. Tela (Leningrad) **21** (5), 1444 (1979) [Sov. Phys. Solid State **21**, 832 (1979)].
8. S. Luding, C. Enss, P. Strehlow, and S. Hunklinger, Phys. Rev. Lett. **88**, 075501 (2002).
9. P. Strehlow, C. Enss, and S. Hunklinger, Phys. Rev. Lett. **80** (24), 5361 (1998).
10. P. Strehlow, M. Wohlfahrt, A. G. M. Lansen, *et al.*, Phys. Rev. Lett. **84** (9), 1938 (2000).
11. J. Le Cochec, F. Ladien, and P. Pari, Phys. Rev. B **66**, 064203 (2002).
12. M. A. Isakovich and I. A. Chaban, Zh. Éksp. Teor. Fiz. **50** (5), 1343 (1966) [Sov. Phys. JETP **23**, 893 (1966)].
13. E. N. Kozhevnikov and I. A. Chaban, Akust. Zh. **20** (4), 565 (1974) [Sov. Phys. Acoust. **20**, 340 (1974)].
14. I. A. Chaban, Zh. Éksp. Teor. Fiz. **53** (8), 556 (1967) [Sov. Phys. JETP **26**, 361 (1967)].
15. A. G. Favret and R. Meister, J. Chem. Phys. **41** (4), 1011 (1964).
16. N. Blombergen, E. M. Purcell, and P. V. Pound, Phys. Rev. **73** (7), 679 (1948).
17. R. Kubo and K. Tomita, J. Phys. Soc. Jpn. **9** (6), 888 (1954).
18. J. Szeftel and H. Alloul, Phys. Rev. Lett. **34** (11), 657 (1975).
19. S. Hunklinger and C. Enss, J. Low Temp. Phys. **131** (1–2), 89 (2003).

Translated by G. Skrebtsov

Physics of the Solid State, Vol. 45, No. 11, 2003, pp. 2104–2109. Translated from Fizika Tverdogo Tela, Vol. 45, No. 11, 2003, pp. 2002–2007.

DEFECTS, DISLOCATIONS, AND PHYSICS OF STRENGTH

Simulation of the Dynamics of a Two-Dimensional Dislocation–Disclination Ensemble

K. N. Mikaelyan*, M. Seefeldt, M. Yu. Gutkin*, P. Klimanek***, and A. E. Romanov******

** Institute of Problems of Mechanical Engineering, Russian Academy of Sciences, Vasil'evskiĭ ostrov, Bol'shoĭ pr. 61, St. Petersburg, 199178 Russia*

e-mail: gutkin@def.ipme.ru

*** Catholic University of Leuven, Department of Metallurgy and Materials Engineering, Heverlee B-3001, Belgium*

**** Freiberg University of Mining and Technology, Institute of Physical Metallurgy, Freiberg D-09596, Germany*

***** Ioffe Physicotechnical Institute, Russian Academy of Sciences, Politekhnicheskaya ul. 26, St. Petersburg, 194021 Russia*

Received April 2, 2003

Abstract—A computer code for simulating the dynamics of an arbitrary 2D dislocation–disclination ensemble is developed. The code is constructed according to the molecular-dynamics principles; individual interacting particles are taken to be edge dislocations and dipoles of partial wedge disclinations. Pure copper is considered as an example for simulating the glide of one dislocation near an immobile dipole for various orientations of the dipole and under various initial conditions of the problem. The dislocation dynamics is shown to be mainly determined by the distribution of the elastic field of the disclination dipole rather than by the initial velocity of the dislocation. © *2003 MAIK "Nauka/Interperiodica".*

1. INTRODUCTION

In the last two decades, disclination concepts have been widely applied to describe mesoscopic defect structures forming in metals and alloys subjected to severe plastic deformation [1–6]. The notion of disclination is also used to construct models that describe the structural and mechanical behavior of nanostructured and noncrystalline materials [7–9], interfaces in various thin-film structures [10–14], martensitic transformations [15, 16], etc. Most disclination models of plastic deformation include a dislocation–disclination elastic interaction, which often plays a decisive role in these models.

For example, in [17], a dislocation–disclination model of propagation of a misorientation band (MB) was proposed. The basic idea of this model consisted in that the elastic-stress fields of a dipole of partial disclinations separate a neutral (with respect to a dislocation charge [1]) ensemble of edge dislocations chaotically distributed in front of an MB into groups of conventionally positive and negative dislocations. These positive and negative dislocations are trapped by positive and negative disclinations, respectively. The entrapment of each new dislocation dipole is an elementary act of the conservative propagation of the MB front. The mechanism proposed in [17] was corroborated by the experimental data reviewed in [1, 2] and then widely applied to simulate dislocation–disclination kinetics in severely deformed metals [4–6, 18–21]. Similar schemes were used to design new disclination models of MB nucleation and development near grain-boundary kinks and junctions [22]. However, comprehensive analysis of this mechanism brings up questions that have not yet been answered. In particular, the details of the process of dislocation trapping by a disclination dipole have not been determined. The effective entrapment length (i.e., the distance from a disclination line at which an edge dislocation of the corresponding sign should stop in front of an MB to make the conservative motion of this disclination possible) has likewise not been estimated.

To obtain missing information, it is necessary to study the dynamics of the development of complex dislocation structures at the site of MB nucleation and then in front of the nucleated MB. It is obvious that, in the general 3D case, this problem is extremely complex. However, for the 2D formulation of the problem, where the lines of all dislocations and partial disclinations are considered to be parallel to each other, the problem can be solved using computer simulation in terms of dislocation–disclination dynamics. Note that the simulation of discrete dislocation ensembles is now one of the most popular trends in theoretical materials science. 2D and 3D models of the dynamics of interacting dislocations have been extensively developed since the late 1980s (see, e.g., reviews [23, 24] and the recent papers dealing with 2D [25, 26] and 3D [27, 28] mesoscopic computer models). However, nobody has attempted to construct a correct mesoscopic model for a dislocation–disclination ensemble. The computational models proposed in [4–6, 18–21] describe the joint evolution kinetics of dislocations and partial disclinations but do not take into account elastic interactions between them.

In this work, we present the first results of simulating the joint dynamics of a partial-disclination dipole

and edge dislocations in a 2D approximation to reveal elastic interaction between these defects. We consider the particular case of one edge dislocation gliding near a biaxial dipole of wedge partial disclinations. The data obtained will be used to check and refine the existing theoretical (not computational) models of developing an MB.

2. COMPUTATIONAL MODEL

To study the dynamics of a 2D dislocation–disclination ensemble under an applied load, we used a computer code based on a program of molecular dynamical simulation of point defects. Particles were considered to be dislocations and dipoles of partial disclinations having an effective mass and self-fields of elastic stresses. Linear edge dislocations and wedge disclinations were distributed over a 2D rectangular region in an infinite elastically isotropic medium (Fig. 1). The defect lines were normal to the plane of this region, and its size was 1×1 mm.

Each edge dislocation was characterized by a Burgers vector $\mathbf{b}_x$ or $\mathbf{b}_y$, coordinates $(x^{(i)}, y^{(i)})$, and velocities $(\dot{x}^{(i)}, \dot{y}^{(i)})$; here, $i = 1, \ldots, n$, with n being the number of dislocations.

Dipoles were made up of unlike disclinations, which were assumed to be immobile in test calculations and considered only as sources of elastic fields. Each dipole was characterized by a strength $\omega^{(j)}$, the length and orientation of its arm, and the coordinates of the central point $(X^{(j)}, Y^{(j)})$; here, $j = 1, \ldots, N$, with N being the number of disclination dipoles. As shown in Fig. 1, each disclination represents the edge of a low-angle dislocation tilt wall. This means that all disclinations are partial rather than perfect [1].

In this model, dislocations can move by gliding or climbing under the action of forces caused by an applied load, the elastic fields of the other defects, and dynamic friction. In this case, the p component of the total force acting on dislocation i has the form

$$F_p^{(i)} = F_p^{\text{ext}(i)} + F_p^{\text{def}(i)} + F_p^{\text{fr}(i)}, \qquad (1)$$

where $F_p^{\text{ext}(i)} = \tau^{\text{ext}} b_p^{(i)}$ is the applied driving force, $F_p^{\text{def}(i)} = e_{mpl}\sigma_{lk}^{(i)} b_k^{(i)} s_m^{(i)}$ is the force of interaction with the other defects, $F_p^{\text{fr}(i)} = -\tau(v) b_p^{(i)}$ is the dynamic-friction force, τ^{ext} is the shear stress induced by the applied load, $b_p^{(i)}$ is the p component of the Burgers vector of the ith dislocation, e_{mpl} is the permutation symbol, $\sigma_{lk}^{(i)}$ is the total field of elastic stresses produced by the other defects and operating at the point of location of the ith dislocation, and $s_m^{(i)}$ is the m component of the unit vector tangent to the dislocation line. All subscripts p, m, l, and k can designate the x or y components. The shear stress $\tau(v)$ characterizes the friction of a crystal lattice and depends on the dislocation velocity v.

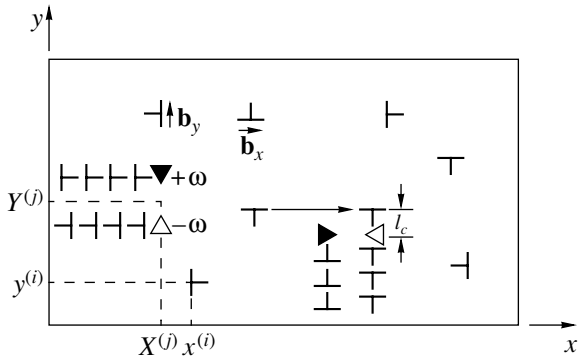

Fig. 1. 2D region of simulation of a dislocation–disclination ensemble. l_c is the characteristic capture length of a dislocation by a disclination dipole.

Dislocation dynamics is described by Newton's equations

$$m^{(i)}\ddot{x}^{(i)} = F_x^{(i)}, \quad m^{(i)}\ddot{y}^{(i)} = F_y^{(i)}, \qquad (2)$$

where $m^{(i)}$ is the effective mass of the ith dislocation and $\ddot{x}^{(i)}$ and $\ddot{y}^{(i)}$ are the components of its acceleration. Each defect receives initial coordinates and velocities, and then Eqs. (2) are solved numerically to yield time dependences of the defect coordinates $(x^{(i)}, y^{(i)})$ and velocities $(\dot{x}^{(i)}, \dot{y}^{i})$. When solving the equations, we use periodic boundary conditions for the spatial variables.

Using this approach, we studied the elastic interaction of a glide edge dislocation with a biaxial dipole of wedge disclinations in pure copper. The Burgers vector of the dislocation was taken to be $b_x = 0.256$ nm, and the effective mass per unit dislocation length [29] was estimated to be $m = \rho b_x^2/2 \approx 1.4 \times 10^{-9}$ kg m^{-1}, where ρ is the copper density. The middle of the disclination-dipole arm was fixed at the central point ($X = 500$ μm, $Y = 500$ μm) of the chosen region in the elastic space. The dipole arm length $2a$ was constant (100 nm), and only its orientation and the disclination strength were varied. To analyze only the dislocation–disclination interaction, the applied force F_p^{ext} was assumed to be zero. The elastic force $F_p^{\text{def}} = \sigma_{xy} b_x$ was determined using the stress field of a disclination dipole σ_{xy} [1]. The dynamic-friction force F_p^{fr} was taken in the form $F_p^{\text{fr}}(t) = -Bv(t)$, where $B = 1.7 \times 10^{-5}$ Pa s for pure copper [30] (see also [29, p. 76]).

In test calculations, we considered some typical situations at various orientations of the dipole arm and the initial dislocation positions and velocities. We took into account only the conservative dislocation gliding, and

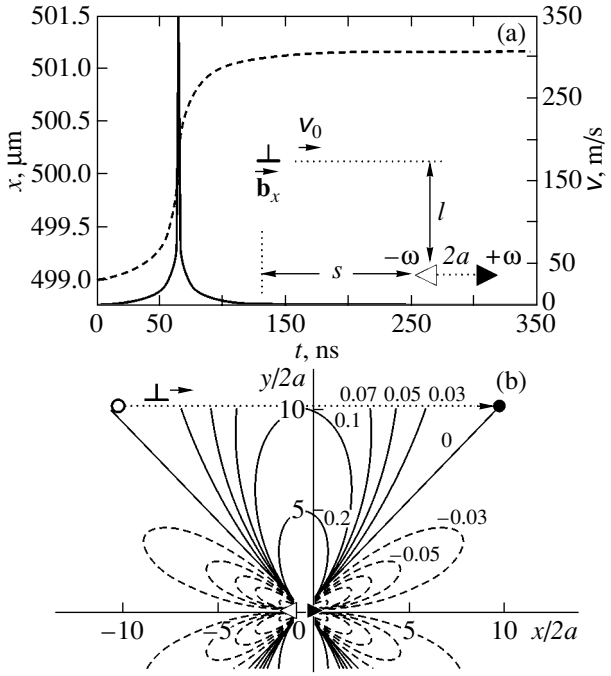

Fig. 2. Accelerated motion of an edge dislocation along the disclination-dipole arm: (a) time dependences of the coordinate $x(t)$ (dashed line) and velocity $v(t)$ (solid line) of the dislocation gliding in (b) the field of positive long-range shear stresses σ_{xy} of the dipole.

dislocation climbing was blocked by an infinite resistance to motion along the normal to the glide plane. The results of calculations are given in the following sections.

3. DISLOCATION GLIDE ALONG THE DISCLINATION-DIPOLE ARM

We first consider a disclination dipole of strength $\omega = 0.01$ and a dislocation gliding along its arm. The dislocation begins to move when it is rather far from the dipole, at the point ($x_0 = 499.0$ μm, $y_0 = 501.1$ μm), and its initial velocity is $v_0 = 0.01$ m s^{-1}. The initial position of the dislocation with respect to the dipole is characterized by the distances $s = 1000$ nm and $l = 1100$ nm, which are substantially longer than the dipole arm (Fig. 2). The solution to this problem is shown in Fig. 2a in the form of the time dependences of the dislocation coordinate $x(t)$ (dashed line) and velocity $v(t) = \dot{x}(t)$ (solid line). For clarification, Fig. 2b gives the contour distribution of the dipole elastic stresses σ_{xy} measured in units of $G\omega/[2\pi(1 - \nu)]$, where G is the shear modulus and ν is Poisson's ratio. The initial position of the dislocation is marked by the open circle in the top left-hand corner in Fig. 2b, and its final position, by the solid circle in the top right-hand corner (all following figures are constructed similarly, and the designations in them are the same).

The initial dislocation position is seen to be chosen so that the dislocation falls in the region of positive values of σ_{xy} from the very beginning of its motion. These values first increase and then decrease as the dislocation moves from left to right. Correspondingly, the dislocation first strongly accelerates and its velocity reaches a maximum in the region right above the dipole, where the dipole stress σ_{xy} is maximum (Fig. 2). Therefore, the dynamic-friction force, which is directly proportional to the dislocation velocity, is also maximum in this region. When the dislocation starts to leave the region of maximum stresses above the dipole, its velocity sharply decreases. As a result, the dislocation stops at the point where the stress σ_{xy} vanishes, i.e., at the point of intersection of the dislocation glide plane with the zero-level line of σ_{xy} (Fig. 2b). It is obvious that, in this case, the dislocation simply passes by the dipole without being trapped by it.

This raises the following question: What are the conditions for the dislocation to be trapped by the dipole (i.e., for the dislocation to stop immediately above the positive disclination) in this configuration? Our calculations showed that the capture is possible only at a very low strength of the dipole ω and only in the case when the dislocation is initially located immediately above the dipole. For example, let us assume that the strength of the dipole is ten times lower ($\omega = 0.001$), the initial dislocation velocity is zero ($v_0 = 0$), and the dislocation is initially located at the point ($x_0 = 500.050$ μm, $y_0 = 500.001$ μm), i.e., at a distance $l = 1$ nm from the dipole immediately above its center (Fig. 3). In this case, from the very beginning, the dislocation is in the region of the strong field σ_{xy} of the dipole, rapidly picks up speed, and reaches the line of zero σ_{xy}, where the dislocation stops in the immediate vicinity of the positive disclination after several damped oscillations. At such a small distance from the disclination, the line of zero σ_{xy} virtually coincides with the y axis and the dislocation may be trapped by the dipole. However, this entrapment is possible only within a very small distance from the dipole (here, $l = 1$ nm), which is significantly smaller than the distance $l_c \approx b_x/\omega = 256$ nm between dislocations in low-angle tilt walls whose edges are described by this disclination dipole. Obviously, due to such a small capture length, conservative motion of the disclination dipole along the normal to its arm by trapped edge dislocations is impossible.

Thus, simulation shows that the existing models of the motion of a disclination dipole should be refined with allowance for the findings of this study. New models are likely to have to include an intermediate rearrangement of a dislocation ensemble in front of a disclination dipole and/or the transformation of the dipole itself.

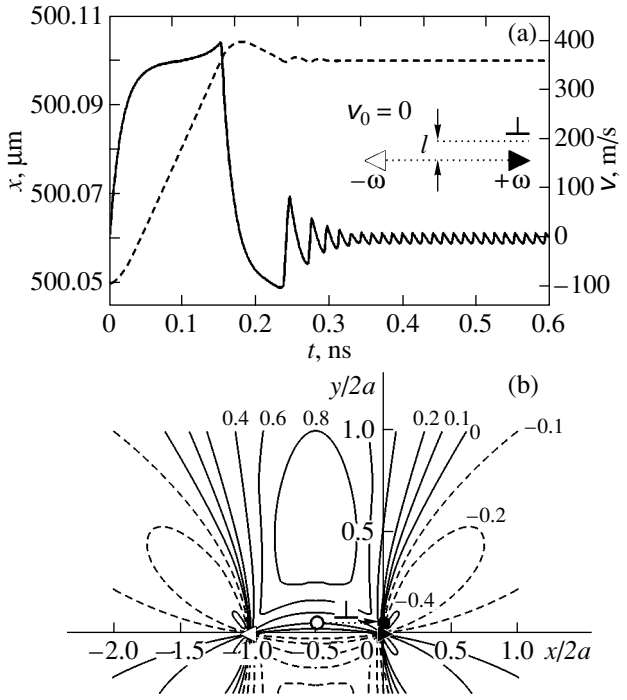

Fig. 3. Accelerated motion of an edge dislocation along the disclination-dipole arm and its capture by this dipole: (a) time dependences of the coordinate $x(t)$ (dashed line) and velocity $v(t)$ (solid line) of the dislocation gliding in (b) the field of positive short-range shear stresses σ_{xy} of the dipole.

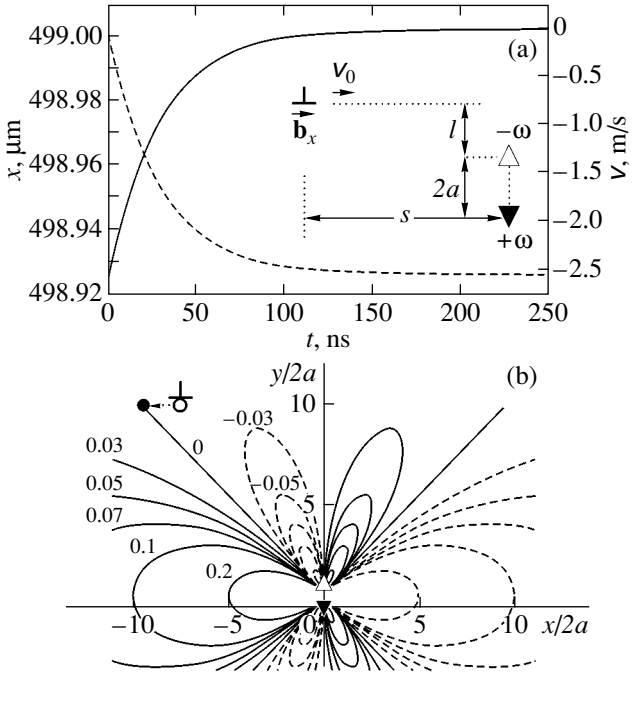

Fig. 4. Repulsion of a gliding edge dislocation by the disclination dipole: (a) time dependences of the coordinate $x(t)$ (dashed line) and velocity $v(t)$ (solid line) of the dislocation gliding in (b) the field of negative long-range shear stresses σ_{xy} of the dipole.

4. DISLOCATION GLIDE ACROSS THE DISCLINATION-DIPOLE ARM

Now, we rotate the disclination-dipole arm of strength $\omega = 0.01$ by 90° (Fig. 4a) and consider a dislocation gliding across this arm. The dislocation starts to move at an initial velocity $v_0 = 0.01$ m s^{-1} from the point ($x_0 = 499$ μm, $y_0 = 501$ μm), so that its initial position with respect to the dipole is specified by the distances $s = 1000$ and $l = 1025$ nm. Thus, the dislocation starts from a point located relatively far from the dipole, in the zone where its shear stress σ_{xy} is negative (Fig. 4b). As a result, the dislocation is repulsed by the dipole, its velocity immediately changes sign, and the dislocation moves with a negative acceleration from the dipole until it achieves the line of zero value of σ_{xy} (the top left-hand corner in Fig. 4b). The corresponding time dependences of the dislocation coordinate $x(t)$ and velocity $v(t)$ are given in Fig. 4a (dashed and solid lines, respectively).

Keeping the same general geometry of the problem, we displace the glide plane by 1 μm toward the dipole (Fig. 5a). Let the dislocation start at the same initial velocity from the point ($x_0 = 499$ μm, $y_0 = 500$ μm), for which $s = 1000$ nm and $l = 25$ nm. Here, the dislocation is in the zone of strong positive stresses σ_{xy} from the very beginning (Fig. 5b). The dislocation picks up a speed $v \approx 450$ m s^{-1} very rapidly (in $t \le 0.1$ ns), glides at approximately the same speed for the following ≈1.2 ns, and then decelerates and stops at the line of zero value of σ_{xy} in ≈1.9 ns.

Let us return to the first example considered in this section (Fig. 4) and interchange the positions of the positive and negative disclinations, all other things being equal (Fig. 6). The dislocation starts to move from the same point at the same initial velocity. It first accelerates under the action of increasing stress σ_{xy} and then decelerates when this stress begins to decrease (Fig. 6b). Within approximately 83 ns after the beginning of motion, the dislocation reaches the line of zero value of σ_{xy} and is trapped by the disclination dipole. This example confirms that the dipole can move conservatively along the direction parallel to its arm by trapping dislocations, contrary to the case of its motion along the normal to its arm (see Section 3).

The examples considered above show that the dislocation dynamics is controlled completely by the elastic field of the disclination dipole: the dislocation accelerates, if it is in the region of the increasing field, and then, when the field begins to decrease, the dislocation is braked by the dynamic-friction force. The dislocation always stops when it reaches the line of zero value of the shear-stress field of the dipole. Thus, the behavior of the dislocation is specified by its initial position with respect to the dipole and is virtually independent of its initial velocity (for the velocities considered in these

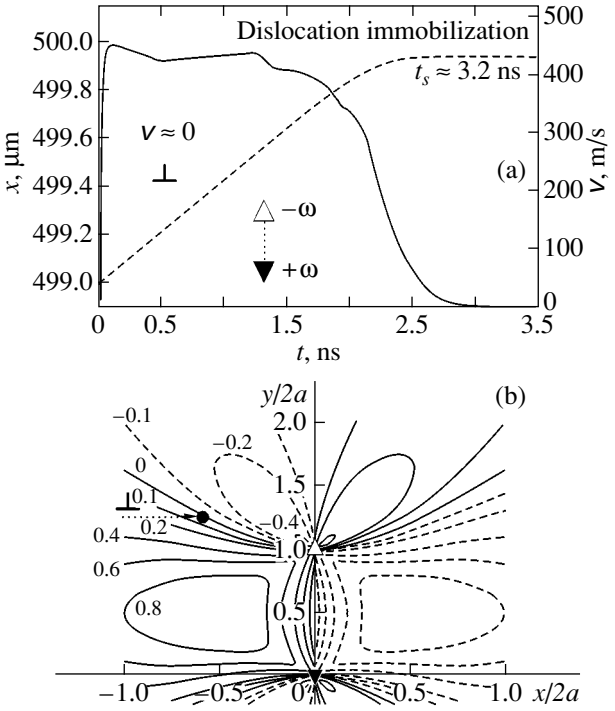

Fig. 5. Attraction and stop of a gliding edge dislocation in the elastic field of the disclination dipole: (a) time dependences of the coordinate $x(t)$ (dashed line) and velocity $v(t)$ (solid line) of the dislocation gliding in (b) the field of positive short-range shear stresses σ_{xy} of the dipole.

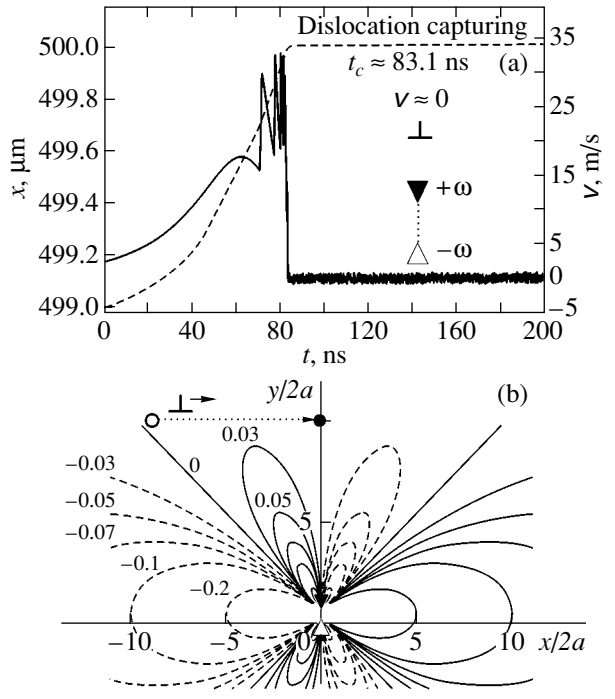

Fig. 6. Accelerated motion of an edge dislocation across the disclination-dipole arm and its capture by this dipole: (a) time dependences of the coordinate $x(t)$ (dashed line) and velocity $v(t)$ (solid line) of the dislocation gliding in (b) the field of positive long-range shear stresses σ_{xy} of the dipole.

calculations). Our computer simulation confirmed that a dipole of wedge disclinations could move conservatively along the direction parallel to its arm by trapping edge dislocations; however, its motion along the normal to its arm cannot be explained in the context of the existing theoretical models and requires further investigations.

5. CONCLUSIONS

The results of the test calculations show that the computer code proposed here can be applied for simulating more complex defect configurations under various conditions of an applied load. At the same time, these results are of interest in themselves, since they clearly illustrate the dynamics of dislocation–disclination elastic interactions and raise interest in studying the collective behavior of defects in solids subjected to severe plastic deformation.

ACKNOWLEDGMENTS

The authors are grateful to U.K. Rössler (Dresden, Germany), who designed the initial version of the molecular-dynamics computer code and provided it to us for the following transformation into a program for molecular dynamical simulation of dislocation–disclination dynamics.

This work was supported in part by the Volkswagen Foundation (grant no. 05019225), the program "Physics of Solid Nanostructures" of the Ministry of Industry of the Russian Federation, and the program "Integration" (project no. B0026).

REFERENCES

1. V. I. Vladimirov and A. E. Romanov, *Disclinations in Crystals* (Nauka, Leningrad, 1986).
2. V. V. Rybin, *Large Plastic Deformations and Fracture of Metals* (Metallurgiya, Moscow, 1986).
3. A. D. Korotaev, A. N. Tyumentsev, and Yu. P. Pinzhin, Fiz. Mezomekh. **1** (1), 23 (1998).
4. M. Seefeldt, Rev. Adv. Mater. Sci. **2** (1), 44 (2001).
5. P. Klimanek, V. Klemm, A. E. Romanov, and M. Seefeldt, Adv. Eng. Mater. **3** (11), 877 (2001).
6. *Local Lattice Rotations and Disclinations in Microstructures of Distorted Crystalline Materials*, Ed. by P. Klimanek, A. E. Romanov, and M. Seefeldt (2002), Solid State Phenom., Vol. 87.
7. A. E. Romanov, in *Nanostructured Materials: Science and Technology*, Ed. by G. M. Chow and N. I. Noskova (Kluwer Academic, Dordrecht, 1998), p. 207.
8. V. A. Likhachev and V. E. Shudegov, *Organization Principles of Amorphous Structures* (S.-Peterb. Gos. Univ., St. Petersburg, 1999).
9. M. Yu. Gutkin and I. A. Ovid'ko, *Physical Mechanics of Deformed Nanostructures*, Vol. 1: *Nanocrystalline Materials* (Yanus, St. Petersburg, 2003).

10. J. S. Speck, A. C. Daykin, A. Seifert, *et al.*, J. Appl. Phys. **78** (3), 1696 (1995).
11. N. A. Pertsev and A. G. Zembilgotov, J. Appl. Phys. **78** (10), 6170 (1995).
12. P. Müllner, H. Gao, and C. S. Ozkan, Philos. Mag. A **75** (4), 925 (1997).
13. I. A. Ovid'ko, Fiz. Tverd. Tela (St. Petersburg) **41** (9), 1637 (1999) [Phys. Solid State **41**, 1500 (1999)].
14. A. G. Sheinerman and M. Yu. Gutkin, Phys. Status Solidi A **184** (2), 485 (2001).
15. M. Yu. Gutkin, K. N. Mikaelyan, and V. E. Verijenko, Acta Mater. **49**, 3811 (2001).
16. M. Yu. Gutkin, K. N. Mikaelyan, V. E. Verijenko, and L. D. Thompson, Metall. Mater. Trans. A **33**, 1351 (2002).
17. V. I. Vladimirov and A. E. Romanov, Fiz. Tverd. Tela (Leningrad) **20** (10), 3114 (1978) [Sov. Phys. Solid State **20**, 1795 (1978)].
18. B. K. Barakhtin, V. I. Vladimirov, S. A. Ivanov, *et al.*, Fiz. Met. Metalloved. **63** (6), 1185 (1987).
19. A. E. Romanov and E. C. Aifantis, Scr. Metall. Mater. **29** (4), 707 (1993).
20. M. Seefeldt and P. Klimanek, Mater. Sci. Eng. A **234–236**, 758 (1997).
21. M. Seefeldt and P. Klimanek, Modell. Simul. Mater. Sci. Eng. **6**, 349 (1998).
22. M. Yu. Gutkin, K. N. Mikaelyan, A. E. Romanov, and P. Klimanek, Phys. Status Solidi A **193** (1), 35 (2002).
23. A. Needleman, Acta Mater. **48**, 105 (2000).
24. B. Devincre, L. P. Kubin, C. Lemarchand, and R. Madec, Mater. Sci. Eng. A **309–310**, 211 (2001).
25. L. Nicola, E. van der Giessen, and A. Needleman, Mater. Sci. Eng. A **309–310**, 274 (2001).
26. N. Argaman, O. Levy, and G. Makov, Mater. Sci. Eng. A **309–310**, 386 (2001).
27. O. Politano and J. M. Salazar, Mater. Sci. Eng. A **309–310**, 261 (2001).
28. H. Yasin, H. M. Zbib, and M. A. Khaleel, Mater. Sci. Eng. A **309–310**, 294 (2001).
29. U. F. Kocks, A. S. Argon, and M. F. Ashby, Prog. Mater. Sci. **19**, 73 (1975).
30. K. M. Jassby and T. Vreeland, Jr., Philos. Mag. **21**, 1147 (1970).

Translated by K. Shakhlevich

Physics of the Solid State, Vol. 45, No. 11, 2003, pp. 2110–2114. Translated from Fizika Tverdogo Tela, Vol. 45, No. 11, 2003, pp. 2008–2012.

DEFECTS, DISLOCATIONS, AND PHYSICS OF STRENGTH

Superplasticity of a Microcrystalline Aluminum–Lithium Alloy under Torsion

V. V. Shpeĭzman[1], M. M. Myshlyaev[2,3], M. M. Kamalov[3], and M. M. Myshlyaeva[3]

[1] *Ioffe Physicotechnical Institute, Russian Academy of Sciences, Politekhnicheskaya ul. 26, St. Petersburg, 194021 Russia*
e-mail: shpeizm.v@mail.ioffe.ru

[2] *Baikov Institute of Metallurgy and Materials Science, Russian Academy of Sciences, Leninskiĭ pr. 49, Moscow, 119991 Russia*

[3] *Institute of Solid State Physics, Russian Academy of Sciences, Chernogolovka, Moscow oblast, 142432 Russia*
e-mail: myshlyae@issp.ac.ru

Received March 19, 2003

Abstract—The deformation of an aluminum–lithium alloy under torsion in the temperature range 523–673 K at angular velocities of 0.322 and 0.0322 rad/s is studied. The shear strain γ prior to failure is found to increase with decreasing strain rate, and its temperature dependence has a maximum at 553 K ($\gamma \approx 30$). The initial loading-induced jump in the dependence of the torque on the angle of rotation (stress–strain curve) is followed by a softening stage, which changes into a hardening stage or a stage with a constant torque at all temperatures except those near 673 K. The stress distribution over a cross section is analyzed, and the dependence of the shear-strain rate $\dot{\gamma}$ on the stress τ and temperature T is found to be $\dot{\gamma} \sim \tau^n \exp(-U/kT)$. The results are compared with those obtained earlier from tensile tests of this alloy. © *2003 MAIK "Nauka/Interperiodica".*

1. INTRODUCTION

The superplasticity of microcrystalline materials produced, in particular, through equal-channel angular pressing (ECAP) has attracted considerable research interest in recent years [1–6]. A titanium alloy [1], various aluminum alloys [2–5], and brass [6] were studied under the conditions of uniaxial tension at constant strain rates and temperatures. The strain rate was rather high in those studies (10^{-3}–10^{-1} s^{-1}). The maximum strains prior to fracture were found to be 575% in the Ti–6Al–4V alloy [1], 1220 [2] and 1900% [4, 5] in various Al–Li alloys, 2280% in the Al–3Mg–0.2Sc alloy [3], and 640% in the Cu–40Zn brass [6]. It is known, however, that significantly higher strains can be achieved under torsion [7–10]. The disadvantage of torsion tests at high strains of continuous cylindrical samples is that the stress state at various distances from the torsion axis cannot be calculated exactly. Thin-walled tube samples, in which stresses can be considered to be constant over a cross section, can be tested at only relatively small strains, since such samples loose their stability upon high deformation. The authors of [7–10] analyzed the stress state under torsion assuming that tangential stresses in the cross section normal to the sample axis were independent of the distance from this axis. This assumption was based on the existence of a sufficiently long steady-state deformation stage under the conditions of both creep and tension at a constant rate [7–10]. This means that deformation occurs under the conditions of a constant structure, namely, without hardening and softening. In this work, we analyzed the stress state under torsion of continuous cylindrical samples in the superplasticity region and obtained the dependence of the shear-strain rate on the flow stress and temperature.

2. EXPERIMENTAL

For experiments, we used an aluminum–lithium alloy containing (in wt %) 5.5 Mg, 2.2 Li, 0.12 Zr, and the balance in Al. The workpieces for ECAP were rods 15 mm in diameter and 80 mm long cut from a hot-rolled plate with a recrystallized structure having 20-μm grains. The workpieces were water-quenched from 743 K and then subjected to ten-times-repeated ECAP in air at 643K [11]; a rod was rotated through 90° after each pass following the technique described in [12]. The mean grain size after ECAP was about 2 μm. Grains contained subgrains, dislocation cells and tangles, and isolated dislocations. Moreover, precipitates of the Al_2LiMg phase and particles of the δ' (Al_3Li) phase were observed both inside the grains and along their boundaries.

The rods subjected to ECAP were used to produce samples for torsion tests; the sample axis coincided with the rod axis, and the cylindrical gage portion was 3 mm in diameter and 5 mm long. The sample heads had a 5×5-mm cross section. For torsion tests, we designed a device in which the rate of rotation of a mobile grip was set by an electric motor with a reduction gear. The force (torque) was measured with a standard Instron transducer having a range of 10 N. Signals

from this transducer were processed using the controller of an Instron testing machine and were recorded to a computer hard drive. The strain rate (rate of rotation) and torque were measured with an accuracy of 2.5 and 1%, respectively. During tests, the temperature was maintained constant to within an error of ±3 K. Tests were performed in the temperature range 523–673 K at torsional rates (changes in the angle of rotation of the mobile head of a sample with respect to its fixed head) of 0.322 and 0.0322 rad/s.

3. RESULTS AND DISCUSSION

3.1. Torsional Stress–Strain Diagrams under the Conditions of Superplasticity

Figure 1 shows the typical dependences of the torque M on the angle of rotation θ (torsion diagrams) at various temperatures and strain rates. All curves initially exhibit a hardening stage, which is very short as compared to the length covered by the whole diagram and is followed by transition to the stage of softening. As the temperature increases or the strain rate decreases, this transition becomes more pronounced and the hardening stage shortens. In most diagrams recorded with a time resolution of 10^{-2} s, this stage cannot be distinguished from the quasi-elastic segment, whose slope is specified by the rigidity of the loading device and force transducer (Figs. 1a–1c). The transition from the hardening to the softening stage becomes smooth only at a high rate of rotation and at temperatures close to the lower boundary of the temperature range under study (Fig. 1d). At low temperatures and strain rates, softening changes into hardening (Fig. 1b). As the temperature or strain rate increases, this segment becomes progressively less pronounced and transforms into a horizontal line (Fig. 1c). Then, the torque decreases as the angle of rotation increases at a rate (slope) lower than that in the previous segment (Fig. 1a). In all cases, the sample eventually fails by shearing along the plane normal to its axis. The angle strain prior to failure increases with decreasing strain rate, and its temperature dependence has a maximum $\theta_f \approx 100$ rad at 553 K (see table); this maximum corresponds to a surface shear $\gamma_f \approx 30$. Note that this value exceeds the shear strain of this material reached under tension by a factor of more than three [4, 5].

As mentioned above, it is difficult to calculate the shear (tangential) stresses and the shear strain under torsion of a continuous cylinder at high strains. Based on the hypothesis of plane sections and the assumption of a linear increase in the shear with the distance from the rotation axis (the radii remain straight lines), one may conclude that, in the softening range, the inner layers of a sample rather than the outer ones become max-

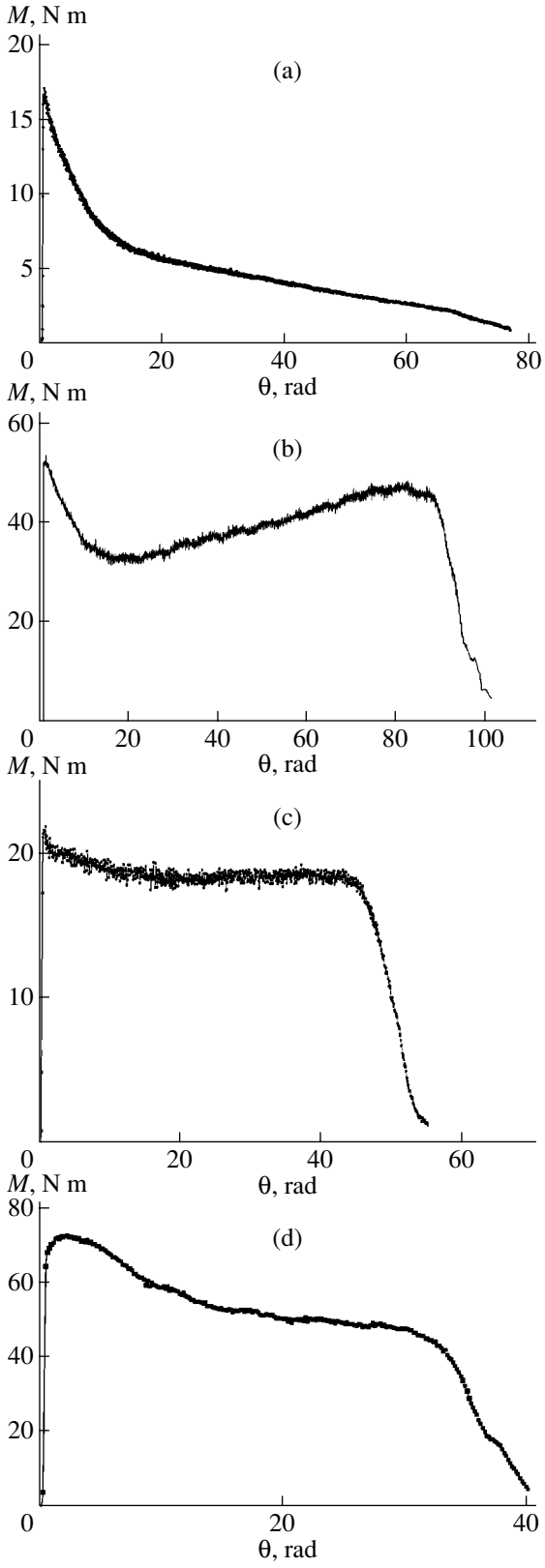

Fig. 1. Dependence of torque M on angle of rotation θ at (a, c) T = 673 and (b, d) 553 K for a torsion rate of (a, b) 0.0322 and (c, d) 0.322 rad/s.

Angle strain to failure θ at various temperatures for torsion rates $\dot{\theta}_1 = 0.0322$ rad/s and $\dot{\theta}_2 = 0.322$ rad/s

T, K	θ, rad	
	for $\dot{\theta}_1$	for $\dot{\theta}_2$
523	69	–
553	100	40
588	90	–
613	90	50
643	76	50
663	75	55
673	70	52

imally stressed. In this case, in the formula for tangential stresses τ_a in the outer layers of a sample [13]

$$\tau_a = \frac{1}{2\pi a^3}\left(3M + \theta\frac{dM}{d\theta}\right) \quad (1)$$

(a is the sample radius), the term $dM/d\theta$ is negative. Under these conditions, $\tau_a < \tau_m$, where $\tau_m = 3M/2\pi a^3$.

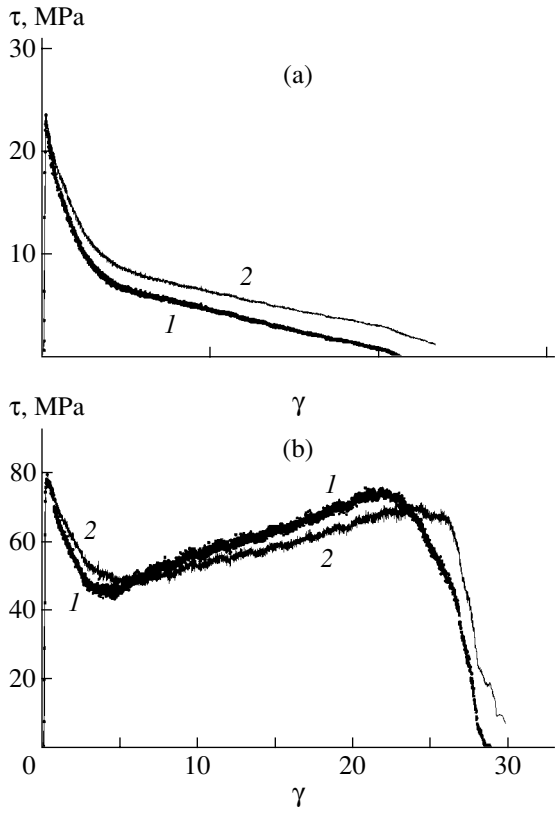

Fig. 2. Stress–strain curves for torsion plotted as tangential stress τ versus shear strain γ for the torsion conditions corresponding to Figs. 1a and 1b. (*1*) Calculation with Eq. (1) and (*2*) calculation for the case of radius-independent stresses.

This means that the surface stresses are lower than the stresses corresponding to "ideally plastic" torsion, where stresses in a cross section are independent of the distance from the axis (see Fig. 2, showing τ_m and τ_a for the torsion diagrams given in Figs. 1a, 1b). Since the torque created by stresses should be equal to the applied torque, the inequality $\tau_r > \tau_a$ should be valid at certain values of $r < a$ when the inequality $\tau_a < \tau_m$ holds true. When plotting Fig. 2, we calculated τ_a using Eq. (1) over the whole θ range, excluding the initial hardening stage. In that stage, we assume that $\tau_a = \tau_m$, since, as noted above, the slope of a stress-strain diagram in this region is specified by the rigidity of the loading device; the application of Eq. (1) here would result in overestimated stresses.

It should be noted that the short analysis of torsion (stress-strain) diagrams and the calculation of stresses performed above are only a first approximation. The calculation is based on assumptions which are not always true at high strains. Our measurements show that the gage diameter and length are not constant at high angles of rotation. For example, an increase in the diameter prior to the failure of the sample whose torsion diagram is given in Fig. 1a is about 10%. If the diameter is also assumed to increase in the hardening stage (Fig. 1b), this reduces the effect by a factor of approximately three and makes the diagram similar to that calculated from the data in Fig. 1c. It is also essential that the increase in the diameter and decrease in the length of a sample are not consistent with the accepted calculation procedure based on the hypothesis of plane sections. In earlier studies on torsion [14], samples were found to elongate at low angles of rotation. Conceivably, a sample subjected to torsion can be considered as a spring that is first wound up (the spring elongates) and then unwound (shortens).

Although, as noted above, the stress calculation is approximate, the conclusion that, at high torsional strains, the layers close to the rotation axis rather than outer layers can be stressed to the highest degree is grounded physically. Indeed, if we assume that the strain is proportional to the distance from the sample axis, then the greater the strain, the less the shear stress should operate in the softening range.

3.2. Dependence of the Strain Rate on Stress and Temperature

Deformation at elevated temperatures is described, as a rule, by a power-law dependence of the strain rate on stress [4, 9, 15]. For a shear-strain rate $\dot{\gamma}$ and tangential stresses, this dependence has the form

$$\dot{\gamma} = A(\tau/\tau_0)^n \exp(-U/kT), \quad (2)$$

where $\tau_0 = 1$ MPa is introduced from dimensional considerations (τ is measured in megapascals), U is the activation energy for plastic deformation, and the coef-

ficient $A \sim T^{-1}$. Our estimations based on the experimental variation of the stresses $\Delta\tau$ with temperature showed that the contribution from the factor T^{-1} to $\Delta\tau$ at a constant γ is less than 1.5% of the contribution from the exponential in the temperature range studied. This conclusion follows from a comparison of the quantities $\ln T$ and Un/kT at the minimal and maximal test temperatures. The insignificant role played by the factor T^{-1} in the determination of the activation energy from Eq. (2) was also pointed out in [4]. Therefore, to determine n and U, we can use the $\tau(T^{-1})$ dependences obtained for two torsion rates. The stress τ is taken to be the stress τ_1 corresponding to the transition from the initial hardening to softening (the case of small strains), and the stress τ_2 is the flow stress at the given shear ($\gamma = 10$).

Figure 3a shows the $\tau_1(T^{-1})$ dependences plotted for two test rates. In the semilogarithmic coordinates, these dependences can be approximated by the straight lines $\tau_1 = \tau_0\exp(-2.17 + 3600/T)$ for $\dot{\gamma} = 10^{-1}$ s^{-1} and $\tau_1 = 1.76\tau_0\exp(-2.17 + 3600/T)$ for $\dot{\gamma} = 10^{-2}$ s^{-1}. The data in Fig. 3b can be approximated by the lines $\tau_2 = \tau_0\exp(-4.8 + 4800/T)$ and $\tau_2 = 2.8\tau_0\exp(-4.8 + 4800/T)$ for the same rates, respectively. As can be seen from Fig. 3b, the data for the maximum test temperature (673 K) and the low strain rate differ from the other data in that the flow stresses are low, which is likely due to changes in the structure that occur during long-term holding at an elevated temperature.

The values of n and U can be determined using the parameters of the dependences given above. By equating the natural logarithms of coefficients 1.76 and 2.8 to $\ln 10/n$, we find that $n = 4.07$ for small deformations and $n = 2.24$ for large deformations. The coefficients of $1/T$ in the formulas for τ_1 and τ_2 give an activation energy $U = 1.28$ eV for the initial deformation stage and $U = 0.94$ eV for large deformations. The value of n obtained for large deformations is close to that given in [4] for a tensile test of this material and is typical of superplastic deformation; this value corresponds to the strain-rate sensitivity $m = 1/n = 0.45$. Such a high value of n (close to four) is usually characteristic of the range of small deformations or elevated temperatures [16], which is likely the reason it appears in the initial deformation stage. The value $U = 1.28$ eV is close to the activation energy measured under torsion of aluminum samples and alloys with an ordinary grain size (about 50 μm or greater), and the value $U = 0.94$ eV is close to that determined under tension of microcrystalline samples of this alloy [4].

To make a more reliable estimation of n and U at large deformations, we determined them experimentally by using the method of a temperature jump or a jump in torsion rate. An example of a torsion diagram with a strain-rate jump at large deformations is given in Fig. 4. The values of n and U calculated using this method are $n = 2.37$ and $U = 1.01$ eV; they are close to the values given above.

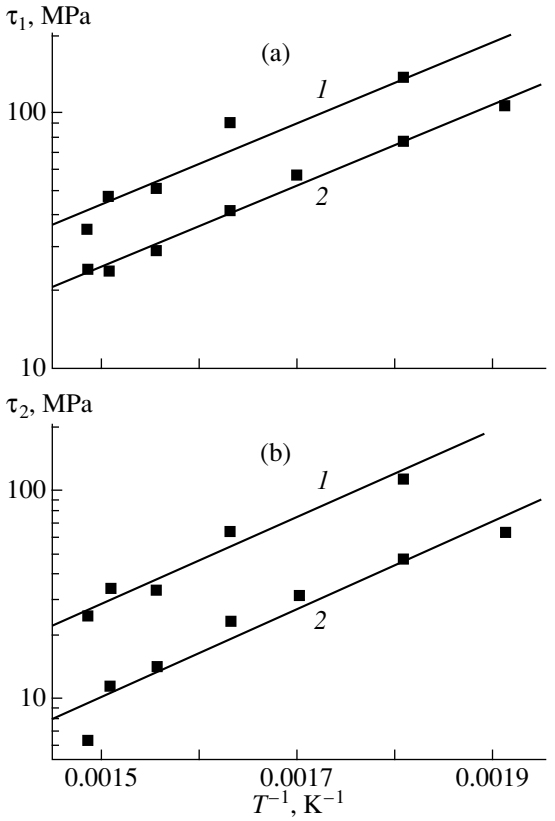

Fig. 3. Inverse-temperature dependences (a) of the stresses corresponding to the transition from the hardening to the softening stage and (b) of the flow stresses for $\gamma = 10$ at strain rates of (*1*) 10^{-1} and (*2*) 10^{-2} s^{-1}.

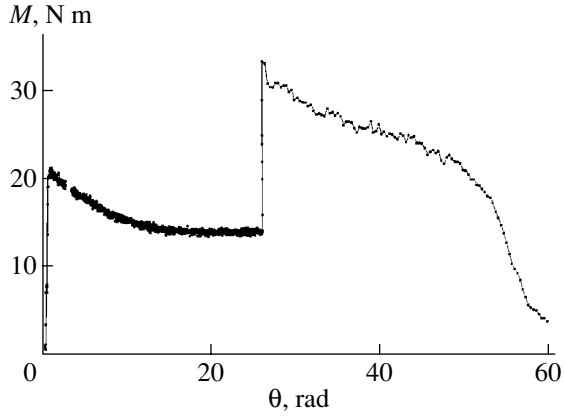

Fig. 4. Torsion diagram. At $\theta = 27$ rad, the strain rate increases jumpwise from 0.0322 to 0.322 rad/s. $T = 643$ K.

4. CONCLUSIONS

Thus, we showed in this work that samples of the Al–Li alloy subjected to ECAP exhibit superplasticity

under torsion at elevated temperatures. The torsion diagrams exhibit a short hardening stage followed by a softening stage where the inner layers of a sample rather than the peripheral layers are maximally stressed. A comparison with the tensile-test data for samples with the same structure shows that the shear strains achieved under torsion are higher than those achieved under tension. The superplasticity range as detected under torsion shifts toward low temperatures. It should be noted that the stresses required for reaching the limiting strains under torsion are higher than the corresponding stresses for tension. As for the mechanism of superplastic deformation, it is likely the same for deformation by tension and torsion.

ACKNOWLEDGMENTS

This work was supported in part by the Russian Foundation for Basic Research (project nos. 01-02-16505, 02-02-81021) and the Ministry of Industry, Science, and Technologies of the Russian Federation (the program "Solid-State Nanostructures").

REFERENCES

1. A. V. Sergueeva, V. V. Stolyarov, R. Z. Valiev, and A. K. Mukherjee, Scr. Mater. **43** (9), 819 (2000).
2. A. M. Shammazov, N. K. Tsenev, R. Z. Valiev, *et al.*, Fiz. Met. Metalloved. **89** (3), 107 (2000).
3. Z. Horita, M. Furukawa, M. Nemoto, *et al.*, Acta Mater. **48** (14), 3633 (2000).
4. M. M. Myshlyaev, M. A. Prokunin, and V. V. Shpeĭzman, Fiz. Tverd. Tela (St. Petersburg) **43** (5), 833 (2001) [Phys. Solid State **43**, 865 (2001)].
5. M. M. Myshlyaev, V. V. Shpeĭzman, and M. M. Kamalov, Fiz. Tverd. Tela (St. Petersburg) **43** (11), 2015 (2001) [Phys. Solid State **43**, 2099 (2001)].
6. K. Neishi, Z. Horita, and T. G. Langdon, Scr. Mater. **45** (8), 965 (2001).
7. V. A. Stepanov and V. V. Shpeĭzman, in *Thermal Stability of Metals and Construction Elements* (Naukova Dumka, Kiev, 1969), p. 82.
8. G. V. Vladimirova, V. A. Likhachev, M. M. Myshlyaev, and S. S. Olevskiĭ, Fiz. Met. Metalloved. **31** (2), 177 (1971).
9. A. N. Orlov, V. A. Stepanov, and V. V. Shpeĭzman, in *Physics of Metals and Physical Metallurgy* (LPI, Leningrad, 1975), No. 341, p. 3.
10. V. A. Likhachev, M. M. Myshlyaev, and O. N. Sen'kov, *Laws of the Superplastic Behavior of Aluminum in Torsion* (Lawrence Livermore National Laboratory, Livermore, 1987), p. 45.
11. M. M. Myshlyaev, M. M. Kamalov, M. A. Prokunin, and M. M. Myshlyaeva, Metally, No. 1, 99 (2003).
12. M. Furukava, Y. Iwahashi, Z. Horita, *et al.*, Mater. Sci. Eng. A **257**, 328 (1998).
13. A. Nadai, *Theory of Flow and Fracture of Solids* (McGraw-Hill, New York, 1950; Inostrannaya Literatura, Moscow, 1954).
14. J. H. Pointing, Proc. R. Soc. London **86**, 534 (1912).
15. J. Friedel, *Dislocations* (Pergamon Press, Oxford, 1964; Mir, Moscow, 1967).
16. J. Weertman and J. R. Weertman, in *Physical Metallurgy*, Ed. by R. W. Cahn (North-Holland, Amsterdam, 1965; Mir, Moscow, 1968), Chap. 16.

Translated by K. Shakhlevich

Physics of the Solid State, Vol. 45, No. 11, 2003, pp. 2115–2118. Translated from Fizika Tverdogo Tela, Vol. 45, No. 11, 2003, pp. 2013–2016.

DEFECTS, DISLOCATIONS, AND PHYSICS OF STRENGTH

Effect of Point Defect Concentration in NaCl and LiF Crystals on the Saturation Field of the Magnetoplastic Effect

E. V. Darinskaya* and E. Hartmann**

** Shubnikov Institute of Crystallography, Russian Academy of Sciences, Leninskiĭ pr. 59, Moscow, 119333 Russia*
e-mail: darin@ns.crys.ras.ru

*** Research Institute for Solid State Physics and Optics, Hungarian Academy of Sciences, Budapest XII, H-1121 Hungary*

Received April 14, 2003

Abstract—The effect is studied of the calcium impurity concentration in NaCl crystals and of preliminary x-ray irradiation of NaCl and LiF crystals on the magnetic saturation field B_0 characterizing the transition from the conventional proportionality of the dislocation mean path length l to the magnetic induction B squared ($l \propto B^2$) to saturation (l = const). B_0 is shown to increase with the calcium concentration in NaCl crystals and with the dose of x-ray irradiation of NaCl and LiF. This finding indicates that the dislocation breakaway from local defects in weak magnetic fields is controlled by the mechanism of longitudinal spin relaxation in a system of radical pairs that form due to interaction between dislocation cores and paramagnetic centers. © *2003 MAIK "Nauka/Interperiodica".*

The magnetoplastic effect (MPE), detected as the motion of dislocations in NaCl crystals in a static magnetic field in the absence of a mechanical load [1], has been studied in detail on a number of alkali-halide crystals, nonmagnetic metals, and semiconductors in the last decade [2–6]. Moreover, the effect of a magnetic field on the macroscopic characteristics (yield strength, microhardness, internal friction, creep rate) of nonmagnetic crystals has also been studied [7–12]. The experimental data obtained indicate that an applied magnetic field creates conditions for the breakaway of dislocations from local defects either by changing the spin state of the dislocation–paramagnetic center system [3, 13, 14] or by modifying the structure of point defects in a crystal [4, 15, 16]. The first effect is more universal and is observed in both annealed and quenched crystals. The direct effect of a magnetic field on the restructuring of impurity centers requires an initial nonequilibrium structure of these centers and is detected only on quenched crystals. Hereafter, we will discuss effects of only the first type, i.e., the case where a magnetic field directly affects the dislocation–impurity system and lifts the forbiddenness of certain electronic transitions in this system. As a result, a barrier for dislocation motion decreases or even vanishes. However, the total energy of the dislocation–paramagnetic center system remains virtually the same, since the spin-dependent transitions in question in a magnetic field do not require energy delivery to this system. A similar principle of spin selectivity is inherent to a set of phenomena related to the effect of weak magnetic fields on various chemical and physical processes [17, 18].

In [13], a transition from the conventional proportionality of the dislocation mean path length to the magnetic induction squared ($l \propto B^2$) to saturation (l = const) was observed when studying MPE in LiF crystals in relatively high magnetic fields. Experimental points [13] in the $l(B)$ curve were found to be described well by the dependence

$$l(B) \propto [(B_0/B)^2 + 1]^{-1}, \quad (1)$$

typical of the known mechanism of longitudinal spin relaxation in a system of radical pairs [19]. In Eq. (1), $B_0 = \hbar/\mu_B\tau_d$ is the saturation field (μ_B is the Bohr magneton) determined by the characteristic frequency τ_d^{-1} of natural oscillations of dislocation segments [1]. This frequency depends on the average length l_d of dislocation segments as $\tau_d^{-1} \sim c/l_d$ (c is the sound velocity) and can depend on the impurity concentration. Since an increase in the impurity concentration leads to a decrease in the average length of a dislocation segment and, hence, in the characteristic time τ_d, it was concluded in [13] that B_0 increases with the impurity concentration if the mechanism of longitudinal spin relaxation is actually predominant for the dislocation breakaway from a local obstacle in a magnetic field.

In this work, we study the effect of the calcium impurity concentration on the magnetic saturation field B_0 in NaCl crystals. Since x-ray irradiation creates additional magnetosensitive defects that change the MPE kinetics [20], we also studied the effect of preliminary x-ray irradiation of NaCl and LiF crystals on B_0.

For experiments, we used NaCl crystals of two types differing in calcium impurity concentration (NaCl-I with $C = 2 \times 10^{-5}$ wt % and NaCl-II with $C = 10^{-2}$ wt %) and having yield strengths τ_{y1} = 150 and τ_{y2} = 600 kPa,

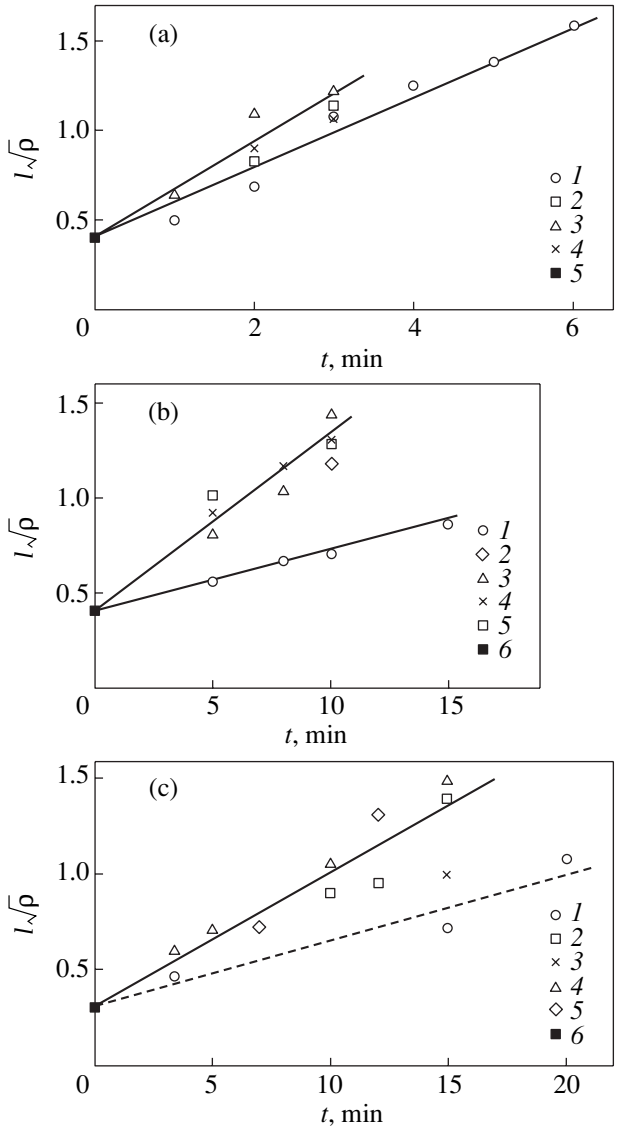

Fig. 1. Dependence of the normalized mean path length $l\sqrt{\rho}$ of dislocations on the time t of holding samples in a magnetic field at various values of induction B: (a) NaCl-I for (*1*) B = 0.5 [14], (*2*) 0.7, (*3*) 1, and (*4*) 1.4 T and (*5*) l_0; (b) NaCl-II for (*1*) B = 0.5, (*2*) 0.7, (*3*) 0.8, (*4*) 1, and (*5*) 1.4 T and (*6*) l_0; and (c) preliminary irradiated LiF for (*1*) B = 0.6, (*2*) 0.8, (*3*) 0.7, (*4*) 1, and (*5*) 1.2 T and (*6*) l_0.

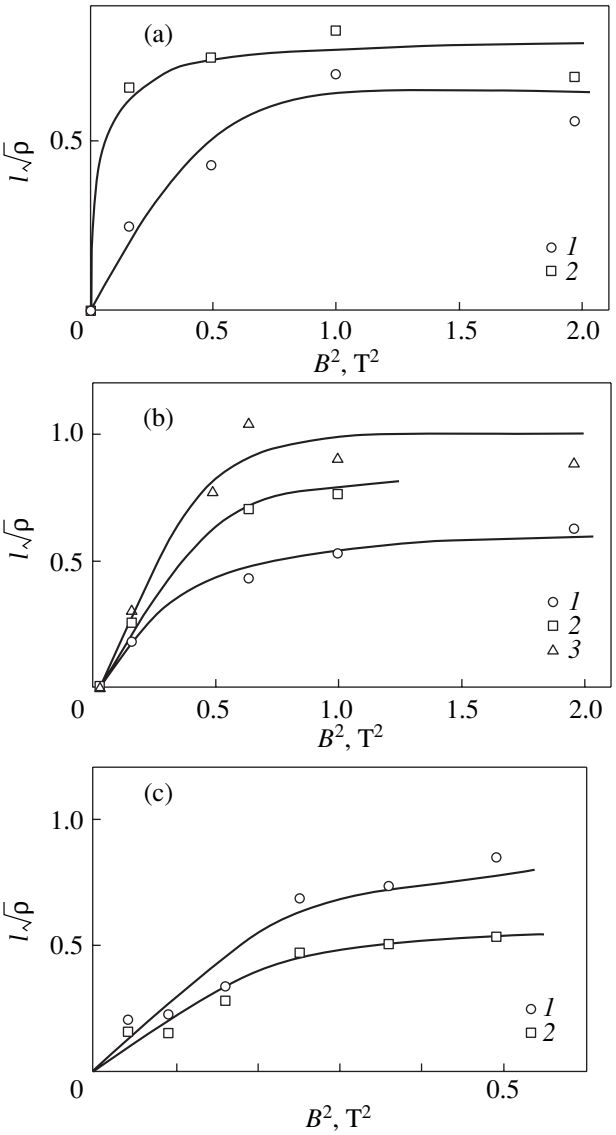

Fig. 2. Saturation of dislocation paths in high magnetic fields at various times of (a, b) magnetic treatment t and (c) preliminary x-ray irradiation t_{ir} of the NaCl crystals: (a) NaCl-I (t_{ir} = 0) for (*1*) t = 2 and (*2*) 3 min; (b) NaCl-II for (*1*) t = 5, (*2*) 8, and (*3*) 10 min; and (c) NaCl-I (t = 5 min) for (*1*) t_{ir} = 5 and (*2*) 10 s.

respectively. The concentration of other impurities was lower than 5×10^{-5} wt % [21]. Fresh dislocations of density $\rho_d \sim p$ were introduced into preliminarily annealed samples with a dislocation density of $\rho \sim 10^4$ cm^{-2} through impaction. Their initial positions were detected through selective etching of a crystal. Then, a sample was exposed to a static magnetic field B = (0.5–1.4) T for a time t = (1–15) min at room temperature without mechanical loading. After the magnetically induced breakaway from local defects, dislocations moved under the action of long-range internal stress fields created by other dislocations. The positions of dislocations after the magnetic treatment was determined by repeated selective etching. In this work, we studied the mobility of only edge dislocations, which provide more complete path histograms. We also studied LiF crystals (with a total impurity concentration lower than 10^{-4} wt %) belonging to the same series of nonirradiated samples as that studied in [13]; these crystals were preliminarily irradiated with x rays for 5 s. To analyze the effect of preliminary x-ray irradiation of the NaCl-I crystals on the magnetic saturation field B_0, we used the data from [20].

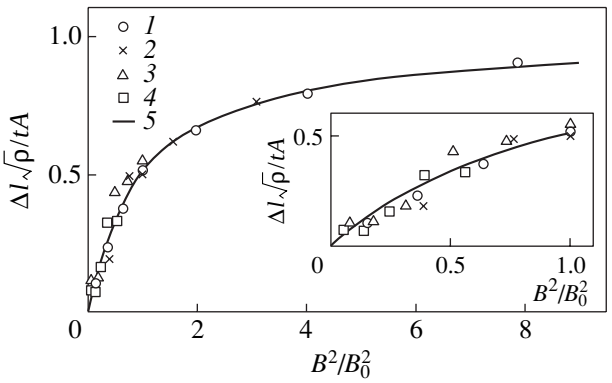

Fig. 3. Experimental data from Fig. 2 [replotted in the coordinates $\Delta l\sqrt{\rho}/At$ versus $(B/B_0)^2$] and the corresponding theoretical dependence $[(B_0/B)^2 + 1]^{-1}$ (solid curve *5*) for (*1*) NaCl-I, $B_0 = 0.5$ T, $A = 0.35$; (*2*) NaCl-II, $B_0 = 0.8$ T, $A = 0.16$; (*3*) NaCl-I, $t_{ir} = 5$ s, $B_0 = 0.7$ T, $A = 0.3$; and (*4*) NaCl-I, $t_{ir} = 10$ s, $B_0 = 0.8$ T, $A = 0.28$.

Figure 1 shows the dependence of the mean path length of edge dislocations l normalized to the average spacing of dislocations $1/\sqrt{\rho}$ [3, 22] on the magnetic-treatment time t at various values of B for the NaCl crystals (Figs. 1a, 1b) and for the preliminarily irradiated LiF crystals (Fig. 1c). The background mean path l_0 at $t = 0$ was determined by removing near-surface barriers with etching and was found to be independent of the experimental conditions. The slope of the linear $l(t)$ dependence is seen to be constant at rather high fields. The saturation of the mean path length with increasing magnetic field is most pronounced in Δl versus B^2 plots, where $\Delta l = l - l_0$ (Figs. 2a, 2b). Similar dependences were obtained for the NaCl-I crystals (Fig. 2c) preliminarily irradiated with x rays for 5 and 10 s and for the irradiated LiF samples. As in [13], the level of saturation decreases with decreasing magnetic-treatment time (Figs. 2a, 2b). Thus, the saturation level turns out to be independent of the geometric limit ($1/\sqrt{\rho} \approx 1.4$), which is characteristic of dislocation relaxation in alkali-halide crystals in an internal-stress field. Moreover, it is seen from Fig. 2c that an increase in the time of preliminary irradiation decreases the level mean-path saturation. The dependences obtained are similar to the experimental curves given in [1]. In Fig. 3, the experimental data from Fig. 2 are replotted in the coordinates $\Delta l\rho/At$ versus B^2/B_0^2 for four values of parameter A determined from the slopes of the linear dependence of the saturation level in Fig. 1. It is seen that these data are described well by the function $[(B_0/B)^2 + 1]^{-1}$ (see Eq. (1)) at B_0 lying in the range 0.5–0.8 T (solid line). An increase in the calcium concentration in the NaCl crystals from $C = 2 \times 10^{-5}$ to 10^{-2} wt % was found to increase B_0 by a factor of more than 1.5 ($B_0 = 0.5$ T for NaCl-I and 0.8 T for NaCl-II). The preliminary x-ray irradiation of the NaCl-I crystals for 5 s increases B_0 from 0.5 to 0.7 T, and that for 10 s, to 0.8 T. The same tendency is observed for the preliminarily irradiated LiF samples.

Thus, the prediction (made in [13]) that the magnetic saturation field B_0 increases with the impurity concentration in a crystal is confirmed, which further supports the hypothesis that the mechanism of longitudinal spin relaxation plays a decisive role in the process of dislocations breaking away from local defects in a magnetic field.

ACKNOWLEDGMENTS

We thank V.I. Al'shits for detailed discussion of the results and V.P. Kisel' for his assistance in preparing the samples. The NaCl (Ca) crystals were supplied by the Research Institute for Solid State Physics and Optics, Hungarian Academy of Sciences.

This work was supported in part by the Russian Academy of Sciences (6th Competition of Scientific Projects of Young Scientists), the Hungarian Scientific Research Foundation (OTKA T23092, T035044), and the Russian Foundation for Basic Research (project no. 03-02-17021).

REFERENCES

1. V. I. Al'shits, E. V. Darinskaya, T. M. Perekalina, and A. A. Urusovskaya, Fiz. Tverd. Tela (Leningrad) **29** (2), 467 (1987) [Sov. Phys. Solid State **29**, 265 (1987)].
2. V. I. Al'shits, E. V. Darinskaya, I. V. Gektina, and F. F. Lavrent'ev, Kristallografiya **35** (4), 1014 (1990) [Sov. Phys. Crystallogr. **35**, 597 (1990)].
3. V. I. Alshits, E. V. Darinskaya, O. L. Kazakova, *et al.*, Mater. Sci. Eng. A **234–236**, 617 (1997).
4. Yu. I. Golovin and R. B. Morgunov, Zh. Éksp. Teor. Fiz. **115** (2), 605 (1999) [JETP **88**, 332 (1999)].
5. E. V. Darinskaya, E. A. Petrzhik, S. A. Erofeeva, and V. P. Kisel', Pis'ma Zh. Éksp. Teor. Fiz. **70** (4), 298 (1999) [JETP Lett. **70**, 309 (1999)].
6. A. M. Orlov, A. A. Skvortsov, and A. A. Solov'ev, Zh. Éksp. Teor. Fiz. **123**, 590 (2003) [JETP **96**, 523 (2003)].
7. V. I. Al'shits, N. N. Bekkauer, A. S. Smirnov, and A. A. Urusovskaya, Zh. Éksp. Teor. Fiz. **115**, 951 (1999) [JETP **88**, 523 (1999)].
8. V. I. Al'shits, A. A. Urusovskaya, A. S. Smirnov, and N. N. Bekkauer, Fiz. Tverd. Tela (St. Petersburg) **42** (2), 270 (2000) [Phys. Solid State **42**, 277 (2000)].
9. N. A. Tyapunina, V. L. Krasnikov, and É. P. Belozerova, Izv. Ross. Akad. Nauk, Ser. Fiz. **64** (9), 1776 (2000).
10. O. I. Datsko, Fiz. Tverd. Tela (St. Petersburg) **44** (2), 289 (2002) [Phys. Solid State **44**, 300 (2002)].
11. Yu. A. Osip'yan, Yu. I. Golovin, R. B. Morgunov, *et al.*, Fiz. Tverd. Tela (St. Petersburg) **43** (7), 1333 (2001) [Phys. Solid State **43**, 1389 (2001)].
12. B. I. Smirnov, N. N. Peschanskaya, and V. I. Nikolaev, Fiz. Tverd. Tela (St. Petersburg) **43** (12), 2154 (2001) [Phys. Solid State **43**, 2250 (2001)].

13. V. I. Al'shits and E. V. Darinskaya, Pis'ma Zh. Éksp. Teor. Fiz. **70** (11), 749 (1999) [JETP Lett. **70**, 761 (1999)].
14. V. I. Al'shits, E. V. Darinskaya, O. L. Kazakova, *et al.*, Pis'ma Zh. Éksp. Teor. Fiz. **63** (8), 628 (1996) [JETP Lett. **63**, 668 (1996)].
15. Yu. I. Golovin, R. B. Morgunov, V. E. Ivanov, *et al.*, Pis'ma Zh. Éksp. Teor. Fiz. **68** (5), 400 (1998) [JETP Lett. **68**, 426 (1998)].
16. R. B. Morgunov and A. A. Baskakov, Fiz. Tverd. Tela (St. Petersburg) **43** (9), 1632 (2001) [Phys. Solid State **43**, 1700 (2001)]; Fiz. Tverd. Tela (St. Petersburg) **45** (1), 91 (2003) [Phys. Solid State **45**, 94 (2003)].
17. Ya. B. Zel'dovich, A. L. Buchachenko, and E. L. Frankevich, Usp. Fiz. Nauk **155** (1), 3 (1988) [Sov. Phys. Usp. **31**, 385 (1988)].
18. A. L. Buchachenko, R. Z. Sagdeev, and K. M. Salikhov, *Magnetic and Spin Effects in Chemical Reactions* (Nauka, Novosibirsk, 1978).
19. B. Brocklehurst, Nature **221**, 921 (1969).
20. V. I. Al'shits, E. V. Darinskaya, and O. L. Kazakova, Zh. Éksp. Teor. Fiz. **111** (2), 615 (1997) [JETP **84**, 338 (1997)].
21. A. A. Urusovskaya, E. V. Darinskaya, R. Voszka, and J. Jansky, Cryst. Res. Technol. **16** (5), 597 (1981).
22. V. I. Al'shits, E. V. Darinskaya, and M. V. Koldaeva, Fiz. Tverd. Tela (St. Petersburg) **43** (9), 1635 (2001) [Phys. Solid State **43**, 1703 (2001)].

Translated by K. Shakhlevich

Physics of the Solid State, Vol. 45, No. 11, 2003, pp. 2119–2123. Translated from Fizika Tverdogo Tela, Vol. 45, No. 11, 2003, pp. 2017–2021.

DEFECTS, DISLOCATIONS, AND PHYSICS OF STRENGTH

Recovery of Young's Modulus upon Annealing of Nanostructured Niobium Produced through Severe Plastic Deformation

Yu. A. Burenkov*, S. P. Nikanorov*, B. I. Smirnov*, and V. I. Kopylov**

** Ioffe Physicotechnical Institute, Russian Academy of Sciences, Politekhnicheskaya ul. 26, St. Petersburg, 194021 Russia*
e-mail: smir.bi@mail.ioffe.ru

*** Physicotechnical Institute, Belarussian Academy of Sciences, ul. Tskhodinskaya 4, Minsk, 220730 Belarus*

Received April 24, 2003

Abstract—The effect of temperature (in the range 20–500°C) on the Young's modulus of nanostructured niobium with Ta impurity content <0.5 wt % and that of O_2 < 0.1 wt % and with a mean grain size of ≅200 nm is studied. The transformation of polycrystalline niobium into a nanostructured state is performed through severe plastic deformation by equal-channel angular pressing. The Young's modulus is found to increase in two stages as the temperature of isothermal annealing is gradually increased. The mechanisms of recovery of the elastic modulus upon annealing of the nanostructured niobium are discussed in the context of the modern concepts of the defect structure of deformed metals. © *2003 MAIK "Nauka/Interperiodica".*

1. INTRODUCTION

Nanostructured materials are of great interest from both scientific and applied viewpoints owing to their unique physical-mechanical properties and microstructural features [1–4]. Such materials have been studied extensively over the past decade. A number of methods for producing nanostructured materials have been developed [4]. To produce bulky pore-free materials with a superfine-grained structure, severe plastic simple-shear deformation during equal-channel angular pressing (ECAP) is widely applied [5]. This treatment allows one to refine a polycrystalline structure to nanograins. It is well known [6] that plastic deformation leads to a considerable decrease in the elastic moduli of materials as a result of weakening of interatomic bonds in a crystal lattice due to structural distortions and an increase in the specific volume of a material. This decrease in the elastic moduli is maximum in pure materials (Al, Cu) and low alloys [7, 8].

In this work, we study the effect of temperature and isothermal annealing on the Young's modulus of nanostructured niobium (NS-Nb). The results obtained are used to discuss the possible mechanisms of recovery of the Young's modulus E upon annealing of NS-Nb to the values characteristic of coarse-grained Nb.

2. EXPERIMENTAL

The initial 22 × 22 × 160-mm NS-Nb bar was produced through ECAP of polycrystalline coarse-grained Nb having an impurity content of Ta < 0.5 wt % and of O_2 < 0.1 wt % subjected to electron-beam remelting. The essence of ECAP consists in multiple pushing of a bulk workpiece through two orthogonally intersecting channels of the same cross section; in the plane of intersection of these channels, a uniform high-intensity simple-shear deformation is concentrated [5]. This method provides a uniform deformation of the whole volume of a workpiece and virtually pore-free samples. High internal stresses that appear during severe plastic deformation of Nb relax through the formation and movement of point defects and excess dislocations, which results in restructuring into a superfine-grained state. During such plastic deformation, when a structure is strongly refined, the sizes of fragments and blocks decrease and their misorientation with respect to each other increases to form boundaries with a strongly distorted crystal lattice. Electron microscopic examinations showed that a nanostructure with a mean grain size $d \cong 200$ nm uniformly distributed over the whole cross section forms in Nb after ECAP.

Samples in the form of 3 × 3 × 15-mm bars were spark-cut from the initial bar. To estimate possible anisotropy in the elastic modulus because of a crystallographic texture appearing upon severe plastic deformation, the Young's modulus was measured on samples cut along three mutually perpendicular spatial directions, namely, (I) along the direction of the first channel, (II) along the axis of turning the channels, and (III) along the direction of the second channel.

The Young's modulus was determined using a resonance method in which longitudinal elastic vibrations of a sample were excited electrostatically; the modulus was calculated from the formula $E = 4\rho l^2 f^2 n^{-2}/(1 + \Delta l/l)$, where ρ is the material density, l is the sample length, f is the resonance frequency of longitudinal

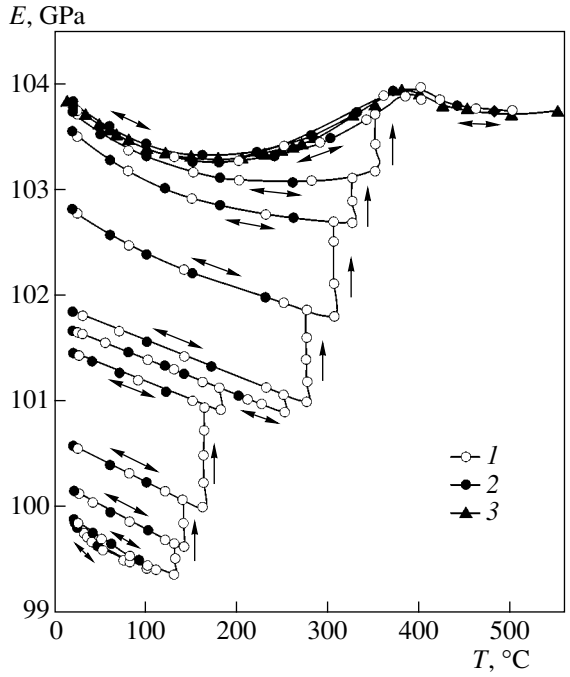

Fig. 1. Temperature dependences of the Young's modulus measured in the course of sequential thermal heating–annealing cycles for 2 h at each temperature T_a followed by cooling for an NS-Nb sample cut along direction II: (*1*) heating, (*2*) cooling, and (*3*) data on $E(T)$ for coarse-grained niobium taken from [16].

vibrations of the sample, n is the index of the excited harmonic ($n = 1$ in our case), and Δl is the temperature-induced elongation of the sample [9]. The density of the samples was measured at room temperature by hydrostatic weighing. Direct measurements showed that the density of the NS samples was identical to that of coarse-grained undeformed Nb (8.57 g/cm^3). The resonance frequencies of longitudinal vibrations of the samples were 117–129 kHz.

We performed the experiments at $T = 20$–500°C. To improve heat exchange, the furnace containing a sample was located in a chamber filled with gaseous helium. At temperatures above 300°C, measurements were carried out in vacuum. The heating and cooling rates were about 2 K/min. Each experimental point in the $E(T)$ dependences was measured after the temperature in the chamber was stabilized. The data on the thermal expansion of Nb were taken from [10]. The grain sizes of samples annealed at various temperatures T_a were measured, using the linear intercept method, from micrographs taken with electron ($T_a < 250$°C) and optical ($T_a > 250$°C) microscopes.

3. RESULTS AND DISCUSSION

Measurements at room temperature show that the Young's modulus of the NS-Nb samples depends on the direction of their cutting from the deformed bar: $E_{\mathrm{I}} = 98.6 \pm 0.3$, $E_{\mathrm{II}} = 99.8 \pm 0.1$, and $E_{\mathrm{III}} = 101.4 \pm 0.3$ GPa. Small differences in the absolute values of E measured along the different directions of propagating ultrasound are likely due to a deformation texture. The Young's modulus of the samples of undeformed coarse-grained Nb cut along direction II was found to be 103.8 ± 0.1 GPa at 20°C. Hence, the contribution of the defect structure of the deformed Nb to the Young's modulus is about 4%.

This change in the Young's modulus is caused by a specific atomically disordered structure, which forms during severe plastic deformation and is characterized by imperfect nonequilibrium grain boundaries [11]. The structure and properties of grain boundaries under nonequilibrium conditions differ substantially from those of ordinary grain boundaries with a low-energy structure. According to a structural model of nanomaterials [4], nonequilibrium boundaries, unlike ordinary equilibrium high-angle boundaries, have long-range elastic fields of internal stresses and a high energy due to the high density of various defects (vacancies, interstitial atoms, randomly distributed ensembles of dislocations and disclinations) introduced into these boundaries during the formation of a nanostructure. The experimentally detected decrease in the elastic modulus of the NS-Nb as compared to the ordinary coarse-grained Nb is caused by two factors. One of them is a high density of excess vacancies pinned by impurity atoms. Pinning is possible when a metal contains at least an insignificant amount (up to 0.1 wt %) of impurity atoms, which can trap vacancies and decrease their mobility [12]. The other factor is related to the process of dislocation redistribution and multiplication in grain boundaries. The dislocation density in grain boundaries can be as high as 10^{12} cm^{-2} for severe plastic deformation, although a relatively low dislocation density (10^8 cm^{-2}, which is characteristic of ordinary, well-annealed, coarse-grained polycrystals) or even an absence of dislocations is observed in the bulk of grains [5, 13, 14]. The latter is caused by dislocations climbing from the bulk of grains to their boundaries, i.e., by their flowing to intergrain regions. The main contribution to the decrease in the Young's modulus of NS-Nb at room temperature is brought about by the second factor, i.e., by the motion of grain-boundary dislocations in the field of mechanical stresses induced by the sound wave. The dynamics of grain-boundary defects resulting in a decrease in the elastic moduli of severely deformed metals is considered in [15].

Nonequilibrium grain boundaries also exert a significant effect on the behavior of materials upon annealing, in particular, on the recovery of their elastic moduli [4]. In this work, the $E(T)$ dependences of the NS-Nb samples were measured in the course of sequential experiments, including gradual heating to a certain temperature, annealing at this temperature for 2 h, and cooling at a constant rate to room temperature. The results obtained during the treatment of sample II in the

temperature range 20–500°C are given in Fig. 1. The elastic modulus is seen to decrease smoothly in the temperature range 20–100°C. The coincidence of the $E(T)$ curves measured upon heating and cooling indicates that we have a stable system in this temperature range. At $T > 100$°C and certain annealing temperatures T_a, E increases as a function of the holding time t. As an example, Fig. 2 shows the $E(t)$ dependence at T_a = 162°C. It can be seen that, during annealing, E first rapidly grows due to structural relaxation and then slowly increases to saturation. The main changes (80%), followed by saturation, occur in 1 h.

After annealing at various T_a in the range 100–350°C, temperature hysteresis of the elastic modulus (i.e., a difference between the $E(T)$ curves recorded upon heating and upon cooling) is observed. The $E(T)$ dependences measured upon cooling after annealing lie above the heating curves and are stable. At the same time, annealing at $T_a \geq 350$°C results in the shape of the $E(T)$ dependence upon cooling becoming similar to that observed for the coarse-grained Nb [16], with the character of the $E(T)$ dependences remaining unchanged during repeated thermal heating–annealing–cooling cycles (the direct and reverse curves coincide). It is notable that a weak and unusual T dependence of E was observed after annealing in the temperature range studied. For the coarse-grained Nb, a small change in E and unusual behavior of $E(T)$ were observed up to 1000°C [16].

Figure 3 shows the relative change in the Young's modulus of the NS-Nb measured at room temperature after each annealing as a function of T_a. Data are given for a large number of measurements performed on the samples cut along directions I, II, and III. The sample with orientation II was studied in detail. According to these results, five stages can be distinguished in the T_a dependence of $\Delta E/E_0$: (1) $20 < T_a < 100$°C, with the modulus E constant; (2) $100 < T_a < 175$°C, with E increasing; (3) $175 < T_a < 240$°C, with E almost independent of T_a; (4) $240 < T_a < 320$°C, with E sharply increasing; and (5) $320 < T_a < 500$°C, with E only weakly dependent on T_a. The dependences of $\Delta E/E_0$ on T_a obtained for different samples demonstrate good agreement. The recovery of the modulus E of the NS-Nb upon annealing is seen to proceed in stages for all directions of ultrasound propagation.

Figure 4 illustrates the dependence of the mean grain size d in the NS-Nb on the temperature of two-hour annealing. As is seen, annealing at temperatures below 100°C does not affect d. A further increase in T_a results in significant grain growth, with the grain size increasing exponentially with temperature. A similar $d(T_a)$ dependence for NS-Cu was observed in [7]. Thus, in the initial stage of annealing (stage 1), no considerable changes are detected in the Young's modulus and grain size of the NS-Nb.

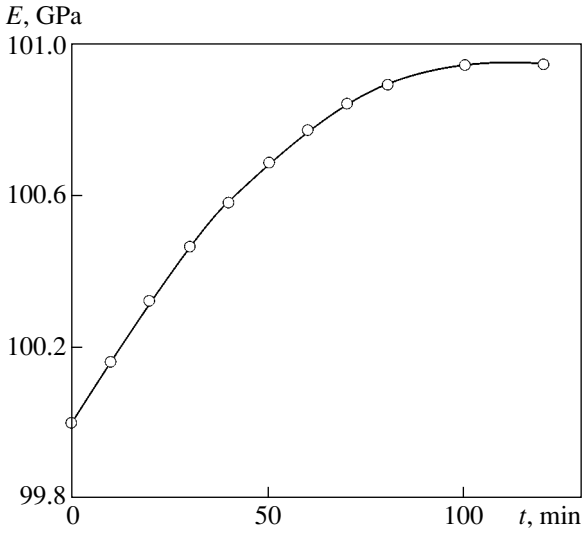

Fig. 2. Typical dependence of the Young's modulus on the time of isothermal annealing. NS-Nb sample with orientation II. T_a = 162°C.

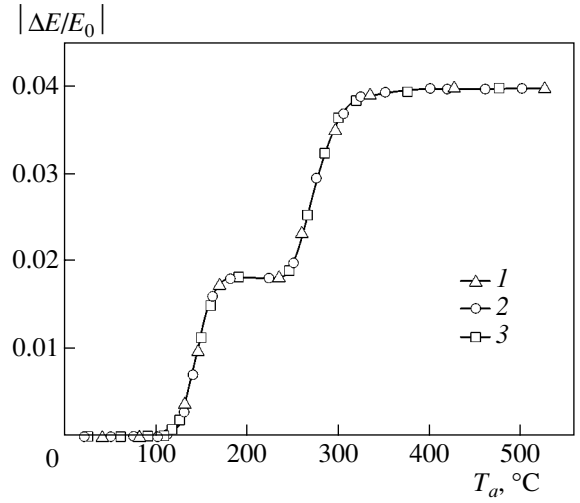

Fig. 3. Relative change in the Young's modulus measured at room temperature as a function of the annealing temperature for NS-Nb samples with various orientations: (*1*) I, (*2*) II, and (*3*) III. E_0 is the value of E before annealing for samples of the corresponding directions.

In stage 2, the Young's modulus increases sharply and grains start to grow, which indicates substantial structural changes in the samples. Such an increase in E upon annealing can be due to a combination of several relaxation processes occurring in the defect structure of the samples. In particular, the breakaway of vacancies from impurity atoms, especially from atoms of dissolved oxygen (which is always present in Nb), occurs. This is the so-called vacancy recovery or the "purification" of vacancies from impurities. As a result, beginning from a certain critical temperature, the impurities precipitate and are accumulated at dislocations, thereby

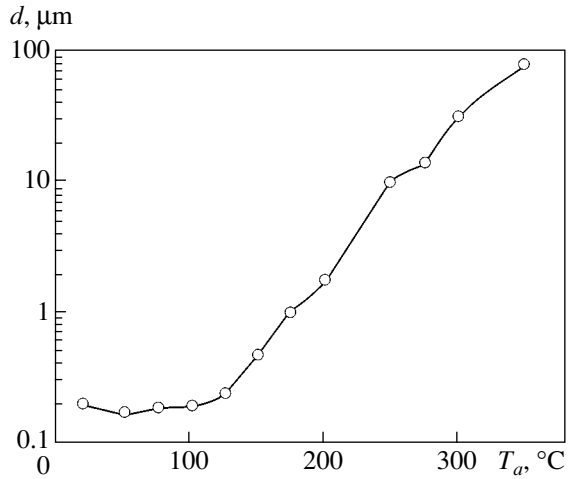

Fig. 4. Dependence of the mean grain size in samples of deformed Nb cut along direction II on the temperature of two-hour annealing.

pinning them and hindering their motion. Firstov and Sarzhan [11] showed that the modulus defect in severely deformed metals could change by 1% because of mobile-dislocation pinning (blocking) as a result of the breakaway of vacancies from impurity atoms at a vacancy concentration of 10^{-14} per atom. The kinetics of annealing of ensembles of grain-boundary dislocations introduced into nanostructured materials is described in [17]. Annealing also leads to transformation of the grain-boundary structure; the structure of nonequilibrium grain boundaries is rearranged to reach a more equilibrium state, and the density of introduced dislocations decreases gradually. These processes are related to the development of primary recrystallization, which decreases the level of internal stresses, changes the grain sizes and the character of grain boundaries, and removes most lattice distortions. The fraction of regions with coarser grains increases to yield a structure with a mean grain size d = 0.3–0.9 μm. Grain growth at relatively low temperatures has been detected in many nanostructured materials [4, 7]. During recrystallization, a structure with a minimum amount of defects forms, which results in a significant decrease in the total density of mobile dislocations and favors an increase in E. The total increase in E in stage 2 is about 1.8%.

Annealing of the samples in stage 3 virtually does not increase E; however, the mean grain size increases to 6 μm. Such a considerable increase in d leads to a decrease in the volume fraction of the grain-boundary phase and is likely the main cause of the constancy of E at this stage.

In stage 4, an increase in T_a again results in a rapid increase in E by about 2%. It is known [3, 7, 18] that, as NS metals are annealed at T_a values above the temperature of primary recrystallization, d still increases rapidly, the volume fraction of boundaries drops, and their structure is transformed. As follows from Fig. 4, d = 6–40 μm in this temperature range; that is, regions with fine grains completely disappear. The processes of secondary recrystallization begin to operate. At this stage, the grain boundary structure is close to equilibrium. After the dislocation density has decreased to its ordinary level (and become virtually constant), the main factor that specifies changes in E becomes the mean free path of lattice dislocations controlled by interaction between dislocations and impurity atoms. An increase in E could also result from changes in the texture of the samples. However, it can be seen from Fig. 3 that, after annealing, the values of $\Delta E/E_0$ are the same for samples with different orientations. Hence, the texture of the NS-Nb samples prepared through ECAP does not change upon annealing.

In stage 5, at $T_a > 350$°C, the Young's modulus is completely recovered to the level corresponding to the undeformed state. The defects disappear, thus removing the majority of lattice distortions. Upon annealing of the NS-Nb in all stages, the total modulus defect is about 4%. The variation of the structural state during annealing at temperatures up to T_a = 500°C is not accompanied by a noticeable change in the density of the samples measured at room temperature.

A multistage process of the irreversible recovery of the Young's modulus was also observed upon annealing of NS-Cu [7], but it started at higher temperatures T_a than in the case of the NS-Nb. The differences found can be caused by a smaller impurity content in the case of niobium or a higher deformation energy stored because of a higher pressure being applied during severe plastic deformation. The authors of [7, 19] also detected different values of the Young's modulus when NS-Cu samples were cooled after annealing at various fixed temperatures, which meant that they observed the memory effect with respect to the value of the modulus E in the preceding structural state. In the case of the NS-Nb, no Young's modulus memory effect was detected.

4. CONCLUSIONS

Thus, the experimental data obtained by us indicate that, when niobium is transformed into a nanostructured state, its Young's modulus decreases and recovers upon heating and subsequent isothermal anneals at temperatures up to 350°C. The main recovery of the elastic modulus proceeds in two stages. The dominant mechanism of the variation of the modulus upon heating of the NS-Nb samples is irreversible structural relaxation in the bulk of the metal, which decreases the internal stresses, changes the grain sizes, transforms nonequilibrium grain boundaries into equilibrium ones, and results in a gradual removal of lattice defects.

ACKNOWLEDGMENTS

This work was supported by the Ministry of Industry, Science, and Technology of the Russian Federation (program "Solid-State Nanostructures").

REFERENCES

1. V. G. Gryaznov and L. I. Trusov, Prog. Mater. Sci. **37** (4), 289 (1993).
2. H. Gleiter, Nanostruct. Mater. **6** (1–4), 3 (1995).
3. K. Lu, Mater. Sci. Eng. R **16** (4), 161 (1996).
4. R. Z. Valiev and I. V. Aleksandrov, *Nanostructure Materials Produced through Intensive Plastic Deformation* (Logos, Moscow, 2000).
5. V. M. Segal, V. I. Reznikov, V. I. Kopylov, D. A. Pavlic, and V. F. Malyshev, *Processes of Plastic Structural Transformation of Metals* (Nauka i Tekhnika, Minsk, 1994).
6. S. A. Golovin, A. Pushkar, and D. M. Levin, *Elastic and Damping Properties of Construction Metal Materials* (Metallurgiya, Moscow, 1987).
7. A. B. Lebedev, Yu. A. Burenkov, V. I. Kopylov, *et al.*, Fiz. Tverd. Tela (St. Petersburg) **38** (6), 1775 (1996) [Phys. Solid State **38**, 978 (1996)].
8. A. B. Lebedev, Yu. A. Burenkov, S. A. Pul'nev, *et al.*, Izv. Ross. Akad. Nauk, Ser. Fiz. **64** (2), 381 (2000).
9. Yu. A. Burenkov, S. P. Nikanorov, and A. V. Stepanov, Izv. Akad. Nauk SSSR, Ser. Fiz. **35** (3), 525 (1971).
10. S. I. Novikova, *Thermal Expansion of Solids* (Nauka, Moscow, 1974).
11. S. A. Firstov and G. F. Sarzhan, Izv. Vyssh. Uchebn. Zaved., Fiz. **34** (3), 23 (1991).
12. H. Dinel, in *Internal-Friction Mechanisms in Solids* (Nauka, Moscow, 1976), p. 11.
13. H. Conrad, in *Ultrafine Grain in Metals* (Syracuse Univ. Press, Syracuse, New York, 1970; Metallurgiya, Moscow, 1973).
14. C. Y. Barlow, B. Bay, and N. Hansen, Philos. Mag. A **51** (2), 253 (1985).
15. A. A. Nazarov, A. E. Romanov, and R. Z. Valiev, Acta Metall. Mater. **41** (4), 1033 (1993).
16. Yu. A. Burenkov, Zh. Tekh. Fiz. **73** (5), 94 (2003) [Tech. Phys. **48**, 616 (2003)].
17. A. A. Nazarov, in *Structure, Phase Transformations, and Properties of Nanocrystalline Alloys*, Ed. by G. G. Taluts and N. I. Noskova (Ural. Otd. Ross. Akad. Nauk, Yekaterinburg, 1997), pp. 70–79.
18. L. C. Chen and F. Spaepen, Nanostruct. Mater. **1** (1), 59 (1992).
19. A. B. Lebedev, Yu. A. Burenkov, V. I. Kopylov, *et al.*, Philos. Mag. Lett. **73** (5), 241 (1996).

Translated by K. Shakhlevich

Physics of the Solid State, Vol. 45, No. 11, 2003, pp. 2124–2127. Translated from Fizika Tverdogo Tela, Vol. 45, No. 11, 2003, pp. 2022–2024.

MAGNETISM AND FERROELECTRICITY

On the Local Magnetization Reversal in Front of a Domain Wall Moving in a Garnet Ferrite Film with Orthorhombic Magnetic Anisotropy

V. V. Randoshkin

Joint Laboratory of Magneto-Optoelectronics, Institute of General Physics, Russian Academy of Sciences, Mordovian State University, Bol'shevistskaya ul. 68, Saransk, 430000 Russia

Received November 26, 2002

Abstract—The experimentally observed shapes of dynamic domains in garnet ferrite single-crystal films with (110) and (210) orientations are explained in terms of in-plane magnetic anisotropy of these films. © *2003 MAIK "Nauka/Interperiodica".*

1. INTRODUCTION

Telesnin *et al.* [1] performed an electron optical chronographic study of the collapse of bubble domains in ytterbium-containing garnet ferrite single-crystal films with the (111) orientation and revealed the threshold effect of a drastic increase in the differential domain-wall mobility in a portion (following the saturation portion) of the dependence of the domain-wall velocity V on the amplitude of the pulsed magnetic field H_p. Later, Martynov *et al.* [2] carried out high-speed photographic observations of dynamic domains in samarium-containing films and established that a similar portion in the $V(H_p)$ curve corresponds to a dynamic domain wall with a broader image. The observed broadening of the image of the moving domain wall was explained as resulting from the local rotation of magnetization in front of this wall [2].

Ivanov *et al.* [3] carried out high-speed photographic investigations of the dynamic expansion of both bubble and strip domains in thulium-containing garnet ferrite single-crystal films with the (111) orientation in a pulsed magnetic field H_p applied along the normal to the film and revealed the generation of the so-called magnetic perturbations. These perturbations brought about the formation of microdomains in front of a moving domain wall. As a result, the translational velocity of the region separating magnetic domains with a polarity opposite to the polarity of this region increased abruptly and a portion with an increased differential mobility appeared in the dependence $V(H_p)$ [4].

A similar effect was also observed upon the expansion of reversed domains during pulsed magnetization reversal of garnet ferrite single-crystal films of different compositions with the (111) orientation under the condition that the content of rapidly relaxing rare-earth ions was sufficiently low (the Gilbert damping parameter α is less than 0.15) [5].

Earlier [5], we made the assumption that the generation of microdomains in front of a moving domain wall can be initiated by spin waves induced by this wall. Khodenkov [6] theoretically considered this process and demonstrated that the radiation of spin waves at a pulsed magnetic field amplitude $H_p^* < H_p < H_p^{**}$, where

$$H_p^* \approx H_b + H_K/3, \tag{1}$$

$$H_p^{**} \approx H_b + 2H_K/3, \tag{2}$$

H_b is the constant magnetic bias field, and H_K is the field of uniaxial magnetic anisotropy.

For the path length of a spin wave, Khodenkov derived the following expression:

$$\lambda_{sw} \approx (2\pi\Delta_0/\alpha)(H_K/H)(3H/H_K - 1)^{1/2}, \tag{3}$$

where Δ_0 is the parameter characterizing the width of the domain wall and $H = H_p - H_b$ is the acting magnetic field.

The validity of relationship (1) was experimentally verified in [5]. It should be noted that, for nonuniform garnet ferrite single-crystal films, this relationship should involve the field H_K for a layer with a weak magnetic anisotropy; i.e., it is in this layer that the generation of microdomains starts. The validity of expression (2) was demonstrated using the example of a special garnet ferrite single-crystal film containing neither rapidly relaxing ions nor a layer with weak magnetic anisotropy [7].

In [8], it was established that application of a sufficiently strong in-plane magnetic field H_{in} suppresses the generation of microdomains in front of a moving domain wall. On this basis, it was concluded that the dimensionless damping parameter α is not a constant of the material but depends on the in-plane magnetic field H_{in} [8].

1063-7834/03/4511-2124$24.00

In my recent work [9], I inferred that spin waves induced by a moving domain wall initiate local rotations of the magnetization vectors in front of this wall. For small parameters α, these rotations look like the generation of microdomains. For large parameters α, they manifest themselves as a broadening of the domain-wall image. The presence of a portion with an increased differential mobility in the $V(H)$ curve is common to both processes.

The investigation into the dynamics of domain walls in $(Bi,Y,Lu)_3(Fe,Ga)_5O_{12}$ garnet ferrite single-crystal films with the (110) orientation demonstrated that, despite the absence of rapidly relaxing ions in the films, the generation of microdomains has never been observed in front of a moving domain wall [10]. However, the broadening of the image of the domain wall, which is nonuniform along the perimeter of the dynamic domain, is observed in these films and leads to the formation of diamond-shaped domains. The dynamic domains in garnet ferrite single-crystal films with the (210) orientation have a more complex shape [11, 12].

In [13], it was assumed that the orthorhombic magnetic anisotropy and an external in-plane magnetic field bring about an increase in the damping parameter α. In this case, both the threshold field of spin wave radiation and the damping parameter α depend on the direction of the domain-wall motion in the film plane.

The purpose of the present work was to explain qualitatively the main features of the formation of dynamic domains in garnet ferrite single-crystal films with orthorhombic magnetic anisotropy under the assumption made in [13].

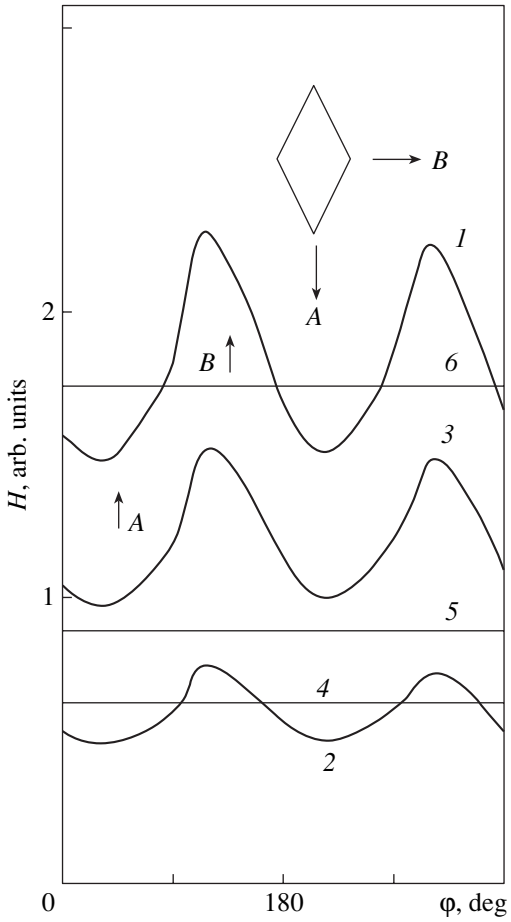

Fig. 1. Azimuthal dependences of (*1*) the saturation field H_s and threshold fields (*2*) H^* and (*3*) H^{**} in the range of acting magnetic fields with possible radiation of spin waves (in arbitrary units). Acting magnetic fields: (*4*) H_1, (*5*) H_2, and (*6*) H_3.

2. RESULTS AND DISCUSSION

For garnet ferrite single-crystal films with the (111) orientation, the weakest possible in-plane magnetic field, which is required to rotate the magnetization vector in the film plane (the saturation field H_s), is virtually entirely independent of the direction of this field and is close in magnitude to the field of uniaxial magnetic anisotropy H_K. Therefore, in relationships (1) and (2), the saturation field H_s can be substituted for the field H_K.

For garnet ferrite single-crystal films with orthorhombic magnetic anisotropy, the magnitude of the saturation field H_s depends on the direction in the film plane, which is specified by the azimuthal angle φ. As an example, Fig. 1 shows the azimuthal dependence of the saturation field $H_s(\varphi)$ (curve *1*), which is characteristic of $(Bi,Y,Lu)_3(Fe,Ga)_5O_{12}$ garnet ferrite single-crystal films with the (110) orientation. The orientation of the diamond-shaped domain in the film plane is also shown in Fig. 1. It should be noted that the longer axis of this domain is aligned with nearly the same direction along which the saturation field H_s is minimum in magnitude. It can also be seen from Fig. 1 that the maximum and minimum values of the saturation field H_s differ by a factor of approximately 1.5.

Unfortunately, to date, a theory of spin wave radiation induced by a moving domain wall in films with orthorhombic magnetic anisotropy has not been developed. Under the assumption that relationships (1) and (2) change insignificantly with the inclusion of the orthorhombic magnetic anisotropy, they can be rewritten in the form

$$H^*(\varphi) \approx H_s(\varphi)/3, \quad (4)$$

$$H^{**}(\varphi) \approx 2H_s(\varphi)/3. \quad (5)$$

The azimuthal dependences of the threshold fields $H^*(\varphi)$ and $H^{**}(\varphi)$ are depicted in Fig. 1 (curves *2* and *3*, respectively). The set of (φ, H) values bounded by these curves corresponds to conditions at which a moving domain wall induces spin waves. Specifically, for a magnetic field $H = H_1$ (Fig. 1, straight line *4*), spin wave radiation is possible in two ranges of angles $\varphi = -21°$–$97°$ and $161°$–$276°$. This situation takes place with a

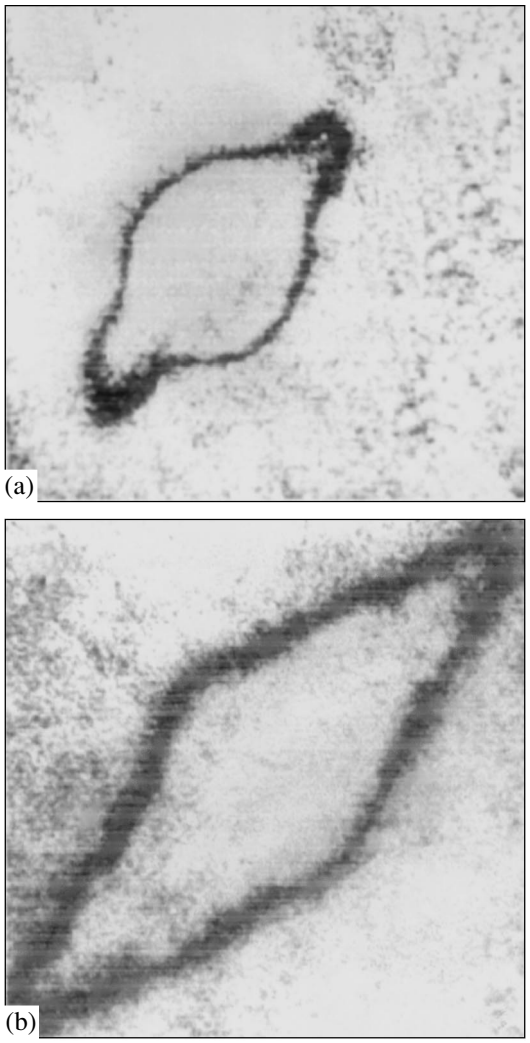

Fig. 2. Dynamic domains in the $(Bi,Y,Lu)_3(Fe,Ga)_5O_{12}$ garnet ferrite single-crystal film with the (110) orientation in acting magnetic fields (a) $H = H_1$ and (b) $H = H_2 > H_1$.

dynamic domain for which local rotation of the magnetization in the vicinity of the domain wall occurs at opposite ends (Fig. 2a). At $H = H_2$ (Fig. 1, straight line *5*), spin waves can be induced at all angles φ, i.e., along the whole perimeter of the dynamic domain (Fig. 2b). This situation becomes possible when the anisotropy in the film plane is insufficiently strong.

For a magnetic field $H = H_2$ (Fig. 1, straight line *6*), spin wave radiation is impossible at all angles φ. However, in the ranges φ = –4°–41° and 88°–132°, there exist two regions in which the film undergoes magnetization reversal due to irregular rotation of the magnetization. A similar situation was observed in the experiments performed with the use of $(Bi,Y,Gd,Yb)_3(Fe,Ga)_5O_{12}$ garnet ferrite single-crystal films with the (110) orientation [14].

Figure 3 shows the azimuthal dependence of the saturation field $H_s(\varphi)$ (curve *1*), which is characteristic of

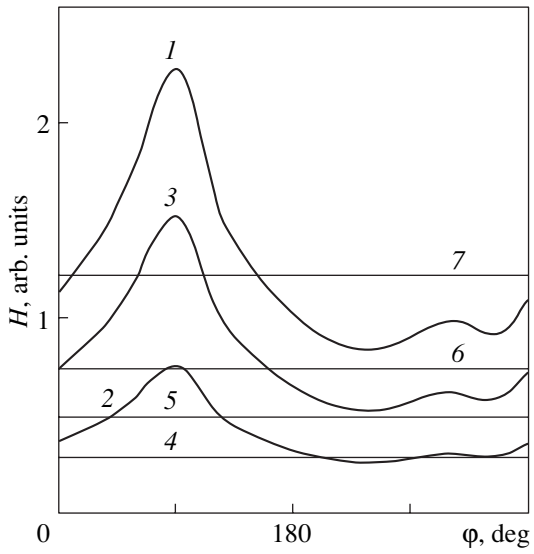

Fig. 3. Azimuthal dependences of (*1*) the saturation field H_s and threshold fields (*2*) H^* and (*3*) H^{**} in the range of acting magnetic fields with possible radiation of spin waves (in arbitrary units). Acting magnetic fields: (*4*) H_1, (*5*) H_2, (*6*) H_3, and (*7*) H_4.

$(Bi,Y,Lu,Pr)_3(Fe,Ga)_5O_{12}$ garnet ferrite single-crystal films with the (210) orientation and the azimuthal dependences of the threshold fields $H^*(\varphi)$ (curve *2*) and $H^{**}(\varphi)$ (curve *3*).

For a magnetic field $H = H_1$ (Fig. 3, straight line *4*), the threshold of generation of spin wave radiation is slightly exceeded and the broadening of the domain walls occurs in a narrow range (φ = 206°–265°); i.e., unidirectional anisotropy of the domain-wall velocity takes place.

At $H = H_2 > H_1$ (Fig. 3, straight line *5*), spin waves are induced over a wide range (except for angles φ = 38°–129°). This situation can be interpreted as a unidirectional decrease in the domain-wall velocity, even though portions of the larger part of the domain perimeter are broadened.

At $H = H_3 > H_2$ (Fig. 3, straight line *6*), the broadening of the domain wall occurs in the range φ = 0–160°; i.e., unidirectional anisotropy (increase) of the domain-wall velocity also takes place.

At $H = H_4 > H_3$ (Fig. 3, straight line *7*), the spin wave radiation and broadening of domain walls are observed in a narrower range (φ = 62°–111°). However, in the range φ = 154°–371°, dynamic domains are absent because of irregular rotation of the magnetization.

The observed changes in the direction of the unidirectional anisotropy of the domain-wall velocity can be interpreted as a rotation of the dynamic domain with variations in the acting magnetic field.

A variety of shapes of dynamic domains, a unidirectional increase and decrease in the domain-wall velocity, instability and distortions in segments of domain

walls, and changes in the orientation of a dynamic domain have been observed experimentally [11, 15].

3. CONCLUSIONS

The dependences $H_s(\varphi)$ presented in this paper (Figs. 1, 3; curves *1*) do not exhaust the great variety of curves $H_s(\varphi)$, because they strongly depend on the particular characteristics of garnet ferrite single-crystal films with orthorhombic magnetic anisotropy. However, their use makes it possible to explain the dynamic effects at least qualitatively. From analyzing these dependences, one can determine only the directions along which local rotation of the magnetization vectors occurs at a given magnetic field. In order to establish the shape of a dynamic domain, it is necessary to know the dependence $\alpha(\varphi, H)$. Unfortunately, these investigations have not been performed until now.

REFERENCES

1. R. V. Telesnin, S. M. Zimacheva, and V. V. Randoshkin, Fiz. Tverd. Tela (Leningrad) **19** (3), 907 (1977) [Sov. Phys. Solid State **19**, 528 (1977)].
2. A. F. Martynov, V. V. Randoshkin, and R. V. Telesnin, Pis'ma Zh. Tekh. Fiz. **8** (3), 803 (1982) [Sov. Tech. Phys. Lett. **8**, 348 (1982)].
3. L. P. Ivanov, A. S. Logginov, and G. S. Nepokoĭchitskiĭ, Preprint, Fiz. Fak. MGU (Physical Department of Moscow State Univ., Moscow, 1982).
4. L. P. Ivanov, A. S. Logginov, and G. S. Nepokoĭchitskiĭ, Zh. Éksp. Teor. Fiz. **84** (3), 1006 (1983) [Sov. Phys. JETP **57**, 583 (1983)].
5. V. V. Randoshkin and V. B. Sigachev, Fiz. Tverd. Tela (Leningrad) **28** (5), 1522 (1986) [Sov. Phys. Solid State **28**, 859 (1986)].
6. G. E. Khodenkov, Fiz. Met. Metalloved. **39** (3), 466 (1984).
7. M. V. Logunov and V. V. Randoshkin, Zh. Tekh. Fiz. **64** (7), 197 (1994) [Tech. Phys. **39**, 741 (1994)].
8. V. V. Randoshkin and M. V. Logunov, Fiz. Tverd. Tela (St. Petersburg) **36** (12), 3498 (1994) [Phys. Solid State **36**, 1858 (1994)].
9. V. V. Randoshkin, Fiz. Tverd. Tela (St. Petersburg) **37** (10), 3056 (1995) [Phys. Solid State **37**, 1684 (1995)].
10. V. V. Randoshkin, V. B. Sigachev, V. I. Chani, and A. Ya. Chervonenkis, Fiz. Tverd. Tela (Leningrad) **31** (7), 70 (1989) [Sov. Phys. Solid State **31**, 1138 (1989)].
11. M. V. Logunov, V. V. Randoshkin, and Yu. N. Sazhin, Fiz. Tverd. Tela (Leningrad) **32** (5), 1456 (1990) [Sov. Phys. Solid State **32**, 849 (1990)].
12. V. V. Randoshkin, M. V. Logunov, and Yu. N. Sazhin, Zh. Tekh. Fiz. **66** (4), 201 (1996) [Tech. Phys. **41**, 404 (1996)].
13. V. V. Randoshkin, Fiz. Tverd. Tela (St. Petersburg) **39** (8), 1421 (1997) [Phys. Solid State **39**, 1260 (1997)].
14. F. V. Lisovskiĭ, A. S. Logginov, E. G. Mansvetova, *et al.*, in *Abstracts of X All-Union School–Seminar on New Magnetic Materials in Microelectronics, Riga, 1986*, p. 189.
15. F. V. Lisovskii, A. S. Logginov, G. A. Nepokoĭchitskiĭ, and T. V. Rozanova, Pis'ma Zh. Éksp. Teor. Fiz. **45** (7), 339 (1987) [JETP Lett. **45**, 430 (1987)].

Translated by N. Korovin

Physics of the Solid State, Vol. 45, No. 11, 2003, pp. 2128–2130. Translated from Fizika Tverdogo Tela, Vol. 45, No. 11, 2003, pp. 2025–2027.

MAGNETISM AND FERROELECTRICITY

Preparation and Investigation of Weakly Ferromagnetic $Fe_{1-x}Ga_xBO_3$ Single Crystals

A. S. Kamzin*, L. P. Ol'khovik, and E. V. Snetkova***

**Ioffe Physicotechnical Institute, Russian Academy of Sciences, Politekhnicheskaya ul. 26, St. Petersburg, 194021 Russia*
e-mail: kamzin@pop.ioffe.rssi.ru
***Kharkov National University, pl. Svobody 4, Kharkov, 61077 Ukraine*

Received February 12, 2003

Abstract—Single crystals of iron borate $FeBO_3$, with part of the iron ions substituted for by Ga diamagnetic ions, were grown through spontaneous crystallization from a melt solution. The chemical composition of the crystals thus prepared, $Fe_{1-x}Ga_xBO_3$ ($x = 0$, 0.15, 0.25, 0.3), was derived from x-ray microprobe analysis data. Mössbauer spectroscopy and magnetometry were employed to determine the hyperfine interaction parameters (effective magnetic fields at the iron nucleus sites, quadrupole splittings, isomer chemical shifts) and Néel temperatures for these crystals and to derive their temperature behavior. © *2003 MAIK "Nauka/Interperiodica".*

$FeBO_3$ and Fe_3BO_6 crystals, first prepared and described in [1, 2], respectively, have been attracting considerable interest because of their remarkable inherent properties. For instance, Fe_3BO_6 was found to undergo spin-orientational phase transitions [3, 4] with characteristic features not observed earlier in other compounds. Substitution of Ga or Al diamagnetic ions for the iron ions in Fe_3BO_6 results in a substantial downshift of the Néel and orientational transition temperatures [5]. Replacing iron ions with a combination of Co and Ti ions up to 6 at. % lowers the spin reorientation temperature from 415 to 0 K [6]. A further increase in the Co and Ti concentrations gives rise to the formation of a new antiferromagnetic phase [6]. Studies of $Fe_{3-x}Ga_xBO_6$ have revealed that substitution of gallium ions for only 9 at. % of iron ions causes an order of magnitude increase in the thickness of a surface layer whose properties differ from those of the crystal bulk [7].

While $FeBO_3$ has a simple magnetic structure similar to that of hematite, its magnetic properties distinguish it from weakly ferromagnetic ferrites [8]. This offered the possibility of using $FeBO_3$ as a model single crystal in studies of the properties of surface layers and to detect a number of new phenomena (see [9, 10] and references therein). Further investigation of the surface properties of macroscopic crystals requires that the scope of objects to be studied be broadened. This accounts for the interest in the investigation of the effect of diamagnetic substitution on the properties of both the crystal as a whole and a thin surface layer by using $FeBO_3$ as a suitable example.

The goal of the present work was (i) to study the conditions conducive to preparation of $Fe_{1-x}Ga_xBO_3$ single crystals in which iron ions are partially replaced ($0 \le x \le 0.45$) by gallium diamagnetic ions and (ii) to investigate the crystal and magnetic properties of the compounds thus obtained. We chose spontaneous crystallization from a melt solution to grow the single crystals desired. The growth conditions accepted were based on the observations [1, 8, 11] of growth of both impurity-free $FeBO_3$ crystals and of $FeBO_3$ doped by various ions. The solvent was a mixture of Fe_2O_3, B_2O_3, PbF_2 (all were of OSCh grade), and KhCh-grade PbO. The iron oxide used had the natural content of the Fe-57 isotope. The reagents were dried for 12 h at 200°C. After the drying, the reagents were ground and sieved. Next, the required amounts of the components were weighed and intimately mixed. The charge thus obtained was placed into an electric furnace with a programmed temperature ramp rate. The crystal growth temperature regime was as follows. The charge was melted at 1073 K, heated at a rate of 200 K/h to 1373 K, and maintained at this temperature for 10 h. After this, the temperature was lowered at a rate of 3 K/h. On reaching 873 K, the furnace was switched off and left to cool to room temperature. The crystals were extracted from the solidified melt with a hot 20 vol % water solution of nitric acid.

The $Fe_{1-x}Ga_xBO_6$ crystals thus obtained, with the gallium ion concentration $0 \le x \le 0.45$, were in the shape of hexahedral plates up to 6×6 mm in area and up to 0.5 mm thick. The lattice parameters of the grown crystals as derived from x-ray diffraction analysis coincided with those quoted in [12].

The composition of these single crystals was studied using x-ray microprobe analysis. The results of the analysis identified the compositions as $Fe_{1-x}Ga_xBO_6$ with $x = 0$, 0.15, 0.25, 0.3, and 0.45. The magnetic properties of the crystals were studied using magnetometric techniques. Mössbauer measurements were conducted with a computerized spectrometer in transmis-

1063-7834/03/4511-2128$24.00

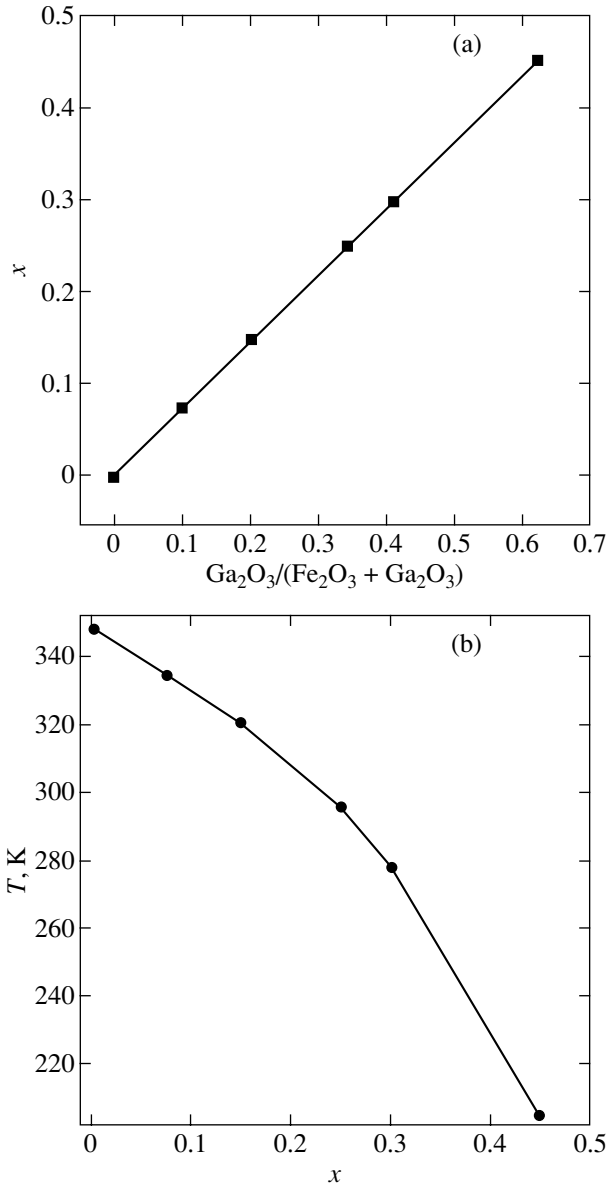

Fig. 1. Dependences (a) of gallium ion concentration (x) in the compounds synthesized on the composition of the charge [$Ga_2O_3/(Fe_2O_3 + Ga_2O_3)$] and (b) of the Néel temperature on the content of gallium ions (x) in the crystals.

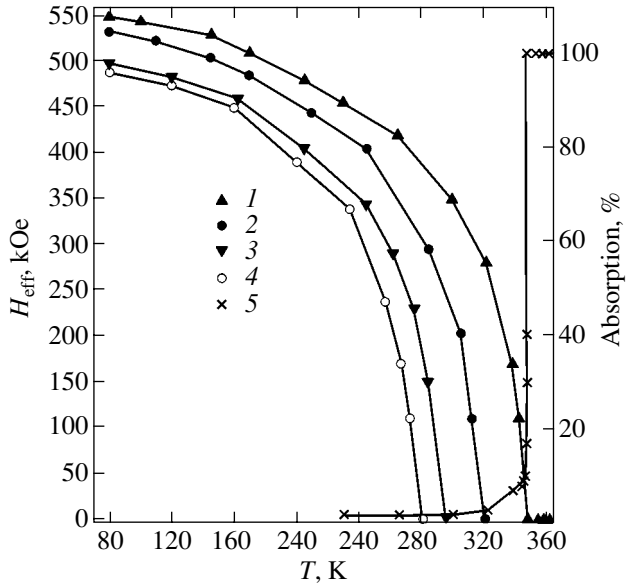

Fig. 2. Temperature dependences (*1–4*) of effective magnetic fields for iron ions in $Fe_{1-x}Ga_xBO_3$ and (*5*) of the number of detected pulses for zero gamma-ray source velocity. The points are connected by lines to aid the eye. x: (*1*) 0, (*2*) 0.15, (*3*) 0.25, and (*4*) 0.3.

sion geometry. The time dependence of the velocity of the gamma-ray source was described by a triangular curve, with its linearity corrected by an additional channel. The gamma-ray source employed was Co^{57} embedded in an Rh matrix. A small-gradient furnace was used in temperature measurements. The studies were performed on plate-shaped single crystals less than 0.1 mm thick.

As follows from the x-ray diffraction measurements, the $Fe_{1-x}Ga_xBO_6$ crystals prepared have the orthorhombic crystal structure and belong to space group D_{3d}^6. The crystallographic and magnetic cells are equivalent. X-ray diffraction identified the faces of the single-crystal plates with the (111) basal plane. The unit cell contains two magnetic ions, whose magnetic moments lie in the basal plane and are almost oppositely oriented to create a weak ferromagnetic moment directed along the [111] crystallographic axis.

Figure 1 relates the gallium concentration in the charge to its content in the crystals obtained. The experimentally obtained dependences of the magnetic moment on temperature and gallium content were used to derive the Néel temperatures presented in Fig. 1. The transition temperature to the paramagnetic state was also determined using Mössbauer spectroscopy methods: namely, (i) experimental spectra measured in the region of the phase transition were used to construct the spectrum with a zero Zeeman splitting and with only the quadrupole lines of the paramagnetic phase present; the temperature at which the Zeeman lines disappeared was accepted as the Curie point; and (ii) temperature sweeping was performed, and the phase transition point was extracted from the temperature dependence of the number of photons recorded by a detector when the gamma-ray source moved with a constant velocity (or was fixed). Figure 2 shows an experimental curve obtained for $x = 0$ using the second method. To make the graph more revealing, the plots drawn for crystals with other gallium concentrations are not shown. As seen from the experimental curve in Fig. 2, the number of photons measured by the detector increases as one approaches the phase transition point from the low-temperature side. At the transition point, the curve saturates, so that the number of recorded photons does not

change with a further increase in temperature. The transition temperatures to the paramagnetic state obtained using the above methods coincided both with one another and with the data quoted in [13]. Doping with diamagnetic ions lowers the magnetic moment and, as is evident from Fig. 1, the Néel temperature as well.

Mössbauer spectra of our crystals measured in the paramagnetic temperature region consist of two quadrupole-splitting lines. In the magnetically ordered region, the spectra exhibit one Zeeman sextuplet, whose linewidths increase with increasing gallium concentration in the crystals. The relative positions of the lines in the spectra suggest that the magnetic moments in the crystals lie in the (111) plane. The experimental spectra were used to determine the hyperfine interaction parameters. Figure 2 plots the effective magnetic fields acting on the iron nuclei as a function of temperature and of the iron ion content in the crystals. As seen from Fig. 2, the effective magnetic fields in $Fe_{1-x}Ga_xBO_3$ decrease with increasing gallium ion concentration. The temperature dependences of the spontaneous magnetic moment and of the effective magnetic field, which is proportional to the sample magnetization, coincide to within experimental error. This gives one grounds to conclude that the canting angle of the magnetic sublattices is independent of temperature, which is in agreement with the conclusions drawn in [7, 12]. The quadrupole splitting in the paramagnetic temperature region is 0.76 ± 0.05 mm/s and does not change, to within experimental error, with increasing gallium ion concentration. This may possibly be accounted for by the fact that replacement of the iron with gallium, which has a similar ion radius, brings about only a slight lattice distortion. The isomer chemical shift, found to be 0.26 ± 0.05 mm/s with respect to the Co-57 source in Rh, is likewise independent of the extent to which the iron ions were substituted in the compounds under study.

The results obtained can be summed up as follows. We have determined the composition of the components and the temperature conditions favorable for growing $Fe_{1-x}Ga_xBO_3$ single crystals, with x varied from 0 to 0.45. The magnetic properties of the $Fe_{1-x}Ga_xBO_3$ crystals with $x = 0$, 0.15, 0.25, 0.3, and 0.45 have been studied. It was found that at these levels of diamagnetic substitution of Ga for iron (i) the crystal and magnetic structures do not change and (ii) the Néel temperature decreases with increasing gallium ion concentration.

ACKNOWLEDGMENTS

This study was supported by the Russian Foundation for Basic Research, project no. 01-02-17889.

REFERENCES

1. L. Bernal, C. W. Struck, and J. G. White, Acta Crystallogr. **16** (8), 849 (1963).
2. J. G. White, A. Miller, and R. E. Nielsen, Acta Crystallogr. **19** (6), 1060 (1965).
3. R. Wolfe, R. D. Pierce, M. Eibschutz, and J. W. Nielsen, Solid State Commun. **7** (13), 949 (1969).
4. A. S. Kamzin, V. A. Bokov, and M. K. Chizhov, Fiz. Tverd. Tela (Leningrad) **18** (9), 2795 (1976) [Sov. Phys. Solid State **18**, 1631 (1976)]; A. S. Kamzin and V. A. Bokov, Fiz. Tverd. Tela (Leningrad) **19** (7), 2131 (1977) [Sov. Phys. Solid State **19**, 1247 (1977)].
5. N. Koshizuka, M. Hirano, T. Okuda, *et al.*, in *Proceedings of 20th Conference on Magnetism and Magnetic Materials, 1974*, Part 1, p. 61.
6. M. Hirano, T. Okuda, T. Tsushima, *et al.*, Solid State Commun. **15** (6), 1129 (1971).
7. A. S. Kamzin, L. A. Grigor'ev, and S. A. Kamzin, Fiz. Tverd. Tela (St. Petersburg) **36** (5), 1399 (1994) [Phys. Solid State **36**, 765 (1994)]; Fiz. Tverd. Tela (St. Petersburg) **37** (1), 66 (1995) [Phys. Solid State **37**, 33 (1995)].
8. L. V. Velikov, A. S. Prokhorov, E. G. Rudashevskiĭ, and V. N. Seleznev, Zh. Éksp. Teor. Fiz. **66** (5), 1847 (1974) [Sov. Phys. JETP **39**, 909 (1974)].
9. V. E. Zubov, G. S. Krinchik, V. N. Seleznev, and M. B. Strugatskiĭ, Zh. Éksp. Teor. Fiz. **94** (10), 290 (1988) [Sov. Phys. JETP **67**, 2122 (1988)]; V. E. Zubov, G. S. Krinchik, V. N. Seleznyov, and M. B. Strugatsky, J. Magn. Magn. Mater. **86**, 105 (1990).
10. A. S. Kamzin, B. Stahl, E. Kankeleit, *et al.*, Pis'ma Zh. Éksp. Teor. Fiz. **71** (10), 643 (2000) [JETP Lett. **71**, 442 (2000)]; B. Stahl, E. Kankeleit, R. Gellert, *et al.*, Phys. Rev. Lett. **84** (24), 5632 (2000).
11. R. C. LeCraw, R. Wolfe, and J. W. Nielsen, Appl. Phys. Lett. **14** (11), 352 (1969).
12. J. C. Joubert, T. Shiek, W. B. White, and R. Roy, Mater. Res. Bull. **3**, 671 (1968).
13. O. A. Bayukov, V. P. Ikonnikov, M. P. Petrov, *et al.*, in *Proceedings of International Conference on Magnetism, Moscow, 1974*, Vol. 3, p. 313.

Translated by G. Skrebtsov

Physics of the Solid State, Vol. 45, No. 11, 2003, pp. 2131–2135. Translated from Fizika Tverdogo Tela, Vol. 45, No. 11, 2003, pp. 2028–2036.

MAGNETISM AND FERROELECTRICITY

Phonon Mechanism of the Antiferromagnetic Photogalvanic Effect

V. V. Men'shenin

Institute of Metal Physics, Ural Division, Russian Academy of Sciences, ul. S. Kovalevskoĭ 18, Yekaterinburg, 620219 Russia

e-mail: menshenin@imp.uran.ru

Received March 14, 2003

Abstract—The phonon mechanism of generation of photogalvanic current in centroantisymmetric tetragonal antiferromagnets with magnetic symmetry excluding the occurrence of a toroidal momentum is considered. It is demonstrated that photocurrent can be caused by scattering of charge carriers by phonons with a polarization other than longitudinal. The polarization of the phonons involved in scattering is determined by the long-range part of the electron–phonon interaction induced by polarization of the lattice due to the magnetoelectric effect. Conditions are given for the observation of photogalvanic current in easy-axis antiferromagnets. © *2003 MAIK "Nauka/Interperiodica".*

1. INTRODUCTION

The photogalvanic effect consists in the optical generation of direct current in a medium in the absence of an external constant electric field and spatial inhomogeneities. This phenomenon has been thoroughly investigated in nonmagnetic crystals without a center of symmetry [1].

The physical nature of the photogalvanic effect is characterized by a number of features. One of these features is that the detailed balancing principle does not hold in materials without an inversion center, because this principle does not account for any spatial–temporal symmetry properties. The violation of the detailed balancing principle leads to asymmetry of electron scattering events, which substantially changes the kinetic properties of the crystal and offers possibilities for generating electric current in a nonequilibrium stationary state [1]. Photogalvanic current is generated in a nonequilibrium state caused by external illumination, and the direction of this current is determined by the crystal symmetry alone.

Earlier [2], we predicted the antiferromagnetic photogalvanic effect in centroantisymmetric antiferromagnets from symmetry considerations. The point is that, when writing invariant relationships for material tensors, energy, etc., within the phenomenological description of a phenomenon, one should proceed from crystal-chemical symmetry (Fedorov group G_F), provided the vector parameter of antiferromagnetic order **L** (antiferromagnetic vector) violating this symmetry is given in an explicit form in these relationships. Under these conditions, the transformation properties of the vector **L** play a significant role in the atomic rearrangement produced by an element of the G_F group. In media where all magnetic atoms belong to a single crystal-chemical position and the G_F group contains the center of symmetry $\bar{1}$, the symmetry element, depending on its spatial location, can transfer a particular magnetic atom either to the same magnetic sublattice (even element) or to a sublattice with an oppositely oriented magnetization (odd element). In the former case, the action of the symmetry element on the vector **L** does not at all differ from that of an element of the point group, even if this element is a screw axis or a glide plane. In the latter case (centroantisymmetric structure), the vector **L** additionally changes sign:

$$\bar{1}\mathbf{L} = -\mathbf{L}. \quad (1)$$

The centroantisymmetric antiferromagnets under consideration have no center of symmetry and, hence, can exhibit a photogalvanic effect. In the framework of the phenomenological description, the density of photoinduced direct electric current can be written in the form

$$j_i = \beta_{ijkl} L_j e_k e_l^* J, \quad (2)$$

where **e** is the unit vector of polarization of a monochromatic light wave and J is the light intensity. It is evident that equality (2) is satisfied only in the case of centroantisymmetric antiferromagnets for which the change in sign of the vector **j** under the action of the center of symmetry $\bar{1}$, according to relationship (1), is compensated by the change in sign of the vector **L** on the right-hand side.

In this paper, an attempt is made to elucidate one of the possible microscopic mechanisms of the origin of the antiferromagnetic photogalvanic effect, namely, the phonon mechanism. Let us first call attention to the fact that, among nonmagnetic crystalline materials, photogalvanic current has been observed in piezoelectric

crystals [3]. The interaction of electrons with phonons as one of the possible factors responsible for photocurrent in piezoelectrics was investigated by Belinicher and Sturman [4]. It was demonstrated that a significant role in the electron–phonon interaction is played by its long-range part, which appears upon polarization of the crystal lattice in the course of phonon propagation.

The centroantisymmetric antiferromagnets do not exhibit a piezoelectric effect, as can be judged from the symmetry of the crystals, and, seemingly, the phonon mechanism does not work. However, it is necessary to take into account the fact that these crystals are characterized by the magnetoelectric effect, which can lead to polarization of the crystal lattice.

2. ELECTRON–PHONON INTERACTION IN CENTROANTISYMMETRIC ANTIFERROMAGNETS

Let us consider a medium in the form of tetragonal centroantisymmetric antiferromagnets [5] with the exchange magnetic structure $\bar{1}(-)4_z(-)2_d(+)$. As was noted above, the polarization of the lattice of these antiferromagnets arises from the magnetoelectric effect. Consequently, the lattice polarization is indirectly affected by phonons through the magnetic subsystem of the crystal. In this situation, it is necessary to take into account not longitudinal but transverse phonons, which, as a rule, are related to the magnetic subsystem in a linear approximation. Belinicher and Sturman [4] described the short-range part of the electron–phonon interaction in terms of the Frelich Hamiltonian and, hence, ignored the polarization of phonons, because this Hamiltonian accounts only for longitudinal lattice vibrations. This Hamiltonian is unsuitable for the problem under consideration. The electron–phonon interaction should be described using a more general relationship that takes into account phonons with a polarization different from the longitudinal polarization. The physical considerations allowing one to obtain a more general expression for the short-range part of this interaction are presented in monographs [6, 7]. The operator $\hat{H}_{ep}^{(1)}$, which describes the change in the energy of charge carriers due to the displacement of the lattice atoms, has the form [6]

$$\hat{H}_{ep}^{(1)} = \sum_{i,j} D_{ij}(\mathbf{r})\varepsilon_{ij}(\mathbf{r}), \tag{3}$$

where $\varepsilon_{ij}(\mathbf{r})$ is the strain tensor. It is assumed that an electron is localized in a nondegenerate band. In the representation of secondary quantization, the Hamiltonian $\hat{H}_{ep}^{(1)}$ can be written in the following form:

$$\hat{H}_{ep}^{(1)} = i\sum_{\mathbf{p},\mathbf{q},s,j} \Gamma_j^s(\mathbf{p},\mathbf{q}) q_j C_{\mathbf{p}+\mathbf{q}}^+ C_{\mathbf{p}}(b_{\mathbf{q},s} + b_{-\mathbf{q},s}^+), \tag{4}$$

where

$$\Gamma_j^s(\mathbf{p},\mathbf{q}) = \sum_i D_{ij}(\mathbf{q}+\mathbf{p},\mathbf{q}) e_i(\mathbf{q},s)\sqrt{\frac{\hbar}{2\rho V\omega_{\mathbf{q},s}}}. \tag{5}$$

In relationships (4) and (5), $C_{\mathbf{p}}^+$ and $C_{\mathbf{p}}$ are the operators of production and annihilation of electrons, respectively; $b_{\mathbf{q},s}^+$ and $b_{\mathbf{q},s}$ are the operators of production and annihilation of phonons, respectively; $\mathbf{e}(\mathbf{q}, s)$ is the polarization vector of a phonon with wave vector $\mathbf{q}$, which is related to the sth acoustic mode; $\hbar$ is the Planck constant; ρ and V are the density and the volume of the medium, respectively; $\omega_{\mathbf{q},s}$ is the phonon frequency; and

$$D_{ij}(\mathbf{p}+\mathbf{q},\mathbf{p})\delta_{\mathbf{p}+\mathbf{q},\mathbf{k}} = \frac{1}{V}\int_V D_{ij}(\mathbf{r})u_{\mathbf{k}}^*(\mathbf{r})u_{\mathbf{p}}(\mathbf{r})\exp\{i(\mathbf{p}+\mathbf{q}-\mathbf{k})\mathbf{r}\}d\mathbf{r}. \tag{6}$$

Equality (6) takes into account that the quantities $D_{ij}(\mathbf{r})$ and Bloch amplitudes of the electron wave functions $u_{\mathbf{k}}(\mathbf{r})$ and $u_{\mathbf{p}}(\mathbf{r})$ are periodic functions. In this equality, the integral does not vanish only in the case when $\mathbf{p} + \mathbf{q} = \mathbf{k}$ (normal processes).

The number of components of the matrix element $(1/V)\int_V D_{ij}(\mathbf{r})u_{\mathbf{k}}(\mathbf{r})u_{\mathbf{k}}^*(\mathbf{r})d\mathbf{r}$ is determined by the group of the wave vector $G_{\mathbf{k}}$ [6]. As a consequence, for an arbitrary wave vector $\mathbf{k}$ in the Brillouin zone of the crystal, all nine components of the tensor $D_{ij}(\mathbf{r})$ can be nonzero.

The Hamiltonian describing the change in the energy of charge carriers with the participation of two phonons can be represented in a similar manner:

$$\hat{H}_{ep}^{(2)} = \sum_{\mathbf{p},\mathbf{q},\mathbf{l},s,s',ij} \Gamma_{ij}^{s,s'}(\mathbf{p}+\mathbf{q}+\mathbf{l},\mathbf{p},\mathbf{q}) C_{\mathbf{p}+\mathbf{q}+\mathbf{l}}^+ \times C_{\mathbf{l}}(b_{\mathbf{q},s} + b_{-\mathbf{q},s}^+)(b_{\mathbf{p},s'} + b_{-\mathbf{p},s'}^+) q_i p_j. \tag{7}$$

The designations in formula (7) are the same as those in relationships (4) and (5), except for the vertex part, which can be represented by the following expression:

$$\Gamma_{ij}^{s,s'}(\mathbf{p}+\mathbf{q}+\mathbf{l},\mathbf{p},\mathbf{q}) = \sum_{n,m} D_{nmij}(\mathbf{p}+\mathbf{q}+\mathbf{l},\mathbf{p},\mathbf{q}) \times e_n(\mathbf{q},s)e_m(\mathbf{p},s')\frac{\hbar}{2\rho V}\sqrt{\frac{1}{\omega_{\mathbf{q},s}\omega_{\mathbf{p},s'}}}, \tag{8}$$

$$D_{nmij}(\mathbf{p}+\mathbf{q}+\mathbf{l},\mathbf{p},\mathbf{q})\delta_{\mathbf{p}+\mathbf{q}+\mathbf{l},\mathbf{k}} = \frac{1}{V}\int_V D_{nmij}(\mathbf{r})u_{\mathbf{k}}^*(\mathbf{r})u_{\mathbf{l}}(\mathbf{r})\exp\{i(\mathbf{p}+\mathbf{q}+\mathbf{l}-\mathbf{k})\mathbf{r}\}d\mathbf{r}. \tag{9}$$

Now, we consider the long-range part of the electron–phonon interaction associated with the lattice polarization. Since this polarization in centroantisymmetric antiferromagnets arises from the magnetoelectric effect, we assume that an external constant magnetic field **H** is applied to the medium along the principal axis of the tetragonal antiferromagnet. We choose the magnetic state of the crystal in such a way that the antiferromagnetic vector at equilibrium will be oriented along the principal axis.

Next, let us use the phenomenological description and assume that the relationship between the lattice polarization **P** and the antiferromagnetic vector **L** has the same form for both the statics and dynamical processes and that these vectors follow the elastic strains in a quasi-equilibrium manner. In this case, we can demonstrate the validity of the following relationships:

$$P_x = \kappa_\perp \gamma_3 \chi H \frac{2B_{44} l_z^0}{\tilde{K}} \varepsilon_{xz}, \quad P_y = \kappa_\perp \gamma_3 \chi H \frac{2B_{44} l_z^0}{\tilde{K}} \varepsilon_{yz},$$
$$P_z = \frac{2B_{44}^2 H \gamma_4 \kappa}{l_z^0 \tilde{K}^2} (\varepsilon_{xz}^2 + \varepsilon_{yz}^2), \tag{10}$$

where ε_{ij} are the components of the strain tensor; B_{44} is the magnetoelastic constant; $\tilde{K}$ is the renormalized constant of the uniaxial anisotropy [8]; χ is the magnetic susceptibility; $\kappa_\perp$ and κ are the transverse and longitudinal electric susceptibilities, respectively; l_z^0 is the reduced antiferromagnetic vector in the ground state; and $\gamma_{3,4}$ are the magnetoelectric constants [8].

The polarization of the lattice gives rise to the scalar potential acting on the charge carriers. In the representation of second quantization, the long-range part of the electron–phonon interaction, which is related to the scalar potential, can be represented by the following expression for electrons:

$$\hat{H}_{\text{ep}}^{\text{Ir}(1)} = e \sum_{\mathbf{p}, \mathbf{q}, s} \Gamma_i^{\text{Ir}}(\mathbf{q}) e_i(\mathbf{q}, s) C_{\mathbf{p}+\mathbf{q}}^+ C_{\mathbf{p}} (b_{\mathbf{q}, s} + b_{-\mathbf{q}, s}^+), \tag{11}$$

where

$$\Gamma_i^{\text{Ir}}(\mathbf{q}) = \frac{4\pi}{\xi_{st} q_s q_t V} \kappa_\perp \gamma_3 \chi H \frac{B_{44}}{\tilde{K}} \sqrt{\frac{\hbar}{2\rho V \omega_{\mathbf{q}, s}}}$$
$$\times [\delta_{iz}(\delta_{xn}\delta_{xl} + \delta_{yn}\delta_{yl}) + \delta_{ix}\delta_{xn}\delta_{zl} + \delta_{iy}\delta_{zn}\delta_{yl}] q_n q_l \tag{12}$$
$$\times \int_V u_{\mathbf{k}}^*(\mathbf{r}) u_{\mathbf{p}}(\mathbf{r}) \exp[i(\mathbf{p} + \mathbf{q} - \mathbf{k})\mathbf{r}] d\mathbf{r}.$$

Here, ξ_{ij} are the components of the permittivity tensor, **e** is the elementary charge, and **e**(**q**, *s*) is the phonon polarization.

As is known [1], the properties of a scattering center are characterized by the probability $W_{\mathbf{kk}'}$ of transferring a particle scattered by this potential from a state with angular momentum **k**' to a state with angular momentum **k**. In media without a center of symmetry, the probability $W_{\mathbf{kk}'}$ can be separated into two parts, one of which is symmetric with respect to the permutation of the angular momenta **k** and **k**' (this corresponds to detailed balancing) and the other is antisymmetric with respect to this permutation [4]:

$$W_{\mathbf{kk}'} = W_{\mathbf{kk}'}^{\text{s}} + W_{\mathbf{kk}'}^{\text{a}}, \quad W_{\mathbf{kk}'}^{\text{s}} = W_{\mathbf{k}'\mathbf{k}}^{\text{s}} = W_{-\mathbf{k}-\mathbf{k}'}^{\text{s}},$$
$$W_{\mathbf{kk}'}^{\text{a}} = -W_{\mathbf{k}'\mathbf{k}}^{\text{a}} = -W_{-\mathbf{k}-\mathbf{k}'}^{\text{a}}. \tag{13}$$

It is this antisymmetric part of the probability $W_{\mathbf{kk}'}^{\text{a}}$ that is responsible for the effects associated with the absence of a center of symmetry. In order to calculate the antisymmetric part of the scattering probability, it is necessary to go beyond the scope of the Born approximation. Then, it can be demonstrated that the antisymmetric part of the probability $W_{\mathbf{kk}'}^{\text{a}}$ has the form [1]

$$W_{\mathbf{kk}'}^{\text{a}} = \frac{2\pi V}{\hbar} \int_V d\mathbf{q} \delta(E_{\mathbf{k}} - E_{\mathbf{k}'}) \delta(E_{\mathbf{k}} - E_{\mathbf{q}})$$
$$\times \text{Im} \langle \mathbf{k}|\hat{H}|\mathbf{q}\rangle \langle \mathbf{q}|\hat{H}|\mathbf{k}'\rangle \langle \mathbf{k}'|\hat{H}|\mathbf{k}\rangle, \tag{14}$$

where $E_{\mathbf{k}}$ is the energy of an electron with wave vector **k** and $\hat{H}$ is the scattering potential, which, in our case, is defined as $\hat{H}_{\text{ep}}^{(1)} + \hat{H}_{\text{ep}}^{(2)} + \hat{H}_{\text{ep}}^{\text{Ir}(1)}$. Upon substituting the last expression into equality (14), we obtain

$$W_{\mathbf{kk}'}^{\text{a}} = \sum_{\mathbf{q}} \sum_{\nu=1}^{3} \zeta_{\mathbf{kqk}'}^{\nu},$$

$$\zeta_{\mathbf{kqk}'}^1 = \frac{\pi^2}{\hbar} \text{Im} \sum_{j, m, r, t} \sum_{\alpha, \beta, s} [i\Gamma_j^s(\mathbf{q}, \mathbf{k}-\mathbf{q})(\mathbf{k}-\mathbf{q})_j$$
$$+ e e_\alpha(\mathbf{q}, s) \Gamma_\alpha^{\text{Ir}}(\mathbf{k}-\mathbf{q})] [i\Gamma_m^s(\mathbf{k}', \mathbf{q}-\mathbf{k}')(\mathbf{q}-\mathbf{k}')_m$$
$$+ e e_\beta(\mathbf{q}, s) \Gamma_\beta^{\text{Ir}}(\mathbf{q}-\mathbf{k}')] \Gamma_{rt}^{ss}(\mathbf{k}', \mathbf{k}'-\mathbf{q}, \mathbf{q}-\mathbf{k})$$
$$\times (\mathbf{q}-\mathbf{k}')_r (\mathbf{k}-\mathbf{q})_t \sum_{\eta, \mu = \pm 1} (2n_{\mathbf{k}-\mathbf{q}, s} + \eta + 1)$$
$$\times (2n_{\mathbf{k}'-\mathbf{q}, s} + \mu + 1) \delta(E_{\mathbf{k}} - E_{\mathbf{q}} - \eta\hbar\omega_{\mathbf{k}-\mathbf{q}, s})$$
$$\times \delta(E_{\mathbf{q}} - E_{\mathbf{k}'} - \mu\hbar\omega_{\mathbf{k}'-\mathbf{q}, s}), \tag{15}$$

$$\zeta_{\mathbf{kqk}'}^2 = -\zeta_{\mathbf{kk}'\mathbf{q}}^1, \quad \zeta_{\mathbf{kqk}'}^3 = -\zeta_{\mathbf{k}'\mathbf{qk}}^1.$$

It follows from equalities (15) that the contribution to the probability $W_{\mathbf{kk}'}^{\text{a}}$ is made by both nonlinear elec-

tron–phonon interactions and single-phonon interactions of electrons with the lattice. The necessity of taking into account the long-range part of the electron–phonon interactions is of considerable importance. For this reason, we had to include the magnetoelectric effect in the consideration of the antiferromagnetic photogalvanic effect.

The photogalvanic current density is determined by the following expression [1]:

$$\mathbf{j} = \frac{e}{\hbar}\int\frac{\partial\varepsilon}{\partial\mathbf{k}}f^{a}_{\mathbf{k}}d\mathbf{k},$$

where $f^{a}_{\mathbf{k}}$ is the antisymmetric part of the distribution function for charge carriers and ε is the energy of the charge carriers.

In order to determine the function $f^{a}_{\mathbf{k}}$ it is necessary to know the processes responsible for electrons in the conduction band of the antiferromagnet. For simplicity, we consider only the excitation of photoelectrons at impurity *s* centers, i.e., impurity–band transitions. In this case, the function $f^{a}_{\mathbf{k}}$ can be represented by the relationship [1]

$$f^{a}_{\mathbf{k}} = \frac{1}{\Gamma^{2}}\int W^{a}_{\mathbf{k}\mathbf{k}'}I_{\mathbf{k}'}d\mathbf{k}'.$$

Here, Γ^{-1} is the time of relaxation with respect to the momentum. In the last formula, it is assumed that the volume of the system is equal to unity and the quantity $I_{\mathbf{k}}$ having the meaning of the electron excitation rate is given by the formula

$$I_{\mathbf{k}} = \frac{2\lambda J}{4\pi k^{4}\hbar\omega}(\mathbf{k}\mathbf{e}(\mathbf{k}))^{2}\delta(\mathbf{k}-\mathbf{k}_{0}).$$

Here, $\mathbf{e}(\mathbf{k})$ is the polarization vector of the electromagnetic wave; λ is the coefficient of light absorption; and $\mathbf{k}_0$ is the limiting momentum of the photoelectron, which is determined from the condition $\hbar\omega = \Delta + \varepsilon_{\mathbf{k}_0}$. As a result, the expression for the density of photocurrent takes the form

$$\mathbf{j} = \frac{2\lambda Je}{4\pi\hbar^{2}\omega\Gamma^{2}}\int\frac{\partial\varepsilon}{\partial\mathbf{k}}W^{a}_{\mathbf{k}\mathbf{k}'}\frac{(\mathbf{k}'\mathbf{e}(\mathbf{k}'))^{2}}{k'^{4}}\delta(\mathbf{k}'-\mathbf{k}_{0})d\mathbf{k}d\mathbf{k}'. \quad (16)$$

3. RESULTS AND DISCUSSION

As was already mentioned, the antiferromagnetic photogalvanic effect should be described with due regard for the interaction of electrons and phonons characterized by a polarization other than longitudinal. It follows from relationships (12) and (15) that, for the chosen direction of the external magnetic field, the electrons interacting with two groups of phonons contribute to the photocurrent. The first group consists of transverse phonons that are polarized along the principal axis of the crystal and propagate along the *x* or *y* axis. The second group consists of phonons propagating in the *xz* and *yz* planes with the polarization vector directed along the *x* and *y* axes, respectively. All other phonons do not participate in the generation of the photocurrent.

Earlier [5], we performed a macroscopic analysis of the antiferromagnetic photogalvanic effect and proved that, for uniaxial tetragonal antiferromagnets at $\mathbf{L} \parallel \mathbf{z}$, the photocurrent can flow only along the fourfold axis. On this basis, the direction of the external magnetic field $\mathbf{H}$ was chosen in such a way that the occurrence of additional components of the photocurrent would be impossible.

In [4], the antisymmetric part of the probability $W^{a}_{\mathbf{k}\mathbf{k}'}$ of an electron transferring from a state with wave vector $\mathbf{k}'$ to a state with wave vector $\mathbf{k}$ due to scattering by phonons was calculated for normal processes of scattering in nonmagnetic crystals under the assumption that electrons obey the square isotropic law of dispersion. In our case, this assumption cannot be used, because, according to this law of dispersion of charge carriers, transverse phonons cannot initiate normal processes of scattering [7]. Therefore, the analytical calculation of Eqs. (15) should be carried out without invoking this approximation, which significantly complicates its execution. However, even without these calculations, we can draw certain conclusions regarding the possibility of the quantity $W^{a}_{\mathbf{k}\mathbf{k}'}$ nonvanishing in our case. Indeed, for arbitrary wave vectors $\mathbf{k}$, when the group of the wave vector $G_{\mathbf{k}}$ contains only the unit element, the Fourier components $D_{ij}(\mathbf{k})$ and $D_{ijkl}(\mathbf{k})$ and, correspondingly, all the vertex parts considered above do not vanish upon the interaction of electrons with phonons having the aforementioned polarizations. The last circumstance allows us to state that the contribution to the probability $W^{a}_{\mathbf{k}\mathbf{k}'}$ from the summation over vectors $\mathbf{q}$ for which $\mathbf{k}-\mathbf{q}$ and $\mathbf{k}'-\mathbf{q}$ are the low-symmetry points of the Brillouin zone does not vanish. The contribution associated with the high-symmetry points of the Brillouin zone can be totally absent because the tensors $D_{ij}(\mathbf{k})$ and $D_{ijkl}(\mathbf{k})$ have no components for the description of the electron interaction with lattice vibrations of the required polarization.

Let us estimate the photocurrent density. In the estimation, we assume that the quantities $\Gamma^{s}_{j}(\mathbf{q}, \mathbf{k}-\mathbf{q})$ and $\Gamma^{ss}_{ij}(\mathbf{k}', \mathbf{k}'-\mathbf{q}, \mathbf{q}-\mathbf{k})$ weakly depend on the wave vectors and $(1/V)\int u^{*}_{\mathbf{k}}(\mathbf{r})u_{\mathbf{p}}(\mathbf{r})\exp(i\{\mathbf{p}+\mathbf{q}-\mathbf{k}\}\mathbf{r})d\mathbf{r} \propto 1$. Then, the expression for the photocurrent density can be represented in the form

$$j \propto \frac{me}{\hbar^{4}}(\Gamma^{(1)}_{\mathrm{ep}})(\Gamma^{(2)}_{\mathrm{ep}})(e\Gamma^{\mathrm{Ir}}_{\mathrm{ep}})\frac{\lambda J}{\hbar\omega\Gamma^{2}}\frac{T^{2}}{(\hbar c_{s})^{2}}k_{0}. \quad (17)$$

Here, e is the electron charge, m is the electron mass,

$$\Gamma_{ep}^{(1)} \propto \{D_{xz}, D_{yz}\}_{\max}\sqrt{\hbar/2\rho V c_s},$$

$$\Gamma_{ep}^{(2)} \propto \{D_{zzxx}, D_{zzyy}, D_{xzxz}, D_{yzyz}\}_{\max}(\hbar/2\rho V c_s),$$

$$\Gamma_{ep}^{\mathrm{Ir}} \propto \frac{4\pi l_z^0}{\xi_0}\kappa_\perp\gamma_3\chi H\frac{B_{44}}{\tilde{K}}\sqrt{\hbar/2\rho V c_s}.$$

Under the assumption that $\{D_{xz}, D_{yz}\}_{\max} \propto 1.6 \times 10^{-12}$ erg, $\{D_{zzxx}, D_{zzyy}, D_{zxzx}, D_{yzyz}\}_{\max} \propto 1.6\times 10^{-13}$ erg, $\lambda \propto 1$ cm^{-1}, $c_s \propto 10^5$ cm s^{-1}, $T \propto k_B 10$ erg, $H \propto 10^3$ Oe, $\xi_0 \propto 10$, $\kappa_\perp\gamma_3\chi l_z^0 \propto 10^{-2}$, $B_{44}/\tilde{K} \propto 10^3$, $2\rho V \propto 1$ g, $\hbar\omega \propto 5 \times 10^{-12}$erg, and $k_0 \propto 10^{-7}$ cm^{-1}, we obtain j (CGS) $\propto 10^{-5} J$ (erg/cm^2 s).

One additional remark needs to be made. In [9, 10], when studying strong electron–hole correlations in "exciton" dielectrics, considerable attention was given to the current states and, in particular, the photogalvanic effect. It was demonstrated that the bulk photogalvanic effect manifests itself on the microscopic level under the condition of existence of the imaginary part of the singlet order parameter in the system [9, 10], which is macroscopically equivalent to the existence of the antisymmetric components of the magnetoelectric tensor (toroidal momentum) of the medium. The occurrence of these components of the magnetoelectric tensor in tetragonal crystals becomes possible in the case when their class of magnetic symmetry is $D_{4h}(C_{4v})$ [11]. However, the rare-earth phosphates and vanadates which I considered in this paper have magnetic symmetry $D_{4h}(D_{2d})$. Therefore, these crystals do not exhibit effects that are associated with the electron–hole correlations and cause photogalvanic currents.

4. CONCLUSIONS

From the above analysis, it can be inferred that, in centroantisymmetric antiferromagnets, the antiferromagnetic photogalvanic effect is caused by scattering of charge carriers by phonons.

REFERENCES

1. B. I. Sturman and V. M. Fridkin, *Photogalvanic Effect* (Nauka, Moscow, 1992).
2. V. V. Men'shenin and E. A. Turov, Pis'ma Zh. Éksp. Teor. Fiz. **72** (1), 23 (2000) [JETP Lett. **72**, 14 (2000)].
3. A. V. Andrianov and I. D. Yaroshchetskiĭ, Fiz. Tekh. Poluprovodn. (Leningrad) **16** (4), 706 (1982) [Sov. Phys. Semicond. **16**, 454 (1982)].
4. V. I. Belinicher and B. I. Sturman, Fiz. Tverd. Tela (Leningrad) **20** (3), 821 (1978) [Sov. Phys. Solid State **20**, 476 (1978)].
5. V. V. Men'shenin and E. A. Turov, Zh. Éksp. Teor. Fiz. **108** (6), 2061 (1995) [JETP **81**, 1124 (1995)].
6. G. L. Bir and G. E. Pikus, *Symmetry and Stain-Induced Effects in Semiconductors* (Nauka, Moscow, 1972; Wiley, New York, 1975).
7. J. M. Ziman, *Principles of the Theory of Solids*, 2nd ed. (Cambridge Univ. Press, Cambridge, 1972; Mir, Moscow, 1974).
8. E. A. Turov, V. V. Men'shenin, and V. V. Nikolaev, Zh. Éksp. Teor. Fiz. **104** (6), 4157 (1993) [JETP **77**, 1014 (1993)].
9. A. A. Gorbatsevich, Yu. V. Kopaev, and V. V. Tugushev, Zh. Éksp. Teor. Fiz. **85** (3), 1107 (1983) [Sov. Phys. JETP **58**, 643 (1983)].
10. Yu. A. Artamonov, A. A. Gorbatsevich, and Yu. V. Kopaev, Zh. Éksp. Teor. Fiz. **101** (2), 557 (1992) [Sov. Phys. JETP **74**, 296 (1992)].
11. Yu. A. Artamonov and A. A. Gorbatsevich, Zh. Éksp. Teor. Fiz. **89** (3), 1078 (1985) [Sov. Phys. JETP **62**, 621 (1985)].

Translated by O. Moskalev

Physics of the Solid State, Vol. 45, No. 11, 2003, pp. 2136–2139. Translated from Fizika Tverdogo Tela, Vol. 45, No. 11, 2003, pp. 2033–2036.

MAGNETISM AND FERROELECTRICITY

Magnetic State of a System of Barium Hexaferrite Nanocrystals in the Vicinity of the Curie Temperature

L. P. Ol'khovik*, Z. I. Sizova*, and A. S. Kamzin**

**Kharkov National University, pl. Svobody 4, Kharkov, 61077 Ukraine*

e-mail: Larisa.P.Olkhovik@univer.kharkov.ua

***Ioffe Physicotechnical Institute, Russian Academy of Sciences, Politekhnicheskaya ul. 26, St. Petersburg, 194021 Russia*

Received March 21, 2003

Abstract—In order to study the magnetic state of a system of nanocrystals of highly anisotropic hexagonal barium ferrite in the vicinity of the Curie temperature, a macrocrystal surface layer comparable in thickness to the particles of the system is chosen as a model. As revealed by simultaneous application of gamma-, x-ray, and electron Mössbauer spectroscopy, the transition of a ~200-nm-thick surface layer to the paramagnetic state starts 55 K and is complete 3 K below the Curie temperature of the bulk of the crystal. This temperature range overlaps the range where the particles transfer from the magnetically stable to the superparamagnetic state. The data obtained made it possible to refine the high-temperature part of the *H–T* diagram for particles with a close-to-critical volume. The regions of the diagram where mixed magnetic states originating simultaneously from the size and surface factors coexist are identified. © *2003 MAIK "Nauka/Interperiodica".*

A number of publications deal with the issue of the physical mechanisms responsible for the magnetic properties of the nanocrystalline system of highly anisotropic barium ferrite ($BaFe_{12}O_{19}$) [1–3]. In particular, an *H–T* magnetic state diagram has been constructed for the temperature range 300 K–T_C and for fields *H* extending from zero to 20 kOe. The diagram specifies regions where the magnetic states specific to a particle system under study exist. One of such regions bounds the superparamagnetic (SPM) state. The temperature extent of this region for a system acted upon by an external magnetic field is ~300 K. In spite of the fact that the smallest particle size of the system of interest is close to the lower limit of the single-domain dimension, only at 30 K below the Curie temperature of the system does the high magnetocrystalline anisotropy energy make possible a transition to the SPM state due to thermal fluctuations with no magnetic field applied.

The goal of the present study was to refine the magnetic state diagram for a system of nanocrystals approaching the Curie temperature.

Information on the magnetic structure can be gained from using Mössbauer spectroscopy. The validity of this approach as applied to a system of small particles with a close-to-critical volume seems, however, questionable for a number of reasons. First, the dispersed form of the material and the real particle size distribution bring about a considerable line broadening of the barium ferrite spectrum, which is originally complex and poorly resolvable at high temperatures. Second, the transition of about 70% of the particles in a system to the superparamagnetic state [2] should become manifest in the appearance in the spectrum of a paramagnetic doublet in addition to the sextuplets, provided the superparamagnetic relaxation time τ is much shorter than the time of experimental observation τ_m [4]. Under these conditions, unambiguous interpretation of a magnetic state at a temperature close to the transition temperature to the paramagnetic state becomes dubious.

The earlier layer-by-layer analysis of the $BaFe_{12}O_{19}$ single crystal performed in [5] showed that the thickness of the surface layer with a magnetic structure different from that of the bulk for $T > 600$ K is ~200 nm, which is comparable to the thickness *h* even of the largest nanocrystals of the system. This is why the surface layer of a macroscopic sample was chosen as the model for a nanocrystal in our Mössbauer studies.

This is the first time the problem of the mechanisms through which the magnetic state of small particles forms in the high-temperature range is treated using this method.

The Mössbauer spectra were obtained through simultaneous gamma-, x-ray, and electron Mössbauer spectroscopy [6]. Measurements were performed on the basal plane of a single crystal with a natural abundance of ^{57}Fe (2% of the total number of iron ions). This choice is motivated by the fact that, compared to a side face, a free basal-plane surface is a stronger source of perturbation of the crystalline and, accordingly, magnetic structure of a platelet nanocrystal.

1063-7834/03/4511-2136$24.00 © 2003 MAIK "Nauka/Interperiodica"

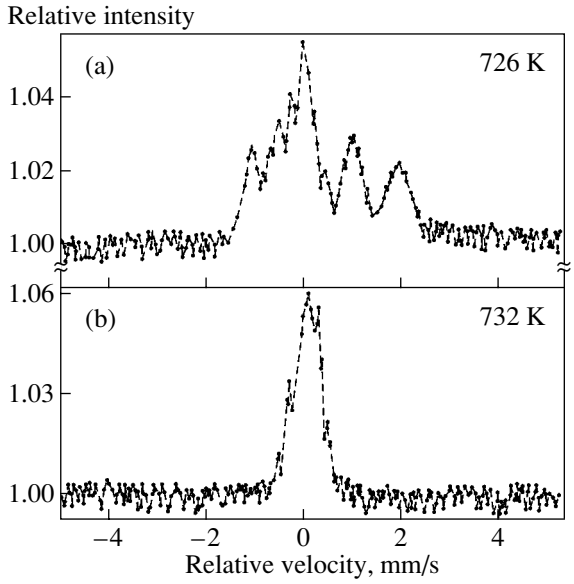

Fig. 1. Mössbauer spectra of a barium hexaferrite single crystal obtained by measuring the conversion and Auger electrons emitted from a surface layer ~200 nm thick.

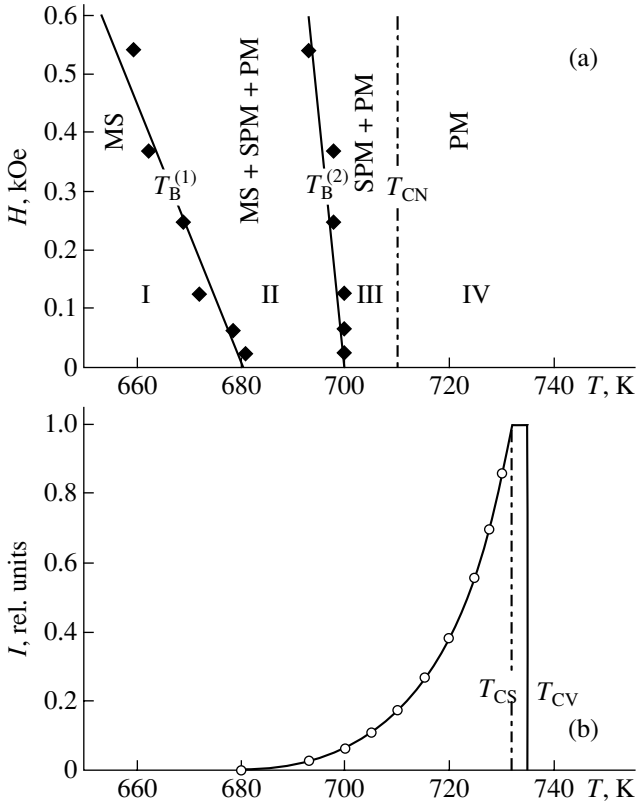

Fig. 2. (a) High-temperature fragment of the *H–T* magnetic state diagram of a system of barium hexaferrite nanocrystals and (b) temperature dependence of the intensity of the paramagnetic line in the Mössbauer spectrum obtained from the surface layer of the macrocrystal. MS stands for magnetically stable, SPM for superparamagnetic, and PM for paramagnetic state.

The $BaFe_{12}O_{19}$ single crystal was grown from a melt solution [7]. Plates 100 μm thick and 9 mm in diameter were cut parallel to the basal plane from the single crystal. The x-ray studies showed the *c* crystallographic axis to be perpendicular to the plate surface prepared for study. Particular attention was focused on the quality of the surface to be studied. Preliminary experiments revealed that a high surface quality of a hexagonal single crystal can be reached through chemical polishing in orthophosphoric acid at 90°C for 1 min. This treatment provided good reproducibility and, hence, reliability of the results obtained.

The geometry of the experiment was chosen such that the crystallographic *c* axis, which is the easy magnetization direction, was parallel to the wave vector of the gamma radiation. This orientation makes an NGR spectrum more revealing, because the second and fifth lines of the sextuplets for a collinear magnetic structure should have zero intensity in this case [8].

Figure 1 illustrates high-temperature Mössbauer spectra obtained by detecting conversion and Auger electrons emitted from a ~200-nm-thick surface layer. The spectrum measured at $T = 726$ K exhibits a paramagnetic doublet against the background of weakly resolved sextuplets, which indicates the coexistence of a magnetically ordered and a paramagnetic phase. The intensity of this doublet, as seen from Fig. 2b, increases with a further increase in temperature. The large width of the paramagnetic phase transition in temperature (680–732 K) may be attributed to the fact that the density of structural defects [5] and, hence, of broken and modified Fe–O–Fe exchange bonds in the near-surface region falls off monotonically away from the surface. In this case, the temperature $T = 680$ K may be identified with the Curie point of the free crystal surface. At $T = 732$ K, the spectrum exhibits only the paramagnetic doublet lines (Fig. 1), which indicates that the whole near-surface region transferred to the paramagnetic state. The temperature at which the Zeeman splitting lines disappeared was assumed to be the Curie temperature of the surface layer T_{CS}. As seen from Fig. 2b, T_{CS} is 3 K lower than the Curie point of the crystal bulk, T_{CV} [9]. Note that the temperature and its gradient across the sample were maintained to within ±0.1 K.

The information obtained on the variation of the magnetic state in the crystal surface layer as the Curie temperature was approached permitted us to refine the high-temperature region of the *H–T* magnetic state diagram obtained earlier for a system of $BaFe_{12}O_{19}$ nanocrystals [2].

This system was prepared using a nonstandard cryochemical technology, which provided chemical and granulometric homogeneity of the ferrite-forming mix-

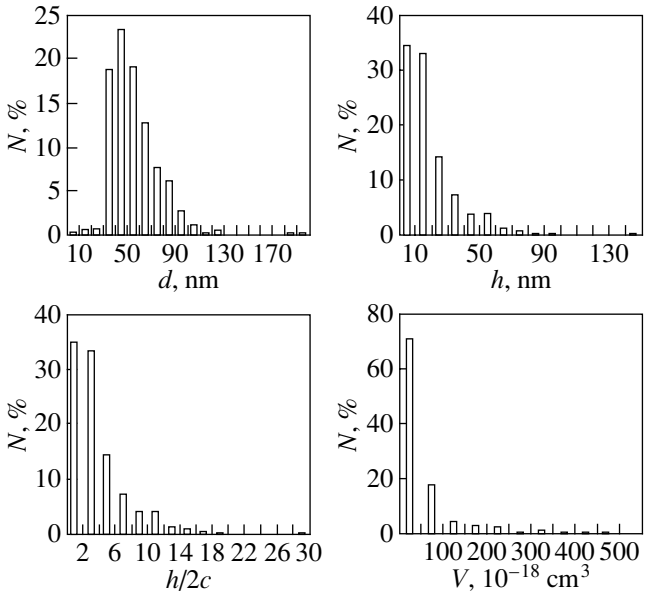

Fig. 3. Size distribution of nanocrystalline powder particles: d is the diameter, h is the thickness, V is the particle volume, and c is the lattice parameter. Sampling size N = 520 particles.

ture and thereby offered the possibility of carrying out ferritization at comparatively low temperatures (800°C, 4 h) [10, 11], with the end product being a nanodispersed powder. Figure 3 presents electron microscopy data on the size distribution of the particles.

A fragment of the H–T diagram is displayed in Fig. 2a. The interval 650–740 K is rich in phase transitions. A 100-K broad temperature region encompasses three consecutively arising phases, namely, magnetically stable (MS), superparamagnetic (SPM), and paramagnetic (PM) phases. The regions of the diagram where various phases exist are separated by the following lines. Line $T_B^{(1)}(H)$ indicates the beginning of the transition of particles in the system from the MS to SPM state (at $H = 0$, $T_B^{(1)} = 681$ K), and line $T_B^{(2)}(H)$ closes the region of the SPM transition for the particles having critical volume in the specified temperature interval [12]. The region beyond the dash-dotted line relates to the paramagnetic state of a system of nanoparticles as a whole. The temperature $T_{CN} = 710 \pm 2$ K, derived from the temperature dependence of magnetization in a low field ($H \sim 25$ Oe) [1], was identified with the Curie temperature of a nanocrystalline sample. The fact that T_{CN} is lower (by 20 K) than T_{CS} should be assigned to the exchange coupling in the surface layer of a macrocrystal being less perturbed (because of the favorable effect exerted by the bulk) than the coupling in a nanocrystal.

The available high-temperature Mössbauer data for a macrocrystal permitted us to correlate the H–T diagram discussed here with the temperature region within which the paramagnetic phase develops in a surface layer comparable in thickness to nanocrystals. A remarkable feature is the overlap of the temperature range 680–700 K, where nanocrystals undergo an SPM transition through thermal fluctuations alone ($H = 0$), with the range where the transition to the paramagnetic state begins (Fig. 2b). Accordingly, regions II and III in the diagram correspond to mixed states; namely, region II corresponds to MS + SPM + PM, and region III, to SPM + PM.

The nanodisperse system under study is specific in that the temperature $T_B^{(1)}$ of the onset of the SPM transition in $BaFe_{12}O_{19}$ nanocrystals adjoins the lower boundary of the temperature-broadened paramagnetic region, because the effective magnetic anisotropy energy is high. The paramagnetic phase in an ultrathin particle ($h/2c = 2$–4, Fig. 3c) nucleates primarily on the free surface containing iron vacancies and broken exchange bonds [5]. The density of broken bonds within the surface layer decreases monotonically with depth, which makes propagation of the paramagnetic phase extended in temperature. An additional energy equivalent to 50 K is needed to completely destroy magnetic order in the volume of such particles.

Note that the hypothesis put forward in [13] on the existence of a magnetically dead (paramagnetic) layer on the surface of small particles may be valid. In highly anisotropic barium ferrite, however, this situation can only be realized at temperatures above 650 K.

ACKNOWLEDGMENTS

This study was supported by the Ministry of Education and Science of Ukraine (basic research program, project no. 2201020) and, in part, by the Russian Foundation for Basic Research (project nos. 01-02-17889, 02-02-39006).

REFERENCES

1. L. P. Ol'khovik, T. G. Kuz'micheva, Yu. A. Mamaluĭ, and A. S. Kamzin, Fiz. Tverd. Tela (St. Petersburg) **38** (11), 3420 (1996) [Phys. Solid State **38**, 1865 (1996)].
2. L. P. Ol'khovik, Z. I. Sizova, Z. V. Golubenko, and T. G. Kuz'micheva, J. Magn. Magn. Mater. **183**, 181 (1998).
3. A. S. Kamzin, L. P. Ol'khovik, and Z. I. Sizova, Visn. Khar'k. Derzh. Univ., Ser. Fiz., No. 440 (3), 115 (1999).
4. *Application of Mössbauer Spectroscopy*, Ed. by L. R. Cohen (Academic, New York, 1980), Vol. 2.
5. A. S. Kamzin, V. L. Rozenbaum, L. P. Ol'khovik, and E. D. Kovtun, J. Magn. Magn. Mater. **161**, 139 (1996).
6. A. S. Kamzin, S. M. Irkaev, Yu. N. Mal'tsev, and L. A. Grigor'ev, Prib. Tekh. Éksp., No. 1, 80 (1993).

7. H. J. van Hook, J. Am. Ceram. Soc. **47**, 579 (1964).
8. V. S. Shpinel', *Nuclear Gamma Resonance in Crystals* (Nauka, Moscow, 1968).
9. J. Smit and H. P. J. Wijn, *Ferrites* (Wiley, New York, 1959; Inostrannaya Literatura, Moscow, 1962).
10. T. G. Kuz'micheva, L. P. Ol'khovik, and V. P. Shabatin, Ukr. Patent No. 1,724,584 (7 April 1992).
11. L. P. Ol'khovik, N. M. Borisova, T. G. Kuz'micheva, and V. P. Shabatin, Funkts. Mater. **3** (1), 84 (1996).
12. H. Pfeiffer and W. Schüppel, J. Magn. Magn. Mater. **130**, 92 (1994).
13. P. Görnert, H. Pfeiffer, E. Sinn, *et al.*, IEEE Trans. Magn. **30** (2), 714 (1994).

Translated by G. Skrebtsov

Physics of the Solid State, Vol. 45, No. 11, 2003, pp. 2140–2146. Translated from Fizika Tverdogo Tela, Vol. 45, No. 11, 2003, pp. 2037–2042.

MAGNETISM AND FERROELECTRICITY

Calculation of Longitudinal Susceptibility of Superparamagnetic Particles

Yu. P. Kalmykov* and S. V. Titov**

**Centre d'Études Fondamentales, Université de Perpignan, Perpignan Cedex, 66860 France*

e-mail: kalmykov@univ-perp.fr

***Institute of Radio Engineering and Electronics, Russian Academy of Sciences, pl. Vvedenskogo 1, Fryazino, Moscow oblast, 141190 Russia*

e-mail: svt245@ire216.msk.su

Received December 10, 2002; in final form, April 7, 2003

Abstract—Simple analytical expressions are derived for the complex longitudinal susceptibility $\chi_{\parallel}(\omega)$ of a system of noninteracting superparamagnetic particles with uniaxial and cubic anisotropy within the continuous-diffusion model in the cases of moderate and strong damping. *© 2003 MAIK "Nauka/Interperiodica".*

1. INTRODUCTION

Single-domain ferromagnetic particles are characterized by an internal anisotropic potential with several minima separated by barriers. If the size of a particle is small (~10 nm), the barriers are relatively low. In this case, due to thermal fluctuations, the magnetization vector $\mathbf{M}(t)$ can overcome a barrier and change direction. Thermal instability of magnetization accounts for the phenomenon of superparamagnetism of particles [1–3]; each particle behaves as a paramagnetic atom with a magnetic moment of ~10^4–10^5 Bohr magnetons. The dynamics of the magnetization of single-domain ferromagnetic particles is described by the Landau–Lifshitz equation [4]. An analogous equation was proposed by Gilbert in [5]. Based on these equations, Brown [2, 6] has described the dynamics of the magnetization of an individual particle using the Langevin equation method from the theory of Brownian motion. The Langevin equation was taken in the form of the Gilbert equation with a fluctuating field [5, 6]:

$$\dot{\mathbf{M}}(t) = \gamma[\mathbf{M}(t) \times [\mathbf{H}(t) + \mathbf{h}(t) - \eta\dot{\mathbf{M}}(t)]], \qquad (1)$$

where γ is the gyromagnetic ratio and η is the damping parameter. The total magnetic field consists of externally applied fields, the effective magnetic anisotropy field (all denoted by $\mathbf{H}$), and a random field $\mathbf{h}(t)$. From Eq. (1), Brown derived the Fokker–Planck equation for the probability density function $W(\mathbf{M}, t)$ of magnetization $\mathbf{M}$ [2, 6]:

$$\frac{\partial}{\partial t}W = L_{\mathrm{FP}}W = \frac{1}{2\tau_N} \times \{\beta[\alpha^{-1}\mathbf{u} \cdot (\nabla V \times \nabla W) + \nabla(W\nabla V)] + \Delta W\}. \qquad (2)$$

Here, L_{FP} is the Fokker–Planck operator; Δ and ∇ are the Laplace operator and the gradient operator, respectively, on the unit-sphere surface; V is the free energy density of a particle; $\mathbf{u}$ is a unit vector along the magnetization vector $\mathbf{M}$; $\beta = v/kT$, where v is the volume of the particle, k is the Boltzmann constant, and T is the temperature; and $\tau_N = \beta M_s(1 + \alpha^2)/2\gamma\alpha$ is the characteristic (diffusion) time, where M_s is the magnetization of the material of the particle and $\alpha = \gamma\eta M_s$ is the dimensionless damping parameter, which characterizes the intensity of thermal fluctuations. In deriving Eq. (1), it was assumed that the magnetization is uniform over a particle and that only the direction of the magnetization and not its magnitude varies with time. Furthermore, interparticle interactions and memory effects were not taken into account. A detailed discussion of the conditions under which the Gilbert equation (1) and the Fokker–Planck equation (2) are valid can be found, e.g., in [7, 8]. Formally, Eq. (2) can be solved by expanding the distribution function W in spherical harmonics $Y_{l,m}(\vartheta, \varphi)$ [7, 9] (ϑ and φ are the polar and azimuth angles, respectively). In this case, the problem reduces to the solution of an infinite set of recurrence equations for averaged spherical harmonics (moments) [9]. An equivalent set of equations for the moments can be derived by averaging the Gilbert equation (1) without recourse to the Fokker–Planck equation [10, 11].

The kinetics of magnetization of single-domain particles is determined chiefly by the anisotropy of the free energy V. In this paper, we consider two types of anisotropy. One of them corresponds to uniaxial particles placed in an external static magnetic field $\mathbf{H}_0$, which is assumed to be directed along the symmetry axis of the internal potential of a particle. In this case, the free energy density has the form [6]

$$\beta V(\vartheta) = -\sigma\cos^2\vartheta - \xi\cos\vartheta, \qquad (3)$$

where $\sigma = vK/kT$, with K being the anisotropy constant, and $\xi = vM_sH_0/kT$. The other type of anisotropy corresponds to particles of cubic crystals, for which the free energy density is [6]

$$\beta V(\vartheta, \varphi) = \sigma'(\sin^4\vartheta\sin^2 2\varphi + \sin^2 2\vartheta), \quad (4)$$

where $\sigma' = vK/4kT$ is a dimensionless anisotropy parameter that can be both positive and negative.

The kinetic characteristics of magnetization of uniaxial particles were investigated, e.g., in [2, 6, 12–22]. In particular, the eigenvalue problem for the Fokker–Planck operator (2) was considered in [2, 6, 12, 19]. An exact expression for the relaxation time τ of the longitudinal magnetization was derived in [13, 14]. The complex longitudinal susceptibility and the relaxation time τ were calculated in [15] using the matrix continued fraction method. In the case of cubic anisotropy, the discrete-orientation approximation has mainly been used and the asymptotic solutions of the Fokker–Planck equation (2) have been investigated (see, e.g., [6, 9, 23–27]). In recent papers [28–31], the relaxation time τ of the longitudinal magnetization and the dynamic magnetic susceptibility $\chi_\parallel(\omega)$ of particles with cubic anisotropy were calculated using the matrix continued fraction method.

In this paper, we derive simple expressions for computing the complex longitudinal magnetic susceptibility $\chi_\parallel(\omega)$ of a system of noninteracting single-domain particles with uniaxial and cubic anisotropy in the case of moderate and strong damping ($\alpha \geq 1$), where the effect of the transverse modes on longitudinal relaxation can be ignored. These expressions are shown to agree with the results of numerical calculations carried out by using matrix continued fractions [15, 29, 30].

2. LONGITUDINAL MAGNETIZATION RELAXATION

In terms of the linear-response theory [32], the longitudinal component $\chi_\parallel(\omega)$ of the complex magnetic susceptibility tensor is written as

$$\chi_\parallel(\omega) = \chi_\parallel'(\omega) - i\chi_\parallel''(\omega) = \chi_\parallel\left[1 - i\omega\int_0^\infty e^{-i\omega t}C_\parallel(t)dt\right], \quad (5)$$

where

$$C_\parallel(t) = \frac{\langle\cos\vartheta(0)\cos\vartheta(t)\rangle_0 - \langle\cos\vartheta(0)\rangle_0^2}{\langle\cos^2\vartheta(0)\rangle_0 - \langle\cos\vartheta(0)\rangle_0^2} \quad (6)$$

is the normalized equilibrium autocorrelation function for the longitudinal component of the magnetization **M**,

$$\chi_\parallel = \frac{v^2M_s^2N_0}{kT}[\langle\cos^2\vartheta(0)\rangle_0 - \langle\cos\vartheta(0)\rangle_0^2] \quad (7)$$

is the longitudinal component of the static magnetic susceptibility tensor, and N_0 is the concentration of particles. The angular brackets $\langle\ \rangle_0$ signify the equilibrium ensemble average.

According to Eq. (5), in order to calculate $\chi_\parallel(\omega)$, one needs to determine the spectrum (one-sided Fourier transform) of the equilibrium autocorrelation function $C_\parallel(t)$. Therefore, the spectrum of $\chi_\parallel(\omega)$ is determined entirely by the time evolution of the function $C_\parallel(t)$, which, in turn, depends on the kinetics of the magnetization of a particle and is characterized by three time constants. Variations in $C_\parallel(t)$ on a long time scale are controlled by long-lived relaxation modes, which are associated with reorientation of the magnetization **M** between metastable states. This (low-frequency) process is characterized by the smallest eigenvalue λ_1 of the Fokker–Planck operator L_{FP} in Eq. (2). The $C_\parallel(t)$ dependence on a short time scale is controlled by the high-frequency intrawell modes and is characterized by the effective relaxation time τ^{eff}, defined as

$$\tau^{eff} = -1/\dot{C}_\parallel(0). \quad (8)$$

In general terms, the $C_\parallel(t)$ dependence is characterized by the integral relaxation time τ, which coincides with the correlation time of $C_\parallel(t)$ and is defined as the area under the $C_\parallel(t)$ curve:

$$\tau = \int_0^\infty C_\parallel(t)dt. \quad (9)$$

The relaxation times τ^{eff} and τ can also be expressed in terms of the eigenvalues λ_k of the Fokker–Planck operator L_{FP}. Using the formal expansion of the function $C_\parallel(t)$ in terms of the relaxation modes

$$C_\parallel(t) = \sum_k c_k e^{-\lambda_k t}, \quad (10)$$

we obtain from Eqs. (8)–(10)

$$\tau^{eff} = \left(\sum_k \lambda_k c_k\right)^{-1}, \quad \tau = \sum_k c_k/\lambda_k. \quad (11)$$

Here, $\sum_k c_k = 1$. In general, the dependences of the relaxation times τ, τ^{eff}, and $1/\lambda_1$ on the parameters of the problem (such as the external field strength and anisotropy constant) can differ considerably [15].

As seen from Eqs. (11), all eigenvalues λ_k contribute to τ^{eff} and τ. For this reason, Eqs. (11) are unsuitable for calculating τ^{eff} and τ and it is more convenient to use Eqs. (8) and (9). In order to derive a working formula for the effective relaxation time τ^{eff} from Eq. (8) for anisotropy of an arbitrary type, we use the Gilbert equa-

tion for the average magnetization written in polar coordinates:

$$2\tau_N \frac{d}{dt}\cos\vartheta = -2\cos\vartheta + \beta\sin\vartheta\frac{\partial V}{\partial\vartheta} - \frac{\beta}{\alpha}\frac{\partial V}{\partial\varphi}. \quad (12)$$

From Eq. (12), it follows that

$$\left\langle \cos\vartheta\frac{d}{dt}\cos\vartheta\right\rangle_0 = -\frac{1}{\tau_N}\left\langle \cos^2\vartheta - \frac{\beta\sin 2\vartheta}{4}\frac{\partial V}{\partial\vartheta} + \frac{\beta}{2\alpha}\cos\vartheta\frac{\partial V}{\partial\varphi}\right\rangle_0 = -\frac{1}{2\tau_N}(1-\langle\cos^2\vartheta\rangle_0). \quad (13)$$

Using Eqs. (6), (8), and (13), we obtain

$$\tau^{\text{eff}} = 2\tau_N\frac{\langle\cos^2\vartheta\rangle_0 - \langle\cos\vartheta\rangle_0^2}{1-\langle\cos^2\vartheta\rangle_0}. \quad (14)$$

For the particular case of uniaxial particles, Eq. (14) was derived in [33]. The integral relaxation time τ can be reduced to quadratures only for an axially symmetric potential V [14, 34]:

$$\tau = \int_0^\infty C_\parallel(t)dt = \frac{2\tau_N}{Z(\langle\cos^2\vartheta\rangle_0 - \langle\cos\vartheta\rangle_0^2)} \times \int_{-1}^{1}\left[\int_{-1}^{z}(z' - \langle\cos\vartheta\rangle_0)e^{-\beta V(z')}dz'\right]^2\frac{e^{\beta V(z)}}{1-z^2}dz. \quad (15)$$

Here,

$$Z = \int_{-1}^{1} e^{-\beta V(x)}dx,$$
$$\langle\cos^n\vartheta\rangle_0 = \frac{1}{Z}\int_{-1}^{1}x^n e^{-\beta V(x)}dx \quad (n = 1, 2). \quad (16)$$

For the case of arbitrary anisotropy, an analogous analytical expression for τ has not been derived. However, the time τ can be calculated from Eq. (9) numerically [15, 21, 29–31].

3. ESTIMATION OF THE MAGNETIC SUSCEPTIBILITY

Using Eqs. (5), (8), and (9) and certain properties of the Fourier transformation, we obtain the following expressions for the longitudinal susceptibility $\chi_\parallel(\omega)$ in the extreme cases of low ($\omega \longrightarrow 0$) and high ($\omega \longrightarrow \infty$) frequencies:

$$\frac{\chi_\parallel(\omega)}{\chi_\parallel} = 1 - i\omega\int_0^\infty C_\parallel(t)dt + O(\omega^2) = 1 - i\omega\tau + O(\omega^2), \quad (17)$$

$$\frac{\chi_\parallel(\omega)}{\chi_\parallel} \sim -\frac{\dot C_\parallel(0)}{i\omega} + O(\omega^{-2}) = -\frac{i}{\omega\tau^{\text{eff}}} + O(\omega^{-2}). \quad (18)$$

According to Eqs. (17) and (18), the low- and high-frequency parts of the spectrum of the magnetic loss $\chi_\parallel''(\omega)$ are determined by the relaxation times τ and τ^{eff}, respectively. We note that the asymptotic expressions (17) and (18) are general and hold for an arbitrary system of noninteracting superparamagnetic particles.

According to Eq. (10), the correlation function $C_\parallel(t)$ generally involves an infinite number of exponentially decaying modes with characteristic frequencies equal to the eigenvalues λ_k. For bistable and multistable potentials (to which the free energies of uniaxial and cubic crystals belong), the eigenvalues λ_k can be classified into two groups. One group consists of eigenvalues (or, in certain cases, of only one eigenvalue λ_1, as in the case of uniaxial particles [12, 19]) that characterize long-lived longitudinal modes associated with magnetization reorientation through overcoming potential barriers. With decreasing temperature (increasing barrier heights), such eigenvalues vanish exponentially, so that we have $\lambda_1\tau_N \ll 1$. The other group includes all remaining eigenvalues, which characterize high-frequency intrawell modes. As the temperature is decreased, the characteristic frequencies of these modes increase and the main contribution to the susceptibility comes from a few modes with frequencies close to each other [15, 19]. For uniaxial and cubic anisotropy, the eigenvalues exhibit such behavior in the cases of moderate and strong damping [15, 19, 24–26]. Therefore, in these cases, diffusion within a potential well is a much faster process than are jumps over a barrier and we can use the following expression to describe the correlation function $C_\parallel(t)$ in Eq. (10):

$$C_\parallel(t) \approx \Delta_1 e^{-\lambda_1 t} + (1-\Delta_1)e^{-t/\tau_W}. \quad (19)$$

Accordingly, the spectrum of $\chi_\parallel(\omega)$ can be represented as the sum of two Lorentzians with the characteristic frequencies λ_1 and τ_W^{-1}:

$$\frac{\chi_\parallel(\omega)}{\chi_\parallel} = \frac{\Delta_1}{1+i\omega/\lambda_1} + \frac{1-\Delta_1}{1+i\omega\tau_W}. \quad (20)$$

The parameters Δ_1 and τ_W can be determined by comparing Eqs. (19) and (20) in the extreme cases of low

($\omega \longrightarrow 0$) and high ($\omega \longrightarrow \infty$) frequencies with asymptotically exact Eqs. (17) and (18):

$$\Delta_1 = \frac{\tau/\tau^{\text{eff}} - 1}{\lambda_1\tau - 2 + 1/(\lambda_1\tau^{\text{eff}})}, \tag{21}$$

$$\tau_W = \frac{\lambda_1\tau - 1}{\lambda_1 - 1/\tau^{\text{eff}}} \tag{22}$$

(Δ_1 and τ_W are found by solving a quadratic equation, only one root of which has physical meaning). Thus, by making the estimates of τ, τ^{eff}, and λ_1 independent, one can calculate Δ_1 and τ_W from Eqs. (20)–(22) and predict the spectrum of $\chi_\parallel(\omega)$ over the entire spectral range $0 \le \omega < \infty$.

It should be noted that, for a superparamagnetic particle with arbitrary anisotropy, the contribution from the high-frequency intrawell modes to the quantity given by Eq. (20) can be approximated by one Lorentzian only in the case of moderate and large values of the damping parameter, $\alpha \ge 1$, because only in this case can the effect of the transverse modes on the longitudinal response be neglected. The exception to this conclusion is the case of a uniaxial particle in an external static field $\mathbf{H}_0$ applied along the anisotropy axis. In this case, the quantities $\chi_\parallel(\omega)$, τ, τ^{eff}, and $1/\lambda_1$ do not depend explicitly on α.

4. UNIAXIAL PARTICLES

The complex longitudinal susceptibility of uniaxial particles with the free energy density V given by Eq. (3) was calculated in [15] by exactly solving (in terms of matrix continued fractions) an infinite set of recurrence equations for longitudinal correlation functions $f_n(t)$:

$$\begin{aligned}\frac{2\tau_N}{n(n+1)}\frac{d}{dt}f_n(t) + \left[1 - \frac{2\sigma}{(2n-1)(2n+3)}\right]f_n(t) \\ = \frac{\xi}{2n+1}[f_{n-1}(t) - f_{n+1}(t)] \\ + 2\sigma\left[\frac{n-1}{(2n-1)(2n+1)}f_{n-2}(t)\right. \\ \left. - \frac{n+2}{(2n+1)(2n+3)}f_{n+2}(t)\right], \\ n = 1, 2, \ldots,\end{aligned} \tag{23}$$

where

$$\begin{aligned}f_n(t) = \langle \cos\vartheta(0) P_n[\cos\vartheta(t)]\rangle_0 \\ - \langle \cos\vartheta(0)\rangle_0 \langle P_n[\cos\vartheta(0)]\rangle_0,\end{aligned}$$

with $P_n(z)$ being the Legendre polynomials. Introducing the quantity $f_1(t)/f_1(0) \equiv C_\parallel(t)$ and using Eq. (5), we can calculate the complex susceptibility [15]. The smallest eigenvalue λ_1 of the Fokker–Planck operator

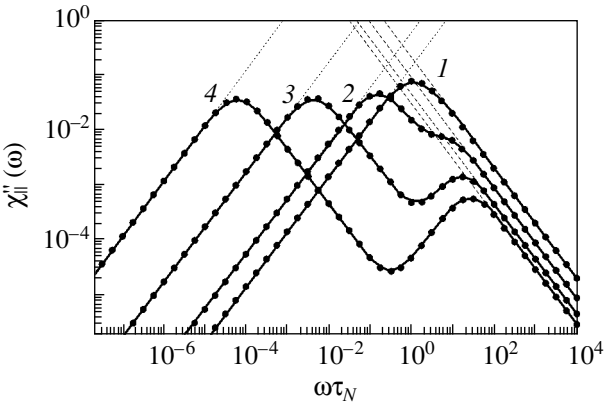

Fig. 1. Calculated $\chi''_\parallel(\omega)$ for $\xi = 2$ and different values of σ: (*1*) 1, (*2*) 5, (*3*) 10, and (*4*) 15. Solid curves are the exact solution found in terms of matrix continued fractions [15]; dots are calculations from Eq. (20) with values of τ, τ^{eff}, and $1/\lambda_1$ taken from the table; and dotted and dashed lines are low-frequency and high-frequency asymptotes calculated from Eqs. (15), (17) and Eqs. (14), (18), respectively.

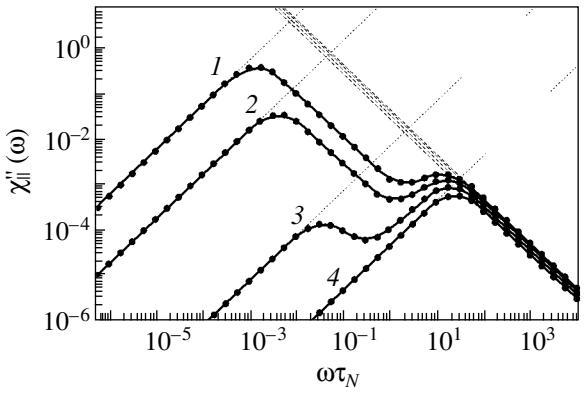

Fig. 2. Same as in Fig. 1 but for $\sigma = 10$ and various values of ξ: (*1*) 0, (*2*) 2, (*3*) 5, and (*4*) 10.

can be found from the set of recurrence equations (23), which we represent in the matrix form [15]

$$\dot{\mathbf{X}} = \hat{\mathbf{A}}\mathbf{X}, \tag{24}$$

where $\hat{\mathbf{A}}$ is a five-diagonal matrix and $\mathbf{X}$ is a vector consisting of the functions $f_n(t)$. The effective relaxation time τ^{eff} can be found from Eq. (14), in which the equilibrium averages (16) are calculated for the given potential (3). Finally, the general relaxation time τ can be calculated from the analytical formula (15).

Figures 1 and 2 compare the results from calculating the spectrum of the imaginary part $\chi_\parallel(\omega)$ of the complex susceptibility of uniaxial particles using matrix continued fractions [15] and approximate expressions (20)–(22) for various values of the parameters ξ and σ and of the quantities $1/\lambda_1$, τ, and τ^{eff} listed in the table (in the

Values of τ, τ^{eff}, $1/\lambda_1$, and τ_W as calculated from Eqs. (15), (14), (23), and (22), respectively

$\sigma = 10$	$\xi = 0$	$\xi = 2$	$\xi = 5$	$\xi = 10$
τ_N/λ_1	693.9	232.5	26.82	2.265
τ/τ_N	691.0	224.1	3.398	0.0386
τ^{eff}/τ_N	16.64	1.690	0.0565	0.0384
τ_W/τ_N	0.0714	0.0615	0.0495	0.0384
$\xi = 2$	$\sigma = 1$	$\sigma = 5$	$\sigma = 10$	$\sigma = 15$
τ_N/λ_1	0.9763	6.387	232.5	16484
τ/τ_N	0.8912	5.720	224.1	16221
τ^{eff}/τ_N	0.7528	1.097	1.610	2.366
τ_W/τ_N	0.2866	0.1383	0.0615	0.0377

calculations, it was assumed that $\nu^2 M_s^2 N_0/kT = 1$). Two clearly defined bands can be seen in the spectrum of $\chi''(\omega)$. The frequency and half-width of the low-frequency band are determined by λ_1. The high-frequency band is associated with the high-frequency intrawell modes. Despite the large number of such modes involved in relaxation, the latter band can be closely approximated by one Lorentzian. From Figs. 1 and 2, it is seen that approximate expression (20) adequately describes the exact solution [15] (the maximum difference between the results is observed in the range $0.1 < \omega\tau_N < 10$ and is of the order of 5%). Calculations also show that there is good agreement between the exactly and approximately calculated values of the real part of the susceptibility $\chi_\parallel(\omega)$ in the range of parameter values $0 \le (\sigma, \xi) < 100$.

5. CUBIC ANISOTROPY

The longitudinal susceptibility of particles with cubic anisotropy described by Eq. (4) was calculated in [28–30] (using matrix continued fractions) by exactly solving an infinite set of recurrence equations for the equilibrium correlation functions $c_{l,m}(t) = \langle \cos\vartheta(0) Y_{l,m}[\vartheta(t), \varphi(t)]\rangle_0$. In the extreme case of $\alpha \gg 1$, this set can be represented in the form

$$\tau_N \frac{d}{dt} c_{l,m}(t) = \sum_{s=-1}^{1} \sum_{r=-2}^{2} d_{l,m,l+2r,m+4s} c_{l+2r,m+4s}(t). \quad (25)$$

Explicit expressions for the coefficients $d_{n,m,r,s}$ can be found in [29, 30]. The longitudinal susceptibility is given by Eq. (5), where $C_\parallel(t) = c_{1,0}(t)/c_{1,0}(0)$. The static susceptibility is $\chi_\parallel = \nu^2 M_s^2 N_0/3kT$, because, in terms of the symmetry, we have

$$\langle \cos^2\vartheta\rangle_0 = 1/3. \quad (26)$$

The effective relaxation time τ^{eff} can be calculated from Eq. (14). Using Eq. (26), we obtain

$$\tau^{eff} = \tau_N. \quad (27)$$

The dependence of the relaxation time τ on σ' was investigated in detail in [29, 30], where it was shown, in particular, that $\tau \approx \lambda_1^{-1}$ at any temperature in the case of moderate and strong damping; therefore, the value of τ is mainly determined by the lowest frequency relaxation mode. The exact values of λ_1 and $\tau_\parallel$ can be found from the recurrence equation (25), represented in the matrix form (24), or by using matrix continued fractions [29, 30]. In the case of cubic anisotropy, the values of λ_1^{-1} can also be calculated from the approximate formulas [35]

$$\lambda_1^{-1} \approx \tau_N \frac{(e^{\sigma'} - 1)}{\sigma'}\left[\frac{\pi}{8\sqrt{2}} + \left(1 - \frac{\pi}{8\sqrt{2}}\right)2^{-\sigma'}\right] \quad (28)$$

for $\sigma' \ge 0$ and

$$\lambda_1^{-1} \approx -3\tau_N \frac{(e^{-\sigma'/3} - 1)}{\sigma'}\left[\frac{\pi}{4\sqrt{2}} + \left(1 - \frac{\pi}{4\sqrt{2}}\right)2^{\sigma'/3}\right] \quad (29)$$

for $\sigma' \le 0$. Equations (28) and (29) closely approximate both λ_1^{-1} and τ in the entire range of values of the parameter σ' [35]. In addition, the amplitude Δ_1 and the time τ_W in Eq. (20) can also be evaluated (for $|\sigma'| > 3$) from the simple expressions [35]

$$\Delta_1 \approx 1 - 1/4\sigma', \quad \tau_W \approx \tau_N/(4\sigma') \quad (30)$$

for positive values of the anisotropy constant and

$$\Delta_1 \approx 1 - 3/(8|\sigma'|), \quad \tau_W \approx 3\tau_N/(8|\sigma'|) \quad (31)$$

for a negative anisotropy constant.

Figures 3 and 4 compare the calculated spectra of $\chi''(\omega)$ using approximate and exact formulas for different values of σ' in the case of cubic anisotropy. It can be seen that the approximate expression (20) ade-

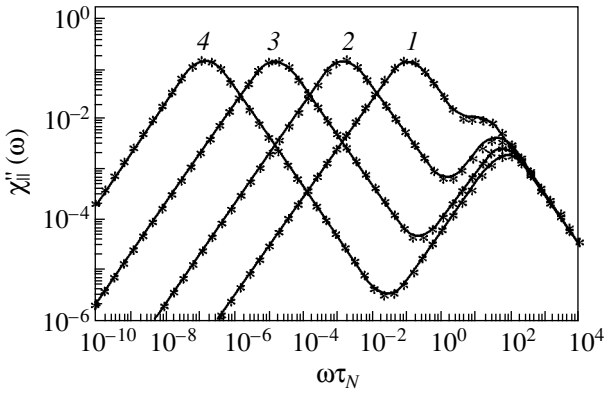

Fig. 3. Calculated $\chi''_{\|}(\omega)$ as a function of $\omega\tau_N$ for various values of $\sigma' > 0$: (*1*) 5, (*2*) 10, (*3*) 15, and (*4*) 20. Solid curves are the exact solution found in terms of matrix continued fractions [29, 30], and asterisks are calculations from Eqs. (20), (28), and (30).

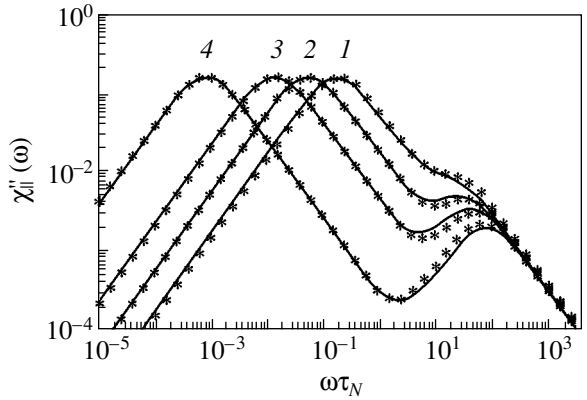

Fig. 4. Same as in Fig. 3 but for various values of $\sigma' < 0$: (*1*) –10, (*2*) –15, (*3*) –20, and (*4*) –30. Asterisks are calculations from Eqs. (20), (29), and (31).

quately describes the spectrum of $\chi''(\omega)$ in both the case of positive and negative values of the anisotropy constant. In accordance with Eq. (20), the low-frequency and high-frequency modes are each approximated closely by one relaxation mode. Calculations show that approximate formula (20) is fairly accurate even in the case of small values of the parameter σ' ($1 \le |\sigma'| \le 3$).

6. CONCLUSION

Thus, we have developed a simple method for calculating the longitudinal magnetic susceptibility $\chi_{\|}(\omega)$ of a system of superparamagnetic particles with uniaxial and cubic anisotropy in the case of moderate and strong damping. It has been shown that, using three time constants characterizing the magnetic relaxation, namely, the correlation time τ, the effective relaxation time τ^{eff}, and the reciprocal of the smallest eigenvalue λ_1 of the Fokker–Planck operator, the spectrum of $\chi_{\|}(\omega)$ can be adequately described over a wide frequency range. Furthermore, calculations showed that Eq. (20) can also be used for particles with other types of anisotropy (for example, for particles of a cubic crystal in a strong dc magnetic field). These results will be published elsewhere.

ACKNOWLEDGMENTS

The authors are grateful to W.T. Coffey (Trinity College, Dublin) for valuable suggestions.

This study was supported by the Russian Foundation for Basic Research (project no. 01-02-16050) and INTAS (grant no. 01-2341).

REFERENCES

1. L. Néel, Ann. Geophys. **5**, 99 (1949).
2. W. F. Brown, Jr., Phys. Rev. **130**, 1677 (1963).
3. C. P. Bean and J. D. Livingston, J. Appl. Phys. (Suppl.) **30**, 1205 (1959).
4. L. D. Landau and E. M. Lifshitz, Phys. Z. Sowjetunion **8**, 153 (1935).
5. T. L. Gilbert, Phys. Rev. **100**, 1243 (1956).
6. W. F. Brown, Jr., IEEE Trans. Magn. **15**, 1196 (1979).
7. Yu. L. Raikher and M. I. Shliomis, Adv. Chem. Phys. **87**, 595 (1994).
8. I. Klik and L. Gunther, J. Stat. Phys. **60**, 473 (1990).
9. L. J. Geoghegan, W. T. Coffey, and B. Mulligan, Adv. Chem. Phys. **100**, 475 (1997).
10. Yu. P. Kalmykov and S. V. Titov, Phys. Rev. Lett. **82** (14), 2967 (1999).
11. Yu. P. Kalmykov and S. V. Titov, Fiz. Tverd. Tela (St. Petersburg) **41** (11), 2020 (1999) [Phys. Solid State **41**, 1854 (1999)].
12. A. Aharoni, Phys. Rev. **177** (2), 793 (1969).
13. D. A. Garanin, V. V. Ishchenko, and L. V. Panina, Teor. Mat. Fiz. **82**, 242 (1990).
14. D. A. Garanin, Phys. Rev. E **54** (4), 3250 (1996).
15. W. T. Coffey, D. S. F. Crothers, Yu. P. Kalmykov, and J. T. Waldron, Phys. Rev. B **51** (22), 15947 (1995).
16. É. K. Sadykov and A. G. Isavnin, Fiz. Tverd. Tela (St. Petersburg) **38**, 2104 (1996) [Phys. Solid State **38**, 1160 (1996)].
17. Yu. L. Raikher and V. I. Stepanov, Phys. Rev. B **55** (22), 15005 (1997).
18. Yu. L. Raikher, V. I. Stepanov, A. N. Grigirenko, and P. I. Nikitin, Phys. Rev. E **56** (11), 6400 (1997).
19. I. Klik and Y. D. Yao, J. Magn. Magn. Mater. **182**, 335 (1998).
20. J. L. Garcia-Palacios, Adv. Chem. Phys. **112**, 1 (2000).
21. Yu. P. Kalmykov and S. V. Titov, Fiz. Tverd. Tela (St. Petersburg) **40** (9), 1642 (1998) [Phys. Solid State **40**, 1492 (1998)].
22. Yu. P. Kalmykov and S. V. Titov, Fiz. Tverd. Tela (St. Petersburg) **42** (5), 893 (2000) [Phys. Solid State **42**, 918 (2000)].
23. A. Aharoni, Phys. Rev. B **7** (3), 1103 (1973).

24. D. A. Smith and F. A. de Rosario, J. Magn. Magn. Mater. **3**, 219 (1976).
25. I. Eisenshtein and A. Aharoni, Phys. Rev. B **16** (3), 1278 (1977).
26. I. Eisenshtein and A. Aharoni, Phys. Rev. B **16** (3), 1285 (1977).
27. I. Klik and L. Gunther, J. Appl. Phys. **67**, 4505 (1990).
28. Yu. P. Kalmykov and S. V. Titov, Fiz. Tverd. Tela (St. Petersburg) **40** (10), 1898 (1998) [Phys. Solid State **40**, 1721 (1998)].
29. Yu. P. Kalmykov, S. V. Titov, and W. T. Coffey, Phys. Rev. B **58** (6), 3267 (1998).
30. Yu. P. Kalmykov and S. V. Titov, Zh. Éksp. Teor. Fiz. **115**, 101 (1999) [JETP **88**, 58 (1999)].
31. Yu. P. Kalmykov, Phys. Rev. B **61** (9), 6205 (2000).
32. D. Forster, *Hydrodynamic Fluctuations, Broken Symmetry, and Correlation Functions* (Benjamin, Reading, MA, 1975).
33. W. T. Coffey, P. J. Cregg, and Yu. P. Kalmykov, Adv. Chem. Phys. **83**, 263 (1993).
34. Yu. P. Kalmykov, J. L. Déjardin, and W. T. Coffey, Phys. Rev. E **55** (3), 2509 (1997).
35. J. L. Déjardin and Yu. P. Kalmykov, J. Chem. Phys. **111**, 3644 (1999).

Translated by Yu. Epifanov

Physics of the Solid State, Vol. 45, No. 11, 2003, pp. 2147–2151. Translated from Fizika Tverdogo Tela, Vol. 45, No. 11, 2003, pp. 2043–2047.

MAGNETISM AND FERROELECTRICITY

Nuclear Superstructure {1/2, 0, 1/2} of an $La_{0.93}Sr_{0.07}MnO_3$ Manganite Orthorhombic Crystal

S. F. Dubinin, V. E. Arkhipov, S. G. Teploukhov, and V. D. Parkhomenko

Institute of Metal Physics, Ural Division, Russian Academy of Sciences, ul. S. Kovalevskoĭ 18, Yekaterinburg, 620219 Russia

e-mail: dubinin@uraltc.ru

Received April 18, 2003

Abstract—The {1/2, 0, 1/2} nuclear superstructure in an $La_{0.93}Sr_{0.07}MnO_3$ manganite orthorhombic crystal is revealed using thermal-neutron diffraction. It is demonstrated that this superlattice belongs to the class of distortion-type structures and is directly associated with a 1/16-type ordering of Mn^{4+} and Mn^{3+} ions in a collinear ferromagnetic phase of the $La_{0.93}Sr_{0.07}MnO_3$ manganite. © *2003 MAIK "Nauka/Interperiodica".*

1. INTRODUCTION

Yamada *et al.* [1] and Vasiliu-Doloc *et al.* [2] demonstrated that $La_{1-x}Sr_xMnO_3$ manganite crystals have a nuclear superstructure with the wave vector

$$q = (0.5, 0, 0.5)_0. \quad (1)$$

According to the neutron diffraction data obtained in [1, 2], the superstructure with wave vector (1) in these manganites is observed only in the orthorhombic phase in the range $0.1 \le x \le 0.15$. The location of superstructure reflections of type (1) in the a^*c^* plane of the reciprocal lattice of the $La_{0.85}Sr_{0.15}MnO_3$ manganite orthorhombic crystal studied in [1] is schematically drawn in Fig. 1. In this figure, the main Bragg reflections of the orthorhombic crystal are depicted by closed circles. The superstructure reflections are indicated by open circles. Yamada *et al.* [1] made the inference that the superstructure with wave vector (1) belongs to the class of distortion-type structures. However, the origin of this superstructure was not discussed in [1].

Vasiliu-Doloc *et al.* [2] assumed that the scattering pattern shown in Fig. 1 corresponds to the superstructure with another wave vector,

$$q = (0, 1, 0)_0, \quad (2)$$

which is very close in magnitude to wave vector (1). This superstructure can also be schematically drawn in the a^*c^* plane with due regard for the domain structure of manganite crystals. In principle, this situation can take place. However, in our earlier work [3], in which the diffraction experiments were performed with an $La_{0.85}Sr_{0.15}MnO_3$ manganite crystal of good quality, we did not reveal indications of b^*-type domains in the a^*c^* plane of the reciprocal lattice but observed the superstructure with wave vector (1).

In our opinion, the superstructure with wave vector (1) is directly associated with charge ordering of Mn^{3+} and Mn^{4+} ions in the crystal lattice of the $La_{0.85}Sr_{0.15}MnO_3$ orthorhombic manganite. In this case, the nuclear component of the intensity of the superstructure reflection appears in the neutron diffraction pattern of the crystal, because the Mn^{4+} ions do not affect the surrounding oxygen octahedra (since these ions have no orbital angular momentum), whereas the Mn^{3+} ions strongly distort their own oxygen environments due to interaction of the $d(z^2)$ orbitals of the ions with the crystal lattice. Within this model, the unit cell parameters of the superstructure with allowance made for wave vectors (1) and (2) should be determined by the quantities $2a$, $2c$, and b (where a, c, and b are the parameters of the original orthorhombic crystal lattice). It is easy to verify that the unit cell with the above parameters contains 16 manganese ions [4]. In particular, for charge ordering with the ion ratio $x\mathrm{Mn}^{4+}/[x\mathrm{Mn}^{4+} + (1-x)\mathrm{Mn}^{3+}] =$

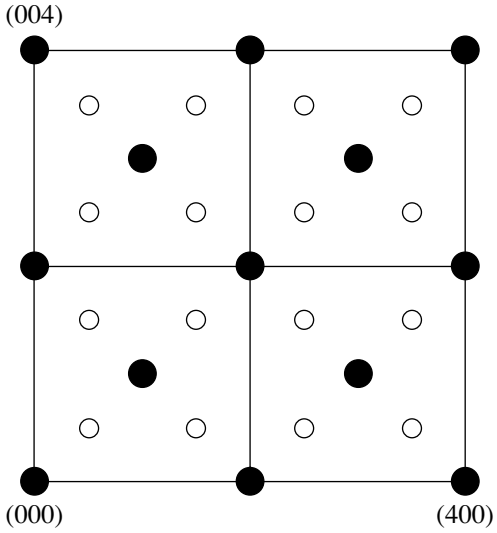

Fig. 1. Schematic drawing of the {1/2, 0, 1/2} nuclear superstructure in the a^*c^* plane of the $La_{0.85}Sr_{0.15}MnO_3$ manganite orthorhombic crystal at 4.2 K [1].

Basic parameters of the spin system of the $La_{0.93}Sr_{0.07}MnO_3$ manganite

Phase **1** (*O*')				Phase **2** (*O**)	
volume fraction in the crystal	canting angle, deg	T_N, K	T_C, K	volume fraction in the crystal	T_C, K
0.9	25	121	128	0.1	≅128

1/8, this means that two out of sixteen positions in the unit cell are occupied by Mn^{4+} ions. This situation occurs in the $La_{0.85}Sr_{0.15}MnO_3$ crystal [4]. In the aforementioned unit cell, the charge ordering corresponding to a stoichiometry of 1/16 becomes possible as well. In this case, only one out of sixteen positions in the unit cell is occupied by Mn^{4+} ions. It is this assumption of a 1/16-type charge ordering that provides the simplest explanation of large-scale phase separation of the spin system in the $La_{0.93}Sr_{0.07}MnO_3$ manganite crystal [5].

The main objective of the present work was to validate the proposed hypothesis for an $La_{0.93}Sr_{0.07}MnO_3$ manganite crystal ($0.07 \cong 1/16$). In this study, the neutron diffraction technique was used as a direct method of revealing and characterizing superlattices of type (1).

2. SAMPLES AND EXPERIMENTAL TECHNIQUE

The $La_{0.93}Sr_{0.07}MnO_3$ manganite crystal was grown by zone melting upon radiation heating in an argon atmosphere [6]. A sample was prepared in the form of a cylinder with linear sizes $d = 4$ mm and $l = 10$ mm. The manganite compound had a single-phase composition and an *O*' orthorhombic structure with the unit cell parameters $a_0 = 5.600$ Å, $b_0 = 7.753$ Å, and $c_0 = 5.549$ Å, which were determined by x-ray diffraction at room temperature in [7].

Experiments on elastic scattering of thermal neutrons were performed using a special multidetector diffractometer designed for single-crystal investigations. The wavelength λ of neutrons incident on the sample was equal to 1.567 Å. This was provided by a double crystal monochromator prepared from pyrolytic carbon and germanium. The efficient monochromatization of the primary beam and the appropriate choice of the wavelength of monochromatic neutrons made it possible to suppress multiple diffraction harmonics in the neutron diffraction pattern of the single crystal. This appreciably increased the sensitivity of our neutron diffraction technique.

3. RESULTS AND DISCUSSION

Before proceeding further, we recall the important parameters determined for the spin system of the $La_{0.93}Sr_{0.07}MnO_3$ manganite crystal in our previous work [5]. In [5], we established that this compound in the magnetic state holds a unique position among solid solutions in the $La_{1-x}Sr_xMnO_3$ system, in which an increase in the content x leads to a transition from antiferromagnetic ordering ($LaMnO_3$, $T_N = 139.5$ K) to ferromagnetic ordering ($La_{0.9}Sr_{0.1}MnO_3$, $T_C = 152$ K). The basic parameters of the spin system of the $La_{0.93}Sr_{0.07}MnO_3$ manganite crystal are presented in the table.

As can be seen from the table, the transition state in the $La_{0.93}Sr_{0.07}MnO_3$ compound is governed by large-scale spin configurations of two types: (i) regions of the collinear ferromagnetic phase (phase **2**) with a mean linear size of 200 Å occupy approximately 10% of the volume of the crystal [5], and (ii) the other volume of the crystal is occupied by the phase with an inhomogeneous canted magnetic structure (phase **1**). Information on the spin configuration in the ground state is necessary for analyzing the nuclear superstructure of the $La_{0.93}Sr_{0.07}MnO_3$ manganite.

In our opinion, the most characteristic neutron diffraction patterns of the $La_{0.93}Sr_{0.07}MnO_3$ manganite crystal are observed in the a^*c^* plane of the reciprocal lattice in the vicinity of the (1.5, 0, 1.5) point. In these diffraction patterns, the scattering angle is relatively small ($2\theta \cong 35.5°$), which ensures sufficient (for our purposes) instrumental resolution. The experimental intensities of neutron scattering in the diffraction pattern of the crystal upon scanning along the scattering vector $\kappa = 4\pi\sin\theta/\lambda$ over a wide temperature range (78–550 K) are presented in Fig. 2. In this figure, closed circles are the experimental intensities measured upon cooling of the sample from a temperature of 550 K and open circles are the experimental intensities measured upon subsequent heating from the liquid-nitrogen temperature.

It can be seen from Fig. 2 that the $La_{0.93}Sr_{0.07}MnO_3$ manganite crystal is characterized by a superstructure of type (1). However, the diffraction pattern of this crystal is rather complicated. For example, the diffraction reflections exhibit a complex structure at certain temperatures and a temperature hysteresis of the intensity of diffraction reflections is observed in the range $78 < T < 380$ K. In order to elucidate the nature of the superstructure observed, we examine in more detail the neutron diffraction patterns shown in Figs. 2a and 2c.

(i) First, we consider the experimental diffraction pattern depicted by open circles in Fig. 2c. As is seen from this figure, the diffraction pattern measured at a temperature of 290 K (i.e., above the Curie point T_C of the manganite) exhibits a single nuclear superstructure reflection corresponding to the (1.5, 0, 1.5) indices.

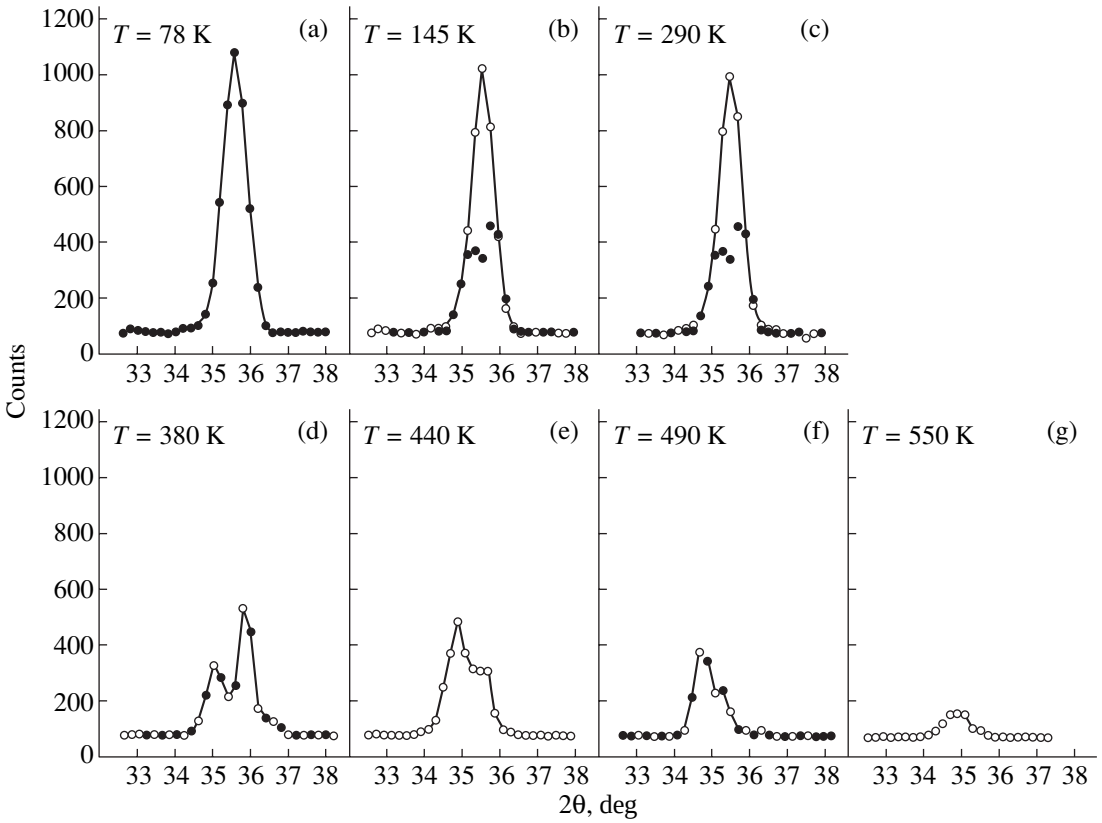

Fig. 2. Experimental intensities of neutron scattering in the vicinity of the (1.5, 0, 1.5) reciprocal lattice point in the diffraction pattern of the $La_{0.93}Sr_{0.07}MnO_3$ crystal at different temperatures.

Figure 3 shows the neutron diffraction pattern of the $La_{0.93}Sr_{0.07}MnO_3$ manganite crystal measured along the [ξ, 0, 0.5] crystallographic direction (Fig. 1) under the same temperature conditions. This diffraction pattern contains three reflections of series (1), namely, the (2.5, 0, 0.5), (3.5, 0, 0.5), and (4.5, 0, 0.5) reflections. It can be seen from Fig. 3 that the intensities of the reflections increase monotonically with an increase in the distance from the origin of the reciprocal lattice. This is consistent with the standard relationship

$$I(\kappa) \sim (\boldsymbol{\kappa} \cdot \mathbf{u})^2, \quad (3)$$

where **u** is the small vector of structural distortions and **κ** is the scattering vector. Therefore, the nuclear superstructure observed belongs to the class of distortion-type structures.

(ii) Second, let us demonstrate that nuclear superstructure of type (1) in the case under consideration is characteristic not of the whole volume of the sample but only of the crystal regions occupied (in the ground state) by the collinear ferromagnetic phase **2** (see table).

In this respect, we discuss in greater detail the diffraction pattern depicted by closed circles in Fig. 2c. The same pattern is shown on an enlarged scale in Fig. 4. Dashed and solid lines in this figure correspond to the results of the profile analysis of the intensities of the studied reflections. As can be seen from Fig. 4, the experimental data fit two peaks (*1*, *2*) with a Gaussian shape fairly well (in this case, the *R* factor is approximately equal to 1%). It is easy to verify that the diffraction doublet is associated with the domain structure. In actual fact, any coherent effect of scattering measured in the diffraction pattern of the domain orthorhombic crystal along the [101] direction can exhibit no more

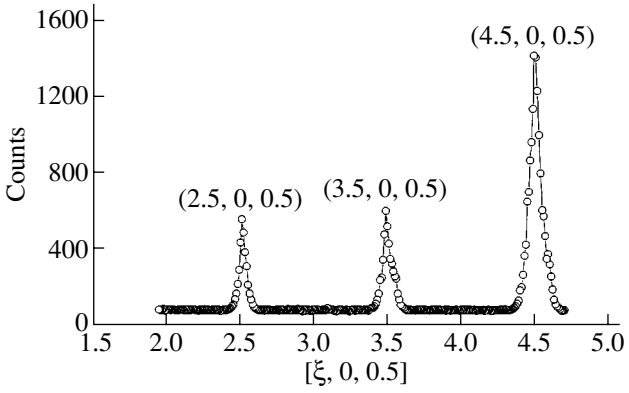

Fig. 3. Neutron diffraction pattern of the $La_{0.93}Sr_{0.07}MnO_3$ crystal measured at 290 K (after preliminary cooling to 78 K) along the [ξ, 0, 0.5] crystallographic direction.

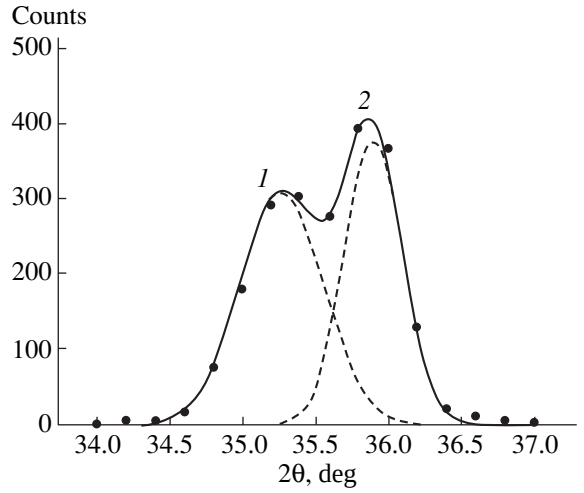

Fig. 4. Profile analysis of the intensity of neutron scattering in the vicinity of the (1.5, 0, 1.5) reciprocal lattice point in the neutron diffraction pattern of the $La_{0.93}Sr_{0.07}MnO_3$ crystal measured at 290 K (after cooling from T = 550 K) along the [101] direction. Points are experimental data. The solid line corresponds to the results of calculations. Dashed lines indicate the contributions of domains *1* and *2* to the intensity of neutron scattering.

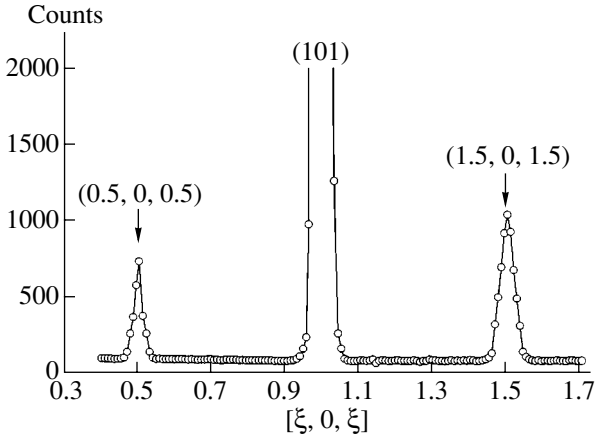

Fig. 5. Neutron diffraction pattern of the $La_{0.93}Sr_{0.07}MnO_3$ crystal at 78 K along the [101] direction.

than two closely spaced peaks. In our case, the first peak in Fig. 4 should represent a superposition of (1.5, 0, 1.5) reflections of two domains, namely, a^*c^* and c^*a^*, with identical scattering angles. The second peak in Fig. 4 should correspond to the (030) reflection of the b^* domain. This model is confirmed by the fact that the lattice parameters determined from the angular positions of peaks *1* and *2* in Fig. 4 are in good agreement with the unit cell parameters a_0, b_0, and c_0 obtained in [7] (see above).

Let us now compare the shapes and half-widths at half-maxima of the superstructure reflections in Fig. 4 with those of the main Bragg reflections (101) and (202). The main Bragg reflections in the neutron diffraction pattern of the $La_{0.93}Sr_{0.07}MnO_3$ manganite crystal at 78 K are shown in Fig. 5. The half-widths of these reflections are equal to 0.52° and 0.85° (it is known that the instrumental width of reflections increases with an increase in the scattering angle), which is considerably less than the total half-width [$\Delta(2\theta)$ = 1.15°] for the coherent effect of scattering observed in Fig. 4.

The above experimental results (Figs. 4, 5), which might appear at first glance to be contradictory, can be explained as follows. The {1/2, 0, 1/2} nuclear superstructure corresponds to the crystal regions occupied by domain phase **2** whose volume fraction in the crystal is approximately equal to 10%. At the same time, the shape and half-width of the high-intensity superstructure reflections in the diffraction pattern are governed primarily by phase **1** in which the b^* domains are absent in the a^*c^* plane of the reciprocal lattice. The proposed scheme agrees well with the neutron diffraction pattern shown in Figs. 2a and 5. This pattern will be analyzed below.

Figure 5 shows the neutron diffraction pattern of the $La_{0.93}Sr_{0.07}MnO_3$ crystal along the [101] direction. This pattern was measured at the liquid-nitrogen temperature, i.e., below the Curie point T_C = 128 K and the Néel point T_N = 121 K of the manganite crystal. The diffraction pattern contains two superstructure reflections of series (1), namely, the (0.5, 0, 0.5) and (1.5, 0, 1.5) reflections (Fig. 2a shows only one reflection). The low intensity of the (0.5, 0, 0.5) reflection in Fig. 5 is of special interest for the following reasons. Indeed, if structural domains of the b^* type in the original crystal were oriented with an equal probability with respect to three axes of the perovskite cube, the intensity of the (0.5, 0, 0.5) superstructure reflection at our times of exposure would be one order of magnitude higher than the experimental intensity, because the intensity of this reflection would be determined primarily by the large antiferromagnetic contribution, i.e., (010)b^* [5].

The relatively low intensities of the superstructure reflections (Fig. 5) indicate that the {1/2, 0, 1/2} nuclear superstructure is formed not in the whole volume of the sample but only in the crystal regions occupied (in the ground state) by the collinear ferromagnetic phase **2** (crystal structure O^*). It is in these crystal regions that the superstructure of the manganite has a domain character at higher temperatures (Fig. 4).

The size of regions occupied by phase **2** can be determined from the data presented in Fig. 2a. It is common knowledge that the size $\bar{L}$ of a crystal region can be calculated from the formula

$$\bar{L} \cong 2\pi/\Delta q, \tag{4}$$

where Δq is the half-width of the (1.5, 0, 1.5) superstructure reflection in the wave vector space. For a neutron diffraction peak of Gaussian shape, the half-width Δq can be expressed through the observed half-width Δq_{obs} and the instrumental half-width Δq_{inst} according

to the standard relationship $\Delta q = (\Delta q_{obs} - \Delta q_{inst})^{1/2}$. In our case, the effective instrumental half-width at half-maximum of the (1.5, 0, 1.5) reflection is determined by two terms: (i) the true instrumental resolution in this range of scattering angles and (ii) the physical broadening of the peak due to deviation of the real structure *O** from a perfect cubic structure. The lattice parameters of the manganite crystal with an *O** structure were taken from [8]. Within the approximations used in the present work, the size of regions with ordering of type (1) is approximately equal to 150 Å. This value is in good agreement with more accurate estimates obtained in our previous work [5] for the linear size of regions occupied by phase **2**.

Thus, the results of the detailed analysis of the characteristic diffraction patterns make it possible to interpret the diffraction patterns shown in Fig. 2. Let us first consider the high-temperature diffraction patterns. It can be seen from Fig. 2g that electron correlations of the Mn^{3+}–Mn^{4+}–Mn^{3+} type appear in the $La_{0.93}Sr_{0.07}MnO_3$ crystal at high temperatures, i.e., when the cooperative Jahn–Teller effect does not manifest itself in the manganite. According to the experimental data, the correlation wavelength in the perovskite cubic lattice corresponds to wave vector (1). It is known that a decrease in the temperature (see Figs. 2f–2b) leads to a structural phase transformation of the manganite into the phase with an *O*' structure. The crystal lattice of this phase is characterized by two types of electron correlations along the [101] direction: (i) electron correlations with a larger (compared to the case of a perovskite cubic lattice) wavelength (domains of the *a***c** and *c***a** types) and (ii) electron correlations with a smaller wavelength (domains of the *b** type).

The diffraction pattern of the manganite crystal substantially changes upon cooling to 78 K, i.e., below temperatures T_N and T_C, at which the spin system undergoes large-scale separation (first-order magnetic phase transition) [5]. As can be seen from Fig. 2a, the diffraction pattern exhibits a single peak whose intensity increases significantly. This finding is the main result of the present work, because it indicates that ferromagnetic crystal regions with finite linear sizes undergo an $O' \longrightarrow O^*$ structural transformation due to charge ordering of Mn^{4+} and Mn^{3+} ions.

Upon subsequent heating of the manganite crystal (Figs. 2b–2d), the $O^* \longrightarrow O'$ reverse structural transition in phase **2** is observed only at room temperature. It is well known that temperature hysteresis is a characteristic feature of first-order structural phase transitions, because these transitions occur through a number of metastable states.

4. CONCLUSIONS

The main result obtained in this study can be formulated as follows. The {1/2, 0, 1/2} nuclear superstructure was revealed in an $La_{0.93}Sr_{0.07}MnO_3$ manganite orthorhombic crystal. It was demonstrated that this superlattice belongs to the class of distortion-type structures and is directly associated with a 1/16-type ordering of Mn^{4+} and Mn^{3+} ions in the collinear ferromagnetic phase of the $La_{0.93}Sr_{0.07}MnO_3$ manganite.

ACKNOWLEDGMENTS

We would like to thank A.M. Balbashev for supplying the $La_{0.93}Sr_{0.07}MnO_3$ manganite crystal used in structural investigations.

This work was supported by the State Scientific and Technical Program of the Russian Federation (contract no. 40.012.1.1.1150), the State Program of Support for Leading Scientific Schools of the Russian Federation (project no. 00-15-96581), and the Russian Foundation for Basic Research (project no. 02-02-16425).

REFERENCES

1. Y. Yamada, O. Hino, S. Nohdo, *et al.*, Phys. Rev. Lett. **77** (5), 904 (1996).
2. L. Vasiliu-Doloc, J. W. Lynn, A. H. Moudden, *et al.*, Phys. Rev. B **58** (22), 14913 (1998).
3. S. F. Dubinin, V. E. Arkhipov, Ya. M. Mukovskiĭ, *et al.*, Fiz. Met. Metallogr. **93** (3), 506 (2002).
4. S. F. Dubinin, V. E. Arkhipov, S. G. Teploukhov, and Ya. M. Mukovskiĭ, Fiz. Tverd. Tela (St. Petersburg) **45** (1), 113 (2003) [Phys. Solid State **45**, 118 (2003)].
5. S. F. Dubinin, V. E. Arkhipov, S. G. Teploukhov, *et al.*, Fiz. Tverd. Tela (St. Petersburg) (in press).
6. A. M. Balbashov, S. G. Karabashev, Ya. M. Mukovskii, and S. A. Zverkov, J. Cryst. Growth **167**, 365 (1996).
7. N. N. Loshkareva, A. V. Korolev, T. I. Arbuzova, *et al.*, Fiz. Tverd. Tela (St. Petersburg) **44** (10), 1827 (2002) [Phys. Solid State **44**, 1916 (2002)].
8. V. S. Gaviko, V. E. Arkhipov, A. V. Korolev, *et al.*, Fiz. Tverd. Tela (St. Petersburg) **41** (6), 1064 (1999) [Phys. Solid State **41**, 969 (1999)].

Translated by O. Borovik-Romanova

Physics of the Solid State, Vol. 45, No. 11, 2003, pp. 2152–2154. Translated from Fizika Tverdogo Tela, Vol. 45, No. 11, 2003, pp. 2048–2050.

MAGNETISM AND FERROELECTRICITY

Changes in Local Magnetic Fields on ^{57}Fe Nuclei in $BaFe_{12}O_{19}$ with Temperature Variations

A. A. Bezlepkin and S. P. Kuntsevich

Kharkov National University, pl. Svobody 4, Kharkov, 61077 Ukraine

Received April 22, 2003

Abstract—Changes in local magnetic fields on ^{57}Fe nuclei of Fe^{3+} ions in bipyramidal (2*b*) and tetrahedral ($4f_1$) positions of the $BaFe_{12}O_{19}$ hexaferrite with variations in temperature are investigated using nuclear magnetic resonance in the temperature range 4.2–295 K. The applicability of the Bloch spin wave theory to the description of the thermal behavior of local magnetic fields on ^{57}Fe nuclei is considered. Low-temperature deviations from the Bloch law are revealed for bipyramidal positions. The model describing the dynamics of an iron ion in these positions is refined. © *2003 MAIK "Nauka/Interperiodica".*

1. INTRODUCTION

Hexaferrites of the structure type *M*, namely, $MeFe_{12}O_{19}$ (where $Me = Ba^{2+}$, Sr^{2+}, or Pb^{2+}), contain only one type of magnetoactive ions, Fe^{3+} ions. These ions are located at lattice sites with octahedral ($4f_2$, 2*a*, 12*k*), tetrahedral ($4f_1$), and bipyramidal (2*b*) oxygen environments [1]. The bipyramidal environment has the form of a trigonal bipyramid. This environment is not characteristic of iron oxides and has been the subject of many investigations. In particular, Townes *et al.* [2] performed an x-ray diffraction study of the $BaFe_{12}O_{19}$ hexaferrite and drew the conclusion that, at room temperature, the iron ions occupying the 2*b* positions in this structure are located not in the mirror plane of the bipyramid but are randomly arranged on each side of this plane at a mean distance of 0.16 Å. Mössbauer investigations of $BaFe_{12}O_{19}$ (BaM) and $SrFe_{12}O_{19}$ (SrM) hexaferrites [1, 3] revealed strong anisotropy of thermal vibrations of iron ions in the 2*b* positions at high temperatures. It was also inferred that, at low temperatures ($T < 100$ K), these ions occupy two pseudohedral positions inside the bipyramid. The specific dynamics of iron ions in the 2*b* positions can affect the distribution of the electron and spin densities and, correspondingly, the local magnetic fields on ^{57}Fe nuclei. In our earlier work [4], the BaM hexaferrite was studied using the nuclear magnetic resonance (NMR) method in the temperature range 4.2–77 K. It was found that a decrease in temperature in this range is accompanied by an anomalous decrease in the local magnetic field on iron nuclei in the 2*b* positions. In the present work, we carried out an NMR investigation of the local magnetic fields on ^{57}Fe nuclei of Fe^{3+} ions in bipyramidal (2*b*) and tetrahedral ($4f_1$) positions of the BaM hexaferrite in the temperature range 4.2–295 K. Moreover, we analyzed the applicability of the Bloch spin wave theory to the description of the changes observed in local magnetic fields in the $4f_1$ and 2*b* positions with variations in temperature.

2. SAMPLES AND EXPERIMENTAL TECHNIQUE

The experiments were carried out using BaM single crystals enriched to 95% with a ^{57}Fe isotope. The single crystals were grown from a $BaO \cdot B_2O_3$ melt according to the solution-growth technique. The synthesis was performed through crystallization on a rotating seed in the temperature range 1420–1300 K. The phase composition of the crystals grown was checked using x-ray diffraction. The lattice parameters at room temperature are $a = 0.589$ nm and $c = 2.319$ nm. The ^{57}Fe nuclear magnetic resonance was examined in domain regions of the Bloch domain walls according to the stationary technique with the use of an instrument described in [5]. The rf voltage across the *LC* circuit containing the studied sample did not exceed 10^{-2} V. The frequencies of NMR signals from domain layers (domain-wall edges), which were determined by the stationary technique at a temperature of 77 K, coincided accurate to within 0.2% with the frequencies of nuclei signals in the domains, which were determined using the spin-echo method at a high level of the excitation voltage (~1.5 kV). The error in determining the frequencies of NMR signals did not exceed 0.1%.

3. RESULTS AND DISCUSSION

Figure 1 shows the temperature dependences of local magnetic fields H_{loc} on ^{57}Fe nuclei of iron ions in bipyramidal 2*b* and tetrahedral $4f_1$ positions. It can be seen from Fig. 1 that, for the 2*b* positions, a decrease in the temperature from 77 to 4.2 K leads to an anomalous decrease in the local magnetic field H_{loc}. For the $4f_1$ positions, no anomaly is observed and the local field increases monotonically as the temperature decreases from 295 to 4.2 K.

As is known, the dominant contribution to the local magnetic field on nuclei of Fe^{3+} ions is made by uncom-

1063-7834/03/4511-2152$24.00

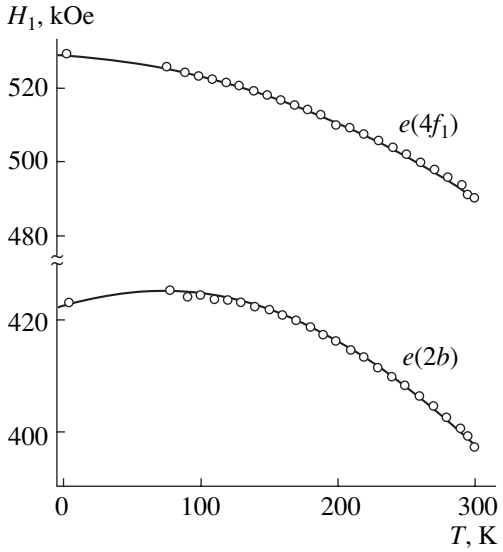

Fig. 1. Temperature dependences of the local magnetic field on ^{57}Fe nuclei of the sublattices *c* and *e* of the $BaFe_{12}O_{19}$ hexaferrite.

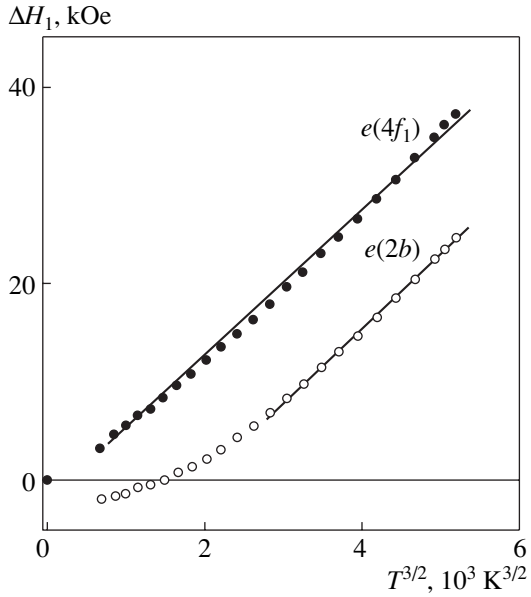

Fig. 2. Temperature dependences of the change in the local magnetic field on ^{57}Fe nuclei of the sublattices *c* ($4f_1$) and *e* ($2b$) of the $BaFe_{12}O_{19}$ hexaferrite.

pensated spins of the electron shell; hence, it is assumed that, to a first approximation, the local magnetic field $H_i(T)$ on nuclei of iron ions of the *i*th sublattice is proportional to the magnetization of this sublattice $M_i(T)$ [6]. It follows from the spin wave theory that, if the interionic dipole–dipole interaction and the interaction of spin waves are ignored, the square dispersion law for acoustical magnons holds at low temperatures. In the *M*-type hexaferrites, the dipole magnetic fields of the sublattices are two orders of magnitude smaller than the effective exchange fields [7, 8]. Therefore, in this case, the magnetization of the sublattices should obey the Bloch three-halves power law [9]:

$$M_i(t) = M_i(0) - A_i T^{3/2}, \quad (1)$$

where *i* is the index of the sublattice and A_i is the temperature-independent quantity.

It follows from expression (1) that the local magnetic field $H_i(T)$ of the *i*th sublattice has the form

$$H_i(0) - H_i(T) = \Delta H_i(T) = B_i T^{3/2}, \quad (2)$$

where $H_i(0)$ is the local magnetic field for ^{57}Fe nuclei of the *i*th sublattice at $T \longrightarrow 0$ and B_i is the temperature-independent quantity.

The dependences $\Delta H_i(T)$ obtained from experimental data on the local magnetic fields H_i for the sublattices *e* (positions $2b$) and *c* (positions $4f_1$) are shown in Fig. 2. As can be seen from this figure, the experimental data for Fe^{3+} ions in the tetrahedral positions are adequately described by relationship (2). For Fe^{3+} iron ions in the bipyramidal positions, relationship (2) does not hold at low temperatures. This result is in rather poor agreement with the model concepts advanced by Belozerskiĭ and Khimich [1], according to which the iron ions in bipyramidal positions at $T < 100$ K are located at two tetrahedral sites of the trigonal bipyramid. For this arrangement, one could expect a linear dependence of the change in the local magnetic field ΔH_i on the quantity $T^{3/2}$ at low temperatures, as is the case with the tetrahedral positions.

The experimental results obtained are consistent with the model proposed by Fontcuberta *et al.* [10]. These authors argued that the tunneling mechanism of iron ion transfer through a barrier between two potential wells is in good agreement with the experimental data of Mössbauer investigations. The change in the length of the jump between the pseudotetrahedral sites is due to the evolution of the double potential well, which, at temperatures close to absolute zero, transforms into a single well and corresponds to the arrangement of iron ions in the mirror plane of the bipyramid.

The evolution of the potential barriers can manifest itself in anharmonicity of thermal lattice vibrations. In this connection, we examined the temperature dependence of the lattice parameter along the hexagonal axis **c**. Figure 3 depicts this dependence in the temperature range 80–295 K. As can be seen from Fig. 3, the temperature dependence of the lattice parameter $c(T)$ exhibits specific features in the temperature range 80–150 K. A comparison of Figs. 2 and 3 shows that the linear temperature dependence of the lattice parameter $c(T)$ in the temperature range 150–295 K corresponds to the linear dependence of ΔH_i on the quantity $T^{3/2}$ for iron ions in the $2b$ positions (sublattice *e*).

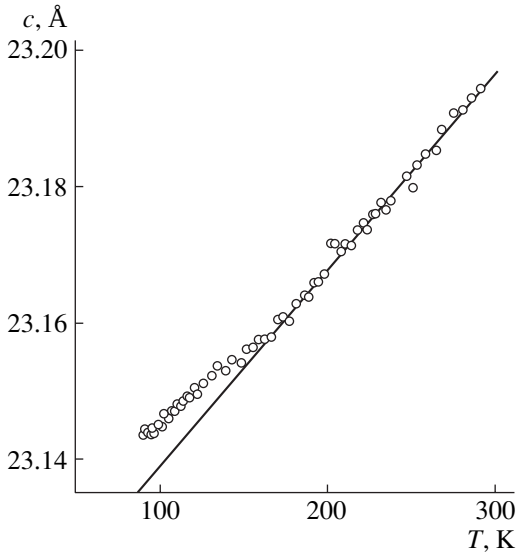

Fig. 3. Temperature dependence of the lattice parameter *c* of the $BaFe_{12}O_{19}$ hexaferrite.

Belozerskiĭ and Khimich [1] carried our the Mössbauer investigation of the temperature dependence of the lattice parameter *a*, which characterizes the anisotropy of thermal vibrations of iron ions in the 2*b* positions of the BaM hexaferrite:

$$a = (\bar{\chi}_{\parallel}^2 - \bar{\chi}_{\perp}^2)/\lambda^2, \quad (3)$$

where $\bar{\chi}_{\parallel}^2$ is the mean-square displacement along the **c** axis, $\bar{\chi}_{\perp}^2$ is the mean-square displacement in the direction perpendicular to the **c** axis, and λ is the wavelength of gamma quanta.

It follows from the results obtained in [1] that, in the temperature range 100–300 K, the BaM hexaferrite is characterized by a strong anisotropy of thermal vibrations and the lattice parameter *a* increases linearly with an increase in the temperature.

4. CONCLUSIONS

The results of our investigation and the data obtained in [1, 3] demonstrate that the low-temperature deviations from the Bloch law are associated not with the anisotropy of thermal vibrations but with the redistribution of the spin and electron densities due to the low-temperature evolution of the potential barriers in the region of pseudotetrahedral sites of the bipyramidal 2*b* positions of the iron ions.

ACKNOWLEDGMENTS

This work was supported in part by the Ministry of Education and Science of Ukraine.

REFERENCES

1. G. I. Belozerskiĭ and Yu. P. Khimich, Fiz. Tverd. Tela (Leningrad) **17** (5), 1352 (1975) [Sov. Phys. Solid State **17**, 871 (1975)].
2. W. D. Townes, J. H. Fang, and A. J. Perrota, Z. Kristallogr. B **125**, 437 (1967).
3. Yu. A. Mamaluĭ, V. P. Romanov, and K. M. Matsievskiĭ, Fiz. Tverd. Tela (Leningrad) **21** (1), 201 (1979) [Sov. Phys. Solid State **21**, 117 (1979)].
4. S. P. Kuntsevich and A. A. Bezlepkin, Fiz. Nizk. Temp. **12** (11), 1200 (1986) [Sov. J. Low Temp. Phys. **12**, 677 (1986)].
5. S. P. Kuntsevich, A. A. Bezlepkin, and Yu. A. Popkov, Zh. Éksp. Teor. Fiz. **88** (5), 1820 (1985) [Sov. Phys. JETP **61**, 1079 (1985)].
6. E. A. Turov and M. P. Petrov, *Nuclear Magnetic Resonance in Ferro- and Antiferromagnets* (Nauka, Moscow, 1969; Wiley, New York, 1972).
7. S. P. Kuntsevich, Fiz. Nizk. Temp. **24** (8), 754 (1998) [Low Temp. Phys. **24**, 568 (1998)].
8. A. A. Bezlepkin and S. P. Kuntsevich, Fiz. Tverd. Tela (St. Petersburg) **43** (7), 1214 (2001) [Phys. Solid State **43**, 1260 (2001)].
9. A. I. Akhiezer, V. G. Bar'yakhtar, and S. V. Peletminskiĭ, *Spin Waves* (Nauka, Moscow, 1967; North-Holland, Amsterdam, 1968).
10. J. Fontcuberta, A. Isalque, and X. Obradors, Z. Phys. B: Condens. Matter **70** (3), 379 (1988).

Translated by O. Moskalev

Physics of the Solid State, Vol. 45, No. 11, 2003, pp. 2155–2159. Translated from Fizika Tverdogo Tela, Vol. 45, No. 11, 2003, pp. 2051–2055.

MAGNETISM AND FERROELECTRICITY

Effect of Gd–Mn Exchange on Phase Transitions in $GdMn_2O_5$ Induced by a Strong Magnetic Field

Yu. F. Popov, A. M. Kadomtseva, G. P. Vorob'ev, S. S. Krotov, K. I. Kamilov, and M. M. Lukina

Faculty of Physics, Moscow State University, Vorob'evy gory, Moscow, 119899 Russia

e-mail: Kadomts@plms.phys.msu.ru

Received April 28, 2003

Abstract—Complex studies of the magnetic, magnetoelectric, and magnetoelastic properties of $GdMn_2O_5$ single crystals in strong pulsed magnetic fields are carried out in order to obtain additional indirect information on the character of the rare-earth and manganese spin ordering. It is shown that magnetic ordering of Gd^{3+} spins affects the manganese sublattice spin orientation and initiates new magnetic phase transitions. The observed magnetoelectric properties of the $GdMn_2O_5$ system are interpreted in terms of the theory of phase transitions.

1. INTRODUCTION

Rare-earth manganates of the RMn_2O_5 family, where R^{3+} stands for a rare-earth ion, are ferroelectric antiferromagnets, i.e., systems exhibiting not only the onset of antiferromagnetic (AFM) order but also ferroelectric properties [1]. The crystal structure of these manganates has been studied in detail only for $DyMn_2O_5$ at a temperature of 298 K [2]. The data presented in [2] favor assigning these systems to orthorhombic space group *Pbam* (D_{2h}^9). The unit cells of the RMn_2O_5 compounds contain four formula units. Three magnetic subsystems made up by the R^{3+}, Mn^{3+}, and Mn^{4+} ions account for the specific physical properties of these compounds. The Mn^{3+} and Mn^{4+} ions occupy the 4*h* and 4*f* positions inside the oxygen pyramid and octahedron, respectively. As follows from neutron diffraction data [3, 4], their spin moments order at a temperature $T_{N1} \sim 40$ K to form a spatially modulated (helical) spin structure with a wave vector $k = (1/2, 0, \tau)$, with $\tau \sim 1/3$. In the low-temperature range, below T_{N2}, the spins of the *R* ions occupying the 4*g* crystallographic position also form an antiferromagnetically ordered inhomogeneous structure. In the case of $GdMn_2O_5$ of interest here, the Gd^{3+} spins order at $T_{N2} = 15$ K. At $T_C = 26$ K, a ferroelectric phase transition occurs, which is accompanied by the onset of spontaneous electric polarization along the *b* axis of the crystal [5]. It should be pointed out, however, that no neutron diffraction measurements are available for $GdMn_2O_5$, which leaves its magnetic structure an open problem. It was of interest to conduct a complex investigation of the magnetic, magnetoelectric, and magnetoelastic properties of $GdMn_2O_5$ single crystals in strong pulsed magnetic fields to obtain indirect additional information on the character of magnetic ordering of the rare-earth and manganese spins. It was expected that the magnetic ordering of the Gd^{3+} spins should modify the spin orientation of the manganese sublattices and initiate new magnetic phase transitions.

2. EXPERIMENTAL

We studied the magnetization, electric polarization, and longitudinal magnetostriction in $GdMn_2O_5$ single crystals along the *a*, *b*, and *c* axes in strong magnetic fields up to 250 kOe and in the temperature interval 10–50 K. The magnetization was measured using the induction method, and the electric polarization and magnetostriction, by following the technique described in [6]: the $GdMn_2O_5$ single crystals were grown through spontaneous crystallization from a melt solution [7].

To make the discussion of the experimental results obtained more revealing, we split the analysis into three cases covering three magnetic field orientations, namely, $\mathbf{H} \parallel a$, $\mathbf{H} \parallel b$, and $\mathbf{H} \parallel c$.

2.1. $\mathbf{H} \parallel a$ *Case*

With the magnetic field oriented along the *a* axis of the $GdMn_2O_5$ single crystal, a strong increase was observed in the magnetization and magnetostriction at low temperatures, $T \leq 15$ K, in fields $H_p \sim 60$ kOe (Fig. 1), which is associated with a spin-flop transition of ordered Gd^{3+} ions. Measurements of the electric polarization $P_b(H_a)$ at $T \leq 15$ K revealed a clearly pronounced maximum in the field dependence of the polarization at the spin-flop transition field (Fig. 2). In addition to the spin-flop transition, a second field-driven transition occurred at temperatures $T > 15$ K, which was accompanied by noticeable jumps in the electric polarization and was apparently caused by the magnetic

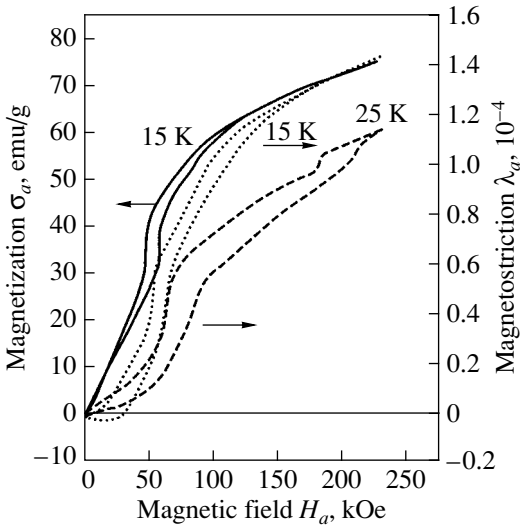

Fig. 1. Magnetization and longitudinal magnetostriction along the *a* axis of a $GdMn_2O_5$ single crystal plotted vs. magnetic field.

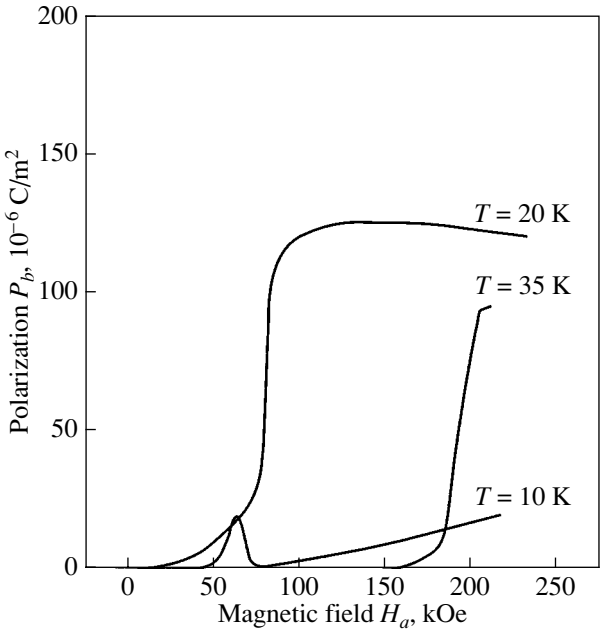

Fig. 2. Dependence of the electric polarization **P** ∥ *b* in $GdMn_2O_5$ on magnetic field **H** ∥ *a* measured at different temperatures.

structure of the manganese subsystem undergoing rearrangement. This transition was also accompanied by the onset of magnetostriction-induced strains.

As the temperature was increased, the transition changed in character. At 35 K, the electric polarization $P_b(H_a)$ was zero up to 150 kOe and then increased subsequently in a jump (Fig. 2). This is possibly due to the *a*-oriented magnetic field ~150 kOe inducing a ferroelectric transition (similar to that observed in YMn_2O_5 [8]) accompanied by the onset of spontaneous electric polarization along the *b* axis of the crystal at 35 K; with no field applied, this transition occurred at 26 K. In other words, a magnetic field ~150 kOe shifts the ferroelectric transition point up by 9 K. Note that no polarization jump was observed in a strong magnetic field along the *a* axis.

2.2. **H** ∥ *b Case*

When the magnetic field was applied along the *b* axis of the crystal, jumps in the longitudinal polarization in the range 10–40 K were only observed in strong fields, $H_p \sim 150$ kOe (Fig. 3). The transverse polarization components along the *a* and *c* axes behaved similarly, but their jumps were substantially smaller than the jumps in the component along the *b* axis, which was apparently due to the spontaneous polarization in $GdMn_2O_5$ being aligned with the *b* crystal axis. At $T_{N1} \sim 40$ K, the electric polarization decreased by an order of magnitude, reversed sign, and did not exhibit any anomalies in strong magnetic fields because the crystal was in the paramagnetic state.

In the temperature interval $T_{N2} < T < T_{N1}$, we also measured the longitudinal magnetostriction, which likewise exhibited an abrupt change at $H_p \sim 150$ kOe (Fig. 4). Contributions to the magnetostriction came apparently not only from the manganese but also from the gadolinium subsystem, because for $T \leq 15$ K the Gd^{3+} spins were ordered and the magnetostriction jump was a few times greater than its values observed in the range $T_{N2} < T < T_{N1}$. A comparison of the polarization jump behavior in various temperature intervals suggests that it was the manganese subsystem that was primarily responsible for the jumps observed in the region

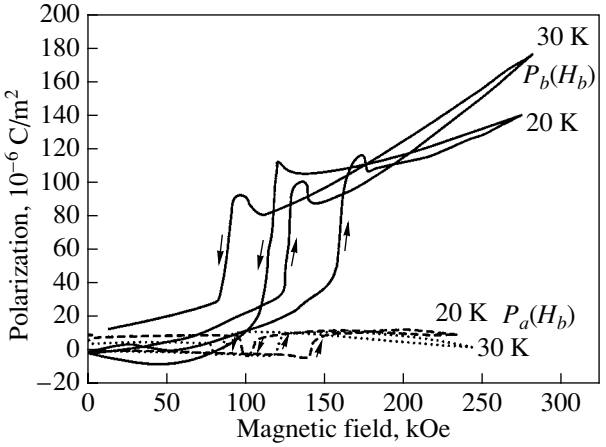

Fig. 3. Dependences of the electric polarizations **P** ∥ *a* and **P** ∥ *b* in $GdMn_2O_5$ on magnetic field **H** ∥ *b* measured at different temperatures.

$T_{N2} < T < T_{N1}$. The above anomalies observed for **H** || *b* in fields $H_p \sim 150$ kOe indicate rearrangement of the magnetic structure of the manganese subsystem, which is correlated (due to the Gd–Mn exchange) with the gadolinium subsystem undergoing ordering with decreasing temperature.

2.3. **H** || *c Case*

When the magnetic field was oriented along the *c* axis, the electric polarization along the *a*, *b*, and *c* axes of the crystal and the magnetostriction (along the *c* axis) also exhibited jumps at a certain threshold field, whose magnitude varied with increasing temperature from $H_p \sim 140$ kOe at 10 K to $H_p \sim 80$ kOe at 35 K (Figs. 5, 6). No anomalies were observed at 40 K in the $\lambda_c(H_c)$ and $P_{a,b,c}(H_c)$ dependences because the crystal transferred to the paramagnetic state. At the threshold fields specified in Figs. 5 and 6, the magnetization curves obtained along the *c* axis for $T < T_{N2}$ revealed clearly pronounced magnetization anomalies, which indicate spin rearrangement of the antiferromagnetically ordered gadolinium subsystem (Fig. 7).

These findings suggest that, for $T < T_{N2}$, the spins of at least the Gd^{3+} ions have components not only in the *ab* plane but also along the *c* axis, which, due to the Gd–Mn exchange, gives rise to spatial reorientation of the Mn^{3+} and Mn^{4+} spins and their eventually leaving the *ab* plane. This conclusion is supported by the above-mentioned anomalies in the magnetic, magnetoelectric, and magnetoelastic properties of the $GdMn_2O_5$ system observed to occur with the magnetic field **H** oriented in the *a*, *b*, and *c* axes of the crystal.

3. DISCUSSION OF RESULTS

As already pointed out, the unit cell of the $GdMn_2O_5$ crystal contains four ions of each of the species Gd^{3+}, Mn^{3+}, and Mn^{4+}. Therefore, magnetic order in the system should be governed by the behavior of the spins of Gd^{3+} ($\sigma_1, \sigma_2, \sigma_3, \sigma_4$), Mn^{3+} (S_1, S_2, S_3, S_4), and Mn^{4+} (S_5, S_6, S_7, S_8). In accordance with the theory of space group representations, in order to construct the thermodynamic potential of a system (we use here the approach developed in [9]), one has to construct (on the basis of individual spins of the Gd^{3+}, Mn^{3+}, and Mn^{4+} ions) basis functions of irreducible representations that correspond, in general, to the star of the wave vector $\mathbf{k} = \left\{\frac{1}{2}, 0, \tau\right\}$, i.e., the vector of propagation of the magnetic structure forming below T_{N1}. One can readily verify that, in our case of one-ray ordering, the magnetic amplitudes of the corresponding basis functions will be the spin basis functions of irreducible representations of the wave-vector group G_k. Therefore, the irreducible magnetic representation of interest to us here is two-

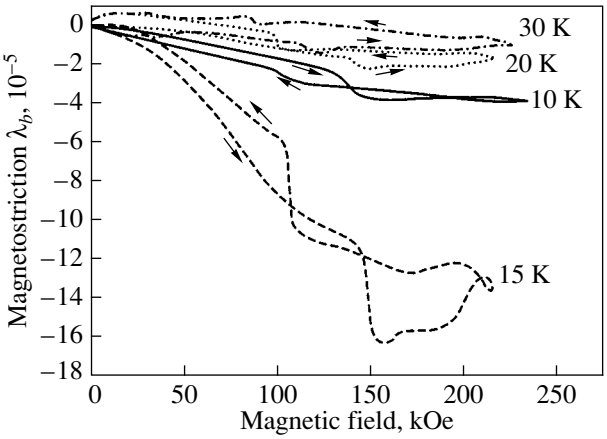

Fig. 4. Magnetic field dependence of longitudinal magnetostriction λ || *b* in $GdMn_2O_5$ measured at different temperatures.

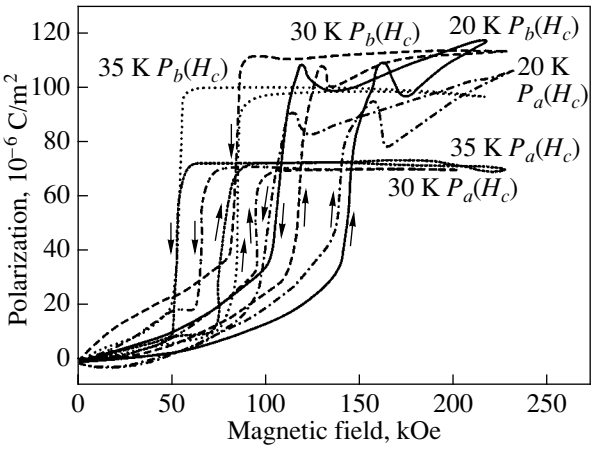

Fig. 5. Dependences of the electric polarizations **P** || *a* and **P** || *b* in $GdMn_2O_5$ on magnetic field **H** || *c* measured at different temperatures.

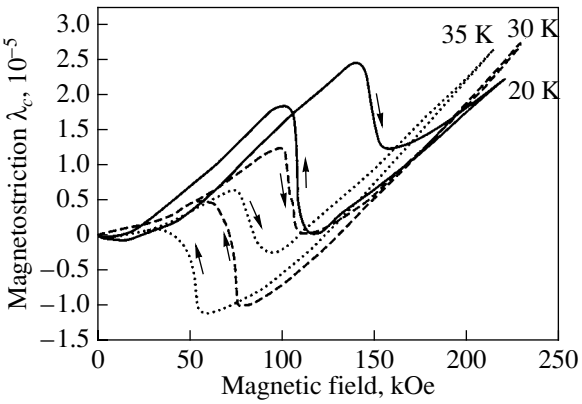

Fig. 6. Longitudinal magnetostriction λ || *c* in $GdMn_2O_5$ measured as a function of magnetic field **H** || *c* at different temperatures.

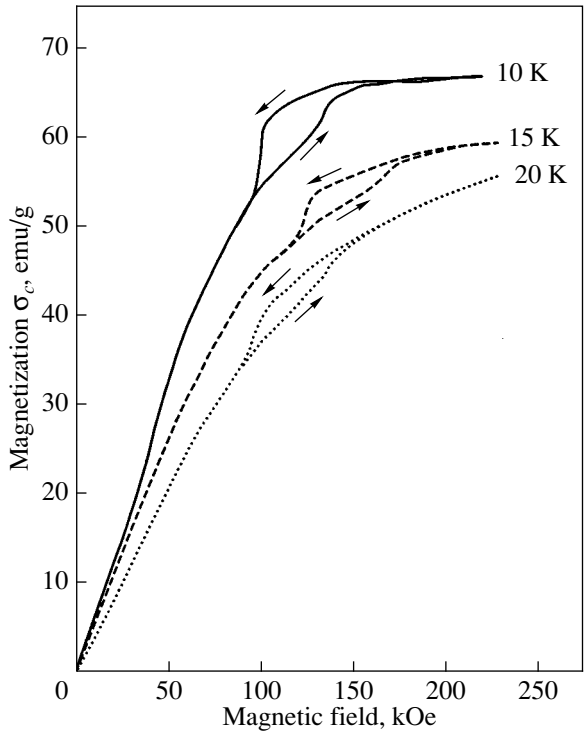

Fig. 7. Magnetization curves measured in $GdMn_2O_5$ at low temperatures along the *c* axis.

dimensional, with the basis function pairs (in the exchange approximation) given by the combinations

$$\left\{\begin{array}{l} S_1 - S_2 - S_3 + S_4 = A_1 \\ S_1 - S_2 + S_3 - S_4 = G_1 \end{array}\right\}; \quad \left\{\begin{array}{l} S_5 + S_6 - S_7 - S_8 = C_2 \\ S_5 + S_6 + S_7 + S_8 = F_2 \end{array}\right\};$$
$$\left\{\begin{array}{l} \sigma_1 - \sigma_2 - \sigma_3 + \sigma_4 = A_3 \\ \sigma_1 - \sigma_2 + \sigma_3 - \sigma_4 = G_3 \end{array}\right\}. \qquad (1)$$

These combinations allow for the character of the Mn^{3+}–Mn^{3+} and Mn^{4+}–Mn^{4+} exchange interactions [3] and correspond to the case of antiferromagnetic Gd^{3+}–Gd^{3+} exchange (the case of their ferromagnetic exchange can be considered in a similar manner and does not significantly affect the conclusions drawn further on). The quadratic-in-spin contribution to the free energy of the system can be written as

$$\Delta F^{(2)} = \Lambda_1(A_1^2 + G_1^2) + \Lambda_2(F_2^2 + C_2^2) + \Lambda_3(A_3^2 + G_3^2) + \Lambda_{12}(A_1C_2 + G_1F_2) + \Lambda_{13}(A_1A_3 + G_1G_3) + \Lambda_{23}(C_2A_3 + F_2G_3). \qquad (2)$$

Obviously enough, the type of the magnetic structure appearing in a phase transition should depend on which of the quantities Λ_1, Λ_2, and Λ_3 in Eq. (2) will be the first to vanish with decreasing temperature. Let it be Λ_1 (as in paper [8], where the behavior of the YMn_2O_5 system is discussed), which corresponds to the AFM phase transition at $T = T_{N1}$. The presence of cross terms in Eq. (2) is evidence of a correlated rearrangement of the Mn and Gd subsystems due to the *f–d* exchange below T_{N1}. In these conditions, the general pattern of the ordering is determined by the Mn^{3+}–Mn^{4+}, Mn^{3+}–Mn^{3+}, and Mn^{4+}–Mn^{4+} exchange energies, with the *f–d* exchange playing the role of a correction only. However, as the temperature decreases, the Gd–Mn exchange gains importance and independent Gd ion spin ordering occurs, with the consequence that one more phase transition will appear at $T = T_{N2}$ and will have the same magnetic structure vector $\mathbf{k} = \left\{\frac{1}{2}, 0, \tau\right\}$. Analyzed from the symmetry viewpoint, our system allows the existence of two independent Lifshitz invariants with linear derivatives along the *c* and *a* axes, respectively; therefore, in this phase transition, inhomogeneous exchange could, in principle, produce an incommensurate magnetic structure along the *a* axis as well, exactly as was observed to occur in $EuMn_2O_5$ in [10]. Each of the above structures (which appear at $T = T_{N1}$ and T_{N2}) is exchange-noncollinear, and each of them can be characterized by a pair of vectors, L_1, L_2 and L_3, L_4, respectively. Because of the Gd–Mn exchange (in contrast to the YMn_2O_5 system), the ferroelectric ordering temperature will be $T_C \sim 26$ K. The presence of the exchange invariants $P_Y(L_1L_3 - L_2L_4)$ and $P_x(L_1L_4 - L_2L_3)$ will give rise to jumps in the electric polarization vector in a strong magnetic field along both the *b* and the *a* axes, which are not present in the YMn_2O_5 system. In addition, if we include the obvious invariant contributions of the form

$$\Delta F = aP^2 - \gamma P^2 H^2, \qquad (3)$$

a shift of the Curie point will become possible in a strong magnetic field, exactly as is observed in the curves in Figs. 2–5.

Observation of spin-flop transitions with a magnetic field applied along any coordinate direction suggests that the magnetic structure is three-dimensional rather than planar (as in [8]). Treated phenomenologically, this means that even if the pair of vectors L_1 and L_2 lies in the basal *ab* plane, the vector pair L_3 and L_4, appearing with increasing Gd–Mn exchange, will lie in the *ac* plane, and therefore the total magnetic structure will become three-dimensional.

The behavior of magnetostriction is well known to be directly determined by the symmetry of the strain tensor, i.e., in our particular case, by the symmetry of the three longitudinal components, which correspond to the diagonal components of the shear strain tensor.

Because all longitudinal components of the strain tensor correspond to the unit representation of the point group of the high-symmetry phase, all spin-flop transitions possible in the system will be accompanied by jumps in the field dependences of the magnetostriction

because of a reorientation of the antiferromagnetism vectors.

ACKNOWLEDGMENTS

This study was supported by the Russian Foundation for Basic Research, project no. 01-02-16468.

REFERENCES

1. G. A. Smolenskiĭ and I. E. Chupis, Usp. Fiz. Nauk **137**, 415 (1982) [Sov. Phys. Usp. **25**, 475 (1982)].
2. S. C. Abrahams and J. L. Bernstein, J. Chem. Phys. **46**, 3776 (1967).
3. G. Buisson, Phys. Status Solidi A **17**, 191 (1993).
4. C. Wilkinson, F. Sinclair, P. Gardner, *et al.*, J. Phys. C **14**, 1671 (1981).
5. K. Kohn, Ferroelectrics **162**, 1 (1994).
6. Yu. F. Popov, A. K. Zvezdin, G. P. Vorob'ev, *et al.*, Pis'ma Zh. Éksp. Teor. Fiz. **57** (1), 65 (1993) [JETP Lett. **57**, 69 (1993)].
7. V. A. Sanina, A. M. Sapozhnikova, E. I. Golovenchits, and N. V. Morozov, Fiz. Tverd. Tela (Leningrad) **30**, 3015 (1988) [Sov. Phys. Solid State **30**, 1736 (1988)].
8. Yu. F. Popov, A. M. Kadomtseva, S. S. Krotov, *et al.*, Zh. Éksp. Teor. Fiz. **123** (5), 1090 (2003) [JETP **96**, 961 (2003)].
9. Yu. A. Izyumov, V. E. Naĭsh, and R. L. Ozerov, *Neutron Diffraction of Magnetic Materials* (Atomizdat, Moscow, 1981).
10. V. Polyakov, V. Plakhty, M. Bonnet, *et al.*, Physica B (Amsterdam) **297**, 208 (2001).

Translated by G. Skrebtsov

Physics of the Solid State, Vol. 45, No. 11, 2003, pp. 2160–2165. Translated from Fizika Tverdogo Tela, Vol. 45, No. 11, 2003, pp. 2056–2061.

MAGNETISM AND FERROELECTRICITY

Specific Features of Propagation of Electromagnetic Waves in Layered Magnetic Photonic Crystals

Yu. I. Bespyatykh, I. E. Dikshteĭn, V. P. Mal'tsev, S. A. Nikitov, and V. Vasilevskiĭ

Institute of Radio Engineering and Electronics (Fryazino Branch), Russian Academy of Sciences, pl. Vvedenskogo 1, Fryazino, Moscow oblast, 141190 Russia

Received April 29, 2003

Abstract—The general regularities of the evolution of the spectrum of magnetostatic waves in a periodic system composed of alternating ferromagnetic and nonmagnetic layers are analyzed. The spectrum of electromagnetic waves in an infinite periodic system and the coefficient of reflection of a plane electromagnetic wave from a half-space periodically filled with ferromagnetic and nonmagnetic layers are calculated. The dispersion relation is derived and analyzed for surface magnetostatic waves at the interface between the periodic system of layers and vacuum. © *2003 MAIK "Nauka/Interperiodica".*

1. INTRODUCTION

In recent years, considerable interest has been expressed by researchers in the properties of different-type waves propagating in periodic structures. First and foremost, the case in point is photonic crystals. Photonic crystals belong to artificially created structures whose refractive index varies periodically. The properties of electromagnetic waves in these structures resemble the properties of electrons in crystals. The spectrum of electromagnetic waves involves band gaps similar to those observed for semiconductors. At present, the properties of the photonic crystals grown have been studied in sufficient detail (see, for example, [1–4]). This has given impetus to the study of other materials in which waves of different natures, namely, phonons (acoustic waves) and magnons (spin waves), possess similar properties. These materials are referred to as phononic [5–7] and magnonic [8–10] crystals. The properties of spin waves in magnonic crystals have become subjects of scientific research only in recent years. The spectrum of spin-wave excitations in ferrites has a number of specific features (for example, the occurrence of surface waves, angles of cutoff, etc.). Therefore, the band structure of the spectrum of magnonic crystals should differ significantly from those of photonic and phononic crystals. Investigation of the propagation of magnetostatic waves in magnonic crystals is of great practical importance.

The region of slow spin waves with wave vectors $k_0 \ll k \ll \alpha^{-1/2}$ (where $k_0 = \omega/c$, ω is the wave frequency, c is the speed of light in free space, and α is the inhomogeneous exchange constant) is conventionally termed the magnetostatic-wave region [11]. The dispersion of magnetostatic waves in sufficiently thick ferromagnetic films weakly depends on both the electromagnetic retardation and the inhomogeneous exchange and is determined primarily by the film thickness. To put it differently, the dispersion of magnetostatic waves is geometric in character. Magnetostatic waves cannot propagate in bulk samples. Since the frequency of magnetostatic excitations depends only on the direction of the wave vector, their spatial damping decrement appears to be large. In multilayer systems, unlike isolated ferromagnetic films, the energy can be transferred by magnetostatic waves in the plane of layers and in the direction perpendicular to this plane due to the magnetic dipole interaction between layers.

2. THEORETICAL ANALYSIS

Let us consider a periodic structure composed of alternating ferromagnetic and nonmagnetic layers with different material parameters. The period of the structure involves $2n$ components. The parameters of the ith pair of ferromagnet–nonmagnet layers are designated by the index i. For definiteness, it is assumed that, in each pair, a nonmagnetic layer is located above a ferromagnetic layer. The number of a layer pair increases with an increase in the coordinate of its surfaces. We assume that the layer surfaces are parallel to the yz plane of the Cartesian coordinate system. The structure is placed in a constant external magnetic field $\mathbf{H}_e$ aligned with the $\mathbf{n}_z$ axis in the layer plane. We will restrict our consideration to the transverse electric mode with the polarization (h_x, h_y, e_z) of the high-frequency field and the wave vector $\mathbf{k}$ perpendicular to the external field ($k_z = 0$).

The general expression for the electric field component $e_{z,i}$ in the ith ferromagnetic layer can be written in the form

$$e_{z,i} = [a_{1,i}\exp(\gamma_i x_i) + a_{2,i}\exp(-\gamma_i x_i)] \times \exp[i(\omega t - k_y y)], \quad (1)$$

1063-7834/03/4511-2160$24.00 © 2003 MAIK "Nauka/Interperiodica"

where $x_i = x - \Delta_i$, Δ_i is the coordinate of the upper surface of the ith ferromagnetic layer, $\gamma_i = (k_y^2 - k_0^2\varepsilon_{fi}\mu_\perp)^{1/2}$, $\mu_{\perp i} = (\mu_i^2 - \nu_i^2)/\mu_i$, $\mu_i = 1 + \omega_{Hi}\omega_{Mi}/(\omega_{Hi}^2 - \omega^2)$, $\nu_i = -\omega\omega_{Mi}/(\omega_{Hi}^2 - \omega^2)$, $\omega_{Hi} = |g_i|(H_e + j\Delta H_i)$, $\omega_{Mi} = 4\pi|g_i|M_{0i}$, ε_{fi} is the permittivity of the lattice, ΔH_i is the half-width of the resonance line, g_i is the gyromagnetic ratio, and d_i is the thickness of the magnetic layer.

Let the vector with components (a_{1i}, a_{2i}) be designated as $\mathbf{a}_i$. Then, from the Maxwell equations, the constitutive equations, and the conditions at the interface, we obtain the equation relating the components of the vectors $\mathbf{a}_{i+1}$ and $\mathbf{a}_i$:

$$\mathbf{a}_{i+1} = \hat{\rho}_i\mathbf{a}_i. \tag{2}$$

The elements of the matrix $\hat{\rho}_i = \rho_{0i}\hat{\rho}_i'$ are as follows:

$$\begin{aligned}
\rho_{11i}' &= -\exp(\gamma_{i+1}d_{i+1})[\exp(-\beta_i b_i)(1 - p_{i+1}/\beta_i)\\
&\times(1 - q_i/\beta_i) - \exp(\beta_i b_i)(1 + p_{i+1}/\beta_i)(1 + q_i/\beta_i)],\\
\rho_{22i}' &= \exp(-\gamma_{i+1}d_{i+1})[\exp(-\beta_i b_i)(1 + q_{i+1}/\beta_i)\\
&\times(1 + p_i/\beta_i) - \exp(\beta_i b_i)(1 - q_{i+1}/\beta_i)(1 - p_i/\beta_i)],\\
\rho_{12i}' &= -\exp(\gamma_{i+1}d_{i+1})[\exp(-\beta_i b_i)(1 - p_{i+1}/\beta_i)\\
&\times(1 + p_i/\beta_i) - \exp(\beta_i b_i)(1 + p_{i+1}/\beta_i)(1 - p_i/\beta_i)],\\
\rho_{21i}' &= \exp(-\gamma_{i+1}d_{i+1})[\exp(-\beta_i b_i)(1 + q_{i+1}/\beta_i)\\
&\times(1 - q_i/\beta_i) - \exp(\beta_i b_i)(1 - q_{i+1}/\beta_i)(1 + q_i/\beta_i)].
\end{aligned} \tag{3}$$

Here, $\rho_{0i} = \mu_{\perp i+1}\beta_i/(4\gamma_{i+1})$, $p_i = (\mu_i\gamma_i - \nu_i k_y)/(\mu_i\mu_{\perp i})$, $q_i = (\mu_i\gamma_i + \nu_i k_y)/(\mu_i\mu_{\perp i})$, $\gamma_i = (k_y^2 - k_0^2\varepsilon_{fi}\mu_{\perp i})^{1/2}$, $\beta_i = (k_y^2 - k_0^2\varepsilon_{si})^{1/2}$, ε_{si} is the permittivity of the lattice, and b_i is the thickness of the nonmagnetic layer. When nonmagnetic layers are absent in the structure, the values of b_i should be taken equal to zero.

According to the Bloch theorem [12] and formula (2), the vectors $\mathbf{a}_{i+n}$ and $\mathbf{a}_i$ are related by the expression

$$\mathbf{a}_{i+n} = \mathbf{a}_i\exp(-ik_xD) = \hat{\lambda}_{ni}\mathbf{a}_i, \tag{4}$$

where $\hat{\lambda}_{ni} = \hat{\rho}_{n+i-1} \times \ldots \times \hat{\rho}_i$, $D = \sum_{l=1}^{n}(b_l + d_l)$ is the period of the structure, and k_x is the wave vector component along the x axis ($-\pi/D \le k_x \le \pi/D$). Equation (4) is a set of two homogeneous linear equations. From the condition for the existence of a nontrivial solution of this set of equations and the equality

$$\det\hat{\lambda}_{ni} = 1 \tag{5}$$

we obtain the following dispersion relation for electromagnetic waves in the structure:

$$2\cos k_xD - \mathrm{Sp}\,\hat{\lambda}_{ni} = 0. \tag{6}$$

Since $\mathrm{Sp}\,\hat{\lambda}_{ni} = \mathrm{Sp}(\hat{\rho}_{n+i-1} \times \ldots \times \hat{\rho}_i)$ is invariant with respect to the cyclic permutation of factors, relation (6) does not depend on the index i. The solution of this equation has the form

$$k_x = \frac{i}{D}\ln\frac{\mathrm{Sp}\,\hat{\lambda}_{ni} \pm \sqrt{(\mathrm{Sp}\,\hat{\lambda}_{ni})^2 - 4}}{2}. \tag{7}$$

The choice of the branch of the logarithm in expression (7) is immaterial, because the quantity k_x enters only into the term $\exp(-ik_xD)$ and the two signs in this expression correspond to two directions of electromagnetic-wave propagation. In the absence of damping in the system, the values of k_x are real at $|\mathrm{Sp}\,\hat{\lambda}_{ni}| \le 4$. In the general case, the values of k_x are complex.

The wave polarization, i.e., the relation between the quantities $a_{i1,2}$, is defined by either of the two equations from set (4):

$$a_{i2} = a_{i1}\{\lambda_{ni21}/[\exp(-ik_xD) - \lambda_{ni22}]\} = \Gamma_i a_{i1}, \tag{8}$$

where

$$\Gamma = \frac{\mathrm{Sp}\,\hat{\lambda}_{ni} - 2\lambda_{ni11} \pm \sqrt{(\mathrm{Sp}\,\hat{\lambda}_{ni})^2 - 4}}{2\lambda_{ni12}}.$$

The second term in relation (6) depends on the frequency ω and the wave vector component k_y. It can be seen from relation (6) that the function $k_x(\omega)$ is a single-valued function in either of the two ranges $-\pi/D \le k_x \le 0$ and $0 \le k_x \le \pi/D$.

The spectrum of magnetostatic waves with a field distribution over the thickness of ferromagnetic layers, which is described by hyperbolic functions, can be obtained from relation (6) by changing over to the magnetostatic case ($\beta_i = \gamma_i = |k_y|$). In the absence of damping at fixed k_x and k_y, Eq. (6) possesses n roots, so that the number of branches of magnetostatic waves $\omega(k_y)$ at fixed k_x coincides with the number of ferromagnetic layers in the period of the structure.

If all ferromagnetic layers consist of the same material, the spectrum of magnetostatic waves in the periodic structure exhibits two features. First, by using the symmetry properties of the matrix $\hat{\rho}_i$ in the magnetostatic case,

$$\begin{aligned}
\rho_{rli}(k_y) &= \rho_{rli}(-k_y), \quad r = l,\\
\rho_{rli}(k_y)\rho_{rlj}(k_y) &= \rho_{rli}(-k_y)\rho_{rlj}(-k_y), \quad r \ne l,
\end{aligned} \tag{9}$$

it is easy to show that the dispersion relation remains unchanged upon replacing k_y by $-k_y$. Hence, it follows that the spectrum is symmetric with respect to a change in the sign of any wave vector component of magneto-

static waves in ferromagnet–nonmagnet layered structures, including nonperiodic structures. Second, the spectrum of magnetostatic waves is invariant with respect to the replacement $b_i \rightleftarrows d_i$, i.e., the replacement of a ferromagnetic material by a nonmagnetic material and vice versa. Apparently, this property of the spectrum of magnetostatic waves is observed for both periodic and nonperiodic structures; however, this is true only in the case when $k_z = 0$.

The spectrum of magnetostatic waves in structures containing magnetic layers with different magnetic parameters is also symmetric with respect to the replacement $k_y \longrightarrow -k_y$ when the structure has a symmetry plane parallel to the layer surface. In the general case, this symmetry of the spectrum is absent.

Now, we analyze in greater detail the simplest periodic structure in which all ferromagnetic and all nonmagnetic layers are identical ($b_i \equiv b$, $d_i \equiv d$, $\beta_i \equiv \beta$, $\gamma_i \equiv \gamma$, $\mu_i \equiv \mu$, $\nu_i \equiv \nu$, $\mu_{\perp i} \equiv \mu_\perp$. In this case, relation (6) takes the form

$$\cos k_x D - \cosh\gamma d \cosh\beta b - \frac{\mu_\perp}{2\beta\gamma}\left(\beta^2 + \frac{\gamma^2}{\mu\mu_\perp}\right)\sinh\beta b \sinh\gamma d = 0. \quad (10)$$

Note that the expression on the left-hand side of relation (10) has no branch points. The same holds for the general relation (6).

According to relation (10), the dispersion of the magnetostatic wave is described by the expression

$$\omega^2 = \omega_H(\omega_H + \omega_M) + \frac{\omega_M^2}{2}\frac{\sinh k_y b \sinh k_y d}{\cosh k_y D - \cos k_x D}. \quad (11)$$

The spectrum of magnetostatic waves in the periodic structure, like the spectrum of surface magnetostatic waves in an isolated ferromagnetic layer, lies in the frequency range $[\omega_H(\omega_H + \omega_M)]^{1/2} \le \omega \le \omega_H + \omega_M/2$. At a fixed wave vector component k_y, the smaller the value of $\cos k_x D$, i.e., the closer the value of k_x to the Brillouin zone boundaries $k_x = \pm\pi/D$, the lower the wave frequency. The case $k_x = 0$, when the frequency is lowest, corresponds to inphase perturbations of the magnetization in all the ferromagnetic layers, and the case $k_x = \pm\pi/D$, when the frequency is highest, corresponds to antiphase perturbations of the magnetization in adjacent layers. The group velocity component along the normal to the interfaces becomes zero at the center and boundaries of the Brillouin zone. The energy transfer in the transverse direction also vanishes in the limiting cases $|k_y| \longrightarrow 0$ and $|k_y| \longrightarrow \infty$. As for the isolated ferromagnetic layer, magnetostatic modes with a field distribution over the thickness of ferromagnetic layers, which is described by trigonometric functions, are absent for the direction of the wave vector under consideration.

In the microwave frequency range, the electromagnetic wavelength in free space, as a rule, considerably exceeds the period of the structure. Therefore, at frequencies far from the frequency of uniform ferromagnetic resonance $\omega = [\omega_H(\omega_H + \omega_M)]^{1/2}$ ($\mu_\perp \longrightarrow \infty$), the following conditions are satisfied:

$$|\beta b| \ll 1, \quad |\gamma d| \ll 1. \quad (12)$$

Taking into account terms up to the second order in the expansions of trigonometric and hyperbolic functions in terms of small parameters βb and γd, we obtain the expression characterizing the electromagnetic-wave dispersion for the structure:

$$k^2 = k_0^2[\varepsilon_{zz}\mu b^2 + \varepsilon_f\mu_\perp\mu d^2 + \mu_\perp(\varepsilon_{zz}\mu + \varepsilon_f)bd] \times \{\mu D^2 + [(\mu - 1)^2 - \nu^2]bd\sin^2\varphi\}^{-1}, \quad (13)$$

where $k = (k_x^2 + k_y^2)^{1/2}$ and $\varphi = \arctan(k_y/k_x)$. The condition of vanishing the wave vector of the electromagnetic wave ($k = 0$) is reduced to the condition $\omega = 0$ and the biquadratic equation for determining two additional intersection points of the dispersion surface with the ω axis. The roots $\omega_{1,2}$ of this biquadratic equation at $d = b$ and $\varepsilon_f = \varepsilon_s$ are represented by the expression

$$\omega_{1,2}^2 = [8\omega_H^2 + 10\omega_H\omega_M + 3\omega_M^2 \pm \omega_M\sqrt{(20\omega_H^2 + 28\omega_H\omega_M + 9\omega_M^2)}]/8. \quad (14)$$

It should be noted that a thick ferromagnetic layer with permittivity ε_f and transverse permeability $\mu_\perp$ does not transmit electromagnetic waves in the frequency range $\sqrt{\omega_H(\omega_H + \omega_M)} \le \omega \le \omega_H + \omega_M$, because the permeability $\mu_\perp$ is negative at these frequencies. At the same time, the periodic structure can transmit a high-frequency signal in this frequency range.

For convenience of numerical analysis, we introduce the dimensionless frequencies $\Omega_H = \omega_H/\omega_M$ and $\Omega = \omega/\omega_M$. The dispersion of electromagnetic waves in the periodic structure composed of alternating layers of yttrium iron garnet ($4\pi M_0 = 1750$ G, $g = 2.8 \times 10^6$ Hz/Oe) and gadolinium gallium garnet is illustrated in Figs. 1–5. In this case, only the solutions of Eq. (6) with $\mathrm{Re}[k_x(\Omega, k_y)] > 0$ are given because relation (6) involves the square of the wave vector component k_x. In calculations, it is assumed that $\Omega_H = 1/2$ and the thicknesses and the permittivities of the magnetic and nonmagnetic layers are identical: $d = b = 5 \times 10^{-4}$ cm and $\varepsilon_f = \varepsilon_s = 16$.

The dispersion surface of magnetostatic waves over a wide range of wavelengths and the dispersion surface of electromagnetic waves in the long-wavelength range are depicted in Figs. 1 and 2, respectively. It can be seen from Fig. 2 that the transmission of electromagnetic waves with wave vectors $k < 16$ is absent in the frequency range corresponding to the existence of magne-

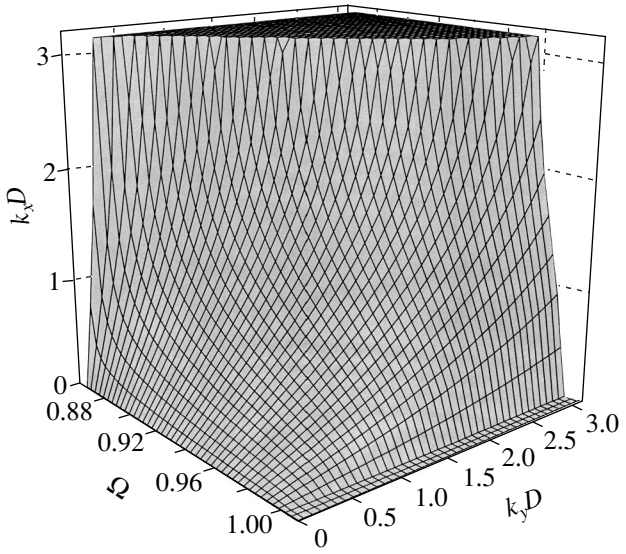

Fig. 1. Spectrum of magnetostatic waves in a periodic system composed of alternating ferromagnetic and nonmagnetic layers.

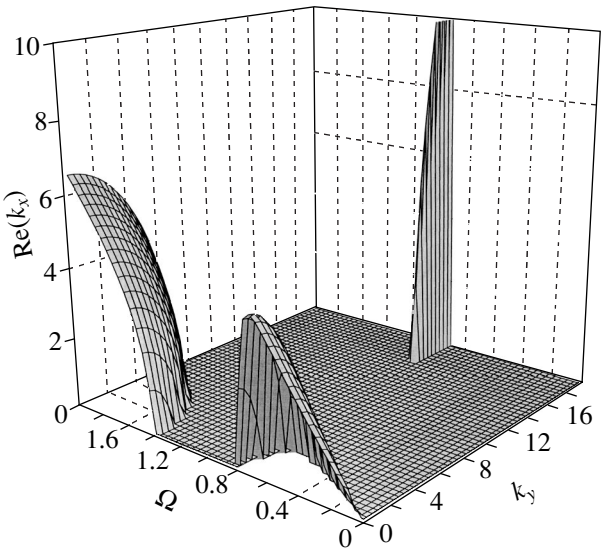

Fig. 2. A general view of the dispersion surface Re[$k_x(\Omega, k_y)$] in the range of long electromagnetic waves.

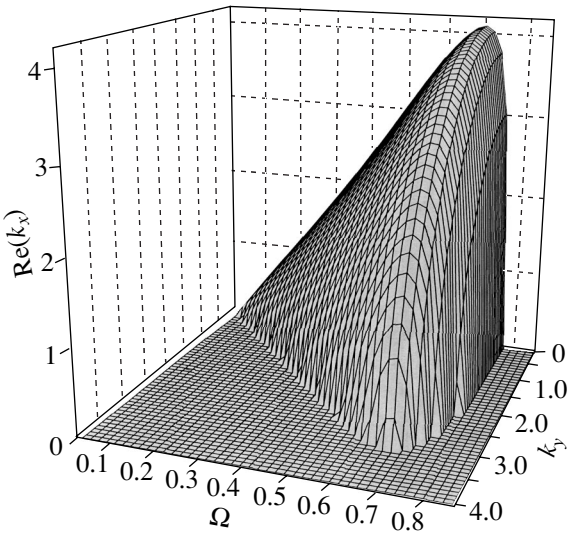

Fig. 3. Dependence Re[$k_x(\Omega, k_y)$] in the frequency range $0 \le \Omega \le [\Omega_H(\Omega_H + 1)]^{1/2}$.

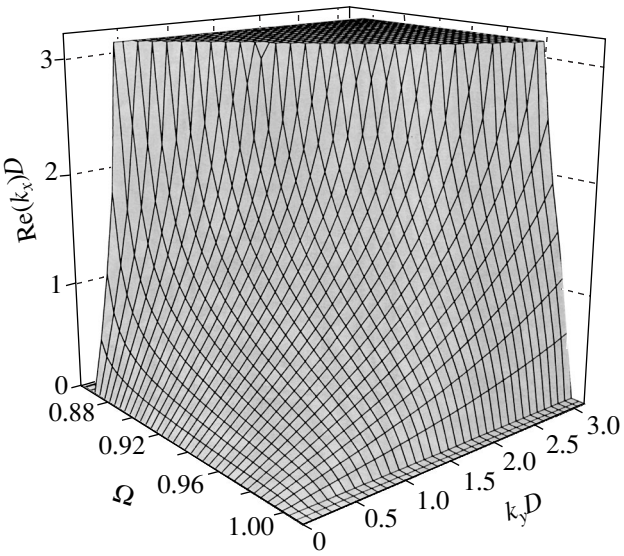

Fig. 4. Dependence Re[$k_x(\Omega, k_y)$] in the frequency range $[\Omega_H(\Omega_H + 1)]^{1/2} \le \Omega \le \Omega_H + 1/2$.

tostatic waves. This fact and the numerical estimates indicate that the magnetostatic approximation for the system with the aforementioned parameters becomes applicable beginning with $k \propto 10^2$ cm^{-1}. The dispersion of long electromagnetic waves is well described by formula (13) over the entire microwave range, except for a narrow frequency range close to the frequency of uniform ferromagnetic resonance $\Omega = [\Omega_H(\Omega_H + 1)]^{1/2}$.

Figure 3 shows the dependence Re[$k_x(\Omega, k_y)$] in the frequency range $0 \le \Omega \le [\Omega_H(\Omega_H + 1)]^{1/2}$. The wave vector of electromagnetic waves vanishes at the frequencies $\Omega = 0$ and $\Omega = \Omega_1 = \omega_1/\omega_M$ [see formula (14)]. In the nonpropagation region, we have Re[$k_x(\Omega, k_y)$] = 0 and Im[$k_x(\Omega, k_y)$] ≠ 0.

The dependence Re[$k_x(\Omega, k_y)$] over a wide range of wavelengths in the frequency range $[\Omega_H(\Omega_H + 1)]^{1/2} \le \Omega \le \Omega_H + 1/2$ is plotted in Fig. 4. A comparison of Figs. 1 and 4 shows that the effect of electromagnetic retardation on the spectrum of short electromagnetic waves is negligible. In the nonpropagation region, we have Re[$k_x(\Omega, k_y)$] = π/D and Im[$k_x(\Omega, k_y)$] ≠ 0.

The dependence Re[$k_x(\Omega, k_y)$] in the frequency range $\Omega \ge \Omega_H + 1/2$ is depicted in Fig. 5. The wave vec-

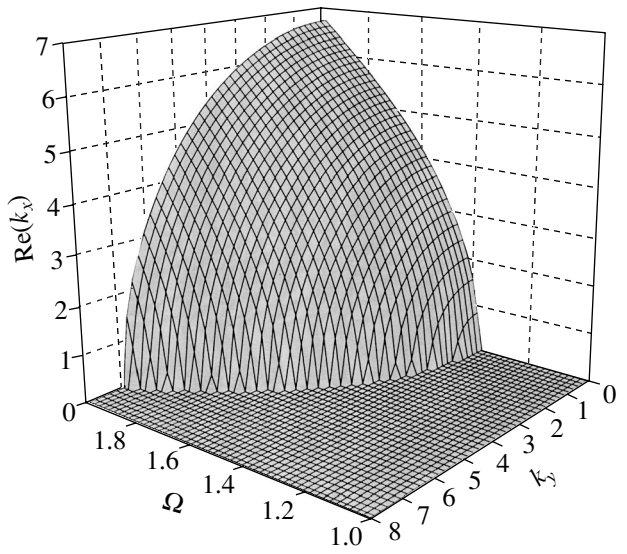

Fig. 5. Dependence Re[$k_x(\Omega, k_y)$] in the frequency range $\Omega \geq \Omega_H + 1/2$.

tor of electromagnetic waves becomes zero at $\Omega = \Omega_2 = \omega_2/\omega_M$, where ω_2 is given by expression (14). In the nonpropagation region, we have $\mathrm{Re}[k_x(\Omega, k_y)] = 0$ and $\mathrm{Im}[k_x(\Omega, k_y)] \neq 0$.

Now, we assume that the half-space $x > 0$ is a homogeneous isotropic medium with permittivity ε_0 and permeability $\mu_0 = 1$ and the half-space $x < 0$ represents the above medium composed of alternating ferromagnetic and nonmagnetic layers with a period equal to two layers. All magnetic and all nonmagnetic layers have identical parameters. For definiteness, we assume that, in the periodic structure, the upper layer is ferromagnetic and its upper surface coincides with the plane $x = 0$. We calculate the reflectivity for a plane electromagnetic wave that has the polarization (h_x, h_y, e_z)] and is incident on the periodic structure. The expression for the sole nonzero component of the electric field in the half-space $x > 0$ is conveniently represented in the form

$$e_{z,0} = [\exp(ik_x x) + R\exp(-ik_x x)] \times \exp[i(\omega t - k_y y)], \quad (15)$$

where

$$k_x = k_{x0} = \sqrt{k_0^2\varepsilon_0 - k_y^2}, \quad k_y^2 \leq k_0^2\varepsilon_0,$$

and R is the amplitude reflectivity of the electromagnetic wave. The electric field and its polarization in the ferromagnetic layer are described by expressions (1) and (8). From the boundary conditions at the surface $x = 0$, we find that the reflectivity R is given by the expression

$$R = \frac{(i\mu\mu_\perp k_{x0} + \nu k_y)(1+\Gamma) - \mu\gamma(1-\Gamma)}{(i\mu\mu_\perp k_{x0} - \nu k_y)(1+\Gamma) + \mu\gamma(1-\Gamma)}. \quad (16)$$

It is easy to demonstrate that the reflectivity defined by expression (16) does not depend on the choice of the branches β and γ.

The condition for the nonpropagation of the electromagnetic wave $|R| = 1$ in the absence of damping at $\mathrm{Im}\,k_{x0} = 0$ is satisfied at $\gamma^2 > 0$ if

$$\mu(\mu^2 - \nu^2)k_{x0}\gamma\,\mathrm{Im}\,\Gamma = 0. \quad (17)$$

The first and second factors in expression (17) vanish at the frequencies $\omega = [\omega_H(\omega_H + \omega_M)]^{1/2}$ and $\omega = \omega_H + \omega_M$, respectively. The equality $k_{x0} = 0$ is the condition for propagation of the electromagnetic wave along the yz plane. From matrix (3) and expression (7), it follows that the inequality $(\mathrm{Sp}\,\hat{\lambda})^2 > 4$ is a sufficient condition for Γ to be a real quantity.

At $\mathrm{Im}\,k_{x0} = 0$ and $\gamma^2 < 0$, the equality

$$\mu(\mu^2 - \nu^2)k_{x0}(1 - |\Gamma|^2)\mathrm{Im}\,\gamma = 0 \quad (18)$$

is the condition for total reflection of the electromagnetic wave from the boundary with the periodic medium.

In the general case, the system without damping does not transmit the electromagnetic wave when real roots $k_x(\omega, k_y)$ of the dispersion relation (6) are absent, i.e., at $(\mathrm{Sp}\,\hat{\lambda})^2 > 4$.

In the system formed by the homogeneous half-space and the periodic structure, there can exist surface electromagnetic waves whose field amplitude is maximum at the boundary of the upper ferromagnetic layer $x = 0$ and exponentially decreases deep in the periodic structure. The dispersion relation for these waves is the condition of vanishing the denominator in expression (16); that is,

$$(i\mu\mu_\perp k_{x0} - \nu k_y)(1+\Gamma) + \mu\gamma(1-\Gamma) = 0. \quad (19)$$

In addition, the electromagnetic wave radiation should be absent in the half-spaces $x > 0$ and $x < 0$; i.e., the following conditions should be satisfied:

$$k_y^2 > k_0^2\varepsilon_0, \quad \mathrm{Im}\,k_{x0} < 0, \quad (\mathrm{Sp}\,\hat{\lambda})^2 > 4. \quad (20)$$

At $\gamma^2 > 0$ and in the absence of damping, the quantity Γ is real and Eq. (19) does not involve the imaginary part. At $\gamma^2 < 0$, the left-hand side of Eq. (19) is complex and it does not possess solutions.

For surface magnetostatic waves, dispersion relation (19) takes the form

$$\frac{\mu}{\nu^2 - \mu^2 + \xi\nu} = \frac{1+\Gamma}{1-\Gamma}, \quad (21)$$

where $k_y \equiv k$ and $\xi = k/\sqrt{k^2}$. Recall that, in a semi-infinite ferromagnet, surface magnetostatic waves are absent because the frequency of magnetostatic excitations does not depend on the magnitude of the wave

vector. For surface magnetostatic waves described by relation (19), the dispersion is observed because the system is characterized by two spatial scales, namely, the thicknesses of ferromagnetic and nonmagnetic layers. The results obtained from analyzing relations (19) and (21) and also the dependences $\mathrm{Im}[k_x(\Omega, k_y)]$ are not presented to economize space.

3. CONCLUSIONS

Thus, it was demonstrated that the magnetic interaction of partial surface magnetostatic waves in ferromagnetic layers leads to the formation of a magnetostatic-wave region and provides the possibility of transferring the energy of the high-frequency magnetic field in the direction perpendicular to the layer interfaces. The group velocity of these waves becomes zero at the center and at the boundary of the Brillouin zone. The situation considered in the present work differs from that observed in nongyrotropic crystals, in which, by contrast, the periodic inhomogeneity brings about the formation of energy band gaps.

The standard band structure of the spectrum of electromagnetic waves was not analyzed in this work. Since the thickness of ferromagnetic layers is usually equal to 10–100 μm, the band gaps should be located in the high-frequency range $\omega \propto 10^{13}$–10^{14} s^{-1}.

ACKNOWLEDGMENTS

This work was supported by the Russian Foundation for Basic Research (project nos. 02-02-16794, 02-02-17166), the International Center of Science and Technology (project no. 1522), and the Committee of Scientific Research of Poland.

REFERENCES

1. J. D. Joannopoulos, R. D. Mead, and J. N. Winn, *Photonic Crystals: Molding the Flow of Light* (Princeton Univ. Press, Princeton, N.J., 1995).
2. *Photonic Band Gap Materials: Proceedings of the NATO ASI, Elounda, Crete, Greece, 1995*, Ed. by Costas M. Soukoulis (Kluwer Academic, Dordrecht, 1996).
3. K. Sakoda, *Optical Properties of Photonic Crystals* (Springer, Berlin, 2001), Springer Ser. Opt. Sci., Vol. 80.
4. S. G. Johnson and J. D. Joannopoulos, *Photonic Crystals: The Road from Theory to Practice* (Kluwer, Boston, 2002).
5. M. Sigalas and E. N. Economou, Europhys. Lett. **36** (2), 241 (1996).
6. J. O. Vasseur, P. A. Deymer, G. Ftziskonis, *et al.*, J. Phys.: Condens. Matter **10** (27), 6051 (1998).
7. A. M. Steinberg, P. G. Kwist, and R. Y. Chiao, Phys. Rev. Lett. **71** (5), 708 (1993).
8. J. O. Vasseur, L. Dobrzynski, B. Dijafari-Rouhani, and H. Puszkarski, Phys. Rev. B **54** (2), 1043 (1996).
9. A. Figotin and I. Vitebsky, Phys. Rev. E **63**, 066609 (2001).
10. S. A. Nikitov, Ph. Tailhades, and C. S. Tsai, J. Magn. Magn. Mater. **236** (1), 320 (2001).
11. B. Lax and K. J. Button, *Microwave Ferrites and Ferrimagnetics* (McGraw-Hill, New York, 1962; Mir, Moscow, 1965).
12. C. Kittel, *Introduction to Solid State Physics*, 5th ed. (Wiley, New York, 1976; Fizmatgiz, Moscow, 1962).

Translated by O. Borovik-Romanova

Physics of the Solid State, Vol. 45, No. 11, 2003, pp. 2166–2170. Translated from Fizika Tverdogo Tela, Vol. 45, No. 11, 2003, pp. 2062–2066.

MAGNETISM AND FERROELECTRICITY

Inhomogeneous States of a Thin-Film Incommensurate Ferroelectric

S. A. Ktitorov*, O. S. Pogorelova, and E. V. Charnaya*****

**Ioffe Physicotechnical Institute, Russian Academy of Sciences, Politekhnicheskaya ul. 26, St. Petersburg, 194021 Russia*
e-mail: ktitorov@mail.ioffe.ru
***St. Petersburg Mechnikov State Medical University, St. Petersburg, 195067 Russia*
****Fock Institute of Physics, St. Petersburg State University, ul. Pervogo Maya 100, Petrodvorets, St. Petersburg, 198504 Russia*

Received February 28, 2003

Abstract—Nonuniform distributions of the order parameter in a film of an incommensurate ferroelectric whose free energy expansion does not contain Lifshitz invariants are considered. An equation describing the order parameter distribution over the film thickness is derived in the approximation of slowly varying amplitudes. The effect of film thickness and surface properties on the temperature of transition to the incommensurate phase is analyzed. © *2003 MAIK "Nauka/Interperiodica".*

1. INTRODUCTION

A large number of publications dealing with experimental [1–4] and theoretical [5–8] investigations of the ferroelectric transition in samples with significantly limited spatial dimensions, such as films, small particles, and clusters, are presently available. Size constraints entail, as a rule, a decrease in the temperature of the phase transition and its becoming diffuse, which makes transformation into an ordered state impossible starting from a certain size. This is accompanied by a change in the spontaneous polarization, susceptibility, and coercive and switching fields.

Many of these features can be described in terms of a theoretical model developed recently for ferroelectrics (see [5–8] and references therein). Specifically, a phenomenological approach to ferroelectric phase transitions in thin films and small particles was proposed in [5]. The phase transition in thin films and small particles was treated later in terms of the Landau theory [8]. All those studies dealt with a transition to a nonmodulated phase; for this reason, a nonuniformity in the order parameter could appear only as a consequence of boundary conditions, with domains and fluctuations disregarded altogether.

We consider here the effect of a limited size of the sample and of boundary conditions on the modulated structure that arises during a phase transition to an incommensurate phase. It is worth mentioning that experiments have been performed recently on thin films of an incommensurate ferroelectric [9].

Below, we present a phenomenological description of a phase transition in thin films of an incommensurate ferroelectric.

2. EQUATION FOR THE ORDER PARAMETER

We analyze the case where incommensurability appears not as a result of symmetry, as in the presence of the Lifshitz invariant, but rather accidentally, because of phonon mode softening at an arbitrary point of the Brillouin zone. In these conditions, one can choose a one-component order parameter (corresponding to the maximum bare instability of the homogeneous state); in contrast, however, to the cases of ferroelectrics and antiferroelectrics [10], the equation written in the self-consistent field approximation for the order parameter is a fourth-order nonlinear differential equation and it is the associated problems whose solution is dealt with in this communication. In particular, the de Gennes boundary conditions [11], introduced for phenomenological description of superconducting films and employed subsequently for similar treatment of the size effect in substances of various natures, were found to be inadequate here.

Consider a one-dimensional distribution of the order parameter in a film of thickness L, with the origin $x = 0$ placed at the center of the film. The dependence of the order parameter on x can be determined by minimizing the thermodynamic potential described by the Landau functional

$$\Phi = \int_{-L/2}^{L/2} dx\left[\frac{1}{2}A_0(T-T_0)\eta^2 + \frac{1}{4}B\eta^4 + \frac{1}{2}C\left(\frac{d\eta}{dx}\right)^2 + \frac{1}{2}D\left(\frac{d^2\eta}{dx^2}\right)^2\right] + \psi(\eta(L/2)) - \varphi(\eta(-L/2)). \quad (1)$$

By varying functional (1), one can obtain Euler's equation complete with the corresponding natural boundary

conditions [12]. Because more symmetric (in particular, even) distributions usually have a lower free energy, we limit ourselves, in what follows, to order parameter distributions which are even functions of the x coordinate, $\eta(-x) = \eta(x)$, and discuss the behavior of the order parameter only for $x \geq 0$:

$$\frac{d^4\eta}{dx^4} - \frac{C}{D}\frac{d^2\eta}{dx^2} + \frac{B}{D}\eta^3 + \frac{A}{D}\eta = 0, \quad (2)$$

$$\left[\frac{d\psi(\eta)}{d\eta} + \frac{dF}{d\eta'} + \frac{d}{dx}\frac{\partial F}{\partial \eta''}\right]_{x = L/2} = 0, \quad (3)$$

$$\left.\frac{\partial F}{\partial \eta''}\right|_{L/2} = 0, \quad (4)$$

where $F(\eta(x), \eta', \eta'')$ is the integrand of functional (1), $\eta' = d\eta/dx$ and $\eta'' = d^2\eta/dx^2$; $\varphi(\eta(-L/2))$ and $\psi(\eta(L/2))$ are given functions of the order parameter at the boundaries $x = \pm L/2$. It appears only natural to consider these functions as a surface energy contribution, which can be approximated by a quadratic expression of the type

$$\psi(\eta(-L/2)) = \alpha\frac{\eta^2}{2}. \quad (5)$$

In view of Eqs. (3)–(5), as well as recalling the form of functional (1), the natural boundary condition for $x \geq 0$ becomes

$$\left[\alpha\eta(x) + C\frac{d\eta(x)}{dx} + D\frac{d^3\eta(x)}{dx^3}\right]_{L/2} = 0, \quad (6)$$

$$\left.\frac{d^2\eta(x)}{dx^2}\right|_{L/2} = 0. \quad (7)$$

The nonlinear fourth-order differential equation thus obtained allows us to find only a numerical solution. It appears, however, important to derive a more tractable equation which could be solved analytically and, thus, would permit a comparatively simple analysis of the results.

3. METHOD OF SLOWLY VARYING AMPLITUDES

This method can be used assuming the film thickness to be large compared to the period of spatial oscillations of the order parameter in an incommensurate ferroelectric, $qL \gg 1$, where q is the oscillation wavenumber. Following the method of slowly varying amplitudes, we make the substitution

$$\eta(x) = u(x)\cos(qx), \quad (8)$$

where $u(x)$ is the slowly varying amplitude and the wavenumber q can be found by minimizing the sum of terms with derivatives in functional (1) for u = const. We do this under the assumption that the boundary conditions in a thick enough film virtually do not affect the spatial oscillation frequency

$$q = \sqrt{-\frac{C}{2D}}. \quad (9)$$

Substituting Eq. (8) into Eq. (2) and neglecting all higher derivatives of the amplitude $u(x)$, we come to a second-order differential equation,

$$\frac{d^2u}{dx^2} = -\frac{3B}{8C}u^3 + \frac{C^2 - 4AD}{8CD}u, \quad (10)$$

which can now be solved analytically. This equation, combined with general homogeneous boundary conditions (which were employed by de Gennes and define the extrapolation length in the Ginzburg–Landau phenomenological theory of superconductivity [11]),

$$\frac{d\ln u}{dx} = \pm\frac{1}{\delta} \quad (11)$$

constitutes the boundary-value problem to be considered below. As in the Ginzburg–Landau theory, we call the parameter δ the extrapolation length. It describes the effect of the surface on the order parameter distribution over the film thickness. Prior to solving the equation, however, we consider the relation between the boundary conditions for the fourth- and second-order equations.

4. BOUNDARY CONDITIONS FOR THE SECOND-ORDER EQUATION

Equation (10) for the amplitude u(x) should be complemented by boundary conditions, which can be derived from Eqs. (6) and (7) by using the method of slowly varying amplitudes. To do this, we substitute Eq. (8) into Eqs. (6) and (7) and, neglecting all but the first derivatives of $u(x)$, we obtain coupled equations

$$\left[(C + 3Dq^2)\left(\frac{u'}{u}\right) + \alpha\right]\cos\left(\frac{qL}{2}\right) = q(C + Dq^2)\sin\left(\frac{qL}{2}\right), \quad (12)$$

$$q^2\cos\left(\frac{qL}{2}\right) = -2q\left(\frac{u'}{u}\right)\sin\left(\frac{qL}{2}\right). \quad (13)$$

Eliminating the sine and the cosine in Eqs. (12) and (13) and recalling Eq. (11), we obtain a quadratic equation for the logarithmic derivative (11),

$$(C + Dq^2)\frac{q^2}{2}\delta^2 - \alpha\delta + (C + 3Dq^2) = 0. \quad (14)$$

Its solution can be written as

$$\delta = \frac{\alpha \mp \sqrt{\alpha^2 - 2(C + Dq^2)(C + 3Dq^2)q^2}}{q^2(C + Dq^2)}. \quad (15)$$

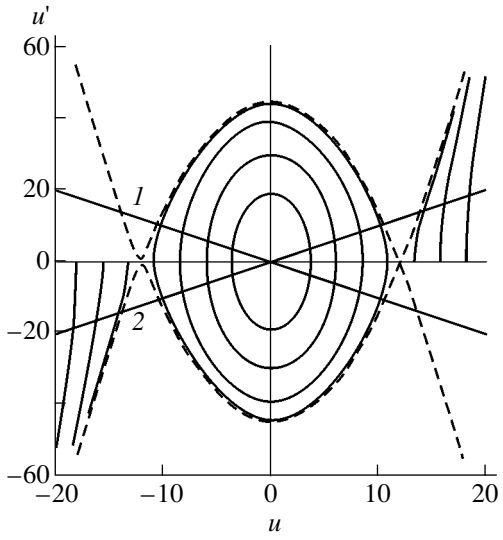

Fig. 1. Phase portrait of Eq. (10). $A = 10\,000$, $B = 100$, $C = -200$, $D = 1$, and $T_0 = 1$. The separatrices are shown by dashed lines. The inclined straight lines relate to linear homogeneous boundary conditions (11) for (*1*) $\delta = 1$ and (*2*) –1.

Relation (11) plays the part of a boundary condition for the amplitude equation. Because δ is real, the inequality $\alpha^2 - 2(C + Dq^2)(C + 3Dq^2)q^2 \geq 0$ should be met. Inserting Eq. (9) for q, we come to

$$\delta = -\frac{4D}{C^2}\left(\alpha \pm \sqrt{\alpha^2 - \frac{C^3}{4D}}\right). \quad (16)$$

The discriminant $\alpha^2 - C^3/4D$ is always positive, because $C < 0$ and $D > 0$; hence, δ is always real. The two roots of Eq. (14) have opposite signs, but only one of them has physical meaning for the given value of qL. Indeed, the compatibility of Eqs. (12) and (13) requires that the equality

$$\operatorname{sgn}\delta = \operatorname{sgn}\tan\frac{qL}{2} \quad (17)$$

be met.

We assumed the quantity q to be strictly defined by condition (9). In this case, we obtain an oscillatory dependence of the logarithmic derivative of the amplitude at the boundary on the "phase thickness" of the sample at the boundary qL and, hence, on temperature. This is not, however, the only possible scenario. The behavior of a real system is governed by more complex equations than those derived by us in the slowly varying amplitude approximation. This means that, in searching for a configuration that would minimize the free energy, a real system can violate some of our assumptions. A possible scenario is to adjust the value of q such that the energy is minimum. For films that are thick enough, qL is large and a small correction to it may suffice to minimize the energy. Another possibility consists in varying the wavenumber q only within a certain boundary layer. Only numerical analysis of the fourth-order equation can determine the path a real system would follow.

Obviously enough, under our assumptions, the problem of a phase transition to an incommensurate phase reduces to a boundary problem that is similar, from a mathematical viewpoint, to that of a ferroelectric phase transition in a thin film. The extrapolation length δ in Eq. (11) describes the difference between the surface and bulk properties and can be both positive and negative. It appears natural to assume that δ should be positive for a film with a free surface. Size effects in a thin film become noticeable when the extrapolation length is comparable to the film thickness. Thus, if the film thickness L is large compared to the spatial modulation period $2\pi/q$, then we also have $\delta \gg 2\pi/q$. In the next section, we treat analytical solutions to the second-order equation.

5. ANALYSIS OF SOLUTIONS TO THE SECOND-ORDER EQUATION

We start our discussion appropriately with an analysis of the phase portrait of Eq. (10) displayed in Fig. 1. The two regions of solutions are separated in Fig. 1 by dashed lines representing separatrices. The closed curves, corresponding to the periodic solutions of Eq. (10), lie within the region Ω bounded by the separatrices. The boundary conditions (11) are represented in the phase diagram by straight lines with a negative and a positive slope for positive and negative extrapolation lengths, respectively. As seen from Fig. 1, in the case of positive extrapolation lengths, all possible solutions are confined within Ω.

The analytical solution to Eq. (10) can be written as

$$u(x) = u_0\frac{\operatorname{cn}(Qx, k)}{\operatorname{dn}(Qx, k)}, \quad Q = \sqrt{\frac{4DA - C^2}{8DC} + \frac{3Bu_0^2}{16C}}, \quad (18)$$

where $u_0 = u(x = 0)$ is the value of u at the film center and k is the elliptic modulus

$$k = u_0/\sqrt{\frac{4(C^2 - 4DA)}{3DB} - u_0^2}, \quad (19)$$

with u_0 being related to δ as

$$\delta = (1 - k^2)\frac{\operatorname{dn}(QL/2, k)}{Q\operatorname{tn}(QL/2, k)}. \quad (20)$$

Here, cn, tn, and dn are Jacobian elliptic functions [13]. The solutions obtained by us describe the order-parameter amplitude distribution over the sample thickness for arbitrary values of the phenomenological parameters of the substance, film thickness, and temperature. They also permit one to find the dependence of the tran-

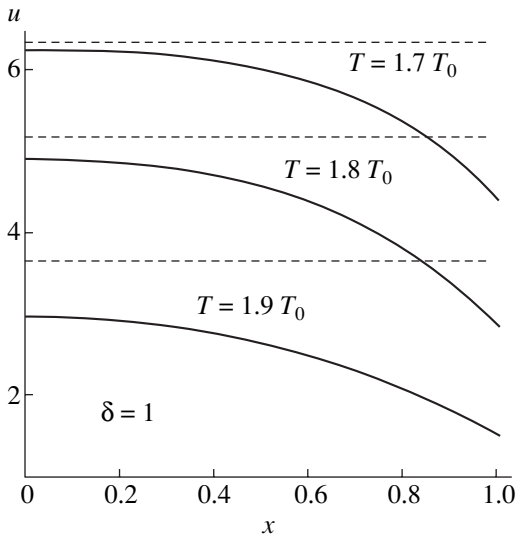

Fig. 2. Order-parameter amplitude u plotted vs. coordinate $x \geq 0$ for positive values of δ and various temperatures. The values of the phenomenological parameters are the same as those in Fig. 1; $L = 2$. Dashed straight lines specify the amplitudes in bulk samples for the same temperatures.

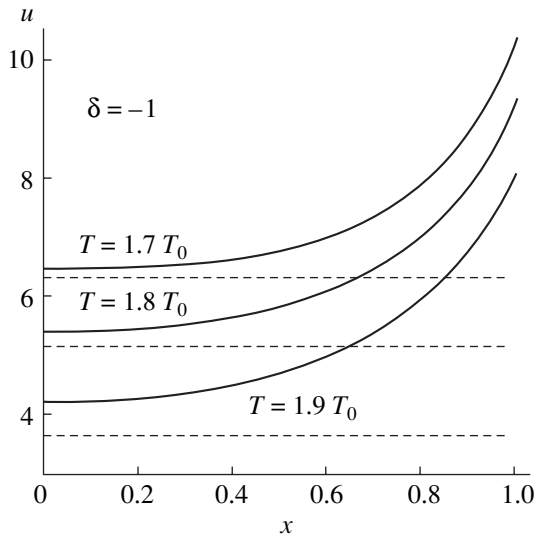

Fig. 3. Order-parameter amplitude u plotted vs. coordinate $x \geq 0$ for negative values of δ and various temperatures. The values of the phenomenological parameters are the same as those in Fig. 1; $L = 2$. Dashed straight lines specify the amplitudes in bulk samples for the same temperatures.

sition temperature T_i on film thickness for various values of the phenomenological parameters (T_i is the temperature at which u_0 and, hence, $u(x)$ vanish).

The dependences of the order-parameter amplitude u on x for positive and negative values of δ are depicted in Figs. 2 and 3 for several temperatures. The phenomenological parameters used are given in the caption to Fig. 1. The behavior of $u(x)$ for positive δ is similar to that of the spontaneous polarization in thin ferroelectric films; namely, the amplitude u decreases as one approaches the film surface and its value at the film center is less than that in the corresponding bulk sample (Fig. 2).

For negative extrapolation lengths, according to the phase diagram (Fig. 1), there are two types of solutions for $u(x)$. The solutions displayed in Fig. 3 behave similarly to the polarization in ferroelectric films; more specifically, the amplitude u increases as one approaches the film surface and its magnitude at the film center is higher than that in the corresponding bulk sample.

For the second type of solutions, the amplitude u in the film is smaller than that in the bulk sample and its magnitude decreases as one approaches the surface, with the amplitude reversing sign at a certain value of x, which corresponds to a jump in the wave phase. Calculation of the contributions from the two solutions to the thermodynamic potential of the film made for negative δ reveals, however, that the solution of the first type (for which the value of u at the boundary is larger than in the bulk) is energetically preferable.

The dependence of the incommensurate phase transition temperature on film thickness is plotted in Fig. 4 for both positive and negative extrapolation lengths. T_i is seen to decrease with decreasing film thickness for a positive extrapolation length δ and vanishes at a certain critical thickness. A similar dependence has been obtained for a ferroelectric and an antiferroelectric film with δ assumed to be positive [5, 8]. The thickness dependence of T_i obtained for negative δ follows the reverse pattern.

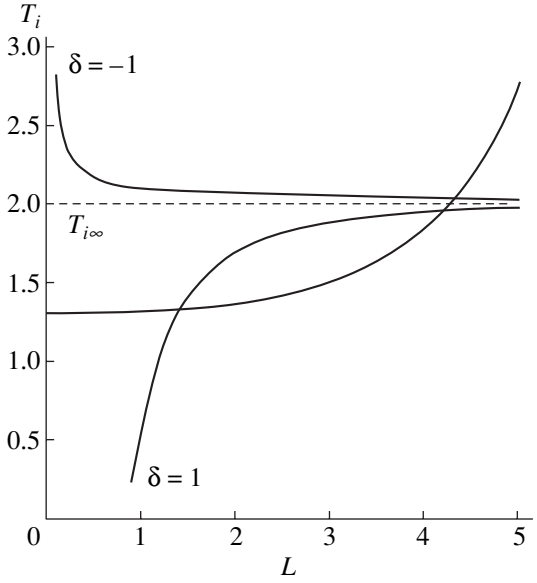

Fig. 4. Temperature T_i of the transition to an incommensurate phase plotted vs. film thickness L for $\delta = 1$ and –1. The phenomenological parameters are the same as those in Fig. 1.

REFERENCES

1. K. Ishikawa, K. Yoshikawa, and N. Okada, Phys. Rev. B **37** (10), 5852 (1988).
2. E. V. Colla, A. V. Fokin, and Yu. A. Kumzerov, Solid State Commun. **103** (2), 127 (1997).
3. J. F. Scott, H. M. Duiker, P. D. Beale, *et al.*, Physica B (Amsterdam) **150** (1), 160 (1988).
4. S. Chattopadhyay, P. Ayyub, V. R. Palkar, and M. Multani, Phys. Rev. B **52** (18), 13177 (1995).
5. D. R. Tilley, in *Ferroelectric Ceramics*, Ed. by N. Setter and E. L. Colla (Birkhause, Basel, 1993), p. 163.
6. W. L. Zhong, Y. G. Wang, P. L. Zhang, and B. D. Qu, Phys. Rev. B **50** (2), 698 (1994).
7. Y. G. Wang, W. L. Zhong, and P. L. Zhang, Phys. Rev. B **53** (17), 11439 (1996).
8. E. V. Charnaya, O. S. Pogorelova, and C. Tien, Physica B (Amsterdam) **305** (2), 97 (2001).
9. J. Schneider, C. Schürrer, and A. Brunetti, Phys. Rev. B **54** (5), 2972 (1996).
10. M. E. Lines and A. M. Glass, *Principles and Applications of Ferroelectrics and Related Materials* (Oxford Univ. Press, Oxford, 1977; Mir, Moscow, 1981).
11. P. G. de Gennes, *Superconductivity of Metals and Alloys* (Benjamin, New York, 1966; Mir, Moscow, 1968).
12. V. I. Smirnov, *A Course of Higher Mathematics*, 6th ed. (Addison-Wesley, Reading, Mass., 1964; Nauka, Moscow, 1981), Vol. 4.
13. *Higher Transcendental Functions (Bateman Manuscript Project)*, Ed. by A. Erdelyi (McGraw-Hill, New York, 1955; Nauka, Moscow, 1967), Vol. 3.

Translated by G. Skrebtsov

Physics of the Solid State, Vol. 45, No. 11, 2003, pp. 2171–2177. Translated from Fizika Tverdogo Tela, Vol. 45, No. 11, 2003, pp. 2067–2073.

MAGNETISM AND FERROELECTRICITY

Specific Features in the Ferroelectric Properties of $Sr_{0.75}Ba_{0.25}Nb_2O_6$ Crystals

V. V. Gladkiĭ, V. A. Kirikov, T. R. Volk, D. V. Isakov, and E. S. Ivanova

Shubnikov Institute of Crystallography, Russian Academy of Sciences, Leninskiĭ pr. 59, Moscow, 119333 Russia

Received April 9, 2003

Abstract—The dielectric properties of strontium–barium niobate crystals with a strontium concentration of 0.75, which corresponds to the most smeared ferroelectric phase transition, were measured. The dielectric hysteresis loops and the polarization relaxation are shown to exhibit clearly pronounced features characteristic of crystals with structural disorder and a broad distribution of a random internal electric field. The measurements were performed in dc, slowly varying (quasi-static), and pulsed electric fields. The experimental data obtained are used to construct the distribution function for the coercive field in the crystal bulk. © *2003 MAIK "Nauka/Interperiodica".*

1. INTRODUCTION

Oxide solid solutions with perovskite-like crystal structure (general formula ABO_3) [1–4] are highly inhomogeneous materials with structural disorder which reveal unusual ferroelectric properties. Such crystals have been named relaxor ferroelectrics (or relaxors). In particular, structural disorder in $Sr_xB_{1-x}Nb_2O_6$ crystals with tungsten bronze structure, which are the subject of the present study, originates from 1/6 of the *A*-cation positions being unfilled [2, 3], with the degree of disorder being determined by the pattern of filling of the *A*2 structural channel by Ba and Sr ions [5]. The structural disorder brings about inhomogeneous strains and internal electric fields in the bulk of the crystal, due to which the local site symmetry is reduced and the symmetric double-minimum local free energy function of polarization transforms into an asymmetric function, with a random distribution of its parameters over the crystal volume [4]. As a result, dielectric hysteresis loops acquire (as shown to be valid for SBN crystals of various compositions [6–8]) an anomalous shape with open and nonreproducing first polarization switching cycles and with clear indications of the absence of a definite coercive field. The actual degree of diffuseness of the phase transition and the relaxor properties of the SBN compounds are determined by the chemical composition. Increasing the Sr content [2, 3] and doping the compound with rare-earth elements [9] lowers the temperature of the maximum of dielectric permittivity considerably increases the diffuseness of the phase transition, and makes the characteristic properties of the relaxors more pronounced.

The goal of the present work was to investigate the polarization processes occurring in the relaxor ferroelectric SBN-0.75. The behavior of the various properties of SBN-0.75, in particular, of the dispersion characteristics of its dielectric permittivity in the region of the phase transition, has been a subject of many publications (see, e.g., [10]). Research has been focused on SBN-0.75 because it has the largest diffuseness of the phase transition and the most clearly pronounced relaxor properties of this composition among all other SBN compounds. It is in SBN-0.75 that nanodomains [11] known to be specific to relaxor ferroelectrics have been observed. At the same time, polarization processes (polarization kinetics, quasi-static dielectric hysteresis loops), whose investigation in other compositions have revealed a number of features characteristic of relaxors [6–8], have not been studied in the SBN-0.75.

Our present investigation of polarization processes in SBN-0.75 was performed in various field regimes, namely, under the application of dc, slowly varying (quasi-static), and pulsed electric fields. Measurements in dc and quasi-static fields make it possible to obtain a response of longest lived metastable states of a crystal and polarizations which most closely approach levels of thermodynamic equilibrium. The experimental technique employed in our previous studies [6, 7] offered the possibility of investigating the slow part of the polarization kinetics for times in excess of 15 s. The broadened scope of techniques employed in this study also made it possible to explore the kinetics of the fast stage of the process.

2. EXPERIMENTAL TECHNIQUES

The polarization variation in dc and quasi-static fields was measured with an equal-arm electrometric bridge, with the sample under study and the source of polarizing voltage V connected in one arm, a reference capacitor C and the source of compensating voltage v connected in the other, and a V7-29 electrometer serving as a null indicator when balancing the bridge across the bridge diagonal. The voltage compensation across the diagonal was attained automatically with an IBM PC and

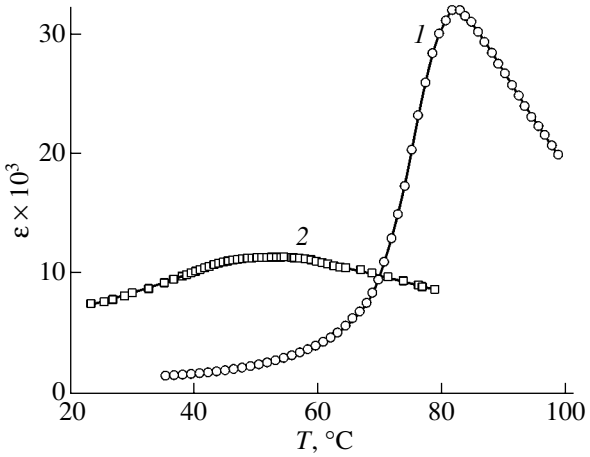

Fig. 1. Temperature behavior of the dielectric permittivity ε of (*1*) SBN-0.61 and (*2*) SBN-0.75.

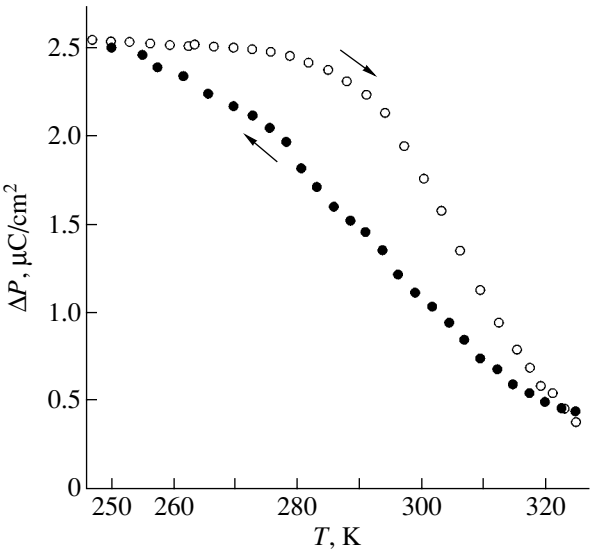

Fig. 2. Variation of the polarization Δ*P* of the SBN-0.75 crystal with temperature in a zero electric field.

controllable peripherals. The maximum bridge sensitivity in voltage was 20 μV, and in charge, 2×10^{-9} μC (C = 10 pF). The compensating voltage v displayed on the monitor, the time t, the field strength $E = V/d$, and the polarization P are related through the expression $v(t) = SP(t)/C + ESt/\rho C$, where S is the sample electrode area and ρ is the sample electrical resistivity. After estimating the smallest possible value of ρ for long times, where the relaxation of the polarization P practically stops and the $v(t)$ curve becomes a straight line ($v(t) = ESt/\rho C$), the polarization P was calculated. For a high electrical resistivity ρ, the electrical conductivity may be neglected and we can write $P(t) = Cv(t)/S$ to sufficient accuracy. All measurements of the SBN-0.75 polarization were corrected for the electrical conductivity. The computerized bridge used for electrometric measurements of the polarization is described in considerable detail in [12, 13]. The polarization was measured in two electric field variation modes; in one of them, the polarization relaxation after switching on and switching off the dc field (the polarization and depolarization processes) was investigated, and in the other, the polarization was measured under a slow periodic field variation (quasi-static loops of the dielectric hysteresis). The fast component of the polarization relaxation was determined under application of pulsed fields by measuring the switching currents using the Merz technique [2]. We used pulsed fields with a leading edge of not longer than 25×10^{-9} s and a duration from 3×10^{-4} to 10 s; the highest field strength was 10–12 kV/cm. The signal was measured with a high-frequency ADC board interfaced with an IBM PC, and the variation of the polarization (switching) current with time, $i(t)$, was displayed in real time on the monitor. The maximum signal resolution was 2×10^{-8} s. The dielectric permittivity was measured using the standard bridge method at a frequency of 1 kHz. The sample used in the studies was a rectangular plate $3 \times 3 \times 0.5$ mm in size whose major faces were perpendicular to the Z axis. Electrodes were deposited on these faces with conducting silver paste.

The ferroelectric characteristics of the crystals studied are displayed graphically in Figs. 1 and 2. Figure 1 presents temperature dependences of the dielectric permittivity ε_{33} of SBN-0.75 and SBN-0.61 crystals. The greater part of the diffuseness in $\varepsilon_{33}(T)$ for SBN-0.75 is in agreement with the data reported in [2, 3, 10]. The variation of the polarization with temperature in the SBN-0.75 sample was measured in a zero electric field is shown in Fig. 2 (the pyroelectric effect); the variation is seen to extend over a broad temperature range including the maximum in dielectric permittivity as a result of the total sample polarization being uncompensated (the unipolarity). We readily see that the polarization grows nearly linearly with temperature under cooling and that the pyroelectric coefficient is a constant and does not exhibit any anomalies; furthermore, there is a clearly pronounced temperature hysteresis. The pyroelectric coefficient is 0.04 μC/K.

3. RESULTS AND DISCUSSION

Recall that in conventional homogeneous ferroelectrics that are described satisfactorily in terms of the Landau–Ginzburg–Devonshire theory [1, 2] the free energy $F = \alpha_0(T - \Theta)P^2/2 + \beta P^4/4$ in the polar phase at $T < \Theta$ has the form of a double-minimum function of polarization P, where α_0 and β are constants; the spontaneous polarization $P_s = [\alpha_0(T - \Theta)/2\beta]^{1/2}$ and the coercive field $E_c = [2\alpha_0(T - \Theta)/3][2\alpha_0(T - \Theta)/3\beta]^{1/2}$, which is equal to one half the width of the dielectric hysteresis loop, are unambiguously defined, while the

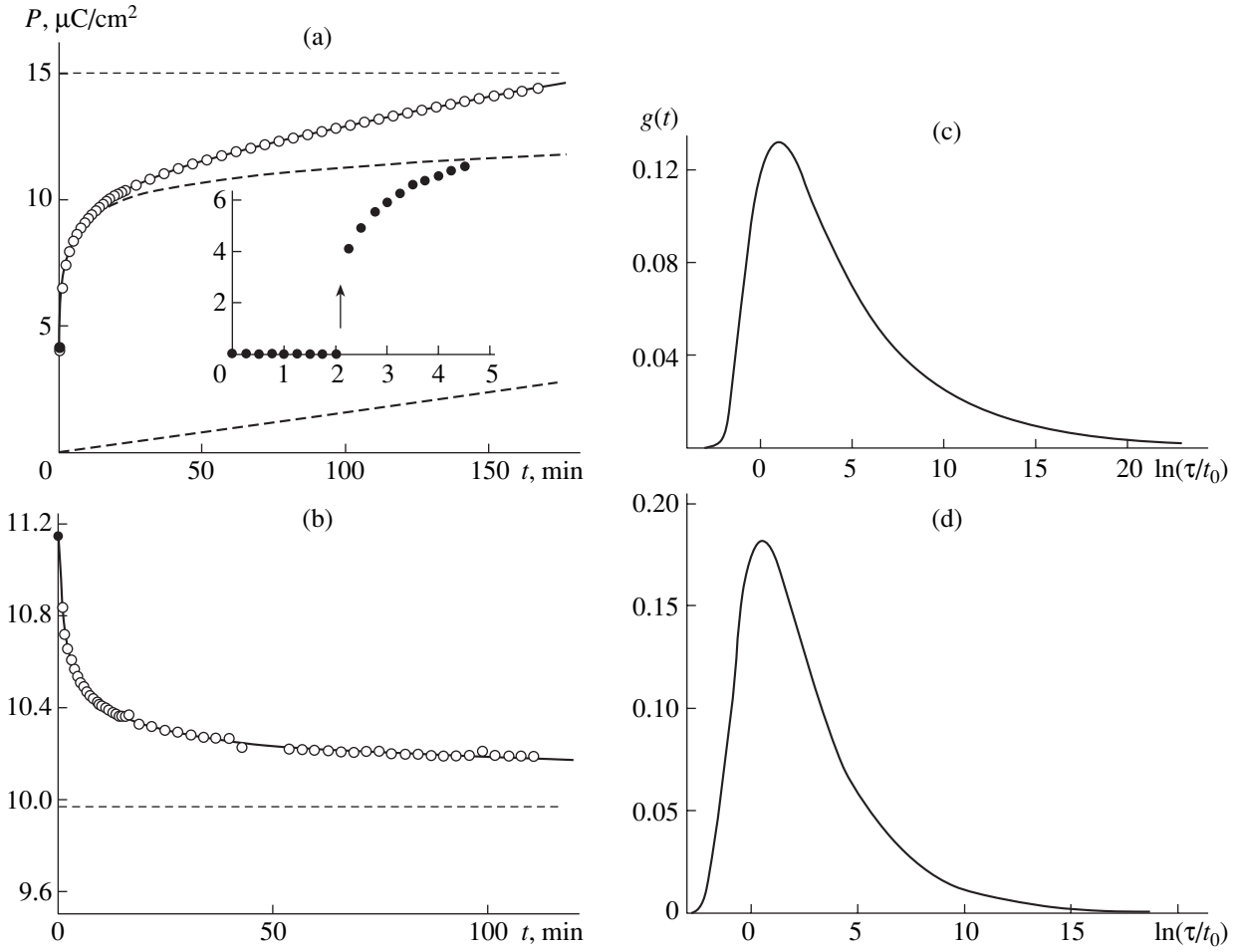

Fig. 3. (a, b) Slow stage in relaxation of the polarization P and (c, d) distribution spectra $g(\ln\tau)$ of relaxation time τ measured on SBN-0.75 at (a, c) E = 2 kV/cm (polarization process) and (b, d) E = 3.75 kV/cm (depolarization). T = 279.7 K. Experimental data are shown by symbols, the solid line represents calculation, and the nonlinear and linear polarization components and the equilibrium polarization P_e are plotted in dashed lines. Inset shows the onset of relaxation (a polarization jump, identified by an arrow).

experimentally measured values of E_c, as is well known, can be substantially smaller than those predicted from theory. The polarization relaxation in the polar phase after application of a field $E < E_c$ is a slow, thermally activated process, without an initial jump in the polarization P. A jump appears only in high fields, $E > E_c$, when one of the two minima in function F disappears under application of the field and a fast, avalanche-like poling process sets in. The equilibrium polarization P_e is always equal to the spontaneous polarization P_s, irrespective of the magnitude of the external field E applied [14]. The polarization kinetics of SBN-0.75 crystals described below, like that of other SBN compositions studied earlier [6, 7, 13, 14], differs radically from this model scenario.

3.1. Polarization Kinetics

Let us discuss the kinetics of the slow (t > 15 s) and fast (3 μs < t < 10 s) polarization stages.

3.1.1. The slow polarization relaxation stage

Figure 3a illustrates the slow stage in the relaxation of polarization P in a dc field E = 2 kV/cm, which is lower than the half-width of the hysteresis loop; this stage follows the fast stage (starting from the polarization P_0 = 4 μC/cm^2). The polarization P was calculated with allowance for the conductivity. In the depolarization process, the polarization behaves similarly; namely, the first, fast stage is followed by a slow decay (Fig. 3b). The variation of $P(t)$ with time can be fitted satisfactorily by a power law,

$$p(t) = (P_e - P(t))/(P_e - P_0) = 1/(1 + t/a)^n, \quad (1)$$

where a and n, as well as the equilibrium polarization P_e, are free parameters.

The solid lines in Fig. 3 plot the results of calculation made with the parameters a and n listed in the table, P_e = 15 ± 0.11 μC/cm^2 for the polarization process, and P_e = 9.97 ± 0.01 μC/cm^2 for the depolariza-

Relaxation parameters (a, n) of SBN-0.75 crystals

Process	a		n	
	fast stage	slow stage	fast stage	slow stage
Polarization, E = 2 kV/cm	0.68 μs	0.52 ± 0.008 min	0.035	0.206 ± 0.004
Depolarization		0.51 ± 0.02 min		0.32 ± 0.01

tion process. The symbols indicate experimental data. The nonexponential relaxation $p(t)$ is related to the normalized distribution function $f(\tau)$ of relaxation times τ (assuming the relaxation centers to be independent) through

$$p(t) = \int_0^\infty f(\tau)\exp(-t/\tau)d\tau, \qquad (2)$$

and the normalized dimensionless function $g(\ln\tau) = \tau f(\tau)$, which characterizes the $\ln\tau$ distribution, or the distribution of barrier energies for relaxation centers $U = kT\ln(\tau/\tau_0)$, is connected with the power-law relaxation (1) through the Laplace transform [15] and can be written as

$$g(\ln\tau) = (1/\Gamma(n))(a/\tau)^n\exp(-a/\tau). \qquad (3)$$

Broad $g(\ln\tau)$ functions including very large values of τ characteristic of relaxors are also presented in Fig. 3 for the polarization and depolarization processes.

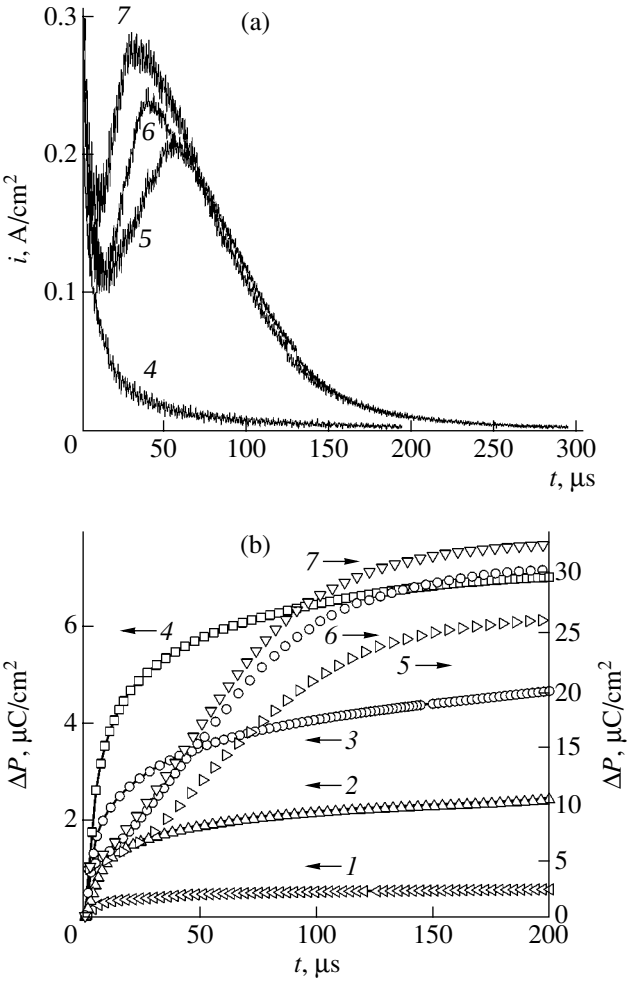

Fig. 4. Evolution (a) of the switching current i and (b) of the polarization P in the fast polarization relaxation stage obtained on an SBN-0.75 crystal in various pulsed electric fields E: (*1*) 1, (*2*) 2, (*3*) 4, (*4*) 6, (*5*) 7, (*6*) 8, and (*7*) 9 kV/cm.

3.1.2. The fast polarization relaxation stage

Figure 4 displays the fast stage of the polarization (polarization jump) in SBN-0.75, which ends at the initial point P_0 of the slow relaxation in Fig. 3. In contrast to homogeneous ferroelectrics [1, 2], where switching currents for $E > E_c$ exhibit characteristic maxima indicating a change in polarization with acceleration, in SBN-0.75 crystals an abrupt process starts, as a rule, in fields far exceeding the half-width of the dielectric hysteresis loop or is not observed altogether up to breakdown fields. Figure 4a illustrates the dependence of the switching currents $i(t)$ on time in an (originally polydomain) SBN-0.75 crystal. An abrupt process, qualitatively similar to that observed to occur in homogeneous ferroelectrics, starts in fields considerably in excess of the coercive field E_c (the quantity E_c is discussed below). In lower fields, including those less than the half-width of the hysteresis loop, the switching currents decay rapidly and nonexponentially. The variation of polarization $P(t)$ with time for this interval of fields (Fig. 4b) follows power-law relation (1) to sufficient accuracy. The parameters a and n of the polarization relaxation are listed in the table. Figure 5 displays the $P(E)$ relations for the original poly- and single-domain crystals; these relations were obtained by integrating the current $i(t)$ (Fig. 4) with respect to time. The $P(E)$ relations are characterized in all the crystals by a smooth growth of P with increasing field (up to $E \gg E_c$ in polydomain samples, which indicates the increase in the poled volume with the field), with the saturated value of the switched charge P in the single-domain state being far less than that in the polydomain state. It should be stressed that the $P(E)$ curves obtained on samples of the same composition differ strongly in shape; therefore, the case illustrated in Fig. 4 is not actually characteristic of the given composition. The absence of a switching fields maximum over a broad interval of currents in SBN crystals may be accounted

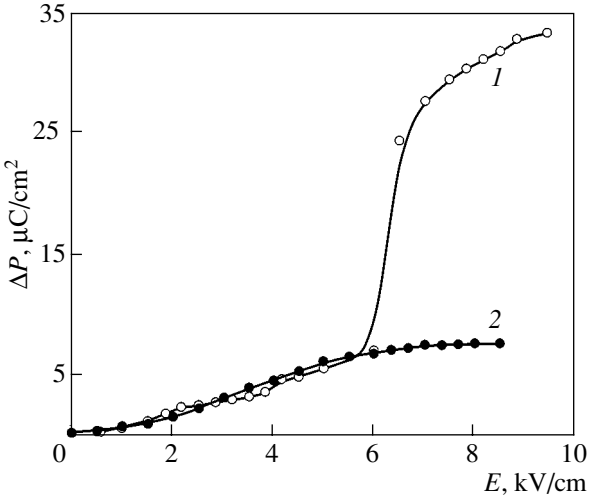

Fig. 5. Switchable polarization P plotted vs. electric field E for (*1*) a polydomain and (*2*) a single-domain SBN-0.75 crystal.

for qualitatively as being due to the broad distribution of relaxation times within the volume of an inhomogeneous crystal. The abrupt process observed to occur in higher fields, which qualitatively resembles that seen in homogeneous ferroelectrics, likewise cannot be discussed in terms of the switching times, the language accepted for a model description of the process [2], because the polarization P (proportional to the poled volume) grows as the field increases.

Summing up the above studies of the fast and slow polarization stages, one may conclude that the poling kinetics in external fields, both less and larger than the half-width of the hysteresis loop, can be fitted satisfactorily, on the whole, by power law (1). The table lists the polarization relaxation parameters for the fast and slow stages calculated for a field of 2 kV/cm.

3.2. Quasi-Static Dielectric Hysteresis Loops

Structural disorder, which is responsible for the generation in relaxor ferroelectrics of an internal electric field randomly distributed over the crystal volume, not only smears the dielectric permittivity maximum and the phase transition to the polar state but also brings about an anomalous shape of the dielectric hysteresis loops. Figure 6 displays hysteresis loops in the dependence of polarization P on field E obtained in SBN-0.75 in a slowly varying (quasi-static) periodic field with a period of 1 h, which corresponds to a frequency of 10^{-4} Hz, and in a 60-Hz field at T = 275.7 K. The loops obtained in the quasi-static field feature an unusual shape; indeed, the first cycles are open nonreproducing trajectories with a gradually decreasing polarization amplitude, after which the amplitude practically ceases to decrease, thus making all subsequent cycles reproducing. The first cycles obtained in a 60-Hz ac field are not fixed; therefore, the loops have the common elongated, nonsquare shape typical of most conventional ferroelectrics and their amplitude is small because only part of the crystal volume is involved in polarization switching in the field of chosen strength and frequency. Both loops have unipolarity of the same sign, which sets in in the sample after the first few switching cycles. Note that the difference in the polarization amplitudes between the first few quasi-static dielectric hysteresis loops and the diffuseness of the phase transition are particularly large in SBN-0.75 and SBN-0.61 doped by La and Ce [6, 7].

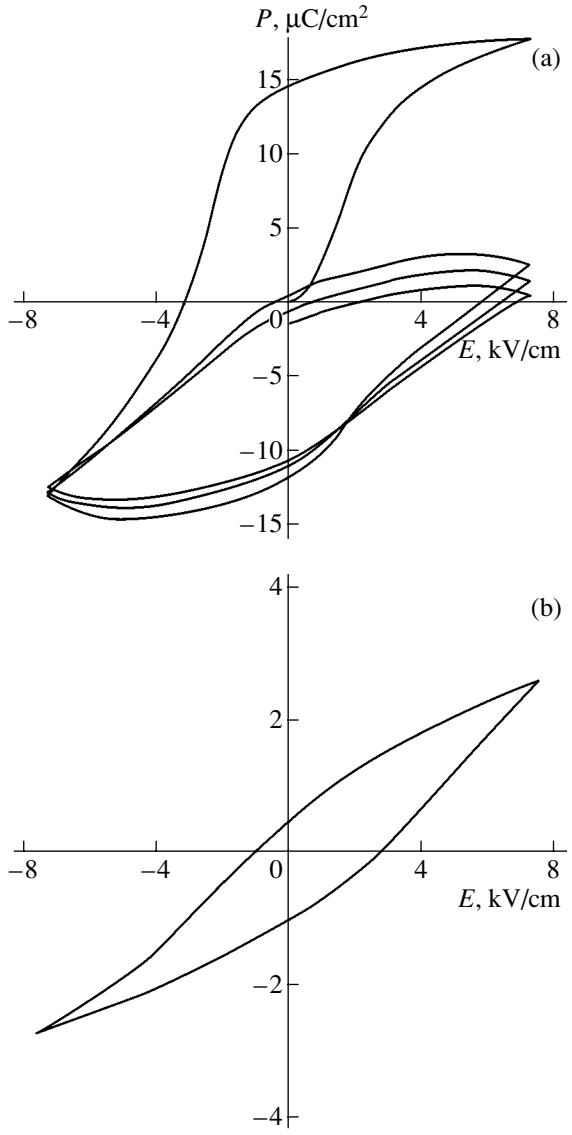

Fig. 6. Dielectric hysteresis loops obtained in SBN-0.75 in (a) a quasi-static and (b) a 60-Hz electric field.

The randomly distributed internal field E_i can quite possibly affect the observed shape of the quasi-static hysteresis loop. The field E_i distorts the symmetric double-minimum free-energy function, which becomes asymmetric with minima of different depth correspond-

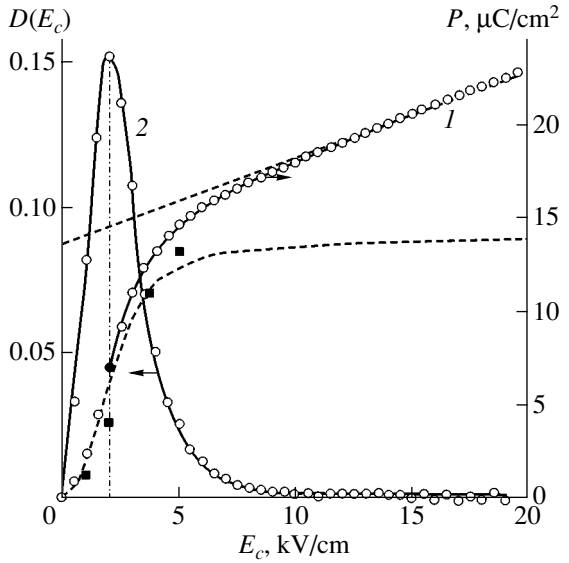

Fig. 7. (*1*) Dependence of polarization P on field E and (*2*) distribution $D(E_c)$ of the coercive field E_c in the SBN-0.75 crystal. Circles are experimental data on P, solid line is the calculated power-law dependence of P on E, squares are jumps in P upon sudden application of a field E, and dashed lines relate to the linear and nonlinear components of the polarization $P(E)$.

ing to a metastable and a stable state. Because E_i is a random quantity, the depths of the minima, their mutual positions in the sample volume, and the heights of the barriers separating these states are likewise random quantities. Before application of an external electric field, the crystal sample resides in a mixed state, with one part of the crystal being in the stable and the other in the metastable state, with a deep and a shallow minimum, respectively. After a field of a given strength and duration has been switched on, transitions from metastable to stable states with deep minima start in the volume of the crystal and will be accompanied by an increase in the polarization opposing the applied field. The reverse transition in an oppositely directed field of a limited magnitude may turn out impossible in practice, because the barriers are too high, as a result of which part of the crystal will not be capable of participating in further polarization switching and the loop amplitude will decrease [6]. It may also be conjectured that at certain fields the deep minima act as local traps, or pinning centers for the polarization, thus eliminating it from the further process [8]. Complete susceptibility of the loop can possibly be reached if the external field is so strong that the internal fields E_i are exceeded throughout the crystal volume.

3.3. Distribution of the Coercive Field in a Relaxor

Investigation of the relaxation within a broad range of dc electric fields E shows that relaxors do not have a definite coercive field E_c, because (unlike the case of a homogeneous ferroelectric), irrespective of the field E, a large part of the initial variation of the polarization in a relaxor is always a fast (jumplike) process which apparently takes place in the crystal regions where the shallow metastable minimum of the local free energy in a field E is either very small or altogether absent (see Section 3.1). Our experimental data, complemented with fairly simple assumptions, make it possible to construct a possible distribution of the coercive field over the SBN-0.75 crystal volume. The fractional volume with a definite coercive field E_c is proportional to the amplitude of the fast polarization appearing abruptly upon application of a field $E = E_c$, without taking into account its linear component along this field. Figure 7 presents, in graphical form, the dependence of polarization P on field E, which is one quarter of the period of the hysteresis loop shown in Fig. 6a. The values of P are close to those of the jumps in P denoted by squares in Fig. 7, which permits us to assume that the $P(E)$ dependence roughly reflects the behavior of the fast part of polarization under application of the field E. The $P(E)$ dependence can be satisfactorily described by the same power-law function as the polarization relaxation $P(t)$:

$$P(E) = P_n(E) + \chi E, \tag{4}$$

where $P_n(E) = P_\infty - (P_\infty - P_0)/(1 + E/b)^c$ is the nonlinear component, P_∞ is the limiting value of P_n for $E \longrightarrow \infty$, and P_∞, b, and c are free parameters used in fitting the experimental data. The solid line in Fig. 7 is a calculated curve with parameters χ = 0.44–0.47 μC/kV cm, P_∞ = 15.3–14.7 μC/cm^2, b = 2.0–3.5 kV/cm, and c = 1.4–2.7, and the circles are the experimental data. Consider the integral $\int_0^\infty \frac{dP_n(E)}{dE} dE = P_\infty$. Because $P_n(E)$ may be considered proportional to the fraction of the crystal volume becoming poled under the application of field E, which is the coercive field for this volume fraction ($P_n = kv$), and $P_\infty = kV$ (V is the total volume of the crystal), the function $D(E_c) = dv/VdE_c = dP_n/P_\infty dE_c$ characterizes the probability density of the coercive field E_c in the crystal and $\int_0^\infty D(E_c)dE_c = 1$; i.e., this function is normalized. The most probable value of E_c coinciding with the maximum in the $D(E_c)$ distribution is seen to correspond to 2 kV/cm.

The probability density $D(E_c)$ of E_c should vary slightly, because the $P(E)$ curves used to construct it are, generally speaking, not reproducing. In particular, the $P(E)$ curves and the distribution functions $D(E_c)$ will be different in the cases where a crystal is polarized from initial polydomain and single-domain states. Note that homogeneous ferroelectrics with a slim canted hysteresis loop may also have broad coercive-field distributions [16] (in contrast to a homogeneous ideal ferroelectric with a square-shaped hysteresis loop, whose $D(E_c)$ is always a delta function).

4. CONCLUSIONS

Thus, the features observed in the dielectric properties of SBN-0.75 crystals and reported here are indications of a structural disorder characteristic of ferroelectric relaxors. These features are most pronounced in this composition of the strontium–barium niobate solid solution and may be considered as a measure of disorder in the structure. Because of the long relaxation times and of the broad distribution spectrum of these times in the crystal volume, they are reliably revealed only in slow measurements.

ACKNOWLEDGMENTS

This study was supported by the Russian Foundation for Basic Research (project no. 02-02-16823) and INTAS (grant no. 01-0173).

REFERENCES

1. G. A. Smolenskiĭ, V. A. Bokov, V. A. Isupov, N. N. Kraĭnik, R. E. Pasynkov, and M. S. Shur, *Ferroelectrics and Antiferroelectrics* (Nauka, Leningrad, 1971), p. 355.
2. M. E. Lines and A. M. Glass, *Principles and Applications of Ferroelectrics and Related Materials* (Oxford Univ. Press, Oxford, 1977; Mir, Moscow, 1981).
3. Yu. S. Kuz'minov, *Ferroelectric Crystals for Controlling Laser Radiation* (Nauka, Moscow, 1982), p. 400.
4. L. E. Cross, Ferroelectrics **76**, 241 (1987).
5. T. S. Chernaya, B. A. Maksimov, T. R. Volk, *et al.*, Fiz. Tverd. Tela (St. Petersburg) **42**, 1668 (2000) [Phys. Solid State **42**, 1716 (2000)].
6. V. V. Gladkiĭ, V. A. Kirikov, S. V. Nekhlyudov, *et al.*, Pis'ma Zh. Éksp. Teor. Fiz. **71** (1), 38 (2000) [JETP Lett. **71**, 24 (2000)].
7. V. V. Gladkiĭ, V. A. Kirikov, T. R. Volk, and L. I. Ivleva, Zh. Éksp. Teor. Fiz. **120** (3), 678 (2001) [JETP **93**, 596 (2001)].
8. T. Granzow, V. Dorfler, Th. Woike, *et al.*, Phys. Rev. B **63**, 174101 (2001).
9. T. R. Volk, V. Yu. Salobutin, L. I. Ivleva, *et al.*, Fiz. Tverd. Tela (St. Petersburg) **42** (11), 2006 (2000) [Phys. Solid State **42**, 2129 (2000)].
10. W. H. Huang, D. Viehland, and R. R. Neurgaonkar, J. Appl. Phys. **76**, 490 (1994); R. R. Neurgaonkar, J. R. Oliver, W. K. Cory, *et al.*, Ferroelectrics **160**, 269 (1994).
11. D. Viehland, Z. Xu, and W.-H. Huang, Philos. Mag. A **71**, 205 (1995).
12. V. V. Gladkiĭ, V. A. Kirikov, S. V. Nekhlyudov, and E. S. Ivanova, Fiz. Tverd. Tela (St. Petersburg) **39** (11), 2046 (1997) [Phys. Solid State **39**, 1829 (1997)].
13. V. V. Gladkiĭ, V. A. Kirikov, S. V. Nekhlyudov, *et al.*, Fiz. Tverd. Tela (St. Petersburg) **42** (7), 1296 (2000) [Phys. Solid State **42**, 1334 (2000)].
14. V. V. Gladkiĭ, V. A. Kirikov, and T. R. Volk, Fiz. Tverd. Tela (St. Petersburg) **44** (2), 351 (2002) [Phys. Solid State **44**, 365 (2002)].
15. V. I. Ditkin and A. P. Prudnikov, *Handbook on Operational Calculus* (Vysshaya Shkola, Moscow, 1965), p. 466.
16. V. V. Gladkiĭ, V. A. Kirikov, S. V. Nekhlyudov, and E. S. Ivanova, Fiz. Tverd. Tela (St. Petersburg) **41** (3), 499 (1999) [Phys. Solid State **41**, 447 (1999)].

Translated by G. Skrebtsov

Physics of the Solid State, Vol. 45, No. 11, 2003, pp. 2178–2182. Translated from Fizika Tverdogo Tela, Vol. 45, No. 11, 2003, pp. 2074–2078.

MAGNETISM AND FERROELECTRICITY

Electroluminescence and Internal Screening of Domains upon Polarization Switching of Ferroelectric Ceramics in a Pulsed Self-Consistent Field

S. A. Sadykov* and A. V. Turik**

** Dagestan State University, Makhachkala, 367025 Russia*
e-mail: ssadyk@mail.dgu.ru
*** Rostov State University, ul. Zorge 5, Rostov-on-Don, 344090 Russia*
Received January 30, 2003; in final form, April 21, 2003

Abstract—This paper reports on the results of investigations into the electroluminescence induced by polarization switching of a ferroelectric ceramic material in an electric field with a rapidly increasing strength. A correlation between the polarization switching and luminescence kinetics is revealed. It is demonstrated that tunneling of electrons to the conduction band and impact ionization in field concentrators are the main mechanisms of generation of free charge carriers responsible for the electroluminescence and internal screening of switching domains. © *2003 MAIK "Nauka/Interperiodica".*

1. INTRODUCTION

It is known that, during polarization switching of ferroelectrics, nucleation and growth of domains can be retarded by a depolarizing field of bound polarization charges. This effect becomes weaker due to compensation of the polarization charges. The screening of polarization charges substantially affects the domain structure and the mechanism of polarization switching [1]. The transformation of the domain structure in an external electric field is accompanied by screening throughout the switching of domains. Although the problem of screening has attracted considerable research attention, the mechanism of this process remains unclear. It has been experimentally demonstrated that the time of polarization switching depends on the conditions of screening of the spontaneous polarization P_s. The screening occurs through the capture of charge carriers by local active centers in a surface region of the ferroelectric and in the vicinity of the domain walls. In polycrystalline (ceramic) materials, the polarization charge can be compensated by both free charges in the bulk of grains and charges at grain boundaries [2]. The screening can be external (dependent on the external compensation for the bound charge) and internal (produced by the space charge). In ferroelectric materials, the bulk internal screening plays an important role, because the external screening is not complete owing to the occurrence of a surface dielectric gap [2].

As a rule, the time characteristics of polarization switching can be related to the time constant of the Maxwell relaxation of a nonequilibrium screening space charge. In turn, the Maxwell relaxation time $\tau_d = \varepsilon/\sigma \sim 10^{-1}$–$10^5$ s depends on the permittivity ε and the conductivity σ of the material [3, 4]. For a short polarization switching pulse ($\tau < \tau_d$), space-charge carriers have no time to respond to this pulse and the residual depolarizing field can induce spontaneous inverse polarization switching of the ferroelectric material. However, in our earlier works [5–7], we demonstrated that, upon exposure of ferroelectric ceramic materials to a steep high-voltage pulse, an equilibrium internal field is induced by space charges for times considerably shorter than the Maxwell relaxation time. This makes polarization of ferroelectric ceramic materials for times lying in the microsecond range possible. Note that, at $\tau \ll \tau_d$, slow (primarily, electrodiffusion) mechanisms of bulk screening are highly improbable. The question now arises as to how the domain structure will behave in the case of ultrafast polarization switching when the response times of the ionic and electronic subsystems are comparable in magnitude ($<10^{-6}$ s).

Earlier [5], it was assumed that the main mechanism responsible for the generation of an internal field is associated with the impact ionization of deep levels (at activation energies of 1.5–3.0 eV) with the formation of a short-lived solid-state plasma. The subsequent recombination of charges, charge trapping, and interband transitions through levels of defects are accompanied by emission in the visible range, because, for the majority of the studied materials, luminescence has been observed during the course of pulses. However, the strength of the applied external field (~1 MV/m) was less than the field strength necessary for impact ionization (~10 MV/m). As was shown by Darinskiĭ and Sidorkin [8], these fields can be locally induced in the bulk of samples during the transformation of the domain structure due to interaction of domain walls with point or nonlinear defects.

1063-7834/03/4511-2178$24.00

The electroluminescence induced by polarization switching in ferroelectrics is a sensitive tool for investigations into the mechanism of transformation of the domain structure and specific features of the electron screening associated with this mechanism. The aim of the present work was to elucidate the mechanism of polarization switching in strong electric fields with a rapidly increasing strength and the role played by bulk screening in the process. For this purpose, we analyzed the kinetic characteristics of polarization switching and the attendant luminescence in ferroelectric ceramic materials.

2. EXPERIMENTAL TECHNIQUE

In our experiments, we used a PKR-1 ferroelectric ceramic with the Curie temperature T_C = 628 K and a relatively weak coercive field $E_c \approx 1.0$ kV/mm, which belongs to the $PbTiO_3$–$PbZrO_3$–$PbB'_{1/2}B''_{1/2}O_3$ system of multicomponent solid solutions [9]. Samples in the form of disks 1 mm thick and 10 mm in diameter were prepared by hot pressing. Silver electrodes without rims were applied to the flat surfaces of the disks.

The measurements were performed on a high-voltage setup at rates of electric field rise $\dot{E}$ = 0.1–80 kV/(mm · μs) according to the technique described in [10]. The specific feature of this technique is that a lumped capacitor is connected in the electric circuit in series with a ferroelectric ceramic sample in order to generate pulsed fields with a specified value of $\dot{E}$. When the electric field is applied along the direction of polarization switching (the electric field vector is antiparallel to the polarization vector), the polarization switching current passes through the sample in addition to the capacitive current. Note that the intensity of the former current considerably exceeds the intensity of the latter current. In this case, the voltage oscillogram $V(t)$ is characterized by a plateau corresponding to rapid switching of domains. This process proceeds at the same voltage (Fig. 1a) at which the strength of the electric field playing the role of a dynamic coercive field $E'_c > E_c$ reaches a steady-state value in the bulk of the ferroelectric ceramic sample.

For the studied rates of electric field rise, the dynamic coercive field E'_c monotonically increases with an increase in $\dot{E}$ [10]. The time interval between the point in time at which the electric field in the sample reaches the dynamic coercive field E'_c and the point in time at which the polarization switching is completed, i.e., the plateau length, can be treated as the polarization switching time τ_s. After the completion of the main stage of polarization switching, the current decreases and the electromotive force of the induction changes sign, which leads to a further increase in the field strength to $(2–3)E'_c$. The switching-current curve has a characteristic asymmetric shape with a smooth maximum and a steeply descending tail portion (Fig. 1b). This indicates that, in the course of polarization switching, the voltage across the ferroelectric ceramic sample is controlled by the transient current and the switching processes proceed in the self-consistent electric field.

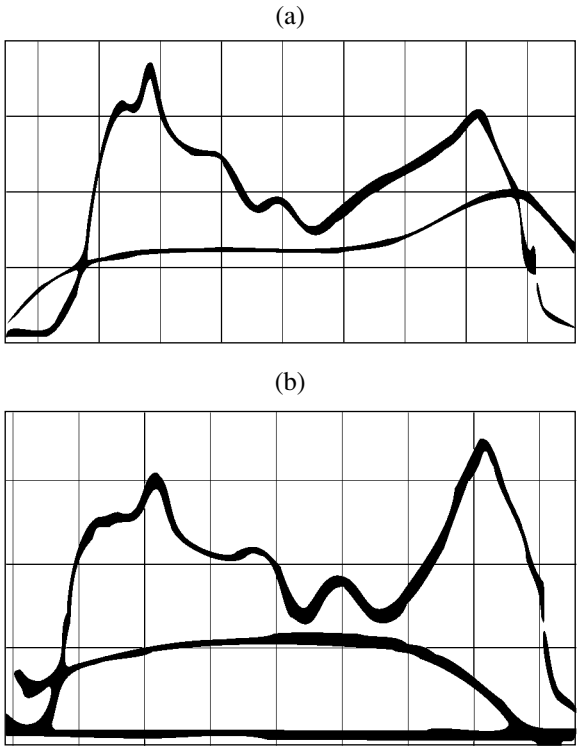

Fig. 1. Correlation of luminescence pulses (upper curves) with (a) the polarizing voltage and (b) the switching current for a PKR-1 ferroelectric ceramic sample. Scale division: 1 μs/div for time, 1.5 kV/div for voltage, and 6 A/div for switching current. T = 293 K.

Luminescence pulses induced by polarization switching of the ferroelectric ceramic sample were measured at lateral surfaces of the sample with the use of photomultipliers covering the spectral range 300–1200 nm. In order to prevent the luminescence stimulated by microdischarges in the electrode regions, the samples were placed in a silicone oil. We investigated the temperature and time dependences of the intensity I_{rad} and energy E_{rad} of electroluminescence of the ferroelectric ceramic material and their relation to the integrated characteristics of polarization switching (such as the time τ_s, the current j_s, and the coercive field E'_c. The luminescence intensity I_{rad} was determined from the amplitude of the luminescence pulse, and the total radiant energy E_{rad} was calculated from the area of the luminescence pulse oscillogram.

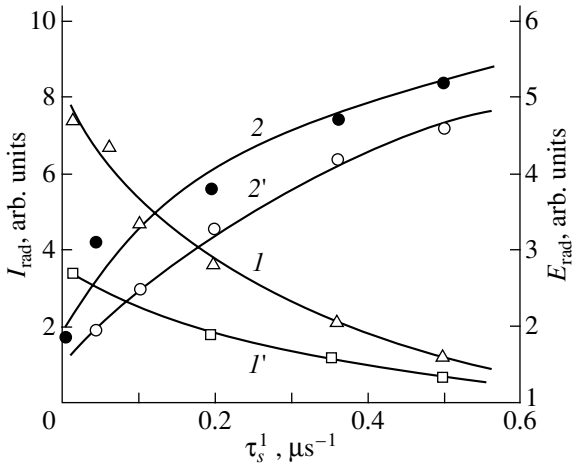

Fig. 2. Dependences of (*1*, *1*') the radiant energy E_{rad} and (*2*, *2*') the luminescence intensity I_{rad} on the reciprocal of the polarization switching time τ_s^{-1} for (*1*, *2*) annealed and (*1*', *2*') unannealed PKR-1 ferroelectric ceramic samples. T = 293 K.

3. EXPERIMENTAL RESULTS

An analysis of the data presented in Fig. 1 shows that there exists a clear correlation between the kinetics of polarization switching of the ferroelectric ceramic material and the electroluminescence kinetics. The luminescence is observed at all stages of polarization switching. The luminescence curve is characterized by several (most frequently, two) pronounced peaks that merge together with an increase in the rate of electric field rise. The specific features in the physical mechanisms of transformation of the domain structure in a self-consistent electric field manifest themselves not only in the shape of the switching-current pulse but also in the luminescence kinetics.

An increase in the rate of electric field rise $\dot{E}$ leads to an increase in the luminescence intensity. The maximum in the luminescence intensity is observed not at the final stage of polarization switching, as is the case in rectangular pulsed fields [11, 12], but is shifted toward the ascending branch of the switching current due to a change in the conditions of nucleation and growth of domains. In the self-consistent field, the luminescence peaks are clearly resolved even at high rates of electric field rise. It is worth noting that the shorter the polarization switching time τ_s, the higher the intensity of the first luminescence peak corresponding to an increase in the current. At short times of polarization switching ($\tau_s \le 1$ μs), the luminescence is observed after vanishing the polarization switching current. This indicates that the processes of screening and domain-wall pinning at defects are incomplete. A decrease in the polarization switching time τ_s leads to an increase in the luminescence intensity I_{rad} (Fig. 2) due to rapid switching of domains.

An increase in the domain-wall velocity can result in an increase in the rate of radiative recombination of charges produced during transformation of the domain structure. Nonetheless, the radiant energy E_{rad} decreases. Preliminary annealing of the samples at a temperature above the Curie point (t = 5 h, T = 770 K) leads to an increase in the energy E_{rad} and the intensity I_{rad} of luminescence (Fig. 2), most likely, due to the dissipation of space charges at domain walls. Upon heating to temperatures considerably above the Curie point, the volume distribution of defects in the sample becomes statistically uniform, which results in the loss of defect memory of the material. The metastability of this state is responsible for the high mobility of domain walls and the related increase in the electroluminescence energy efficiency of the ferroelectric ceramic material. The intensity of the second luminescence peak for the annealed samples is higher than that for the unannealed samples.

The temperature dependences of the intensity I_{rad} and the energy E_{rad} of electroluminescence are similar to those of the integrated characteristics of polarization switching (such as the time τ_s, the current j_s, and the coercive field E_c'). The behavior of the dependences $I_{rad}(T)$ and $E_{rad}(T)$ is governed by the specific features of the polarization switching voltage pulse, which depend on the polarization switching temperature (Fig. 3a). As the Curie temperature T_C is approached, the coercive field E_c' and the polarization switching time τ_s decrease (Fig. 3b). A decrease in the time τ_s corresponds to an increase in the recombination rate of screening charges, which become nonequilibrium after depinning of domain walls from defects. This results in an increase in the luminescence intensity. It should be noted that the increase in the transformation rate of the domain structure upon heating of the ferroelectric ceramic sample is caused by the increase in the mobility of domain walls, whereas the transformation of the domain structure at room temperature is initiated by the relatively strong dynamic coercive field E_c'. As was shown by Novitskiĭ *et al.* [10], at room temperature, an increase in the rate of electric field rise $\dot{E}$ and, hence, the dynamic coercive field E_c' is accompanied by a decrease in the polarization switching time τ_s and vice versa. For fields exceeding 2–2.5 MV/m, the polarization switching time is inversely proportional to the field in which the process takes place: $\tau_s = \text{const} E_c'^{-1}$. For weaker fields, the dependence of τ_s on E_c' is described by an exponential law.

As can be seen from Fig. 3b, the total radiant energy E_{rad} exhibits a clear tendency toward a decrease with increasing temperature T and the temperature dependence of the total radiant energy E_{rad} is similar to that of the remanent polarization $P_r(T)$ for ferroelectric ceram-

ics. The temperature dependence of the luminescence intensity $I_{rad}(T)$ exhibits a maximum. The results obtained indicate that an increase in the temperature brings about not only a decrease in the dynamic coercive field E_c' (which leads to an increase in the switched volume of the sample) but also thermal depolarization of the ferroelectric ceramic material. The decrease in the switched charge is the main reason for the decrease in the total radiant energy, even though the luminescence intensity slightly increases.

4. DISCUSSION

The luminescence occurring during polarization switching was explained by Guro *et al.* [13] in terms of the semiconducting properties of $BaTiO_3$. It was assumed that the internal depolarizing field $E_i \approx 4\pi P_s$(according to the estimates made by Miller and Savage [14], $E_i \sim 3 \times 10^8$ V/m) leads to band bending and generates electron–hole pairs until thermodynamic equilibrium is attained when the field E_i turns out to be screened by excess charge carriers. Therefore, the screening is provided by electrons generated from the valence band through field emission rather than by carriers transferred from the conduction band. Aĭrapetov *et al.* [15] held the same viewpoint. It is their opinion that, owing to the Zener effect, electrons that ensure the screening of bound charges on ends of growing nuclei are transferred from the valence band. Consequently, the growth of nuclei and the screening of their polarization are concurrent processes in the course of rapid switching.

On this basis, the results presented in Figs. 1 and 2 can be interpreted as follows. The mechanism of nucleation is such that, at the initial stage, domains smaller than the critical size continuously nucleate and annihilate in the sample. The domains reach the critical size when the field in the sample approaches the dynamic coercive field E_c'. In this case, the voltage oscillogram exhibits a characteristic plateau that indicates the onset of transformation of the domain structure. At the leading edge of the voltage pulse, 180° domain walls are destabilized and their mobility increases without transforming the original domain structure. Then, 180° tapered domains oriented along the field nucleate and grow in the sample.

It can be assumed that, at the initial stages of polarization switching, the luminescence in the ferroelectric ceramic material is caused by the increase in the mobility of domain walls and the number of domains involved in the switching. These processes lead to an increase in the real part of the permittivity ε' of the sample [7] at the leading edge of the voltage pulse.

In the bulk of the ferroelectric ceramic sample, the inhomogeneity of the electric field, which is especially pronounced on the ends of growing spike-shaped domains, directly determines the probability of electron tunneling to the conduction band. The screening is predominantly enhanced in the immediate vicinity of growing spike-shaped domains and, hence, weakens the depolarizing field in this region. Therefore, the nucleation rate in these regions is considerably higher than that in unswitched regions, which results in intensive nucleation at domain walls.

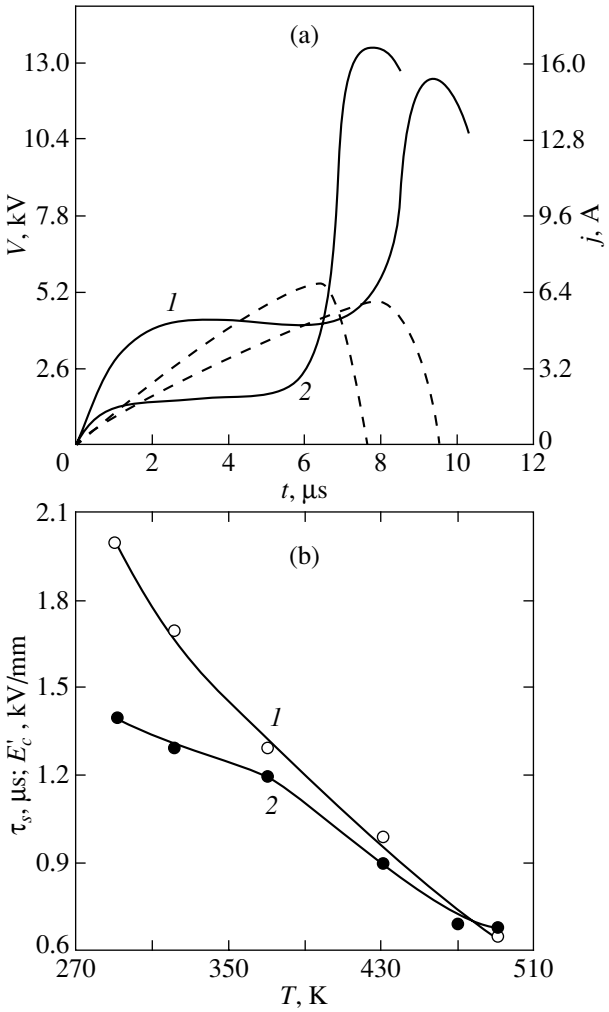

Fig. 3. (a) Oscillograms of the polarization switching voltage $V(t)$ (solid lines) and the polarization switching current $j(t)$ (dashed lines) for a PKR-1 ferroelectric ceramic sample at T = (*1*) 293 and (*2*) 423 K. (b) Temperature dependences of (*1*) the polarization switching time τ_s and (*2*) the coercive field E_c'.

The concurrent processes of recombination of electrons are responsible for the quasi-equilibrium state of the electronic subsystem in which the carrier concentration remains relatively high. The recombination is accompanied by the luminescence. The intensity of the luminescence observed at the early stage of polarization switching in the ferroelectric sample increases out of proportion to the increase in the voltage (Fig. 1). This confirms the assumption regarding the autoelectronic

nature of the internal screening at the initial stage of polarization switching.

The screening of free domain walls leads to the pinning of 180° domains due to the formation of bound space charges. The mobility of screened domain walls is substantially less than that of free domain walls. This brings about a decrease in the domain mobility and, as a consequence, the retardation of polarization switching. Therefore, the screening is attended by a decrease in the luminescence intensity. The participation of 90° domains in the final stage of polarization switching leads to a further increase in the luminescence intensity I_{rad}. Electron microscope examinations of the domain structure of ferroelectric ceramic samples partially polarized in a self-consistent field demonstrated that the transformation of mobile 90° domain walls occurs almost simultaneously with the appearance of the second luminescence peak.

5. CONCLUSIONS

Thus, we proposed a model according to which local inhomogeneous electric fields are induced in the bulk of a ferroelectric material due to the growth of antiparallel spike-shaped domains. These fields provide conditions favorable for the generation of electrons tunneling to the conduction band owing to a considerable band bending. This leads to the formation of an inhomogeneous electron liquid that is predominantly concentrated in the vicinity of the growing-domain ends. The proposed mechanism of the phenomenon under investigation is quasi-static; i.e., it is retained throughout the polarization switching and determines the dynamic features of the rapidly switching domain structure.

The tunneling of electrons to the conduction band and impact ionization in field concentrators are the main mechanisms of generation of free charge carriers responsible for the electroluminescence and internal screening of the domain structure upon ultrafast polarization switching of ferroelectrics in self-consistent electric fields.

REFERENCES

1. V. M. Fridkin, *Ferroelectric Semiconductors* (Nauka, Moscow, 1976).
2. M. E. Lines and A. M. Glass, *Principles and Applications of Ferroelectrics and Related Materials* (Oxford Univ. Press, Oxford, 1977; Mir, Moscow, 1981).
3. V. Ya. Shur, E. L. Rumyantsev, E. V. Nikolaeva, *et al.*, Fiz. Tverd. Tela (St. Petersburg) **44** (11), 2049 (2002) [Phys. Solid State **44**, 2145 (2002)].
4. H. Gundel, J. Handerek, and H. Riege, J. Appl. Phys. **69** (2), 975 (1991).
5. S. A. Sadykov and A. Sh. Agalarov, Pis'ma Zh. Tekh. Fiz. **16** (17), 32 (1990) [Sov. Tech. Phys. Lett. **16**, 655 (1990)].
6. S. A. Sadykov, E. I. Bondarenko, and A. Sh. Agalarov, Zh. Tekh. Fiz. **63** (11), 60 (1993) [Tech. Phys. **38**, 965 (1993)].
7. S. A. Sadykov, V. Z. Borodin, and A. Sh. Agalarov, Zh. Tekh. Fiz. **70** (6), 108 (2000) [Tech. Phys. **45**, 776 (2000)].
8. B. M. Darinskiĭ and A. S. Sidorkin, Fiz. Tverd. Tela (Leningrad) **26** (6), 1634 (1984) [Sov. Phys. Solid State **26**, 992 (1984)].
9. A. Ya. Dantsiger, O. N. Razumovskaya, L. A. Reznichenko, and S. I. Dudkina, *Highly Efficient Piezoceramic Materials* (Paĭk, Rostov-on-Don, 1995).
10. E. G. Novitskiĭ, V. D. Sadunov, S. A. Sadykov, *et al.*, Zh. Tekh. Fiz. **54** (2), 348 (1984) [Sov. Phys. Tech. Phys. **29**, 204 (1984)].
11. S. A. Flerova, Izv. Akad. Nauk SSSR, Ser. Fiz. **48** (6), 1233 (1984).
12. N. N. Kraĭnik, S. A. Popov, and S. A. Flerova, Fiz. Tverd. Tela (St. Petersburg) **39** (2), 341 (1997) [Phys. Solid State **39**, 298 (1997)].
13. G. M. Guro, I. I. Ivanchik, and N. F. Kovtonyuk, *Barium Titanate* (Nauka, Moscow, 1973), p. 71.
14. R. C. Miller and A. Savage, J. Appl. Phys. **31** (4), 662 (1960).
15. A. Sh. Aĭrapetov, I. I. Ivanchik, A. N. Lebedev, *et al.*, Dokl. Akad. Nauk SSSR **311** (3), 594 (1990) [Sov. Phys. Dokl. **35**, 267 (1990)].

Translated by O. Borovik-Romanova

Physics of the Solid State, Vol. 45, No. 11, 2003, pp. 2183–2188. Translated from Fizika Tverdogo Tela, Vol. 45, No. 11, 2003, pp. 2079–2085.

LATTICE DYNAMICS AND PHASE TRANSITIONS

Structure, Ionic Conduction, and Phase Transformations in Lithium Titanate $Li_4Ti_5O_{12}$

I. A. Leonidov, O. N. Leonidova, L. A. Perelyaeva, R. F. Samigullina, S. A. Kovyazina, and M. V. Patrakeev

Institute of Solid-State Chemistry, Ural Division, Russian Academy of Sciences, Pervomaĭskaya ul. 91, Yekaterinburg, 620219 Russia

e-mail: leonidov@imp.uran.ru

Received March 11, 2003

Abstract—The spinel structure of lithium titanate $Li_4Ti_5O_{12}$ is refined by the Rietveld full-profile analysis with the use of x-ray and neutron powder diffraction data. The distribution and coordinates of atoms are determined. The $Li_4Ti_5O_{12}$ compound is studied at high temperatures by differential scanning calorimetry and Raman spectroscopy. The electrical conductivity is measured in the high-temperature range. It is shown that the $Li_4Ti_5O_{12}$ compound with a spinel structure undergoes two successive order–disorder phase transitions due to different distributions of lithium atoms and cation vacancies (□, *V*) in a defect structure of the NaCl type: $(Li)_{8a}[Li_{0.33}Ti_{1.67}]_{16d}O_4 \longrightarrow [Li□]_{16c}[Li_{0.33}Ti_{1.67}]_{16d}O_4 \longrightarrow [Li_{1.33}□_{0.67}]_{16c}[Ti_{1.67}□_{0.33}]_{16d}O_4$. The low-temperature diffusion of lithium predominantly occurs either through the mechanism … $\longrightarrow$ Li(8*a*) $\longrightarrow$ *V*(16*c*) $\longrightarrow$ *V*(8*a*) $\longrightarrow$ … in the spinel phase or through the mechanism … $\longrightarrow$ Li(16*c*) $\longrightarrow$ *V*(8*a*) $\longrightarrow$ *V*(16*c*) $\longrightarrow$ … in an intermediate phase. In the high-temperature phase, the lithium cations also migrate over 48*f* vacancies: … $\longrightarrow$ Li(16*c*) $\longrightarrow$ *V*(8*a*, 48*f*) $\longrightarrow$ *V*(16*c*) $\longrightarrow$ …. © *2003 MAIK "Nauka/Interperiodica".*

1. INTRODUCTION

Lithium titanate $Li_4Ti_5O_{12}$ has a cubic spinel structure with space group $Fd\bar{3}m$ [1–4]. According to Blasse [2], three-fourths of the lithium ions can occupy 8*a* tetrahedral positions, the other Li^+ ions and Ti^{4+} ions are statistically distributed over 16*d* octahedral positions in the ratio 1 : 5, and the formula for this compound is $Li[Li_{1/3}Ti_{5/3}]O_4$. Owing to the presence of vacant cation positions and titanium ions with a variable valence in the spinel structure, this compound can be used as a cathode material for lithium batteries. Ohzuku and Veda [4] synthesized the $Li_2[Li_{1/3}Ti_{5/3}]O_4$ compound with completely occupied 16*c* and 16*d* octahedral positions through the electrochemical intercalation of lithium. These authors made the inference that 16*c* octahedral positions in the initial sample are half-occupied by lithium ions. Proskuryakova *et al.* [5] analyzed the IR and Raman spectra of the $Li_4Ti_5O_{12}$ spinel and drew the conclusion that titanium and lithium ions occupy both octahedral and tetrahedral positions and that the studied compound has the crystal chemical formula $Li_{4/9}Ti_{5/9}[Li_{8/9}Ti_{10/9}]O_4$.

The low electrical conductivity ($\sigma = 5.8 \times 10^{-8}$ S/cm) of the $Li_4Ti_5O_{12}$ spinel [6] suggests that the 8*a* tetrahedral positions are occupied. The higher electrical conductivities ($\sigma \sim 10^{-3}$ S/cm) measured at 670 K [7], most likely, correspond to a disordered state observed in this compound upon a transfer of lithium ions from the 8*a* positions to vacant 16*c* octahedral positions, as is the case in Li_2MCl_4 chloride spinels (*M* = Mg, Mn, Fe) [8–12]. Neutron diffraction and Raman spectroscopic investigations of these compounds at high temperatures have demonstrated that the spinel structure transforms into a defect structure of the NaCl type due to a redistribution of lithium ions.

In this work, the occupancies of cation positions were determined using x-ray and neutron diffraction at room temperature. The electrical conductivity and Raman spectra were studied at high temperatures. It was found that the high lithium conductivity in the $Li_4Ti_5O_{12}$ compound is caused by two successive phase transitions associated with different distributions of lithium ions in the cubic structure.

2. SAMPLE PREPARATION AND EXPERIMENTAL TECHNIQUE

The samples used in our experiments were prepared through solid-phase synthesis. Lithium carbonate Li_2CO_3 and titanium oxide TiO_2 (the content of the main component was no less than 99.9%) served as initial reactants. The initial mixtures of reactants were carefully mixed in a jasper mortar and then were pressed into pellets. The synthesis was performed at temperatures ranging from 800 to 1170 K for 80–100 h with homogenization of intermediate products at 20- to 30-h intervals. The charge transfer was studied using samples in the form of pellets 5–6 mm in diameter and 4–5 mm in height. The density of the ceramic materials synthesized was measured by hydrostatic weighing and

Structural parameters of $Li_4Ti_5O_{12}$

Atom	Position	Atomic coordinates $x = y = z$	Site occupancy	Thermal parameter B, Å^2
Li	8*a*	0	1.00(6)*	0.32*
Li	16*d*	0.625	0.16	0.74
Ti	16*d*	0.625	0.84(3)**	0.74**
O	32*e*	0.3878(6)	1.00(3)*	0.77*

* Parameters determined from the neutron diffraction data.

** Parameters determined from the x-ray diffraction data.

amounted to 85–90% of the x-ray density. Platinum electrodes were applied to flat surfaces of the pellets with the use of a paste prepared from a finely dispersed platinum powder. The platinum electrodes were fired at 1220 K. After this procedure, the cooling rate was 200 K/h in the range 500–1220 K and did not exceed 60 K/h upon cooling to room temperature.

The structural investigation and x-ray powder diffraction analysis were performed on a Stadi-P (Stoe) diffractometer (CuK_α radiation). The intensities of x-ray reflections were measured in the range $2\theta = 5°$–$120°$ with a step width of 0.02°. The neutron diffraction data were collected on a D7a multidetector diffractometer (wavelength $\lambda = 1.515$ Å, angular resolution $\Delta d/d = 0.2\%$). The measurements were carried out at room temperature in the 2θ range from 5° to 111° with a step width of 0.1°. The occupancies of cation and anion positions were determined using the Rietveld full-profile analysis with the Fullprof program [13]. The electrical conductivities were measured by impedance spectroscopy on a Solartron 1260 frequency response analyzer in the frequency range 10–100 kHz, in which the real part of the impedance Z' of the sample remained nearly constant. The activation energy for electrical conduction was calculated from the slope of the dependence $\ln\sigma T$ on the reciprocal of the temperature. The partial pressure of oxygen in the range 10^{-12}–1 atm was maintained and controlled using an electrochemical oxygen pump and sensor, which were fabricated from an yttria-stabilized cubic zirconia. The time required for attaining an equilibrium varied from 20 min to several hours depending on the composition of the gas phase and the temperature of the experiment. The Raman spectra were recorded in the temperature range 300–1000 K on a Renishaw-1000 spectrometer (Ar^+ laser, $\lambda = 514$ nm) equipped with a TS-1500 high-temperature attachment and then were processed with the TMS software package. The differential thermal analysis (DTA) was performed a TG-92 (Setaram) thermoanalyzer.

3. RESULTS AND DISCUSSION

3.1. Distribution of Cations over Crystallographic Positions

The structure of the $Li_4Ti_5O_{12}$ lithium titanate was refined in space group $Fd\bar{3}m$ by varying the unit cell parameters, the coordinates of oxygen atoms, the site occupancies g, and the isotropic thermal parameters B. The site occupancies and coordinates of oxygen atoms and the occupancies of lithium atoms in the 8*a* positions were determined from neutron diffraction data. The occupancies of octahedrally coordinated titanium atoms in the 16*d* positions were refined using x-ray diffraction data, because titanium is more sensitive to x rays. The occupancies of lithium atoms in the 16*d* positions were determined as $g[\mathrm{Li}(16d)] = 1 - g[\mathrm{Ti}(16d)]$; in this case, the thermal parameters were taken to be $B[\mathrm{Li}(16d)] = B(\mathrm{Ti})$. In the final refinement of the x-ray diffraction data, the reliability factors were as follows: $R_p = 12.3$, $R_{wp} = 14.3$, $R_B = 6.2$, $R_E = 4.7$, and $R_F = 5.0$. The results of the refinement are presented in the table.

It was found that, in the structure of the $Li_4Ti_5O_{12}$ titanate, the unit cell parameter is $a = 8.3538(2)$ Å and the M–O bond lengths in the tetrahedral and octahedral environments are equal to 1.9939 and 1.9873 Å, respectively. Since the assumption regarding the possible occupation of the 8*a* positions with titanium atoms led to deterioration of the reliability factors, the presence of the titanium atoms in the tetrahedral positions was ruled out. The above analysis of the site occupancies showed that the compound under investigation has the crystal chemical formula $(\mathrm{Li})[\mathrm{Li}_{0.33}\mathrm{Ti}_{1.67}]\mathrm{O}_4$.

3.2. Electrical Conductivity

The temperature dependence of the electrical conductivity for the $Li_4Ti_5O_{12}$ titanate in the Arrhenius coordinates is shown in Fig. 1. The low conductivities σ at low temperatures can be explained by the absence of both vacancies in the 8*a* positions and interstitial lithium ions in the 16*c* positions. As the temperature increases from 430 to 1230 K, the electrical conductivity increases by almost six orders of magnitude. It can be seen that the dependence $\log\sigma(T^{-1})$ exhibits a complex behavior and involves portions with high activation energies. This suggests that, upon heating, the low-temperature phase of the $Li_4Ti_5O_{12}$ titanate with a spinel structure transforms into high-temperature phases with other distributions of lithium cations over sites. An increase in the electrical conductivity of the $Li_4Ti_5O_{12}$ titanate spinel, unlike the Li_2MCl_4 chloride spinels, can also be associated with the contribution of the electronic conductivity to the total conductivity due to the nonstoichiometry of the sample with respect to oxygen at high temperatures. In order to estimate the electronic contribution, we measured the dependence of the electrical conductivity on the oxygen pressure in

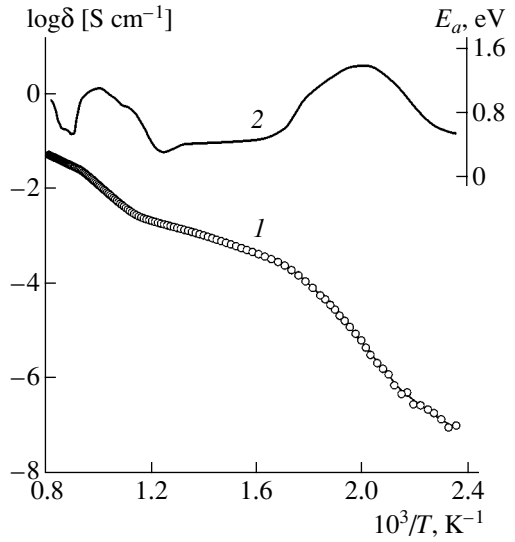

Fig. 1. Temperature dependences of (*1*) the electrical conductivity and (*2*) the activation energy for electrical conduction of the $Li_4Ti_5O_{12}$ compound.

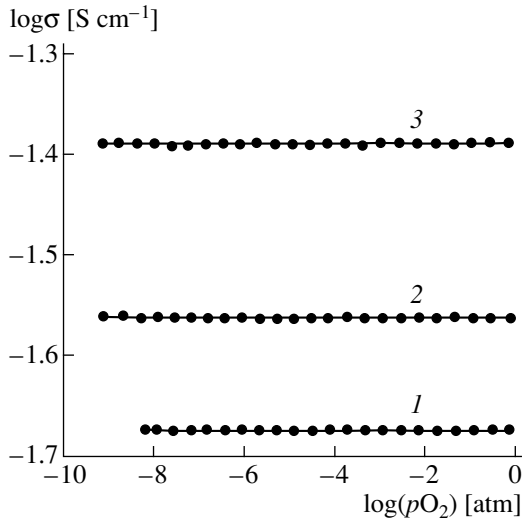

Fig. 2. Dependences of the electrical conductivity of the $Li_4Ti_5O_{12}$ compound on the oxygen partial pressure at T = (*1*) 1023, (*2*) 1073, and (*3*) 1123 K.

the gas phase (Fig. 2). It can be seen from Fig. 2 that the electrical conductivity σ does not depend on the oxygen partial pressure p_{O_2} at T = const. This indicates that the oxygen content in the $Li_4Ti_5O_{12}$ compound remains constant and the measured conductivity σ is determined by the lithium conductivity, which, in turn, does not depend on the oxygen partial pressure p_{O_2}.

Therefore, the substantial increase in the electrical conductivity of the $Li_4Ti_5O_{12}$ titanate is caused only by the disordering of the original spinel structure due to a redistribution of lithium ions among occupied and empty sites. The temperature dependence of the activation energy for lithium conduction $E_a(T)$ exhibits minima at temperatures close to 800 and 1100 K, most likely, upon the completion of two transitions to high-temperature phases of the $Li_4Ti_5O_{12}$ titanate. These phase transitions can be transformations of the spinel structure, first, into an ordered NaCl-type defect structure (space group $Fd\bar{3}m$) and then into a disordered NaCl-type structure (space group $Fm\bar{3}m$), as is the case in Li_2MgCl_4 chloride spinels [10]. The absence of thermal effects in the DTA curves suggests a gradual redistribution of cations over wide temperature ranges and the occurrence of order–disorder phase transitions. *In situ* investigation into the evolution of the Raman spectra with variations in the temperature can provide important information on phase transitions of this type, which was convincingly demonstrated by Wussow *et al.* [10] for lithium chloride spinels.

3.3. High-Temperature Raman Spectroscopy

The Raman spectra of the $Li_4Ti_5O_{12}$ compound at different temperatures are shown in Fig. 3. It can be seen from this figure that an increase in the temperature leads to noticeable changes in the Raman spectra. As a result, only three broad lines are observed at 973 K. The temperature dependences of the frequency location of the principal lines in the Raman spectra are shown in Fig. 4.

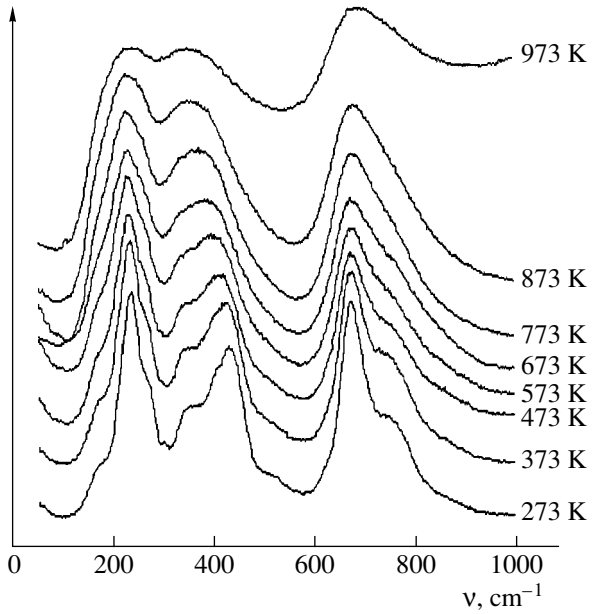

Fig. 3. Raman spectra of the $Li_4Ti_5O_{12}$ compound at different temperatures.

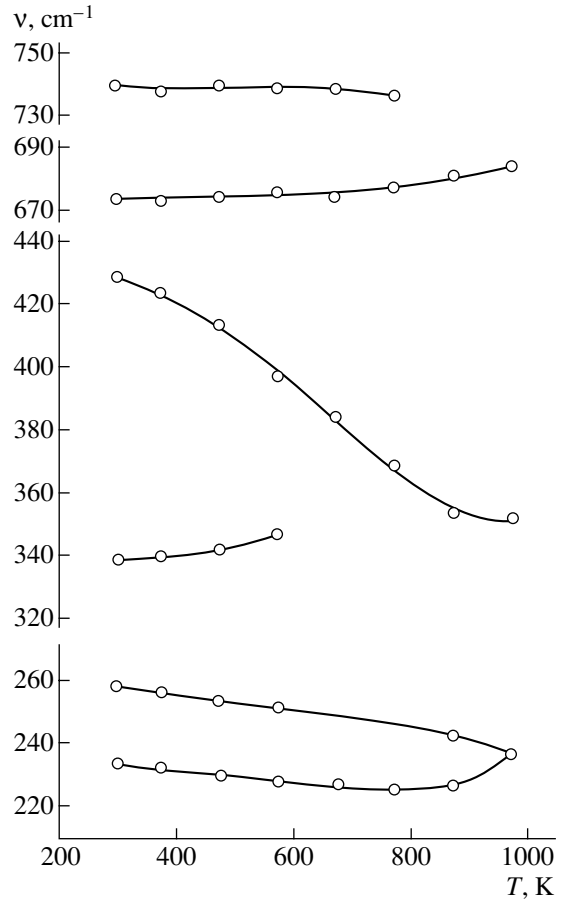

Fig. 4. Temperature dependences of the frequency of bond vibrations in the $Li_4Ti_5O_{12}$ compound.

Proskuryakova *et al.* [5] thoroughly analyzed the IR and Raman spectra of the $Li_4Ti_5O_{12}$ spinel at room temperature. In particular, it was demonstrated that the frequencies of the Ti–O stretching vibrations lie in the range above 460 cm^{-1}. The stretching–bending vibrations of the Li–O bonds in LiO_4 and LiO_6 polyhedra are observed at 430 and 335 cm^{-1}, respectively. The bending vibrations at frequencies below 300 cm^{-1} correspond to the O–Ti–O (235 cm^{-1}) and O–Li–O (160 cm^{-1}) bonds. In the Raman spectra, the lines observed at higher frequencies (675, 740 cm^{-1}) [as compared to the frequencies of the Ti–O stretching vibrations in compounds with octahedral coordination of titanium ($BaTiO_3$, $SrTiO_3$)] were assigned in [5] to vibrations of Ti–O bonds in TiO_4 tetrahedra. However, according to structural investigations (see table), titanium atoms occupy only the 16*d* octahedral positions. Therefore, the high-frequency lines at 675 and 740 cm^{-1} should be attributed to vibrations of Ti–O bonds in TiO_6 octahedra. In AB_2O_4 spinels, oxygen atoms are coordinated by three *B* atoms and one *A* atom (Li atoms at the 8*a* positions). Consequently, the presence of Li^+ ions in the 16*d* positions leads to the nonequivalence of Ti–O bonds. A

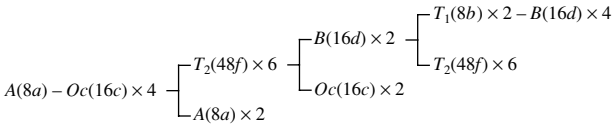

Fig. 5. Schematic diagram of the bonding of coordination polyhedra in the AB_2O_4 spinel structure [14].

number of bonds (Ti–O…Li^+) become shorter, and the frequency of their vibrations is higher than the frequency of vibrations of Ti–O bonds in $ATiO_3$ perovskites.

The redistribution of lithium ions in the structure of the $Li_4Ti_5O_{12}$ titanate upon heating brings about considerable changes in the location and intensity of the lines in the Raman spectra (Figs. 3, 4). A decrease in the intensity ratio of the lines at 430 (LiO_4) and 340 cm^{-1} (LiO_6) is due to a transfer of lithium ions from the 8*a* tetrahedral positions to vacant 16*c* octahedral positions. At 773 K, this transfer is virtually complete and the Raman spectrum exhibits three lines.

An increase in the intensity of the line at ~740 cm^{-1} can be associated with the appearance of a new mode of vibrations of Ti–O … Li(16*c*) bonds. An increase in the frequency of vibrations of Ti–O bonds in TiO_6 octahedra from 675 to 685 cm^{-1} at $T > 800$ K is most likely caused by the transfer of lithium ions from the 16*d* positions to the remaining vacant 16*c* positions. As a consequence, the Coulomb attraction of Ti^{4+} and O^{2-} ions is enhanced and the Ti–O bond becomes shorter. At these temperatures, two lines attributed to vibrations of Li–O bonds in Li(16*d*)O_6 and Li(16*c*)O_6 octahedra merge together.

3.4. Structural Prerequisites of Disordering and Migration of Lithium Ions in the $Li_4Ti_5O_{12}$ Compound

In the structure of AB_2O_4 spinels, BO_6 octahedra are linked by AO_4 isolated tetrahedra through common vertices (oxygen atoms) into a three-dimensional framework. The schematic diagram of the bonding of coordination polyhedra in spinel structures is drawn in Fig. 5. In each pair, BO_6 octahedra are shared by the edge. The framework involves 56 empty tetrahedra of two types, namely, T_1(8*b*) and T_2(48*f*), and 16 empty octahedra *Oc*(16*c*). The occupied cation polyhedra and empty polyhedra are shared by their faces: each *A* position is surrounded by four empty octahedra, four *B* positions surround a T_1 tetrahedron, and two occupied *B* octahedra and two empty octahedra surround a T_2 tetrahedron.

Let us consider possible paths of migration of lithium ions in the $Li_4Ti_5O_{12}$ spinel. In the case when vacancies in *A* positions are absent, an Li^+ ion occupying an *A* position can migrate into an empty octahedron through a common face. Then, the Li^+ ion can either

leave this octahedron and occupy an empty T_2 tetrahedron (scheme *I*) or shift Li from the adjacent position *A*' to an *Oc*' octahedron (scheme *II*). The lithium ion will follow both paths until it occupies a vacancy at an *A*" position formed after the escape of another migrating lithium ion. The activation energy for migration of lithium ions over these sites is higher than the energy for migration of the lithium ion from the *A* position into the empty octahedron, because lithium ions migrating through the T_2 position are repelled either by multiply charged Ti^{4+} ions occupying adjacent positions *B* or by Li^+ ions located at the *A*' positions. However, it seems likely that this activation energy is less than the enthalpy of formation of thermodynamically stable vacancies at the *A* positions due to the transfer of lithium ions to vacant octahedral positions with an increase in the temperature. The particular scheme (*I* or *II*) for migration of the Li^+ ion can be judged from the low-temperature portion of the curve $\log\sigma(T^{-1})$ with the activation energy for electrical conduction $E_a \sim 0.6$ eV.

A considerable increase in the conductivity of the $Li_4Ti_5O_{12}$ titanate above 450 K indicates that the *V*(8*a*) vacancies are formed in the 8*a* positions due to the transfer of the fraction α of lithium ions to *V*(16*c*) empty octahedra in the 16*c* positions. In this case, cations can migrate over the trajectories … Li(8*a*) ⟶ *V*(16*c*) ⟶ *V*(8*a*) ⟶ … (scheme *III*) and Li(16*c*) ⟶ *V*(8*a*) ⟶ *V*(16*c*) ⟶ … (scheme *IV*). The probability of hopping following scheme *III* is proportional to the product of the fraction of charge carriers (Li^+ ions) in the 8*a* positions by the fraction of vacant intermediate positions $[(16 - \alpha)/16]$ and the fraction of vacancies in the 8*a* positions $(\alpha/8)$: $W_3 \sim (8 - \alpha)(1 - \alpha/16)(\alpha/8)$. The probability of hopping following scheme *IV* is proportional to the product of the fraction of Li^+ ions in the 16*c* positions (α) by the fraction of intermediate positions or vacancies in the 8*a* positions $(\alpha/8)$ and the fraction of the remaining vacant 16*c* positions: $W_4 \sim \alpha(\alpha/8)(1 - \alpha/16)$. The dependences of $\log W_{3,4}$ and $\log(W_3 + W_4)$ on the fraction of lithium ions α are shown in Fig. 6. For close values of the activation energies for migration of Li^+ ions according to these two schemes and small values of α, the lithium conduction is governed by lithium migration following scheme *III*. If the quantity α varies over a wide range, lithium ions in both positions are involved in the transfer.

In the case when half the number of lithium ions transfer from the 8*a* positions to the 16*c* positions, the migration of cations following scheme *IV* becomes dominant. The lowest activation energy (0.3 eV) for ionic conduction at approximately 800 K corresponds to the energy of lithium migration following scheme *IV* and indicates a complete transformation of the $Li_4Ti_5O_{12}$ spinel structure into an NaCl-type structure with ordered cation vacancies in the 16*c* positions (space group $Fd\bar{3}m$). The crystal chemical formula

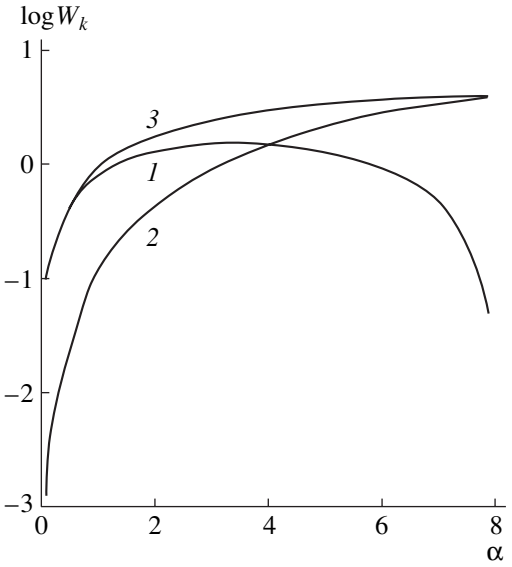

Fig. 6. Dependences of the probability of lithium ions migrating over different trajectories on the fraction α of lithium ions in the 16*c* positions: (*1*) $\log W_3$, (*2*) $\log W_4$, and (*3*) $\log(W_3 + W_4)$.

can be written as follows: $[Li\square]_{16c}[Li_{0.33}Ti_{1.67}]_{16d}O_4$, where $\square$ is a vacancy. According to the group-theoretic analysis performed for Li_2MCl_4 compounds with a similar distribution of cations [10], the Raman spectrum should involve four active modes (A_{1g}, E_g, $2F_{2g}$) instead of five modes characteristic of the spinel (A_{1g}, E_g, $3F_{2g}$). In the Raman spectrum of the $Li_4Ti_5O_{12}$ titanate, three modes are clearly observed at 873 K.

The transfer of lithium ions from the 16*d* positions to vacant 16*c* octahedral positions is most likely responsible for the drastic increase in the electrical conductivity at $T > 800$ K. For Li_2MCl_4 chlorides, the high-temperature phase transition is associated with the transformation of the NaCl-type structure with ordered cation vacancies into a disordered structure and the Raman spectra at temperatures above the phase transition point involve only one line A_{1g} [10]. Note that this transition should be accompanied by the redistribution of multiply charged ions over octahedral positions. Moreover, the diffusion of Ti^{4+} ions in the $Li_4Ti_5O_{12}$ compound is unlikely. Hence, it can be assumed that the high-temperature kink in the temperature dependence of the electrical conductivity at ~1050 K corresponds to the completion of the second phase transition, which results in the complete transfer of lithium ions from the 16*d* positions to the 16*c* positions. In this case, the crystal chemical formula for the $Li_4Ti_5O_{12}$ compound can be written as follows: $[Li_{1.33}\square_{0.67}]_{16c}[Ti_{1.67}\square_{0.33}]_{16d}O_4$. Since the Raman spectrum at 973 K is characterized by three modes, we can assume that the structure of the $Li_4Ti_5O_{12}$ titanate does not transform into a disordered

NaCl-type structure with one imperfect octahedral cation sublattice. At the same time, a decrease in the intensity of the line at ~350 cm^{-1} with an increase in the temperature from 873 to 973 K suggests that the lithium sublattice is disordered.

The probability of Li^+ ions migrating from the 16*c* positions to empty octahedra at the 16*c* positions drastically increases at $T > 800$ K, because these ions can move not only through vacant 8*a* positions (Fig. 6) but also through a number of vacant 48*f* tetrahedral positions [*V*(48*f*)] which are adjacent to vacancies in the *B*(16*d*) positions. Earlier, Abrahams *et al.* [15] observed vacancies in the titanium sublattice of the $Li_2Ti_3O_7$ ramsdellite whose composition is close to that of the $Li_4Ti_5O_{12}$ titanate. The ^7Li NMR spectra of $Li_2Ti_3O_7$ exhibit one peak associated with one sort of crystallographic position of Li^+ cations [16].

It should be noted that the ionic conductivities of $Li_2Ti_3O_7$ [17, 18] and $Li_4Ti_5O_{12}$ compounds at ~1000 K are rather close to each other. An activation energy of ~0.5 eV corresponds to the migration of lithium ions over the trajectory … ⟶ Li(16*c*) ⟶ *V*(48*f*) ⟶ *V*(16*c*) ⟶ …. This activation energy is substantially higher than the activation energy for lithium migration following scheme *IV*, because the Ti^{4+} ion occupies one of two positions *B* surrounding the T_2(48*f*) tetrahedron. An increase in the activation energy for lithium conduction at $T > 1150$ K can be explained by the fact that the other T_2(48*f*) tetrahedral positions surrounded by two TiO_6 octahedra are involved in the ion transfer. This leads to a strong enhancement of the Coulomb interaction of migrating lithium ions with immobile cations.

4. CONCLUSIONS

Thus, the above investigation demonstrated that, in the $Li_4Ti_5O_{12}$ spinel structure, Li^+ ions in the 8*a* regular positions and interstitial ions in the 16*c* positions are involved in diffusion. In high-temperature modifications of the $Li_4Ti_5O_{12}$ compound with an NaCl-type structure, Li^+ cations in the 16*c* positions are charge carriers: lithium cations migrate over vacant 8*a* tetrahedral positions at moderate temperatures and 48*f* positions at temperatures above 800 K.

ACKNOWLEDGMENTS

This work was supported by the Russian Foundation for Basic Research, project nos. 01-03-32472 and 02-03-06544.

REFERENCES

1. G. H. Jonker, *Trabajos de la Tercera Reunion International Sobre Reactividad de la Solidas, Madrid* (1957), Vol. 1, p. 413.
2. G. Blasse, Philips Res. Rep. Suppl. **3**, 121 (1964).
3. G. Izquierdo and A. R. West, Mater. Res. Bull. **15**, 1655 (1980).
4. T. Ohzuku and A. Veda, Solid State Ionics **69**, 201 (1994).
5. E. V. Proskuryakova, O. I. Kondratov, N. V. Porotnikov, and K. I. Petrov, Zh. Neorg. Khim. **28** (6), 1402 (1983).
6. N. V. Porotnikov, N. G. Chaban, and K. I. Petrov, Izv. Akad. Nauk SSSR, Neorg. Mater. **18** (6), 1066 (1982).
7. R. Kanno, Y. Tzkeda, A. Takahashi, *et al.*, J. Solid State Chem. **71**, 196 (1987).
8. C. Cros, L. Hanebali, L. Latié, *et al.*, Solid State Ionics **9–10**, 139 (1983).
9. J. L. Soubeyroux, C. Cros, W. Gang, *et al.*, Solid State Ionics **15**, 293 (1985).
10. K. Wussow, H. Haeuseler, P. Kuske, *et al.*, J. Solid State Chem. **78**, 117 (1989).
11. R. Kanno, Y. Takeda, and O. Yamamoto, Solid State Ionics **28–30**, 1276 (1988).
12. M. Partik and H. D. Lutz, Mater. Res. Bull. **32** (8), 1073 (1997).
13. J. Rodriges-Carvajal, Physica B (Amsterdam) **192**, 55 (1993).
14. B. Zachau-Christiansen, K. West, T. Jacobsen, and S. Atlung, Solid State Ionics **40–41**, 580 (1990).
15. I. Abrahams, P. G. Bruce, W. I. F. David, and A. R. West, J. Solid State Chem. **78**, 170 (1989).
16. S. Garnier, C. Bohnke, O. Bohnke, and J. L. Fourquet, Solid State Ionics **83**, 323 (1996).
17. J. B. Boyce and J. C. Mikkelsen, Solid State Commun. **31**, 741 (1979).
18. A. P. Mozhaev, Yu. A. Pamyatnykh, and Yu. D. Tret'yakov, Izv. Akad. Nauk SSSR, Neorg. Mater. **16** (12), 2193 (1980).

Translated by O. Borovik-Romanova

Physics of the Solid State, Vol. 45, No. 11, 2003, pp. 2189–2193. Translated from Fizika Tverdogo Tela, Vol. 45, No. 11, 2003, pp. 2085–2089.

LOW-DIMENSIONAL SYSTEMS AND SURFACE PHYSICS

Spin Depolarization and a Metal–Insulator Transition in a Two-Dimensional System in Zero Magnetic Field

I. A. Shelykh, N. T. Bagraev, and L. E. Klyachkin

Ioffe Physicotechnical Institute, Russian Academy of Sciences, Politekhnicheskaya ul. 26, St. Petersburg, 194021 Russia
e-mail: impurity.dipole@mail.ioffe.ru

Received January 16, 2003

Abstract—The conditions for spontaneous spin polarization in a two-dimensional system in a zero magnetic field are considered in the case of a partial filling of the lower quantum-well subbands when the energy of exchange interaction of charge carriers exceeds their kinetic energy. The critical density above which the two-dimensional gas of charge carriers undergoes complete spin depolarization is determined in the Hartree–Fock approximation. It is assumed that this process can be due to a transition of the two-dimensional gas to a metallic state.© *2003 MAIK "Nauka/Interperiodica".*

1. INTRODUCTION

Recent considerable progress achieved in nanotechnology has provided a way of producing two-dimensional semiconductor systems characterized by a low density of charge carriers with a high mobility. These systems exhibit ballistic properties under the condition $k_BT\tau/\hbar > 1$, where $\hbar/k_BT$ is the time of electron–electron interaction and $\tau = m^*\mu/e$ is the transport relaxation time [1–14]. It should be noted that the ballistic transport is governed by spin correlations to a greater extent than the diffusive transport ($k_BT\tau/\hbar < 1$) [2–4]. A clear manifestation of spin correlations in charge-carrier transfer is a metal–insulator transition revealed recently in silicon metal-oxide semiconductor (MOS) transistors in a zero magnetic field [1], even though the observation of this phenomenon contradicts the predictions made in the framework of the one-parametric scaling theory of localization, according to which the existence of a metallic state in two-dimensional systems is impossible [5]. Furthermore, the metallic state has been observed in a two-dimensional electron (or hole) gas in Si–Ge [6] and GaAs–GaAlAs [7, 8] heterojunctions. The spin nature of the metallic state primarily manifests itself in the fact that this state is destroyed in a magnetic field applied in the plane of the two-dimensional system and restoring the regime of weak (or strong) localization. It has been found that the contribution to the metal–insulator transition occurring in two-dimensional systems is made by both the spin–orbit interaction [2, 9, 10, 11] and spontaneous spin polarization due to exchange and correlation interparticle interactions [4, 12, 13]. Nonetheless, the mechanism of this transition in two-dimensional systems is not clearly understood. In particular, the field dependences of the conductivity of a two-dimensional electron gas at an electron density close to the critical value n_c corresponding to a metal–insulator transition indicate that, under these conditions, there occurs spontaneous polarization [12, 15]. However, these results disagree with data on the Shubnikov–de Haas oscillations and spin susceptibility, according to which the tendency toward ferromagnetic ordering is accompanied by the transformation of a normal metal into a two-dimensional insulator without transition to a spontaneously polarized state with delocalized wave functions [9, 14, 16]. In this respect, the interrelation between the metal–insulator transition and the critical density of charge carriers above which a spontaneously polarized two-dimensional gas undergoes complete spin depolarization remains a key problem. In the present work, the critical density of charge carriers above which the two-dimensional gas undergoes complete depolarization was determined in the Hartree–Fock approximation. Within this approximation, we analyzed the conditions at which spontaneous spin polarization can arise in a two-dimensional system in a zero magnetic field.

2. SPONTANEOUS SPIN POLARIZATION IN A TWO-DIMENSIONAL SYSTEM IN A ZERO MAGNETIC FIELD

Let us consider a system of fermions described by the Schrödinger equation

$$H\Psi = E\Psi. \quad (1)$$

Here, $H = H_0 + H_1$, where H_0 is the Hamiltonian of noninteracting fermions, which depends on the dimensionality of the system under consideration, and H_1 is the Hamiltonian accounting for the interaction of these fermions.

For two-dimensional systems, specifically for a fermion gas in a quantum well, the kinetic energy is added to the potential energy corresponding to the quantum confinement of motion of a charge carrier along the z

1063-7834/03/4511-2189$24.00

direction perpendicular to the plane of the quantum well; that is,

$$H_0^{2D} = \sum_{j=1}^{N}\left(\frac{\mathbf{p}_j^2}{2m^*} + U(z_j)\right). \quad (2)$$

The unperturbed single-particle wave functions are represented by the products of the wave functions of quantum confinement and the wave functions of plane waves propagating parallel to the quantum well:

$$\psi_{k,m}(\mathbf{r}) = \frac{1}{\sqrt{\Omega_{2D}}}e^{i\mathbf{k}\boldsymbol{\rho}}\varphi_m(z), \quad (3)$$

where m is the number of the quantum-well subband along the z axis, $\boldsymbol{\rho} = \mathbf{i}x + \mathbf{j}y$, and Ω_{2D} is the two-dimensional volume.

If the density of noninteracting carriers is sufficiently low (such that they occupy only the lowest quantum-well subband), the total energy of the electron gas is equal to the kinetic energy and the density of the kinetic energy can easily be calculated from the relationship

$$\varepsilon_{\text{kin}}^{2D} = \sum_{k<k_\text{F}} g_s\frac{\hbar^2k^2}{2m^*} = \frac{\hbar^2}{16\pi m^*}g_sk_\text{F}^4 = \frac{\pi\hbar^2n_{2D}^2}{m^*g_s}. \quad (4)$$

Here, k_F is the Fermi wave number, which can be determined from the condition

$$\pi k_\text{F}^2 = \frac{(2\pi)^2}{g_s}n_{2D}; \quad (5)$$

n_{2D} is the charge-carrier density in the two-dimensional gas; and g_s is the spin factor, which is equal to the number of electrons in a unit cell of the phase space. For a two-dimensional gas, $g_s = 2$ in an unpolarized state, $g_s = 1$ in a completely polarized state, and $1 < g_s < 2$ in a partially spin-polarized state.

Let us now analyze the possibility of spontaneous polarization arising in a quasi-two-dimensional system due to an exchange interaction. The polarized state of a two-dimensional gas of noninteracting fermions is always less energetically favorable, because the kinetic energy of this state is universally higher than that of the unpolarized state. However, for a system of interacting particles, there appears an addition to the energy E_1, which can be illustrated using an infinite sequence of diagrams:

$\varepsilon_{\text{core}} + \varepsilon_{\text{el–el}} =$ 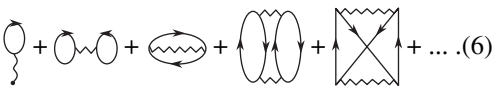 $+ \ldots$.(6)

It can easily be seen that the third and fifth exchange diagrams substantially depend on the spin polarization. Indeed, the spin should be conserved at the vertices of the diagram, because the interaction does not depend on the spin. Therefore, the processes described by the exchange diagrams can proceed only between particles with identical spins. Consequently, the contribution from these diagrams for polarized systems is more significant than that for unpolarized systems. Since the second diagram makes a negative contribution, the spin-polarized state can be more energetically favorable than the unpolarized state.

We will restrict our consideration to the case of the first two diagrams. This corresponds to the inclusion of interparticle interactions in the framework of the Hartree–Fock approximation. As a result, we have

$$E_1 = \frac{1}{2}\sum_{E_K,\,E_L<E_\text{F}}[\langle KL|V|KL\rangle - \langle KL|V|LK\rangle], \quad (7)$$

where the first and second terms are the Hartree and Fock exchange additions to the energy, respectively, and the sum involves summation over spin indices. The first term diverges in the thermodynamic limit $N \longrightarrow \infty$, $\Omega_{2D} \longrightarrow \infty$, and $N/\Omega_{2D} = n_{2D} = \text{const}$. However, this term is canceled out by the term of interaction with a positive background. Therefore, to a first approximation, the exchange component of the interaction plays the decisive role and can be represented in the form

$$E_{\text{exc}} = -\frac{1}{2}\sum_{K,\,L<k_f}\langle KL|V|LK\rangle = -\frac{g_se^2\Omega_{2D}}{2(2\pi)^4}\int e^{-i\mathbf{k}\boldsymbol{\rho}}d\mathbf{k} \times\int e^{i\mathbf{l}\boldsymbol{\rho}}d\mathbf{l}\int\frac{|\varphi(z')|^2|\varphi(z'')|^2}{\sqrt{\boldsymbol{\rho}^2+(z'-z'')^2}}d\boldsymbol{\rho}\,dz'dz''. \quad (8)$$

Here, the quantum-well area Ω_{2D} and the spin factor g_s are introduced when calculating the matrix element of the exchange interaction as the result of summation over spins. The calculation of the integrals with respect to $\mathbf{k}$ and $\mathbf{l}$ leads to the following expression for the exchange interaction energy:

$$E_{\text{exc}} = -\frac{e^2k_\text{F}^2\Omega_{2D}}{4\pi}\int|\varphi(z)|^2|\varphi(z')|^2dz\,dz' \times\int_0^\infty\frac{J_1^2(k_\text{F}\rho)}{\rho\sqrt{\rho^2+(z'-z'')^2}}d\rho, \quad (9)$$

where $J_1(k_\text{F}\rho)$ is the Bessel function. In this expression, the integral I with $\alpha = k_\text{F}|z-z'| \sim k_\text{F}d$ (d is the quantum-well width) can be conveniently estimated under the condition

$$k_\text{F}d \ll 1, \quad (10)$$

which corresponds to a partial filling of the lower quantum-well subbands. In this case, we obtain $I = Ak_\text{F}$, where $A \sim 0.424$. As a result, the density of the

exchange interaction energy for the two-dimensional gas of charge carriers can be written in the form

$$\varepsilon_{exc} = E_{exc}/\Omega_{2D} = -\frac{g_s A e^2 k_F^3}{4\pi}\int |\varphi(z')|^2 |\varphi(z')|^2 dz'dz'' = g_s \frac{A e^2 k_F^3}{4\pi} = -\frac{\beta_{2D}}{g_s^{1/2}} n_{2D}^{3/2}, \quad (11)$$

where $\beta_{2D} = 2\sqrt{\pi} A e^2$. Note that the derived expression for the exchange energy density has negative sign and does not depend on the wave functions of noninteracting particles, i.e., on the quantum-well shape. The dependence of the exchange energy density on n_{2D} can be predicted from dimensional considerations. It should be emphasized once again that expression (11) for the exchange energy density of a two-dimensional electron gas holds only for sufficiently low densities of charge carriers when condition (10) is satisfied.

Now, we estimate the Fermi wave number k_F corresponding to the onset of the filling of the second quantum-well subband. Since the energy at the bottom of the jth subband in a square well is defined as $E_j = \pi^2\hbar^2 j^2/2m^*d^2$, the wave number k_0 corresponding to the onset of the filling of the second subband can be estimated as follows: $E_2 - E_1 \approx 3\pi^2\hbar^2/2m^*d^2 \approx \hbar^2 k_0/2m^*$ and $k_0 d \approx \sqrt{3}\pi \approx 5.44$. Therefore, approximation (10) does not hold for any quantum well with a sole filled subband. In this respect, it is of interest to evaluate the integral I in a limit opposite to the limit specified by relationship (10), i.e., under the condition $k_F d \gg 1$. In this case, we have $I = B/|z - z'|$, where $B \sim 0.498$. Hence, the exchange energy density can be represented in the form

$$\varepsilon_{exc} = -g_s \frac{B e^2 k_F^2}{4\pi}\int \frac{|\varphi(z')|^2 |\varphi(z'')|^2}{|z - z'|} dz'dz'' = -\chi_{2D} n_{2D}, \quad (12)$$
$$\chi_{2D} \approx B e^2 \int \frac{|\varphi(z')|^2 |\varphi(z'')|^2}{|z - z'|} dz'dz''.$$

Therefore, the dependence of the exchange energy density on the charge-carrier density in a two-dimensional system at high carrier densities differs significantly from that at low carrier densities. It is interesting to note that, in the limit of high carrier densities, the exchange energy does not depend on the degree of polarization, because the two-dimensional systems are characterized by the short-range exchange interaction in the k space.

In order to answer the question as to whether the exchange interaction can be responsible for spontaneous spin polarization in low-dimensional systems, it is necessary to compare the total energies of the two-dimensional gas of charge carriers in polarized and unpolarized states. In the limit of low carrier densities, the energy density can be written in the form

$$\varepsilon^{2D} = \varepsilon_{kin} + \varepsilon_{exc} \approx \frac{\pi\hbar^2 n_{2D}^2}{m^* g_s} - \frac{\beta_{2D}}{g_s^{1/2}} n_{2D}^{3/2}. \quad (13)$$

Here, the first and second terms characterize the kinetic energy and the exchange interaction energy, respectively. The energies of the two-dimensional gas in the polarized ($g_s = 1$) and unpolarized ($g_s = 2$) states are given by the relationships $\varepsilon^{2D}\big|_{g_s=1} \approx \pi\hbar^2 n_{2D}^2/m^* - \beta_{2D} n_{2D}^{3/2}$ and $\varepsilon^{2D}\big|_{g_s=2} \approx \pi\hbar^2 n_{2D}^2/2m^* - \beta_{2D} n_{2D}^{3/2}/\sqrt{2}$, respectively.

It can easily be seen from expression (13) that, in the case where the charge-carrier density is higher than the critical density n_0 defined by the formula

$$n_0 = \left[\frac{(2 - \sqrt{2}) m^* \beta_{2D}}{\pi\hbar^2}\right]^2, \quad (14)$$

the kinetic energy exceeds the exchange interaction energy and the unpolarized state is more energetically favorable than the completely polarized state. By contrast, if the charge-carrier density does not exceed the critical value n_0 and the exchange interaction energy is higher than the kinetic energy, the polarized state becomes more energetically favorable. Note that the critical density n_0 depends solely on the effective mass of charge carriers and increases with an increase in its value. In turn, the effective mass decreases with an increase in the charge-carrier density in the two-dimensional system.

It should be noted that the analysis of the mechanism responsible for spontaneous spin polarization of a two-dimensional gas of charge carriers involves two features. First, our consideration refers to the quasi-two-dimensional case where the quantum-confinement functions are introduced in an explicit form. It turns out that nothing depends on these functions in the limit of low carrier densities n_{2D}. Moreover, the possibility of ferromagnetic ordering arising in a quasi-two-dimensional system in the limit of low carrier densities is analyzed for the spontaneous spin polarization in a two-dimensional case where the stability of the ferromagnetic state associated with the exchange interaction is proved with due regard for the correlation corrections [17–19]. Second, the inclusion of the correlation energy is of fundamental importance in determining the charge-carrier density at which the Wigner crystallization takes place in a two-dimensional gas. This process is quite competitive with the above transition to a spontaneously polarized state with delocalized wave functions [20–25]. However, according to theoretical estimates [22–25], a Wigner crystal can be formed when the carrier density n_{2D} is less than $\cong m^2 e^4/r_s^2\hbar^2$. Here, the parameter r_s is the potential-to-kinetic-energy ratio

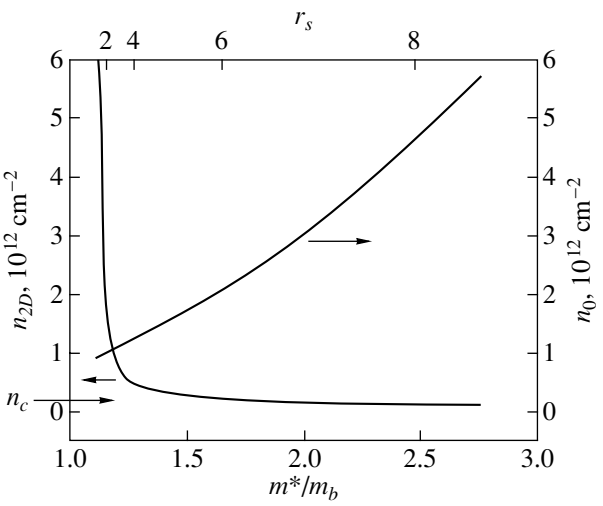

Fig. 1. Dependence of the critical electron density n_0 (corresponding to complete spin depolarization of the two-dimensional electron gas in silicon MOS structures) on the effective mass m^*/m_b and the dependence of the effective mass m^*/m_b on the electron density n_{2D} (taken from [9]). Designations: $m_b = 0.19m_0$ and n_c is the critical electron density corresponding to a metal–insulator transition in silicon MOS structures [9].

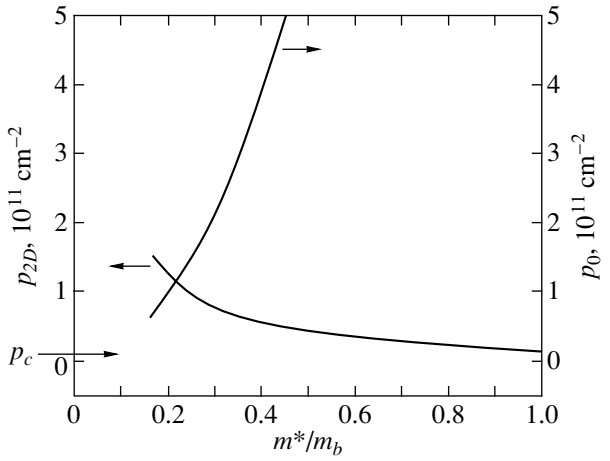

Fig. 2. Dependence of the critical hole density p_0 (corresponding to complete spin depolarization of the two-dimensional hole gas in the GaAs–GaAlAs heterostructure) on the effective mass m^*/m_b and the dependence of the effective mass m^*/m_b on the hole density p_{2D} (taken from [7]). Designations: $m_b = 0.38m_0$ and p_c is the critical hole density corresponding to a metal–insulator transition in the GaAs–GaAlAs heterostructure [7].

corresponding to the transition to a crystalline state. Depending on the chosen model, the parameter $r_s$can vary from 30 to 100 [22–25]. The critical carrier density at which the spontaneously polarized two-dimensional gas of charge carriers undergoes a complete depolarization [see relationship (14)] is estimated as $n_0 \sim 0.5m^2e^4/\hbar^2$. Therefore, the spontaneous spin polarization arises in a two-dimensional system when the kinetic energy is of the order of the potential energy, whereas the Wigner crystallization occurs when the potential-to-kinetic-energy ratio is of the order of 1 : 100. To put it differently, the transition to a crystalline state occurs when the carrier density n_{2D} is two to four orders of magnitude lower than the density corresponding to the transition to a spontaneously polarized state with delocalized wave functions. According to more exact calculations [23–25], the spontaneous spin polarization is limited by the potential-to-kinetic-energy ratio in the range $10 < r_s < 30$. At smaller ratios r_s, the degree of polarization decreases drastically, most likely, due to rigid condition (10). However, this restriction is of no significance in applying the Hartree–Fock approximation to an analysis of ferromagnetic ordering under conditions of exchange interaction (even with the inclusion of correlation corrections) and only indicates the carrier-density range in which the plane-wave approximation can be used as the initial approximation.

It should be emphasized that the above analysis corresponds to the limit of low charge-carrier densities in a two-dimensional system, i.e., the condition $k_F d \ll 1$, which imposes severe restrictions on the quantum-well width ($d \leq 20$ nm), especially when the experimental values of n_c are taken into account [15, 16]. If this condition is not satisfied, the two-dimensional system should be examined in the limit of high charge-carrier densities, i.e., under the condition $k_F d \gg 1$. In this case, the unpolarized state is always more energetically favorable than the polarized state, because the exchange energy does not depend on the spin factor g_s.

3. ON THE POSSIBLE INTERRELATION BETWEEN SPIN DEPOLARIZATION AND A METAL–INSULATOR TRANSITION IN A TWO-DIMENSIONAL SYSTEM

The dependences of the critical density n_0 (p_0) of two-dimensional electrons (holes) on their effective mass m^* at an electron (hole) density close to the critical value n_c (p_c) corresponding to a metal–insulator transition (Figs. 1, 2) were determined from the data obtained in studies on silicon MOS transistors [9] and GaAs–AlGaAs heterojunctions [7]. It can be seen from Figs. 1 and 2 that the spontaneous spin polarization decreases drastically when the density of two-dimensional electron (hole) gas exceeds the critical value n_c. The dependences shown in these figures indicate that fluctuations of the critical carrier density n_c can play a very important role in the elucidation of the tendency toward ferromagnetic ordering of a two-dimensional electron gas in silicon MOS transistors. A comparison of the carrier densities n_0 at $n_c = 8 \times 10^{10}$ cm^{-2} (spontaneous polarization [12, 15]) and $n_c = 1.0 \times 10^{11}$ cm^{-2} (no indication of ferromagnetic ordering [9, 16]) shows that

these values of n_0 differ by two orders of magnitude. Possibly, this difference in the critical density n_0 leads to a drastic decrease in the degree of spontaneous spin polarization of the two-dimensional electron gas in the vicinity of the metal–insulator transition in a two-dimensional system with a higher electron density n_c [9, 16]. However, in this case, the residual effect of spin polarization can manifest itself in deviations of the temperature dependences of the spin susceptibility from the Curie law [14], which makes it possible to reveal a tendency of the two-dimensional electron gas toward superparamagnetism. This explanation is based on the coincidence of the critical carrier densities corresponding to the metal–insulator transition (n_c) and spontaneous spin polarization (n_x) [12, 15] and disagrees with available data on the Shubnikov–de Haas oscillations, which do not confirm the occurrence of spin polarization of charge carriers even at $n_{2D} \approx 7.5 \times 10^{10}$ cm^{-2} [9, 16]. The question as to whether this fact can be explained in terms of a decrease in the carrier density n_0 due to a greater degree of disordering of the MOS structures studied in [9, 16] as compared to those examined in [12, 15] remains open. In this respect, the possible interrelation between the critical carrier densities n_c, n_x, and n_0 calls for further investigation.

ACKNOWLEDGMENTS

We would like to thank V.M. Pudalov for his participation in discussions of the results and helpful remarks.

This work was supported by the International Scientific and Technical Center, project no. 2136.

REFERENCES

1. S. V. Kravchenko, G. V. Kravchenko, J. E. Furneaux, *et al.*, Phys. Rev. B **50**, 8039 (1994).
2. V. M. Pudalov, Usp. Fiz. Nauk **168**, 227 (1998) [Phys. Usp. **41**, 211 (1998)].
3. A. M. Finkel'shteĭn, Zh. Éksp. Teor. Fiz. **84** (1), 168 (1983) [Sov. Phys. JETP **57**, 97 (1983)].
4. G. Zala, B. N. Narozhny, and I. L. Aleiner, Phys. Rev. B **64**, 201201 (2001).
5. E. A. Abrahams, P. W. Anderson, D. C. Licciardello, and T. V. Ramakrishnan, Phys. Rev. Lett. **42**, 673 (1979).
6. P. T. Coleridge, R. L. Williams, Y. Feng, and P. Zawadzkii, Phys. Rev. B **56**, R12764 (1997).
7. Y. Y. Proskuryakov, A. K. Savchenko, S. S. Safonov, *et al.*, Phys. Rev. Lett. **89**, 076406 (2002).
8. Y. Hanein, D. Shahar, C. C. Li, *et al.*, Phys. Rev. B **58**, R13338 (1998).
9. V. M. Pudalov, M. E. Gershenson, H. Kojima, *et al.*, Phys. Rev. Lett. **88**, 196404 (2002).
10. L. E. Golub and S. Pedersen, cond-mat/0205373.
11. E. I. Rashba, J. Supercond. **15**, 1 (2002).
12. A. A. Shashkin, S. V. Kravchenko, V. T. Dolgopolov, and T. M. Klapwijk, Phys. Rev. Lett. **87**, 086801 (2001).
13. S. A. Vitkalov, H. Zheng, K. M. Mertes, *et al.*, Phys. Rev. Lett. **87**, 086401 (2001).
14. O. Prus, Y. Yaish, M. Reznikov, *et al.*, cond-mat/0209142, v1.
15. S. V. Kravchenko, A. A. Shashkin, and V. T. Dolgopolov, Phys. Rev. Lett. **89**, 219701 (2002).
16. V. M. Pudalov, M. E. Gershenson, H. Kojima, *et al.*, Phys. Rev. Lett. **89**, 219702 (2002).
17. F. Stern, Phys. Rev. Lett. **30**, 278 (1973).
18. A. K. Rajagopal and J. C. Kimball, Phys. Rev. B **15**, 2819 (1977).
19. N. Iwamoto, Phys. Rev. B **43**, 2174 (1991).
20. R. S. Crandall and R. W. Williams, Phys. Lett. A **34A**, 404 (1971).
21. P. M. Platzman and H. Fukuyama, Phys. Rev. B **10**, 3150 (1974).
22. H. Fukuyama, P. M. Platzman, and P. W. Anderson, Phys. Rev. B **19**, 5211 (1979).
23. G. Senatore, S. Moroni, and D. Varsano, Solid State Commun. **119**, 333 (2001).
24. B. Bernu, L. Candido, and D. M. Ceperley, Phys. Rev. Lett. **86**, 870 (2001).
25. C. Attaccalite, S. Moroni, P. Gori-Giorgi, and G. B. Bachelet, Phys. Rev. Lett. **88**, 256601 (2002).

Translated by O. Borovik-Romanova

Physics of the Solid State, Vol. 45, No. 11, 2003, pp. 2194–2202. Translated from Fizika Tverdogo Tela, Vol. 45, No. 11, 2003, pp. 2090–2098.

LOW-DIMENSIONAL SYSTEMS AND SURFACE PHYSICS

Molecular-Beam Epitaxy and Properties of Heterostructures with InAs Nanoclusters in an Si Matrix

D. V. Denisov[1], I. T. Serenkov[1], V. I. Sakharov[1], G. É. Tsyrlin[1, 2], and V. M. Ustinov[1]

[1] *Ioffe Physicotechnical Institute, Russian Academy of Sciences, Politekhnicheskaya ul. 26, St. Petersburg, 194021 Russia*
e-mail: denisov@beam.ioffe.rssi.ru

[2] *Institute of Analytical Instrument Making, Russian Academy of Sciences, Rizhskiĭ pr. 26, St. Petersburg, 198103 Russia*

Received March 18, 2003

Abstract—The formation of heteroepitaxial structures with InAs nanoclusters in an Si matrix during molecular-beam epitaxy and variations in the parameters of these structures due to thermal annealing are investigated by reflection high-energy electron diffraction (RHEED), medium-energy ion scattering (MEIS), and scanning electron microscopy (SEM). It is demonstrated that the deposition of InAs onto the Si(100) surface at certain temperatures brings about the formation of tetrahedral nanopyramids with {111} orientation of the lateral faces. It is revealed that InAs nanoislands can be epitaxially overgrown with silicon, which leads to gradual smoothing of the three-dimensional relief. After annealing under vacuum, the Si/InAs/Si(100) structures are stable at temperatures up to 700°C. © *2003 MAIK "Nauka/Interperiodica".*

1. INTRODUCTION

At present, silicon is the most promising material for use in semiconductor electronics. In many respects, this is explained by the natural properties of silicon as an easily producible and relatively inexpensive material. Further progress in silicon microelectronics requires an increase in the integration density and operating frequency, a decrease in the power consumption, and the fabrication of combined microelectronic and optoelectronic integrated circuits in one crystal. However, silicon is an indirect-band-gap semiconductor with a low efficiency of interband radiative recombination, which imposes severe limitations on its applications in optoelectronics. Therefore, the design of new optoelectronic devices that can be physically and technologically compatible with the existing silicon planar technology is an important problem in modern solid-state electronics.

A possible way to solve this problem is to provide the formation of an Si matrix involving a large number of optically active centers: an array composed of closely spaced nanoclusters of a direct-band-gap semiconductor with a band gap narrower than the band gap of silicon [1]. Tsyrlin *et al.* [2] proposed to produce such structures with the use of InAs molecular-beam epitaxy on Si. In this case, the array of nanoclusters is initially formed on the surface due to the formation and self-consistent growth of coherently strained nanoislands during heteroepitaxy of materials with a considerable lattice mismatch. The subsequent overgrowth of nanoclusters with a layer of the main material results in the formation of a structure with quantum dots. This technique was applied by Ledentsov *et al.* [3] to fabricate laser structures with InAs quantum dots in an active region in the traditional InGaAs–AlGaAs heterosystem. In recent years, $Si_{1-x}Ge_x$/Si(100) structures characterized by quasi-direct-band-gap radiative recombination between electrons of silicon and holes of silicon–germanium nanoislands have been investigated extensively [4].

For the InAs–Si heterosystem composed of elemental nonpolar and binary polar semiconductors, the molecular-beam epitaxy has a number of specific features, namely, a large mismatch between the lattice parameters (InAs/Si, 11%; InAs/GaAs, 7%; Ge/Si, 4%), interdiffusion of the heterojunction materials, and the possibility of forming antiphase domains. It should be noted that the InAs and Si homoepitaxy conditions also differ significantly. Actually, InAs is grown at temperatures of 400–500°C and an As vapor pressure of ~10^{-6} Torr [5, 6]. High-quality Si epitaxial layers are prepared at growth temperatures of 600–800°C and a background residual pressure of ~10^{-8} Torr or lower [7] (under these conditions, InAs undergoes thermal dissociation [8]).

In the present work, the specific features of formation and the properties of InAs–Si heterostructures consisting of an Si matrix with an embedded layer of InAs three-dimensional nanoclusters prepared by molecular-beam epitaxy on Si(100) wafers were investigated by reflection high-energy electron diffraction (RHEED), medium-energy ion scattering (MEIS), and scanning electron microscopy (SEM).

2. EXPERIMENTAL TECHNIQUE

Heterostructures in the InAs–Si system were grown by molecular-beam epitaxy on an SUPRA-32 apparatus

equipped with an electron-beam evaporator for producing an Si flow and effusion cells for the evaporation of In and As. The initial pressure in a growth unit of the apparatus was no higher than 3×10^{-10} Torr. When operating the electron-beam evaporator (power, ~1 kW; Si deposition rate, ~1.0 Å/s), the pressure did not exceed 1×10^{-8} Torr. The pressure in the growth chamber and the composition of the background atmosphere were controlled using a Bayard–Alpert vacuum gauge and a quadrupole mass spectrometer. The design of the manipulator made it possible to continuously rotate the sample in the course of growth. A standard tantalum ribbon heater provided thermal heating of the sample to 800°C. The sample temperature was measured by an IRCON-V IR pyrometer and a W–Re thermocouple. The morphology of the growth surface was monitored *in situ* with an RHEED instrument (electron beam energy up to 10 keV) and equipment for recording the diffraction patterns on the basis of a compact digital camera. The epitaxy was performed on *n*-Si(100) substrates with a dopant concentration of 2×10^{15} cm^{-3}.

The structures grown were studied using scanning electron microscopy and medium-energy ion scattering. The electron microscope images of the sample surface were obtained with the use of a CamScan S4-90FE electron microscope. The secondary-emission images were recorded at a probing beam energy of 20 keV. Examination of the samples by medium-energy ion scattering was carried out on a setup described in [9]. Probing was performed with He^+ ions at energies of 96 and 191 keV. Ions backscattered at an angle of 120° were detected using an electrostatic analyzer at a resolution $\Delta E/E = 0.005$ in a random geometry or a channeling geometry along the [100] axis. The samples used in our experiments correspond to the main stages of the formation of the heterostructures with InAs nanoclusters in the Si crystal matrix through molecular-beam epitaxy: (1) Si/Si(100) [the preparation of chemically pure, atomically smooth, structurally perfect Si(100) surface], (2) InAs/ Si(100) (the formation of an array of InAs nanoislands on the Si surface), and (3) Si/InAs/Si(100) (the overgrowth of InAs nanoislands with an Si layer).

In order to obtain reliable information on the nucleation and growth of InAs nanoislands during heteroepitaxy, the surface condition of the initial Si substrate must be taken into account. The use of only reflection high-energy electron diffraction for monitoring the pregrowth treatment of substrates can lead to incorrect inferences, because etch pits can be formed during the removal of the protective oxide [10, 11]. For this reason, the surface condition at all stages of the pre-epitaxial preparation was additionally examined by scanning electron microscopy.

The pregrowth chemical treatment of Si substrates consisted in cleaning and forming a protective thin layer of nonstoichiometric silicon oxide on the operating surface according to the Shiraki method [12]. The samples thus prepared were immediately placed in the apparatus. Immediately prior to the growth, the substrate was sequentially degassed at temperatures of 400 and 750°C for 50 and 20 min, respectively. Then, the silicon oxide layer was removed from the surface in an Si flow (~0.02 Å/s) at a temperature of 750°C for 15–20 min. The pre-epitaxial preparation of substrates under vacuum was monitored by reflection high-energy electron diffraction.

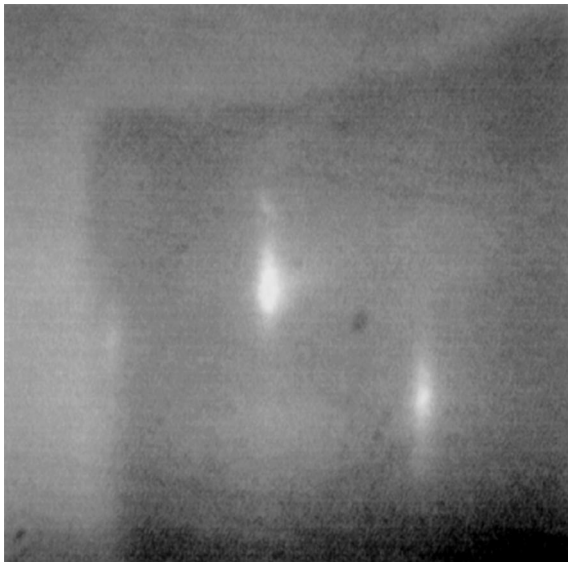

Fig. 1. RHEED pattern of the surface of the Si(100) substrate after pregrowth chemical treatment. The electron energy is equal to 10 keV. The electron beam is incident along the [011] direction.

The silicon substrates used for the growth experiments had a microscopically smooth surface. This could be judged from the absence of topographic contrast in the SEM images. The chemical treatment did not lead to a change in the surface morphology of substrates on the microscopic level. The RHEED patterns of these substrates involve extended diffraction reflections (Fig. 1) corresponding to the Si lattice. This indicates that the substrate surface is atomically smooth and that the thickness of the SiO_2 layer does not exceed several monolayers. According to the SEM and RHEED data (Fig. 2), the removal of the protective oxide layer through heating at 750°C in a flow of Si atoms (~ 0.02 Å/s, t ~ 15–20 min) or heating at 800°C (t ~ 10–15 min) provides a way of producing an atomically smooth, structurally ordered silicon surface. As follows from the x-ray photoelectron spectroscopic data, the surface was free of contaminations to within the sensitivity of the method (less than 0.1 monolayers). The check Si layers 100–500 Å thick were grown on the prepared substrates at temperatures from 350 to 750°C and a deposition rate of 1.0 Å/s. All the samples grown exhibited (2 × 2) diffraction patterns and had surfaces with no microroughnesses.

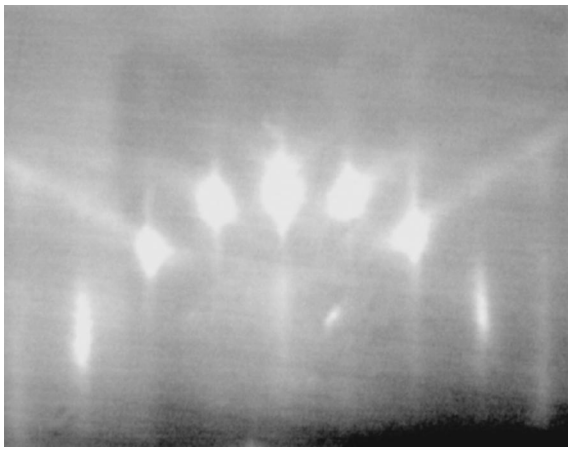

Fig. 2. RHEED pattern of the surface of the Si(100) substrate after removal of the oxide layer. The electron energy is equal to 10 keV. The electron beam is incident along the [011] direction.

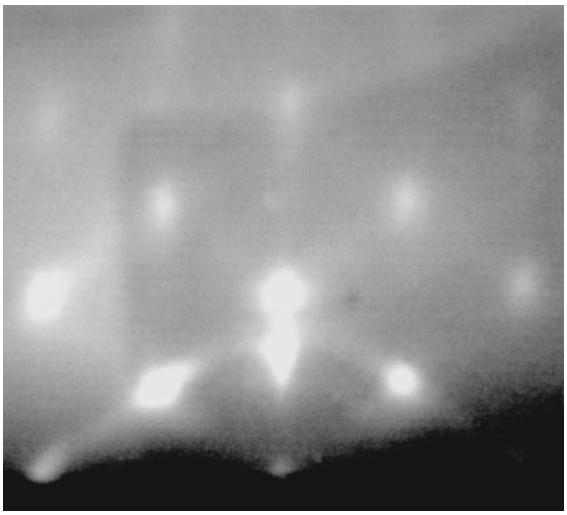

Fig. 3. RHEED pattern of the surface of the InAs/Si(100) structure. The number of InAs monolayers deposited at 400°C is 4. The electron energy is equal to 10 keV. The electron beam is incident along the [011] direction.

Prior to the growth of InAs, the As vapor pressure in the chamber was raised to ~10^{-6}–10^{-5} Torr. Under this pressure, the number of molecules from the background atmosphere that find their way to the sample surface corresponds to approximately a monolayer (ML) formed by adsorbed atoms in a matter of seconds [for the Si(100) surface, 1ML = 6.8×10^{14} atoms/cm^2]. However, since the saturation vapor pressure of As at a temperature of 200°C is approximately equal to 10^{-5} Torr, more than one monolayer of As atoms cannot be adsorbed on the silicon surface heated to temperatures above 200°C. This is confirmed by the data on the electronic state of As atoms on Si [13, 14] and the fact that the As deposition from the background atmosphere or from the flow emerging from the effusion cell does not lead to a change in the (2×2) diffraction pattern of the Si(100) surface heated to temperatures above 200°C. On the other hand, according to x-ray photoelectron spectroscopy, thermal desorption of As from the Si(100) surface is observed at temperatures above 600°C [15, 16]. Consequently, even prior to the growth, the Si surface is covered with a monolayer of regularly arranged As atoms, which is in agreement with the conclusions drawn by Alstrin *et al.* [17].

The deposition of InAs was performed under the following growth conditions: the As vapor pressure in the chamber was approximately equal to ~2–5×10^{-6} Torr, the rate of In flow from the effusion source was specified so that the growth rate of InAs was equal to 0.1 ML/s, and the ratio between the In and As flow rates was maintained in the range from 1 : 2 to 1 : 5. The temperature of different samples was varied from 350 to 500°C. The heteroepitaxial growth of InAs on the Si(100) surface was controlled using the RHEED patterns.

3. RESULTS AND DISCUSSION

At the early stage of the InAs deposition, the initial (2×2) diffraction pattern corresponding to the Si(100) surface changes in the same way in all the growth experiments. The superstructure reflections disappear at a deposited InAs layer thickness of ~ 1/3 ML. The deposition of ~ 2/3 ML InAs results in a weakening and smearing of the main reflections and in an enhancement of the diffuse background.

Further evolution of the diffraction pattern in the course of the InAs deposition is governed by the sample temperature. At 400°C and lower temperatures, the point reflections appeared almost simultaneously with a weakening of the main reflections. In the range from 410 to 440°C, the point reflections became noticeable when the thickness of the InAs layer on Si was equal to 2–20 ML. Note that, as the upper limit of this temperature range was approached, the point reflections became less pronounced and the amount of deposited InAs necessary for their appearance must be increased. For the samples heated above 450°C, no point reflections were observed even after deposition of several tens of InAs monolayers. In this case, the RHEED pattern exhibits a specular reflection against the background of strong diffuse scattering.

The appearance of point reflections in the RHEED patterns (Figs. 3, 4) unambiguously indicates the three-dimensional character of InAs growth. An analysis of the geometry of the diffraction patterns along different directions showed that the lattice spacing of deposited InAs corresponds to the lattice spacing of the bulk material and the lattice orientation coincides with the orientation of the Si substrate. Along the [011] direction, there appear point reflections and, simultaneously, diffraction lines corresponding to a faceted surface with

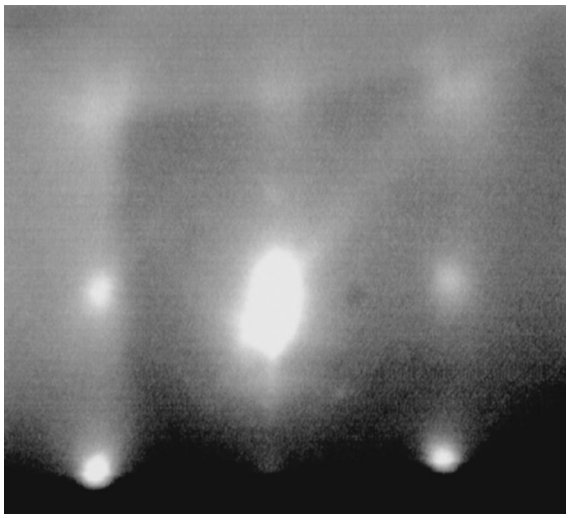

Fig. 4. RHEED pattern of the surface of the InAs/Si(100) structure. The number of InAs monolayers deposited at 400°C is 4. The electron energy is equal to 10 keV. The electron beam is incident along the [010] direction.

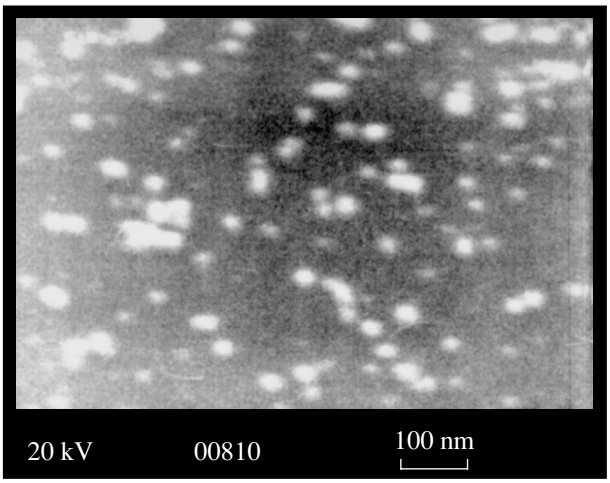

Fig. 5. SEM image of the surface of the InAs/Si(100) structure. The number of InAs monolayers deposited at 400°C is 4. Image sides are parallel to the [011] and [0 –11] directions.

{111} microfaces. The diffraction patterns of the samples grown at temperatures below 400°C also exhibit the main and superstructure reflections associated with the Si(100) surface. The RHEED patterns of the samples deposited at higher temperatures involve only the point reflections of InAs. Figure 5 displays the SEM image of the surface that is typical of InAs/Si(100) structures. Nanoobjects formed on the initially smooth surface are clearly distinguished in the SEM image. The foregoing allows us to make the inference that the three-dimensional relief arising upon InAs deposition on the Si(100) surface at temperatures of 350–430°C is formed by an array of InAs nanoislands in the form of tetrahedral pyramids with lateral faces parallel to the {111} planes. The lateral sizes and the surface density of three-dimensional islands were estimated from the SEM data at ~200–400 Å and ~$1–3 \times 10^{10}$ cm^{-2}, respectively. The islands in the form of regular tetragonal pyramids faceted by the {111} planes are easily calculated to have a height of ~140–280 Å. From these estimates, it follows that the total number of InAs molecules in islands is equal to $(1–7) \times 10^{15}$ per square centimeter and the fractional coverage of the substrate surface is 10–60%.

It should be noted that even the deposition of less than 1.0 ML InAs leads to a considerable change in the initial (2×2) diffraction pattern. Most likely, this is caused by the aforementioned difference between the lattice parameters of components in the InAs/Si heterostructure. The 1.0-ML-thick InAs islands occupying slightly more than 1/3 of the area induce elastic stresses in the surface layer, which results in disappearance of the ordered reconstruction of the Si(100) surface. Upon deposition of 2/3 ML InAs, the crystal lattice of the Si surface layer is distorted to a depth of several monolayers. This is accompanied by a weakening of the main reflections and an enhancement of the diffuse background.

Thus, from the above analysis of the RHEED patterns, we can draw the inference that the critical thickness at which the deposited InAs layer undergoes transformation depends on the deposition temperature. At 400°C and lower temperatures, the nanoislands are formed directly on the Si surface. In this case, owing to the partial release of elastic stresses, open Si surface regions contribute to the diffraction pattern and are responsible for the main and superstructure reflections. At temperatures in the range 410–430°C, the nanoislands grow above the wetting InAs layer. This layer is pseudomorphic and merely enhances the total diffuse background during electron diffraction. The deposition at temperatures above 440°C results in the growth of the InAs layer with a disordered crystal lattice (the evaporation rate of stoichiometric InAs at 440–500°C is substantially less than 0.1 ML/s [18]) without the formation of nanoislands.

Investigation of InAs/Si(100) structures by medium-energy ion scattering made it possible to obtain both information supporting the inferences drawn on the basis of the RHEED study and new data on the InAs nanoclusters.

The MEIS spectra of one of the studied samples are depicted in Fig. 6. The He^+ ions with initial energy E_0 = 96 keV were used as probing particles. The scattering angle was equal to 120°. Channel no. 329 corresponds to the initial energy E_0. Figure 6 shows two experimental spectra measured in channeling (*I*) and random (*II*) geometries. In the former case, the ion-beam direction coincided with the [100] axis of the Si single-crystal substrate. There are a number of points to be made. The

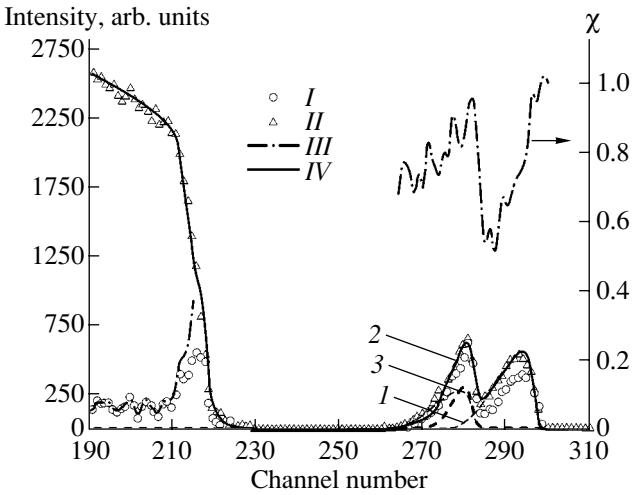

Fig. 6. MEIS spectra of the InAs/Si(100) structure: (*I*) channeling spectrum, (*II*) random spectrum, (*III*) minimum yield χ_{min}, (*IV*) simulated spectrum, (*1*) partial spectrum of In, (*2*) partial spectrum of As, and (*3*) partial spectrum of excess arsenic.

intensity ratio of the channeling and random spectra or the minimum yield χ_{min} (the dot-dashed line in Fig. 6) for the spectral portion corresponding to the Si surface layers (channel nos. 190–210 in Fig. 6) is equal to 5%, which is characteristic of a good Si single crystal. Channeling is also observed in the spectral portions corresponding to In and As (channels no. 260–300). This suggests an ordered crystal structure of nanoclusters. Note that the minimum yield $\chi_{min} = 0.75$–0.85 for the peak associated with the ion scattering by As atoms (channel nos. 280–285) exceeds the minimum yield $\chi_{min} = 0.55$–0.75 for the peak attributed to the ion scattering by In atoms (channel nos. 285–300). These findings can be explained only by the fact that a number of As atoms are not involved in the composition of InAs single crystals and form a polycrystalline or amorphous phase. This agrees with the fact that the amplitude ratio of the peaks corresponding to scattering by As and In atoms is close to unity, whereas, for the InAs single crystal, it should be equal to the ratio of the nuclear charges squared, i.e., 0.45. Consequently, we can assume that excess amorphous As is deposited on the surface upon cooling of the sample.

More detailed information on the structure of InAs clusters can be obtained from the simulation, i.e., comparison of the calculated and experimental spectra. In some cases, only the simulation makes it possible to draw unique inferences. The simulated spectrum that is in best agreement with the experimental spectrum is depicted by the solid line in Fig. 6. The dashed and dotted lines indicate the partial spectra of In (curve *1*) and As (curves *2*, *3*). The spectrum of As is represented as the sum of two components, namely, spectrum *2* corresponding to stoichiometric arsenic in the InAs compound and spectrum *3* corresponding to excess arsenic. The amount of excess arsenic was estimated at 2.6×10^{14} atoms/cm^2. We considered two variants of the structure of the excess arsenic. In the first case, the excess arsenic formed a monolayer on the sample surface. This variant led to a considerable discrepancy between the calculated and experimental spectra. In the second case, the structure of the excess arsenic was simulated in the form of islands having a mean thickness of 8.8×10^{15} atoms/cm^2 and occupying 3% of the substrate surface. The latter variant provided good agreement with the experimental spectrum.

The results of simulation can be summarized as follows. (i) The InAs clusters occupy 7% of the substrate surface. (ii) The mean cluster thickness is determined to be $h_{mean} = 8.4 \times 10^{15}$ InAs molecules/cm^2, which corresponds to 47 Å for single-crystal InAs. (iii) The scatter in the thicknesses is evaluated to be $\sigma = 7 \times 10^{15}$ molecules/cm^2 [19]. It follows from these data that the total amount of InAs in the clusters is equal to 6×10^{14} molecules/cm^2.

The relationship $h_{mean} \cong \sigma$ agrees with the above inference regarding the pyramidal shape of the clusters. Under this assumption, it is possible to determine the total height of the pyramids, which is equal to $3h_{mean}$, i.e., approximately 150 Å.

Therefore, the results obtained in the analysis of the MEIS spectra are in reasonable agreement with the above estimates made for the geometric parameters of clusters on the basis of the SEM and RHEED data.

The overgrowth of InAs nanoclusters with an Si layer was investigated under the conditions corresponding to the maximum and minimum As vapor pressures in the growth chamber: ~10^{-6} Torr in the first series of experiments (as in the case of the InAs deposition) and lower than 10^{-8} Torr in the second series of experiments (as for the Si homoepitaxy). The substrate temperature and the Si deposition rate for all samples were equal to 400°C and 1.0 Å/s, respectively. A relatively low substrate temperature for the silicon molecular-beam epitaxy during overgrowth was chosen in order to avoid undesirable processes, such as thermal decomposition of InAs and interdiffusion of heterosystem components.

In the first series of experiments, an Si layer up to 400 Å in thickness was grown immediately after InAs deposition. The growth was attended by an insignificant change in the point reflections in the RHEED pattern. The Si deposition led to an increase in the intensity of the background associated with the diffuse scattering and to smearing of the point reflections.

In the second series of experiments, the samples were overgrown with Si after reducing the background arsenic pressure. The holding of the InAs/Si(100) structures for several tens of minutes at a temperature of 400°C and a pressure lower than the growth pressure by several orders of magnitude was not accompanied by a noticeable change in the diffraction pattern. Under these conditions of the overgrowth of InAs clusters, the point reflections in the diffraction patterns were observed only at the early stage. Then, the Si deposition

led to a weakening of point reflections and the appearance of the main reflections. As a result, the diffraction pattern corresponding to the (1×1) structure of the Si surface was observed at an Si layer thickness of ~150 Å (Fig. 7). It should be noted that the diffraction patterns do not contain superstructure reflections but involve more intense main reflections, which form the pattern typical of diffraction by a three-dimensional crystal lattice of silicon.

The overgrowth of InAs nanoclusters was also investigated by medium-energy ion scattering. Figure 8 depicts the fragments of the MEIS spectra (He^+ ions, $E_0 = 191$ keV) of the initial uncovered sample (curve *1*) and the samples with Si overlayers ~50 Å (curve *2*) and ~130 Å (curve *3*) thick. Only the signals (peaks) corresponding to ion scattering by In atoms are shown. The specific feature of spectrum *1* is that the slope of the ascending Branch (channel nos. 585–595) is considerably larger than the slope of the descending Branch (channel nos. 565–580), which suggests that InAs clusters are pyramidal in shape. The data presented in Fig. 8 indicate that, at an Si overlayer thickness of ~50 Å, the InAs islands are incompletely covered with silicon and partially extend above the surface. This can be judged from the coincidence of the initial points (channel no. 593) of the ascending Branches of spectra *1* and *2*. At the same time, the shift in the upper part of the ascending Branch of spectrum *2* with respect to spectrum *1* (channel nos. 580–585) is caused by the partial coverage of InAs nanoclusters with silicon. For an Si overlayer thickness of ~130 Å (spectrum *3*), no indium occurs on the surface, because the peak is shifted toward the low-energy range. By using the simulation, it is possible to show that the spectrum of In (spectrum *3*) in which the slope of the ascending Branch (channel nos. 560–580) is substantially smaller than the slope of the descending Branch (channel nos. 550–560) corresponds to the situation where the pyramidal islands are completely covered with silicon and the overlayer surface is smooth and does not follow the relief of the initial structure.

In the third and fourth series of experiments, InAs was not deposited. The Si(100) substrates were exposed to an As flow from the effusion source at a background pressure of $\sim 10^{-6}$ Torr in the chamber, followed by Si homoepitaxy under the conditions corresponding to the overgrowth of InAs nanoclusters in the first and second series of experiments.

At a pressure of $\sim 10^{-9}$ Torr in the chamber, the homoepitaxial growth of silicon proceeded through the two-dimensional mechanism. The observed diffraction patterns exhibited a (2×2) structure. According to the SEM data, the surface remained microscopically smooth. An increase in the background arsenic pressure to $\sim 10^{-6}$ Torr led to three-dimensional growth. A three-dimensional relief was observed in the SEM images (Fig. 9). The RHEED patterns showed almost point reflections [15].

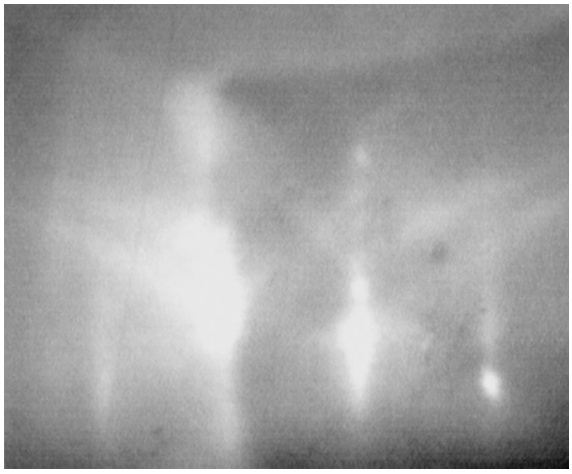

Fig. 7. RHEED pattern of the surface of the Si/InAs/Si(100) heteroepitaxial structure. The number of InAs monolayers deposited at 400°C is 4. The Si overlayer 200 Å thick is grown at 400°C and a background pressure of 9×10^{-9} Torr. The electron energy is equal to 10 keV. The electron beam is incident along the [011] direction.

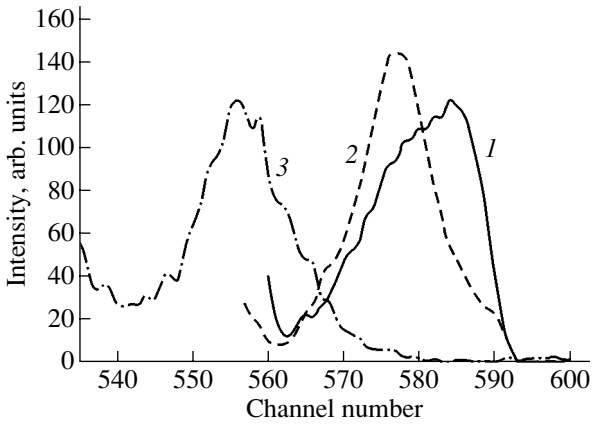

Fig. 8. Fragments of the MEIS spectra (ion scattering by In atoms) of (*1*) the uncovered InAs/Si(100) heteroepitaxial structure and the Si/InAs/Si(100) heteroepitaxial structures with Si overlayers (*2*) ~50 and (*3*) ~130 Å thick.

The MEIS investigation into the formation of the Si layer covering the InAs nanoclusters revealed that the relative concentration of arsenic in this layer can be as high as 6.5% depending on the growth conditions (primarily, on the silicon substrate temperature). Figure 10 shows the MEIS spectra of the sample that does not involve InAs clusters, i.e., that was prepared through the deposition of silicon onto the clean Si(100) substrate under exposure to an As flow. The spectra depicted in Fig. 10 were recorded for two orientations of the probing beam: (i) the beam incident along the [100] direction of the normal to the Si substrate surface (channeling spectrum *I*) and (ii) the beam deviating from this direction by angles larger than 9° (random spectrum *II*). The solid lines represent the simulated

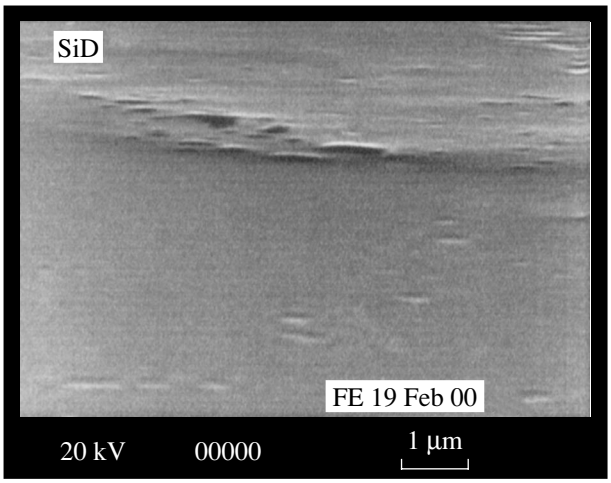

Fig. 9. SEM image of the surface of the Si homoepitaxial layer grown in the presence of background arsenic. The thickness of the Si layer deposited at 400°C is equal to 130 Å. Image sides are parallel to the [011] and [0 –11] directions.

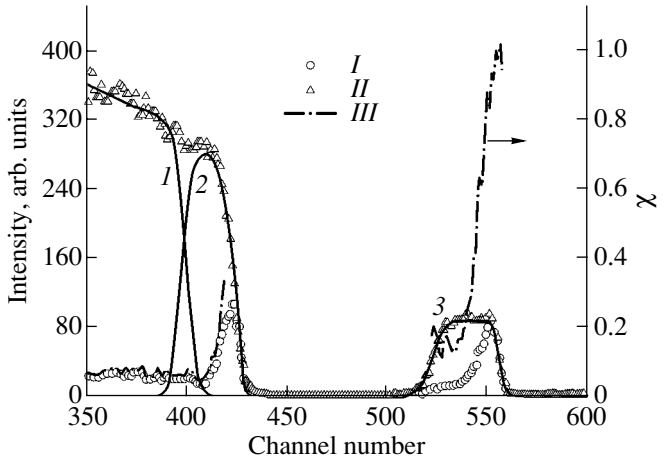

Fig. 10. MEIS spectra of homoepitaxial silicon grown in the presence of background arsenic: (*I*) incidence of the ion beam along the [100] direction of an Si single crystal, (*II*) random (nonchanneling) direction of incidence of the ion beam, and (*III*) the intensity ratio of the channeling and random spectra. Solid lines are the simulated spectra of (*1*) the silicon substrate, (*2*) homoepitaxial silicon, and (*3*) As atoms.

partial random spectra of the substrate (spectrum *1*), the deposited Si layer (spectrum *2*), and As atoms (spectrum *3*). Analysis of the spectra allows us to make the following inferences.

(1) The minimum yield χ_{Si} for the grown Si layer is approximately equal to 5%, which corresponds to a good Si single crystal.

(2) In the Si layer, As atoms are characterized by the channeling with the minimum yield $\chi_{As} \sim 15\%$, which suggests that As atoms are incorporated into the Si matrix. This assumption is confirmed by the results of investigation into the dependence of the yield of backscattered ions on the angle between the beam direction and the [100] crystallographic direction of the sample (with the use of the electrostatic analyzer tuned to channel no. 530).

(3) No channeling effect is observed for the initial (closest to the surface) portion of the spectrum of As (channel nos. 540–555). This can be explained by the fact that this portion of the spectrum corresponds to As atoms deposited on the Si layer from the background atmosphere after the growth is complete. This inference is supported by the results obtained for the Si layer grown at higher temperatures, in which the concentration of As atoms incorporated into the Si lattice is several orders of magnitude lower (see table) while the intensity of the peak attributed to the As surface is close in magnitude.

The characteristics of a number of samples with an Si overlayer grown at different substrate temperatures T_s and background arsenic pressures P_{As} are listed in the table. The parameters used are as follows: the relative atomic concentration of arsenic n_{As}/n_{Si}, the minimum yield χ_{Si} characterizing the ordering of the crystal lattice of the Si layer, the minimum yield χ_{As} characterizing the incorporation of As atoms into the Si lattice, and the silicon layer thickness d_{Si}.

The data presented in the table demonstrate that, at identical background arsenic pressures, an increase in the substrate temperature used during growth of the Si

Characteristics of the Si overlayer grown under different conditions

Sample no.	T_{sub}, °C	P_{As}, Torr	n_{As}/n_{Si}	χ_{Si}	χ_{As}	d_{Si}, nm
1	700	1.2×10^{-9}	1.4×10^{-4}	0.033	0.44	17.0
2	700	1.0×10^{-8}	3.0×10^{-4}	0.034	0.27	17.0
3	600	1.0×10^{-8}	3.4×10^{-4}	0.048	0.41	27.0
4	550	1.0×10^{-8}	4.0×10^{-4}	0.025	0.21	>27
5	400	3.4×10^{-7}	6.5×10^{-2}	0.040	0.15	10.8
6	400	7.1×10^{-8}	1.0×10^{-2}	0.040	0.20	13.6
7	400	5.3×10^{-9}	0.5×10^{-2}	0.025	0.20	12.8

layer results in a sharp (by two orders of magnitude) decrease in the number of As atoms incorporated into the Si lattice. As follows from our data, the quality of the crystal structure of the Si layer is virtually independent of the temperature.

Therefore, the overgrowth of InAs nanoclusters with silicon is epitaxial in character and occurs with a gradual smoothing of the initial three-dimensional relief. It is clear that the height of InAs pyramids in the samples of the second series does not exceed 150 Å. The three-dimensional relief and the strong diffuse background in the RHEED patterns of the samples of the first series are associated with the influence of As vapors on the growth of the Si overlayer.

The thermal stability of the InAs/Si(100) structures was studied at an As vapor pressure of ~10^{-6} Torr, which corresponds to the conditions of InAs deposition in our experiments. The results obtained demonstrate that the temperature of thermal dissociation of the deposited InAs on the Si(100) surface is higher than that of the bulk InAs. Actually, with an increase in the temperature above 500°C, a (2 × 4) diffraction pattern of an atomically smooth As-terminated InAs(100) surface transforms for a minute into a diffraction pattern with point reflections and then the intensity of the RHEED pattern decreases considerably. For InAs/Si(100) structures with an array of coherent InAs nanoclusters, the diffraction pattern with point reflections remains unchained up to 540°C. With a further increase in the temperature, the point reflections are smeared and completely disappear at 560–590°C; as a result, there appears the (2 × 2) RHEED pattern corresponding to the pattern of the Si(100) surface. The diffraction pattern of the samples with a continuous InAs layer deposited at temperatures above 440°C changes in the same manner upon heating. According to the RHEED data, the InAs layer remains stable up to 540°C. At higher temperatures, the intensities of the diffuse background and the specular reflection in the diffraction pattern decrease and the (2 × 2) pattern of the Si(100) surface appears at 560–590°C. The same temperatures were obtained by Oostra *et al.* [20], who applied the thermally stimulated desorption technique to investigate the adsorption and desorption of indium on an Si(100) surface partially covered with arsenic.

The thermal stability of the Si/InAs/Si(100) overgrown structures was investigated upon short-term (for ~ 10–20 min) annealing at 700°C. We studied the samples with the Si overlayer grown at low (~10^{-9} Torr) and high (~10^{-7}–10^{-6} Torr) background arsenic pressures. In both cases, the diffraction patterns with point reflections and the (1 × 1) diffraction patterns transform into (2 × 2) diffraction patterns at 650°C. For a layer thickness of 50 Å, uncovered InAs islands undergo complete thermal desorption upon annealing. In the samples with an Si overlayer 150 Å in thickness, InAs nanoclusters in the Si matrix are retained and can be seen using a scanning electron microscope after annealing. This implies that an Si layer with a thickness of 100 Å or greater protects the heterostructures with InAs nanoclusters from thermal desorption in the temperature range up to 750°C.

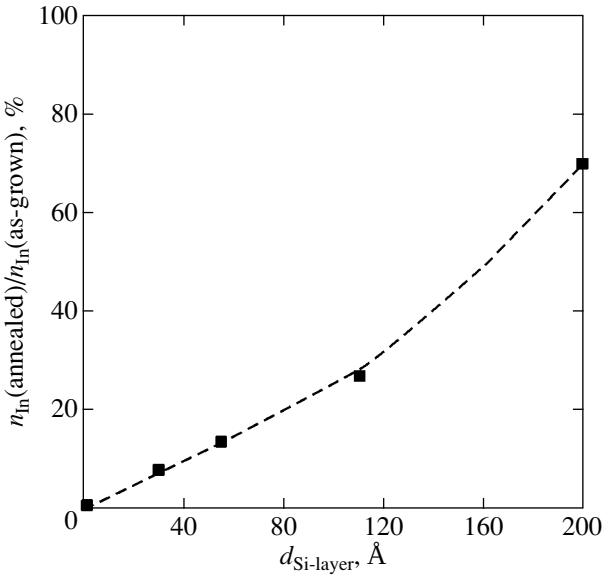

Fig. 11. Dependence of the fraction of InAs not evaporated upon annealing on the thickness *d* of the Si overlayer in the Si/InAs/Si(100) heteroepitaxial structures.

The amount of the material retained in the InAs nanoclusters after heat treatment was estimated from the integrated intensity of the peak attributed to indium in the random MEIS spectra. The results obtained are presented in Fig. 11, in which the ratios (in percent) between the amounts of indium in the annealed and unannealed structures (the amounts of as-deposited InAs and Si in the corresponding pairs of structures were identical) are plotted on the vertical axis and the thicknesses of the Si overlayer are plotted on the horizontal axis.

It can be seen from Fig. 11 that, even for the Si overlayer 200 Å thick, a substantial part (~30%) of the indium evaporates upon annealing. In our opinion, this can be explained by the following mechanism of overgrowth of InAs nanoclusters. The Si adatoms migrate over the surface, are predominantly incorporated into the crystal lattice in planar surface regions between InAs nanoclusters, occupy the initial three-dimensional surface of the InAs/Si(100) structures, and, thus, smooth down the surface. In this case, since InAs nanoclusters differ in height, the vertices of the largest clusters remain uncovered with the Si layer and these nanoclusters evaporate upon annealing. As the amount of deposited Si increases, the number of uncovered nanoclusters decreases, which leads to an increase in the fraction of indium retained after annealing.

It seems likely that morphological transformations of the surface at 650°C are caused by the thermal desorption of arsenic, because the diffraction pattern with point

reflections transforms into a (2×2) diffraction pattern at the same temperature during Si homoepitaxy at high background pressures of As vapors (~10^{-7}–10^{-6} Torr) [15].

4. CONCLUSIONS

Thus, the results obtained allowed us to draw the following inferences.

(1) Depending on the deposition conditions, the formation and growth of InAs nanoclusters in the InAs–Si heterosystem during molecular-beam epitaxy can proceed through both the Volmer–Weber mechanism, i.e., directly on the Si(100) surface (at lower temperatures), and the Stranski–Krastanov mechanism, i.e., above the wetting layer (at higher temperatures). In this case, nanoislands can be formed even when less than one InAs monolayer occurs on the surface. At temperatures above the critical point (in our case, 440°C), nanoclusters are not formed and InAs is deposited on the Si(100) surface in the form of a layer with a poorly ordered crystal lattice.

(2) The orientation of the crystal lattice in InAs nanoclusters is identical to that in the initial Si(100) substrate. The nanoclusters have the shape of regular tetragonal pyramids with {111} lateral faces. The elastic stresses caused by the mismatch between the lattice spacings of Si and InAs relax within the bulk of nanoclusters. The characteristic lateral size of nanoislands, their surface density, and the fractional coverage of the Si(100) surface upon deposition of several InAs monolayers are equal to ~200–400 Å, $1–3 \times 10^{10}$ cm^{-2}, and 10–60%, respectively.

(3) It was revealed that InAs nanoclusters grown on the Si(100) surface can be epitaxially overgrown with the formation of Si/InAs/Si(100) planar structures. In this case, the Si deposition does not occur in the form of a uniform layer but provides a gradual smoothing of the initial three-dimensional relief. The lateral faces of InAs nanopyramids are overgrown with an increase in the thickness of the Si layer on planar surface regions between nanopyramids.

(4) The structures with InAs nanoclusters embedded in the Si crystal lattice are thermally stable upon short-term (~ 10–20 min) heating to 700°C. In the course of annealing, the thermal desorption of part of the as-deposited InAs is most likely associated with the size spread of the InAs nanoclusters and, as a consequence, with the incomplete overgrowth of the highest nanoclusters.

(5) The presence of background arsenic vapors during molecular-beam epitaxy of the InAs/Si(100) and Si/InAs/Si(100) heterostructures results in the capture and incorporation of a large number of As atoms (up to 6.5% in the Si layers grown at 400°C and an As pressure of ~10^{-6} Torr) into the lattice sites of the growing Si layer and also in the precipitation of arsenic in the form of amorphous islands on the surface upon cooling.

ACKNOWLEDGMENTS

This work was supported in part by the Scientific Programs of the Ministry of Science and Technology of the Russian Federation and the Russian Foundation for Basic Research. G.É. Tsyrlin acknowledges the support of the Alexander von Humbolt Stiftug.

REFERENCES

1. N. N. Ledentsov, in *Proceedings of 23rd International Conference on Physics of Semiconductors, Berlin, 1996*, Ed. by M. Scheffler and R. Zimmermann (World Sci., Singapore, 1996), Vol. 1, p. 19.
2. G. É. Tsyrlin, V. N. Petrov, V. G. Dubrovskiĭ, *et al.*, Pis'ma Zh. Tekh. Fiz. **24** (8), 10 (1998) [Tech. Phys. Lett. **24**, 290 (1998)].
3. N. N. Ledentsov, V. A. Shchukin, M. Grundmann, *et al.*, Phys. Rev. B **54**, 8743 (1996).
4. G. E. Cirlin, V. G. Talalaev, N. D. Zakharov, *et al.*, Phys. Status Solidi B **232**, R1 (2002).
5. S. N. Newstead, R. A. A. Kubiak, and E. H. C. Parker, J. Cryst. Growth **81**, 49 (1987).
6. P. S. Kop'ev and N. N. Ledentsov, Fiz. Tekh. Poluprovodn. (Leningrad) **22** (10), 1729 (1988) [Sov. Phys. Semicond. **22**, 1093 (1988)].
7. W.-X. Ni, W. M. Chen, I. A. Buyanjva, *et al.*, J. Cryst. Growth **157**, 242 (1995).
8. C. Sasaoka, Y. Kato, and A. Usui, Appl. Phys. Lett. **62**, 2338 (1993).
9. V. V. Afrosimov, G. O. Dzyuba, R. N. Il'in, *et al.*, Zh. Tekh. Fiz. **66** (12), 76 (1996) [Tech. Phys. **41**, 1240 (1996)].
10. G. D. Wilk, Yi Wei, Hal Edwards, and R. M. Wallace, Appl. Phys. Lett. **70**, 2288 (1997).
11. E. Kasper, M. Bauer, and M. Oehme, Thin Solid Films **321**, 148 (1998).
12. A. Ishizaka and Y. Shiraki, J. Electrochem. Soc. **666**, 133 (1986).
13. T. Mano, H. Fujioka, K. Ono, *et al.*, Appl. Surf. Sci. **130–132**, 760 (1998).
14. R. I. G. Uhrberg, R. D. Bringans, R. Z. Bachrach, and J. E. Northrup, Phys. Rev. Lett. **56**, 520 (1986).
15. G. É. Tsyrlin, V. N. Petrov, N. K. Polyakov, *et al.*, Fiz. Tekh. Poluprovodn. (St. Petersburg) **33** (10), 1158 (1999) [Semiconductors **33**, 1054 (1999)].
16. A. K. Ott, S. M. Casey, and S. R. Leone, Surf. Sci. **405**, 228 (1998).
17. A. L. Alstrin, P. G. Strupp, and S. R. Leone, Appl. Phys. Lett. **63**, 815 (1993).
18. A. N. Alexeev, S. Yu. Karpov, M. A. Maiorov, *et al.*, J. Cryst. Growth **166**, 167 (1996).
19. V. V. Afrosimov, R. N. Il'in, S. F. Karmanenko, *et al.*, Fiz. Tverd. Tela (St. Petersburg) **41** (4), 588 (1999) [Phys. Solid State **41**, 527 (1999)].
20. D. J. Oostra, R. V. Smilgys, and S. R. Leone, Appl. Phys. Lett. **55**, 1333 (1989).

Translated by O. Borovik-Romanova

Physics of the Solid State, Vol. 45, No. 11, 2003, pp. 2203–2208. Translated from Fizika Tverdogo Tela, Vol. 45, No. 11, 2003, pp. 2099–2103.

LOW-DIMENSIONAL SYSTEMS AND SURFACE PHYSICS

Dielectric Multilayer Nanostructures of Tantalum and Aluminum Oxides

Yu. K. Ezhovskiĭ and A. I. Klusevich

St. Petersburg Technological Institute (Technical University), Moskovskiĭ pr. 26, St. Petersburg, 198013 Russia

Received January 22, 2003; in final form, April 4, 2003

Abstract—This paper reports on the experimental results of investigations into the mechanism of formation and dielectric characteristics of multilayer nanostructures prepared through the molecular layer-by-layer growth of tantalum and aluminum oxides. It is demonstrated that the permittivity of the multilayer nanostructures varies almost linearly with a change in the content of the components. The electrical conductivity depends on the ratio between the Al_2O_3 layer thickness d_i and the Ta_2O_5 layer thickness d_j. For a layer thickness d_i (d_j) < 5 nm, the tunneling phenomena contribute significantly to the permittivity and conductivity of these nanostructures. © *2003 MAIK "Nauka/Interperiodica".*

1. INTRODUCTION

Recent progress in nanoelectronics has been achieved in many respects owing to the considerable advances made in research into the mechanism of formation and the properties of low-dimensional systems, which, in turn, has given impetus to the development of nanotechnology for these systems. Among the large variety of methods used in the chemical nanotechnology of low-dimensional systems, the molecular layer-by-layer growth technique has enjoyed the widest application. This technique involves the growth of nanostructures due to a chemical surface reaction upon sequential introduction of reactants and makes it possible not only to control the composition and thickness of prepared nanostructures within a monolayer but also to synthesize multilayer nanostructures whose properties differ significantly from those of the constituent materials.

Multilayer nanostructures based on tantalum and aluminum oxides are very promising for use as dielectric materials in microwave technology. Moreover, they can be used in the design of metal–dielectric–semiconductor structures. For a dielectric superlattice of this type, the permittivity and distribution of the electrical potential over the layer thickness can be varied depending on the superlattice composition and the sequence of layers.

This paper reports on the results of investigations into the dielectric characteristics (such as conductivity and permittivity) of multilayer nanostructures consisting of tantalum and aluminum oxide layers of different thicknesses.

2. SAMPLE PREPARATION AND EXPERIMENTAL TECHNIQUE

Multilayer nanostructures composed of tantalum and aluminum oxide layers of different thicknesses were prepared using the molecular layer-by-layer growth technique. The layer thickness was determined by measuring the elliptic polarization angles Δ and Ψ and was then calculated in the framework of the Drude–Tronston single-layer model [1]. The angles Δ and Ψ were measured on an ellipsometer assembled according to the PQSA scheme [2] with a static compensator. An LG-75 laser with an emission wavelength of 632.8 nm served as a source of linearly polarized light. In order to increase the accuracy of measurement, the light beam was subjected to magnetic modulation. The error in determining the angles Δ and Ψ did not exceed $\pm 0.01'$.

The composition of ultrathin layers was controlled using x-ray photoelectron spectroscopy. The x-ray photoelectron spectra were recorded on NR-5950A (AlK_α radiation, $E_{K\alpha}$ = 1486 eV) and SÉR-1 (MgK_α radiation, $E_{K\alpha}$ = 1253 eV) spectrometers. The energy was measured with respect to the C $1s_{1/2}$ line (E_{st} = 285.0 eV). The maximum depth of penetration of the probe into the surface layer at the above energies did not exceed 8 nm [3]. The assignment of the lines observed at energies E_s in the x-ray photoelectron spectra was performed according to the data taken from [4, 5]. For quantitative analysis of the composition of the surface layers, we used the relationship [3]

$$\frac{I_1}{I_2} \approx \frac{n_1\sigma_1\sqrt{E_{K2}}}{n_2\sigma_2\sqrt{E_{K1}}}, \quad (1)$$

where I_1 and I_2 are the intensities of the lines of aluminum and tantalum atoms, respectively; σ_1 and σ_2 are the

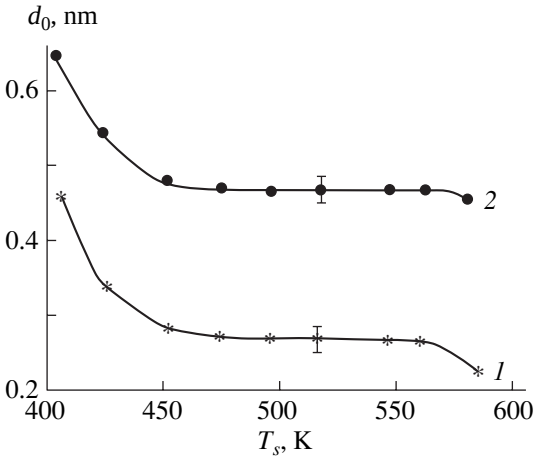

Fig. 1. Dependences of the growth parameter for (*1*) tantalum and (*2*) aluminum oxide layers on the synthesis temperature.

relative ionization cross sections of the corresponding energy levels; n_1 and n_2 are the concentrations of aluminum and tantalum atoms, respectively; and E_{K1} and E_{K2} are the kinetic energies of electrons of aluminum and tantalum atoms, respectively. Here, $E_K = E_{K\alpha} - E_s - \varphi_s$, where φ_s is the work function of the spectrometer material. The spectra were processed with a special computer program using the Gaussian approximation of the curves. Moreover, the composition of the layers was controlled ellipsometrically against the refractive indices, which were determined by the Holmes method [2].

The nanostructures were prepared using sequential treatment of the surfaces of KÉF-7.5 silicon(100), aluminum, and tantalum matrices in vapors of halides of the corresponding metal (P = 1–10 Pa) and water ($P \sim$ 100 Pa) in a vacuum–flow-type chamber. The residual pressure was no higher than 10^{-1} Pa. Metallic substrates in the form of 0.1- to 0.2-μm-thick films of aluminum or tantalum on silicon were prepared by vacuum deposition or magnetron sputtering.

The preparation of oxide layers through the molecular layer growth is based on self-organization processes of chemisorption of a metal halide and water vapors with a limiting (close to a monolayer) coverage of the surface. For example, this process on a hydroxylated silicon surface proceeds through the following reactions:

$$(\equiv\text{Si–OH})_m + Me\text{Cl}_n \longrightarrow (\equiv\text{Si–O–})_m Me\text{Cl}_{n-m} + m\text{HCl}, \quad (I)$$

$$(\equiv\text{Si–O–})_m Me\text{Cl}_{n-m} + (n-m)\text{H}_2\text{O} \longrightarrow (\equiv\text{Si–O–})_m Me(\text{OH})_{n-m} + (n-m)\text{HCl}. \quad (II)$$

Reactions (*I*) and (*II*), when repeated as many times as necessary, result in the formation of an oxide layer of a specified thickness d. As was shown earlier by Kol'tsov *et al.* [6, 7], the thickness d is proportional to the number of cycles N of surface treatment:

$$d = d_0 N, \quad (2)$$

where d_0 is the proportionality coefficient, which characterizes the structure of the prepared layer and corresponds to the film thickness averaged over one complete cycle of treatment with both components.

Relationship (2) is characteristic of processes of chemical assembly [8]. Experimental verification of this relationship for multilayer structures was carried out using the example of alternating layers of silicon and titanium oxides [8] and chalcogenide structures [9] on a silicon surface.

The coefficient d_0 is referred to as the layer growth parameter. This parameter is an important characteristic of the process and makes it possible to evaluate the coverage of the surface, which serves as a guideline in elucidating the mechanism of formation of nanostructures. At present, particular interest has been expressed by researchers in the layer mechanism of formation of nanostructures. The formation of nanostructures through the layer mechanism occurs upon complete hydroxylation of the surface and under nonequilibrium conditions of the proceeding reactions (*I*) and (*II*). These conditions can be provided by rapid elimination of liberated hydrogen chloride in combination with a sufficiently high reactivity of OH groups of the hydroxylated surface. Earlier [10, 11], it was demonstrated that hydroxyl groups on a silicon surface with an oxide layer thinner than 1 nm exhibit weak proton-donor properties. Taking into account these results, the activation of the surface reactions of aluminum and tantalum halides with hydroxyl groups was carried out with an exchange activator, namely, triethylamine. Owing to its well-pronounced proton-acceptor properties, triethylamine stabilized the hydroxylated surface via hydrogen bonds, activated the surface reaction due to the formation of an intermediate complex, and bound hydrogen chloride. A similar situation most likely occurs with a metallic matrix involving a thin oxide layer. In this case, the inhibiting effect caused by the electron-saturated metallic matrix also decreases the proton-donor ability of the hydroxyl groups. In the course of the synthesis, triethylamine (incapable of entering into nucleophilic substitution reactions) was introduced together with water vapors $\text{H}_2\text{O} + \text{N}(\text{C}_2\text{H}_5)_3$.

From analyzing the dependences of the layer thickness on the number of cycles of surface treatment $d = f(N)$ at different substrate temperatures T_s for Al_2O_3 and Ta_2O_5 layers, we determined the growth parameter d_0 involved in expression (2) for each temperature T_s. Moreover, it was established that, in the temperature range T_s = 443–553 K, the formation of nanostructures occurs through the layer mechanism (Fig. 1). Under these conditions, the growth parameter d_0 was found to be approximately equal to double the metal–oxygen interplanar spacing typical of the given oxide. It turned

out that the growth parameter d_0 for aluminum oxide exceeds the growth parameter for tantalum oxide. This can be associated with the chemisorption of an Al_2X_6 dimer (X = Cl, Br) in different orientations [12], which, in turn, brings about the formation of bimolecular layers. In all cases, the coverage of the silicon surface with hydroxyl groups ensured bonding with no more than two hydroxyl groups of the surface [11]. It is worth nothing that the vapor pressures of tantalum and aluminum halides are close to each other. Moreover, the temperature conditions of layer growth of the tantalum oxide system are similar to those of the aluminum oxide system. This circumstance considerably simplified the synthesis of multilayer nanostructures based on tantalum and aluminum oxides, which required heating the whole system for supplying reactants into the reaction chamber to a temperature of the vapor source.

It should be noted that the preparation of aluminum oxide layers through treatment of the tantalum oxide surface in aluminum halide vapors can be accompanied by the substitution reaction

$$Ta_2O_5 + AlX_3 \longrightarrow Al_2O_3 + TaX_5. \qquad (III)$$

In this case, we evaluated the thermal effects and calculated the equilibrium constants $K_{f,T}$ according to the Temkin–Schwartzman method in terms of the equations for the thermodynamic potential: $\Delta G_T = 2.3RT\log K_{f,T}$ and $\Delta G_T^0 = \Delta H_T^0 - T\Delta S_T^0$.

The calculations performed for aluminum chloride and aluminum bromide showed that the substitution reaction is virtually ruled out when the molecular layer-by-layer growth of multilayer structures occurs at $T_s <$ 470 K for $AlBr_3$ and $T_s < 600$ K for $AlCl_3$. Making allowance for these conditions, we prepared layers with the use of tantalum and aluminum chlorides at T_s = 473 K, which corresponds to the layer growth conditions of each component of the multilayer nanostructure (Fig. 1).

3. RESULTS AND DISCUSSION

The ellipsometric investigation into the growth kinetics of the multilayer nanostructures demonstrated that, for all the studied matrices, the dependence $d = f(N)$ at parameters $d_0 \approx 0.3$ nm for Ta_2O_5 and $d_0 \approx 0.45$ nm for Al_2O_3, which are characteristic of the layer growth of these oxides, remains linear within a layer (Fig. 1). Figure 2 depicts the dependences of the thickness of multilayer oxide nanostructures prepared on a silicon surface on the number of cycles N of layer growth. As can be seen from Fig. 2, the thickness of the multilayer nanostructure varies in proportion to the growth parameter for both oxides. Hence, it can be concluded that the multilayer nanostructures are formed through the layer mechanism irrespective of the number of growth cycles and that no diffusion processes leading to mixing occur. This inference is confirmed by the results of x-ray photoelectron and Auger spectro-

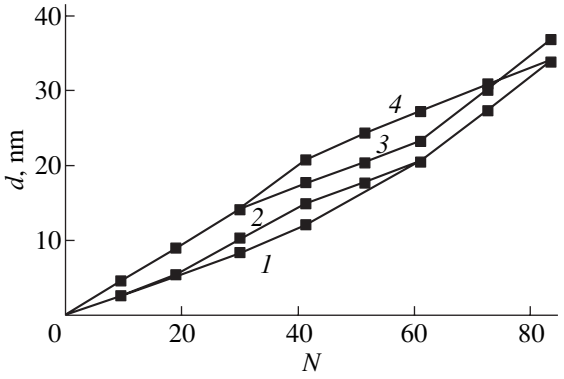

Fig. 2. Dependences of the thickness of multilayer oxide nanostructures prepared at T_s = 473 K on the number of cycles N of layer growth: (*1*) $40Ta_2O_5 + 40Al_2O_3$, (*2*) $20Ta_2O_5 + 20Al_2O_3 + 20Ta_2O_5 + 20Al_2O_3$, (*3*) $30Al_2O_3 + 30Ta_2O_5 + 20Al_2O_3$, and (*4*) $40Ta_2O_5 + 40Al_2O_3$.

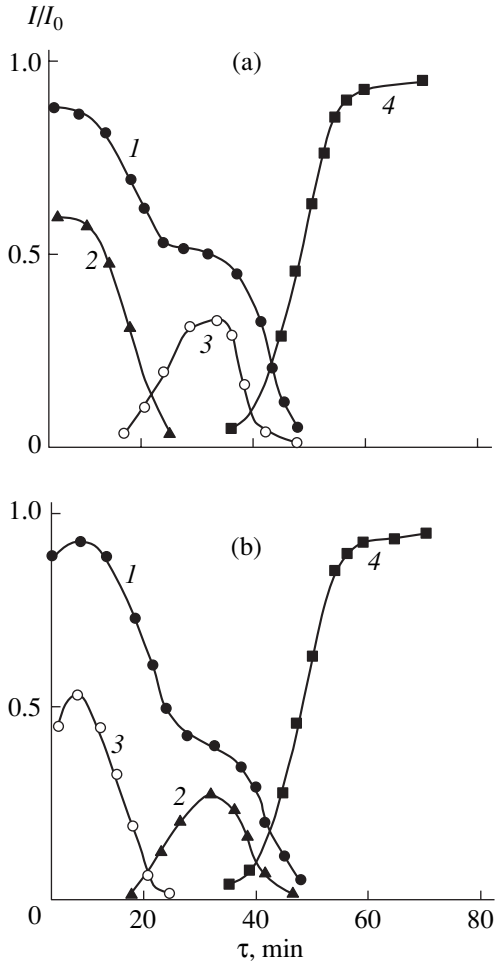

Fig. 3. Variation in the intensity of Auger signals of (*1*) oxygen, (*2*) aluminum, (*3*) tantalum, and (*4*) silicon upon layer-by-layer etching of (a) Si–Ta_2O_5–Al_2O_3 and (b) Si–Al_2O_3–Ta_2O_5 nanostructures with a layer thickness of approximately 10 nm.

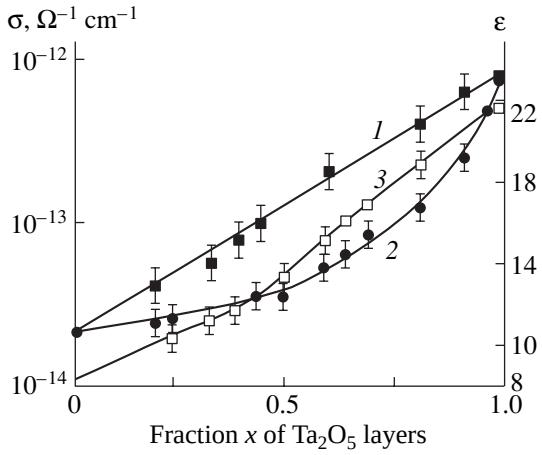

Fig. 4. Dependences of (*1*, *2*) the conductivity and (*3*) the permittivity of the Al_2O_3–Ta_2O_5 multilayer nanostructure on the fraction x of Ta_2O_5 layers at a total thickness $d \approx 40$ nm: (*1*) d_i (d_j) ≥ 5 nm and (*2*) d_i (d_j) ≈ 1 nm.

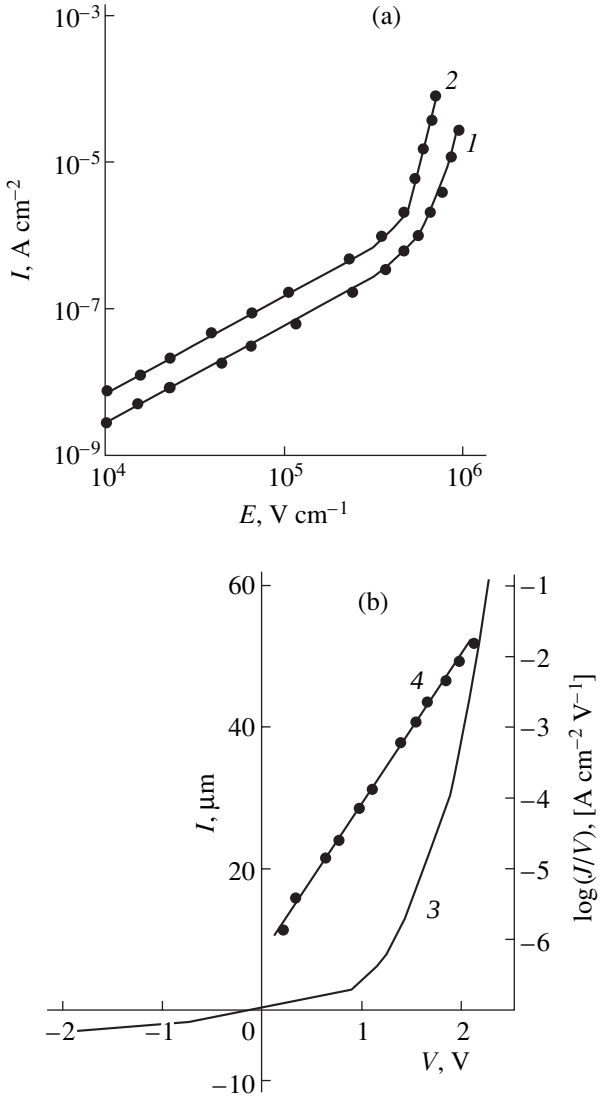

Fig. 5. Current–voltage characteristics (a) in the coordinates I–E for (*1*) Al_2O_3 (d = 20 nm) and (*2*) Ta_2O_5 (d = 20 nm) nanostructures and (b) in the coordinates (*3*) I–V and (*4*) $\log(J/V)$–V for the Ta–Al_2O_3–Ni tunneling nanostructure with a dielectric layer thickness d = 5 nm and sign "±" at the nickel electrode.

scopic investigations into the composition and distribution of elements over the layer thickness for Si–Al_2O_3–Ta_2O_5 and Si–Ta_2O_5–Al_2O_3 bilayer structures with a layer thickness not exceeding 20 nm. It turned out that the x-ray photoelectron spectra do not exhibit maxima characteristic of halogens and silicon. This indicates that, in our case, the surface reactions proceed to completion and the prepared layers of the specified thickness are continuous.

The x-ray photoelectron spectra of the multilayer nanostructures prepared contain lines at energies E_s = 118.9 and 74.8 eV, which correspond to the Al 2*s* and Al 2*p* levels, and lines at energy E_s = 26.8 eV, which is characteristic of the Ta 4*f* level.

The Auger electron spectra were recorded upon layer-by-layer etching with argon ions. The etching rate was equal to 0.5 nm/min. An analysis of the Auger electron spectra (Fig. 3) revealed that, for nanostructures (d_0 > 10 nm) prepared at T_s = 473 K, the distribution of tantalum and aluminum corresponds to the sequence of their oxide layers. It should be noted that, upon preparation of multilayer nanostructures at T_s = 573 K with the use of aluminum bromide, the distribution of tantalum and aluminum corresponds to a greater extent to a mixture of their oxides. This confirms the correctness of the estimate obtained for the synthesis conditions from the change in the thermodynamic potential of the system.

As can be seen from Fig. 3, the signal associated with the silicon matrix is observed only after etching for 40 min. This is in good agreement with the total thickness of the oxide structure for a given eating rate. For aluminum and tantalum matrices, the formation of multilayer nanostructures proceeds in a similar way.

An analysis of the Auger electron spectra demonstrated that, unlike the oxide mixtures, the materials prepared are characterized by a zonal distribution of each metal (Fig. 3). Therefore, these materials should exhibit a number of specific properties, the most important among which are permittivity, conductivity, and electric strength.

The electrical properties of nanostructures were investigated using the example of Al(Ta)–Al_2O_3(d_i)–Ta_2O_5(d_j)–Ni and Si–Al_2O_3(d_i)–Ta_2O_5(d_j)–Ni structures synthesized at T_s = 453 K. For these nanostructures, we varied the Al_2O_3 layer thickness d_i, the Ta_2O_5 layer thickness d_j, and the sequence of layers. The total thickness of each nanostructure ranged from 50 to 60 nm. The influence of high-temperature treatment (at T = 873 K)

Permittivities ε of Al_2O_3–Ta_2O_5 multilayer nanostructures of different compositions

Sample no.	Al_2O_3 layer thickness d_i, nm	Number n_i of Al_2O_3 layers	Ta_2O_5 layer thickness d_j, nm	Number n_j of Ta_2O_5 layers	Sequence of layers in the nanostructure	ε		
						Experiment	Calculation	Experiment after heat treatment
1	5	6	5	6	ATATATATATAT	13.6	14.8	14.8
2	10	3	10	3	ATATAT	13.7	14.8	14.7
3	25	1	25	1	AT	13.7	14.8	14.1
4	10	3	5	4	TATATAT	12.2	13.0	12.8
5	20	2	5	3	TATAT	11.2	11.7	11.2
6	20	2	10	2	TATA	12.2	13.0	12.7
7	10	2	20	2	ATAT	15.8	16.9	16.2
8	10	1	50	1	AT	18.1	19.35	18.5
9	5	3	20	2	ATATA	17.7	18.7	18.7

Designations: A is a layer of aluminum oxide, and T is a layer of tantalum oxide.

on the properties of dielectric multilayer nanostructures was examined using structures with a silicon matrix. As was noted above, the permittivity ε is an important characteristic of multilayer nanostructures. This quantity can be estimated by different techniques [13]. A comparison of the experimental data with the permittivities ε calculated according to the Landau–Lifshitz model for a statistical mixture of dielectric materials showed that, in all cases, the experimental permittivity of the multilayer nanostructure does not exceed the calculated value (see table). Therefore, the dielectric multilayer nanostructure prepared cannot be considered a mixture of oxide layers. However, after a two-hour heat treatment of multilayer nanostructures at $T = 873$ K, the experimental values of ε become close to the permittivities calculated for a mixture of dielectrics. The best agreement was achieved for samples with a small layer thickness (d_i, $d_j \cong 5$ nm) for at least one component of the multilayer nanostructure (sample nos. 1, 4, 5, 9 in table). This suggests that the diffusion processes occurring at $T = 873$ K contribute to the permittivity only for nanostructures with layers of a small thickness.

Examination of the dependence of the permittivity of multilayer nanostructures on their composition (Fig. 4, curve *3*) revealed that the permittivity ε almost linearly depends on the ratio of the components rather than on the layer thicknesses d_i and d_j. At the same time, the electrical conductivity of multilayer nanostructures is governed not only by the ratio of the components but also by the thicknesses of their constituent layers.

Let us now consider a multilayer nanostructure in the form of a chain consisting of resistors that are connected in series and possess conductivities σ_i and σ_j. For a layer thickness d_i (d_j) > 5 nm, the electrical conductivity of this nanostructure can be adequately described by the relationship for the conductivity of an equivalent circuit:

$$1/\sigma = \sum 1/\sigma_i + \sum 1/\sigma_j .$$

In this case, the electrical conductivity exhibits almost linear behavior in the $\log\sigma$–x coordinates, where x is the fraction of Ta_2O_5 layers (Fig. 4, curve *1*). When the layer thickness of at least one component of the multilayer nanostructure decreases and becomes less than 5 nm, the dependence of the electrical conductivity on the fraction x changes and gradually becomes similar to curve *2* (Fig. 4), which is characteristic of layer thicknesses d_i (d_j) ≈ 1 nm. In our opinion, the above behavior of the electrical conductivity can be associated with both the tunneling mechanism of charge transfer at d_i (d_j) < 5 nm and the formation of charge states at interfaces of the multilayer nanostructure. This assumption is confirmed by the current–voltage characteristics of oxide nanostructures (Fig. 5). It can be seen from Fig. 5a that, for nanostructures with a layer thickness d > 10 nm, the ohmic behavior of the current–voltage characteristics in weak fields ($E < 10^5$ V cm^{-1}) gives way to an exponential behavior. This dependence is typical of charge transfer occurring in disordered systems through the mechanism of electron hopping over localized states [14]. Judging from the current–voltage characteristics, the tunneling mechanism of charge transfer dominates in nanostructures with a dielectric layer whose thickness is less than 5 nm. This inference is also supported by the fact that the current–voltage characteristics are linear in the $\log(J/V)$–V coordinates, where J is the current density. Even with electrodes characterized by close values of the work functions ($\varphi_{Ni} = 4.84$ eV, $\varphi_{Ta} = 4.45$ eV [15]), the asymmetry observed in the electrical conductivity (Fig. 5b) stems from the fact that the barrier height is determined by the

charge states at the metal–dielectric interface rather than by the work function. In dielectric multilayer nanostructures, the presence of additional interfaces between oxide layers and interfaces with the metal oxide of the matrix should decrease the tunneling current.

It should be noted that, for a dielectric layer with a total thickness $d > 3$ nm, no short circuits are observed in tunneling structures, even though there exist regions with a decreased electric strength. For the multilayer nanostructures under investigation, the electric strength falls in the range from 3×10^5 (small fractions of Al_2O_3 layers) to 5×10^6 V cm^{-1} (small fractions of Ta_2O_5 layers) and depends linearly on the ratio of their constituent layers. It is established that even small fractions of aluminum oxide in the Al_2O_3–Ta_2O_5 multilayer nanostructure bring about a substantial increase in the electric strength due to the specific features of the field distribution in the system and charge states at the interfaces.

4. CONCLUSIONS

The results of the above investigations have demonstrated that, by varying the composition and the thickness ratio of the constituent layers in a multilayer nanostructure, it is possible to prepare a dielectric material that will be characterized by a conductivity and (or) electric strength of one component and a permittivity predominantly determined by another component. These nanostructures can be used as materials in micro- and nanoelectronic devices.

REFERENCES

1. R. M. Azzam and N. M. Bashara, *Ellipsometry and Polarized Light* (North-Holland, Amsterdam, 1977; Mir, Moscow, 1981).
2. V. K. Gromov, *Introduction to Ellipsometry* (Leningr. Gos. Univ., Leningrad, 1986).
3. V. I. Nefedov and V. T. Cherepin, *Physical Methods for Studying Solid Surfaces* (Nauka, Moscow, 1983).
4. V. I. Nefedov, *X-ray Photoelectron Spectroscopy of Chemical Compounds* (Khimiya, Moscow, 1984).
5. *Handbook of X-ray Photoelectron Spectroscopy* (Physical Electronics, Eden Prairie, MN, 1978).
6. S. I. Kol'tsov, G. V. Sveshnikova, and V. B. Aleskovskiĭ, Zh. Prikl. Khim. (Leningrad) **43** (5), 1150 (1970).
7. S. I. Kol'tsov, V. E. Drozd, and T. A. Redrova, Dokl. Akad. Nauk SSSR **235** (5), 1090 (1977).
8. V. B. Aleskovskiĭ, Vestn. Akad. Nauk SSSR **6**, 52 (1975).
9. V. B. Aleskovskiĭ, V. K. Adamchuk, V. E. Drozd, *et al.*, Dokl. Akad. Nauk SSSR **303** (6), 1390 (1988).
10. Yu. K. Ezhovskiĭ and P. M. Vaĭnshteĭn, Zh. Fiz. Khim. **71** (12), 2222 (1997).
11. Yu. K. Ezhovskiĭ and P. M. Vaĭnshteĭn, Zh. Prikl. Khim. (St. Petersburg) **71** (2), 227 (1998).
12. Yu. K. Ezhovskiĭ, G. V. Anikeev, and S. I. Kol'tsov, Izv. Akad. Nauk SSSR, Neorg. Mater. **24**, 619 (1988).
13. V. B. Lazarev, V. G. Krasov, and I. S. Shaplygin, *Electrical Conductivity of Oxide Systems and Film Structures* (Nauka, Moscow, 1979).
14. N. F. Mott and E. A. Davis, *Electronic Processes in Non-Crystalline Materials*, 2nd ed. (Clarendon Press, Oxford, 1979; Mir, Moscow, 1982).
15. S. M. Sze, *Physics of Semiconductor Devices*, 2nd ed. (Wiley, New York, 1981; Mir, Moscow, 1984).

Translated by O. Borovik-Romanova

Physics of the Solid State, Vol. 45, No. 11, 2003, pp. 2209–2212. Translated from Fizika Tverdogo Tela, Vol. 45, No. 11, 2003, pp. 2104–2107.

LOW-DIMENSIONAL SYSTEMS AND SURFACE PHYSICS

Radiative Transitions and Spectral-Hole Burning in MgO : Cr^{3+} Nanocrystals

R. I. Zakharchenya*, A. A. Kaplyanskiĭ*, A. B. Kulinkin*, R. S. Meltzer, and S. P. Feofilov***

**Ioffe Physicotechnical Institute, Russian Academy of Sciences, Politekhnicheskaya ul. 26, St. Petersburg, 194021 Russia*

***Georgia University, Athens, GA, 30602 USA*

Received April 28, 2003

Abstract—Luminescence spectra of Cr^{3+} ions in nanocrystalline MgO obtained by sol-gel technology were studied. The radiative lifetime of excited ^2E states of cubic and tetragonal Cr^{3+} centers was found to be considerably longer than that of bulk single crystals. This effect is caused by a modified effective refractive index of the inhomogeneous medium. Burning of long-lived spectral holes in the $^4A_2$–^2E transition profile of cubic centers was observed, which sets nanocrystalline samples strongly apart from bulk crystals, where no hole burning was found. © *2003 MAIK "Nauka/Interperiodica".*

Dielectric nanocrystals doped by rare-earth (RE) or transition metal (TM) ions are of considerable interest because of their optical properties. Impurity ions can serve as spectroscopic probes for exploring dynamic processes in nanocrystals. Another feature that attracts attention is the modification of the spectroscopic properties of impurity ions induced by spatial confinement. To date, a number of effects in optical properties that are directly associated with spatial confinement have been revealed (see [1] and references therein). Interest in the optical properties of dielectric nanocrystals doped by RE and TM ions is spurred to a considerable extent by the possible application potential of these materials. Indeed, in view of doped crystals and glasses being employed in laser technology and as luminophors, the new properties induced by nanocrystallinity may prove useful for applications.

MgO : Cr^{3+}, as well as ruby, is a classical subject in the spectroscopy of doped crystals. MgO : Cr^{3+} crystals were used in the pioneering studies of piezospectroscopic effects in spectra of impurity centers [2] and of inhomogeneous spectral-line broadening caused by two-phonon Raman processes [3]. The Cr^{3+} ions in the MgO cubic lattice substitute for Mg^{2+} ions, and the excess charge of the impurity ions needs to be compensated. The excess positive charge of $Cr^{3+}(Mg^{2+})$ in MgO : Cr^{3+} is compensated by cation vacancies. These vacancies can occupy a cation position close to the Cr^{3+} ion or be at a large distance from it. As a result, the Cr^{3+} ions in the MgO lattice form both $Cr^{3+}(Mg^{2+})$–vacancy complexes and $Cr^{3+}(Mg^{2+})$ cubic centers [2, 4, 5]. In a center with a nearby cation vacancy, the latter may be located differently with respect to the Cr^{3+} ion, which gives rise to the existence of a variety of noncubic centers (tetragonal, rhombic) differing in symmetry [4, 5]. The presence of centers of different symmetries in MgO : Cr^{3+} crystal makes it particularly attractive for spectroscopic studies. The lowest ^2E excited level of the Cr^{3+} ion in the spectra of cubic centers is not split; therefore, the spectra exhibit a single ^2E–$^4A_2$ (R) line, whereas in centers of lower symmetry the ^2E state splits into a doublet, with the spectra revealing pairs of ^2E–$^4A_2$ lines (sometimes called N lines) [4, 5].

We studied the luminescence spectra of nanocrystalline MgO : Cr^{3+} samples. The samples were prepared using sol-gel technology [6], with magnesium alkoxide used as the starting material. The final annealing was carried out at 750 or 850°C. In the course of the sol-gel process, chromium (~0.1%) was added to the samples. The samples were fine-grained powders consisting of nanocrystals merged in clusters. X-ray analysis showed (through x-ray reflection broadening) the nanocrystals in the samples to be ~5 nm in size.

Figure 1 presents a luminescence spectrum of nanocrystalline MgO : Cr^{3+} in the ^2E–$^4A_2$ transition region excited at T = 77 K by an argon laser. Also shown for comparison is the spectrum of an MgO : Cr^{3+} single crystal taken in the same conditions. The luminescence spectra are seen to be practically identical. The spectrum is dominated by lines due to cubic and tetragonal centers. The only difference is the larger inhomogeneous broadening of the ^2E–$^4A_2$ transitions in nanocrystalline MgO : Cr^{3+}, which is 0.25 nm for cubic centers, compared with 0.03 nm for the bulk sample. This broadening originates from the contribution of Cr^{3+} ions located close to the surface and/or a larger concentration of defects in the nanocrystals.

1063-7834/03/4511-2209$24.00 © 2003 MAIK "Nauka/Interperiodica"

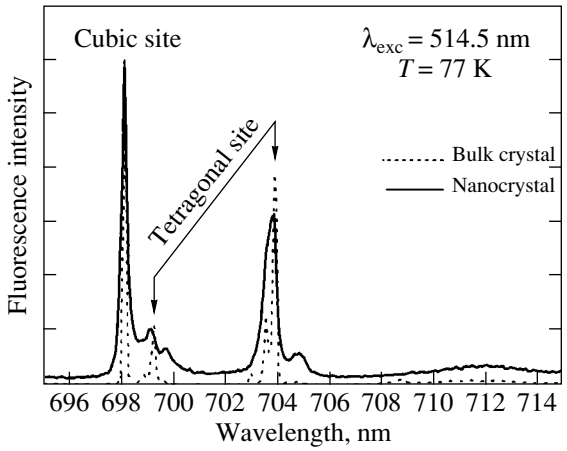

Fig. 1. ^2E–$^4A_2$ luminescence lines of Cr^{3+} ions in bulk and nanocrystalline MgO.

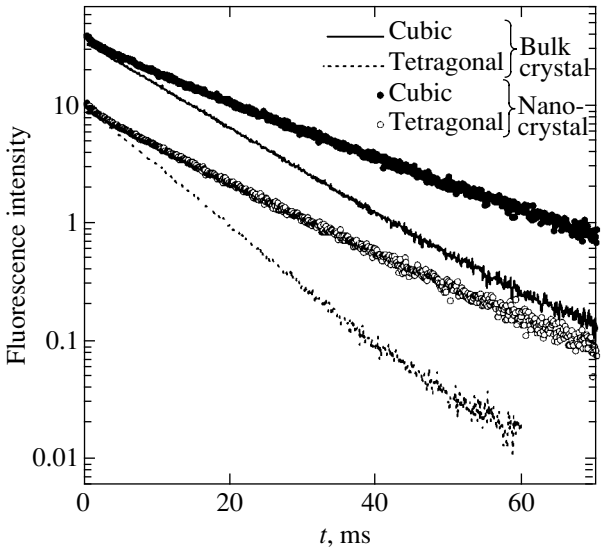

Fig. 2. Decay of ^2E–$^4A_2$ luminescence of cubic and tetragonal Cr^{3+} centers in bulk and nanocrystalline MgO. To make graphs more revealing, the intensities are shown normalized.

Figure 2 displays luminescence decay in the Cr^{3+} cubic and tetragonal centers in nanocrystalline and bulk MgO measured at the frequencies of zero-phonon ^2E–$^4A_2$ transitions at T = 77 K under modulated Ar-laser radiation. The powder samples were pressed between two thin glass plates fixed by glue around the perimeter and were isolated against penetration of liquid nitrogen. One readily sees a sharp (nearly twofold) slowing of the luminescence decay in nanocrystalline MgO.

At low temperatures, the quantum yield of Cr^{3+} fluorescence is close to unity and its decay is fully due to radiative transitions [5]. Thus, the ^2E–$^4A_2$ fluorescence decay at 77 K is dominated practically completely by radiative relaxation, with nonradiative processes being insignificant. The large difference in the radiative lifetime τ_R between the nanocrystalline and microcrystalline samples may be accounted for by the changes in the nanoparticles induced by the surrounding medium [7]. When the particle size is substantially smaller than the light wavelength, the local electric field acting on the Cr^{3+} ion is determined both by the material of the particles and by the substance filling the space between them. The radiative lifetime of an ion embedded in a medium can be written as

$$\tau_R \sim \frac{1}{f(ED)} \frac{\lambda_0^2}{\left[\frac{1}{3}(n^2+2)\right]^2 n}, \qquad (1)$$

where $f(ED)$ is the oscillator strength for an electric dipole transition, λ_0 is the wavelength of light in vacuum, and n is the refractive index. The dependence of τ_R on the refractive index n originates from (i) the change in the photon density of states in a medium with a lower velocity of light and (ii) modification of the polarizability of the medium in which the ion is embedded. Nanoparticles occupy only a fraction of the sample volume. Therefore, in order to make possible comparison of experimental data with Eq. (1), one has to introduce an effective refractive index n_{eff} of the medium consisting of MgO nanoparticles (n = 1.735) surrounded by air with a refractive index n = 1. We assume that $n_{eff}(x) = xn_{MgO} + (1 - x)$, where x (<1) is the filling coefficient specifying the fraction of space occupied by MgO nanoparticles. For the nanoparticles, n in Eq. (1) is replaced by $n_{eff}(x)$. Using n_{eff} is valid if the average nanoparticle size is far smaller than the wavelength of light; this condition is definitely met for the samples studied here.

The experimentally observed values of τ_R in nanocrystalline MgO : Cr^{3+} were 19 ms for the cubic centers and 14 ms for the tetragonal centers (compare with τ_R = 11.7 ms for the cubic centers and 8.4 ms for the tetragonal centers in bulk single crystals; see also [5]). To account for the experimentally observed increase in τ_R by a factor of approximately 1.6 for centers of both types, one has to set $n = n_{eff}$ = 1.49 in Eq. (1), which corresponds to x = 0.67 and means that MgO nanocrystals occupy 67% of the sample volume.

The use of Eq. (1) for τ_R for an electric dipole transition in cubic centers, in which Cr^{3+} ions occupy positions with inversion symmetry (O_h) and the zero-phonon line is associated with a magnetic dipole transition, requires validation. The excited-state lifetime is governed by both pure electronic and vibronic transitions. According to [8, 9], vibronic sidebands of a zero-phonon (magnetic-dipole) line in cubic centers originate from electric dipole transitions induced by the interaction with odd-parity lattice vibrations. The intensity ratio of the vibronic sideband to zero-phonon line is 4 : 1 [5]. Thus, τ_R in cubic centers is dominated by

vibronic electric-dipole transitions and, hence, the use of Eq. (1) is valid. Application of Eq. (1) to tetragonal centers, in which zero-phonon transitions are primarily of the electric-dipole type, with the addition of a magnetic-dipole component [4] is even more valid.

Our experiments provided supportive evidence for the conclusion [7] that nanocrystalline materials offer the unique possibility of modifying the refractive index of a medium without changing the local structure of the centers. This permits one to verify Eq. (1), which relates the oscillator strength to the radiative lifetime. The observed effect permitted us to determine the filling coefficient, i.e., the fraction of the sample volume occupied by nanocrystals.

The materials in which long-lived holes can be burned in inhomogeneously broadened spectra of impurity ions by a photophysical or a photochemical method are of considerable interest both from the viewpoint of fundamental investigation of the processes occurring in impurity centers and in connection with the possibility of using them in optical information recording systems. This stimulated our search for new objects for hole burning among materials prepared using sol-gel technology. It was demonstrated in [10] that a nanocrystalline structure offers specific possibilities for burning narrow holes in Eu^{3+} spectra in γ-Al_2O_3 obtained through sol-gel technology. It was conjectured in [10] that photoinduced reorientation of nanocrystals enhanced by localization of the excitation energy in nanocrystals can favor burning of long-lived holes in the Eu^{3+} spectrum. Effective photochemical spectral-hole burning caused by two-step photoionization of impurity centers was observed to occur in α-$Al_2O_3 : Mn^{4+}$ ceramics prepared using sol-gel technology [11].

Experiments on spectral-hole burning in $MgO : Cr^{3+}$ crystals were carried out at a temperature of 1.7 K. A single-mode ring dye laser (Coherent 899-21, frequency instability ~2 MHz) was tuned to the $^4A_2$–^2E transition. The beam power was 50 mW, and the beam was focused to a 1-mm spot on the sample. To detect holes, the laser frequency was swept within a range 5 GHz wide in a time of ~0.5 s. Holes were detected using the fluorescence in the vibronic sideband of the Cr^{3+} $^4A_2$–^2E transition, which was isolated with an interference filter. Figure 3 shows a typical spectral hole observed in our experiments in the *R* line of cubic Cr^{3+} centers. The hole width was ~0.4 GHz, and the relative depth was ~1%; i.e., it was very small. Nevertheless, holes were reliably observed in the *R* lines of cubic Cr^{3+} centers in all the samples studied. The holes lived for at least a few minutes. No hole burning was observed in the spectrum of tetragonal centers (probably, for technical reasons). Nor was hole burning detected in bulk $MgO : Cr^{3+}$ crystals.

We believe the hole burning in $MgO : Cr^{3+}$ nanocrystals to be due to the photophysical process of rearrangement of the Cr^{3+} environment, in particular, due to photostimulated processes on the surface of nanocrystals and/or photoinduced nanocrystal rearrangement in clusters. As follows from our experiments, the possibility of photophysical hole burning in nanocrystalline systems is a fairly general property of these systems [10–12]. Indeed, both in $MgO : Cr^{3+}$ and in $Li_2Ge_7O_{15} : Cr^{3+}$ [12], spectral-hole burning is observed to occur in nanocrystalline samples only, whereas in the bulk material no hole burning is seen. This indicates that nanocrystalline systems are more susceptible to photoinduced processes. One cannot, however, totally exclude the photochemical mechanism of hole burning involving capture of the detrapped carrier at the nanocrystal surface.

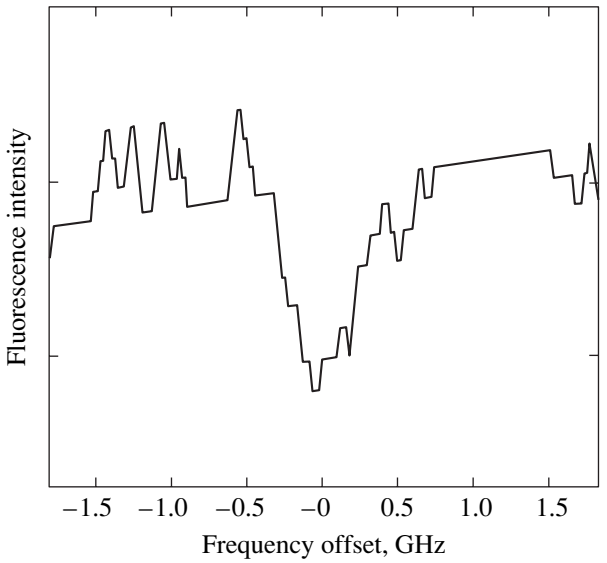

Fig. 3. Long-lived hole in the *R*-line spectrum of cubic Cr^{3+} centers in nanocrystalline MgO.

On the whole, the experiments performed have once more demonstrated the common nature of a number of effects observed in the optical properties of nanocrystalline materials prepared by sol-gel technology and originating from the smallness of crystal particles.

ACKNOWLEDGMENTS

The authors are indebted to L.S. Sochava for providing the MgO : Cr single crystal sample.

This study was supported by the Russian Foundation for Basic Research, project no. 02-02-17662.

REFERENCES

1. S. P. Feofilov, Fiz. Tverd. Tela (St. Petersburg) **44**, 1348 (2002) [Phys. Solid State **44**, 1407 (2002)].
2. A. L. Schawlow, J. Appl. Phys., Suppl. **33**, 395 (1962).

3. G. F. Imbusch, W. M. Yen, A. L. Schawlow, *et al.*, Phys. Rev. **133**, A1029 (1964).
4. J. P. Larkin, G. F. Imbusch, and F. Dravnieks, Phys. Rev. B **7**, 495 (1973).
5. M. O. Henry, J. P. Larkin, and G. F. Imbusch, Phys. Rev. B **13**, 1893 (1976).
6. S. P. Feofilov, A. A. Kaplyanskii, A. B. Kulinkin, *et al.*, J. Sol-Gel Sci. Technol. **21**, 135 (2001).
7. R. S. Meltzer, S. P. Feofilov, B. Tissue, and H. B. Yuan, Phys. Rev. B **60**, R14012 (1999).
8. M. J. L. Sangster, Phys. Rev. B **6**, 254 (1972).
9. S. E. Stokowski, S. A. Johnson, and P. L. Scott, Phys. Rev. **147**, 544 (1966).
10. S. P. Feofilov, A. A. Kaplyanskii, R. I. Zakharchenya, *et al.*, Phys. Rev. B **54**, 3690 (1996).
11. S. P. Feofilov, A. B. Kulinkin, A. B. Kutsenko, and R. I. Zakharchenya, J. Lumin. **76–77**, 217 (1998).
12. S. P. Feofilov, A. A. Kaplyanskii, A. B. Kulinkin, *et al.*, J. Lumin. **100**, 155 (2002).

Translated by G. Skrebtsov